MICROBEAM ANALYSIS
1980

David B. Wittry, *Editor*

Proceedings of the 15th Annual Conference
of the
Microbeam Analysis Society
San Francisco, 4-8 August 1980

PUBLISHER'S NOTICE

Proceedings of the Annual Conference of the Microbeam Analysis Society are published in hard covers starting with the 14th (1979). Back copies are available from San Francisco Press at $25 each. Spiral-bound copies of the 1974, 1975, 1976, and 1978 Proceedings are also available from San Francisco Press, at $20 each. The 1977 issue is out of print, but selected papers from that meeting (held in conjunction with the 8th International Conference on X-ray Optics and Microanalysis) have been published in full length and are available as a separate publication at $90.

Table of Contents*

---

*An Author Index appears on p. 334.   †Invited paper.

---

†Invited paper.

---

†Invited paper.

Officers of the Microbeam Analysis Society (1980)

MAS Executive Council:

President: Oliver C. Wells
                    IBM Thomas J. Watson Research Center
                    Box 218
                    Yorktown Heights, NY 10598

Past President: David F. Kyser
                    K63-282
                    IBM Research Laboratory
                    San Jose, CA 95193

President Elect: James R. Coleman
                    Department of Radiation Biology and Biophysics
                    University of Rochester Medical Center
                    Rochester, NY 14620

Treasurer: Roger B. Bolon
                    General Electric Co.
                    Box 8
                    Schenectady, NY 12301

Secretary: Charles E. Fiori
                    Room 3W13, Building 13
                    National Institutes of Health
                    Bethesda, MD 20205

Members at Large

Noel C. MacDonald
Physical Electronics Industries
6509 Flying Cloud Drive
Eden Prairie, MN 55343

Dale E. Newbury
Chemistry A121
National Bureau of Standards
Washington, DC 20234

Peter Statham
Link Systems Ltd.
Halifax Road
High Wycombe, Bucks.,
England HP12 3SE

David C. Joy
Room ID343
Bell Laboratories
Murray Hill, NJ 07974

Phillip B. DeNee
Inhalation Toxicology Research Institute
Box 5890
Albuquerque, NM 87115

Honorary Members

L. S. Birks
Naval Research Laboratory
Washington, DC 20390

Raymond Castaing
University of Paris
Faculté des Sciences
Orsay, France

I. B. Borovskii
Institute of Solid State Physics
Academy of Sciences
Moscow, U.S.S.R.

Peter Duncumb
Tube Investments Research
  Laboratories
North Saffron Walden,
Essex, England

Gunji Shinoda
Osaka University
Osaka, Japan

V. E. Cosslett
The Cavendish Laboratory
University of Cambridge
Cambridge, England

Sustaining Members' Information

AMRAY INC.

160 Middlesex Turnpike
Bedford, MA 01730

Contact: Kenneth A. Lindberg, (617) 275-1400

Product Line: Manufacturer and distributor of scanning electron microscopes and a complete line of accessories.

Sales Offices:
  George Russell, Gerald Cameron Jr., and Ken Benoit, Merchantsville, N.J., (609) 662-3922
  Parker Brinkman, Cleveland, Ohio, (216) 579-0035
  Tom Levesque, Dallas, Tex., (214) 247-3542
  Henry Levesque, Bedford, Mass., (617) 275-1400
  Don Pollock, Lico, Inc., Bedford, Mass., (617) 275-8310
  Fritz Healey, Laguna Hills, Calif., (714) 830-1332
  Dr. Werner Noli, Leitz-AMR GmbH, Wetzlar, Federal Republic of Germany, (06441) 292352

APPLIED RESEARCH LABORATORIES

9545 Wentworth Street
Box 129
Sunland, CA 91040

Contact: Bryce I. Hanna, (213) 352-6011

Product Line: Electron microprobes, ion microprobes, optical emission spectrometers, x-ray fluorescence instrumentation.

Sales Offices:
  4 Elm St., Salisbury, MA 01950
  Dearborn, Mich., (313) 336-3900
  842 Hamilton Mall, Allentown, PA 18101, (215) 434-7441
  905 W. Hillgrove Avenue, LaGrange, IL 60525, (312) 352-5990

BABCOCK AND WILCOX RESEARCH CENTER

Alliance Research Center
Box 835
Alliance, OH 44601

Contact: Alex S. Miller, (216) 821-9110, Ext. 360

CAMBRIDGE INSTRUMENTS INC.

40 Robert Pitt Drive
Monsey, NY 10952

Product Line: Research scanning electron microscopes and accessories, research production electron beam microfabrication systems, image analysis equipment.

Contact: Peter W. Boutell, Cambridge Instruments Inc., 40 Robert Pitt Drive, Monsey, NY 10952, 914-356-3331

Sales Offices:
  Dick Harniman, Monsey, N.Y., (914) 356-3331
  Don Nelson, Pittsburgh, (412) 561-0313
  Mike Webber, Atlanta, (404) 926-9636
  John Pong, California, (714) 893-1609
  Jack Oltheten, Montreal, (514) 337-4343

CAMECA INSTRUMENTS, INC.

37 Brownhouse Road
Stamford, CT 06902

Contact: Robert J. Hessler, (203) 348-5252

Product Line: Electron probe analyzers, scanning electron microscopes, combination SEM/
EMP instruments and ion mass analyzers. The IMS-3F, a new SIMS instrument, has the
features of improved performance at a lower price. The new IMS is the only direct
imaging instrument available. The CAMECA MBX is a flexible combination SEM/EMP with
an extensive array of accessories.

Sales Offices:
Robert D. Boies, Box 262, Reedley, CA 93654, (219) 266-6372
Thomas Fisher, 37 Brownhouse Road, Stamford, CT 06902, (203) 348-5252

EDAX INTERNATIONAL, INC.

103 Schelter Road
Box 135
Prairie View, IL 60069

Contact: Peter Blakeslee, (312) 634-0600

Product Line: Manufactures energy-dispersive x-ray analysis systems for x-ray microanaly-
sis in SEMs, TEMs, and electron probes, as well as energy-dispersive x-ray fluorescence
spectrometers. System configurations from basic qualitative to fully automated quanti-
tative (with computer control and data processing) are available, including an automated
WD/ED system with stage and spectrometer controls.

Sales Offices:
V. Balmer, 637 Sunnyside Rd., Vermilion, OH 44089, (216) 967-4148
Frank Mannino, 769 Shadow Lake Dr., Thousand Oaks, CA 91360, (213) 889-2576
E. Martin, Box 547, New Rochelle, NY 10802, (914) 576-3117
J. Moore, Box 2253, Boulder, CO 80306, (303) 443-3610

EG & G/ORTEC

100 Midland Road
Oak Ridge, TN 37830

Contact: Michael J. Kirchoff or Tim Bates, (615) 482-4411, Ext. 500

Product Line: Energy-dispersive systems for electron optical microscopes of all types.
Wavelength-dispersive system electronics. Backscattered electron detection systems.

Sales Offices:
Val Johnson, Box 1678, Boulder, CO 80306, (303) 449-5933
Gene Embry, Box 631, Cary, NC 27511, (919) 467-8028
Charles Thomas, 24222 Via Luisa, Mission Viejo, CA 92675, (800) 251-9732
Nick Alen, 5257 Arquilla Dr., Richton Park, IL 60471, (800) 251-9732
Bob Bardorf, Box 3355, Oak Ridge, TN 37830, (615) 482-9072
Jacqueline Rams, Suite 311, 11800 Sunrise Valley Dr., Reston, VA 22070, (800) 336-0122

GERHARD WITZSTROCK PUBLISHING HOUSE INC.

381 Park Avenue South, Suite 1123
New York, NY 10016

Contact: Monika Magid, (212) 686-7280

Product Line: Publishes. *Scanning: International Journal of Scanning Electron Microscopy
and Related Methods*. *Scanning* provides an international and interdisciplinary medium
for the rapid exchange of information among all scinetists interested in scanning elec-
tron microscopy. It publishes original scholarly papers of a practical nature, report-
in new analytical, methodological, and specimen-preparation aspects of SEM.

HITACHI SCIENTIFIC INSTRUMENTS

460 E. Middlefield Road
Mountain View, CA 94043

Contact: Bruce N. Harley

Product Line: Transmission and scanning electron microscopes and a complete line of accessories.

Sales Offices:
  Ronald Lunn, Box 366, Princeton, MA 01541, (617) 756-5331
  Morton Harloe, 1701 Golf Rd., Rolling Meadows, IL 60008, (312) 981-8750
  Michael E. Mullen, 2909 Oregon Court, Unit B-3, Torrance, CA 90502, (213) 328-9700
  Ronald E. McDuffie, 1383 Piccard Rd., Rockville, MD 20850, (301) 840-1650

INTERNATIONAL SCIENTIFIC INSTRUMENTS, INC.

3255-6C Scott Boulevard
Santa Clara, CA 95051

Contact: Robert Ruscica, (408) 727-9840

Product Line: Scanning electron microscopes with a full complement of accessories including WDX spectrometers. The ISI SEM line includes: Alpha-9, Super IIIA, ISI-40, ISI S-100B, and ISI DS-130. Also in the product line is our new light/transmission electron microscope, the ISI LEM-2000. A complete line of scanning electron microscopes suited for any application and budget.

Sales Offices:
  Bill Maguire, Avon Park South, 20 Tower Lane, Bldg. 2, Avon, CT 06001, (202) 677-0016
  Bud Bowen, 415 W. Golf Rd., Suite 37, Arlington Heights, IL 60005, (312) 437-7790
  Mike McCarthy, Santa Clara, Calif.
  Mike Ivey, Los Angeles, Calif.
  Richard Lois, 6655 Hillcroft, Suite 100, Houston, TX 77081, (713) 777-0321

JEOL U.S.A., INC.

11 Dearborn Road
Peabody, MA 01960

Contact: Robert T. Santorelli, (617) 535-5900

Product Line: Manufacturers and dealers of scanning electron microscopes, transmission electron microscopes, scanning transmission electron microscopes, electron probe microanalyzers, scanning Auger microprobes, and energy loss analyzers.

Sales Offices:
  John Bonnici, New Jersey, (201) 254-5600
  Thayer Brickman, San Francisco, (415) 697-9220
  Paul Enos, Texas, (817) 267-6011
  Jack Francis, Ohio, (513) 232-7350
  Thomas Gildea, Massachusetts, (617) 535-5900
  Ray Gundersdorff, Maryland, (301) 953-2959
  Roland Marti, Los Angeles, (213) 870-8852
  Jean-Pierre Slakmon, Canada, (514) 482-6427 (Soquelec, Ltd.)
  Robert Steiner, Illinois, (312) 825-7164

KEVEX CORPORATION

Box 4050
1101 Chess Drive
Foster City, CA 94404

Contact: Henry S. Culver, (415) 573-5866

Product Line: Analytical systems for x-ray energy spectrometry, wavelength-dispersive x-ray spectrometry and electron energy spectrometry. Kevex detector/cryostats and analytical spectrometer systems are compatible with all electron microprobe, scanning electron microscopes and transmission electron microscopes in current production. Systems are available for both qualitative and quantitative analysis.

Sales Offices:
Dana Kelley, 46 Knollwood, West Hartford, CT 06107, (617) 256-4961
Dennis Ward, 13802 Castle Blvd, #301, Silver Spring, MD 20904, (301) 890-6633
Steven Miller, 602 South Fairview, Park Ridge, IL 60068, (312) 398-1333
Frank Mannino, 769 Shadow Lake Drive, Thousand Oaks, CA 91360, (805) 495-1632
Aptec Engineering, 4251 Steeles Avenue West, Downsview, Ont., Canada M3N 1V7

WALTER C. McCRONE ASSOCIATES, INC.

2820 South Michigan Avenue
Chicago, IL 60616

Contact: Ian M. Stewart, (312) 842-7100

Product Line: Analytical services in desciplines such as pharmaceuticals, forensic sciences, contamination control, metallography, air and water pollution, painting and document authentication, and corrosion. Analytical tools available: electron and ion microprobes, TEM, SEM, EMMA, ESCA, XRD, XRF, GC-MS, IR-UV, optical microscopy, and MOLE, laser Raman microprobe.
Instruments Division, McCrone Accessories and Components, range of instruments and accessories for light and electron microscopy.

MICRON INC.

Box 3536
Lancaster Pike and Centre Road
Wilmington, DE 19807

Contact: James F. Ficca Jr., (302) 998-1184

Product Line: Scanning electron microscopy, electron spectroscopy, electron probe x-ray analysis, transmission electron microscopy, quantitative image analysis, x-ray diffraction, x-ray fluorescence, optical microscopy and metallography, micro hardness, optical emission spectroscopy, differential scanning calorimetry, ultra microtomy, sample preparation.

MICROSPEC CORPORATION

265-G Sobrante Way
Sunnyvale, CA 94086

Contact: Richard C. Wolf or William D. Donnelly, (408) 733-3540

Product Line: WDX-2A wavelength dispersive x-ray spectrometer systems. X-ray microanalysis systems for use as accessories on scanning electron microscopes and other electron beam instruments. Capable of quantitative x-ray analysis of all elements down to beryllium, atomic number 4. Unique design permits attachment to most SEM electron columns without interference to other detectors or operational modes.

3M COMPANY, ANALYTICAL SYSTEMS

Building 53-3
3M Center
St. Paul, MN 55101

Contact: Peggy Willingham

Product Line: Complete ion scattering spectrometer (ISS) and secondary ion mass spectrometer (SIMS) systems with vacuum or as attachments to existing vacuum systems. Ion gun systems for surface analysis and sputtering.

Sales Offices:
  Gerald H. Rosenthal, Box 76, 15 Henderson Dr., West Caldwell, NJ 07006, (201) 575-2123
  Robert W. Geiger, Box 460, Noblesville, IN 46060
  Paul B. Clark, 346 Drexel Ave., Ventura, CA 93003, (213) 726-6417

PERKIN-ELMER ETEC INC.

3392 Investment Boulevard
Hayward, California 94545

Contact: Mrs. P. J. Breton, (415) 783-9210

Product Line: High performance electron microprobes and scanning electron microscopes.
  Modular design allows alternative configurations to be offered with a wide range of
  retrofittable accessories. Instruments are available for manual operation, with auto-
  mated control through dedicated minicomputers, with shielding for imaging and analysis
  of radioactive materials, and for laboratory and manufacturing electron beam litho-
  graphy. Microbeam products include: Autoscan, Omniscan, Autoprobe, LEBES, Vistascan,
  Viewpoint, Biosem, and ADRES.

Sales Offices:
  Throughout the USA, call toll-free (800) 227-1222 or (415) 783-9210

PHILIPS ELECTRONIC INSTRUMENTS, INC.

85-91 McKee Drive
Mahwah, NJ 07430

Contact: J. D. Rodgers, (201) 529-3800

Product Line: Electron optical instrumentation and x-ray analytical instrumentation.

Sales Offices:
  Main Line Professional Building, Suite A 1104, Rt. 130, Cinnaminson, N.J., (609)
  829-4454
  7525 Long Avenue, Skokie, IL 60076, (312) 676-1714
  11141 Georgia Avenue, Suite 210, Silver Spring, Md., (301) 933-3002
  3000 Scott Blvd., Suite 113, Santa Clara, CA 95050, (408) 247-5333
  3760 Cahuenga Blvd. W., Suite 101, North Hollywood, CA 91604, (213) 980-2884

PHYSICAL ELECTRONICS
DIVISION OF PERKIN-ELMER CORP.

6509 Flying Cloud Drive
Eden Prairie, MN 55344

Contact: Robert C. Cargill, (612) 941-5540

Product Line: ESCA/Auger electron spectrometers, scanning Auger microprobes, thin-film
  analyzers, secondary ion mass spectrometers, specialized combination systems, and a
  broad range of components including electron energy analyzers, sputter-etching systems,
  specimen manipulators, x-ray generators, UV sources, and sample introduction stages.
  Also operates an analytical service laboratory for custom surface analysis.

Sales Offices:
  Boston, New York, Washington, Pittsburgh, Chicago, Dallas, Minneapolis, Seattle, San
    Jose, and Los Angeles.
  Contact Minnesota for local contact.

PRINCETON GAMMA-TECH

Box 641
Princeton, N.J. 08540

Contact: Darlene Thompson, (609) 924-7310

Product Line: X-ray energy dispersive microanalysis systems. An application laboratory and extensive program library.

Sales Offices:
  Bill Hendrixson, 405 Vernon Rd., Jenkintown, PA 19046, (215) 885-3077
  Tom Griffin, 701 Morewood Pkwy., Rocky River, OH 44116, (216) 331-0120
  Al Hollaar, Box 4319, Thousand Oaks, CA 91359, (213) 991-3898
  Joe Piersante, Route 2, Box 50-A16, Gainsville, GA 30501, (404) 887-9100
  Don Dunkin, Box 641, Princeton, NJ 08540, (609) 924-7310
  Denny Cannon, Box 36157, Denver, CO 80236, (303) 978-0786
  Rod Jensen, 8408 Bridgetown Dr., Austin, TX 78753, (512) 836-0188
  Ernie Frost, Box 5817, Stanford, CA 94305, (415) 941-3560

QBI INTERNATIONAL

2034 Golden Gate Avenue
San Francisco, CA 94115

Contact: Quentin A. Brown, (415) 929-1622

Product Line: Signal processors for the scanning electron microscope and STEM. Video systems for the electron microprobe. X-ray systems for the electron microprobe. Crystals and detectors. Stage and goniometer drive systems. Computer control of the SEM or electron microprobe. Computerized data acquisition systems.

Sales Office:
  Box 6A, Russell Road, Bloomington, IN 47401, (812) 336-6244

C. M. TAYLOR CORPORATION

Box 7087
Stanford, CA 94305

Contact: Dr. Charles M. Taylor, (408) 245-4229

Product Line: Various types of multi-element standards for microbeam analysis by SEM, microprobe, and ion probe using energy, wavelength, and mass spectrometers. The standards available exceed 135 different metals, alloys, or compounds. Bence-Albee standards are available. Also supply sample holders for ARL-EMX and ARL-EMX-SM stages and many types of sample holders and polishing jigs for sample preparation. Offer analytical services to customers desiring electron beam microprobe analysis, MAC-5 instrument.

TECHNICS EMS INC.

7950 Cluny Court
Springfield, VA 22153

Contact: Diane Hurd or Robert Barr, (703) 569-7200

Product Line: Secondary ion mass spectrometers and electron energy loss spectrometers. Preparation and peripheral equipment for the electron microscope.

Sales Offices:
  1754 Junction Avenue, San Jose, CA 95112
  Milhertshotener-Str. 8, 8000 Munich 40, Federal Republic of Germany

TRACOR NORTHERN

2551 West Beltline Highway
Middleton, WI 53562

Contact: Tyler North, (608) 831-6511

Product Line: Wide range of data processing instrumentation for qualitative and quantitative x-ray analysis. Products include data acquisition, reduction and automation for electron microprobe, SEM, TEM and STEM. Featuring simultaneous EDS/WDS acquisition/

reduction, digital beam control allowing for digital mapping, line scans and other digital image processing. And now particle location, sizing and elemental characterization. Flexible packaging allows instrument to be also used for ELS, Auger, ESCA, SIMS, etc. Other products are used in nuclear, optical, signal averaging and medical applications.

Sales Offices:
  Suite 260, 2425 Bisso Lane, Concord, CA 94520, (415) 825-8190
  Technical Instrument Co., Suite 106, 4215 Beltwood Parkway, Dallas, TX 75234, (214) 387-0606
  Scientific Systems Sales Corp., 6901 Jericho Turnpike, Syosset, NY 11791, (516) 921-3737
  Contemporary Science, Inc., Box 205, 500 E. Northwest Highway, Mt. Prospect, IL 60056, (312) 255-3793
  Pulcir, Inc., Box 357, Oak Ridge, TN 37830, (615) 483-6358
  Trembly Associates, 119 Quincy NE, Albuquerque, NM 87108, (505) 266-8616
  EMCAR Marketing, Inc., 8041 W. I-70 N. Service Rd., Arvada, CO 80002, (303) 424-0108
  Allan Crawford Associates, Ltd., 6503 Northam Dr., Mississauga, Ont., Canada, L4V 1J2, (416) 678-1500
  Alva Nuclear, SA, Apartado Postal 12-626, Mexico 12, D.F., Mexico 5167454
  Tracor Europa, B. V., Schiphol Airport Amsterdam, Bldg. 106, P. O. Box 7553, Amsterdam, The Netherlands, (020) 41-1865
  Also Representatives in: Great Britain, West Germany, France, Japan, India, Malaysia, Taiwan, Singapore, Thailand, Australia, Argentina, and Brazil.

UNITED SCIENTIFIC CORPORATION
ANALYTICAL INSTRUMENT DIVISION

Box 1389
1400 D Stierlin Road
Mountain View, CA 94042

Contact: William D. Stewart, (415) 969-9400

Product Line: Automated x-ray analysis systems, including x-ray tube excited and source excited; Si(Li) x-ray detection systems for use on scanning electron microscopes, transmission electron microscopes and electron microprobes; Si(Li) x-ray detectors for basic research; and portable x-ray spectrometers.

Sales Offices:

  The Buhrke Company, 2180 Sand Hill Road, Menlo Park, Calif., (415) 854-5629
  International Instrument Corp., 64 E. Main St., Marlon, N.J., (609) 983-6550
  Instruments and Technology, 220 E. 14th St., Naperville, Ill., (312) 355-7748
  North Eastern Analytical Corp., 17 Sherman Rd., Millis, Mass., (617) 376-4132
  Technical Instrument Co., 4215 Beltwood Pkwy., Suite 106, Dallas, TX 75234
  Pulcir, Inc., Box 357, Oak Ridge, TN 37830, (615) 483-6358

MICRODIFFRACTION FROM CRYSTALS CONTAINING DEFECTS

R. W. Carpenter

In order to examine defects in crystals using electron diffraction it is desirable to irradiate only the local crystal region containing the defect. Recent improvements in microscope instrumentation, principally in electron optics and vacuum systems, have made convergent-beam electron diffraction a relatively simple experimental method, and it is the method of choice for diffraction investigation of many types of lattice defects. The method itself has been used in crystal physics research for about 40 years, but only recently have applications to materials science problems begun.[1,2] At present, applications of the method are being made to characterization of grain and interphase boundaries, local foil thickness measurement, lattice defect symmetry characterization, small precipitate crystallography, and other problems at various laboratories. In this paper the method is described, its use for Burger's vector direction determination is illustrated, and use of convergent-beam shadow images is discussed.

Experimental Method

Microdiffraction in electron microscopes may be classified according to the method used to select the area for diffraction as probe-selected or aperture-selected microdiffraction. Here, probe-selected microdiffraction is of primary interest. Aperture-selected microdiffraction, more often called "selected-area diffraction" (SAD), is, the better known of the two methods.[3] For SAD a nearly parallel, rather large-diameter incident electron probe is used; the minimum size of the specimen area that can be accurately selected by the field-limiting aperture is determined by lens aberrations and focusing errors, and is about 0.5 μm.[4] The minimum size specimen area for probe-selected microdiffraction is determined by the incident-probe diameter on the specimen; typical probe diameter on the specimen; typical probe diameters range from about 50 down to 0.5 nm. Such small probes are formed by use of the microscope illumination system to converge the electron beam to nearly a point focus at the specimen and probe-selected microdiffraction patterns are often called convergent-beam electron diffraction patterns (CBED). The spatial resolution of CBED is much higher than SAD; thus the displacement field surrounding a lattice defect, such as a dislocation, occupies a much larger fraction of the crystal-diffracting volume in CBED than in SAD, and one may expect the effects on the diffraction pattern to be more easily observed. Because CBED patterns are formed with a convergent incident probe, the specimen is irradiated over a range of angles and the Bragg spot diameter is generally larger than in the case of SAD. In this paper the terms angular resolution and beam divergence, denoted by α_i, have the same meaning and refer to one-half the diameter of a Bragg disk in a diffraction pattern, expressed in radians. Since the spacing of Bragg spots in a diffraction pattern is 2θ, where θ is the Bragg diffraction angle, it is easy to see that Bragg disks in a CBED pattern overlap if $\alpha_i > \theta$. Probe size and divergence obtainable in microdiffraction patterns depend on illumination system parameters such as electron source size, excitation of condenser lenses, and condenser aperture size. The relationships among these parameters have recently been described in detail elsewhere.[5] It has been shown that probe size and divergence are inversely related; for CBED experiments the probe is usually focused on the specimen using illumination system lenses and then a divergence appropriate for the application is fixed by choice of second condenser aperture size. The first applications of CBED to materials science systems made use of the small probe (high spatial resolution) to obtain single-phase diffraction patterns from each distinct phase in fine grain size multiphase specimens such as lamellar precipitates in Cu-Ti alloys.[6] These patterns are usually taken at high angular resolutions to

resolve closely spaced Bragg spots (i.e., with small second condenser aperture), especially if the crystal structure of the phase is not well known. However, diffraction patterns of larger divergence (larger Bragg disk diameter) also contain very useful information. In particular, convergent-beam diffraction patterns from specimens of appropriate thickness contain three-dimensional lattice information. This feature is a consequence of excitation of Bragg reflections in higher-order Laue zones (HOLZ) (i.e., Bragg reflections in reciprocal lattice planes above those in the plane containing the origin).
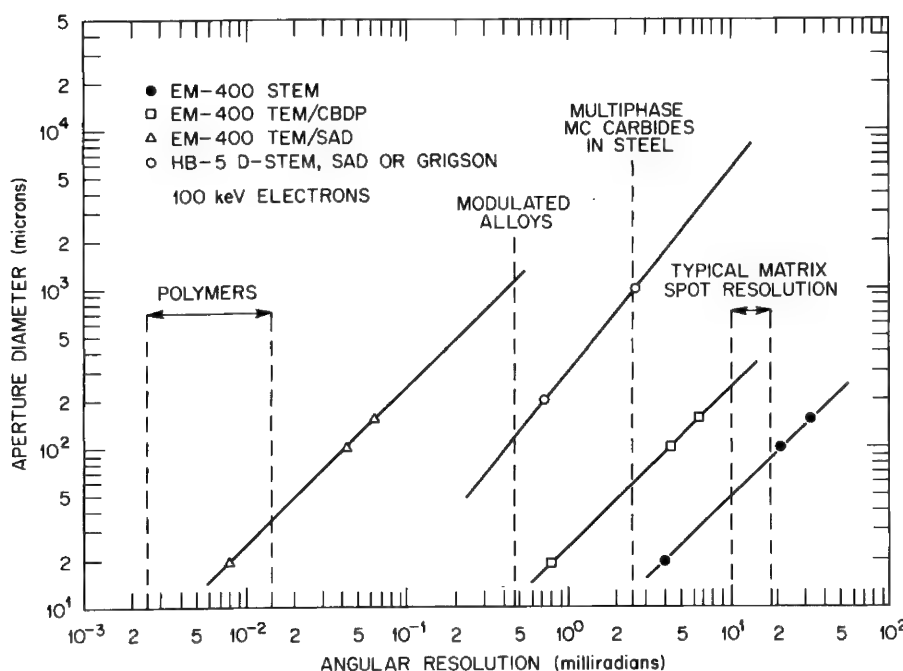
FIG. 1.--Experimentally determined angular resolution dependence on probe-forming aperture diameter for two analytical electron microscopes in various operating modes. Typical angular resolution ranges for particular applications are indicated. EM 400 TEM/STEM used is fitted with field-emission source.

A more detailed description of HOLZ terminology has been given by Jones et al.[7] Diffraction vectors corresponding to HOLZ reflections have significant components antiparallel to the incident-beam direction. Thus, three-dimensional information is contained in these diffraction patterns. It is clear that incident-probe divergence α_i is one of the most important experimental variables for electron diffraction. Figure 1 shows the range of angular resolution attainable as a function of aperture diameter for several operating modes of two microscopes, and the approximate values of angular resolution required to examine specific diffraction phenomena. To examine the lattice distortions caused by various lattice defects, such as chemical segragation, stacking faults, dislocations, and others, it is useful to choose a larger value of α_i such that a number of HOLZ reflections are excited to produce Kikuchi lines corresponding to HOLZ reflections and HOLZ line detail that can be observed in the central Bragg disk at large camera lengths.

Experimental Determination of Burgers Vector in Silicon

A CBED pattern from a silicon crystal, with the approximately 10nm-diameter incident probe centered on a 60° dislocation in the plane of the (111) foil, is shown in Fig. 2(a). For comparison, a similar pattern from a perfect silicon crystal in the same orientation is shown in Fig. 2(b). These patterns were recorded with a relatively short camera length, so that a large area of reciprocal space is visible. The bright ring of Bragg disk near the edge of the patterns is composed of excited First-order Laue Zone (FOLZ) reflections. Two Kikuchi bands corresponding to FOLZ reflections are indexed in Fig. 2(a): [$33\bar{5}$] and [$\bar{3}\bar{3}7$]. Note that $\bar{B} \cdot \tilde{g} = 1$, where B = [111], for both FOLZ reflections. Comparison of Figs. 2(a) and 2(b) shows that all the Kikuchi lines in Fig. 2(a) are split into fringes parallel to the original (unsplit) Kikuchi line direction except the [$\bar{3}\bar{3}7$], [$33\bar{5}$], and $\pm$[$22\bar{4}$] lines. These unsplit lines correspond to diffraction vectors not affected by the presence of the dislocation in the irradiated volume. The direction of the Burgers vector is obtained from the cross product of the indices of any two of the unsplit Kikuchi lines, and is $\pm$[$1\bar{1}0$]. This information is obtained easily from a single

zone axis CBED pattern because many beams are excited. Corresponding two-beam image contrast experiments confirmed the Burgers vector direction. The unsplit Kikuchi lines of Fig. 2(a) correspond to three diffraction vectors in the plane orthogonal to $\bar{b}$.
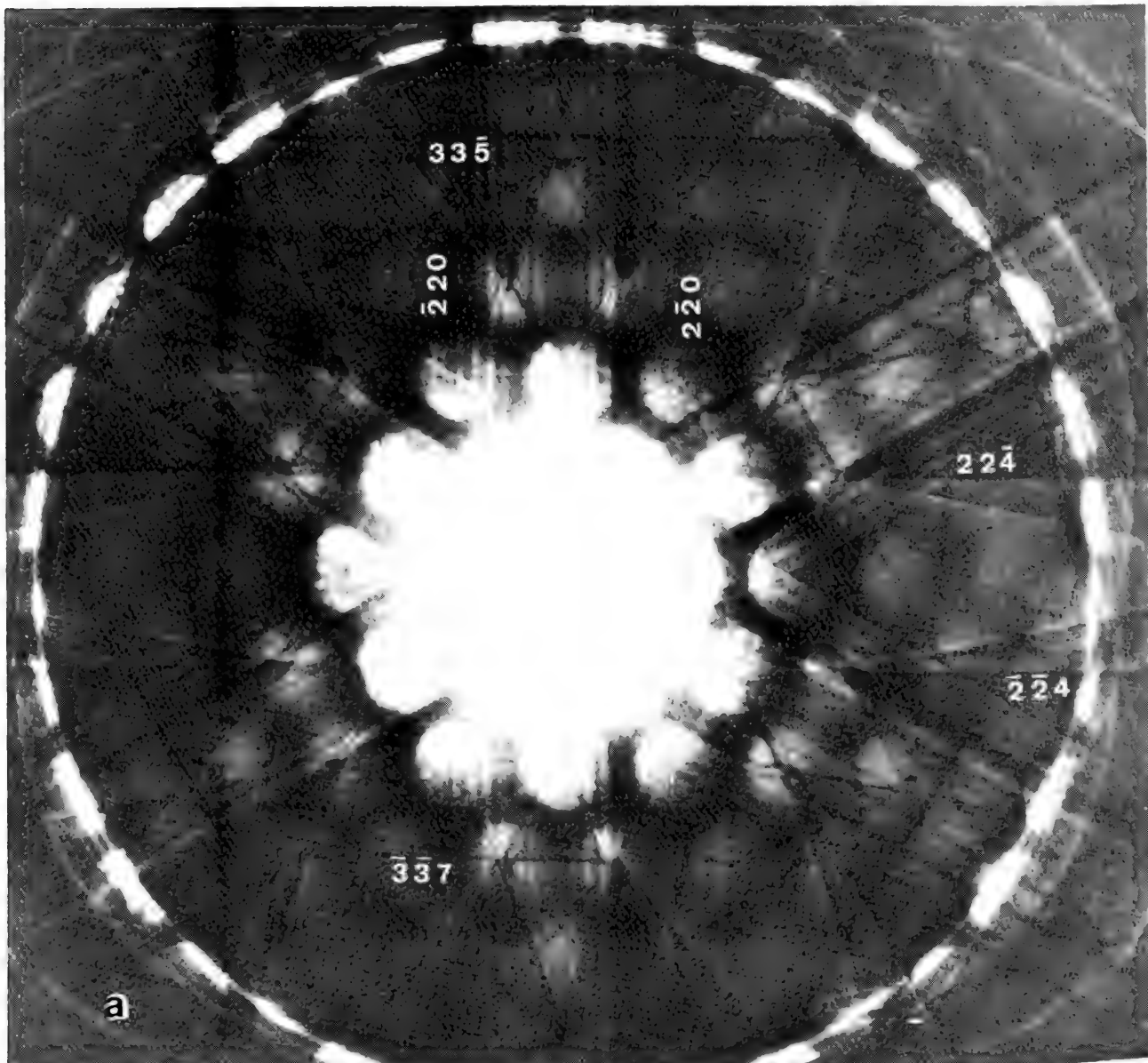
FIG. 2.--CBED patterns taken from silicon crystal at relatively low camera length show Kikuchi lines from zero- and first-order Laue zones: (a) pattern with dislocation under probe, (b) pattern from perfect crystal; 120 keV, α_i = 6.6 mr.

At larger camera lengths one may observe FOLZ line detail in the central Bragg disk as shown in Fig. 3. The pattern from the perfect crystal shows unsplit FOLZ lines, which are indexed. When the probe is placed over a dislocation, all FOLZ lines except the [11, $\bar{5}$, $\bar{5}$] were observed to split, such as seen at the [$\bar{1}$99] position denoted by A-A in Fig. 3(b). Other experiments showed $\bar{b}$ = ±1/2[0$\bar{1}$1] in this case. Note the strong disturbance of the pendellösung fringes by the dislocation.
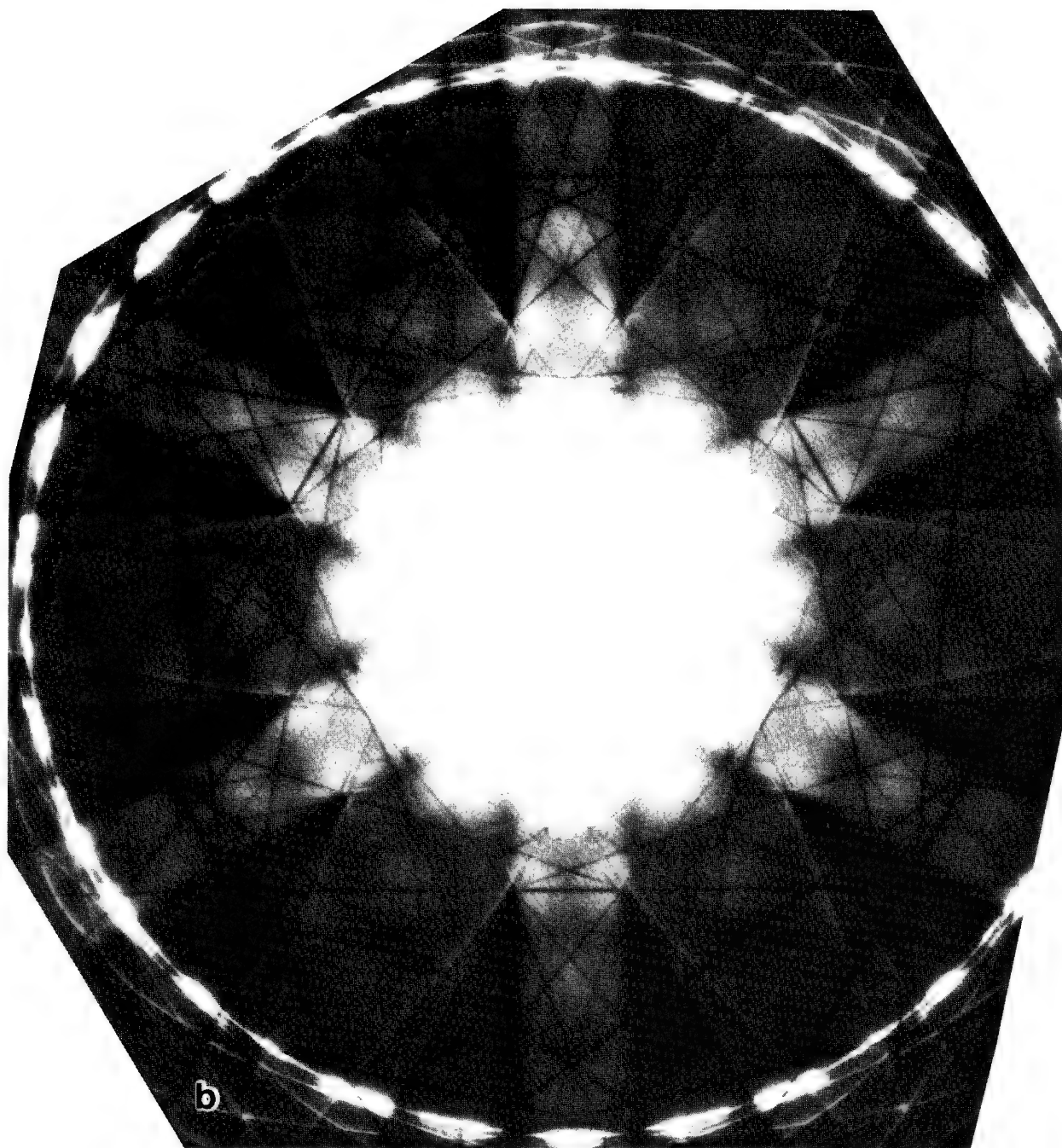
Dynamical interactions among the diffracted beams in a perfect crystal can also cause HOLZ line splitting, and the complexity of a pattern containing splitting from both dislocations and dynamical interactions may preclude quantitative analysis. This problem can often be avoided by adjustment of the operating voltage of the microscope so that the HOLZ line pattern from a perfect crystal of the material of interest can be indexed by straightforward application of geometry. The splitting observed when the irradiated volume contains a lattice defect should then be attributable to lattice distortion, at least in simple materials. Further details of this method of defect analysis will be published in due course.[8]
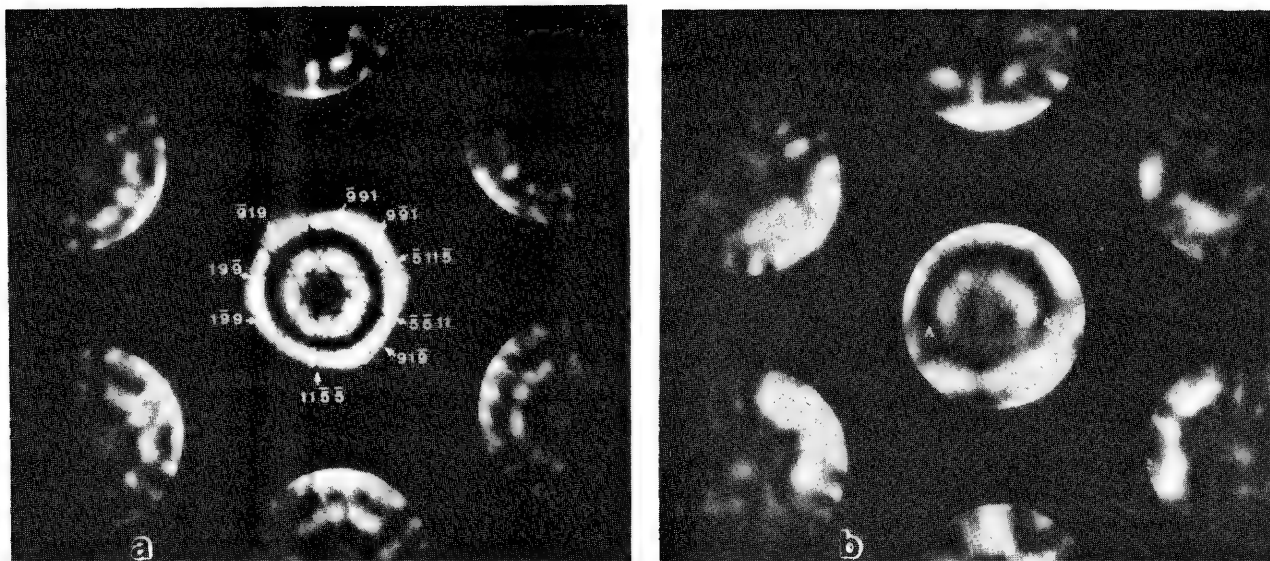
FIG. 3.--CBED patterns taken from a silicon crystal at large camera length to show FOLZ lines in the central Bragg disk: (a) perfect crystal, (b) probe on dislocation; 100 keV.

Use of CBED Shadow Images

A practical problem associated with identification of defects from CBED patterns is placing the probe on small defects. A related problem is keeping track of a small area (such as 20nm-size grains in a sintered ceramic) during large-angle tilting experiments in an analytical electron microscope. These tasks can be most easily accomplished if the observer views the shadow image of the specimen area of interest in the direct beam disk of a CBED pattern, while observing the CBED pattern itself on the final viewing screen.

A shadow image is formed in a CBED pattern by a change in the current in the probe-forming lens from the focused-probe value for diffraction (magnification infinite) to a greater or smaller value, so that the incident probe is no longer focused on the specimen; a real space shadow image then becomes visible in the Bragg disks of the diffraction pattern. The magnification of the shadow image depends on the current in the probe-forming lens. An example is shown in Fig. 4. The TEM micrograph shows a portion of cellular colony formed behind a high-angle grain boundary that migrated during an aging treatment to form $L1_2$ long-range order in an Fe-Co-V alloy. The boundary migration direction is indicated by the arrow. The colony is composed of long range ordered matrix, intrinsic stacking faults, and VC carbide particles.[9] The CBED shadow images were formed by defocusing of the second condenser lens in a TEM/STEM analytical microscope. The correspondence between the normal image and the shadow images is obvious. In the lower magnification shadow images only the colony is in contrast in the diffracted beams, and not the grain ahead of the advancing boundary. The shadow images in the diffracted beams are dark-field images, and show clearly that the systematic row of reflections originated within the colony and not in the grain ahead of the migrating boundary. Shadow images are also the most direct and simplest method for accurately aligning the incident probe on a defect, or on a microstructural feature for chemical analysis. The practice of focusing the incident probe on an image feature and then switching the microscope to diffraction mode is strongly discouraged, because in many microscopes the probe changes position on the specimen when one switches from image to diffraction mode. When small microstructural features are of interest such probe movement can be a serious problem.
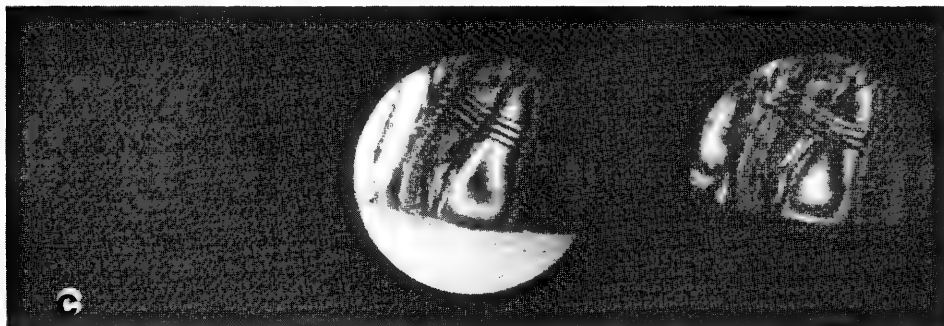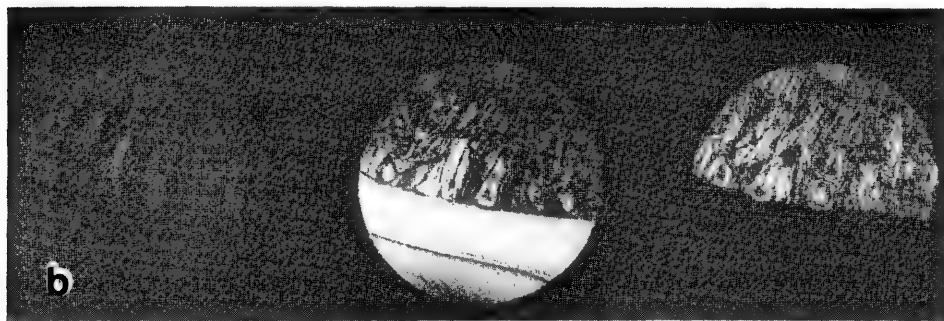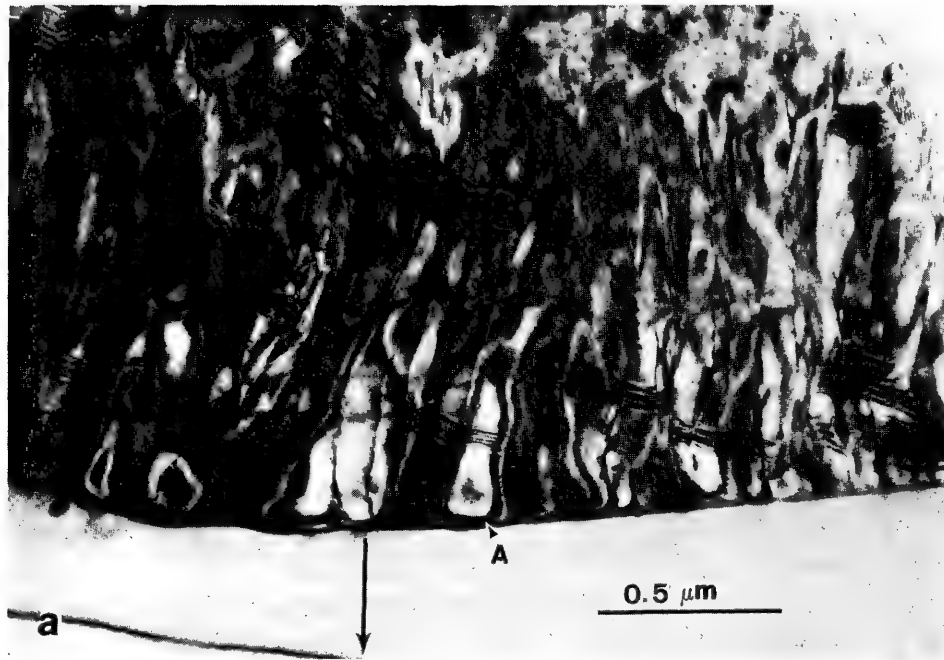
FIG. 4.--Correspondence between TEM image and CBED shadow images of increasing magnification: (a) TEM image, region of interest for CBED marked A. (See text for specimen details.) (b) Low magnification CBED shadow image. (c) Increased magnification CBED shadow image. (d) Focused CBED pattern on region A. Row of systematic diffraction spots is [hhh] type. 100 keV. (Figure continued on next page.)
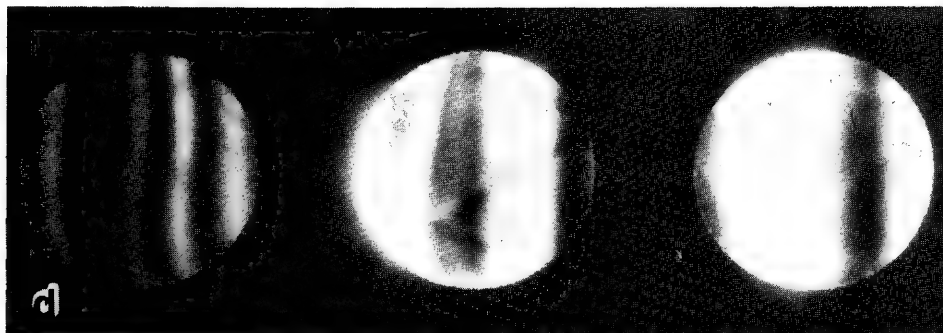
Fig. 4 (Cont'd)

References

1. G. Lehmpfuhl, "Convergent beam electron diffraction," in J. M. Sturgess, Ed., *Electron Microscopy 1978, Proc. 9th Intern. Cong. Elec. Microscopy,* Vol. 3, Mic. Soc. Canada, Toronto, 1978, 304.

2. J. W. Steeds, "Convergent beam electron diffraction," in J. J. Hren, J. I. Goldstein, and D. C. Joy, Eds., *Introduction to Analytical Electron Microscopy,* New York: Plenum Press, 1979, 387.

3. J. B. LePoole, *Philips Tech. Rdsch.* 9: 33, 1947.

4. P. B. Hirsch et al., *Electron Microscopy of Thin Crystals,* Washington: Butterworths, 1965, 1st ed., 5, 18.

5. R. H. Geiss, "Introductory Electron Optics," in J. J. Hren, J. I. Goldstein, and D. C. Joy, Eds., *Introduction to Analytical Electron Microscopy,* New York: Plenum Press, 1979, 43.

6. R. W. Carpenter, J. Bentley, and E. A. Kenik, "Analytical electron microscopy investigation of structural and composition variation in lamellar multiphase alloys," in O. Johari, Ed., *SEM/1977/I,* Chicago: IITRI, 1977, 411.

7. P. M. Jones, G. M. Rackham, and J. W. Steeds, "Higher order Laue zone effects in electron diffraction and their use in lattice parameter determination," *Proc. Roy. Soc. Lond. (A)* 354: 197, 1977; J. W. Steeds, this volume.

8. R. W. Carpenter and J. C. H. Spence (to be published).

9. D. N. Braski, R. W. Carpenter, and E. A. Kenik, "Discontinuous precipitation in ordered $(Fe,Co)_3V$ alloys," in G. Bailey, Ed., *Proc. 37th Ann. Mtg. EMSA,* San Antonio, Claitor's Pub. Div., 1979, 650.

Digital Image and Data Processing Techniques

DIGITAL IMAGE PROCESSING AND THE ELECTRON MICROSCOPE IMAGE

K. R. Castleman and R. Nathan

Computer processing techniques have been applied to images from a variety of sources and for many diverse reasons in the last two decades. It is only in the past few years, however, that the electron microscope image has been receiving its fair share of attention in this field. In this paper we examine some of the processing techniques that have proved useful in digital image analysis, some of the applications where image processing has been helpful, and some of the special problems presented by TEM and SEM images.

We shall consider two classes of image processing techniques, image restoration and pattern recognition. Digital image restoration is an activity aimed at improving the quality of an image that has been unavoidably degraded, usually by noise and distortion in the imaging and image recording systems. Pattern recognition involves finding, measuring, and identifying the objects in an image.

A classic example of digital image restoration is shown in Fig. 1. An image returned from the Surveyor spacecraft on the lunar surface was restored by the process of deconvolution.[1] This is a linear filtering (convolution) technique that compensates for the modulation transfer function. It is limited, however, by noise considerations to resolution increases typically of the order of two. Deconvolution has approximately doubled the resolution of the image in Fig. 1, although the reproduction process partially masks this difference.

Linear filtering techniques can also be used to reduce the noise level in an image. The Wiener (minimum mean equal error) filter[1] is commonly used, but other approaches are also useful.[2] Noise reduction and the enhancement of fine detail usually work at cross purposes because the signal-to-noise ratio is usually lowest at the high spatial frequencies involved.

Figure 2 shows an example of high-resolution electron microscope image synthesis in which a digitally implemented synthetic aperture technique is used.[3,4] The electron diffraction pattern of the organic crystal indanthrene olive was recorded in a series of off-axis dark-field images. The Fourier transform was used to produce the image of the (periodic) crystal structure with about 1Å resolution.

Another EM image restoration example appears in Fig. 3. The image of a damaged specimen of a catalace crystal was divided into unit cells spanning one period. The unit cells were averaged together and the result replicated to form the restored image.[5,6]

Pattern recognition involves finding objects in an image and assigning each to one of several preestablished classes.[1,7] The three steps in the process are (1) image segmentation--finding the boundaries that separate the objects from the background, (2) feature extraction--making a set of measurements on each object, and (3) classification--assigning each object to one of the classes based on the values of its measurements. Image segmentation can be approached in two ways. Once can seek to find the boundaries directly, for example by following a line through the areas where the brightness is changing most rapidly (maximum gradient magnitude). The other approach is to examine each picture point and determine whether it is an interior or background point. The objects are then regions containing only interior points.

A variety of size, shape, and texture measures have been used on digital images.[1] Experience shows the importance of well-calibrated and accurately implemented measurements is quite important, but highly complex measures seldom outperform simpler and more straightforward ones. Classification of each object is done strictly on the basis of its measurements. Techniques from statistical decision theory are used[1,7] and performance is commonly specified by misclassification error rates.

The authors are with the Observational Systems Division, Jet Propulsion Laboratory, California Institute of Technology, Pasadena, CA 91103. The work was supported in part by NASA Contract NAS7-100 and by NIH Contracts HD-30001 and CB-70314, and Grant RR-00443.

FIG. 1.--Digital image restoration by deconvolution approximately doubles resolution.
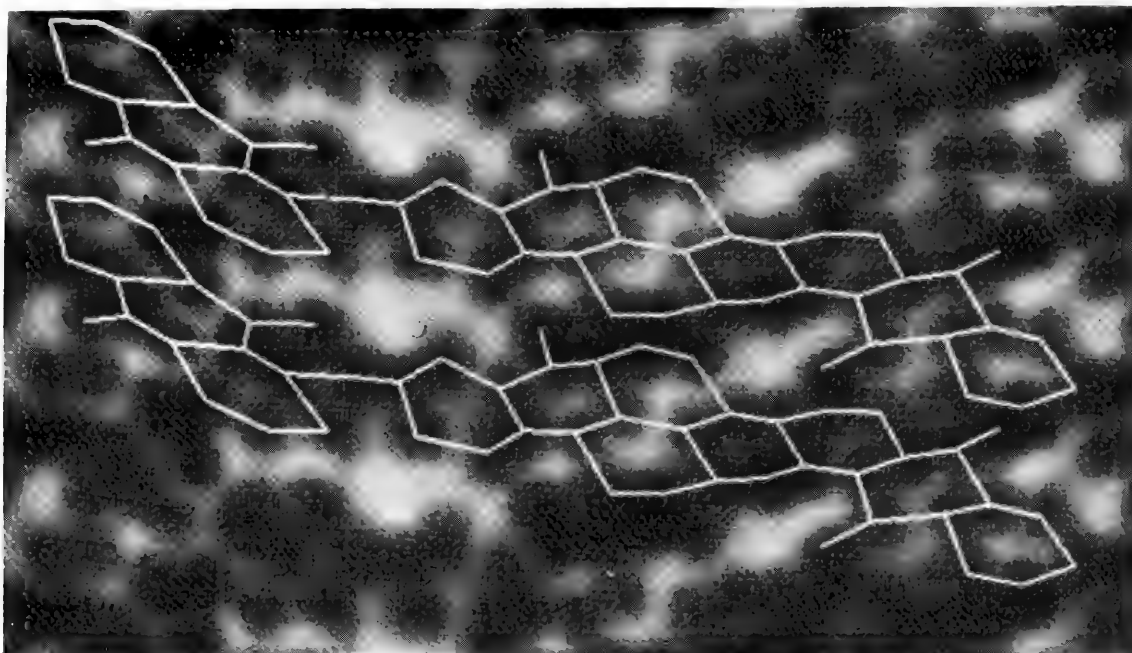
FIG. 2.--Digitally implemented synthetic aperture technique used for EM image synthesis.
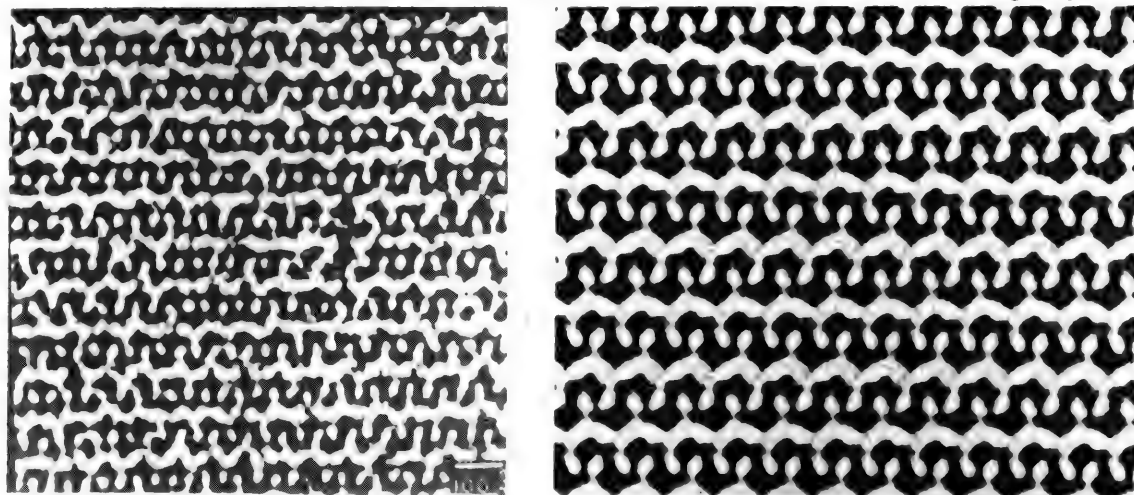
FIG. 3.--Image restoration by replication of crystal cells averaged over several periods.

Pattern recognition has seen considerable application to light-microscope images. Commercially available white blood cell differential counters use it. Clinical prototypes for automated chromosome analysis[1] (Fig. 4) and automated muscle biopsy analysis[8] (Fig. 5) have been developed. Work is in progress on automated Pap smear analysis and a variety of other topics.
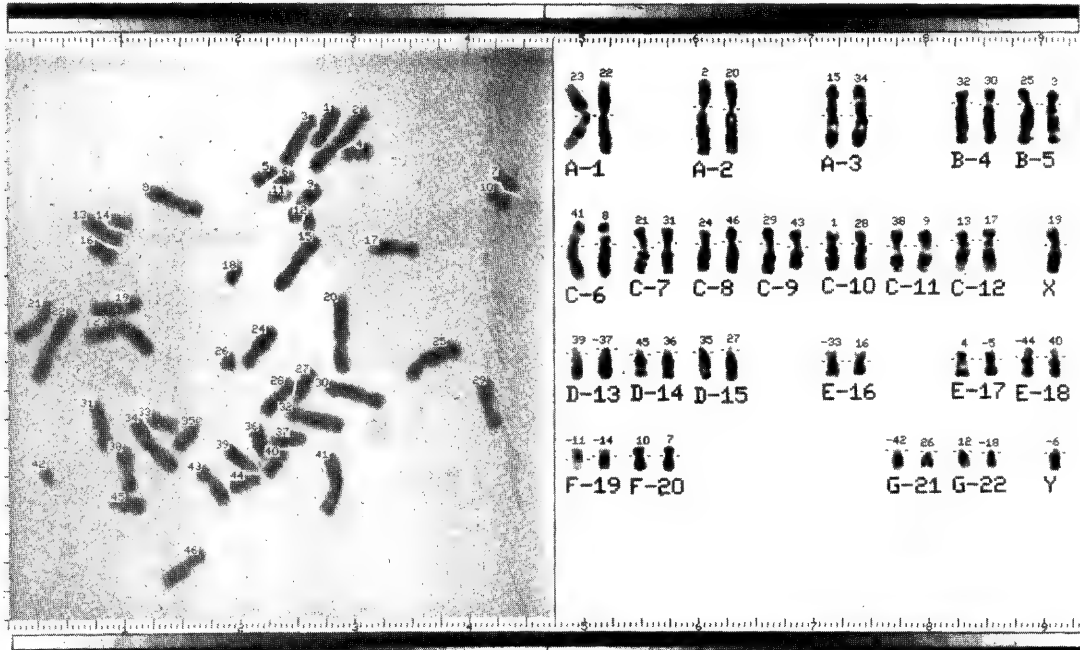
FIG. 4.--The 46 chromosomes from a human white blood cell (left) have been located, oriented, measured, and classified by a computer program and arranged in the standard "karyotype" format (right).
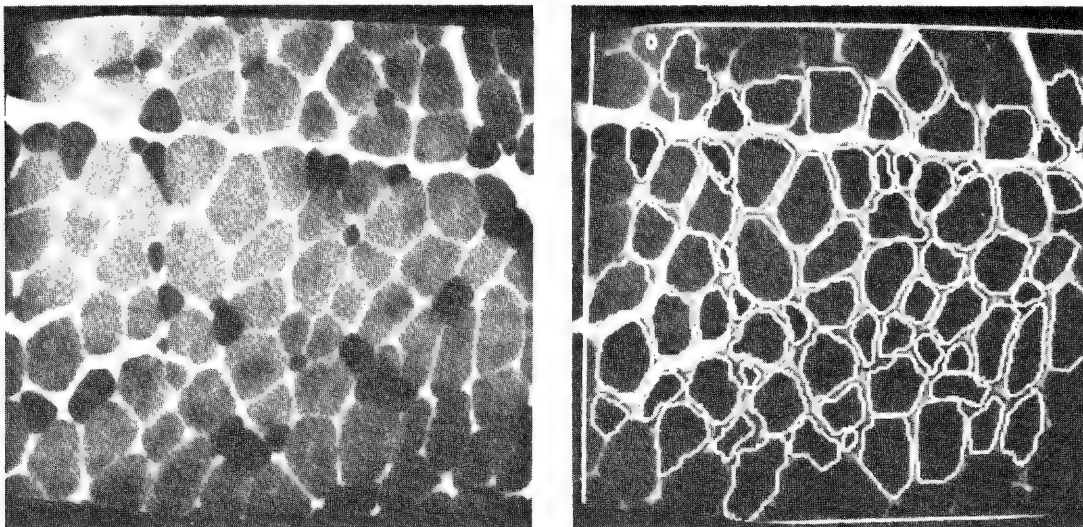
FIG. 5.--A histochemically prepared muscle tissue section from the light microscope (left) has had the individual fibers located, measured and outlined (right).

Both TEM and SEM images possess characteristics that pose special problems not encountered in light microscope images. Biological specimens are commonly stained with a heavy metal to make them visible in high-resolution electron microscopy. This method combines with film grain, phosphor grain, and image sensor noise to produce digitized images that can be quite grainy. This inherent high-frequency noise limits the effectiveness of image enhancement or restoration efforts, and complicates the process of image segmentation. The characteristic surface visualization format of SEM images makes them more complex to process digitally. A cell that appears as a black circle on a white background in the light microscope might show up in the SEM as gray on gray with a highlight on one side and a shadow on the other. Such images require image segmentation algorithms more sophisticated than those commonly employed in light-microscope work.

These EM-specific problems present an interesting challenge to the algorithm designer. As more attention is focused on these problems we can expect to see many successful applications of digital processing to electron microscope images.

References

1. K. R. Castleman, *Digital Image Processing*, Englewood Cliffs, N.J.: Prentice-Hall, 1979.
2. H. C. Andrews and B. R. Hunt, *Digital Image Restoration*, Englewood Cliffs, N.J.: Prentice-Hall, 1977.
3. R. Nathan, "Biological atomic resolution via synthetic aperture," *Eighth Intern. Cong. Electron Microscopy*, Canberra, 1974, vol. 1, 306-307.
4. R. Nathan, "Computer synthesis of high resolution electron micrographs," in K. Preston and M. Onoe, Eds., *Digital Processing of Biomedical Images*, New York: Plenum 1976.
5. R. Nathan, "Image processing for electron microscopy: I. Enhancement procedures," in Barer and Cosslett, Eds., *Advances in Optical and Electron Microscopy*, 1979.
6. R. Nathan, "Computer enhancement of electron micrographs," *Annual Proc. EMSA*, 1970.

APPLICATIONS OF SEM-BASED AUTOMATIC IMAGE ANALYSIS

R. J. Lee and J. F. Kelly

Computer-controlled scanning electron microscopy (CCSEM) is a rapidly evolving techno-
logy. Three factors are responsible: (1) the advent of high-speed minicomputers and
associated electronics is making computer control easier and less expensive; (2) the
serial mode of collecting image information used in the SEM makes the instrument readily
amenable to computer control of the production, recording, and analysis of signals; and
(3) the variety of signals available in the SEM enhance the potential usefulness of com-
puter-controlled instruments.[1,2] In this paper, we briefly summarize the uses of compu-
ter control of microscopes, compare several approaches to automatic image analysis (AIA)
in the SEM, and review the current applications of AIA in materials science.

Computer-controlled Microscopy

The primary advantages of programmable control vs hardwired control lies in the flexi-
bility and potential for interactive operation. For specific applications that do not
require flexibility most computer-controlled functions could be done equally well and
faster with hardwired circuits.[2-4]

Four general areas of computer-controlled microscopy are emerging. First, computers
are being used for automatic setting and optimization of instrumental parameters such as
accelerating voltage, magnification, and focus.[5] Monitoring of the optimal values in
real time can in turn be used to derive information about the sample. For example, moni-
toring changes in focus can be used to measure microtopography or surface roughness.[6]

Second, the production of predetermined patterns on electron sensitive materials
forms the basis for microfabrication or electron-beam lithography. In this highly de-
veloped area, the use of computers is essential to producing the desired pattern.[2]

Third, every electron microscope image has some degradation resulting from system
noise. Often significant improvements in resolution or contrast can be achieved by image
enhancement or restoration techniques. In this case, the computer serves two purposes.
It is used to correlate beam position with the signal at a given point, and to perform
the desired transformations on the digitized image.[3,4,7]

Fourth, computer control of the beam is used to extract textural, geometric, or com-
positional data from the image. This use is termed automatic image analysis (AIA). In
the past "image analysis" has referred to the characterization of geometric parameters
such as feature size and shape. As computer control of the SEM develops, "image analysis"
will logically come to include quantitative analysis of the variations in any or all the
available signals in the SEM. Currently, there are two approaches to SEM-based AIA, as
follows:

1. *Gray level digitizing of the signal at each picture point and storage of the com-
plete digitized image.*[1] In this approach the size and shape of features are obtained by
means of either "on-line" or "off-line" computers.[1,8] This type of image reconstruction
closely parallels the approach of hardwired image analyzers used on optical microscopes.
Its limitations lie in the large storage required for the image data, which restricts the
number of picture points analyzed and thus decreases the speed of the analysis. A sig-
nificant advantage of this approach is the sophistication of the algorithms used in the
analysis. For example, Dixon has used a skeletonization process to extract and measure
low-contrast image features such as asbestos fibers,[8] and Ekelund has developed a histo-
gram method for defining a local threshold.[9] These methods improve the resolution and
detection of image features. Lebiedzik et al. have used a novel variant of this method
to measure microtopography and derive surface-roughness parameters.[10]

2. *Binary coding of the image by use of an analog comparator to define a threshold
level.* Picture-points with signals above the threshold are considered "on-points" (points

The authors are with U.S. Steel Corp.'s Research Laboratory in Monroeville, PA 15146.

on a feature). All other points are considered "off-points" and ignored. Several methods have been used to extract geometrical data.[11-13] In one, the edge coordinates of features are stored and used to derive the perimeter, area, and shape factors.[13] In another, first introduced by LeMont Scientific, a dual picture-point density is used to separate the analysis into "search" and "analyze" modes. A low point density is used until the status of the analog comparator indicates the beam is on a particle or feature. A high point density is then used to measure the dimension of the feature.[11,14] Only the feature dimensions and centroid are stored. This approach is the fastest and requires the least storage area. However, it suffers from the disadvantage that the area and perimeter of features are inferred, rather than directly measured, as is the case in the preceding approaches.

Each approach to extracting image information has merit; the method used should reflect the type of information required. At U.S. Steel Research Laboratory we are primarily interested in materials applications and in correlating microscopic observations with macroscopic properties. Thus, the size/shape/composition distributions and the relative abundance of different chemical species are of most interest. In order to produce such data, we interfaced a LeMont Scientific digital beam-control system with a Tracor Northern 4000 energy dispersive spectrometer (EDS). Software was developed to classify features on the basis of relative x-ray peak intensity. Thus, we are able to take advantage of the reproducibility of EDS spectra to develop a "pattern recognition" capability in AIA comparable to that used by knowledgable microscopists in identifying individual features.[15]

Applications

The AIA methods developed in our laboratory and elsewhere have a wide range of applications. In the following, we summarize the applications reported to date and provide some illustrative results. The details of these applications are described in the references.

Coal. The size and relative abundance of included minerals in coal are significant factors in determining the behavior of a particular coal during combustion, carbonization, or gasification. Bulk measurements can be used to infer the relative abundance of minerals in coal but size data have been difficult to obtain. AIA has been used to measure quantitatively the average mineral content in coals[15] and to measure the projected size distribution of mineral grains in polished coal samples.[16] These measurements are in good agreement with bulk chemistry data and provide direct identification of the individual mineral species as well. AIA results on coal samples spiked with known quantities of individual minerals indicate the technique can be considered quantitative.[17]

Quantitative Metallography. Second-phase particles have an important effect on mechanical properties of steels and other metals. A measurement of volume fraction and size distribution of such particles can be obtained by optical techniques, but the resolution is limited and chemical data are not available. An extensive amount of work has been done with SEM-based AIA to study the effects of size, shape, composition, and number of inclusions on mechanical properties, corrosion resistance, and weld strength.[5,18]
Other AIA studies on steel samples have measured precipitate growth as a function of heat treatment; characterized the effect of rare-earth additions on the development and shape of MnS inclusions; and studied the deformation of MnS inclusions during hot rolling.[19]
Metallographic studies are especially valuable in that the precision and reproducibility of SEM-based AIA over a range of instrumental and software parameters can be easily compared with the results of optical image analysis.[18,20] Such a comparison is shown in Table 1. The AIA and optical results agree well and are highly reproducible. The range of the area percent data reflects inhomogeneity in the inclusion distribution.

Ore Evaluation. Processing of ore generally requires some type of beneficiation procedure to remove accessory minerals. In the past, evaluations of the effectiveness of such treatments have been performed by optical microscopy or by bulk chemical techniques. However, the optical methods are tedious, and (when opaque minerals are involved) unreli-

able. SEM-based AIA has been used successfully to measure the liberation of minerals as a function of the degree of grinding.[12] We have been measuring the relative abundance of specific minerals in rutile-bearing sands. In the Fe-Ti solid solution series, rutile, leucoxene, and ilmenite are very difficult to resolve optically, but readily separable on the basis of the Fe/Ti ratio.

TABLE 1.--Comparison of SEM-based AIA and optical QTM analysis of all inclusions in four low-carbon steels.

QTM		AIA	
Mean*	Range*	Mean*	Range*
.036	.028 - .048	.032	.026 - .036
.040	.034 - .052	.038	.030 - .054
.078	.075 - .086	.074	.060 - .090
.010	.080 - .012	.010	.090 - .011

*Area percent.

Environmental. SEM-based AIA allows direct measurement of the relative abundance and size distribution of airborne particles when collected on suitable filter media. By a comparison of these data with the analysis of reference samples characterizing local emission sources such as automobiles, plant and public roads, coal-fired boilers, and industrial processes, one can calculate the contribution of individual sources.[21,22] This area is in its infancy but promises to play a major role in the development of cost-effective air-pollution control strategies, and (through source characterization) measurement of the effectiveness of dust control devices.

Powders. Numerous industrial processes use powder technologies, and the reliable characterization of the size distribution of these materials is often required. Here, SEM-based AIA is most effective in obtaining particle size distributions below the normal sieving range, and for comparison with alternative methods such as coulter counters or cyclones.

In summary, the applications of automatic image analysis include the traditional areas of scanning microscopy and offer the potential for new areas of use as well. In each, the AIA procedures are most effective when used to define the image features on which to perform more detailed microscopic observations. Then AIA can provide a quantitative link between microscopic and macroscopic data.

References

In the following references, *SEM/(date)* stands for Scanning Electron Microscopy/(date), published by Scanning Electron Microscopy, Box 66507, AMF O'Hare, IL 60666; *MAS/(date)* stands for Microbeam Analysis Society/(date), published or distributed by San Francisco Press, 547 Howard Street, San Francisco, CA 94105.

1. E. W. White, H. A. McKinstry, and G. G. Johnson Jr., "Computer processing of SEM images," *SEM/1968*, 234-240.
2. R. F. Herzog, B. L. Lewis, and T. E. Everhart, "Computer control and the scanning electron microscope," *SEM/1974*, 175-182.
3. M. Oron and D. Gilbert, "Combined SEM-minicomputer system for digital image processing," *SEM/1976*, 121-128.
4. A. V. Jones and K. C. A. Smith, "Image processing for scanning microscopists," *SEM/1979*, 13-26.
5. K. C. A. Smith, "Some aspects of computer aided scanning electron microscopy," *MAS/1977*, 6A-6B.

6. D. M. Holburn and K. C. A. Smith, "On-line topographic analysis in the SEM," *SEM/1979*, 47-52.

7. R. Llinas, R. Spitzer, D. Hillman, and M. Chujo, "Computer graphics analysis of STEM images," *SEM/2979*, 367-374.

8. R. N. Dixon and C. J. Taylor, "Asbestos fibre counting by automatic image analysis," *SEM/1979*, 361-366.

9. S. Ekelund and T. Werlefors, "A system for the quantitative characterization of microstructures by combined image analysis and x-ray discrimination in the scanning electron microscope," *SEM/1976*, 417-424.

10. J. Lebiedzik et al., "Use of microtopography capability in the SEM for analyzing fracture surfaces," *SEM/1979*, 61-66.

11. M. R. Hoover et al., "Automated characterization of particulates and inclusions by computer-controlled SEM/Probe," *MAS/1975*, 54A-54B.

12. G. Grant et al., "Multicompositional particle characterization using the SEM-Microprobe," *SEM/1976*, 402-416.

13. W. R. Stott and E. J. Chatfield, "A precision SEM image analysis system with full-feature EDXA characterization," *SEM/1979*, 53-60.

14. J. J. McCarthy, "Applications of a digital scan generator to EDS analysis," *MAS/1979*, 307-309.

15. R. J. Lee, F. E. Huggins, and G. P. Huffman, "Correlated SEM-Mössbauer studies of coal mineralogy," *SEM/1978*, 561-568.

16. A. K. Moza, L. G. Austin, and G. G. Johnson Jr., "Inorganic element analysis of coal particles using computer evaluation of scanning electron microscopy images," *SEM/1979*, 473-476.

17. F. E. Huggins, G. P. Huffman, and D. A. Kosmack, "Coal mineralogies by SEM automatic image analysis," *SEM/1980* (to be published).

18. T. Werlefors and C. Eskilsson, "Automatic multiparameter characterization of non-metallic inclusions," *Scandinavian J. Metallurgy* 7: 215-222, 1978.

19. R. J. Lee and R. M. Fisher, "Quantitative characterization of particulates by scanning and high voltage electron microscopy," *MAS/1978*, 63.

20. R. J. Lee and J. F. Kelly, "Overview of SEM-based automatic image analysis," *SEM/1980* (to be published).

21. R. J. Lee et al., "Electron-beam particulate analysis," *Industrial Research/Development*, June 1979, pp. 105-108.

22. J. F. Kelly, R. J. Lee, and S. Lentz, "Automated characterization of fine particulates," *SEM/1980* to be published).

Low-loss Imaging Techniques with Solid Specimens in the SEM

SIMPLIFIED MODEL FOR THE SCATTERING OF LOW-LOSS ELECTRONS FROM AN AMORPHOUS OR SINGLE-CRYSTAL SOLID TARGET IN THE SCANNING ELECTRON MICROSCOPE

Oliver C. Wells

Low-loss electrons (LLE) are those which have been scattered from a solid target in the scanning electron microscope (SEM) with an energy loss that is typically less than 1% of the initial energy. They can be collected in the forward scattering direction to form a low-loss image by the use of a retarding field energy filter.[1-6]

The low-loss image from a solid specimen in the SEM is approximately the reciprocal of the *reflection* image in the transmission *electron microscopy* (REM) and the images obtained by the two methods have many features in common.[3] Hojlund Nielsen and Cowley[7] and Osakabe et al.[8] obtained REM images from single-crystal samples with a nearly grazing angle of incidence by selecting a diffracted beam and focusing it to form a topographic image. The arrangement of the specimen for high-resolution reflection electron microscopy in the high-field region of a condenser-objective lens used by Osakabe et al.[8] is the same (except for the reversal of the ray paths) as it is for the high-resolution low-loss method described by Wells, Broers, and Bremer.[6] The REM has the advantage of allowing simultaneous topographic and diffraction studies.[8] The deflection angle of the electrons in the specimen during diffraction studies is, however, limited to a low value by the fact that Bragg reflections cannot occur through wide angles because of thermal vibrations in the crystal.[9] In the low-loss method the glancing angle of incidence can be 30-45°. The low-loss electrons are collected over a large solid angle. Electron channeling contrast then arises as a result of changes in the angle between the incident beam and the lattice planes in the sample.[9] Fine structure in the angular distribution of the low-loss electrons from a single crystal sample (Kikuchi lines) is unlikely to affect the image because of the large collector solid angle, although the general position of the detector is certainly important (see, for example, Fig. 14 in Ref. 5). A similar relationship between the transmission electron microscope (in which diffraction contrast is important) and the STEM (which is advantageous for dark-field work) was pointed out by Cowley.[10]

This paper contains the derivation of a simple mathematical expression for the angular distribution of LLE in the plane of incidence from an amorphous target which is as accurate for all practical purposes as a much more complicated integral expression that was published previously.[3] This theory is then extended to calculate the image contrast at a small step in an otherwise flat surface. This analysis applies to the case of an amorphous specimen of uniform composition (and not one that is covered with a very thin surface layer of a heavy metal, for example). The application of this theory to a single-crystal specimen is then discussed.

Simplified Low-loss Electron Scattering Model. A comparison between the calculated and the measured angular distribution of low-loss electrons from an amorphous target is shown in Fig. 1. The full line in Fig. 1 was calculated on the basis of the low-loss electron scattering model[2-4] shown in Fig. 2. Here, it is assumed that the incident electrons penetrate straight into the specimen along the line AB losing energy at a constant rate and with a certain probability $d\Sigma$ per unit length of being scattered through the angle ϕ into the collector solid angle $d\Omega$ by a single Rutherford wide-angle scattering event. The total path length AB + BC must be smaller than some value L_{max} so that the energy that is lost by the scattered electrons does not exceed some value E_{loss} determined by the energy filter. This imposes an upper limit of AB_{max} on the distance along AB from which low-loss scattering can occur. The glancing angle of incidence θ_1 and the takeoff angle θ_2 are also shown in Fig. 2.
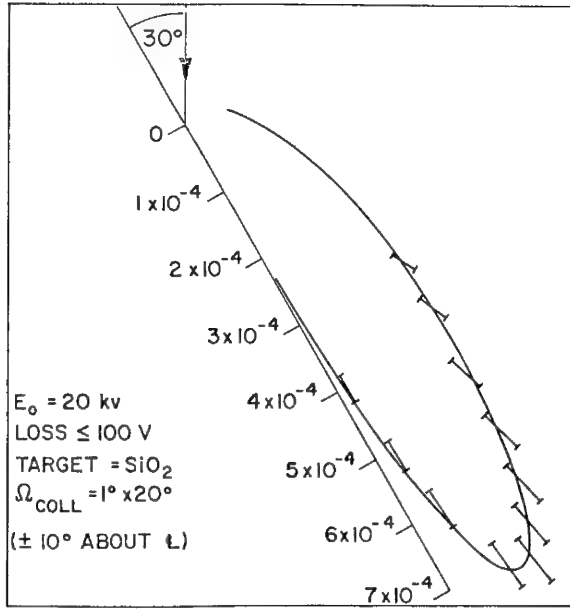
FIG. 1.--Comparison between the calculated angular distribution (full line) and measures values (bars) for low-loss electron scattering from amorphous SiO_2. The measured values were increased by 6% to improve the fit.[4]
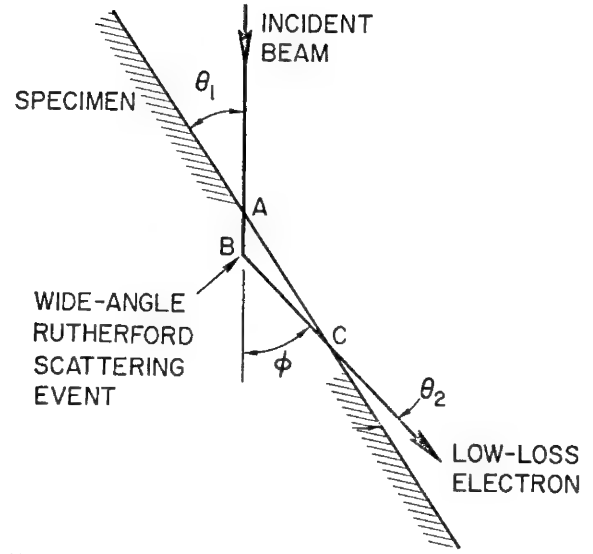
WITH 400 eV LOSS IN Al
AT 20kV   AB + BC ≤ 1000Å

FIG. 2.--Simplified model for low-loss scattering from a flat amorphous target.[2]

Magnitude of L_{max}. If the maximum permitted energy loss E_{loss} is greater than a few tens of eV, then L_{max} is given by the continuous slowing-down approximation as

$$L_{max} = E_{loss} / \left(\frac{dE}{ds} \right)_{Bethe} \qquad (1)$$

where $(dE/ds)_{Bethe}$ is the rate of energy loss as derived from Bethe's equation. If E_{loss} is smaller than a few tens of eV, then a lower limit is imposed on L_{max} by the mean free path between inelastic scattering events in the specimen.[5]

Angular Distribution of Low-loss Electrons. The scattering probability $dn_{low-loss}$ for a LLE into the collector solid angle $d\Omega$ for given values of θ_1 and θ_2 is given as described above by the product of AB_{max} and $d\Sigma$:

$$dn_{low-loss} = AB_{max} \, d\Sigma \qquad (2)$$

$$d\Sigma = n \, \frac{d\sigma}{d\Omega} \, d\Omega \qquad (3)$$

where

    AB_{max} (cm) is the value of AB in Fig. 2 for which AB + BC = L_{max}
    L_{max} (cm) is the average penetration distance in the specimen required to lose the specified energy loss
    $d\Sigma$ (cm^{-1}) is the scattering probability per unit length along AB through the angle ϕ into the collector solid angle $d\Omega$
    n is the number of atoms per cm^3
    $d\sigma/d\Omega$ (cm^2/sterad-atom) is the differential scattering cross section for a deflection ϕ

$d\Omega$ (sterad) is the solid angle of the collector which is assumed to be small

From the geometry of Fig. 2 it can be calculated that

$$AB_{max} = L_{max} \frac{\sin \theta_2}{\sin \theta_1 + \sin \theta_2} \quad (cm) \tag{4}$$

This quantity is zero when $\theta_2 = 0$, and rises to a maximum when $\theta_2 = 90°$.

For a deflection greater than about 15° and for energies greater than 15 keV it is acceptable to assume an unscreened Rutherford scattering cross section:

$$\frac{d\sigma}{d\Omega} = \frac{d^2}{16} \cosec^4 \frac{\phi}{2} \quad (cm^2/sterad-atom) \tag{5}$$

where d (cm) is the distance of closest approach of the incident electron to the scattering nucleus, given nonrelativistically by

$$d^2 \simeq 2.06 \times 10^{-14} Z^2/E_0^2 \quad (cm^2) \tag{6}$$

where Z is the atomic number of the scattering atom and E_0 (eV) is the incident electron energy.

The probability that an incident electron will be scattered into the small collector solid angle $d\Omega$ is therefore given by:

$$d\eta_{low-loss} = 1.29 \times 10^{-15} L_{max} \frac{Z^2 n}{E_0^2} F(\theta_1, \theta_2) \, d\Omega \tag{7}$$

where

$$F(\theta_1, \theta_2) = \frac{\sin \theta_2}{\sin \theta_1 + \sin \theta_2} \cosec^4 \frac{(\theta_1 + \theta_2)}{2} \tag{8}$$

For a given value of θ_1 the angular distribution of low-loss electrons in the plane of the diagram in Fig. 2 is therefore given by $F(\theta_1, \theta_2)$. The shape of the curve obtained when one plots $F(\theta_1, \theta_2)$ for $\theta_1 = 30°$ agrees within the width of the line shown in Fig. 1, which was calculated from a much more cumbersome mathematical expression.[3,4]

Surface Step. The case of a surface step of height h which occurs between A and C is shown in Fig. 3(a). This case may be analyzed as follows: From the geometry of the figure it can be calculated that the value AB_{step} from which scattering can occur when the step is present is related to the value $AB_{no\ step}$ for a flat surface by the equation:

$$\frac{AB_{step}}{AB_{no\ step}} = 1 + \frac{h}{L_{max} \sin \theta_2} \tag{9}$$

The dependence of the low-loss signal on the beam position in the case of a step of height h is therefore as shown in Fig. 3(b). For a fixed value of θ_2 the low-loss signal is increased by the ratio $AB_{step}/AB_{no\ step}$ as long as the step occurs anywhere between A and C. This relationship gives rise to a band of contrast of width W asymmetrically located relative to the surface step, where

$$W = L_{max} \frac{\sin \theta_1 \sin (\theta_1 + \theta_2)}{\sin \theta_1 + \sin \theta_2} \tag{10}$$

For a low takeoff angle θ_2 the percentage increase is largest, but the width of the band in the image over which the scattering is enhanced is also increased. An example is as follows. For Al at 15 kV a lower limit[5] of 205 Å is imposed on L_{max} by the mean free path between inelastic scattering events.[11] If $\theta_1 = 30°$ then the peak of the angular distribution curve as calculated from Eq. (8) occurs at $\theta_2 = 7.75°$. For a step height of
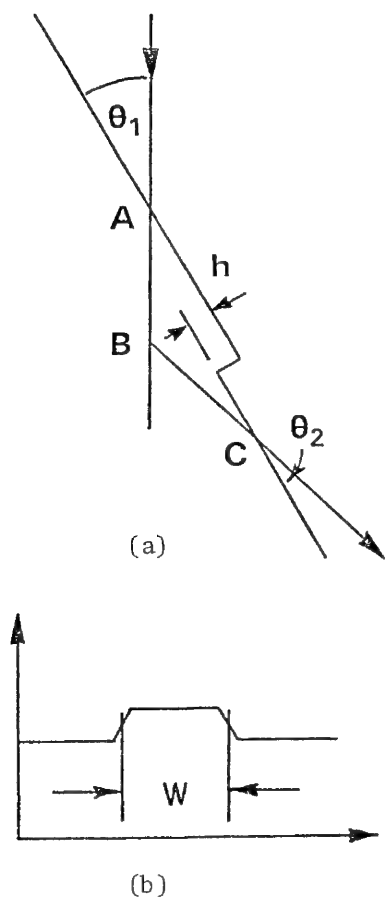
10 Å and with this value of θ_2, $AB_{step}/AB_{no\ step} = 1.36$ from Eq. (9). This step therefore appears in the image as a band of width 100 Å (from Eq. 10) having a 36% increase (or decrease) in the collected signal. For a 2Å step in gold imaged at 60 kV ($L_{max} = 430$Å)[11] and with $\theta_1 = 30°$ the calculated line width and image contrast are 200 Å and 3.4%. This example illustrates the values of image contrast that are to be expected in the low-loss image from a small surface step.

Surface Steps on a Single-crystal Specimen. Low-loss images from single-crystal samples were published as Figs. 7.1(b) and 7.10(c-f) in Wells et al.[3] Topographic contrasts are essentially the same as for an amorphous sample. However, additional strong electron channeling contrasts are caused by variations in the angle between the incident electrons and the lattice planes. These contrasts are similar (although stronger) than the crystalline contrasts reported by Philibert and Tixier.[12] Topographic contrast at surface steps (Fig. 7.1b in Ref. 3) is not affected in any obvious way by electron channeling contrast. Channeling contrast caused by imperfect regions in the crystal reversed as the sample is tilted through the Bragg condition for the incident beam (Figs. 7.10 c-f in Ref. 3).

Two main lines of work have emerged with reference to the low-loss imaging of single-crystal samples. Electron channeling contrast caused by crystal defects is discussed in considerable detail by Morin et al.[13,14] Here, the contrast of interest reverses as the sample is tilted through the Bragg condition. High-resolution low-loss studies of the surfaces of single crystal metal films have been reported by Krakow and Broers.[15] During this work the question arose whether single atomic steps should be visible in the low-loss image. Krakow has pointed out that the above calculation of the contrast at a surface step should also apply if the specimen is a single crystal. If that is the case then it is to be expected that a single atomic step should be detectable by the low-loss method. The applicability of this calculation to the single-crystal case follows from the conclusion reached by Hall and Hirsch[7] that because of thermal vibrations the wide-angle scattering of electrons from a single crystal "...is effectively Rutherford scattering, as usually assumed." In addition, they also pointed out that the wide-angle scattering probability is "...considerably enhanced or decreased depending on the type of Bloch wave excited." These conclusions all agree with the observation that the low-loss image from a single-crystal specimen appears to be essentially the same as for an amorphous sample except for the addition of electron channeling contrast. Specifically, it is to be expected that the contrast at a surface step calculated from Eq. (9) above should apply to a single-crystal as well as to an amorphous sample.

FIG. 3.--(a) Low-loss scattering from a flat surface having a step of height h; (b) signal as a function of beam position.

References

1. O. C. Wells, "Low-loss image for scanning electron microscope," *Appl. Phys. Lett.* 19: 232-235, 1971.
2. O. C. Wells, (1972): Explanation of the low-loss image in the SEM in terms of electron scattering theory. *SEM/1972*, Chicago: IITRI, 169-176.
3. O. C. Wells et al., in *Scanning Electron Microscopy*, New York: McGraw Hill, 1974, 9, 54-62, 139-150, 160-179.
4. O. C. Wells, "Measurements of low-loss electron emission from amorphous targets," *SEM/1975*, Chicago: IITRI, 43-50.
5. O. C. Wells, "Effects of takeoff angle and energy filtering on the BSE image in the SEM," *Scanning* 2: 199-216, 1979.

6. O. C. Wells, A. N. Broers, and C. G. Bremer, "Method for examining solid speci-
mens with improved resolution in the scanning electron microscope (SEM)," *Appl. Phys.
Lett.* 353: 353-355, 1973. (The oxide step height in Fig. 3 should be 2200 Å; the magni-
fication is correct.)

7. P. E. Hojlund Nielsen and J. M. Cowley, "Surface imaging using diffracted elec-
trons," *Surface science* 54: 340-354, 1976.

8. N. Osakabe et al., "Reflection electron microscopy of clean and gold deposited
(111) silicon surfaces," *Surface Science* (submitted for publication).

9. C. R. Hall and P. B. Hirsch, "Effect of thermal diffuse scattering on propaga-
tion of high energy electrons through crystals," *Proc. Roy. Soc.* A286: 158-177 (esp. p.
175), 1965.

10. J. M. Cowley, "Image contrast in a transmission scanning electron microscope,"
Appl. Phys. Lett. 15: 58-59, 1969.

11. D. L. Misell, Collison data reproduced on p. 38 of Ref. 3.

12. J. Philibert and R. Tixier, "Effects de contraste crystalline en microscopie
électronique à balayage," *Micron* 1: 174-186, 1969.

13. P. Morin et al., "Electron channelling imaging in scanning electron microscopy,"
Phil. Mag. 40A: 511-524, 1979.

14. P. Morin et al., "Scanning electron microscope observation of single defects in
solid crystalline materials," Scanning 2: 217-224, 1979.

15. W. Krakow and A. N. Broers, "High resolution low-loss microscopy of crystalline
surfaces," *Proc. 38th Ann. Meeting EMSA,* San Francisco (in press).

APPLICATION OF ELECTRON CHANNELING CONTRAST WITH LOW-LOSS BACKSCATTERED ELECTRON DETECTION TO THE OBSERVATION OF CRYSTALLINE DEFECTS IN SOLID MATERIALS

P. Morin and M. Pitaval

Electron channeling by atomic planes, which gives channeling patterns in SEM, is shown here to give the possibility to observe crystalline defects on solid specimens. Electron channeling patterns (ECP) are obtained when the incidence of a parallel beam changes at the surface of a crystal; the backscattering coefficient is modified near the Bragg direction.[1] The dislocation images occur when a beam in the Bragg direction scans a defect at the surface of the crystal. At high magnification the beam stays parallel to itself, but owing to the local modification of the crystallographic planes near the defect, the incident beam does not stay in the Bragg position and the backscattering coefficient changes.[2] The contrasts of ECP and defect images are highly increased if only low-loss electrons are detected [3,4]; an energy filter must be used to observe individual defects. The beam diameter and the illumination angle must be small; the high-brightness beam of a field-emission gun is needed.[5] The images of defects are very sensitive to the conditions of observation, the influence of the diffracting conditions, the beam parameters, the tilt angle of the specimen, and the energy losses. We show that this technique allows to determine the Burgers' vector of dislocations and the orientation of microtwins.

Observation of Dislocations

Diffracting Conditions. To display a dislocation, the beam must be in the Bragg position. Reflecting conditions are determined with ECP on selected area by the rocking-beam method.[6] The specimen is oriented with an accurate goniometer stage. Let g be the reciprocal lattice vector corresponding to the Bragg position; as in transmission electron microscopy, the contrast of a dislocation depends on the orientation of g with respect to R, the atomic displacement near the core of the dislocation. The contrast is maximum when g is parallel to R and minimum when g is normal to R.[7] An example of dislocations observed in plastically deformed silicon is shown on Fig. 1. The lower part of the dislocation D is a 60° dislocation lying along the [10$\bar{1}$] direction in the (1$\bar{1}$1) slip plane with a Burgers' vector a/2 [110]:

- for g = 220, Fig. 1(a), (g . b) = + 2, a maximum contrast occurs;
- for g = $\bar{2}\bar{2}$0, Fig. 1(b), (g . b) = − 2, the black and white contrast is reversed;
- for g = 2$\bar{2}$0, Fig. 1(c), (g . b) = 0, a minimum contrast of dislocation D is observed.

Influence of Tilt Angle and Energy Losses. (a) *Experimental Procedure.* Low-loss electrons are selected by a retarding field filter. Two spherical grids are centred on the object with a large collection angle (45°). The electrons are detected by a scintillator. The photomultiplier output is connected either to the video preamplifier for specimen imaging, or to the discriminator amplifier of a photon counting system to measure the absolute value of the detected current. The maximum count rate corresponds to 10^{-12} A.

A silicon monocrystal with a (1$\bar{1}$1) surface is oriented to have the ($\bar{2}$02) planes normal to the tilt axis. Intensity profiles of the $\bar{2}$02 band of the ECP were recorded with a 20s line scan for three tilt angles (55°, 70°, 80°) and for various widths ΔV of the filter window. The value of the contrast, defined as $\Delta I / I_{mean}$, was measured on the recorded profiles, where ΔI is the variation of the video signal and I_{mean} its mean value. The contrast is positive when the band has an intensity higher than I_{mean}, and negative when the contrast of the band is reversed, which occurs for high tilt angles.

The authors are at the CNRS Department of Materials Physics of the University of Lyons, 69621 Villeurbanne, France.
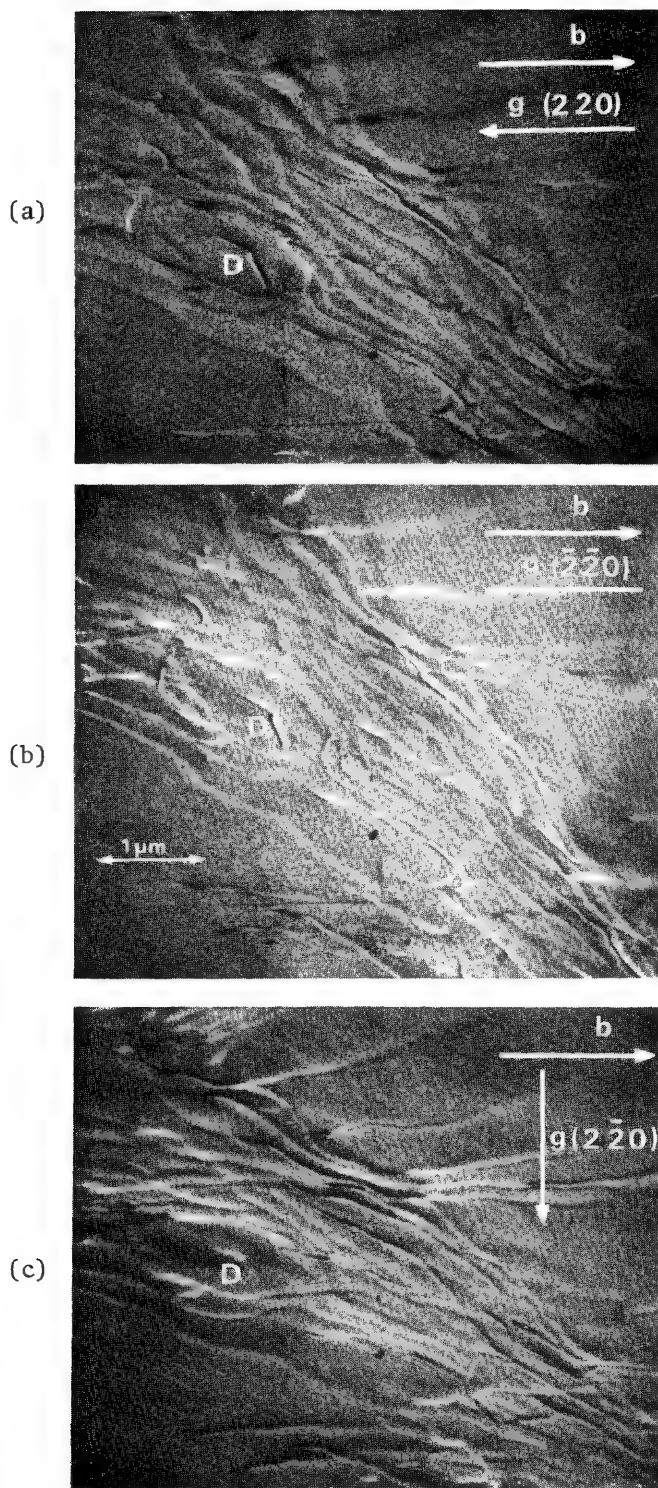
(b) *Discussion of results.* To explain these results, a theoretical model has been developed (to be published in detail elsewhere). The primary electrons in the matter are described in three successive steps.

1. The primary electrons are elastically scattered by the periodic potential. They are described by a transmitted and a diffracted beam with the two-wave approximation of the dynamic theory. At the depth z, $\psi(z)$ is the wave function of these electrons.

2. The electrons are then inelastically scattered from the diffracted and transmitted beams. Let $\sigma(\theta, \phi)$ be the differential cross section where θ and ϕ are respectively the polar and the azimuthal angles; σ includes phonons, plasmons, and individual excitations.

3. These electrons are then treated until they escape through the surface with a Monte Carlo calculation. They have a probability $F(\theta, \phi, z, \Delta V, \alpha)$ to be detected by a filter with a width window ΔV when they are scattered towards the (θ, ϕ) direction at the depth z and for a tilt angle α.

The detected intensity I for a window-filter width ΔV and a given incidence can be calculated from

$$I = \iiint |\psi(z)|^2 \, \sigma(\theta, \phi) \, F(\theta, \phi, z, \Delta V, \alpha) \, dz \, d\theta \, d\phi$$

The dependence of I on the deviation from the (220) Bragg direction gives the contrast of the 220 band. The dependence of this contrast on the width ΔV is shown in Fig. 2 for three tilt angles (55°, 70°, 80°).

At high tilt angle (80°) and with a large filtering window ($\Delta V = 5$ kV), the contrast of the 220 band is reversed. This effect can be explained as follows. The inelastic scattering from Bloch waves occurs nearer the surface inside the band than outside the band, owing to the anomalous absorption effect. For 55° tilt angle, the detection probability $F(\theta, z)$ (Fig. 3) decreases when z increases, so that the band occurs white. For 80° tilt angle, $F(\theta, z)$ increases with z except for θ angles towards the filter entrance, but the scattering cross section of the electrons in this direction is very low and the contribution of these electrons is weak. The detection probability is lower for electrons scattered near the surface than for those scattered in deeper layers, so that the band is black and the contrast is reversed. The experimental and calculated values of ΔV at which the contrast reverses are respectively

FIG. 1.--Dislocations in a $(1\bar{1}1)$ glide plane in deformed silicon: b is Burgers' vector of dislocation D, g is reciprocal lattice vector of excited reflection; (a) gb = + 2, maximum contrast for D; (b) gb = - 2, reversal contrast; (c) gb = 0, minimum contrast for D and maximum contrast for most the other dislocations.

$\Delta V = 1.26$ and 1.56 kV.

The experimental and calculated ratios of the mean detected current to the beam current are also in good agreement, as shown in Fig. 4 for 55° tilt angle. The theoretical and experimental values are fitted by a straight line.

These results show that the contrast increases when the tilt angle and the width of the filter window decrease, but the mean detected current is lowered and the statistical noise has a higher value. From these results a compromise can be found for ΔV and the tilt angle to have the best signal-to-noise ratio.

Influence of beam parameters. This study has been developed elsewhere.[7] It is briefly summed up here.

● In the ECP mode, with a parallel beam, the intensity varies from a maximum to a minimum when the orientation is modified by $\theta_0 = 1/g\xi_g$; around the Bragg angle corresponding to $g\xi_g$ is the extinction distance (with our experimental conditions $\theta_0 \simeq 3.7 \times 10^{-3}$ rad).
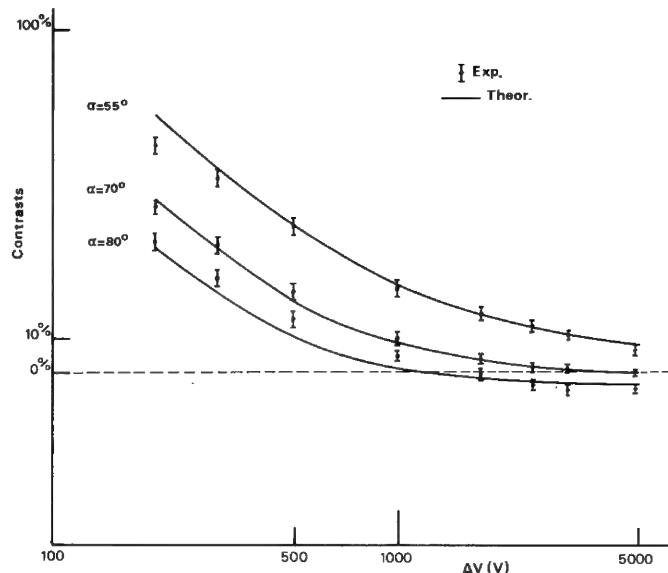
FIG. 2.--Experimental and calculated contrasts as function of width of filter window.
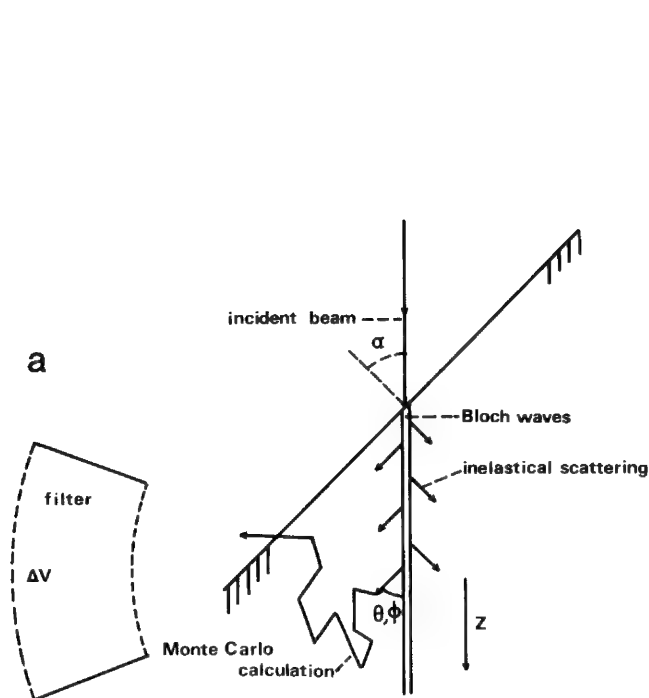
FIG. 3.--Detection probability for electrons leaving the Bloch waves at the Z depth with the θ angle: (a) configuration, (b) tilt angle $\alpha = 55°$, (c) $\alpha = 80°$.
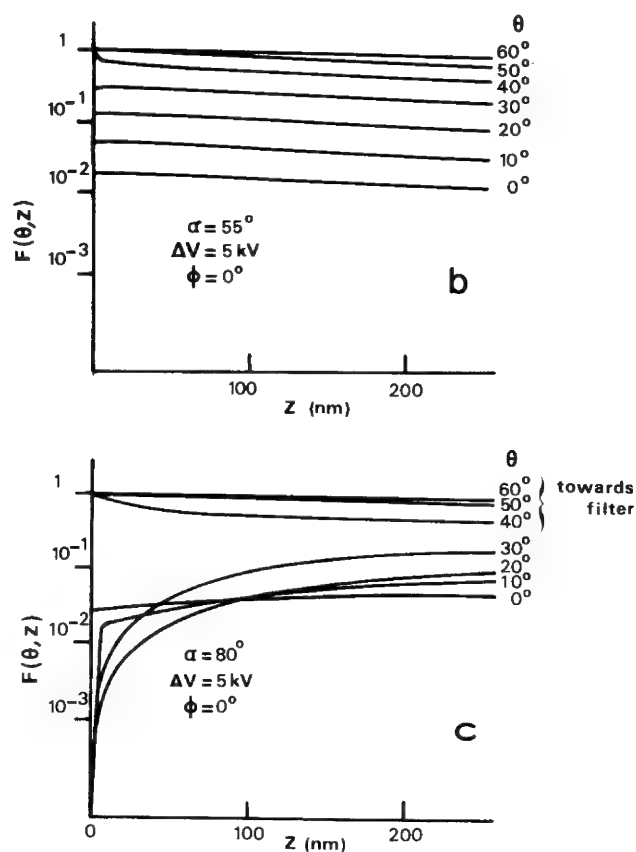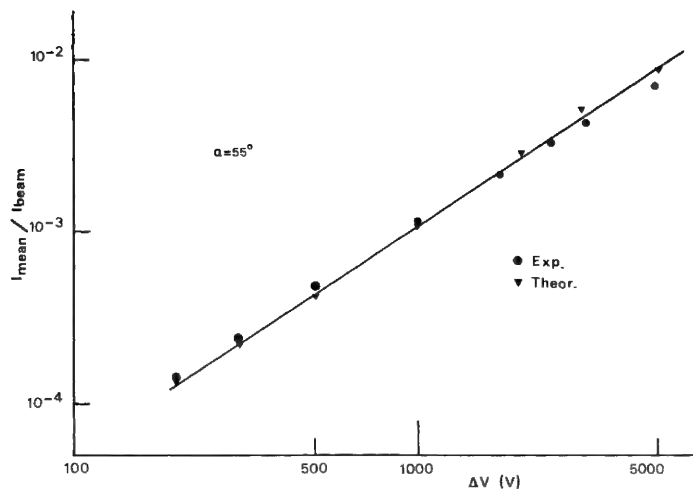
FIG. 4.--Ratio of mean detected current to beam current as a function of filter window width.

• In standard SEM mode, the illumination angle has a similar value, so the contrast is strongly affected by the choice of the illumination angle, which is determined by the objective aperture. As the beam convergence decreases, the contrast increases but the beam intensity decreases and the statistical noise has a higher value; moreover, the beam diameter depends itself on the objective aperture. These three beam parameters must be taken into account in the choice of the illumination angle.

It has been found from this study that for imaging dislocations, experimental conditions must be very critically choosen. These choices result from compromise between the amplitude of the contrast and the mean value of the detected current to obtain the highest signal-to-noise ratio. Typically, to observe dislocations on a (111) surface of silicon crystal, we use a 150μm objective aperture, a width of filtering window equal to 600 V, and a tilt angle of about 55°. If the dislocations are far away below the surface it may become necessary to widen the filter window up to 1000 V. In silicon the maximum depth explored is about 100 nm.

Observation of Microtwins

The crystalline contrast permits the observation of grains on a polycrystalline sample.[8] This contrast corresponds to the excitation of an ECP band when a grain is scanned by the beam: when backscattered electrons are detected, this grain is brighter than other grains that are not oriented for the excitation of an ECP band. This contrast might permit the observation of twins.[5,9] However, the microtwins shown in Fig. 5 are too thin to be imaged with unfiltered backscattered electrons because of poor resolution and low contrast. Thus just as for dislocations imaging, these observations need detection of low-loss electrons. These microtwins are observed on an epitaxially grown silicon layer on a ($\bar{1}$012) oriented sapphire substrate. The silicon layer is 600 nm thick; its surface is (001) oriented. Four microtwinning systems occurs corresponding to the four (111) type planes. For Fig. 5(a), the specimen was oriented to display the center of the [111] pole in ECP mode; ($\bar{1}$11) twinning planes intersect the surface along the [110] direction. These microtwins have a [511] type axis parallel to the incidence direction, fewer electrons are backscattered than for (111) pole, and the twins have a black contrast. In Fig. 5(b), the specimen is oriented for the beam impiging along the [212] axis of the matrix and (0$\bar{1}$0) axis of the microtwins which have their twinning axis along the (1$\bar{1}$1) direction. The 202 band is excited for both the matrix and these microtwins. The incidence corresponds to the center of the band. More electrons are scattered by the microtwins, which appear brighter than the matrix.

By a tilt of a few degrees, the incidence is varied to correspond at the side band, the $\bar{2}$02 planes are in Bragg position (Fig. 5c), and a network of inclined misfit dislocations become visible.

Conclusion

Crystalline defects can be characterized by this method (determination of Burgers' vector for dislocations, orientation of microtwins, etc.). Although the resolution is at present lower than in transmission electron microscopy, we now have a new method of detecting crystalline defects in solid specimens.

FIG. 5.--Microtwins in epitaxial silicon
on sapphire substrate: (a) beam along
[111] matrix zone axis, (b) beam along
[212] axis, (c) beam in Bragg position
for (202) planes.

This technique thus presents new possi-
bilities:

● when thinning of a specimen is diffi-
cult or may modify specimen properties;

● for samples with large sizes--a non-
destructive method that permits observation
of the entire surface;

● in an MEB, the specimen is out of the
magnetic field of the polepieces of the ob-
jective lens; is easily accessible, and may
be available simultaneously for other charac-
terizations (Auger spectroscopy, EBIC, cath-
odoluminescence, dispersive x-ray analysis).

References

1. G. R. Booker, *Discuss. Faraday Soc.*,
38: 298, 1968; *Modern Diffraction and Imaging
Techniques in Materials Science*, London:
North-Holland, 1970.

2. D. G. Coates, *Phil. Mag.* 16: 1179,
1967.

3. E. D. Wolf and T. E. Everhart, *Scan-
ning Electron Microscopy*, Chicago: IITRI,
1969, 41.

4. O. C. Wells, *Appl. Phys. Lett.* 19: 232,
1971; *Scanning Electron Microscopy*, Chicago:
IITRI, 1972, 169.

5. P. Morin et al., *Scanning* 4-2: 218,
1979.

6. E. M. Schulson and C. J. Van Essen,
J. Phys. (E) 22: 247, 1969; *J. Appl. Phys.*
42: 3894, 1971.

7. P. Morin et al., *Phil. Mag. (A)* 40:
511, 524, 1979.

8. J. Philibert and R. Tixier, *Micron*
1: 174, 1969.

9. M. L. Zorrilla et al., ESSDERC, 1979.

ELECTRON CHANNELING PATTERN (ECP) CONTRAST IN THE SCANNING ELECTRON MICROSCOPE (SEM) FROM ION-BOMBARDED GARNET SAMPLES

O. C. Wells, R. J. Savoy, and D. F. Kyser

Ion bombardment is used to change the magnetic properties of garnet films for bubble applications.[1] Electron channeling pattern (ECP) contrast provides a way by which local variations in the crystal properties of a specimen can be studied in the scanning electron microscope (SEM).[2-5] This paper describes the use of ECP contrast in the SEM as a means for studying the geometry of the ion-bombarded regions in garnet films. The backscattered-electron (BSE) image was used in this work as being less susceptible to specimen charging and contamination effects than is the secondary-electron image.

Two samples were used in this work. Sample 1 was a (111) large-area single crystal $Gd_3Ga_5O_{12}$(GGG) garnet substrate. Sample 2 was as Sample 1 but with a 1-2μm epitaxially grown layer of doped garnet which had been ion-bombarded over the whole surface except for certain small regions protected with photoresist, which had then been removed.

The samples were first coated with 100-200 Å of carbon to prevent charging. The thickness was judged by previous experience and was checked by measurement for a detectable conductivity with an ohmeter. In a secondary-electron image obtained from such a sample (Fig. 1a), the surface details are almost completely obscured by contamination caused by the raster scan (dark rectangles) and by charging effects (horizontal streaks). (Specimens processed with photoresist are sometimes more susceptible to contamination effects in the SEM than unprocessed samples.) The BSE image from the same field of view (obtained with the BSE detector in the "high" position as described below) is shown in Fig. 1(b). Here, the charging and contamination effects are absent. The same surface particles and surface scratches can be seen in Fig. 1(b) as in Fig. 1(a). A series of radial stripes (the regions that were *not* ion bombarded) are also seen in Fig. 1(b). These stripes were investigated as follows.

(a)   (b)
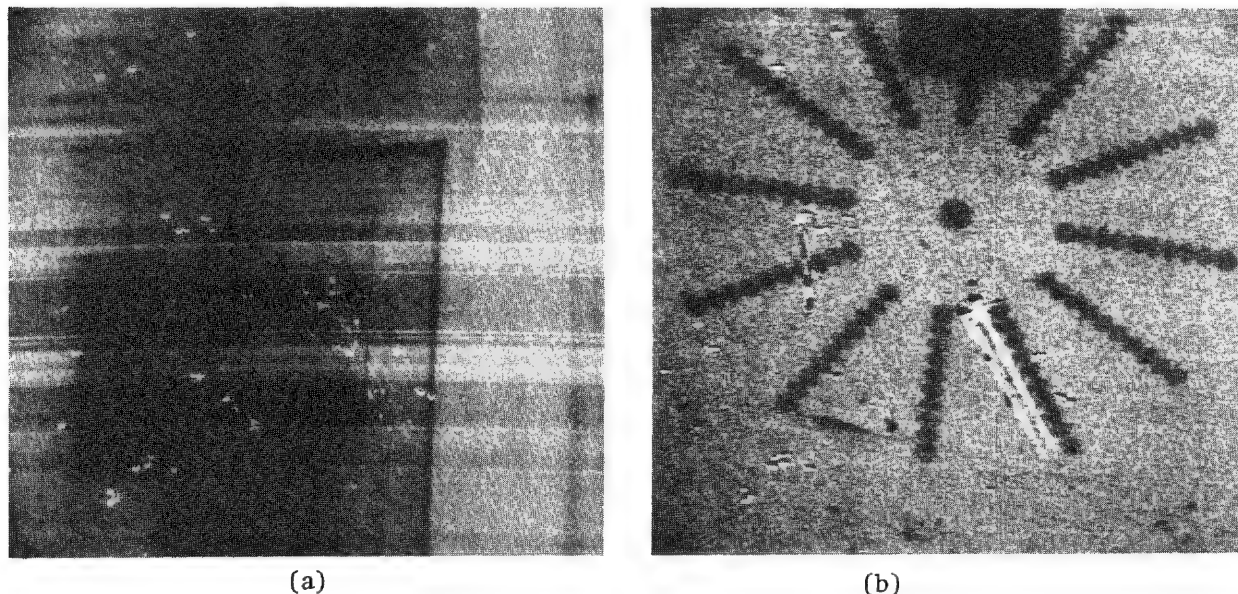
FIG. 1.--Comparison between (a) secondary electron image and (b) BSE image of carbon-coated garnet sample. E_0 = 15 kV, θ_1 = 68°. BSE detector was in "high" position shown in Fig. 2. Horizontal field of view measures 225 μm from left to right.

The authors are at IBM: Wells and Savoy at the Watson Research Center, Box 218, Yorktown Heights, NY 10598; Kyser at the Research Laboratory in San Jose, CA 95193.
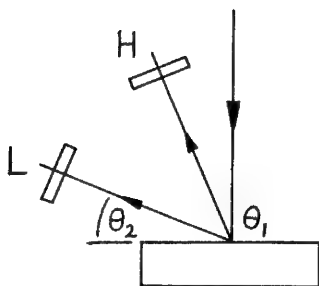
FIG. 2.--"High" and
"low" positions for
the solid-state BSE
detectors. Defini-
tions of θ_1 and θ_2.

The first step is to establish the conditions under which ECP contrast can be obtained from these particular samples. (ECP contrast is a tilt-sensitive contrast that gives information related to the crystal structure, whereas topographic and compositional contrasts are insensitive to small changes in the angle of the specimen.) To determine these conditions, the sample was mounted in the SEM at right angles to the beam. A pair of silicon-diode BSE detectors were mounted, one in the "high" position H with $\theta_2 =$ 67.5° (Fig. 2) and the other in the "low" position L with $\theta_2 =$ 22.5°. The detector was type 55CL manufactured by Optical Coating Laboratories Inc. (This is essentially the same detector system as was used by Wells and Savoy[6] to investigate magnetic contrast from silicon iron at normal incidence--except in that case it was the "high" rather than the "low" image that contained the desired image contrasts.)

A typical BSE image obtained with the "low" detector and with the beam in focus is shown in Fig. 3(a). Surface particles are seen in sharp focus, but the ECP is blurred. The final lens current was then reduced from 0.62 to 0.30 A in order to collimate, rather than focus, the incident beam (Figs. 3b and c). The image has rotated clockwise by about 30°. The spatial magnification has increased by about 20%. The surface particles are now imaged as circles with a uniform diameter related to the final beam-defining aperture in the SEM. The network of lines shown in Figs. 3(a) and (b) is the ECP caused by variations in the incident angle as the specimen was scanned. The image obtained with the BSE detector in the "high" position (Fig. 3b) shows very little ECP contrast. The "low" image (Fig. 3c) shows strong ECP contrast. This observation is important inasmuch as BSE detectors in commercial SEMs are generally in the "high" position; that is, they are in the wrong position to give strong ECP contrasts from these particular samples.

The images shown in Figs. 3(b) and (c) were obtained with a 0.001μF condenser in series with the diode BSE detector. This image therefore shows only the changes in the recorded signal (which are caused, of course, by the changes that occur in the direction of the incident electron beam relative to the crystal lattice as this area is scanned). In reality, the recorded signal is either slightly greater, or slightly less, than the average in the regions of this image that are bounded by the bright or dark lines in Fig. 3(c) (see Fig. 7 below).

The (111) pole ECP obtained from Sample 2 (which *had* been ion bombarded) as shown in Fig. 4 contains less fine structure than the ECP obtained from Sample 1 (which had not) as shown in Fig. 3(c). The degradation of the ECP is related to the crystal damage caused by the ion bombardment.[7-10] This relationship thus provides one way by which this damage can be categorized.

Images obtained from Sample 2 are shown in Figs. 5 and 6. This part of the pattern consists of 12 stripes radiating outward from a central circle. The stripes were protected from the ions by the photoresist; the surrounding crystal was damaged by the ion bombardment. The diameter of the circle that just encloses the outer ends of the stripes is 200 μm. The micrograph obtained with the low BSE detector and with normal electron incidence is shown in Fig. 5(a). The spokes (which are the parts of the surface that were *not* ion-bombarded) are brighter than the background because the central part of the (111) ECP represents a favorable channeling condition (point A in Fig. 7). Progressive tilts of 1.5° are shown in Figs. 5(b) and (c) (points B and C in Fig. 7). The ECP contrast is in the process of changing sign in Fig. 5(b) and can be seen to be of different sign at the upper and lower edges of this micrograph. Topographic contrast is independent of the channeling condition.

Micrographs at higher magnification are shown in Fig. 6. Topographic contrast corresponding to a slight depression of the stripe is also seen in all three micrographs. This result is consistent with an increase in thickness of the ion-bombarded part of the crystal (as is shown in Fig. 1c in Ref. 1, for example). Topographic contrast is enhanced by the low position of the BSE detector. In images obtained with the detector in the "high" position the bombarded areas appear darker than the surrounding crystal regardless of the

specimen tilt (Fig. 1b). The reason for this reduction in the BSE signal from the non-bombarded regions was not established. Topographic contrasts are greatly reduced. The nonreversal of contrast as the specimen is tilted (when the BSE detector is in the high position) is consistent with the weakness of the ECP with Sample 1 in Fig. 3(b).

(a)

(b)

(c)
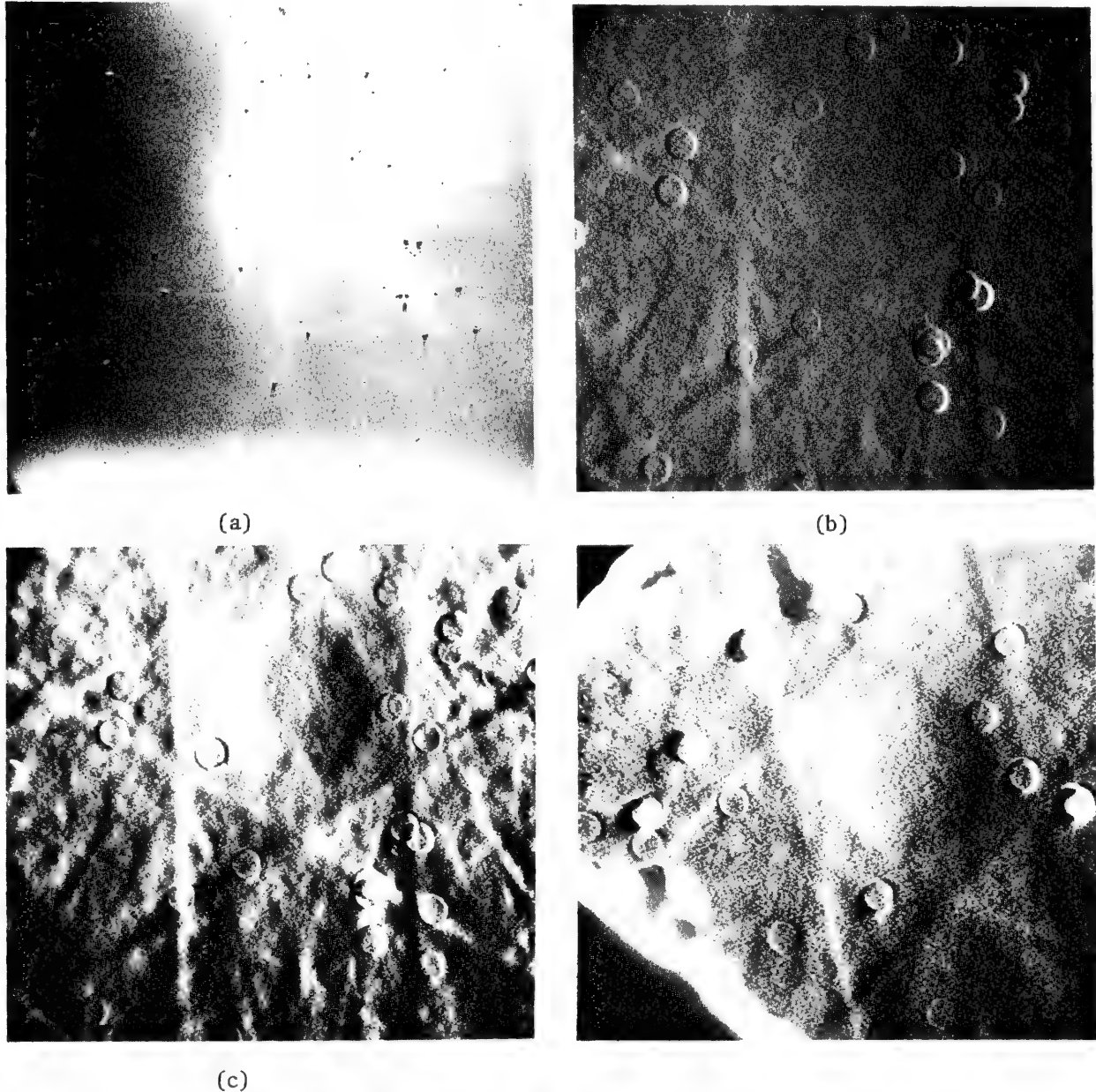
FIG. 3.--BSE images obtained from Sample 1: (a) with final lens in focus, topographic contrast is sharp, ECP pattern is blurred; (b), (c) with final lens current reduced from 0.62 to 0.30 A to collimate incident beam rather than to focus it. Detector was in the "high" position in (b), "low" in (c). E_0 = 25 kV; i_{beam} = 5.5 × 10^{-9} A and C = 1 μF in (a); i_{beam} = 1.2 × 10^{-7} A and C = 0.001 μF in (b) and in (c); 80sec scan, 200μm final aperture diameter. Normal incidence, field of view measures 8000 μm from left to right in (a).

FIG. 4. (bottom right).--ECP obtained from Sample 2: compare with Fig. 3(c). (Less fine structure implies poorer crystal.)

(a)

(b)

(d)

(c)
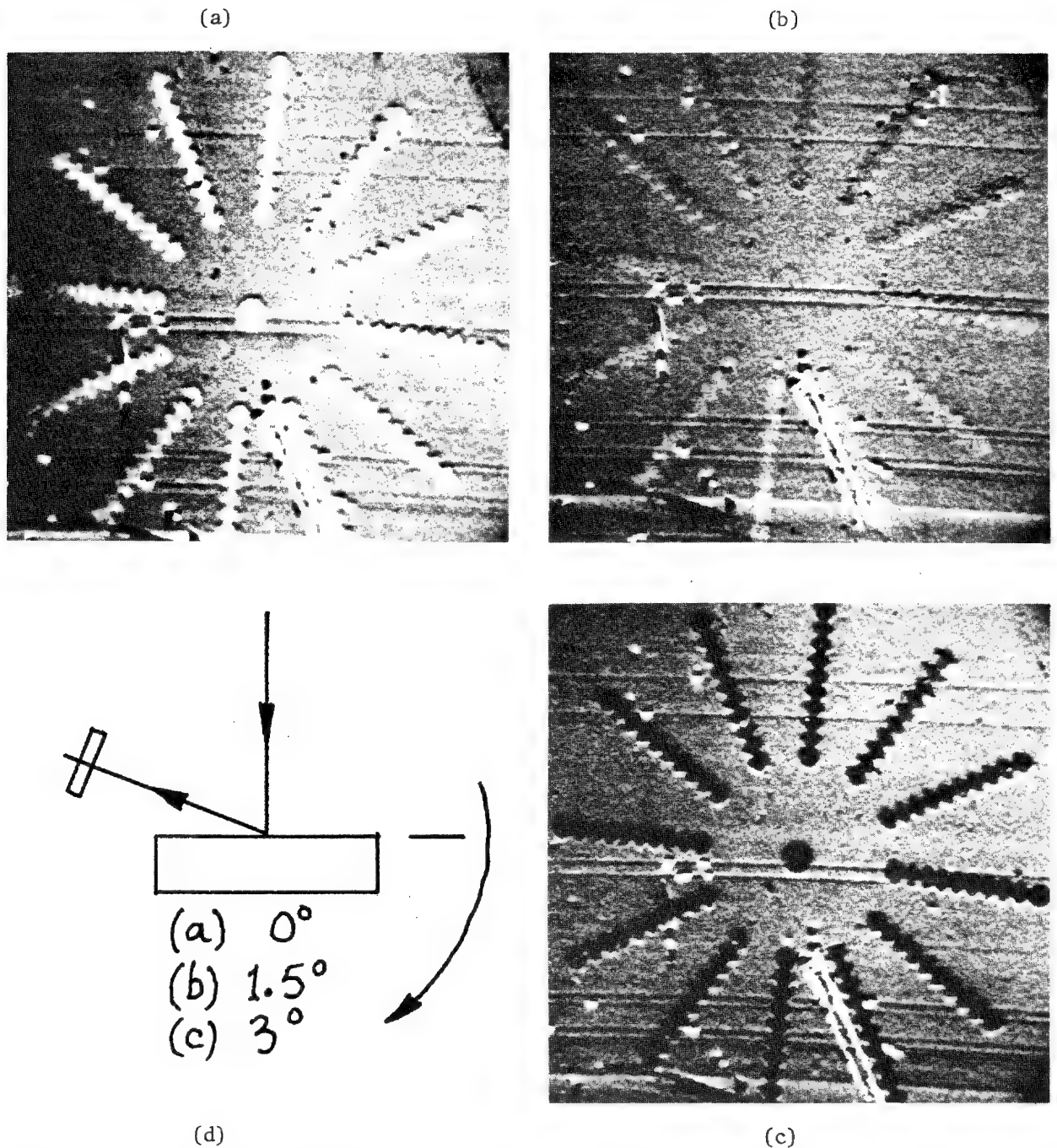
FIG. 5.--Part of the pattern on Sample 2 imaged using "low" BSE detector (spokes are *not* bombarded): (a) with normal incidence (point A in Fig. 7); (b), (c) with 1.5° and 3.0° tilt (points B and C in Fig. 7). E_0 = 25 kV; i_{beam} = 9 × 10^{-9} A; 80sec scan; C = 2 μF. Horizontal field of view measures 200 μm from left to right; (d) Explanatory diagram.

In some experiments we varied the incident beam energy. The effect of increasing the accelerating voltage from 30 to 50 kV is to wash out the topographic contrast while preserving the ECP contrast at a constant value of 0.5% over this voltage range. The fact that the ECP contrast stays sharp as the voltage is raised is consistent with the theory that the ECP information is contained in the low-loss electrons scattered by the thin surface layer.

(a)   (b)

(c)
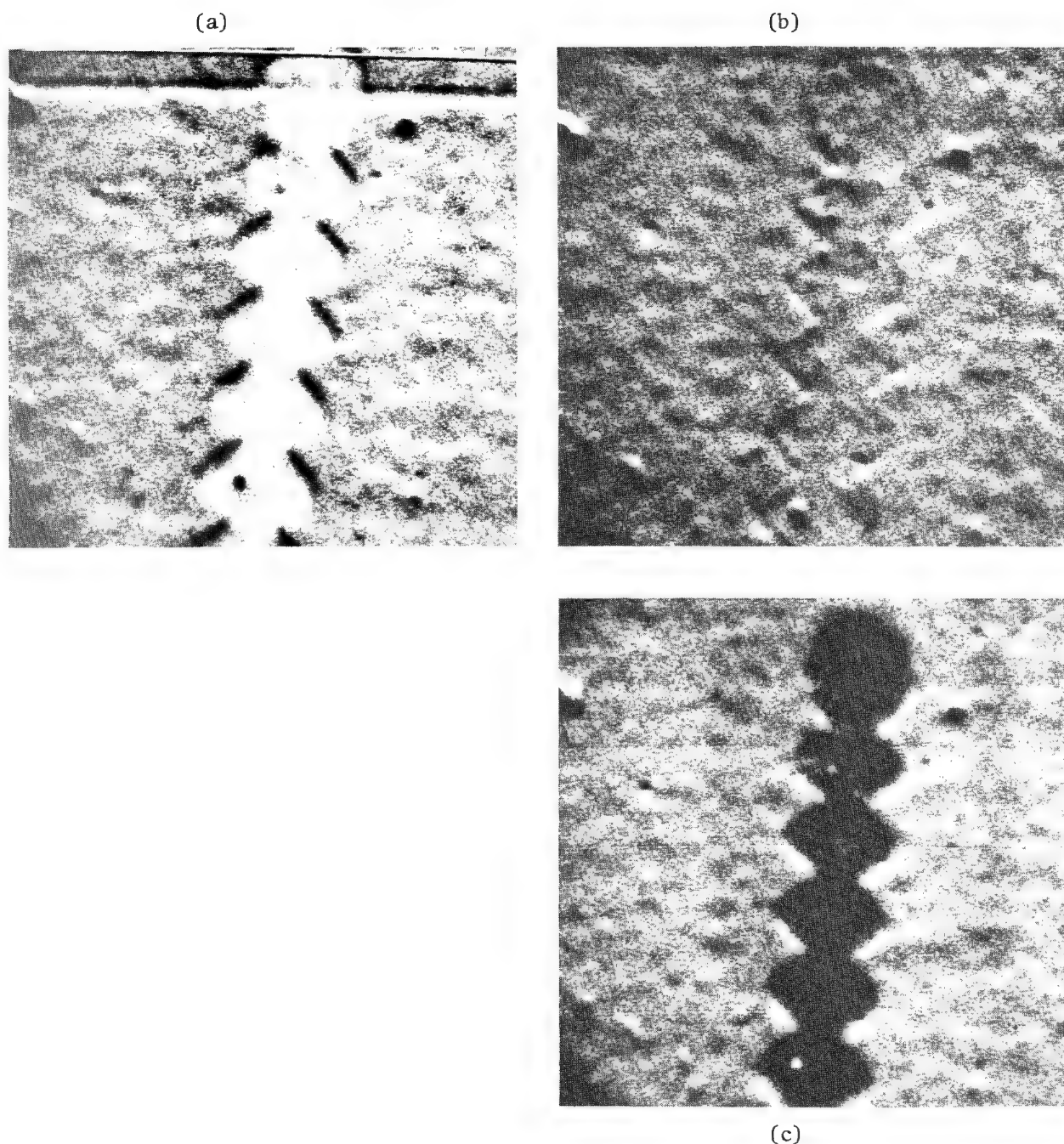
FIG. 6.--(a), (b), (c) are as in Fig. 5, but at higher magnification. Horizontal field of view measures 40 µm from left to right. E_0 = 25 kV; i_{beam} = 5 × 10^{-8} A; 80sec scan; C = 2 µF.

    The general form of the ECP contrast variation at a band edge is shown in Fig. 7. The angular spacing $\Delta\theta$ between the maximum and the minimum signal at the band edge (in their case for silicon) was called the "linewidth" by Farrow and Joy.[11] This value is several times smaller than the 1.5° tilt angle referred to above, which was large enough to tilt the sample onto the level sections shown in Fig. 7. Owing to the irregular nature of the peaks it may be easier in practice to measure the gradient at the neutral point than the linewidth as defined in the above way. Concerning the importance of measuring the linewidth, Farrow and Joy[11] wrote: "...these measurements represent an important step towards the effective use of ECP contrast as a tool for characterizing para-

31
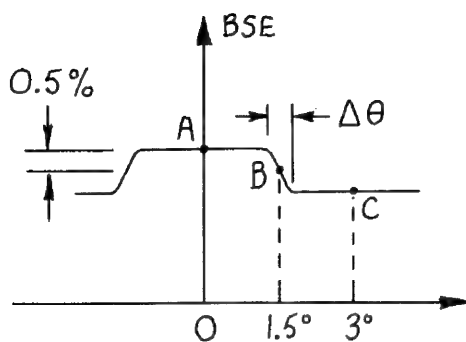
FIG. 7.--Definition of line width $\Delta\theta$. Vertical axis = recorded signal. Horizontal axis = specimen tilt. A, B, C: Beam orientations used to record Figs. %(a), (b), and (c); also 6(a), (b), and (c).

meters of the crystal lattice such as dislocation and point-defect density, and the extent, depth and distribution of damage layers due to ion implantation."

The conclusions reached from this preliminary investigation were therefore as follows: First, it is certainly possible to form an image of the ion-bombarded regions by means of ECP contrast in the BSE image in the SEM; second, the usual position for the BSE detector in commercial SEMs is not the best for this particular problem; and third, it was found that the ECP from Sample 2 contained less fine structure than the ECP from Sample 1. This finding agrees with the results published previously by other workers[7-10] that the damage caused by the ion bombardment reduces the apparent sharpness of the ECP. Thus, this technique will provide a means for studying the damage caused by different ion doses.

References

1. B. Strocka, G. Bartels, and R. Spohr, "Lattice strain in garnet single crystals caused by high-energy heavy ion irradiation, *Appl. Phys.* 21, 141-149, 1980.

2. J. Philibert and R. Tixier, "Effets de contraste crystalline en microscopie électronique à balayage," *Micron* 1: 174-186, 1969.

3. O. C. Wells et al., *Scanning Electron Microscopy*, New York: McGraw-Hill, 1974, 172-177. (Reprinted 1978.)

4. P. Morin et al., "Electron channelling imaging in scanning electron microscopy," *Phil. Mag.* 40A: 511-524, 1979.

5. P. Morin et al., "Scanning electron microscope observation of single defects in solid crystalline materials," *Scanning* 2: 217-224, 1979.

6. O. C. Wells and R. J. Savoy, "Type-2 magnetic contrast with normal electron incidence in the scanning electron microscope (SEM), in *Microbeam Analysis--1979*, San Francisco: San Francisco Press, 1979, 17-21.

7. S. M. Davidson, "Study of radiation damage in silicon with the scanning electron microscope," *Nature* 227: 487-488, 1970.

8. S. M. Davidson and G. R. Booker, "Damage produced by ion implantation in silicon," *Radiat. Eff. (Eng.)* 6: 33-42, 1970.

9. E. D. Wolf and R. G. Hunsperger, "Measurement of ion implantation damage in (111) GaAs using the scanning electron microscope," *Appl. Phys. Lett.* 16: 526-529, 1970.

10. E. D. Wolf and R. G. Hunsperger, "Pseudo-Kikuchi pattern degradation of (111) gallium arsenide induced by 60-keV cadmium ion bombardment," *SEM/1970*, 457-463.

11. R. C. Farrow and D. C. Joy, "Measurements of electron channeling pattern linewidths in silicon," *Scanning* 2: 249-254, 1980.

SURFACE IMAGING AND ANALYSIS WITH REFLECTION-DIFFRACTED ELECTRONS

J. M. Cowley

The idea of using electron beams diffracted from flat surfaces of bulk single-crystal specimens to form images of surface structure was tried briefly in the 1950s[1] and revived in the 1970s with both high-energy (100keV) electrons[2] and medium-energy (5-15keV) electrons.[3] The medium-energy system, with scanning techniques, has been applied successfully for the study of surface reactions[4] and also to the study of diffraction channeling effects.[5] The instrument operates with ultrahigh vacuum and the specimens can be cleaned by ion bombardment and heated *in situ*, but the systems suffers because to date the resolution achieved has been no better than about 300 Å.

By use of 100keV electrons in a standard TEM, the resolution of surface detail has approached 20 Å but, because the diffraction angles are very small and the beam is incident at grazing angles, the images of flat surfaces are severely foreshortened in the beam direction. Also, in most microscopes the pressure of air and organic compounds around the specimen is much too high to allow clean surfaces to be prepared or studied. This last defect of the method has been overcome by Yagi and collaborators in Tokyo who have used an ultrahigh-vacuum 100kV TEM in which specimens may be ion-bombarded and heated to clean and anneal them. With this instrument, this group has observed atom-high steps on clean silicon surfaces, the growth and domain formation of surface-reconstruction super-lattices,[6] and the intersection of dislocations with the surface.[7]

In our HB-5 STEM instrument we have as yet no provision for heating and cleaning the surfaces, but since the pressure in the specimen chamber is 10^{-9} torr or better, surfaces which are initially clean can be maintained in that state.

We have been able to obtain scanning dark-field images with diffracted electron beams reflected from the surfaces of small crystals and have achieved a resolution approaching 10 Å. Furthermore we have been able to analyze these surface-reflected beams with an energy-loss spectrometer and to compare the ELS curves with those for electrons transmitted through thin crystals.

The crystals used have been, for the most part, the larger, roughly cubic crystallites, about 1 μm in diameter, occurring in samples of MgO smoke. Shadow images and convergent beam microdiffraction patterns of these crystals were observed by use of the optical system attached to our STEM instrument[8,9] and were used to align the crystals so that the axial incident beam was inclined to one of the major cube faces by an angle of about 2.6×10^{-2} rad corresponding to the Bragg angle for the (600) reflection. The diffraction geometry is indicated in Fig. 1(a). A typical diffraction pattern, Fig. 1(b), shows doubled diffraction spots (or streaks) because the beams reflected from the surface

(a)   (b)
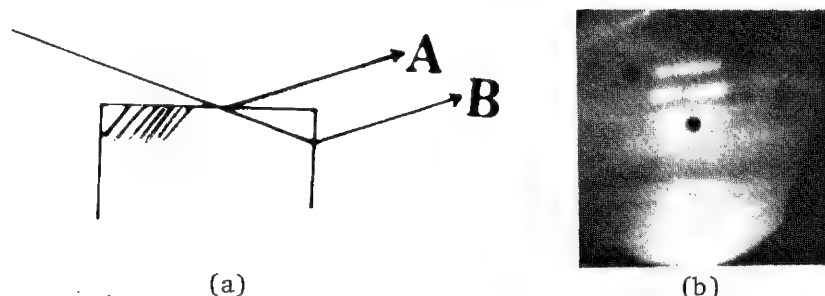
FIG. 1(a).--Diffraction of electrons from small cubic crystal showing diffracted beams reflected from surface A and transmitted through crystal edge B; (b) Convergent-beam diffraction pattern from MgO cubic crystal. The 400, 600, and 800 reflected beams are visible and each is split into the two components, A and B of part (a). Black spot is detector mirror in optical system of STEM instrument.
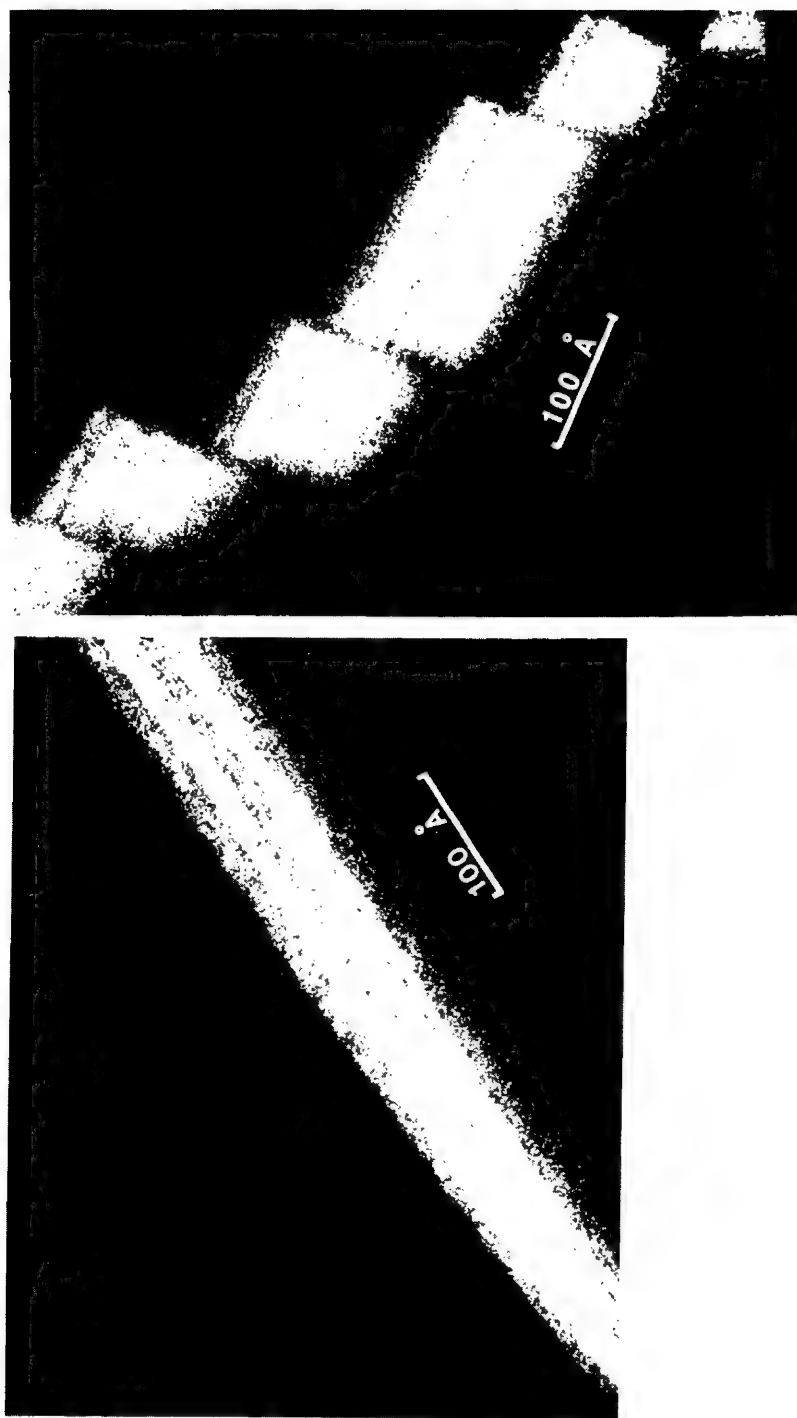
FIG. 2.--Images of faces of MgO cubic crystals obtained by detection of surface-diffracted beam (A in Fig. 1a).
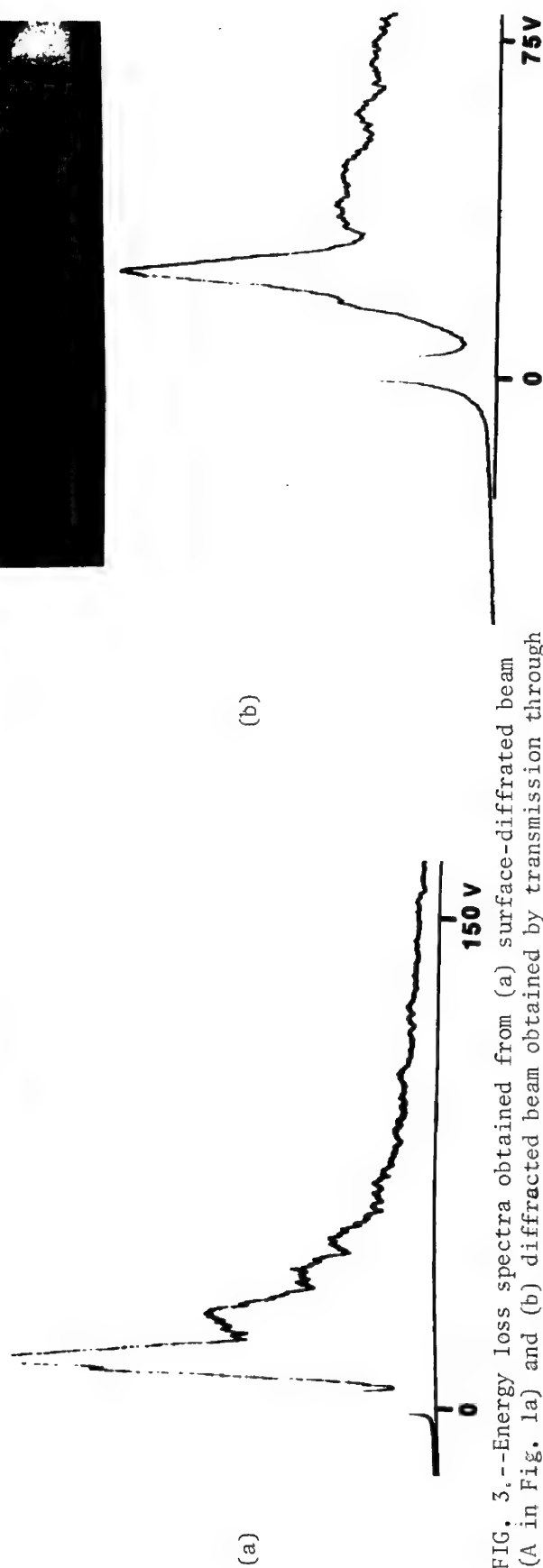
FIG. 3.--Energy loss spectra obtained from (a) surface-diffrated beam (A in Fig. 1a) and (b) diffracted beam obtained by transmission through corner of thin crystal of MgO (B in Fig. 1b).

34

are more deflected by refraction effects than those transmitted through an edge of the crystal. The surface-reflected beam may be detected to form the scanning image by use of a small mirror in the optical system (the black spot in Fig. 1b), or by guiding the selected part of the diffraction pattern through the detector aperture at the entrance to the energy-loss spectrometer.

Figure 2(a) shows the image of an almost flat face of an MgO crystal. The image detail is due to small steps on the surface. Figure 2(b), obtained with the beam almost in the [100] direction, reveals that the rounded corner of a large cube actually consists of steps bounded by {100} MgO planes, about 100-200 Å wide. These large steps are crossed by much finer steps. From the interaction of the small steps with the edges of the large steps it is clear that their heights are in many cases less than 5 Å.

The ELS spectrum obtained from the surface diffracted beam (Fig. 3a) may be compared with that from the diffracted beam transmitted through a corner of the crystal (Fig. 3b). Apart from the differences in relative heights of the peaks due to differences in the effective crystal thickness, the only obvious difference between the two spectra is that the surface-diffracted beam shows a small energy loss peak at about 7 V energy loss, not seen in the other curve.

Since the penetration of a strongly reflected diffracted beam into a flat surface is no more than 10-20 Å, one may expect this ELS method to prove to be a valuable technique for the study of surface concentrations of particular types of atoms or for surface states that may have a profound influence on surface electronic properties or reaction kinetics.

Some interesting interference fringes are observed when images such as those of Fig. 2 from nearly perfect MgO faces are defocused. These fringes arise from interference of the electron waves corresponding to the beams A and B of Fig. 1(a), which leave the crystal at slightly different angles owing to differences in the refraction effect.

Our results to date are of a preliminary nature, designed to explore the possibilities of the techniques and to provide some further basis for the theoretical study of the image contrast[10] and of surface analysis. They are being extended to studies of MgO with thin epitaxed metal films, and to investigations of the surfaces of NiO and other crystals.

References

1. J. S. Halliday and R. C. Newman, *Br. J. Appl. Phys.* 11: 158, 1960.
2. P. E. Højlund Nielsen and J. M. Cowley, *Surface Sci.* 54: 340, 1976.
3. J. M. Cowley et al., *Rev. Sci. Instr.* 46: 86, 1975.
4. G. G. Hembree, J. M. Cowley, and M. A. Otooni, *Oxidation of Metals* 13: 331, 1979.
5. G. G. Hembree and J. M. Cowley, in Om Johari, Ed., *Scanning Electron Microscopy/ 1979*, vol. I, AMF O'Hare, Ill.: SEM Inc. 1979, 145.
6. N. Osakabe, Y. Tanishiro, K. Yagi, and G. Honjo, *Surface Sci.* (1980), in press.
7. K. Yagi, N. Osakabe, Y. Tanishiro, and G. Honjo. *Proc. 4th Int. Conf. on Solid Surfaces*, 1980 (in press).
8. J. M. Cowley and J. C. H. Spence, *Ultramicroscopy* 3: 433, 1979.
9. J. M. Cowley, in *Scanning Electron Microscopy/1980*, in press.
10. H. Shuman, *Ultramicroscopy* 2: 361, 1977.

ON THE PROBLEM OF COATING SAMPLES FOR HIGH-RESOLUTION LOW-LOSS SURFACE SEM

A. N. Broers and Eberhard Spiller

For highest resolution with the low-loss or scanning reflection surface image, it is necessary to coat low-atomic-weight samples with a thin layer of relatively high-atomic-weight metal. The metal layer scatters many more electrons than the underlying sample and gives rise to a predominantly surface image. In practice, it is difficult to make the metal coating smooth enough to allow the full resolution potential of the method to be realized. With the high-resolution low-loss mode, the final lens has a focal length that is ten times shorter than that of the final lens of a conventional secondary-electron SEM, and the lower aberrations of this lens allow the beam diameter to be reduced to below 1 nm.[2] Contrast from surface perturbations is very high; we have been able to detect roughness that is not detected in a conventional secondary-electron SEM. For example, features of 2-5 nm are observed with high contrast in 3-5 nm coatings of AuPd and PtPd films.[3] Similar coatings produce acceptable structureless coatings for the standard SEM.[4,5] Sputtered coatings of about 200 Å used for conventional SEM have structures as large as 10-20 nm when viewed with the low-loss method.[6] Such coatings would obscure a lot of potentially bisible detail on many samples. With the high-resolution low-loss method, films of pure gold show considerable structure that is not visible in the high-resolution SEM.[7]

We have explored a variety of heavy-metal coatings in order to examine their relative roughnesses. We first measure the roughness of the film by monitoring the intensity of a beam of soft x rays reflected from the sample surface. The samples are then examined in a high-resolution SEM with a beam diameter below 1 nm. The x-ray measurements are made during film deposition by monitoring of the oscillations in the reflectivity of the films caused by the interference of the waves reflected at the top and bottom boundaries of the film. The average reflected intensity decreases as the film roughness increases.

For uncoated samples of moderate atomic weight (27-29), an energy filter improves the scanning reflection image: the image then becomes more truly a "low-loss" image, as the filter prevents electrons that suffer too large an energy loss from reaching the detector. The use of a filter was proposed originally as one alternative for the high-resolution low-loss image,[2] but subsequently most samples have been examined in our laboratory without its use. For heavy-atomic-weight samples, or for coated samples, adequate energy selection results from the optics of the objective lens/detector combination. To reach the detector from the center of the condenser-objective lens, electrons must emerge from the sample at a glancing angle (10-20°) to the sample surface.[8] Scattering into this 'fan' of acceptance results predominantly from elastic scattering events close (< 2 nm) to the surface so the image is mainly a surface image. For lower-atomic-weight samples, the depth from which electrons can be scattered into the detector increases; and 'flairing' (which results from electron penetration of surface protuberances) becomes more serious. In these cases the filter improves the image by rejecting electrons that have lost significant energy (> 400 eV). These electrons have travelled too far into the sample, or have travelled through protuberances and therefore no longer yield localized information about the point of impact of the electron beam.

Surface Roughness by Soft X-ray Interference

The interference of soft x rays reflected from the top and bottom boundary of a thin film during the deposition of the film can be utilized to measure changes in the surface

---

roughness of the film during growth. The (complex) amplitude reflectance of a film is given by

$$r_f = \frac{r_t + r_b e^{-i\Delta}}{1 + r_t r_B e^{-i\Delta}} \tag{1a}$$

$$\Delta = 4\pi d\tilde{n}\cos\alpha/\lambda \tag{1b}$$

where r_t and r_b are the amplitude reflection coefficients of the top and bottom boundaries of the film, d is the film thickness, and $n = \tilde{n} - ik$ is the complex refractive index of the film material. In the soft x-ray region at nongrazing incidence, we have $|r_t|$, $|r_b| \ll 1$ and Eq. (1a) can be approximated by

$$r_f \approx r_t + r_b e^{-i\Delta} \tag{2}$$

For the case $|r_t| \gg |r_b|$ the absolute value of the amplitude reflectance $|r_f|$ as a function of the film thickness d represents a damped oscillation around an average value $|r_t|$. Surface roughness reduces $|r_t|$ over that of a perfectly smooth surface; the value of $|r_t|$ decreases if the surface becomes rougher during the deposition, which results in a reduction of the mean value in the observed curve of reflected amplitude ($= \sqrt{R}$) versus thickness. An effective rms surface roughness σ can be determined from

$$|r_t| = |r_{to}| \exp[(2\pi\sigma \cos\alpha)/\lambda]^2 \tag{3}$$

where α is the angle of incidence and $|r_{to}|$ is the extrapolated value of the amplitude reflectance for zero thickness.

The sensitivity of the method can be selected by a proper choice of x-ray wavelength and angle of incidence. Shorter wavelengths and or angles closer to normal incidence give higher sensitivity for the measurements of very small roughnesses. However, because the reflectivity of all materials decreases with decreasing wavelength, smaller signals are obtained for the highest sensitivity. We obtain reflected signals around 1000 photons/sec for characteristic soft x-ray sources ($\lambda = 4.5$ or 6.7 nm) at angles of incidence around 60°. With these parameters, we can determine roughness changes of around 0.2 nm with good signal-to-noise ratio for deposition rates up to about 100 Å/min. Figure 1 shows the measured reflected amplitude, and the roughness calculated from the
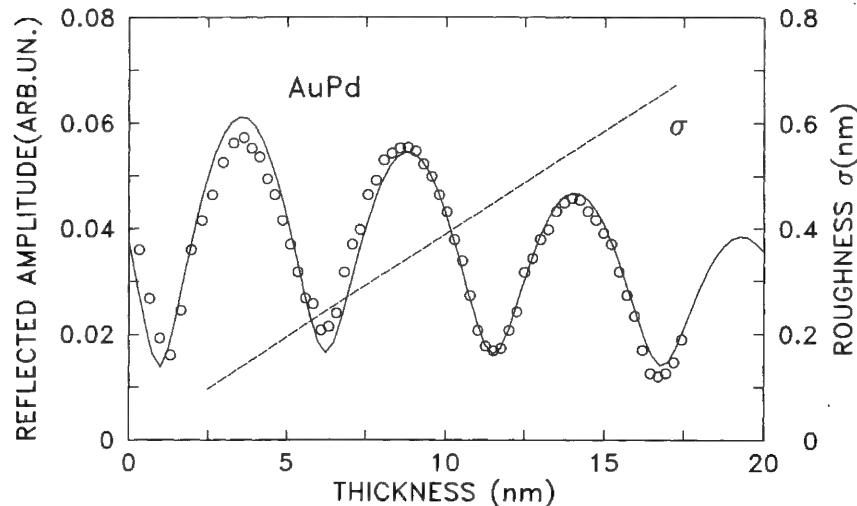
FIG. 1.--Measured (circles) and calculated (full curve) reflected amplitude (arbitrary units) and roughness (nm) of AuPd film vs film thickness. Film thickness was derived from mass thickness as measured with quartz oscillator; 25% lower density for the first 3 nm was necessary to fit the data. Effective roughness of top surface is calculated from decrease in average reflected amplitude. Reflected amplitude is measured for soft x-rays (wavelength, 4.5 nm; angle of incidence $\alpha = 64°$); absorption index k = 0.0055 is used for calculated curve.

reflected amplitude, for an AuPd film. Similar measurements were made for all the metal films examined. The roughnesses are given in the figure captions of the micrographs of the metal films.

Electron Microscopy

The SEM used for this examination has been described previously.[9] The final lens is of the condenser-objective type and has a minimum focal length of 0.8 mm at 50 kV. For this study, both sintered and single-crystal LaB_6 cathodes were used with brightnesses between 5×10^6 and 10^7 A/cm^2ster at 50 kV. Brightnesses were measured by means of the Kohler illumination mode.[10] Beam currents between 10^{-11} and 10^{-10} amp were used for the surface micrographs. Beam diameters were between 0.8 and 1.5 nm. In all cases, STEM micrographs were 'sharper' than surface micrographs obtained with the identical electron beam; the definition in the surface images is evidently set by the electron interaction volume in the sample and not by the diameter of the electron probe.

For surface microscopy, the sample is placed exactly at the center of the polepiece gap. The first half of the magnetic field focuses the beam onto the sample; the second half redirects the scattered electrons back parallel to the axis of the lens so that they pass on to the electron detector. The detector is a plastic scintillator 1 cm in diameter placed 8 cm below the final lens. The surface of the sample is oriented at 20° to the direction of the incident beam. Incident electrons must be therefore scattered through at least this angle in order to pass around the sample edge. Such scattering angles cannot be produced by the lower diffraction orders and contrast is dominated by surface topography. Topographical contrast is assumed to be due to changes in the scattered signal that arise from variations in the local angle of incidence of the beam with the surface. We have observed that steps on the surface produce particularly strong contrast. When the beam is incident on the region above the step, there is a significant increase or decrease in the scattered signal according to whether the step is downward or upward. Such step contrast is treated theoretically by O. C. Wells in this proceedings.[11]

The filter used to obtain the true "low-loss" images, described previously,[12] is a retarding mesh filter with a large acceptance area (~ 1cm diam.) and a resolution of ~400 V.

For the STEM observations, the metal films were deposited on silicon nitride membrane substrates. The films were deposited at the same time as the surface microscopy samples were deposited. The silicon nitride membrane substrates are made from silicon nitride-coated silicon wafers by selective etching of holes through the silicon with an anisotropic etchant. The etchant stops at the silicon nitride and leaves the 30nm-thick nitride membrane covering the hole. For the STEM micrographs shown here, the detector acceptance angle was set to be approximately equal to the illumination angle.

Results

Figure 2 shows surface micrographs of Au, Re, AuPd, PtIr, W, and ReW films. The roughness estimated from the x-ray measurements is given in the figure captions. Some surface roughness is visible in all the micrographs, which shows that this SEM method can detect surface topography of a few tenths of a nanometer. We have found repeatedly that the smoothest films are ReW, although W films appear satisfactory for most surface microscopy applications. Although the ReW films are very smooth, some structure remains visible even in thinner films. For example, Fig. 3 shows the surface of a 9nm-thick ReW film coated onto a freshly cleaved NaCl crystal. Of the more commonly used coating materials, AuPd provides the smoothest coating; however, the residual structure still limits the effective resolution of this method.[3] Pure Au films are quite unacceptable even in very thin layers (see, for example Fig. 4, which shows a 20Å-thick Au layer).

The advantage of using the retarding-field filter for samples of moderate atomic weight is illustrated in the micrographs of a portion of a silicon integrated circuit (Fig. 5). The micrographs show aluminum interconnection wires passing over layers of polysilicon and silicon. The filter reduces flairing and increases the contrast from the surface perturbations.

Figure 6 (STEM micrographs of 18, 6, and 3nm-thick ReW films) shows how the structure in the films becomes finer as the film thickness is reduced.
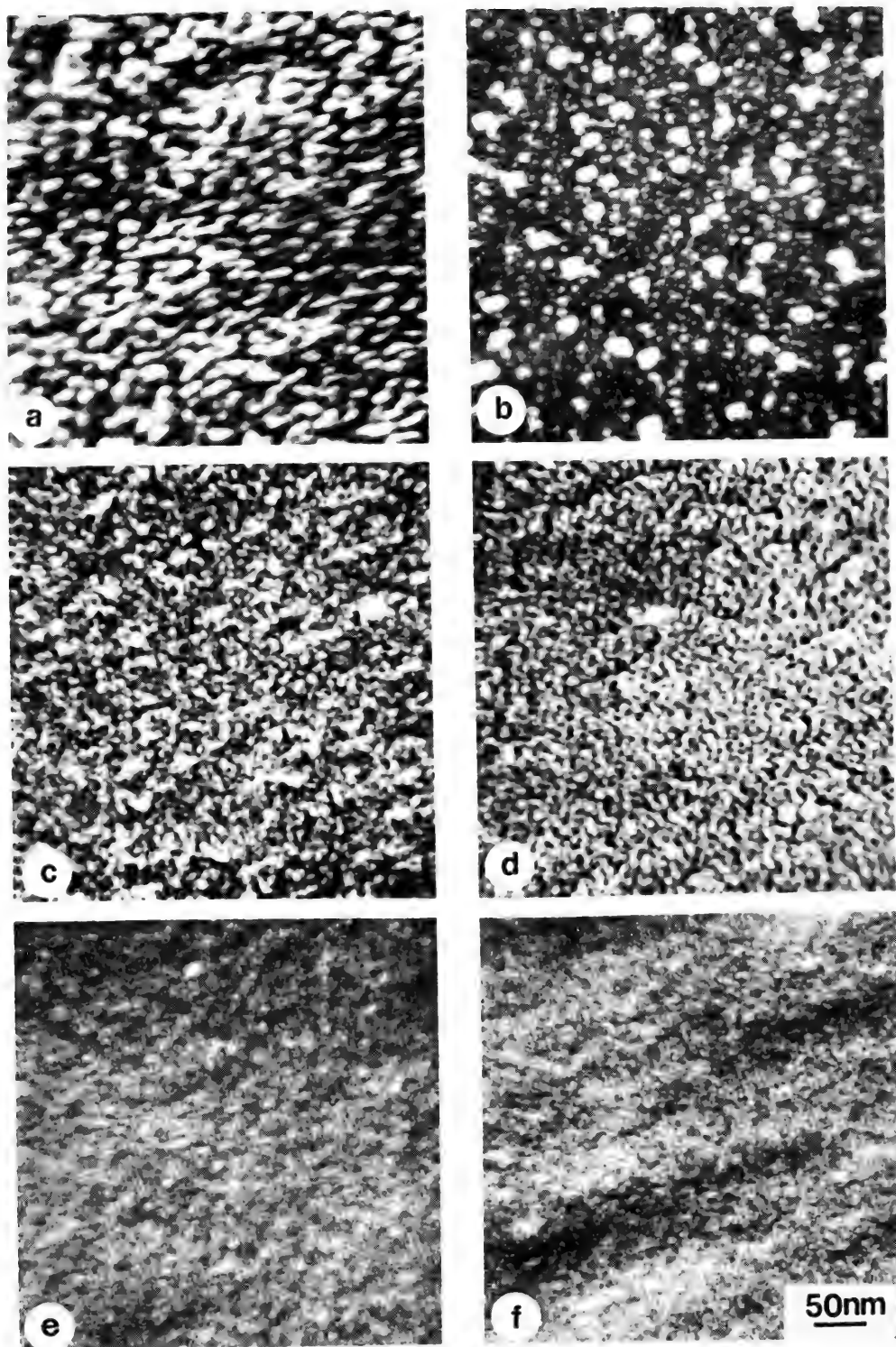
FIG. 2.--High-resolution surface SEM micrographs of 18nm-thick metal films; measured effective surface roughness is shown in parenthesis: (a) Au (1.1 nm), (b) Re (0.75 nm), (c) PtIr (1.05 nm), (d) AuPd (0.6 nm), (e) W (0.55 nm), (f) ReW (0.46 nm).
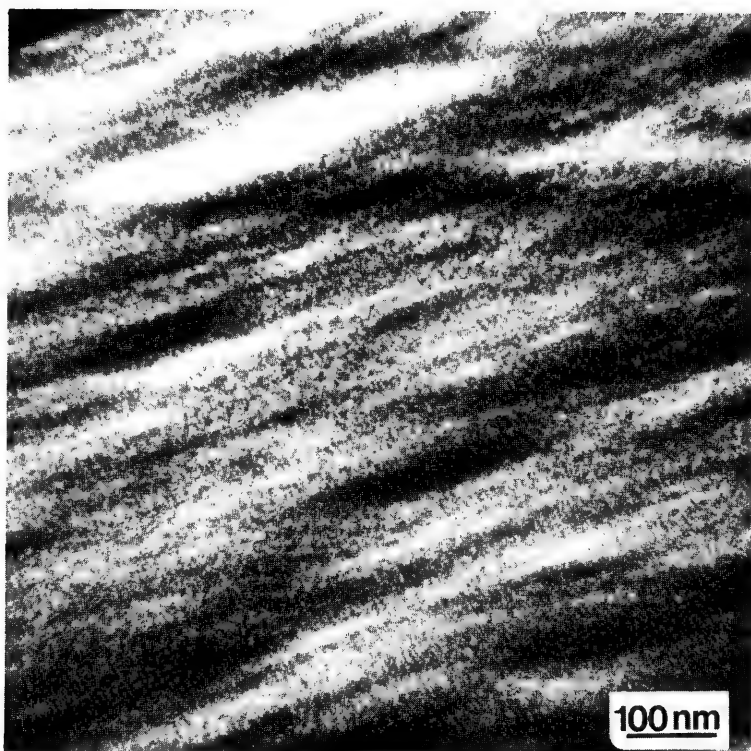
FIG. 3.--Surface of 9nm-thick ReW (68% Re) film deposited on freshly cleaved NaCl crystal. Structure is visible in film although its roughness is estimated from measurements of similar ReW films on silicon substrates to be only about 0.25 nm.
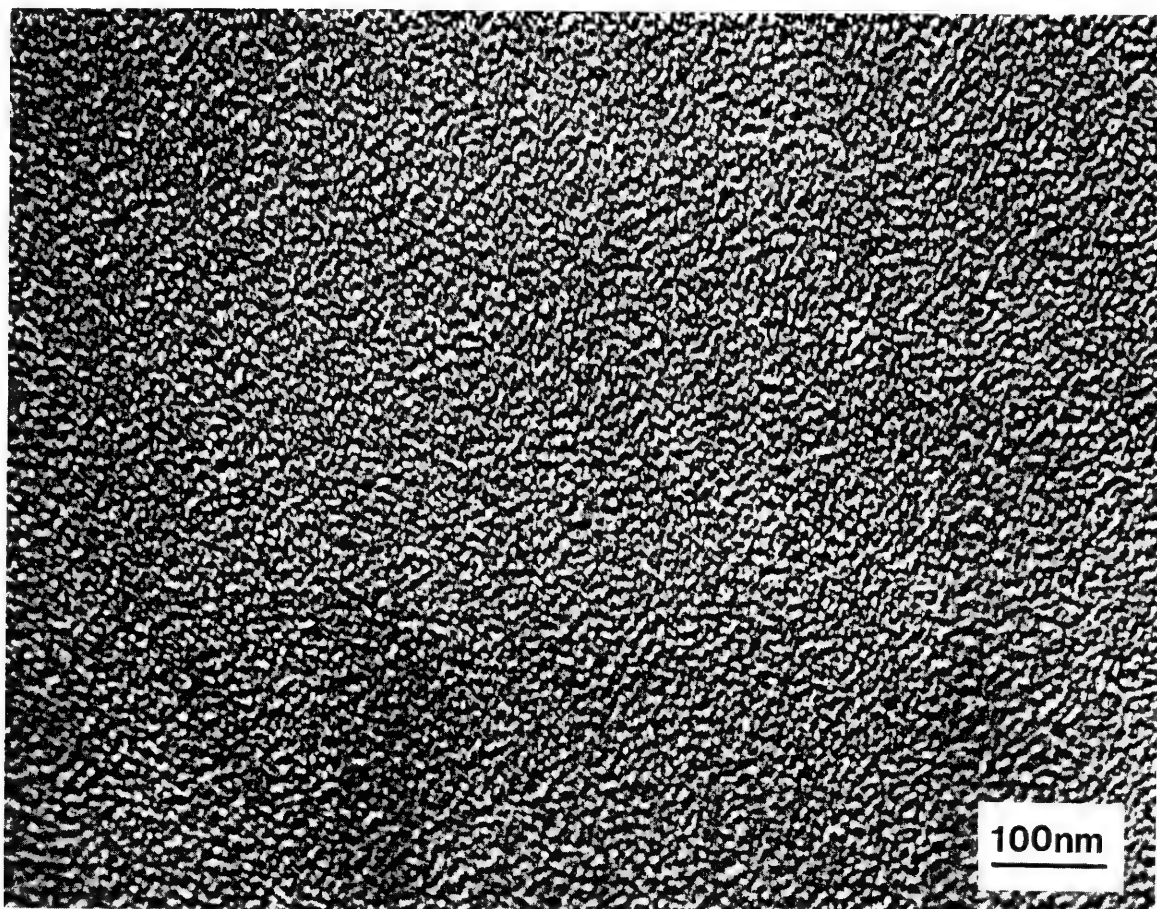
FIG. 4.--Surface micrograph of 2.5nm-thick gold layer on <100> silicon wafer.
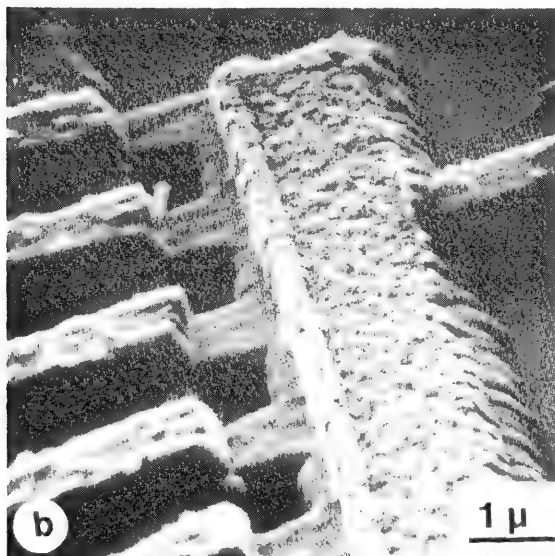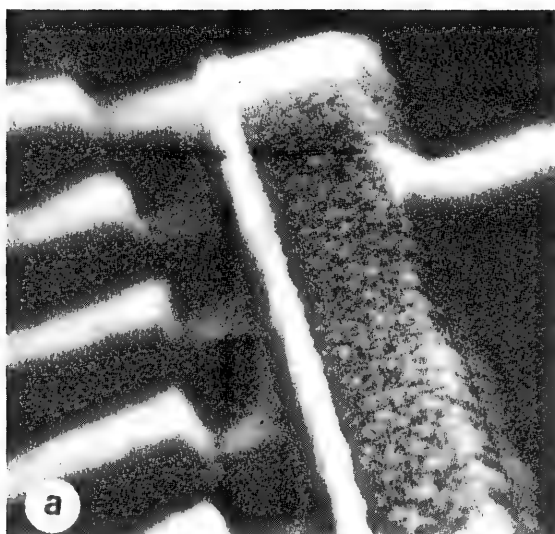
FIG. 5.--Surface micrographs of portion
of silicon integrated circuit showing
aluminum interconnection wires passing
over polysilicon and silicon dioxide
layers: (a) image without filtering sig-
nal reaching detector; (b) image when
retarding field filter is used to filter
out electrons that have lost more than
about 400 eV.
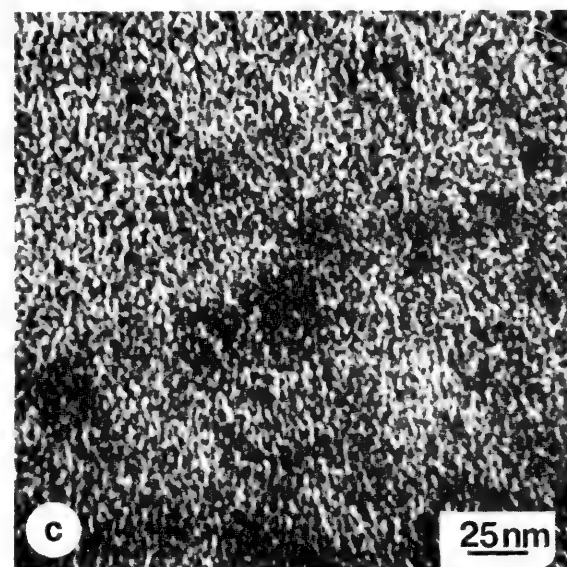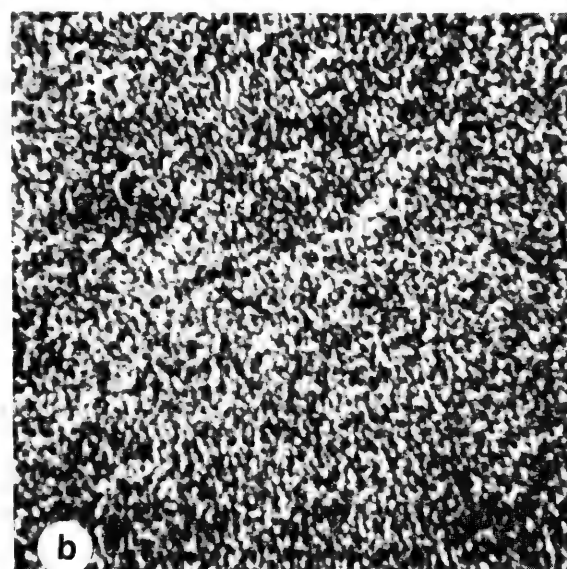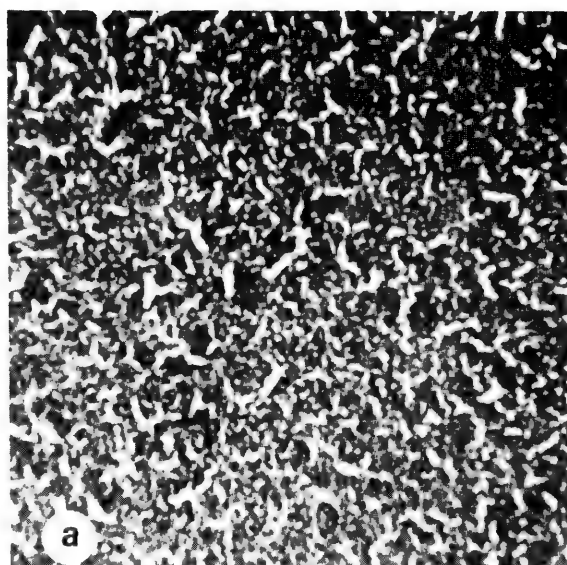
FIG. 6.--STEM micrographs of ReW (68% Re)
films. Measured effective surface rough-
ness is given in parenthesis. Thicknesses
are as follows: (a) 18 nm (0.46 nm), (b)
6 nm (0.27 nm), (c) 3 nm (0.18 nm).

References

1. W. Krakow and A. N. Broers, "High resolution low-loss microscopy of crystalline surfaces," *38th Annual EMSA Proc.*, 1980 (to be published).

2. O. C. Wells, A. N. Broers, and C. G. Bremer, "Method for examining solid specimens with improved resolution in the scanning electron microscope (SEM," *Appl. Phys. Lett.* 23: 353-355, 1973.

3. A. N. Broers, B. J. Panessa, and J. F. Gennaro Jr., "High-resolution scanning electron microscopy of bacteriophages 3C and T4," *Science* 189: 637, 1975.

4. T. Nagatani, and M. Saito, *SEM/1974*.

5. P. Echlin, "Coating techniques for scanning electron microscopy and x-ray microanalysis," *SEM/1978/I*, 109-132; P. Echlin and G. Kaye, *SEM/1979/II*, 21-30.

6. P. Echlin, A. N. Broers, and W. Gee, "Improved resolution of sputter-coated metal films," *SEM/1980* (to be published).

7. K. R. Peters, "Scanning electron microscopy at macromolecular resolution in low energy mode on biological samples coated with ultra-thin metal films," *SEM/1979/II*, 133-148.

8. E. Munro, "The mechanism of surface-image formation in a condenser-objective lens using low-loss scattered electrons," Proc. 8th Intern. Cong. Electron Microscopy, 1974/I, 218-219.

9. A. N. Broers, "High resolution thermionic cathode scanning transmission electron microscope," *Appl. Phys. Lett.* 22: 610-612, 1973.

10. A. N. Broers, "Thermal cathode illumination systems for round beam electron probe systems," *SEM/1979/I*, 1-9.

11. O. C. Wells, "Simplified model for the scattering of low-loss electrons from an amorphous or single-crystal solid target in the scanning electron microscope," *Microbeam Analysis--1980*, San Francisco: San Francisco Press, 1980, 17.

LOW-LOSS ELECTRON IMAGES AND THEIR APPLICATIONS IN InP AND GaAs DEVICE PROCESSING

Aristos Christou

Low-loss electron (LLE) images obtained by filtering out of the slower backscattered electrons results in a line to line resolution of better than 200 Å and a depth perception of better than 100 Å. Auger imaging in an SEM results in line to line resolution of approximately 2000 Å and a depth resolution of 10-20 Å depending on the Auger energy analyzed. Low-loss images can reveal substrate surface texture since the image contrasts from surface details smaller than 200 Å are considerably stronger in the low-loss image than in the secondary-electron image. The substrate surface texture observed with LL electrons can be chemically analyzed and mapped by an increase in the working distance to 20 mm and use of a 20mm-diameter clyindrical mirror analyzer in conjunction with the SEM primary beam in order to obtain an Auger image of the surface texture.

In the present paper, we review techniques for applying LLE and Auger imaging to semiconductor wafer screening and to general materials problems.[1] The low-loss images were obtained with a two-grid filter with a voltage resolution of 3-5%, and 200 to 400V energy loss. The accelerating potential was 15 kV. The techniques for obtaining Auger images have been presented previously. LLE images of Si wafers have identified surface defects previously undetected by secondary-electron microscopy. These defects, directly related to wafer process control, include swirls, striations, edge dislocations and impurity segregations. Direct correlation between LLE and Auger images has been obtained for swirls and impurity segregations near the surface.

Experimental Set-up

In the case of GaAs substrates, defects related to chemical impurities and uncontrolled surface oxides have been studied in detail. In each case, a correlation between LLE images and Auger images has been obtained where the latter identifies the associated elements. Surface oxides on GaAs can be detected topographically in LLE images and further identified by elemental distribution in Auger images. A single-collector system for low-loss electrons was used in the present work that consists of a conventional scintillator-light pipe-photomultiplier detector but with three grids between the detector and the specimen. The grid closest to the scintillator was held at or near the potential of the second grid. The middle grid acts as the filter for removing the inelastically scattered primary electrons.

Experimental Results

Figures 1 and 2 show typical surface defects on GaAs surfaces detected by low loss electrons. These defects are 50-100 Å in depth and cannot be imaged by secondary-electron microscopy. Similar defects introduced by field-effect transistor processing have been analyzed for InP. In addition, surface oxides (InO) on InP have been studied as a function of desorption temperature. Changes in surface stoichiometry as a function of in-situ desorption temperature can be directly imaged with low-loss electrons. These variations, which occur over a depth of up to 100 Å, directly affect microwave and millimeter-wave device performance.

Two basic problems with GaAs wafer processing are the presence of oxides and sulfur contamination on GaAs surfaces. In the present work, the epitaxial GaAs was surface treated by a 2min acetone, methanol rinse followed by a concentrated HCl etch for 2 min. The adsorption of sulfur on GaAs is shown in Fig. 1. The Auger image was taken at an energy of 150 eV corresponding to the sulfur Auger transition. There is a one-to-one correlation between the Auger and low-loss images. The Auger spectrum of the sulfur containing region is shown in Fig. 1 and also indicates the presence of S, Cl, C, and O on the surface. The Auger-low loss correlation was only obtained with the sulfur transi-

---

The author is with the Naval Research Laboratory, Code 6815, Washington, DC 20375.

tion. In the case of surface oxides on GaAs, attempts to desorb them at 10^{-8} Torr and 575°C often result in an irregular surface owing to loss of arsenic. The contrast variation in the low loss images of such surfaces is then due to a lateral inhomogeneity in the GaAs native oxide, which causes both a variation in oxygen concentration and stoichiometry.

The advantage of low-loss images in the study of GaAs and InP surface defects is directly related to the short normal penetration depth for GaAs and InP. The normal penetration depth can be calculated by means of a steplike transmission function F(E) and an energy resolution of 1-2%. The total energy loss is proportional to the total electron penetration times the Bethe loss function. Figure 3 shows that the normal penetration depth can be made to vary between 25 and 50 Å for Ga As, so that LLE images are ideal for the study of surface characteristics of III-V semiconductor compounds.

References

1. A. Christou, *SEM/1977/I*, 159; International Summer School and Conference in Electron and Ion Beams, Spetses, Greece, 1977; "Electron collector for forming low loss images," U.S. Patent 4 179 604, 1979; First Athens Conference on Electron Microscopy and Microanalysis, Athens, 1978.
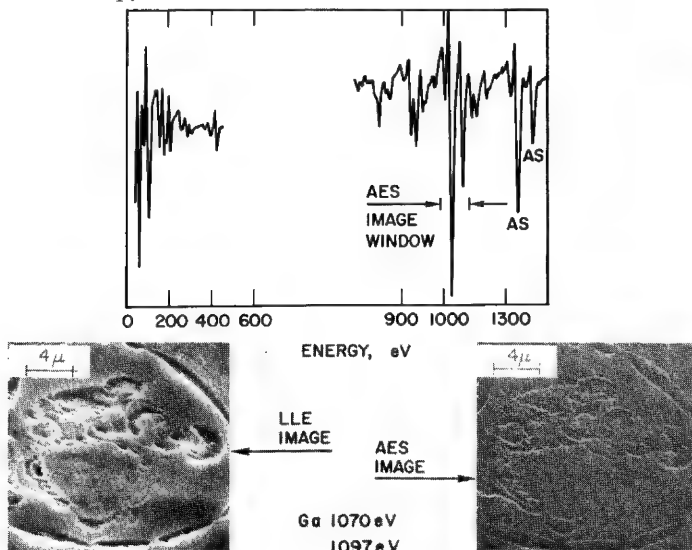
FIG. 1.--AES and LLE images of sulfur contamination on a GaAs substrate.
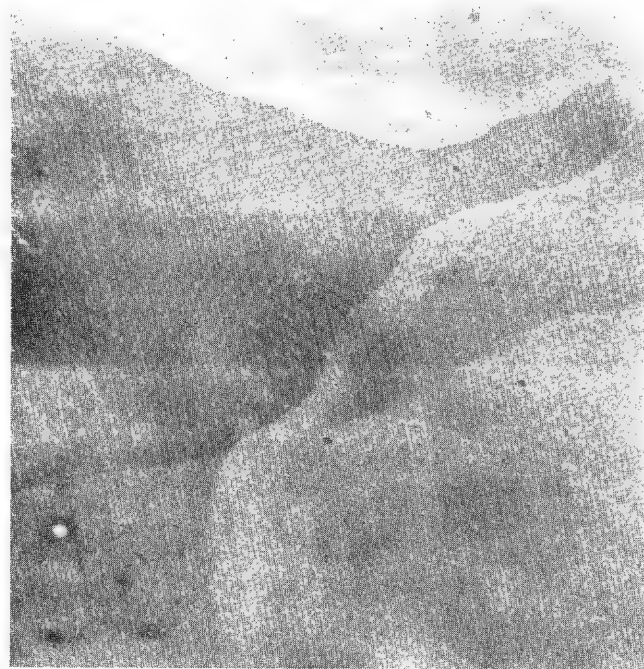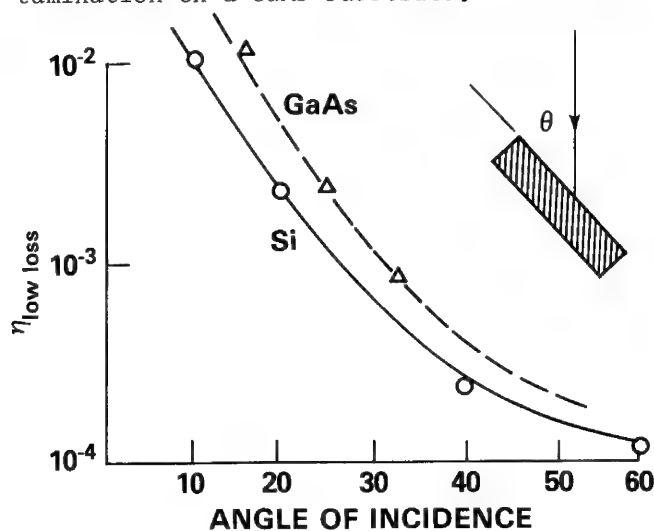
FIG. 2.--LLE image of GaAs surface showing variation in oxide formation.
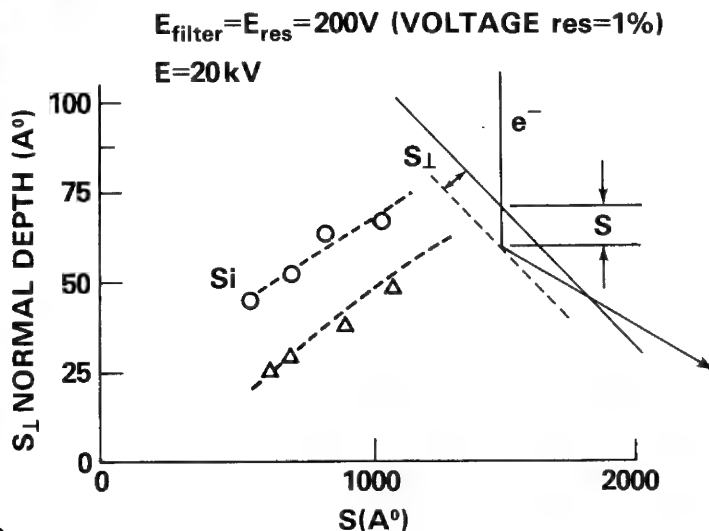
FIG. 3.--Electron penetration curves for Si and GaAs, and backscatter electron curves for low-loss electrons.

4

Quantitative Analysis

CONCERNING X-RAY PRODUCTION AND QUANTITATIVE ANALYSIS

R. H. Packwood and J. D. Brown

For a number of experimentally measured $\phi(\rho z)$ curves, plotting $\ln(\phi(\rho z))$ against $(\rho z)^2$ rather than ρz itself leads to rather remarkable straight lines (Fig. 1). These plots suggest that the $\phi(\rho z)$ curves can be described by a Gaussian $\phi \propto \exp(-\alpha^2(\rho z)^2)$ with the maximum of the Gaussian at the origin ($\rho z = 0$) and the value of α related to the slope of the straight line portion of the curve. Wittry[1] and Kyser[2] had used a Gaussian in an attempt to fit $\phi(\rho z)$ curves to an analytical expression but fitted the maximum of the Gaussian to the maximum in the $\phi(\rho z)$ expression.

In searching for an explanation of the Gaussian dependence of x-ray generation on depth, an analytic expression describing the random-walk approach used in the Monte Carlo calculations of x-ray production was derived. This approach predicts a Gaussian dependence as a function of depth starting from the surface. The deviations from this Gaussian behavior result from the initial conditions of a finely focused beam in which the electrons are traveling perpendicular to the sample surface in one direction. The decreased x-ray production near the surface is a result of the lack of randomization of the electron paths near the surface. An exponential function adequately describes this near-surface behavior so that the entire $\phi(\rho z)$ curve is given by

$$\phi(\rho z) = \gamma_0 e^{-\alpha^2(\rho z)^2}(1 - q e^{-\beta \rho z})$$

The values of α and β have been derived starting from a screened Rutherford scattering cross section[3] and are

$$\alpha = 1.37 \times 10^5 \frac{Z}{A} \frac{Z^{0.16}}{E_0(E_0 - E_c)^{0.5}} \ln[1.166(E_0/J)]^{0.5}$$

$$\beta \simeq 3.5 \times 10^4 \frac{Z^2}{AE_0^2}$$

The values of γ_0 can be shown to lie between $\pi/2$ and π on the basis of a simple backscattering argument; q can be calculated from

$$q = 1 - \frac{\phi(0)}{\gamma_0}$$

The significance of these constants in the calculation of $\phi(\rho z)$ is shown in Fig. 2.

A Simplex procedure was used to fit this formula to the measured $\phi(\rho z)$ data of Brown and Parobek[4] starting from assumed values for the four parameters obtained for the first curves from rough plots, then later by small adjustments of these values. The values of γ_0 and q were constrained to fall within the limits theoretically derived since in perhaps 5% of the total number of curves (which numbered about 200) very large values were obtained for γ_0 and the value of q was close to 1 for an unconstrained fit.

Table 1 gives a comparison of the theoretically derived values of α and the simplex best fit values for some of the low energy curves. Figures 3 and 4 show the fit to the

---

Author Packwood is with the Department of Energy, Mines and Resources, Ottawa, Ontario, Canada; Prof. Brown is with the Faculty of Engineering Science and the Centre for Interdisciplinary Studies in Chemical Physics, University of Western Ontario, London, Ontario, Canada N6A 5B9.
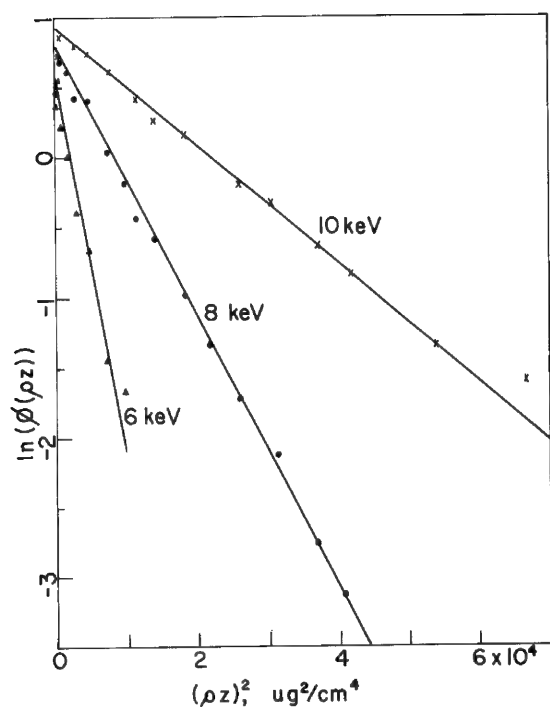
FIG. 1.--Linear relationship between $\ln[\phi(\rho z)]$ and $(\rho z)^2$ for SiKα line in nickel matrix for three electron energies.
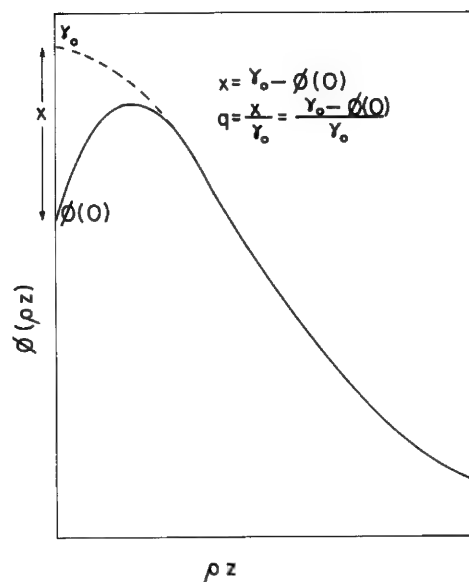
FIG. 2.--Schematic representation of a $\phi(\rho z)$ curve and extrapolated Gaussian showing origin of γ_0 and q.
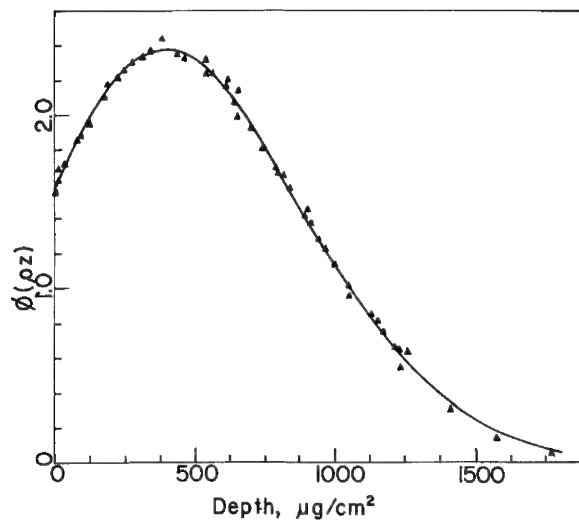
FIG. 3.--$\phi(\rho z)$ curve for CdLα line in aluminum at 30keV electron energy. Points are from Brown and Parobek and curve is best fit to Gaussian expression.
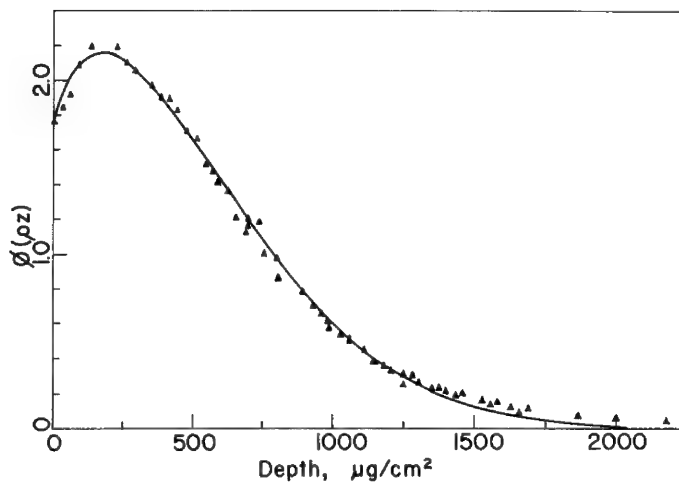
FIG. 4.--Same as Fig. 3 but for ZnKα line in silver matrix. Note that all experimental points lie above calculated curve in tail of curve.

TABLE 1.--Comparison of the values of α obtained from a theoretical expression (T) and from best fits to experimental data (M) for several $\phi(\rho z)$ curves.

	Low Electron Energies, Si Tracer (SiKα)					
	α Coefficients ($\times 10^4$)					
Matrix	6 keV		8 keV		10 keV	
	T	M	T	M	T	M
Al	1.56	1.79	1.01	1.08	0.72	0.65
Ni	1.60	1.72	1.04	0.98	0.74	0.65
Ag	1.47	1.40	0.96	0.83	0.69	0.58
Au	1.33	1.11	0.87	0.71	0.63	0.51

	25 keV Electron Energy			
	α Coefficients ($\times 10^3$)			
Matrix	Cd tracer (CdLα)		Zn tracer (ZnKα)	
	T	M	T	M
Al	2.00	1.69	2.30	1.86
Cu	1.99	1.41	2.33	1.68
Ag	1.94	1.41	2.27	1.70
Au	1.82	1.51	2.14	1.49

experimental curves in a situation of low matrix Z and low energy characteristic x ray where production from the continuum is not important and in a high Z matrix where it is important. The poor fit in the tail of the latter curve shows clearly that the Gaussian expression applies only to x rays directly excited by electrons. The conclusion one can draw is that the Gaussian function can accurately describe the experimental data of x-ray production as a function of depth.

For quantitative analysis, in the absence of fluorescence effects, the intensity ratio

$$K_A = W_A \frac{\int_0^\infty \phi_A(\rho z) e^{-\chi_A \rho z} d(\rho z)}{\int_0^\infty \phi_S(\rho z) e^{-\chi_S \rho z} d(\rho z)}$$

where W_A is weight fraction of element A in the unknown, χ is the absorption factor $\mu \csc \psi$ (where ψ is the x-ray take-off angle), and $\phi_A(\rho z)$ and $\phi_S(\rho z)$ are the depth distributions of x-ray production/unit concentration in the unknown and pure element standard, respectively. This expression includes both absorption and atomic number corrections.

On substituting the Gaussian expression for $\phi(\rho z)$ and integrating, we obtain[6]

$$K_A = W_A \ \frac{\gamma_{OA}}{\gamma_{OS}} \ \sqrt{\frac{\alpha_S}{\alpha_A}} \ \frac{e^{\chi_A^2/4\alpha_A} \ \mathrm{erfc}\left(\dfrac{\chi_A}{2\sqrt{\alpha_A}}\right) - q_A e^{(\beta_A+\chi_A)^2/4\alpha_A} \ \mathrm{erfc}\left(\dfrac{\beta_A+\chi_A}{2\sqrt{\alpha_A}}\right)}{e^{\chi_S^2/4\alpha_S} \ \mathrm{erfc}\left(\dfrac{\chi_S}{2\sqrt{\alpha_S}}\right) - q_S e^{(\beta_S+\chi_S)^2/4\alpha_S} \ \mathrm{erfc}\left(\dfrac{\beta_S+\chi_S}{2\sqrt{\alpha_S}}\right)}$$

where erfc(x) is the complementary error function which is easily approximated by a simple polynomial expression.[5] This equation, which can be programmed easily, puts quantitative electron probe microanalysis on a sound theoretical and experimental basis.

References

1. D. B. Wittry, *J. Appl. Phys.* 29: 1543, 1958.
2. D. F. Kyser, in G. Shinoda, K. Kohra, T. Ichinokawa, Eds., *X-ray Optics and Microanalysis*, Tokyo: University of Tokyo Press, 1972, p. 147.
3. D. E. Newbury and R. L. Myklebust, *Ultramicroscopy* 3: 391, 1979.
4. J. D. Brown and L. Parobek, in Ref. 3, p. 163; J. D. Brown and L. Parobek, *X-Ray Spectrometry* 5: 36, 1976.
5. C. Hastings Jr., *Approximations for Digital Computers*, Princeton, N.J.: Princeton University Press, 1955.
6. K. Milliken, private communication.

BACKSCATTER LOSS IN THE X-RAY CONTINUUM

R. L. Myklebust, D. E. Newbury and J. A. Small

The quantitative analysis of small particles and irregular surfaces in an electron micro-probe or scanning electron microscope has many applications. One method of correcting the x-ray data for particle size effects or for variations due to nonflat surfaces is to make use of the continuum x-ray intensity as a measure of mass of the volume of x-ray generation. This technique has been employed by several authors in conjunction with standard quantitative analysis methods.[1,2]

The peak-to-background method requires knowledge of the x-ray continuum intensities generated at the same energies as the characteristic x-ray peaks needed for the quantitative analysis computations. We have made measurements of the continuum intensities on a large number of elements at several beam energies (5-30 keV, continuum energy 1-10 keV).[3] Before one attempts to fit an empirical expression to the continuum intensities as a function of atomic number, the intensities measured must be corrected for absorption in the specimen and detector components and should be corrected for loss due to electron backscattering.

The NBS Monte Carlo program for computing electron trajectories and generated x rays was used to calculate the continuum x-ray loss due to backscatter in a variety of materials. The continuum x-ray generation cross section of Kirkpatrick and Wiedmann[4] was employed to compute both the continuum x rays generated in the specimen and the continuum x rays that would have been generated by the backscattered electrons if those electrons had remained in the specimen. The fraction of x rays generated within the specimen, R(continuum), was then calculated for each of the continuum energies. The NBS Monte Carlo program is capable of calculating the x-ray continuum intensity at five different energies each time the program is run. The calculation required a considerable amount of time, so that it was not practical to attempt to compute the entire continuum. Selected energies of 1.5, 2.6, 4.6, 7.6, and 8.7 keV were used.

The R(continuum) values obtained agree with the analytic calculations of Rao-Sahib and Wittry[5] as shown in Fig. 1. The Monte Carlo program also confirmed these authors' observation that the x-ray continuum from thick targets may be considered as isotropic over a wide range of Z, but not for small particles, where high-energy electrons are lost through the bottom of the particle. We have observed, in this case, that there is a change in the shape of the x-ray continuum as compared to a polished flat specimen.[6,7] This change in shape does not appear to be related to the excitation volume or the x-ray absorption within the particle.

The largest discrepancy between the Monte Carlo results and the calculations of Rao-Sahib and Wittry was for gold at X = 0.1, where the Monte Carlo data were 4% lower. The Monte Carlo data deviated below the analytic calculations at high atomic number. Additional calculations for elements of high atomic number will be required to determine the origin of this difference.

The Monte Carlo program computes the x-ray absorption within a specimen from the excitation positions within the target and not from a function that requires knowledge of the depth distribution of x-ray excitation. These absorption factors differed by no more than 7% from the absorption factors calculated for characteristic x rays of the same energy. The absorption of the continuum was always slightly more than for a corresponding characteristic x-ray energy.

We have fitted an empirical expression to the data of Rao-Sahib and Wittry[5] that reproduces their table of R(continuum) with an accuracy better than ±2%. A plot of R(continuum) versus Z is shown in Fig. 2, together with some of the Monte Carlo results. The expression is a function of atomic number (Z) and overvoltage (U):

The authors are members of the Microanalysis Group, Center for Analytical Chemistry, National Bureau of Standards, Washington, DC 20234.

$$R(\text{continuum}) = AZ^2 - BZ + C$$

where A, B, and C are defined as follows:

$$A = [1 - \exp(0.361413X^2 + 0.288563X - 0.619466)]10^{-4}$$

$$B = [1 - \exp(0.152782X^2 + 2.04255X - 2.17326)]10^{-2}$$

$$C = 1.00257 + 0.0406679X \quad \text{for } X < 0.7$$

$$C = 1.017 \quad\quad\quad\quad\quad\quad \text{for } X > 0.7$$

The above equations were used to predict the R(continuum) at the x-ray energies measured for a large number of pure elements. Figure 3 is a plot of x rays generated within a pure element target for one x-ray energy at 20KeV beam voltage as a function of atomic number and the same data divided by R(continuum). The corrected data follow a straight line in this case. That may not always be the situation; however, the continuum intensity appears to be a fairly simple function of atomic number at a fixed overvoltage after correction for the intensities for R(continuum).
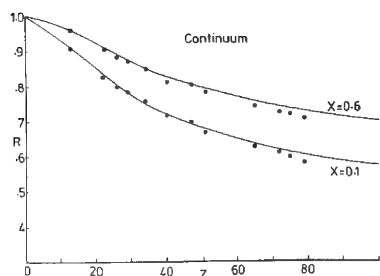
FIG. 1.--R(continuum) vs atomic number for two overvoltages. Curves are from Ref. 5; points are calculated from the NBS Monte Carlo program; X = 1/U.
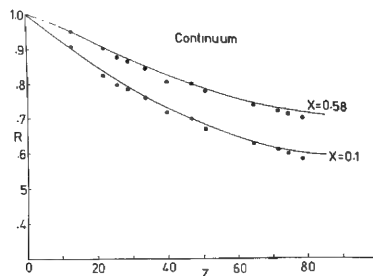
FIG. 2.--R(continuum) vs atomic number for two overvoltages. Curves are empirical fit to data from Ref. 5, points are calculated from the NBS Monte Carlo program.
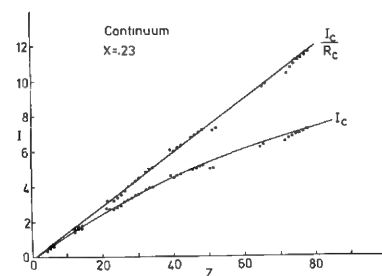
FIG. 3.--Continuum intensity generated at 4.6 keV by a 20 keV electron beam vs atomic number. Both the generated intensity and the generated intensity divided by R(continuum) are shown.

References

1. J. A. Small et al., "The production and characterization of glass fibers and spheres for microanalysis," in O. Johari, Ed., *Proc. 11th SEM Symposium*, Los Angeles, 1978, 445.
2. P. J. Statham and J. B. Pawley, "A new method for particle x-ray microanalysis based on peak-to-background measurements," *Ibid.*, 469.
3. J. A. Small et al., to be published, 1980.
4. P. Kirkpatrick and L. Wiedmann, "Theoretical continuous x-ray energy and polarization," *Phys. Rev.* 67: 321, 1945.
5. T. S. Rao-Sahib and D. B. Wittry, "The x-ray continuum from thick targets," *Proc. 6th ICXOM*, Osaka, Japan, 1971, 131.
6. J. A. Small et al., "Progress in quantitation of single-particle analysis with the electron probe," *Proc. 13th MAS Conf.*, 1978, 56-A.
7. J. A. Small et al., in O. Johari, Ed., "Progress in the development of the peak-to-background method for the quantitative analysis of single particles with the electron probe," SEM, Inc., 1979, 807.

ON THE CONTINUUM FLUORESCENCE CORRECTION IN THE ANALYSIS OF FILMS

J. D. Kuptsis, F. Cardone, and R. J. Savoy

It is common practice in quantitative electron probe microanalysis to overlook the contribution of continuum fluorescence excitation in the correction scheme. This approximation is frequently permissible if the target is similar in atomic number to the standard and is infinitely thick (over 10 μm) relative to the fluorescence excitation range. Accurate calculations of this continuum contribution are complex and require considerable computer time. Hénoc[1] carried out such calculations and found that as much as 7% of the total x-ray production is due to continuum excitation under typical operating conditions in electron microprobe spectroscopy. Green[2] and others[3-5] have also considered this problem. However, the common procedure in quantitative data reduction is to normalize the x-ray intensities of the sample to the x-ray intensity of the pure element standard (also subject to continuum excitation), which usually corrects for this effect to an acceptable level of accuracy.

On the other hand, if the target under investigation is a film of a thickness larger than the primary production range but considerably smaller than the fluorescence excitation range, normalization of the x-ray intensities to pure "bulk" element standards does not eliminate this problem. Indicative of this problem is the experimental observation that the sum of the weight fractions of all constituents after the correction procedure (excluding continuum excitation) is smaller than unity. Forcing the results to unity by normalization makes the invalid assumption that all elements in the target are equally affected by the continuum excitation process. An alternative and more correct approach we frequently take is to measure the x-ray intensity of the pure element standard in the form of a film of a thickness comparable to the actual sample. Deviations from unity after concentration summation are much smaller but the work that is involved in the preparation of such standard films restricts the general usefulness of this technique. A more practical alternative would be a procedure based on the measurement of pure element bulk standards and the inclusion of a continuum fluorescence correction.

Working toward this goal, we have made a series of measurements on pure element films and on pure element bulk standards.

Experimental Procedure

Two electron probes were used, an ARL-SEMQ and an ARL-EMX-SM (takeoff angle 52.5°). Sets of monoelemental films of Ge and Au were prepared to evaluate the relatively large contributions of indirect production to the total intensities measured for GeKα and AuLα. The films ranged in thickness from less than 0.5 μm to several microns. GeKα (9.89 keV) and AuLα (9.71 keV) are the most energetic K and L lines that we can evaluate in first order and also prepare thin films by evaporation in vacuum. In addition, the same set of films can be used to evaluate GeLα (1.2 keV) and AuMα (2.1 keV); however, these relatively low-energy lines are predicted to have little indirect radiation contribution.

The wavelength-dispersive background-corrected peak intensities were plotted as a ratio of I_B (total intensity from bulk standard) to I_F (total intensity from film). In Figs. 1 and 2, GeKα and AuLα ratios are plotted at fixed accelerating voltages as a function of different thicknesses. The intensity ratios for GeKα and AuLα for varying accelerating voltages on individual films are plotted in Figs. 3 and 4. It can be seen that the contribution of indirect radiation can be as large as 9% and that this value decreases with increasing thickness.

Data were also acquired for films of Si, Ti, Cr, Ni, Nb, Pd, and Ta in order to gain a better understanding of the continuum fluorescence effects as a function of atomic number.

The authors are with the IBM Watson Research Center, Box 218, Yorktown Heights, NY 10598.

Discussion

Work is at present in progress to find a semi-empirical relation that would fit our data and permit the analyst to estimate the size of the continuum correction term. It will be assumed that an estimate of the composition (ZAF procedure) and the thickness are known to the analyst.

References

1. J. Hénoc, in K. F. J. Heinrich, Ed., *Quantitative Electron Probe Microanalysis*, NBS Publication 298: 197, 1968.

2. M. Green, "The angular distribution of characteristic X radiation and its origin within a solid target," *Proc. Phys. Soc.* 83: 435, 1964.

3. R. Castaing and J. DesCamps, "Sur les bases physique de l'analyse ponctuelle par spectrographie X," *J. Physique et Radium* 16: 304, 1955.

4. G. Springer, *Neues Jahrbuch für Mineralogie Abbandlungen,* 106: 241, 1967.

5. K. F. J. Heinrich, "Fluorescence excited by the continuum and the accuracy of electron probe microanalysis," *Proc. 10th MAS Conf.*, paper 1, 1975.
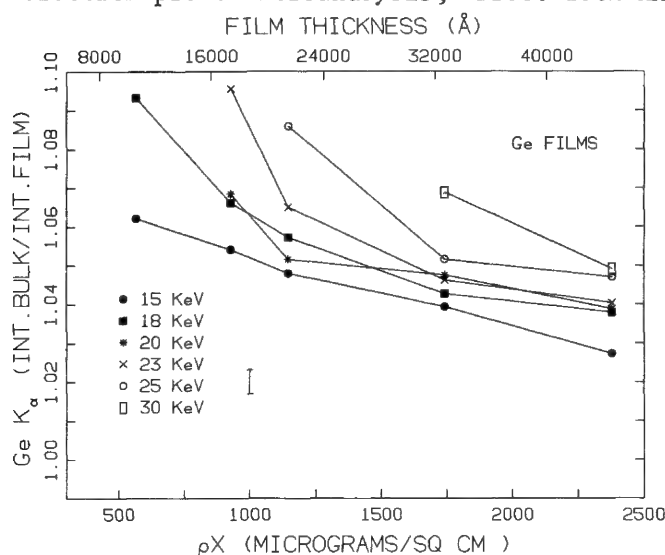
FIG. 1.--Intensity ratio I_B/I_F for Ge Kα at fixed accelerating voltages as function of various thicknesses of Ge.
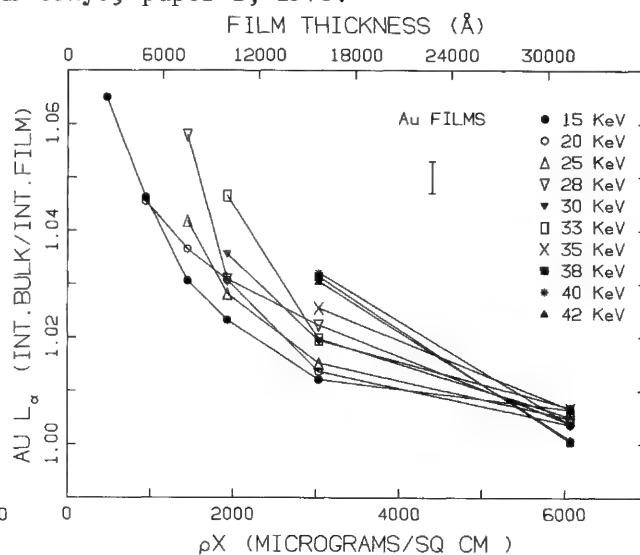
FIG. 2.--Intensity ratio I_B/I_F for Au Lα at fixed accelerating voltages as function of various thicknesses of Au.
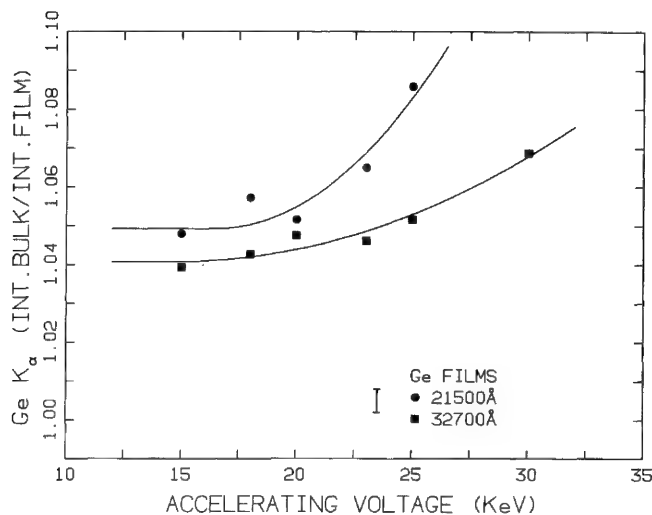
FIG. 3.--Intensity ratio I_B/I_F for Ge Kα for several thicknesses of Ge as function of various accelerating voltages.
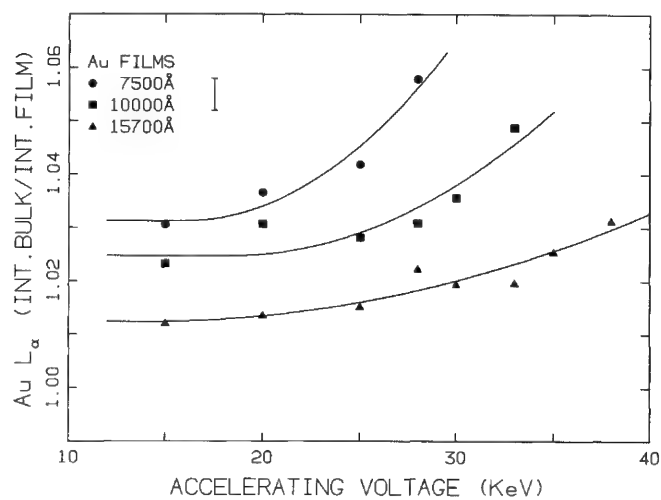
FIG. 4.--Intensity ratio I_B/I_F for Au Lα for several thicknesses of Au as function of various accelerating voltages.

INSTRUMENTAL EFFECTS ON THE GENERATION OF CONTINUUM FROM PURE ELEMENT TARGETS

J. A. Small, D. E. Newbury, and R. L. Myklebust

The quantitative analysis of samples with the various methods based on peak-to-background measurements requires detailed knowledge of the continuum (bremsstrahlung) as a function of specimen and beam parameters.[1,2] In the NBS peak-to-background program, FRAME P, which is currently under development, we would like to use the continuum intensity measured on one pure element standard at a particular energy E_ν to predict the continuum intensity for the various elements of the unknown at all E_ν's of interest. The continuum intensity for the unknown, B_{bulk}, at a given E_ν can then be determined from an estimate of the concentration[3]:

$$B_{bulk} = \sum_i C_i B_{i,e}$$

During the early work on FRAME P, we attempted to use various functions to describe the continuum with respect to the atomic number Z of the target, beam energy E_0, and continuum energy of interest E_ν.[4-6] Since the various functions we tried did not adequately describe the experimentally observed values of continuum intensities, we have been working on an empirical equation relating continuum intensity to Z, E_0, and E_ν. In this paper we discuss a comparison of the continuum intensities from pure-element targets measured on three different electron-beam instruments at two different accelerating voltages. The purpose of this work was to determine whether a single expression relating the continuum to Z, E_0, and E_ν can be applied to various experimental setups.

Of the three electron-beam instruments used in the study, two were electron microprobes with take-off angles of 40 and 52.5°; the third was a scanning electron microscope with a 30° take-off angle. Spectra from polished pure-element targets of C, Al, Ti, Fe, Ge, Nb, Sb, Tb, Ta, Au, and Bi were taken for a live time of 1000 sec at normal beam incidence.

The continuum intensities for five different energy windows 200 eV in width were measured and midpoint energies were used as the E_ν values. Measurements were made at E_ν values of 1.5, 2.6, 4.6, 7.6, and 8.7 keV. The measured intensities were used for the windows where there were no interfering peaks. For the windows where there were interfering peaks, the continuum intensities were determined from the second-order fit used in the analysis procedure FRAME C.[7] All the intensity values were then converted to generated intensities by corrections for specimen absorption and detector efficiency.

To determine whether the Z dependence for the continuum intensity was the same for all three instruments at a given E_0, the intensity values for the various elements determined on a given instrument and at a given E_ν were normalized to the intensity measured on a particular target (e.g., Fe) at the same energy. This normalization compensates for differences in electron dose and geometric efficiency among the three instruments. Figure 1 is a plot of the normalized intensities from the three instruments vs Z at E_ν = 7.6 keV and E_0 = 25 keV. Within experimental uncertainty the points from the three instruments all fall on the same curve. Similar results were also observed for the other energy regions. The Z dependence for the continuum intensity is thus the same for all instruments and can be expressed as a single function.

The second test was to determine whether dependence was the same for the two beam energies, 25 and 17.4 keV. Figure 2 is a plot of the values, again normalized to iron in each set, for instrument 1 plotted vs Z at both 25 and 17.4 keV. The values of the normalized continuum intensities fall nearly on the same curve. The Z dependence of the normalized continuum is thus independent of E_0 to a first approximation, so that the expression derived for 25 keV can also be used to describe the normalized continuum intensity at 17.4 keV. We are currently working on an expression to describe the Z dependence of the continuum intensities after their correction for back-

The authors are at the National Bureau of Standards, Washington, DC 20234.

scattered electron loss.[8]

Z Dependence of Continuum Intensity (Instrument) E_V=7.6 keV E_o=25 keV

instrument 1 = x
" 2 = □
" 3 = ○

$\frac{I_Z}{I_{Fe}}$
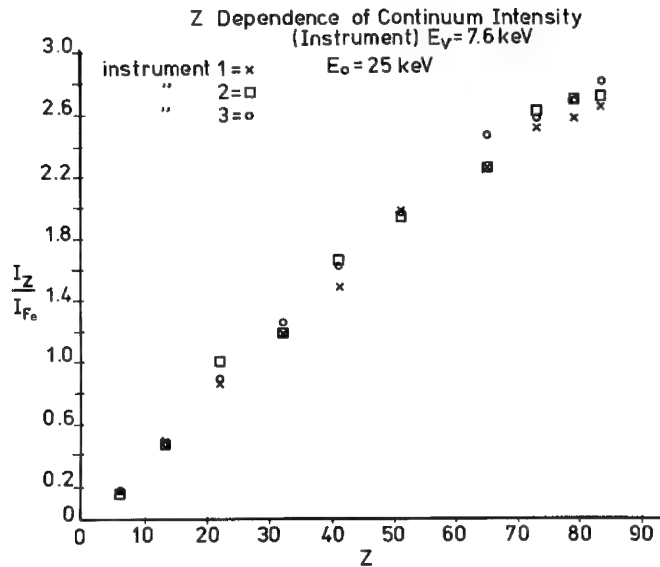
FIG. 1.--Normalized intensities from three instruments vs Z at E_ν = 7.6 and E_0 = 25 keV.

Z Dependence of Continuum Intensity (E_o) E_V=7.6 keV

25 keV = ○
17.4 " = □

$\frac{I_Z}{I_{Fe}}$
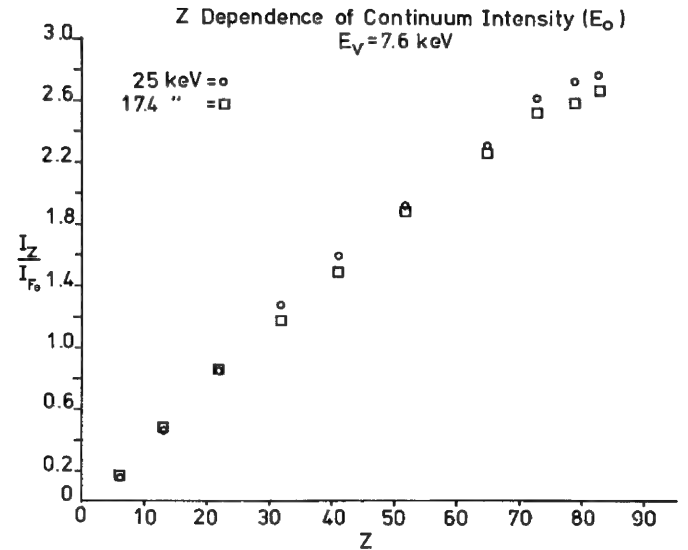
FIG. 2.--Normalized intensities values from instrument 1 vs Z at E_0 = 25 and 17.4 keV.

The final aspect of the continuum we examined was the dependence of the intensity on E_ν. For this work the intensity values for a given element and instrument were normalized to the corresponding value for that element and energy from the run on instrument 1. The results are shown in Fig. 3 for elements 26 and 51 with the values for instrument 1 equal to unity. One would expect the curves for instruments 2 and 3 to be displaced from unity, because of the different electron doses and geometric efficiencies. If all the machines had the same E_ν dependence the curves would be parallel over the energy range. Figure 3 shows that this is not the case. The curve for instrument 2 increases (and that for instrument 3 decreases) with respect to the curve for instrument 1 at higher E_ν values. One possible source of this discrepancy may be a difference in the absolute efficiency of the various detectors over the energy range.

Two conclusions can be drawn from the results of this study. First, it appears that a single expression can be used to describe the Z dependence of the continuum for different experimental set-ups over the range of accelerating voltages 17-25 keV. Second, because the relationship of the continuum to E_ν varies with the instrumental set-up, additional investigation into the correction procedures used to determine continuum intensities is necessary.

E_V Dependence of Continuum Intensity E_o=25 keV

instrument 1

Z = 26 ···○
" " 51 ···□

instrument 3

instrument 2

$\frac{I_{2,3}}{I_1}$

E_V keV

FIG. 3.--Plot of E_ν dependence of continuum elements 26 and 51.

References

1. J. A. Small et al., "The production and characterization of glass fibers and spheres for microanalysis," *SEM/1978/I.*, 445-454.

2. P. Statham and J. Pawley, "A new method for particle x-ray microanalysis based on peak-to-background measurement," *Ibid.*, 469-478.

3. J. A. Small, D. E. Newbury, and R. L. Myklebust, "Analysis of particles and rough surfaces by FRAME P, a ZAF method incorporating peak-to-background measurements," *Microbeam Analysis--1979*, San Francisco: San Francisco Press, 1979, 243.

4. H. A. Kramers, "On the theory of x-ray absorption and the continuous x-ray spectrum," *Phil. Mag.* 48: 836, 1923.

5. D. G. W. Smith, C. M. Gold, and D. A. Tomlinson, "The atomic number dependence of the x-ray continuum intensity and the practical calculation of the background in energy dispersive electron microprobe analysis," *X-ray Spectroscopy* 4: 149, 1975.

6. P. J. Statham, "Generation, absorption and anisotropy of thick-target bremsstrahlung and implications for quantitative energy-dispersive analysis," *X-ray Spectroscopy* 5: 154, 1976.

7. R. L. Myklebust et al., *FRAME C: A Compact Procedure for Quantitative Energy-dispersive Electron Probe X-ray Analysis*, NBS Technical Note 1106, Washington, D.C.: Government Printing Office, 1979.

8. R. L. Myklebust, D. E. Newbury, and J. A. Small, "Backscatter loss in the x-ray continuum," *Microbeam Analysis--1980*, San Francisco: San Francisco Press, 1980, 49.

CRYSTAL EFFICIENCY DETERMINATION FOR RELATIVE LINE INTENSITY MEASUREMENTS

R. B. Marinenko, K. F. J. Heinrich, R. L. Myklebust, and C. E. Fiori

Poor resolution remains the major limitation of energy-dispersive x-ray spectrometry (EDS). Data-reduction procedures such as FRAME C[1] must therefore correct for peak overlap; and this correction requires an accurate knowledge of relative x-ray line intensities.

Recently, ratios have been re-determined for the Kα and Kβ x-ray lines of elements from phosphorus through germanium.[2] The improved accuracy was made possible by the use of EDS for which accurate detector efficiency corrections for the absorption of the beryllium window, gold contact layer, and silicon dead layer, as well as for the detector acceptance angle, can be calculated. The low resolution of EDS does not impose a serious problem in the determination of the K-line ratios. For low-atomic-number elements, Heinrich et al.[2] used a modification of a simplex procedure[3] to make overlap corrections for Kα and Kβ lines.

The L-line overlap is more extensive. Far more than a simple overlap correction procedure would be needed if EDS were used to determine L-line ratios. Therefore, the use of a crystal spectrometer, where the higher resolution reduces the overlap problem, is a potential solution, but the efficiency of a crystal spectrometer cannot be as easily determined as in EDS.

Recently, Bolen et al.[4] measured the relative peak height intensities of the L-lines of samarium with a quartz 10$\bar{1}$1 crystal spectrometer. The crystal spectrometer was calibrated with the help of values of the absolute x-ray yield data for K lines previously determined by Lifshin et al.[5] by EDS.

We have similarly calibrated a crystal spectrometer with the help of EDS, but our procedure is somewhat different from the above. A ratio of integrated intensity obtained with the wavelength-dispersive spectrometer (WDS) to the integrated intensity of the same line obtained with EDS is calculated for most elements from titanium through arsenic. Both the Kα and Kβ lines are used. A plot of these ratios as a function of peak energy gives a smooth curve (Fig. 1). The curve defines the efficiency of this particular crystal spectrometer. Points along the curve can be used to correct L-line integrated intensities obtained on the same crystal spectrometer for more accurate line intensity ratios.

Experimental

A lithium fluoride (LiF) crystal spectrometer was selected for calibration. The K-lines of elements titanium through arsenic fall within the range of this crystal; thus, many calibration points are available. Subsequently, the crystal can be used to measure the L-lines of elements from about indium (at. no. 49) to about bismuth (at. no. 83).

All measurements were made at an excitation potential of 20 kV. The room temperature was maintained at 21-22°C. Beam current measurements were made with a Faraday cup. The sample holder was connected directly to an electrometer followed by a digital voltmeter. Current measurements had to be as accurate as possible so that corrections could be made for current drift and changes from day to day. Beam current regulation was used for collecting all WDS data. Over a 1.5hr scanning time, drift was no greater than about 0.2% for a beam current of 5×10^{-8} A. With this current, the net integrated intensities for the K lines were a million counts or greater except for a few Kβ lines, for which the lowest integrated intensity was about 575 000 counts. A $10 \times 10\mu$m scanning raster was used to reduce sample contamination.

Authors Marinenko and Myklebust are with the Center for Analytical Chemistry, National Bureau of Standards (NBS), Washington, DC 20234; Heinrich is the Chief of the Office of International Relations at NBS; and Fiori is with the Division of Research Services, National Institutes of Health, Bethesda, MD 20205.
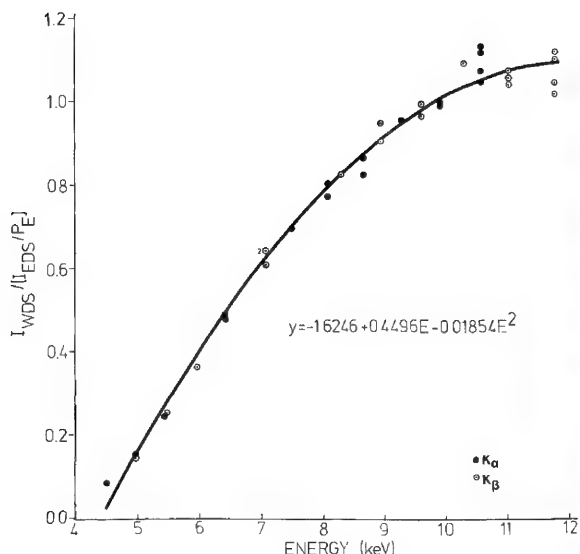
FIG. 1.--Ratio of WDS integrated intensity to corrected EDS integrated intensity as a function of peak energy for LiF crystal.
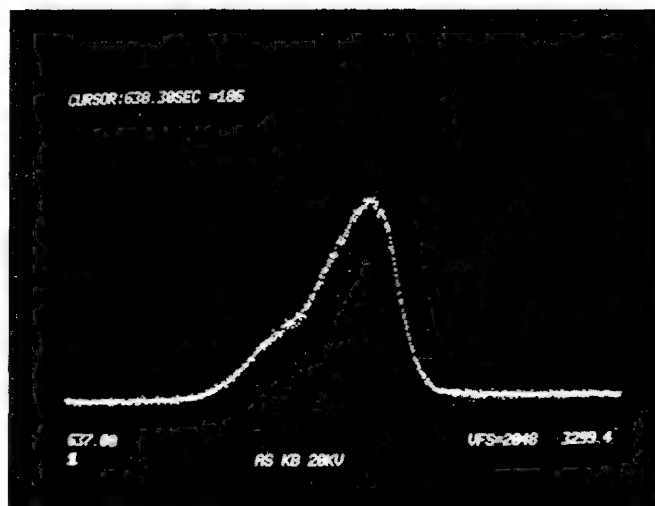
FIG. 2.--A spectrum of the As Kβ line recorded on a MCA from a LiF spectrometer.

The WDS spectra were collected in the multichannel scaling mode of a multichannel analyzer (MCA). There is sufficient MCA memory to store a single Kα or Kβ x-ray line plus background on both sides of the peak (Fig. 2). This method of scanning with the MCA requires a very slow, careful pass through the peak. The resulting spectrum is stored on a floppy disk. The net (i.e., background-corrected) integrated-intensity value is determined from an average of several (usually 16 or more) acceptable integrated intensities.

The dead-time setting used for collecting the WDS data was 0.5 μs, which is approximately the same as the electronic dead time for our instrument. The highest count rate observed was about 15 000 counts/s, for which the dead-time correction is less than 1%. No dead-time corrections have thus far been made; but this correction (within each channel) will be made as we progress in our work.

For each element, the EDS spectrum was recorded just after the WDS spectrum The beam current for the former was approximately 5×10^{-10} A and the live time was 500 s. Net integrated intensities were determined by two methods--a straight line or a calculated background[6] fit. The net Kα integrated intensities obtained from the two methods differed by less than 1% and the Kβ integrated intensities sometimes by no more than 2-3%. For consistency the calculated background fit data were used in these calculations. Some overlap of the Kα and Kβ peaks in EDS occurs for titanium, vanadium, and chromium; it is most serious for titanium. We do intend to correct for this overlap although only a small (1-2%) change in the calculated background fit is expected. All EDS integrated intensities were corrected for detector efficiency.

The expression used to calculate each ratio is

$$I_{WDS}/(I_{EDS}/P_E)$$

where I_{WDS} is the WDS net integrated intensity, I_{EDS} is the EDS net integrated intensity, and P_E is the EDS detector efficiency at the energy of the peak being measured. The x-ray absorption term for the sample, f_p, cancels out as it appears in both numerator and denominator.

Results

All EDS and WDS integrated intensities were normalized to the same beam current; WDS integrated intensities were normalized to a 1 s interval per channel scan and EDS to a 100 s accumulation period. The line drawn through the points (Fig. 1) is a least-squares fit of the data by a quadratic function which appears in the lower right of the figure. Reproducibility of repeated experiments on the same x-ray line (conducted on different days) is good (2-3%) except for the arsenic $K\alpha$ and $K\beta$ lines (about 4%) which occur at the high-energy limit for the crystal. (This discrepancy is not understood at present.)

With the LiF crystal calibrated, we now are collecting L-line data, with the same crystal spectrometer and with the MCA as described previously. Overlap between L-lines, such as the $L\alpha$-lines and the $L\beta$-lines of tungsten, is significant. A procedure is being developed to correct this overlap to obtain good integrated intensity values. Corrections to the L-line integrated intensities will then be made for crystal efficiency with the calibration curve and for sample absorption. The results should yield more accurate L-line intensity ratios than are presently available in the literature.

References

1. R. L. Myklebust, C. E. Fiori, and K. F. J. Heinrich, "Frame C: A compact procedure for quantitative energy-dispersive electron probe x-ray analysis," *Nat. Bur. Stds. Tech. Note* 1106, 1979.

2. K. F. J. Heinrich, C. F. Fiori, and R. L. Myklebust, "Relative transition probabilities for the x-ray lines from the K level," *J. Appl. Phys.* 50: 5589, 1979.

3. C. E. Fiori and R. L. Myklebust, "A simplex method for fitting Gaussian profiles to x-ray spectra obtained with an energy-dispersive detector," *Proc. ANS Conf. on Computers in Activation Analysis and Gamma-Ray Spectroscopy,* Mayaguez, P. R., 1978 DOE Symposium Series CONF-780421, p. 139.

4. R. B. Bolon, M. D. McConnell, and M. E. Gill, "Determination of x-ray WDS efficiency for absolute and relative intensity measurements," *Microbeam Analysis--1979,* San Francisco: San Francisco Press, 1979, 204.

5. E. Lifshin, M. F. Ciccarelli, and R. B. Bolon, "New measurements of the voltage dependence of absolute x-ray yields using energy dispersive spectrometry," *Proc. 8th Inter. Conf. on X-ray Optics and Microanalysis and 12th MAS Conf.,* 1977, 104.

6. C. E. Fiori et al., "Prediction of continuum intensity in energy-dispersive x-ray microanalysis," *Anal. Chem.* 48: 172, 1976.

CORRECTION FOR SIMS MATRIX EFFECTS IN THE ANALYSIS OF HIGH As (>5%)/Se ALLOYS

G. J. Scilla, R. W. LaForce and A. B. Fowler

Quantitative analysis in Secondary Ion Mass Spectrometry (SIMS) is often difficult due to the large matrix effects inherent in the technique. This problem is particularly serious if the sample contains a constituent which is present at high concentration and which varies over a significant range. The matrix effects associated with the SIMS analysis for As in As/Se alloys are so severe that quantitation of As at levels greater than 5 atom % is not practical by standard analytical procedures. The analysis of As at levels below 5% has been previously reported.[1] This paper describes a new method that permits the quantitative analysis of As in Se at levels > 5%. This method should also be applicable to other SIMS analyses were severe matrix effects are encountered.

Theory

Recent work by DeLine et al. has demonstrated that when sputtering is accomplished by means of a reactive primary ion species (i.e., O_2^+, O^-, Cs^+) the SIMS matrix effect is attributable to variations in the matrix sputtering yield.[2,3] Also, since the sputtering yield controls the concentration of implanted primary species,[4] the following relationship holds:

$$n^{\pm}/n^0 \propto (1/S_L)^X \propto [P]^X \tag{1}$$

where $n^{\pm}/n^0$ = positive or negative secondary ion yield, S_L = linear sputtering rate, $[P]$ = concentration of enhancing species (O for positive secondary ions, Cs for negative secondary ions), and X is an experimentally determined constant for each ion species. In quantitative analysis by SIMS it is generally assumed that

$$\frac{C_A}{C_M} \propto \frac{i_A^{\pm}}{i_M^{\pm}} \tag{2}$$

where $i^{\pm}$ is the positive or negative secondary ion current measured at the detector, C is concentration, and the subscripts A and M denote analyte and matrix, respectively. An expression for $i_A^{\pm}/i_M^{\pm}$ can be derived from Eq. (1):

$$\frac{i_A^{\pm}}{i_M^{\pm}} \propto \frac{(n_A^{\pm}/n_A^0)(C_A) \text{ (Volume Sputtered)}}{(n_M^{\pm}/n_M^0)(C_M) \text{ (Volume Sputtered)}} \tag{3}$$

$$\frac{i_A^{\pm}}{i_M^{\pm}} \propto \frac{C_A}{C_M}\left(\frac{1}{S_L}\right)^{X_A-X_M} \propto \frac{C_A}{C_M}[P]^{X_A-X_M} \tag{4}$$

or

$$\frac{C_A}{C_M} \propto \frac{i_A^{\pm}}{i_M^{\pm}} \bigg/ \left(\frac{1}{S_L}\right)^{X_A-X_M} \propto \frac{i_A^{\pm}}{i_M^{\pm}} \bigg/ [P]^{X_A-X_M} \tag{5}$$

The authors are with the Materials Engineering Department of Xerox Corp., Xerox Square - W114, Rochester, NY 14644.

It is therefore evident that Eq. (2) is not valid unless $X_A = X_M$; if X_A differs greatly from X_M, secondary ion intensity ratios must be corrected to yield quantitative results. The analytical procedure employed in our laboratory for the analysis of As in Se calls for monitoring the $^{91}AsO^-/^{80}Se^-$ secondary ion intensity ratio under $^{16}O^-$ bombardment.[1] ($^{91}AsO^-$ is used rather than $^{75}As^-$ for improved sensitivity.) If we consider the effects that oxygen can have on the formation of negative ions,[5] and the fact that molecular oxide species are utilized in the analysis, we might expect that the exponential factors for these ions may differ significantly. If that is the case, a large matrix effect would result if the sputter rate (and thereby [oxygen]) is affected by changes in the As concentration.

Experimental

An Applied Research Laboratories IMMA interfaced to a DEC PDP-11/40 computer was employed in this study. A $^{16}O^-$ primary beam of 1.5 nA at 20 keV and beam diameter of 5 μm is rastered over an area of 80 × 40 μm. The computer system sequentially steps the secondary magnet and collects data for each peak, integrating for 10 sec in the pulse-counting mode. The following negative secondary ions were monitored: $^{16}O^-$, $^{80}Se^-$, $^{91}AsO^-$, and $^{96}SeO^-$. Standards of 5, 10 and 30 atom% As in Se were prepared and certified by XRF and EMPA. An unknown was analyzed by the IMMA and the results were compared with EMPA and TEM/EDXA analyses. All samples were cleaned by sputtering for at least 15 min prior to collecting data. A 40% electronic aperture was employed during data acquisition.

The exponential factors for each analyte and matrix ion of interest were determined by measurement of the intensities of these ions (corrected for concentration) as a function of the $^{16}O^-$ secondary ion intensity in each standard. Exponential factors for each ion species were also determined as funtion of $^{16}O^-/^{80}Se^-$. Since it is often impractical to measure changes in sputtering rate, variations in the exponential factor as a function of S_L were not determined. The $^{16}O^-$ signal and the $^{16}O^-/^{80}Se^-$ ratio in conjunction with the corresponding $(X_A - X_M)$ values were then utilized to correct secondary ion intensity ratios as shown in Eq. (5).

Results

The variation in secondary ion intensity as a function of $^{16}O^-$ intensity is displayed in Fig. 1. The slopes (m) of these curves yield the exponential factors for each ion. As expected, molecular oxide ions are enhanced with increasing oxygen level. The production of the $^{80}Se^-$ ion is inhibited with increasing oxygen.

The "calibration" curve for As in Se obtained from the uncorrected $^{91}AsO^-/^{80}Se^-$ secondary ion intensity ratio is displayed in Fig. 2a; that corresponding to quantitation with $^{91}AsO^-/^{96}SeO^-$, in Fig. 2b. The exponential factors obtained from Fig. 1 were then employed to correct these secondary ion intensity ratios. The corrected data are shown in Fig. 2c. Similar results were obtained when correction was accomplished by use of $^{16}O^-/^{80}Se^-$ and the corresponding $(X_A - X_M)$ values to correct secondary ion intensity ratios. Table 1 displays the data obtained from comparative analyses of an unknown sample of high-As alloy.

TABLE 1.--Comparative analyses of high As in Se alloy.

Technique	Wt % As ± 2 Sigma
EMPA	34.3 ± 1.5 (average 4 analyses)
TEM/EDXA	34.4 ± 1.0
SIMS--no correction	4.9 ± 0.4 (average 5 analyses)
SIMS--correction procedure	34.5 ± 3.3 (average 5 analyses)

These data demonstrate that the correction procedure described in this paper is effective in providing linear calibration curves with improved sensitivity for high concentration As in Se alloys. This correction procedure yields accurate results with fair precision. The procedure has been shown valid for As in the concentration range 5-35

atom %. Below 5%, standard analytical procedures can be employed.

References

1. R. LaForce and K. Johnson, "Quantitative analysis of Se alloy thin films by ion microprobe mass analysis and transmission electron microscopy," *Microbeam Analysis--1979*, San Francisco: San Francisco Press, 1979, 354.

2. V. R. Deline, C. A. Evans Jr. and P. Williams, "A unified explanation for secondary ion yields," *Appl. Phys. Lett.* 33(7): 578, 1978.

3. V. R. DeLine et al., "Mechanism of the SIMS matrix effect," *Appl. Phys. Lett.* 33(9): 832, 1978.

4. H. Liebl, "SIMS and its use in depth profiling," *J. Vac. Sci. Tech.* 12(1): 385, 1975.

5. P. Williams and C. A. Evans Jr., "Anomalous enhancement of negative sputtered ion emission by oxygen," *Surface Sci.* 78. 1978. 324.
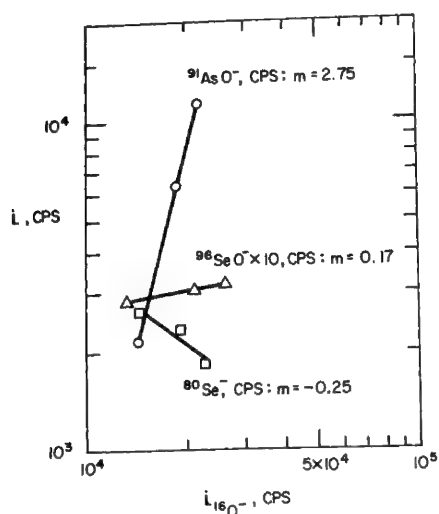
FIG. 1.--Log of intensity of analyte and matrix ions as function of intensity of $^{16}O^-$ ion from 5, 10, and 30 atom % As in Se standards. Slopes m of curves are equal to exponential factors for each ion.
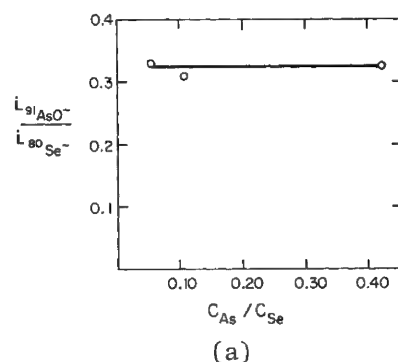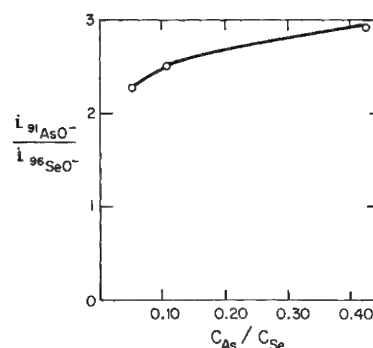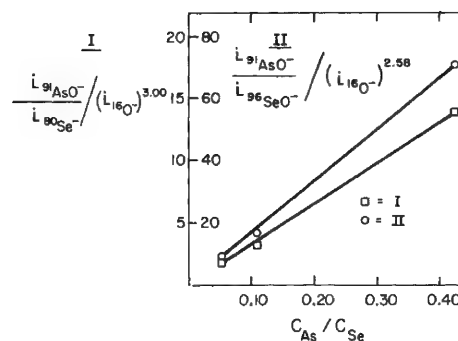
FIG. 2.--(a) Secondary ion intensity ratio for $^{91}AsO^-/^{80}Se^-$ as function of C_{As}/C_{Se}; (b) secondary ion intensity ratio for $^{91}AsO^-/^{96}SeO^-$ as function of C_{As}/C_{Se}; (c) secondary ion intensity ratios corrected by use of $(i_{16_O^-})^{X_A-X_M}$.

QUANTITATIVE X-RAY MICROANALYSIS ON SURFACES WITH UNKNOWN ORIENTATION

J. C. Russ and T. M. Hare

Conventional quantitative x-ray microanalysis requires knowledge of the local surface orientation, for calculation of the ZAF correction factors. For many real samples this parameter is at best difficult and sometimes impossible to measure. We present a new method that uses two sets of intensity values recorded at different, accurately measured acceleration voltages, from which an iterative solution determines an effective x-ray takeoff angle that gives best agreement for the two data sets. No standards are used. Tests with metals and minerals show that the results are comparable with conventional calculations with known angles.

Method

In scanning electron microscopy with energy-dispersive analysis, samples are commonly encountered with irregular surfaces, which may be locally flat so that quantitative corrections can be performed, but for which the local surface orientation is not known, Moll has described the equations for the case in which the stage tilt can be incremented to change the sample angle and the angles obtained from the parallax measurement.[1] Unfortunately, this method is limited to the case in which the surface has no tilt component perpendicular to the stage tilt direction, and hence is not generally applicable. Furthermore, it is a difficult measurement to make accurately, especially at high magnifications where the area may be lost.

The difficulties in measuring the surface orientation--mechanical complexity, imprecision, and the time required--led us to consider other ways to handle the problem. It seemed that measurement of x-ray intensities at two acceleration voltages should provide a series of simultaneous equations of the ZAF relationships that could be solved together for concentrations (and the angle). This method is iterative: we begin by assuming an arbitrary angle (we generally use 15°). Each set of intensities is carried through a complete ZAF calculation which includes oxygen by stoichiometry and a "no-standards" normalization. The latter step is needed since standard intensities at all possible angles and voltages are not practically available, and in any case the fundamental parameter calculations of relative pure intensity have been refined to the point where quite good routine results can be obtained.[2]

After concentrations have been calculated for each set of intensities, the assumed angle is changed (steps of 5° are adequate for the initial stages) and the calculations repeated. The goal is to find an angle at which the two sets of results agree, as defined by the minimization of the sum of squares of the concentration differences (SSD). After results for three angles have been computed, a parabolic "look-ahead" estimate is used to predict the angle yielding the minimum SSD. A parabola is fitted to the three points and its vertex is used for the next angle estimate. The three best (lowest SSD) points are used for the next iteration. When the minimum is found (when the change in predicted SSD or angle is less than a preset amount), the compositions calculated from each set of intensities are averaged, as the best estimate of concentrations. The angle is not of direct interest, except as a means of arriving at the composition.

The calculations, which include fitting background and modified Gaussian peaks with least squares and a full ZAF computation, are programmed in BASIC for an APPLE microcomputer. The optimized ZAF routine for each voltage and assumed angle takes from 1.5 min for the six-element-plus-oxygen clinopyroxene to less than 10 sec for the FeS_2 binary. Four to six iterations of estimated angle are generally needed. The total time is similar to that needed to collect spectra at the two voltages.

The authors are at the School of Engineering of North Carolina State University in Raleigh, NC 27607.

Testing

The program was systematically tested by application to known specimens and known takeoff angles. Table 1 shows results for a mineral (clinopyroxene) measured at 16 and 23° and at accelerating voltages of 9.9, 13, 17, 20, and 25 KV. The average results using a conventional no-standards ZAF approach for individual data sets, and those in which pairs of intensities measured at different voltages are used in the angle-iteration program, show a slightly greater error in the latter, which is due to the inclusion of poorer results when the voltages are both very high and close together.

Table 2 shows results for a stainless steel, expected to present difficulties because the principal elements are all very close together. Data measured at 13 and 23°, at 17, 22.5, 28, and 39 KV gave very good results both in a conventional no-standards ZAF program and, in pairs, in the angle-iteration method. However, we found that the SSD curve had a much flatter minimum in this case than for the mineral, and that a larger error in the angle was obtained. This finding is not of concern since the results for these higher energy lines are less sensitive to angle.

Another mineral sample, an olivine, was analyzed repetitively to assess error sensitivity. Table 3 shows that for five measurements each at 17 and 23 KV, the variation in calculated concentrations is generally similar for the ten conventional ZAF computations and the twenty-five (all combinations) angle-iteration computations, and also to the purely statistical variation in intensities. Table 4 shows what happens when the average intensities are used in the angle-iteration program, but one of the voltages is changed by 500 V. The resulting errors are substantial; an accurately determined accelerating voltage is urgently needed.

Typical application to a real sample is shown in Fig. 1 and Table 5. The grain is iron pyrite (FeS_2), and at each marked location intensities were measured at 16.9 and 24.8 KV; they vary widely. We also found that the ratio of S to Fe P/B ratios, useful in some simple cases as partial compensation for irregular surface effects, varied on these faces by more than 3 to 1. The angle iteration method still gives useful results.

Conclusion

The method described for solving for concentrations by iteration of an assumed takeoff angle by means of two sets of intensity values measured at different accelerating voltages appears to offer a practical solution to the problem of obtaining results on irregular samples. It does not require measuring or knowing the local angle, and replaces the cumbersome and error-prone measurement of angle by the need for an accurate measurement of the accelerating voltages, which can be accomplished with comparative ease and good precision, and for most instruments need only be done once at each voltage for a series of samples or locations.

References

1. S. Moll et al., "Geometrical considerations for ZAF corrections in the SEM," *Proc. Microanalysis Conf.*, 1977, 33.
2. J. C. Russ, "Fast, self-contained, no-standards quantitative program for EDS," *Proc. Microanalysis Conf.*, 1978, 48.

TABLE 1.--Clinopyroxene.

	nominal	conventional ZAF 16 des	23 des	angle iteration 16 des	23 des
SiO2	54.92	55.11 +-.14	54.65 + .30	55.85 + .69	54.82 + 1.21
Al2O3	0.74	0.65 +-.35	0.80 + .27	0.70 + .22	0.84 + .17
FeO	2.95	2.78 +-.32	3.07 + .16	2.57 + .21	3.01 + .42
MgO	16.46	16.88+-1.35	16.62 + .48	17.99 + .65	17.40 + 1.03
MnO	0.25	0.23 +-.05	0.22 + .08	0.21 + .03	0.22 + .07
CaO	24.79	24.34 +-.56	24.63 + .89	22.68 +-1.00	23.71 + 1.77
angle				13.6 + 1.2	20.9 + 7.5

TABLE 2.--**Stainless** steels.

	nominal	conv.ZAF	23 deg	13 deg
Cr	18.37	18.66 +-.20	18.46 +-.13	18.65 +-.13
Mn	1.71	1.77 +-.13	1.66 +-.08	1.86 +-.06
Fe	71.12*	72.35 +-.22	72.39 +-.28	72.34 +-.32
Ni	7.40	7.23 +-.15	7.50 +-.38	7.16 +-.39
angle			20.4	13.5

*by difference

TABLE 3.--Olivine.
average results and (relative variation)

	nominal*	conventional ZAF	angle iteration	inten.
MgO	48.5	48.52 +-.20 (0.4%)	49.43 +-.30 (0.6%)	(0.4%)
SiO2	40.8	42.65 +-.19 (0.4%)	42.28 +-.56 (1.3%)	(1.0%)
CaO	0.21	0.37 +-.04 (9.7%)	0.34 +-.02 (5.9%)	(10.0%)
FeO	9.8	8.47 +-.15 (1.0%)	7.95 +-.01 (10.2%)	(1.6%)

TABLE 4.--Olivine: Sensitivity to voltage error.

kV:	17/22.5	17/23.5	17/23	16.5/23	17.5/23
MgO	50.27	48.87	49.42	48.07	50.64
SiO2	43.57	41.34	42.25	40.28	44.56
CaO	0.28	0.39	0.35	0.44	0.24
FeO	5.88	9.39	7.98	11.21	4.54
angle	8.2	15.0	11.8	17.8	6.9

TABLE 5.-- Iron pyrite.

Point	%S	%Fe	"angle"
A	52.67	47.33	31.3
B	47.34	52.66	4.6
C	56.74	43.26	13.1
D	53.30	46.70	79.8
E	54.37	45.63	30.6
F	in shadow		
aver	52.88	47.12	
+-	3.47		
true	53.45	46.55	
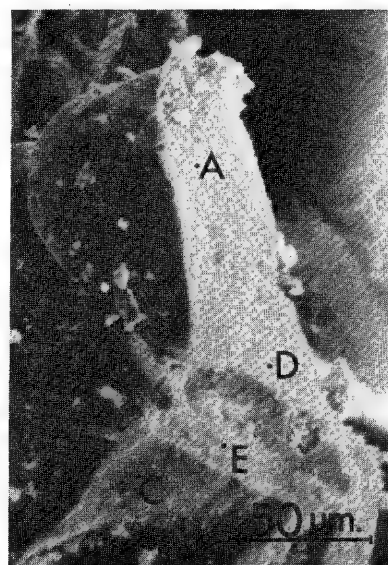
FIG. 1.--Iron pyrite specimen with letters indic-
ating analyzed locations.

DETERMINATION OF THE EFFECTIVE TAKE-OFF ANGLE ON SCANNING ELECTRON MICROSCOPE ENERGY-DISPERSIVE X-RAY ANALYSIS SYSTEMS

M. A. Parker and W. R. Warke

A calibration procedure has been developed that permits rapid and accurate determination of the effective take-off angle on scanning electron microscope energy-dispersive x-ray analysis (SEM-EDX) systems. The method consisted of the measurement of the x-ray absorption on an alloy of known composition, and the subsequent computation of the associated value of the effective take-off angle. The validity of the procedure was checked by use of the resulting values of the effective take-off angle for the analysis of a stainless-steel standard.

Many analysts have attempted recently to employ the SEM-EDX system as a moderately accurate electron probe microanalyzer (EPMA) for quantitative analysis.[1] In many such systems, the detector/sample geometry is poorly defined, and often analysts tilt the specimen to reduce analysis time. A major difficulty encountered in such work is determination of the effective take-off angles that are required for ZAF (atomic number, absorption, and fluorescence) computations of the fluorescence and absorption corrections when the specimen is titled.[2,3]

Experimental Setup

A JEOL U3 SEM, Canberra SiLi detector and amplifier, and Tracor Northern NS 880 spectral analysis system constituted the analytical system. Chamber peaks were eliminated by use of a polepiece shield and a collimator over the EDS detector. Other precautions were taken to assure satisfaction of the conditions for quantitative analysis.

The calibration standard was the W-20% Mo alloy standard reference material, SRM480, which can be obtained from the National Bureau of Standards. A cartridge brass (72.8% Cu and 27.1% Zn), SRM498, and a stainless steel (69.0% Fe, 18.6% Cr, 10.0% Ni, 1.6% Mn, and 0.5% Si) were used to verify the validity of the analytical procedure and the computed values of the effective take-off angle. The Lα,β line of Mo was chosen, because it required a large absorption correction and the fluorescence correction factor was essentially unity.

Calibration Method

The absorption factor for the Mo Lα,β was determined by $A = C/kZ$. The composition C was known; the intensity ratio k was measured; and the atomic number correction Z was calculated.[4,5] Since fluorescence correction for the Mo x-ray line was negligible, the resulting empirically determined value of the absorption correction depended directly on the specimen orientation with respect to the detector given by α_0 and the tilt of the specimen relative to the electron beam θ. Philibert[6,7] has demonstrated a simple dependence of the absorption correction on the effective take-off angle ϵ, which is a function of α_0 and θ. Solution of Philibert's expression for csc ϵ resulted in a simple quadratic equation giving csc ϵ in terms of the empirical absorption correction. In a sense, the calibration was the converse of quantitative analysis.[8]

An alternate method relied on a calibration curve. The calibration curve was developed by modification of the ZAF correction program to compute the intensity ratio as a function of csc ϵ. Once the intensity ratio was measured for a given stage tilt and detector position, the value of csc ϵ was read from the curve (Fig. 1).

The values of csc ϵ were obtained for two stage tilts. The specimen was analyzed in a nominally untilted and tilted position, $-2° \pm 1°$ and $43° \pm 1°$, respectively. The x-ray collimator defined a take-off angle α_0 for the nearly perpendicular electron beam incidence; α_0 equaled $20° \pm 3°$. The values of csc ϵ for the untilted and tilted geometries were 3.47 ± 0.23 and 0.93 ± 0.19, respectively. For the untilted geometry, this arrangement gave a take-off angle of $17° \pm 2°$; good agreement was obtained with the sum of α_0 and θ, $18° \pm 3°$. Controversy regarding the form of the dependence of the effective take-off angle on α_0 and θ made a similar evaluation of accuracy at the tilted geometry difficult; 0.93 agreed qualitatively with direct computations of csc ϵ.[9-13]
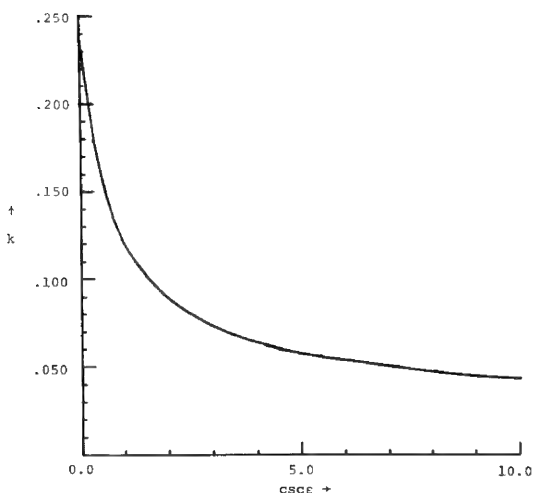
FIG. 1.--Results of simulation of intensity ratio versus take-off angle ϵ for acceleration potential of 25 kV.

Results of Stainless Steel and Brass Analyses

The criterion for acceptance of the calibration procedure was that the analysis of a typical engineering alloy should fall within the limits of acceptable quantitative results. These limits were $\pm 6\%$ relative error for constituents greater than 20% (weight percent) and $\pm 10\%$, for the constituents less than 20%.[14] It was also necessary for the alloy to exhibit strong absorption and fluorescence effects. Stainless steel was chosen, since Ni showed a strong absorption effect and Cr, a strong fluorescence effect. Brass was chosen to verify that the atomic number correction did not exhibit a strong dependence on tilt, since absorption and fluorescence effects were negligible for brass. Analyses were performed on these alloys at the previous untilted and tilted stage geometries.

The analysis of the stainless steel satisfied the criterion. Before application of the ZAF corrections, the intensity ratios were taken as a first approximation of the composition. A large positive relative error in Cr concentration indicated a strong fluorescence effect; a large negative relative error in Ni, a strong absorption effect. After application of ZAF corrections which employed the calibrated values of csc ϵ, and normalization to a total concentration of 97.6% Cr, Fe, and Ni, the Cr and Ni concentrations fell within the limits of acceptance (Tables 1 and 2).

A crucial assumption in the development of the calibration procedure was that the dependence of the atomic number correction Z on tilt was negligible.[15] The results of the analysis verified the legitimacy of this assumption. After ZAF corrections and normalization to 100% total Cu and Zn concentrations, the analyses for Cu and Zn were well within acceptance limits (Tables 1 and 2).

TABLE 1.--Estimates of composition, before and after ZAF corrections, of stainless-steel and cartridge brass standards for two stage tilts.

Alloy	Constituent	Before ZAF		After ZAF	
		$\theta = -2°$	$\theta = 43°$	$\theta = -2°$	$\theta = 43°$
Stainless steel	Cr	23.6%	22.0%	19.3%	18.4%
	Fe	67.1	67.8	68.6	70.1
	Ni	7.5	8.3	9.7	9.2
Cartridge brass	Cu	77.0	66.5	73.9	72.2
	Zn	27.7	26.0	26.1	27.8

TABLE 2.--Relative errors in estimates of composition, before and after ZAF corrections, of stainless-steel and cartridge brass for two stage tilts.

Alloy	Constituent	Before ZAF		After ZAF	
		$\theta = -2°$	$\theta = 43°$	$\theta = -2°$	$\theta = 43°$
Stainless steel	Cr Fe Ni	26.9% -2.8 -25.0	18.3% -1.7 -17.0	3.8% -0.6 -3.0	-1.1% 1.6 8.0
Cartridge brass	Cu Zn	5.8 2.2	8.7 4.1	1.5 -3.7	-0.8 2.6

References

1. E. Lifshin, "Quantitative microprobe analysis with energy dispersive detectors," Syracuse, N.Y.: *General Electric Technical Information Series* 75 CRD 253.
2. H. Yakowitz et al., *Practical Scanning Electron Microscopy*, New York: Plenum Press, 1975, 1st ed., pp. 327-372.
3. L. S. Birks et al., "X-ray absorption and emission," *Analytical Chemistry* 46(5): 360R, 1974.
4. J. Philibert, "Some problems with quantitative electron probe microanalysis," *Special Publication 298*, Washington, D.C.: National Bureau of Standards, 1968.
5. D. R. Beaman, *Electron Beam Microanalysis*, Philadelphia: American Society for Testing and Materials, 1972, STP-506.
6. J. Philibert, "A method for calculating the absorption correction in electron-probe microanalysis," *X-Ray Optics and X-Ray Microanalysis*, New York: Academic Press, 1963, pp. 378-392.
7. H. E. Bishop, "The absorption and atomic number corrections in electron probe microanalysis," *Brit. J. Appl. Physics* 1(2): 673, 1968.
8. M. A. Parker, *The Effective Take-Off Angle for Quantitative Electron Probe Microanalysis*, Thesis, Chicago: IIT, 1978.
9. D. B. Wittry, "Methods of quantitative electron probe analysis," *Adv. X-Ray Analysis* 7:397, 1963.
10. M. Green, "The angular distribution of characteristic x radiation and its origin within a solid target," *Proc. Phys. Society* 83:435, 1964.
11. H. E. Bishop, "A Monte Carlo calculation on the scattering of electrons in copper," *Proc. Phys. Society* 83:435, 1964.
12. N. Gennai et al., "The $f(\chi)$-curves for Fe K_α and Al K_α x-rays in the inclined EPMA targets of Fe, Al and Fe-Al Alloy," *Jap. J. Appl. Physics* 10(4): 491, 1971.
13. S. Moll, "Geometrical considerations for ZAF corrections in the SEM," Technical Bulletin 111-277, Advanced Materials Research Corp., 1977.
14. D. R. Beaman et al., "Accuracy of quantitative electron probe microanalysis with energy dispersive spectrometers," *Analytical Chemistry* 44(9): 1958, 1972.
15. H. Yakowitz, *op. cit.* (Ref. 2).

DEVELOPMENT OF AN ADVANCED ION MICROPROBE ANALYZER

J. M. Gourgout

It has been known for many years that the technique of secondary-ion mass spectroscopy (SIMS) is potentially one of the most sensitive and versatile analytical techniques for microscopic analysis. The first dedicated SIMS instruments were relatively low in resolving power, sensitivity, and imaging performance. These instruments by no means exploited the technique to the full, and their use did not spread very quickly. However, sufficient numbers were manufactured and used for the development of the technique to go on; and the first instrument of the second generation, the IMS 3F, shows marked improvements. It is now possible to solve the frequently encountered problem of spectral interference between peaks from atomic ions and peaks from molecular ions. Sensitivity is now such that n-type phosphorus dopant in silicon-based electronic components can be detected down to concentrations of 10^{15} atoms/cm^3. The ion optics now give an ion image with a resolution of better than 1 µm, a considerable aid in the viewing of the area of analysis.

Automation and use of a minicomputer has made the operation of the instrument faster and much more convenient. Considerable progress has been made in the quantification of results, and the computing facilities will help with the work that still has to be carried out in this field. As always, there is room for improving the instrument facilities by the introduction of new accessories. Three accessories have recently become available:
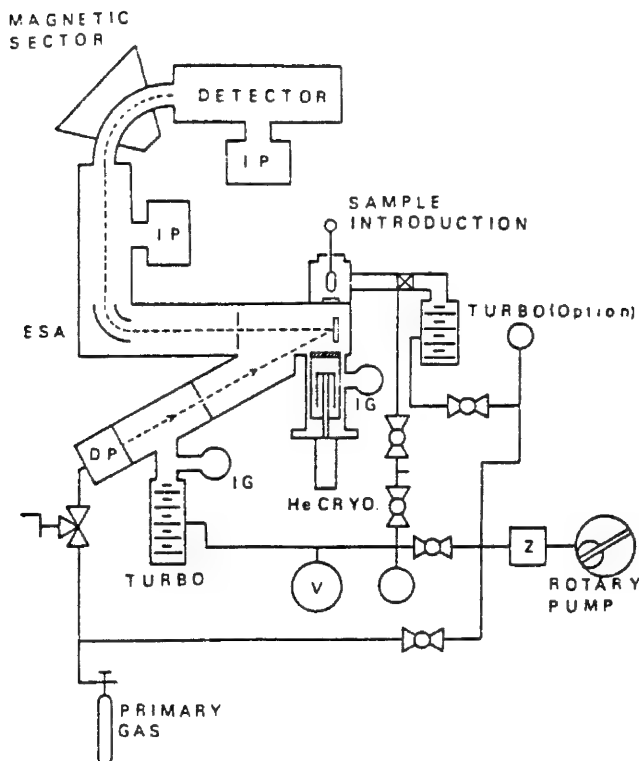
FIG. 1.--IMS 3F vacuum system.   FIG. 2.--Primary-beam filtering.
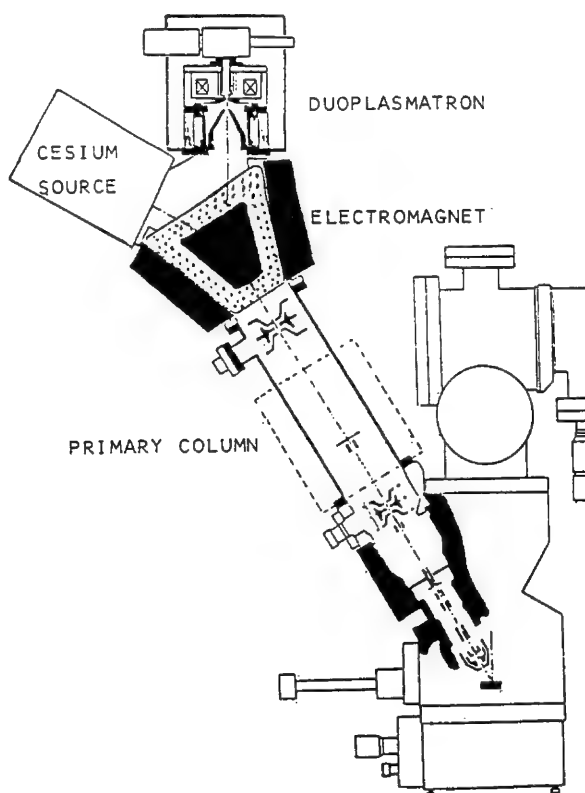
The author is with CAMECA, B.P. 6, F 92403 Courbevoie, France.

1. A cryogenic pumping system (Fig. 1) in the specimen chamber, consisting of a liquid helium cooled plate that collects contaminant hydrogen, carbon, nitrogen, and oxygen molecules that strike it, thus reducing the partial pressure of these gases, and reducing their possible effects on the ionization process.

2. A cesium ion gun that gives a higher secondary ion emission than the duoplasmatron gun for electronegative elements.

3. Magnetic mass filtering of the ion beam from the gun. This technique was devised for two purposes. The first is to filter the primary ion beam so that only one type of ion reaches the specimen, so that, say, hydrogen ions are removed from an oxygen beam. The second purpose is achieved by mounting the duoplasmatron gun and the cesium gun on the magnetic filter (Fig. 2), so that by a mere reversal of the polarity of the magnet the gun may be switched from one ion source to the other. Thus the vacuum need not be broken whenever the ion source is changed and the electronegative and electropositive elements can be analyzed consecutively under the best ionization conditions.

If the dedicated SIMS instrument continues to be used in a widening field of applications, it is essential for instrumental refinements to continue to be developed.

Bibliography

J. E. Chelgren et al., *J. Vac. Sci. Tech.* 16: 324, 1979; J. M. Gourgout, *8th Intern. Conf. X-ray Optics and Analysis,* 1977; J. M. Gourgout, "Secondary ion mass spectrometry SIMS II," *Chem. Phys.* 9: 286, 1979.

THE SCANNING PROTON MICROPROBE

G. J. F. Legge

Some basic principles of ion-atom interactions are reviewed as a way of discussing the characteristics and unique features of a scanning proton microprobe and assessing its potential. After a brief description of the instrument, examples are given of some applications, including spot analysis, depth profiling, and scanning analysis with the Melbourne total data handling technique. This technique is applicable to all scanning probes and is of particular value with sensitive specimens.

The basic requirement of any proton or nuclear microprobe to be used for sensitive microanalysis is a beam of protons or heavier ions with an energy of at least 1 MeV per nucleon and a focused spot size of the order of microns rather than the usual millimeters obtained for focused accelerator beams. The first such probe was developed at Harwell in 1970.[1] When the *Melbourne Proton Micro Probe* (MP) commenced operation early in 1976 there were then five operating focused proton microprobes.[2,3] By 1977 this number had grown to 9; now there are at least 17 such probes and more are under construction. What are the reasons for this activity and what is the need for such instruments? What are the ultimately achievable goals for the proton microprobe? The instrument should be compared with the more familiar electron microprobe, for they have much in common; but the specifics in which they differ are of greatest interest to us, for they define the value and the fields of application. We first compare electron-induced x-ray emission (EIXE) with proton-induced x-ray emission (PIXE).

Ion-Atom Interactions

   (i) Ionization and Energy Requirements. Figure 1 shows the cross sections for K-shell
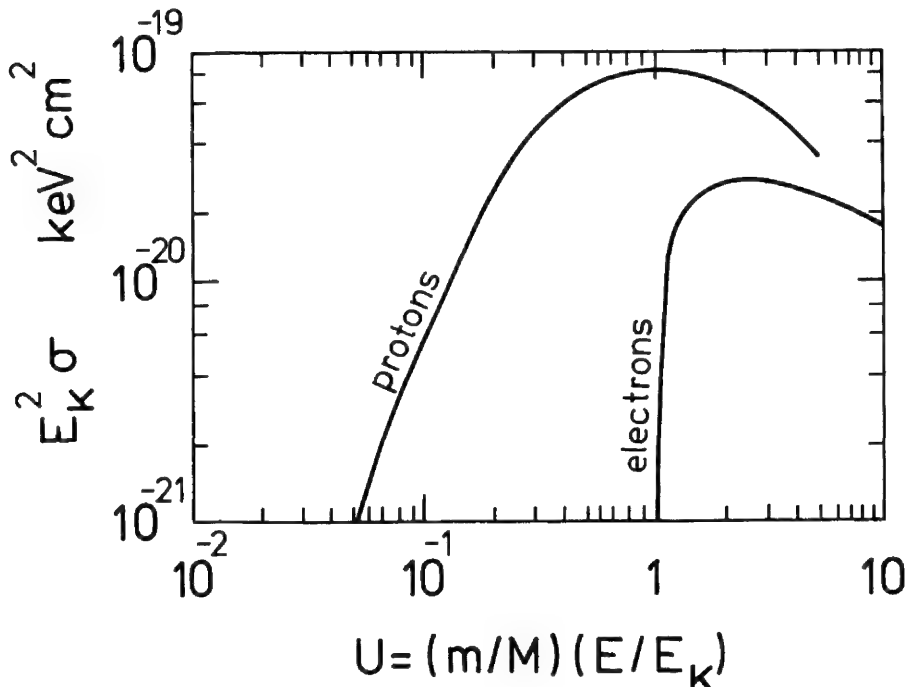
FIG. 1.--Cross sections σ for ionization of K-shell by protons and by electrons of mass M and energy E; m is electronic mass and E_K is ionization energy. Scales are normalized to emphasize velocity dependence of cross section ($U = 1$ for electronic orbital velocity).

$$U = (m/M)(E/E_K)$$

ionization by protons and by electrons as a function of projectile energy. The scales are normalized to remove the dependence on ionization energy E_K and on projectile mass M. Unit energy U then corresponds to the classical electron orbital velocity. Comparison of these two curves shows that protons and electrons of similar high velocities are equally efficient in ionizing the K-shell of target atoms. In this respect, a 10keV electron is the equivalent of an 18MeV proton. However, at velocities approaching the orbital electron velocities (U = 1) the electron-induced cross section falls to zero, whereas the proton-induced cross section peaks; and the proton continues to ionize at velocities well below the orbital velocity. Incoming electrons of suborbital velocities for the K-shell still deposit energy in the target by ionization or excitation of outer shells, although the resultant radiation may not be analytically useful. In contrast, it may be advantageous to use protons of suborbital velocity to minimize background radiation from other sources. Because of their similar Coulomb interactions, protons and electrons of the same velocity transfer energy to the target and produce radiation at similar rates for most processes. The important exceptions are bremsstrahlung and nuclear collisions, which we shall discuss separately. It is sometimes thought that high-energy protons damage a specimen more than the relatively low-energy electrons of the same velocity; however, a single proton produces many more ionizing events than a single electron. The only important parameter, useful ionizing events per energy lost, is similar for the two ions. The comparison is complicated by other factors that cause the electron and proton probes to be operated at different beam velocities. We are not concerned with fluorescence yield in this comparison, because this factor is independent of the means of ionization.

(ii) Bremsstrahlung and Sensitivity. The cross section per unit energy interval for production of bremsstrahlung is approximately inversely proportional to the square of the mass of the radiating ion. Consequently the background level from proton bremsstrahlung in PIXE analysis is more than six orders of magnitude below that from electron bremsstrahlung in EIXE analysis, if ions of the same velocity are employed. The main source of background in PIXE analysis is secondary-electron bremsstrahlung. The large mass ratio between the proton and electron fortunately limits the fraction of energy transferable in their interaction, and the bremsstrahlung contribution from secondary electrons consequently decreases exponentially with increasing photon energy. In Fig. 2 we show a theoretical calculation of the total bremsstrahlung spectrum expected from 3MeV protons traversing a thin kapton foil compared with a spectrum measured on MP.[4] This is an absolute comparison and the agreement is excellent except at energies above 10 keV, where nuclear radiation intervenes. At the top of Fig. 2 is shown the expected shape of the bremsstrahlung spectrum for EIXE. The ratio of these two backgrounds increases rapidly with x-ray energy. For light elements the peak-to-background ratio, and hence the elemental sensitivity, may be comparable for the electron and proton microprobes. However, the sensitivity of the proton microprobe is much greater for the important *heavy metals* and other heavy trace elements; it is about 1 ppm by weight.[4] A typical proton microprobe spectrum for a *thin* specimen is shown in Fig. 3, produced by a 0.25nA, 3MeV beam of protons for 5000 sec on a *silicon cell* in a 30μm-thick epidermal strip of wheat leaf.[5] Even for thick rock specimens the peak-to-background ratio for rare earth detection is greater by a factor of 10^3 on the proton microprobe than on an electron microprobe.[2,6] The absence of a high energy continuum in the proton microprobe means that fluorescence corrections are small, if needed at all.

(iii) Beam Penetration and Divergence in a Specimen. For similar particle velocities, a proton beam has much greater penetrability than an electron beam, since the two beams have very different energies but similar rates of energy loss. The relatively large mass of the proton also results in much smaller deviation from the incident direction as a result of scattering in the specimen. Measurements with thin foils have shown that the divergence of a proton microprobe beam can be accurately calculated from theory.[7] Typically a beam of 3MeV protons loses only 260 keV in traversing 20 μm of unit density biological material and spreads in diameter by only 0.6 μm owing to multiple scattering. This result may be compared with a beam of 30keV electrons, which has a range of only 20 μm in the same material and spreads in diameter by more than 10 μm.[8] Thus a proton microbe is ideal

71

for the study of thick specimens with optimum spatial resolution.
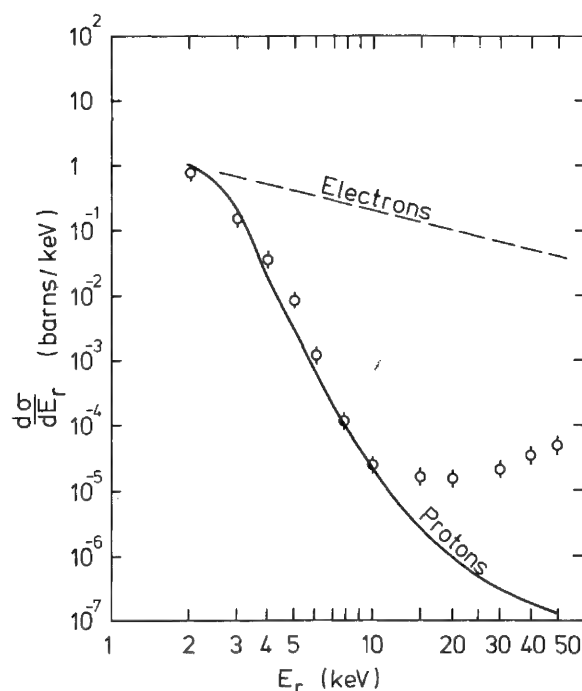
FIG. 2.--Experimental and theoretical spectrum of total bremsstrahlung from 3MeV proton beam in thin target of kapton. (Target is thick to secondary electrons whose contribution dominates at low energies.) Dashed line shows shape of bremsstrahlung spectrum from electron beam for comparison.
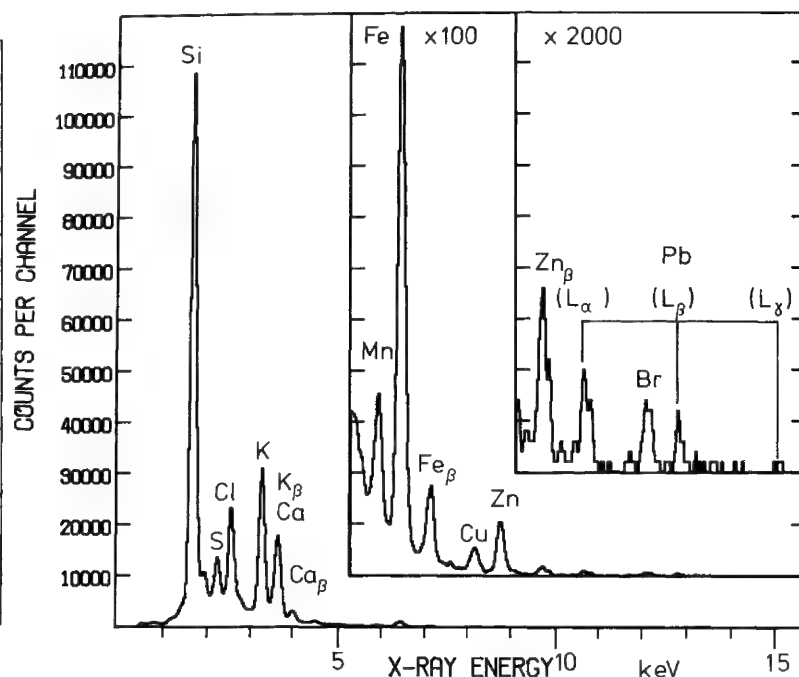
FIG. 3.--X-ray spectrum from *silicon cell* in freeze-dried wheat leaf epidermis, produced by 3MeV proton beam of 0.25 nA for 5000 sec. Except for Pb, all lines are K-radiation and, unless labelled β, are Kα. Si(Li) detector was used with no coating on specimen. Background at high energies is about 1 ppm.

Ion Optics and Construction

The Melbourne proton microprobe (MP) is shown in Fig. 4. A detailed description of this instrument has been given recently.[2] We shall mention here only the basic principles of such an instrument. A nuclear accelerator is used to illuminate a 10-100μm-diam. aperture with a monoenergetic proton beam selectable over the range 1-5 MeV. This aperture is then imaged on the specimen, usually by means of a single-stage compound lens of 0.2-0.5 magnification. The beam spot size and hence the resolution is limited by lens aberrations. The cylindrical iron lenses employed for electrons are much too weak to handle protons of MeV energies. Therefore a combination lens of strong-focusing magnetic quadrupoles is usually employed. MP has a quadrupole quadruplet like the Harwell and Studsvik probes.[1,9] The Zurich, Heidelberg, and Karlsruhe probes have quadrupole doublets, two stages in the case of Zurich.[10-12] As an alternative to quadrupole fields, some groups are trying superconducting magnets, for which similar resolutions are predicted.[13] Three European probes have achieved 2-3μm resolution.[11,12,14] Work is now in progress on the MP lens system to improve on the present resolution of 3 μm.

The proton beam on MP can be scanned in two directions over a range of 2 mm and the specimen accurately located by means of an internal optical microscope and an external micrometer stage to an accuracy of 1 μm. The clean ultra-high vacuum system is appropriate to trace-element analysis. The specimen plane is normal to the beam direction and the x-ray take-off angle of the Si(Li) detector is 135°.

FIG. 4.--Melbourne proton micro-
probe (MP). Energy-analyzing mag-
net of accelerator is at extreme
top left. Center of photo shows
four magnetic quadrupole lenses
preceded by sweep coils. Specimen
chamber at right end of line has
Si(Li) detector at 135°, binocular
microscope at 0° (thick specimens
use stereo microscope through side
window), and micrometer stage be-
low chamber.

Nuclear Scattering: Light Elements and Depth Profiling

We have shown that the proton microprobe can detect trace elements by virtue of the very low background produced in PIXE analysis. Unless a windowless detector is used, this technique is restricted to elements of Z > 11. With thin biological specimens it is possible simultaneously to detect the light elements down to hydrogen by examining the spectrum of protons scattered from the specimen at forward or backward angles.[2,15] The energy lost in scattering is a direct measure of the mass of the target atom and distinct peaks are observed in thin target spectra. With thick targets the peaks broaden to overlap or become steps. However, these wide peaks or steps are indicative of the depth distribution of the corresponding atoms in the sample. It is thus possible, by backscattering from a thick specimen, to measure nondestructively depth profiles simultaneously for several elements in a small area. Figure 5 shows a good example of such a measurement on MP.[16] To increase the depth sensitivity, a beam of 2MeV alpha particles was used. This measurement is particularly interesting because the beam was channelled down the crystal axis of the silicon substrate. The spectrum of Fig. 5 gives information on the depth distribution of implanted As and of a surface film of carbon, the thickness of an amorphous surface layer on the silicon, the degree of channeling, and the presence of a contaminant trace element.

FIG. 5.--Spectrum of backscattered α particles; 2MeV α beam from MP was channeled down axis of implanted Si wafer and scattered beam was observed at grazing (10°) angle of emergence.[16]

Nuclear Reactions: Isotope Detection

Although cross sections for nuclear reactions are much smaller than those for ionization or nuclear scattering, many reactions are available to the various particle beams and, since they are highly selective, they are particularly useful in identifying light elements in a thick heavy matrix. Most work of this nature with microbeams has been done at Harwell, where Be, B, C, N, O, and Si profiles have been measured in metal specimens.[17] A nuclear reaction is specific to an isotope rather than just an element Z or mass A. In theory a microprobe can be used to map the movement of nonradioactive (or radioactive) tracers, but the levels and cross sections involved generally make this procedure impractical.

Scanning Analysis Total Data Handling

MP was conceived from the start as an instrument with a major application to biological and medical problems. Much of the work involves elemental mapping, line scanning, or the collection of elemental

spectra for points or designated regions of a beam-sensitive specimen. We therefore developed a technique that would permanently record and handle all data available from the specimen during a single analysis.[18] Scanning of the MP beam is done by magnetic coils ahead of the lens system (Fig. 4). These coils are driven by independent oscillators, and a storage oscilloscope is used to image the specimen for lining it up in the beam.

MAP BEING DRAWN ON THE
FACE OF THE STORAGE C.R.O.
BY THE SCANNING ELECTRON BEAM

C.R.O.
SWEEP
COILS

TRIGGER

DETECTOR

X RAY

X OSCILLATOR   Y OSCILLATOR

PROTON BEAM

MP
SWEEP
COILS

SPECIMEN BEING SCANNED
BY THE PROTON BEAM

(a)

DISPLAY

PDP 11/40
COMPUTER

FILTER

SORT

KEYBOARD

STORAGE
DISC

PROGRAM
DISC

STORAGE
TAPE

ENERGY   X   Y

DETECTOR
X OSCILLATOR   Y OSCILLATOR

(b)

TO MP SWEEP COILS
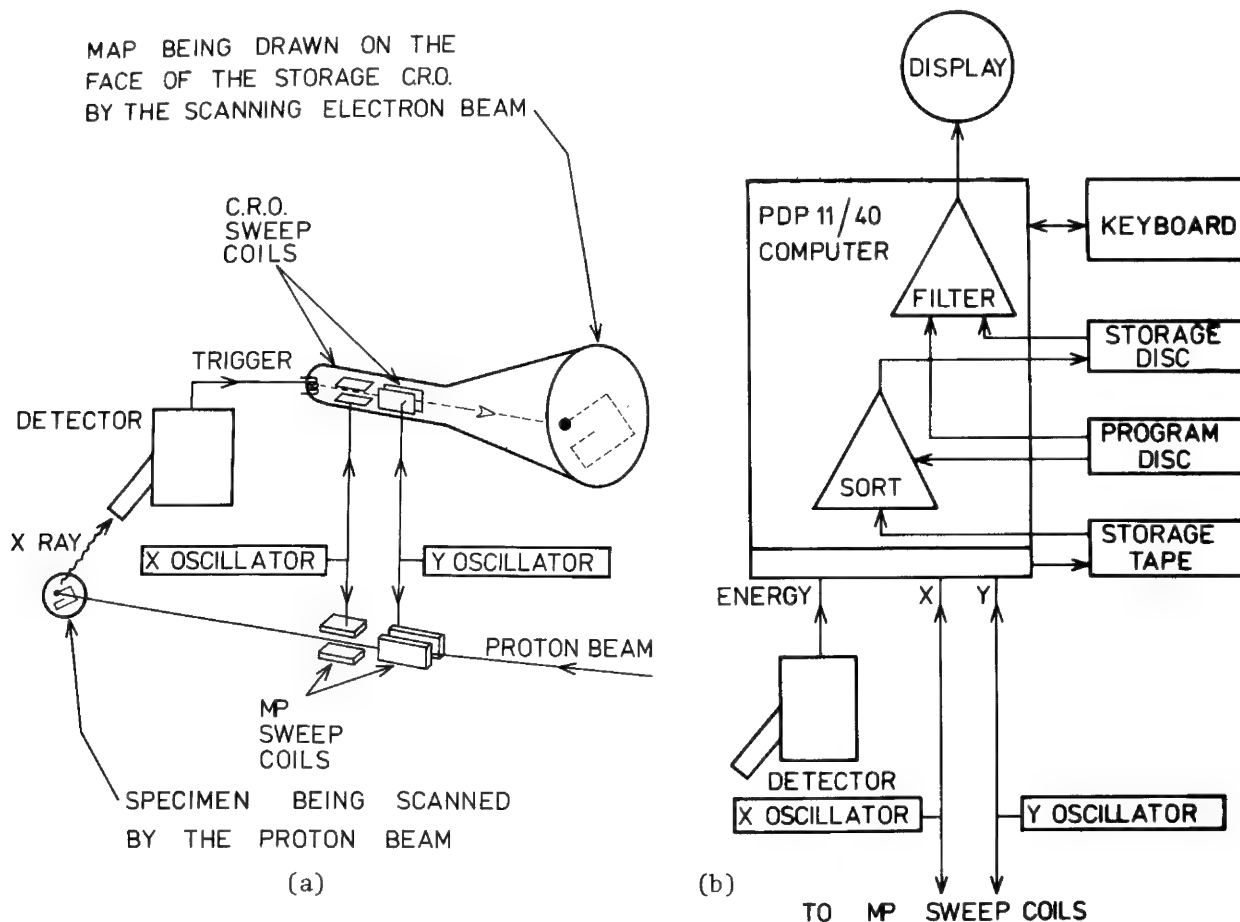
FIG. 6.--Schematic diagram of MP scanning-analysis system, showing (a) basic system similar to that of scanning electron microscope, and (b) additions to basic system that enable simultaneous recording of all information.

The oscilloscope is driven by the same oscillators and triggered by the x-ray detector (Fig. 6a). The energy signal from the x-ray detector and the two oscillator signals are also fed to the analog-to-digital converters of an on-line PDP 11/40 computer (Fig. 6b). Once a run is started, each x-ray event triggers the recording of the x-ray energy value together with the corresponding values of the X and Y beam displacements. As the data come in they are stored on magnetic tape. At any time after run termination, the data can be sorted onto a magnetic disk for rapid access. We can then project on the computer display screen a map or line scan of any element or a spectrum of any region within the analyzed area. With this system no data are thrown away, no resolution is lost, and a vast amount of information is available for immediate or later examination and intercomparison.

An example of some data from the Melbourne system is shown in Fig. 7: four of the many elemental maps and spectra displayed by the computer after a single scanning operation on a section of wheat seed.[19] The specimen was fairly uniform in density over this $1mm^2$ region, as indicated by a map of bremsstrahlung, in contrast to the structure apparent in the elemental maps shown here. The contrast in these maps also serves to emphasize the excellent peak-to-background ratio obtained for the trace elements.
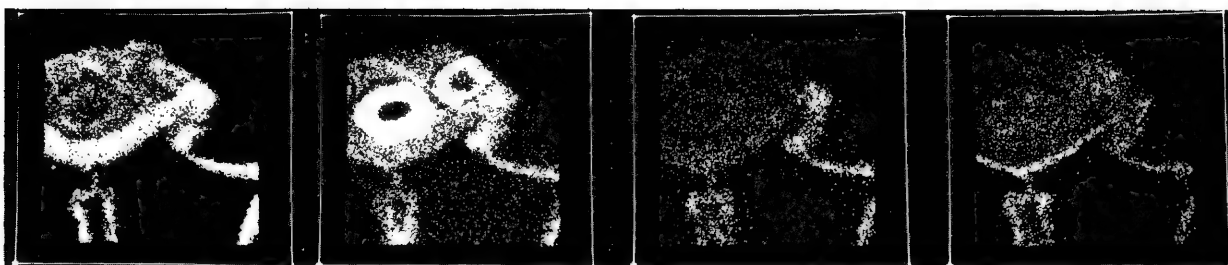
FIG. 7.--Maps of (left to right) K, Mn, Fe, and Zn distributions in thin transverse section of wheat seed, showing strong concentrations of trace metals in or around embryo (top half of scan). Kink in aleurone layer at right is from microtome. Area of scan is 1 mm^2. These and other maps were extracted by computer from data for all elements collected simultaneously.

Measurement of Elemental Losses

Proton microprobe analysis is a nondestructive technique in the same sense as electron microprobe analysis, but both techniques can cause physical damage and, more serious loss of elements under adverse conditions. Because the Melbourne system gives a complete record of the data as they were collected, it is used to detect losses of elements by a study of the PIXE and scattering yields as a function of beam charge collected; the digitized charge pulses are also stored by the system.[20] Figure 8 shows a computer display of such elemental loss under deliberately induced extreme conditions. A beam of 3MeV protons was run unscanned on a 12μm spot at a current of 10 nA instead of the usual 0.1-1 nA. The specimen was a 5μm-thick section of freeze-dried *Mougeotia* (a filamentous alga) embedded in Spur's resin. The support was a nylon foil and no cold stage or coating was used. The initial rate of chlorine loss was very rapid under these extreme conditions, in contrast to the stability of the mass indicated by the bremsstrahlung. Note that half the chlorine disappeared in the first 4.5 sec after the beam hit the specimen. Periodic inspection of the spectrum by the operator would have revealed only a very gradual loss of chlorine.

FIG. 8.--Yield of chlorine and bremsstrahlung (mass) x-rays from 5μm section of *Mougeotia* as function of beam charge, for extreme beam conditions (10 nA unscanned). Scale is effectively 1.5 sec/channel.

Potential of the Scanning Proton Microprobe

We have reviewed the fundamental bases of proton microprobe analysis, the current state of instrumental development, and the development of a special scanning analysis technique. The main potential of the scanning proton microprobe in nondestructive analysis lies in its sensitivity, its deep penetration with minimum loss of spatial resolution, and its ability, when fully instrumented, to collect and analyze a vast amount of quantitative data from one exposure of the specimen. However, some of this instrumentation is adaptable to the scanning-electron microprobe. The sensitivity would remain as a fundamental advantage of the proton instrument and its future appears to lie in *trace* elemental microanalysis. Big technological improvements must be made before the proton instruments can hope to equal the electron instruments in spatial resolution of thin specimens--improvements in ion source brightness, in accelerator optics and stability, and in strong-lens

design. Even then the electron microprobe is likely to remain as the standard in-house instrument for most studies of the major elements in a sample. A rapid increase in the number of scanning proton microprobes should make them increasingly accessible for trace elemental studies.

References

1. J. A. Cookson, A. T. G. Ferguson, and F. D. Pilling, "Proton microbeams, their production and use," *J. Radioanal. Chem.* 12:39, 1972, and *Harwell Report* AERE-R6300, 1970.

2. G. J. F. Legge, C. D. McKenzie, and A. P. Mazzolini, "The Melbourne proton microprobe," *J. Microsc.* 117: 185, 1979, and *Univ. Melb. Report* UM-P-76/43, 1976.

3. G. J. F. Legge, "Proton microprobes: Principles, properties and potentials," *Proc. 2nd Aust. Conf. on Nuc. Tech. of Anal.*, 1978, 18.

4. J. Guy and G. J. F. Legge, "Continuous x-ray spectrum from proton interactions with matter," *ibid.*, 1978, 72.

5. A. P. Mazzolini and G. J. F. Legge, "Elemental analysis of botanical specimens using the Melbourne proton microprobe," *ibid.*, 1978, 27.

6. T. Hughes, C. D. McKenzie, and J. Waschl, "Proton probe analysis for rare earths in minerals," *ibid.*, 1978, 30.

7. A. Roczniok and G. J. F. Legge, "Measurements of beam profile and spread for a proton microbeam," *ibid.*, 1978, 24.

8. S. J. B. Reed, *Electron Microprobe Analysis*, London: Cambridge University Press, 1975, p. 218.

9. D. Brune, U. Lindh and J. Lorenzen, "A proton semi-microbeam device for surface analysis," *Nucl. Instr. Meth.* 142: 51, 1977.

10. G. Bonani et al., "A digitally controlled scanning microprobe for protons and heavy ions," *Nucl. Instr. Meth.* 157: 55, 1978.

11. R. Nobiling et al., "Focussing of proton beams to micrometer dimensions," *Nucl. Instr. Meth.* 142: 49, 1977.

12. D. Heck, "The Karlsruhe proton microbeam system," *Beitr. elektronenmikroskop. Direktabb. Oberfl.* 1979, 259.

13. H. K. Ito and L. Grodzins (MIT) "A superconducting solenoid lens for focusing MeV protons," *Bull. Am. Phys. Soc.* 24: 595, 1979; and C. J. Maggiore, *Los Alamos Progress Report* LA-7872PR, 1979.

14. J. A. Cookson, "The production and use of a nuclear microprobe of ions at MeV energies," *Nucl. Instr. Meth.* 165: 477, 1979.

15. J. A. Cookson and G. J. F. Legge, "Biological analysis with a nuclear microprobe," *Proc. Analyt. Div. Chem. Soc.* 12: 225, 1975.

16. S. A. Ingarfield, C. D. McKenzie, and J. S. Williams, private communication.

17. J. A. Cookson, J. W. McMillan, and T. B. Pierce, "The nuclear microprobe as an analytical tool," *J. Radioanal. Chem.* 48: 337, 1979.

18. G. J. F. Legge and I. Hammond, "Total quantitative recording of elemental maps and spectra with a scanning microprobe," *J. Microsc.* 117: 201, 1979, and G. J. F. Legge, "Some experiments with a proton microbeam," *Abstr. 48th ANZAAS Cong.*, 1977, 25.

19. A. P. Mazzolini, C. K. Pallaghy, and G. J. F. Legge, to be published.

20. G. J. F. Legge and A. P. Mazzolini, "Elemental microanalysis of biological and medical specimens with a scanning proton microprobe," *Nucl. Instr. and Meth.* 168: 563 1980.

PLANAR MICROMETROLOGY IN THE SEM

Stephen Jensen

Accurate dimensional measurements in the scanning electron microscope (SEM) of lateral features on planar structures and particles are becoming increasingly important. Miniaturization in a number of industries--most notably the electronics industry--has led to an increasing need for dimensional metrology at micrometer and submicrometer dimensions. Planar micrometrology currently consists of poorly defined and characterized techniques for measurement. Dimensional measurements made with the SEM generally employ the indicated SEM magnification as a calibration reference without verification of its accuracy. The resulting uncertainty combines with image formation in the SEM to produce significant systematic measurement errors. Two measurement techniques using the SEM are described. One is a comparison method in which the SEM image of the object to be calibrated is compared with the image of a previously calibrated artifact. The second employs optical interferometry to measure the translation of an object beneath a static electron beam in an SEM.

Measurement Process

The linear dimensions of a planar object in an SEM are measured by a two-step process that entails (1) locating the edges of the object and (2) measuring the distance between these edges. Edge location involves establishing an intensity level of the detected signal (e.g., secondary electrons) as being the position in the SEM image that corresponds to the geometric object edge. This position lies within the transition region that defines the image boundary. The difference between the position of the edge-as-located and the geometric edge is a distance δ and is a complex function of instrument and technique variables.

Three kinds of linear dimensional measurements are possible: displacement, spacing, and length. Each involves edge-location and distance-measurement operations. In a displacement measurement, a single edge in the SEM image of an object is located and the corresponding position P_1 noted. The object is then translated. The same edge is relocated and the new position of the edge P_2 is determined. The distance the edge has moved constitutes the displacement measurement. Since only one edge is measured, the edge location error δ is repeated at both image positions and cancels when the displacement D is measured:

$$D = (P_2 + \delta) - (P_1 + \delta) = (P_2 - P_1) \tag{1}$$

For a spacing measurement, two similarly facing edges are located and the distance between them is measured. Since the edges face the same direction, the sign of the two edge location errors in the SEM image is the same. Also, to first order, the magnitude of the edge location error at each edge is the same. If the measured positions and edge location errors for these two edges are denoted by P_1, δ_1 and P_2, δ_2 then the spacing measurement S is

$$S = (P_2 + \delta_2) - (P_1 + \delta_1) = (P_2 - P_1) + (\delta_2 - \delta_1) = (P_2 - P_1) \tag{2}$$

Illustrations of spacing measurements include the measurement of distances between SEM stage micrometer graduations and diffraction grating replica lines. A spacing measurement is made whenever the distance between two similar objects is measured, as shown in Fig. 1 for linespacing measurements.

In a length measurement, two oppositely facing edges are located and the distance between them is measured. Since the edges face in opposite directions, the signs of the two edge location errors are opposite. If the two edges have positions and edge loca-

The author is with the Surface Characterization Group of the National Bureau of Standards, Washington, DC 20234.

tion errors of P_1, δ_1 and P_2, δ_2, respectively, the measured length L is

$$L = (P_2 + \delta_2) - (P_1 - \delta_1) = (P_2 - P_1) + (\delta_2 + \delta_1)$$

$$\simeq (P_2 - P_1) + 2\delta \qquad (3)$$

A length measurement is made whenever the size or width of a single object is determined. Examples of length measurements include linewidth and particle size measurements. For length measurements, the edge location errors add rather than subtract as was the case for spacing measurements. The distinction between a linewidth and a linespacing is illustrated in Fig. 1 for the case of both low-quality and high-quality images indicative of large and small edge-location errors, respectively. The measured linespacings are equal for both images, whereas the linewidth measurements differ and depend on the edge location errors.

In order to perform a measurement of length, spacing, or displacement, a calibration process through which the dimensions of the object being measured are referenced to the standard of length[1] is required. This calibration may be done indirectly through the use of comparator methods or may be performed directly through the use of optical interferometry, where the standard is the wavelength of the laser employed with the interferometer.

SYMMETRY IN LINEWIDTH AND LINESPACING
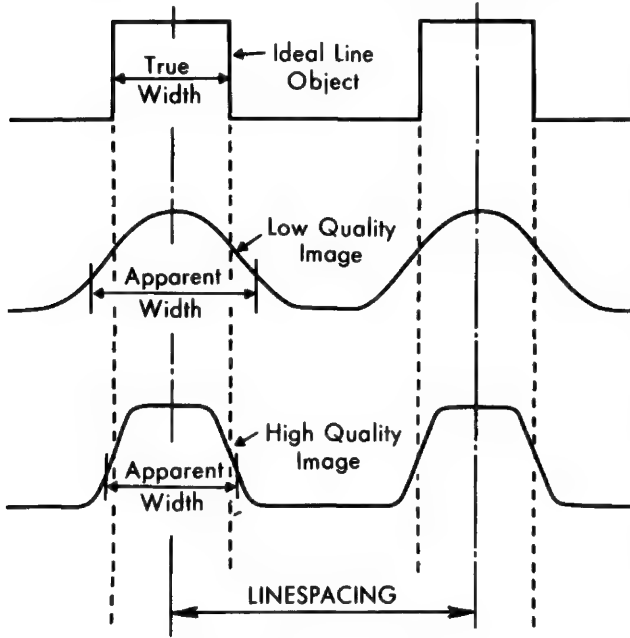
FIG. 1.--Linespacing vs linewidth measurements for low- and high-quality images.

Comparator methods consist of a ratio technique, in which the object to be calibrated (the unknown) is compared with some reference standard which has been previously calibrated. The reference standard may be either a known spacing or a known length. The comparison may be made directly by imaging of both the unknown and the reference standard in the SEM at the same time, or may be done indirectly by calibration of the magnification of the SEM with a spacing reference standard.

There are four possible cases to consider in comparator measurements, since both the unknown and the reference standard may be either a spacing or a length. Each case gives rise to a different measurement error involving the edge location errors. In the discussion that follows, object dimensions are indicated by small letters, image dimensions by capital letters, unknown dimensions by the subscript x and superscript primes, and known (reference standard) dimensions by the subscript o. Edge location errors and position in the SEM image are denoted by δ and P, respectively. The comparator process consists of ratioing the measured dimensions of the images for both the unknown and the known (reference) objects:

$$\frac{\text{Unknown Object Dimension}}{\text{Known Object Dimension}} = \frac{\text{Unknown Image Dimension}}{\text{Known Image Dimension}} \qquad (4)$$

For the comparison of an unknown spacing s_x to a known spacing s_o Eq. (4) becomes

$$\frac{s_x}{s_o} = \frac{(P_2' - P_1') + (\delta_2' - \delta_1')}{(P_2 - P_1) + (\delta_2 - \delta_1)} \simeq \frac{S_x}{S_o} \qquad (5)$$

and the error introduced by the comparison measurement is zero since the edge location errors cancel to first order.

For the comparison of an unknown spacing s_x to a known length ℓ_o as would be the case if latex spheres were used as the reference standards the measurement is

$$\frac{s_x}{\ell_o} = \frac{(P_2' - P_1') + (\delta_2' - \delta_1')}{(P_2 - P_1) + (\delta_2 + \delta_1)} \simeq \frac{S_x}{L_o + 2\delta} \simeq \frac{S_x}{L_o}\left(1 - \frac{2\delta}{L_o}\right) \tag{6}$$

The comparison of an unknown length ℓ_x to a known spacing s_o will result in a similar error

$$\frac{\ell_x}{s_o} = \frac{(P_2' - P_1') + (\delta_2' + \delta_1')}{(P_2 - P_1) + (\delta_2 - \delta_1)} \simeq \frac{L_x + 2\delta'}{S_o} = \frac{L_x}{S_o}\left(1 + \frac{2\delta'}{L_x}\right) \tag{7}$$

The comparison of an unknown length ℓ_x to a known length ℓ_o results in an error of more complicated form:

$$\frac{\ell_x}{\ell_o} = \frac{(P_2' - P_1') + (\delta_2' + \delta_1')}{(P_2 - P_1) + (\delta_2 + \delta_1)} \simeq \frac{L_x + 2\delta'}{L_o + 2\delta} \simeq \frac{L_x}{L_o}\left[1 + \frac{2(L_o\delta' - L_x\delta)}{L_xL_o}\right] \tag{8}$$

Equations (5)-(8) illustrate the manifestations of the edge location errors for different types of comparator measurements. The significance of these errors is described in greater detail elsewhere.[2]

Comparator Measurements in the SEM

The use of a comparator method to measure planar dimensions of objects is by far the most common method employed in the SEM. The comparison of the unknown to the reference standard may be performed by imaging of the two in the SEM either simultaneously or sequentially. An example of simultaneous imaging is the measurement of the diameters of particles mounted on a diffraction grating replica (the reference standard). Sequential measurements, in which the unknown and standard are imaged separately, suffer from the fact that operating conditions influencing magnification may be different for the two images produced.

The uncertainty of comparator measurements depends on both the calibration uncertainty of the reference standard and the image formation and edge definition process in the SEM. Image formation in the SEM is an important source for both systematic and random errors. The errors associated with image formation errors have been reviewed by several authors.[3-5] Possible sources for error include:

1. Uncorrected lens astigmatism
2. Extraneous magnetic and electrostatic fields
3. High-voltage supply instabilities in the electron gun
4. Nonorthogonal deflection by the scan coils
5. Unbalanced and/or nonlinear scan generator circuits
6. Signal processing
7. CRT beam distortions and curvature of the CRT face
8. Camera lens distortion
9. Expansion, contraction, and processing of photographic materials

All of these contribute to changes in apparent magnification and to image distortion. Image distortion may be checked by micrographs of periodic structures such as diffraction grating replicas. The field of SEM photogrammetry provides abundant illustration of the measurement and correction of image distortion.[5,6] The distortion need not be in the SEM itself since the CRT may introduce nonlinearities as large as 16%.[4] The effects of image distortion may be minimized by measurement of the known and unknown at the same position in the SEM image. The spacings or widths of the reference standard should be near in size to the dimensions of the unknown so that they may both be imaged in the same part of the

SEM field of view.

The indicated magnification of the SEM can be in error by an amount typically between 10 and 30%,[3] which shows the need for calibration with a reference standard if dimensional measurements with uncertainties smaller than 30% are desired. Possible sources for change in apparent magnification include electron beam voltage, lens hysteresis, working distance, and objective lens setting. The influence of these parameters on apparent magnification of the SEM must be determined if accurate dimensional measurements are to be made by use of the indicated SEM magnification. Once that is done, there is no assurance that the magnification will remain constant with time. Figure 2 shows an example of the variation of apparent magnification of an SEM with time. It shows measurements on the 2, 5, and 50μm spacings of the control standard for the National Bureau of Standards (NBS) Standard Reference Material (SRM) #484 (an SEM magnification standard).[3,7] Measurements were made on 70 different dates over a period of 1 yr under experimental conditions as nearly identical as possible. Changes as large as 6% are present, which shows that in the more routine operation of an SEM the apparent magnification is generally reliable only to about 10% even though the magnification has once been calibrated with a reference standard. This uncertainty illustrates the importance of simultaneous imaging and comparison of the unknown and the reference standard if accurate dimensional measurements are to be made in an SEM.
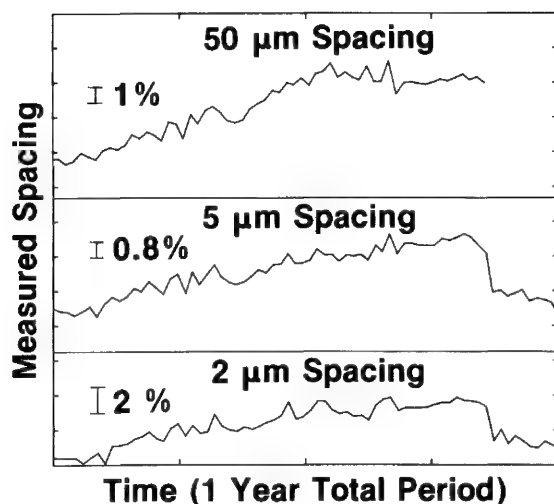
FIG. 2.--Change in magnification of SEM as function of time over 1 yr. Error bars indicate measurement uncertainty for each spacing. (Courtesy David Ballard, NBS).
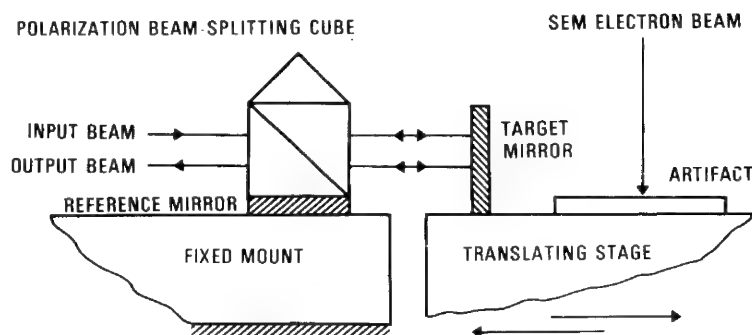
FIG. 3.--Use of scanning stage and optical interferometer in SEM for dimensional measurements.

Interferometer-based Measurements in the SEM

Dimensional measurements by optical interferometry in an SEM date back at least to 1970.[8] Typical operation is shown in Fig. 3. A plane mirror or corner cube reflector is mounted on the translating stage and forms the moving arm of a two-axis interferometer. As the stage moves the specimen is scanned beneath the static electron beam and the signal produced by the electron-specimen interaction is collected along with the sample position as determined by the interferometer. The data then consist of a set of x, I pairs where x is the sample position and I is the signal intensity. This intensity may be the detected secondary, backscattered, or Auger electrons. Since x is known directly in terms of the interferometer laser wavelength, calibration measurements may be performed directly on the unknown without resort to reference standards.

One facility illustrating the use of optical interferometry for dimensional measurements in an SEM is the microlength calibrating electron probe (MCEP) at NBS. Figure 4

ELECTRON OPTICS COLUMN

ELECTRON BEAM SPOT POSITION

D/A CONVERTER

ANNULAR BSE DETECTOR

A/D CONVERTER

SECONDARY ELECTRON DETECTOR

AUGER ANALYZER

TO COMPUTER

SPECIMEN & PZT STAGE

INTERFEROMETER

BCD READOUT

SCAN

LASER

FUNCTION GENERATOR

FROM COMPUTER
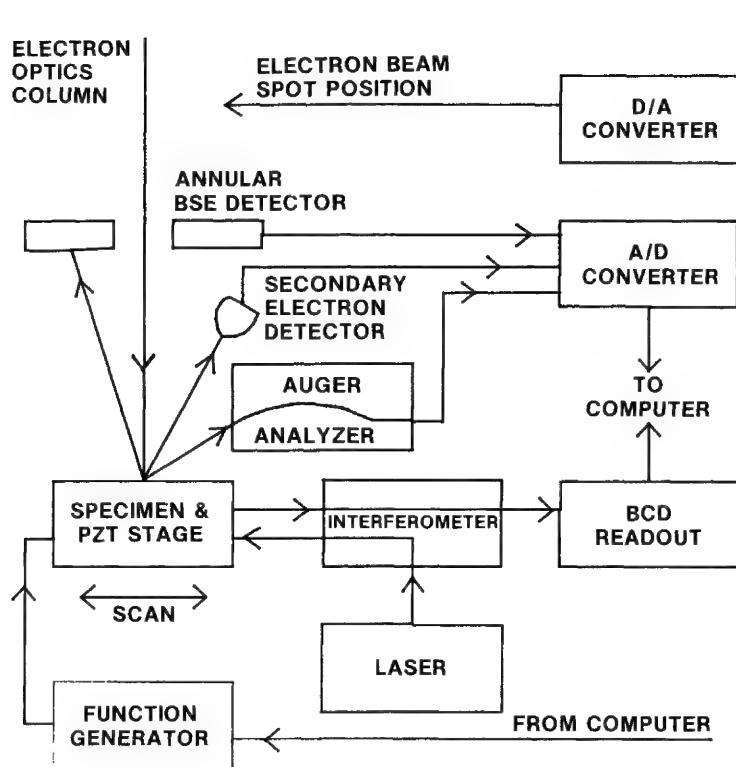
FIG. 4.--Block diagram of NBS microlength calibrating electron probe (MCEP).

shows a block diagram of the facility, which is built around a UHV SEM[9] with a field-emission source. The modified SEM incorporates a piezo-flex stage[10] and an optical interferometer[11] inside the vacuum chamber. The stage consists of a stack of piezoelectric ceramic disks and a flexure-pivot network to amplify the expansion or contraction of the disks. A total scan of 110 µm is possible with roll, pitch, and yaw each less than 5 arc-seconds. The interferometer is a modified Michelson interferometer and is used with a commercial laser measurement system.[12] Secondary, backscattered, or Auger electrons may be detected as the specimen is scanned beneath the static electron beam. Data acquisition as well as stage scanning are under control of a minicomputer. The MCEP is capable of providing calibrations for lateral dimensions on objects between 0.1 and 100 µm in length with a measurement uncertainty as small as 0.01 µm.

Since a static electron beam is employed, image distortion and magnification errors associated with comparator measurements that use a raster-scanned electron beam are avoided. There are, however, a number of sources for calibration uncertainty in such systems:

1. Electron beam size and stability
2. Roll, pitch, and yaw of the stage scan
3. Specimen or interferometer misalignment relative to the stage scan axis
4. Stage and interferometer vibration
5. Interferometer/laser measurement system resolution

The sharpness possible in scanned image profiles is limited by both the size and stability of the electron beam, which combine to produce an effective beam spot size. The MCEP has a beam size of 5 nm (FWHM) and a positional stability of 4 nm over 20 sec. Items (2) and (3) can produce scale factor (cosine) errors as well as additive (sine) errors. These errors are generally quite small and for a well-aligned system with a good scanning stage such as the one employed in the MCEP typically give errors less than 10 nm for measurements on micrometer-sized objects. Interferometer and stage vibrations act along with (1) to limit the sharpness of scanned image profiles. Item (5) determines the least count (and hence the resolution) for the x axis of a calibration scan. A practical least count of 2 nm is possible with the commercially available equipment employed in the MCEP.

Calibration Standards

Several structures with calibrated dimensions smaller than 10 µm are commercially available for use as reference standards in the SEM. Most of them consist of calibrated spacings although a few have calibrated widths. Commercially available calibrated spacings in approximate order of decreasing size include optical stage micrometers, NBS SRM 484, and diffraction grating replicas. Calibrated widths include NBS SRM 474 and polymer spheres. The sizes and uncertainties for these commercially available objects are summarized in Fig. 5, where the calibration uncertainty is plotted as a function of the spacing (or width) of the reference standard.

FIG. 5.--Commercially available SEM reference standards for dimensions less than 10 μm. Calibration uncertainty is plotted as function of standard size.

Optical stage micrometers have calibrated spacings as small as 2 μm. They generally consist of patterned metal lines on a glass substrate and should be carbon coated to minimize charging in the SEM. Most have calibrations that are traceable to the NBS Line Standard Interferometer.[13] An accurately calibrated optical stage micrometer is included as part of NBS SRM 474 (a photomask linewidth standard).[7,14] The spacings range between 2 and 10 μm with uncertainties of 0.02 μm.[15] A stage micrometer specifically intended for use in the SEM is NBS SRM 484.[3,7] The surface of the standard is a polished cross section consisting of alternating lines of gold and nickel. The standard has seven lines of gold (0.04-0.08 μm wide) separated by thicknesses of nickel ranging from 1 to 20 μm. Spacings of 1, 2, 3, 5, and 50 μm are calibrated with uncertainties of 0.039 and 0.476 μm for spacings smaller and larger than 5 μm, respectively. Calibration of these standards is also traceable to the NBS Line Standard Interferometer.

The most useful diffraction grating replicas for the SEM are gold replicas. They are commercially marketed as magnification standards for scanning microscopes.[16] These cross-ruled diffraction grating replicas have spacings of 0.46 μm (2160 lines/mm) and 50 μm (19.7 lines/mm) and offer reasonable contrast when imaged in the SEM. No information is provided with the replica regarding its calibration uncertainty. Irregularities up to 0.05 μm in the edges of individual grooves of the replicas are probably the most significant source for uncertainty in the use of these replicas as spacing reference standards on the micrometer scale.

Calibrated linewidths are provided by NBS SRM 474 for both clear (glass) and opaque (chrome) lines ranging in size from 0.5 to 10 μm. The associated calibration uncertainties are 0.05 μm.[15] A second calibrated-width standard is monodisperse polymer spheres. These spheres are available from a number of domestic suppliers[17] and have calibrated diameters ranging from 0.08 to 100 μm. Spheres smaller than 2 μm have a diameter uncertainty of about 0.01 μm; those larger than about 2 μm have considerably larger uncertainties. The calibration uncertainty is due in part to the distribution in size of spheres in a given (supposedly monodisperse) sample.[2] Since these spheres are composed of polymer material and are thus nonconducting they should be coated for imaging in the SEM.

Standards for the SEM with a calibration uncertainty of about 1% are needed throughout the range from 0.01 to 1 μm. Except for a few of the standards listed above, commercially available length and spacing standards on a submicrometer scale do not exist at present. A promising means for the development of such standards between 0.1 and 1 μm is through new lithographic techniques such as x-ray and STEM lithography.[18] For dimensions smaller than 0.1 μm, structures fabricated by molecular beam epitaxy[19] hold considerable promise.

Modeling

Edge location errors δ can play a significant role in determining the ultimate uncertainty in a dimensional calibration and are an important source for systematic errors in

both comparator and interferometer-based measurements. One may minimize these errors by either improving the image resolution or by modeling the electron-specimen interaction process. Improved image resolution results in a smaller "fuzzy" region of transition between the object and the substrate (or background material). If this "fuzzy" region is made narrower, the potential edge location errors δ are also correspondingly decreased since the edges are located in this region. Alternatively, the electron-specimen interaction may be modeled and theoretical profiles generated for the detected electron signal-intensity as a function of position. In that way one may gain insight into the scatering process and may hope to locate more accurately the geometric specimen edge within the transition region of the image. Methods used to calculate electron-specimen interaction mechanisms are described by Wells[20] and include transport equations, diffusion models, single-event backscattering models, and Monte Carlo methods. Monte Carlo methods find the widest application and are reviewed by Kyser.[21] Part of the appeal of Monte Carlo methods is the fact that they calculate typical electron trajectories and may be easily applied to arbitrary specimen geometries.

Work is needed both in the modeling of the electron-specimen interaction process and in the comparison of calculations to experimental measurements. The use of the SEM for dimensional measurements of planar structures on a submicrometer scale depends both on the success of such modeling and on the availability of reference standards for these dimensions.

References

1. The present internationally accepted standard of length is the wavelength of the transition between the $^2P_{10}$ and the $^5d_5$ levels of the Krypton-86 atom. The de facto standard is the wavelength of the iodine-stabilized He-Ne laser.

2. Dennis Swyt, "A look at techniques for the dimensional calibration of standard microscopic particles," NBS Spec. Publ. 260, to be published August 1980.

3. David Ballard, "A procedure for calibrating the magnification of a scanning electron microscope using NBS SRM 484," NBS Internal Report 77-1248, 1977.

4. David Joy, "SEM parameters and their measurement," *SEM/1974*, Chicago: IIT Research Institute, 327-334.

5. S. Murray and A. H. Windle, "Characterization and correction of distortions in SEM micrographs," in *Scanning Electron Microscopy: Systems and Applications*, London: Institute of Physics, 1973, 88-93.

6. P. G. T. Howell, "A practical method for the correction of distortions in SEM photogrammetry," *SEM/1975*, Chicago: IIT Research Institute, 199-206.

7. Available from the Office of Standard Reference Materials, National Bureau of Standards, Washington, DC 20234.*

8. E. D. Wolf, F. S. Ozdemir, and R. D. Weglein, "Precision electron beam microfabrication of acoustic surface wave devices," *IEEE Ultrasonics Symp. Proc.*, 1973, 510-515.

9. Vacuum Generators Ltd. HB-50A.*

10. Fredric Scire and Clayton Teague, "Piezodriven 50-μm range stage with subnamometer resolution," *Rev. Sci. Instrum.* 49: 1735-1740, 1978.

11. A. W. Hartman, "Polarization interferometers for micrometrology," NBS Internal Report, 1980 (in press).

12. Hewlett Packard #5526.*

13. "Line-standard interferometer," *NBS Tech. News Bull.*, 1967, pp. 43-45.

14. John Jerke, Ed., "Semiconductor measurement technology: Accurate linewidth Measurements on integrated circuit photomasks," NBS Spec. Publ. 400-43, 1980.

15. Diana Nyyssonen, "Spatial coherence: The key to accurate optical micrometrology," *SPIE Proc.* 34-44, 1979.

16. Available from Polaron Instruments and Ted Pella Inc.

*Certain commercially produced equipment or materials are identified in this paper in order to specify experimental and calibration procedures. In no case does such identification imply recommendation or endorsement by the National Bureau of Standards nor does it imply that the material or equipment identified is necessarily the best available for the purpose.

17. Sources include Dow Chemical, Coulter Electronics, Duke Scientific, Microspheres, Pacific Scientific, Particle Information Service, Poly Science, and Royco Instrument.[*]

18. H. I. Smith, D. C. Flanders and D. C. Shaver, "New applications of submicro-meter structures in materials science and biology," *SEM/1978/I*, AMF O'Hare Ill.: SEM Inc., pp. 33-40.

19. A. C. Gossard et al., "Epitaxial structures with alternate-atomic-layer composition modulation," *Appl. Phys. Lett.* 29, 323-325, 1976.

20. Oliver Wells, *Scanning Electron Microscopy*, New York: McGraw-Hill, 1974, 47-49.

21. David Kyser, "Monte Carlo Simulation in Analytical Electron Microscopy," J. Goldstein, and D. Joy, Eds., *Introduction to Analytical Electron Microscopy*, New York: Plenum, 1979, 199-221.

THE SIMS II: A NEW APPROACH TO SIMS ANALYSIS

B. F. Phillips and R. L. Gerlach

Recently the field of Quadrupole Secondary Ion Mass Spectrometry (QSIMS) has grown rapidly. Since the introduction of the Applied Research Laboratories QMAS in 1975,[1] the designs and experiments of Magee[2] of RCA Laboratories and related developments have led to recognition of QSIMS as an analytical technique with high potential for surface studies. First, compact primary ion guns have been developed which can form beams of a small enough diameter so that individual features on specimens can be analyzed. Second, the action of secondary-ion-extraction lenses and energy filters used in conjunction with quadrupole mass spectrometers have become better understood. Third, the instrument control and data acquisition systems have shown great improvement in capabilities over the past several years.

With the introduction of the Physical Electronics Model 3500 SIMS II, the factors mentioned above have been blended together to produce an instrument that truly represents a major advance in SIMS analysis. This SIMS can be mounted in combination with Auger, ESCA, and UPS spectrometers, so that all analyses can be performed on the same area of a specimen. Figure 1 shows some of the important features of the SIMS II. The secondary-ion-extraction lens and oxygen gas jet can be moved over a 2.5in. range with the linear-motion micrometer, so that the best lens position for ion extraction can be used when SIMS only is used and then the lens can be retracted for optimum AES and/or ESCA analysis. The tilt motion allows the whole spectrometer to be moved so that the focal points for AES, ESCA, SIMS, and the primary-ion gun can all be made to coincide on the sample surface. The 90° section spherical capacitor energy analyzer sorts the secondary ion beam by energy so that only ions that match the energy acceptance of the quadrupole are transmitted. The continuous dynode electron multiplier is mounted off axis to reduce susceptibility to noise induced by neutral or high-energy particles. Also, signal gating before ions enter the spherical-sector energy analyzer insures that "crater wall" effects are minimized during depth profiling. In addition, the quadrupole mass spectrometer is designed so that mass ranges of 1-250, 1-500 or 2-1000 can be covered by simple substitution of the corresponding rf-tuning units.

As an example of the capabilities of this system, which has a high ion transmission with high mass-resolving power, NBS Standard Reference Material No. 613 was analyzed (Fig. 2). SRM No. 613 is a glass of nominal composition 72% SiO_2, 12% CaO, 14% Na_2O, and 2% Al_2O_3 with 50 ppm of 61

LINEAR MOTION MICROMETER

LEAK VALVE

TILT MOTION

ELECTRON MULTIPLIER

QUADRUPOLE

SPHERICAL CAPACITOR ENERGY ANALYZER

STANDARD 4½″ O.D. PORT (2½″ I.D.)

EXTRACTION LENS

GAS JET

8.25″ (21 cm) FLANGE TO SAMPLE

FIG. 1.--SIMS II spectrometer outline.

Author Phillips is a senior laboratory scientist with the Surface Sciences Division Laboratories of Perkin-Elmer Corp. and Dr. Gerlach is a senior project scientist with the Perkin-Elmer Physical Electronics Division, Eden Prairie, MN 55344.

other elements added. Note the particular peaks identified in the spectrum, especially in the high-mass range. This spectrum illustrates two points: the ability to use the scanning electron beam of the Auger spectrometer to provide sample surface charge neutralization and the high sensitivity at high mass range of the SIMS II.
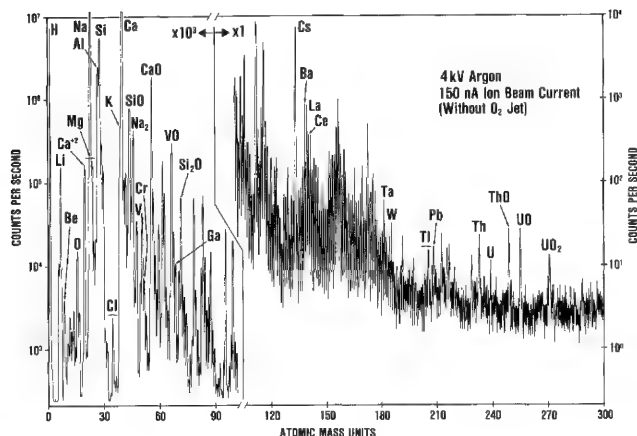
FIG. 2.--NBS SRM 613, 50 PPM of 61 elements.

The second example (Fig. 3) is an analysis of an Si film after an overlayer of Al has been sputtered away. Note particularly the absence of any Al peaks and the extremely low levels of the alkali elements (Li, Na, K) in these spectra. It is apparent that hydrocarbon ions seen in the upper spectrum are a function of the oxygen jet interacting with residual C-containing species in the vacuum and not the specimen itself.

The SIMS II is designed to be integrated into the Physical Electronics MACS (Multiple-technique Analytical Computer System) with both the SIMS and quadrupole under direct digital control of the computer. All spectrometer voltages are adjustable from the graphics display terminal and software control of instrument set-up and operation modes has been developed.

FIG. 3.--Si substrate under Al film.

In conclusion, the SIMS II is presented as an instrument of great capability that can be used in combination with other techniques to provide a complete characterization of both material surfaces and depth profiles.

References

1. H. J. Roden and R. D. Fralick, "The QMAS," *26th Pittsburgh Conf.*, 1975, paper 70.
2. C. W. Magee, W. L. Harrington, and R. E. Honig, "Secondary ion quadrupole mass spectrometer for depth profiling: Design and performance evaluation," *Rev. Sci. Inst.* 49: 477-485, 1978.
3. A. Benninghoven et al., *Secondary Ion Mass Spectrometry SIMS II*, New York: Springer, 1979, vol. 9, 203-205.

THE USE OF CHARGE-COUPLED DEVICES FOR DIRECT ELECTRON RECORDING

J. N. Chapman, R. P. Ferrier, A. M. MacLeod, and P. T. E. Roberts

Introduction

There is a need in electron microscopy for a parallel recording system capable of direct electronic readout. In the conventional transmission electron microscope (CTEM) images are generally viewed on a phosphor screen, yet frequently the current density there is inadequate to observe fine detail or even on occasions to determine whether an object of interest is present. Such instances arise, for example, in the investigation of magnetic structures by Lorentz microscopy, due to stringent coherence requirements, and in the observation of "weak-beam" images of dislocations. A more serious deficiency of the phosphor screen is that images may only be observed while the specimen is being irradiated, a grave limitation in the examination of radiation-sensitive materials. Further disadvantages arise when a CTEM image is to be recorded. Photographic film offers a high information-storage density, but it has a limited dynamic range: it responds linearly only over a part of it. Access to the recorded image is only available after development and fixation, and even then the information is present in an analog form unsuitable for image analysis by digital computer. To obtain quantitative electron intensity data a further stage involving a microdensitometer is required, so that the whole process of obtaining information from the CTEM in a suitable form for image processing is time consuming and remote from the microscope itself.

The scanning transmission electron microscope (STEM) has the advantage that in imaging mode the intensity information from bright- or dark-field detectors is available directly. Recently experimental and theoretical studies of new forms of detector, e.g., split,[1] quadrant,[2] and multi-annular,[3] have been carried out with the aim of obtaining information of more direct relevance to any particular structural feature under investigation. Such detectors are normally placed in the far field and it is advantageous if the effective angle which they subtend at the specimen can be varied over a wide range. It would be extremely useful if a direct output 2-D detector array could be utilized, the information from which would be processed to provide the set of signals appropriate to the form of detector to be simulated.

One system[4] that overcomes some of the disadvantages discussed above uses a low-light-level TV technique involving electron-photon conversion and the subsequent digitization of the output of the TV camera. A simpler approach we have been evaluating is to use a multi-element semiconductor device on which the electrons are directly incident and which provides a signal proportional to the number of electrons received. Devices that may be suitable in this context include self-scanned photodiode arrays (SSPDAs) and charge-coupled devices (CCDs). An investigation of the suitability of the former has been carried out[5]; the use of the latter in direct-bombardment mode with electrons of much lower energies than those of interest in the electron microscope has also been studied.[6,7] In this paper we examine the use of CCDs as a recording medium for electrons in the range 20-100 keV.

Experimental Results

Commercial CCDs and SSPDAs are designed for photon rather than electron imaging. When a photon is incident on one of the cells of the device, an electron-hole pair is produced and the electron is stored in a potential well. After a preset time the contents of the wells are interrogated and the output signal comprises a series of voltage pulses proportional to the number of photons incident on each cell. When electrons of

energy 20-100 keV are incident directly (after the protective optically transparent cover has been removed) on such devices, the principal difference is that rather than one electron-hole pair being produced, each incident electron creates several thousand such pairs, the exact number depending on the incident electron energy and the device geometry. Thus, under direct electron bombardment, the device itself has a high intrinsic gain, an attractive feature for a low-noise imaging system.

The particular device chosen for study in this investigation was the Fairchild CCD 202, which is a 2-dimensional array of 100×100 photocells each of area 18×30 μm. Each cell is essentially an MOS capacitor capable of storing 0.1 pC of charge and comprises a polysilicon electrode, SiO_2 insulator, and a p-type silicon substrate. When a positive potential is applied to the electrodes, the minority carriers created by a high-energy electron are swept towards the insulator and are held in a potential minimum at the substrate-insulator interface. Insertion of a thin channel of n-type silicon at the interface diminishes the likelihood of the collected electrons being trapped in states close to the insulator surface and is responsible for the slight displacement of the minimum away from the interface. To determine the magnitude of the individual charge packets, they are initially clocked from the photocells into the adjacent transport cells (Fig. 1), after which they are clocked along the vertical analog transport registers into a horizontal transport register and subsequently read out through a two-stage gated charge integrator. The content of each cell is read through the same gate, and transport efficiency is very high, so that the noise performance of the device is very good.
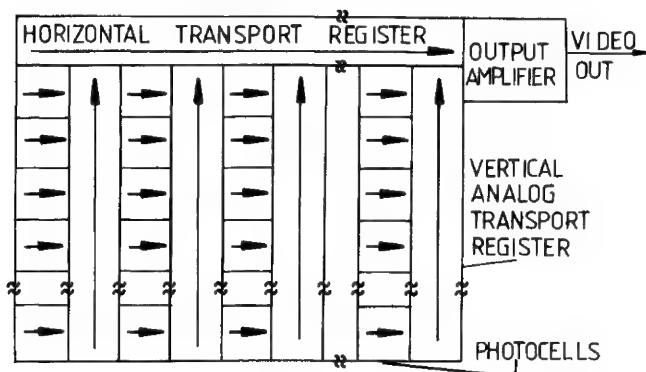
FIG. 1.--Block diagram of the CCD 202 showing directions of charge transfer.
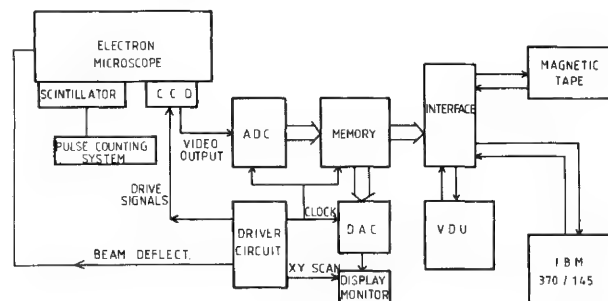
FIG. 2.--Block diagram of the detection and recording system.

Under constant irradiation with photons no image smearing occurs during transfer, since the charge is clocked through the transport cells, which are protected from the photon beam by a thin layer of aluminum. However, under electron irradiation the aluminum layer is virtually transparent, so that secondary electrons are collected in both the photocells and the transport cells. This increase in active area is an advantage when the CCDs are used for electron detection but makes it desirable to operate the microscope in a pulsed-beam mode. In operation and testing of the CCD the experimental arrangement[8,9] illustrated in the block diagram (Fig. 2) was set up. The CCD is located beneath the camera chamber of a JEOL JEM 100C electron microscope and may be cooled to approximately -40°C. Also located there is a scintillator/photomultiplier pulse counting system used to monitor the flux of electrons incident on the CCD. Prior to recording, the illumination is deflected from the specimen; it is then restored for a preset time during which the charge packets build up in the potential wells of the device. The content of the cells are then read out with the illumination once again deflected from the specimen. The analog signals are transferred to the data accumulation system for digitization and storage and the whole process repeated until the desired statistical accuracy is achieved. (This procedure is a consequence of the somewhat limited storage capacity of the cells under electron bombardment.) After accumulation, data can be transferred to a computer via a port which is designed to accept characters from a VDU terminal. Although slow (about 10 min to transfer

4K words), this mode currently allows access to a departmental IBM 370/145 computer for image processing and permanent storage. This arrangement will be soon supplemented by the addition of a new minicomputer system, which will permit greater flexibility and speed of transfer. Alternatively, data can be output on to magnetic tape and subsequently transferred to the computer. A display monitor allows the stored image to be viewed for examination and selection before transfer and enables images to be photographed.

Several experiments were performed to check the performance of the CCD. We investigated the gain of the device by flooding it and the adjacent scintillator with a uniform beam of electrons and measuring the average height of the output pulses from each cell of the CCD; this quantity should be proportional to the average charge collected by each cell. This experiment was performed for three values of the incident electron energy: 20, 60, and 100 keV. The results show that for any electron energy, the gain of the CCD, defined as the number of secondary electrons collected in a potential well for each incident electron, was independent of the incident intensity provided the cell content was below its saturation value. For the incident energy range considered the gain increased nonlinearly with energy; the gains for 20, 60, and 100keV electrons were in the ratio 2:13:20. Such nonlinearity is hardly surprising as the energy of the primary electron is deposited in the electrodes and insulator as well as in the silicon substrate, whereas charge is collected only from secondary electrons generated in the last. The maximum deposition of energy in the overlying layers occurs when 20keV electrons are incident, which further depresses the gain observed at this voltage. Also, the gain does not increase indefinitely with increasing electron energy, since electrons from electron-hole pairs created well beyond the diffusion length in silicon are not collected in the potential well and the proportion of these electrons increases with primary electron energy.

A consequence of the high gain and limited cell capacity of the CCD is that well saturation is achieved with 440, 65, and 45 primary electrons for incident energies of 20, 60, and 100 keV, respectively. If random variation of intensity in an image is to be unimportant, the number of incident electrons per cell should exceed 400 and hence each image must be built up from several cycles of illumination and read out, e.g., at 60keV incident energy a minimum of 8 cycles is required to produce an acceptable image. However with the clocking rates available (> 1 MHz) this requirement presents no real problem.

By shielding part of the CCD from the incident electrons, one may compare the performance of the irradiated and unirradiated cells, by a comparison of the behavior of the two groups of cells when the whole device was uniformly illuminated by light from an LED. As the cumulative dose increased two effects were noted. The dark current (the output of the cells when they are not subject to illumination) increased; it rose to 10% of the saturation level after 10^6 electrons per cell at 60 keV were incident. By cooling to -10°C we reduced this signal substantially and could neglect it. As the cumulative dose increased further, the gain of the irradiated cells was no longer independent of incident electron intensity, but decreased as the output voltage approached the saturation level. Restoration to its original value was achieved by an increase in the voltage applied to the gate electrodes. However, that was only possible over a limited range of doses, and since the gate voltage could not be increased indefinitely, an uncorrectable decrease in gain was ultimately observed. For each value of cumulative dose there was a maximum output voltage below which the gain was normal; if we define the lifetime of the CCD as the dose at which this voltage falls to half of the original saturation level, we have lifetimes of 0.2, 1.2, and 1.5×10^7 incident electrons per cell at 20, 60, and 100 keV respectively. Given that about 10^3 electrons per cell (i.e., 3% shot noise) are desirable for most image analysis procedures in electron microscopy, the lifetime of the device corresponds to 1.2×10^4 recorded images for 60keV electrons.

The overall uniformity of response of the system[10] was measured by irradiation of the CCD with an electron dose of 10^3 electrons/photocell. The output from 4096 cells was transferred to the computer and the distribution of cell contents analyzed. The mean and standard deviation of the distribution were found to be 77 and 2.6, respectively, in arbitrary units and so agreed well with the expected 3% variation due to shot noise in the beam. Similar results were obtained with 60 and 100keV electrons indicating that noise in the detector system is suitably low.

Another characteristic of interest is the spatial resolution of the CCD when used to

detect high energy electrons. Given that the photocell size is 18 × 30 μm and that the diameter of the electron-hole pair cloud created by an incident electron is about 60 μm for a 100keV incident electron and about 10 μm for one of 40 keV,[11] it is clear that some charge collection in cells other than the one struck by the incident electron would be expected. To test this hypothesis, a 75μm-thick copper aperture was placed 500 μm above the CCD to give an abrupt change in electron intensity, and the signal variations across the edge of the aperture were investigated. The results (Fig. 3) indicate that for 40keV electrons there is little spreading of charge to adjacent cells, but for 100keV electrons a significant variation in signal is observed over four photocells, which indicates that charge spreading over about 60 μm has occurred. This result is consistent with the values described above.

CONTENT OF INDIVIDUAL CELL
(ARBITRARY UNITS).

DISTANCE FROM EDGE OF APERTURE (μ m)
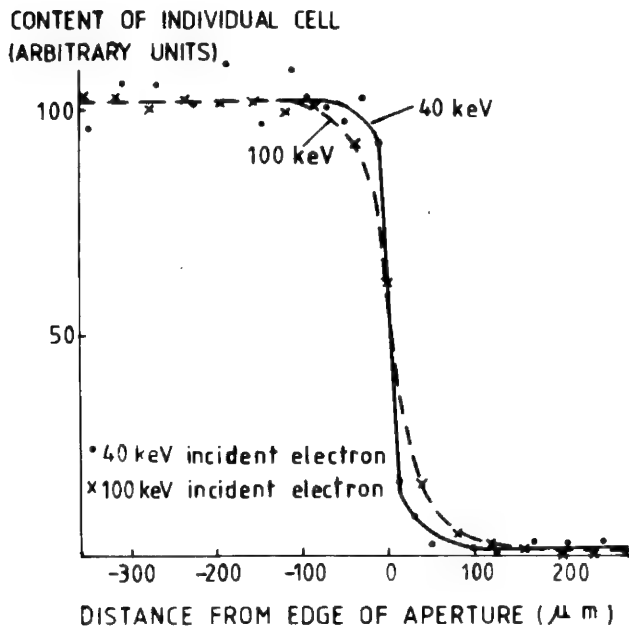
FIG. 3.--Variation of the cell content across an aperture edge for incident electrons of energy 40 and 100 keV.

Electron images obtained with 60keV electrons with the CCD cooled to -20°C are shown in Figs. 4 and 5. To avoid damage to the on-chip amplifiers, the outer area of the device was shielded from the electron beam by a copper mask, leaving an inner area of approximately 82 × 82 photocells and 82 × 41 transport cells to record the image. Figure 4(a) shows the image of a 0.5μm repeat replica diffraction grating, taken with an average number of 630 electrons incident on each photocell. To illustrate that useful information is not restricted to the photocells, Fig. 4(b) shows the image formed from the contents of the transport cells. Figure 5 shows an equivalent pair of images obtained from a specimen of catalase which is frequently used for magnification calibration in electron microscopy. In this case the average content per cell was equivalent to 280 primary electrons. The resolution in these images is consistent with the figures discussed previously.

Discussion

The experimental results for the Fairchild CCD 202 detailed in the previous section may be summarized as follows.

1. The output of each cell of an undamaged device is proportional to the electron flux incident on it, up to the saturation level of the cell.
2. The capacity of each cell expressed in terms of the equivalent number of incident primary electrons decreases with increasing primary electron energy for energies up to 100 keV. The capacity is small (about 50 at 100 keV), which indicates the need for a data accumulation and storage system if reasonable statistical significance is to be obtained in imaging.
3. If the device is cooled, noise from electrons thermally generated in the silicon is negligible.
4. At 100 keV there is inevitable spillage of charge over typically four cells; at 40 keV the spread is less than one cell size. Thus at 100 keV the number of cells available is effectively reduced.
5. After prolonged irradiation the cooled device damages under the beam and a reduction in charge transfer efficiency results. The lifetime of the device is therefore limited and at 100 keV the maximum accumulated dose is 1.5×10^7 primary electrons per photocell.
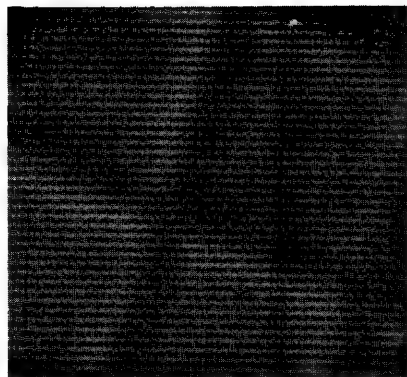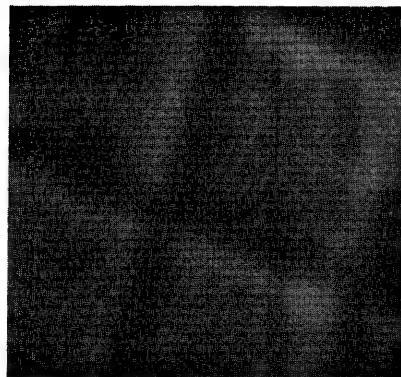
FIG. 4.--Transmission electron image of a replica diffraction grating using 60keV electrons. Number of electrons/photocell = 630. (a) Photocells (b) Transport cells.
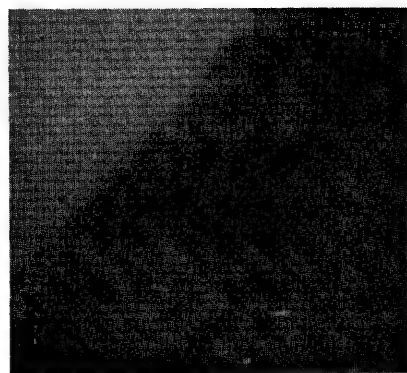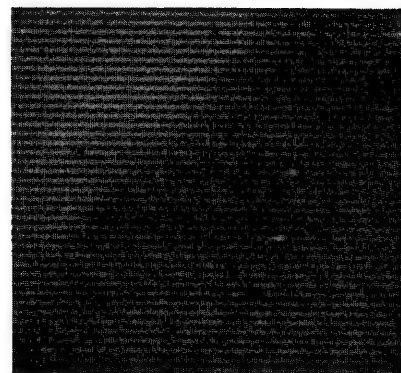
FIG. 5.--Transmission electron image of a catalase crystal. Number of electrons/photocell = 280. (a) Photocells (b) Transport cells.

Of the characteristics described above, (1), (2), and (3) are either advantageous or present no limitation; (4) confirms that the cell size of the CCD 202 is smaller than is required for the higher energy electrons of interest; and (5) is actually disadvantageous: although 10^4 images/device is acceptable, extensive use of the device to locate areas of interest on the specimen and to adjust microscope operating conditions would severely reduce the final number of images available for analysis. It is believed that the damage mechanism is associated with the radiation-induced fixation of positive charge (holes or Na^+ ions) at the oxide-semiconductor interface.[12] However, these particular CCDs, which are now out of production, were not intended for electron imaging.

No other devices known to us have been designed with electron microscopy in mind, yet it is worth considering how some might perform in this role. Recently an examination has been made of a 2-D Integrated Photomatrix SSPDA in the direct electron bombardment mode and an increased resistance to damage has been observed compared with the CCD 202.[13] In SSPDAs the MOS structure is effectively replaced by p-n junctions and although these devices generally seem to have slightly poorer uniformity of response and noise characteristics than CCDs, these considerations are outweighed if a substantially greater lifetime is confirmed. New CCDs are also becoming available that may be more suitable. Such devices should preferably have a structure in which impurities in the oxide and the number of interface states are minimized; the latter desideratum is achieved if growth of the oxide during fabrication is performed at the lowest possible temperature.[14] However, a more satisfactory CCD would be one in which no energy was deposited in the insulator. This requirement could best be achieved by backface irradiation,[15] but that requires a thinned substrate and at present few such devices are commercially available.

We have restricted ourselves to a consideration of the suitability of CCDs, when directly bombarded with electrons, as detectors for electron microscopy. The need for a low-noise parallel detector system also exists in electron energy loss spectroscopy (EELS), but its somewhat more stringent requirements suggest that a directly bombarded CCD would not be satisfactory. Foremost among them are the greater dynamic range typically encountered (frequently above 10^4); and the limited dispersion of many spectrometers, which would severely restrict the resolution in the recorded spectra. Both these problems, and indeed the serious problem of radiation damage, are overcome to some extent if the electron image is initially converted to a photon image before being projected onto the CCD. However, such a system is more complex, more bulky, and unlikely to have as good a noise performance, considerations of differing importance under various circumstances. Thus, before the potential of CCDs or SSPDAs as detectors in electron microsopy and analysis can be fully evaluated, further tests involving direct electron bombardment and photon conversion should be carried out on new devices with an improved performance.

References

1. N. H. Dekkers and H. de Lang, *Optik* 41: 452, 1974.
2. E. M. Waddell and J. N. Chapman, *Optik* 54: 83, 1979.
3. H. Rose, *Ultramicroscopy* 2: 251, 1977.
4. K-H. Herrmann, D. Krahl, and H. P. Rust, *Ultramicroscopy* 3: 227, 1978.
5. D. G. Jenkins et al., in T. Mulvey, Ed., *Developments in Electron Microscopy and Analysis* (IOP Conf. Ser. 52), 1979, 81. B. L. Jones, D. G. Jenkins, and G. R. Booker; in D. L. Misell, Ed., *Developments in Electron Microscopy and Analysis* (IOP Conf. Ser. 36), 1977, 73; D. G. Jenkins et al., *Electronics Letters* 14: 174, 1978.
6. S. Sobieski, *SPIE Low Light Level Devices* 78: 73, 1976.
7. D. G. Currie and J. P. Choisser, *ibid.*, 83, 1976.
8. J. N. Chapman et al., in T. Mulvey, Ed., *Developments in Electron Microscopy and Analysis* (IOP Conf. Ser. 52), 1979, 77.
9. J. N. Chapman et al., submitted to EUREM 80.
10. P. T. E. Roberts, A. M. MacLeod, and J. N. Chapman, in J. Mavor, Ed., *Proc. 5th Intern. Conf. on CCDs* (Univ. of Edinburgh), 1979, 112.
11. K. F. J. Heinrich, D. E. Newbury, and H. Yakowitz, Eds., *Proc. Workshop on Use of Monte Carlo Calculations in Electron Probe Microanalysis and Scanning Electron Microscopy*, NBS Special Publication 460, 1975.
12. J. M. Killiany et al., *Trans. IEEE* NS-21: 193, 1974.
13. G. R. Booker, private communication.
14. J. M. Killiany, *Trans. IEEE* CHMT-1: 353, 1978.
15. L. Caldwell and J. Boyle, *SPIE* 78: 10, 1976.

THERMAL-WAVE MICROSCOPY IN A SCANNING ELECTRON MICROSCOPE

Elmar Brandis and Allan Rosencwaig

In recent years photoacoustic or thermal-wave analysis and imaging of solid samples have been of considerable interest. Although so far all work done involved the use of high-intensity optical illumination, thermal-wave analysis and microscopy can also be performed in a scanning electron microscope.

In thermal-wave microscopy both thermoacoustic and elastoacoustic processes are set up in the sample by the intensity-modulated radiation incident on the surface. Energy levels excited by the incident radiation de-excite by heat-producing processes. Thus, the absorption of intensity-modulated radiation at any point on the surface results in periodic heating. The heat energy is transferred either in a thermal-wave mode for low and moderate modulation frequencies, or in a elastoacoustic mode for high modulation frequencies.

Experimental

The experimental work was conducted in a Cambridge Steroscan MKIIa scanning electron microscope equipped with a LaB_6 electron source. Figure 1 is a schematic diagram for detecting thermal-wave signals. The sample was mounted on a Vernitron piezoelectric transducer with Apiezon wax.
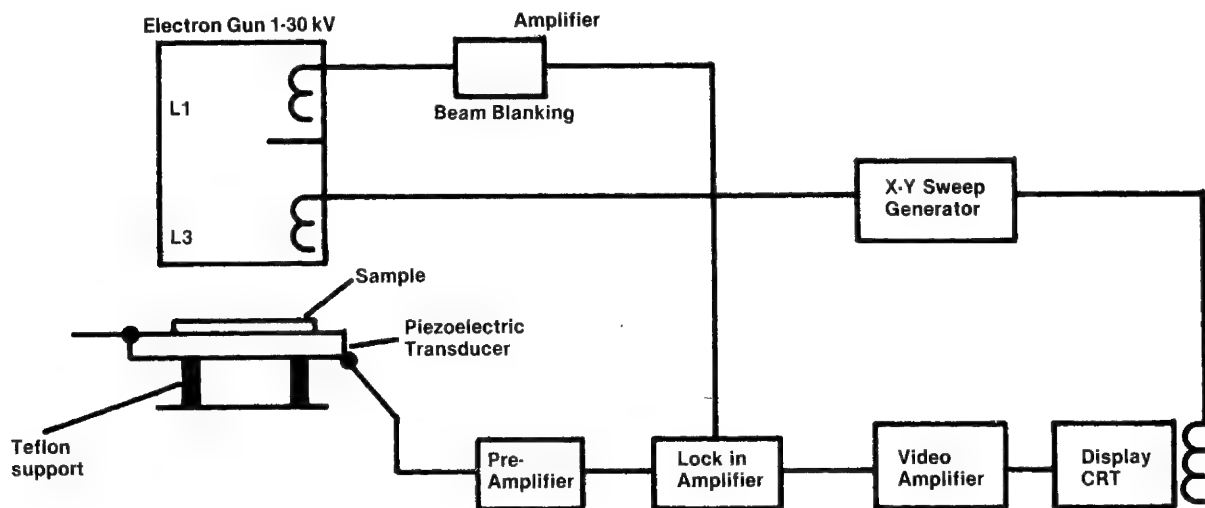
FIG. 1.--Measurement and display of thermal-wave images in SEM.

The electron beam was modulated with a frequency derived from the lock-in amplifier. The amplified signal from the piezoelectric transducer was fed into the video channel of the SEM for the recording of thermal-wave images. An electron beam energy of 30KV and a beam current of 3×10^{-7} A were selected. A modulation frequency of 100 kHz provided the highest signal-to-noise ratio. With a time constant of 3 msec the recording of thermal-wave images with 300 lines per frame required 400 sec.

Results

Generation of thermal-wave images in an SEM was demonstrated by means of a specimen consisting of part of a semiconductor chip with a deep scratch covered with silver paint. A thermal-wave image of the scratched area (Fig. 2) was recorded at a phase that maximized the contrast between the silicon substrate and the scratch. The thermal-wave image is related to both the topography and materials variation of the sample, and the thermal properties of the scratch. The thermal-wave image shows that part of the scratched area contains dark patches that suggest internal voids of varying dimensions within the capillary filled scratch. High-resolution secondary-electron images of the same area indicates only a scratch partially filled with silver paint (Fig. 3).
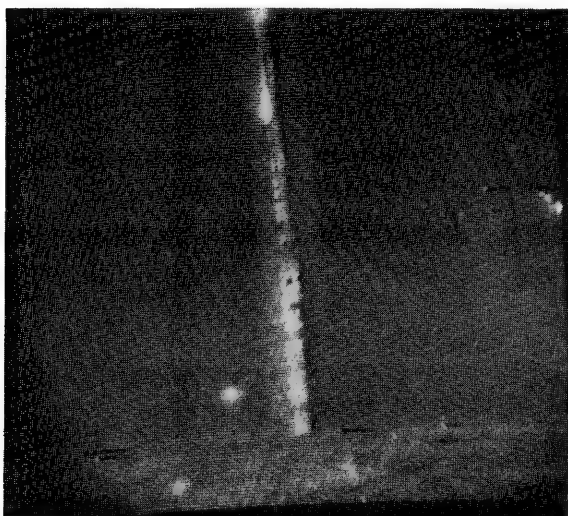
FIG. 2.--Thermal-wave image of scratch capillary filled with silver paint.
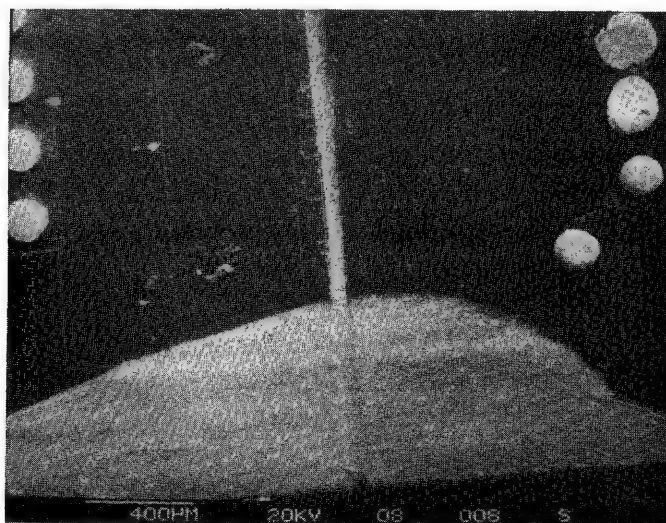
FIG. 3.--Secondary-electron micrograph of scratch capillary filled with silver paint.

The thermal wave produced by the electron beam has a wavelength at 100 kHz of approximately 5 µm and is scattered by the void below the surface. In this manner the microvoid is imaged by thermal waves generated by the electron beam incident on the sample surface.

References

1. Y. H. Wong, R. L. Thomas, and G. F. Hawkins, *Appl. Phys. Lett.* 32: 538, 1979.
2. Y. H. Wong, R. L. Thomas, and J. J. Pouch, *Appl. Phys. Lett.* 35: 368, 1979.
3. M. Luukkala and A. Penttinen, *Elect. Lett.* 15: 326, 1979.
4. H. K. Wickramasinghe et al., *Appl. Phys. Lett.* 33: 923, 1978.
5. G. Busse, *Appl. Phys. Lett.* 35: 759, 1979.
6. G. Busse, *Proc. Topical Meeting on Photoacoustic Spectroscopy,* Ames, Iowa, 1979.
7. R. L. Thomas et al., *J. Appl. Phys.* 51: ;;52, 1980.
8. A. Rosencwaig, *Am. Lab.,* April 1979.
9. E. Brandis and A. Rosencwaig, *Appl. Phys. Lett.* MS L-99.

AN X-RAY SPECTROMETER DATA ACQUISITION SYSTEM WITH A MICROPROCESSOR-BASED COMPUTER

R. S. Lisiecki and D. B. Wittry

A PET microcomputer system[1,2] along with a minimal amount of external hardware has been adapted for control, data acquisition, and data processing with an x-ray spectrometer. This system sets the wavelength of the x-ray spectrometer via a stepper motor and records x-ray counts and specimen current for each spectrometer position. The system provides for automated scanning over a peak and beam current normalization. Signal averaging is obtained by repetitive scanning over a given peak over long time intervals in order to improve the signal to background ratio.

   This system is easily implemented because the PET microcomputer can retrieve or send information to hardware devices in its high-level Basic language. The interface to the PET could have been accomplished either by the IEEE 488 General Purpose Interface Bus provided on the PET or by the memory expansion connector. For this application, the 488 bus required more logic to perform the requisite bidirectional data transfers and also made control programming more difficult. We therefore chose to use the memory-expansion connector, to which we attached the hardware necessary to complete the interface. This arrangement made it possible to write operating programs in Basic for control of the spectrometer position, starting or stopping of the counting, and reading of x-ray counts or counts from the digitized specimen current.

   As shown in Fig. 1, x-ray pulses from the spectrometer go first to an external pulse-height analyzer and then into a 24-bit ripple counter via a Schmitt trigger. The specimen current goes to an external voltage-to-frequency converter and then into another 24-bit ripple counter via a Schmitt trigger. Data from these counters is input to the Pet microcomputer through the 6522 Versatile Interface Adaptors (VIAs),[3] which provide data latching. The time for data recording at a given spectrometer position (1, 2, 5, 10, 20, 50, 100 sec) is determined by a crystal oscillator and divider chain set by the three external switches (X2, X5, X10) and synchronized with timing signals from the VIAs. Outputs from the VIAs send clockwise or counterclockwise pulses to the stepper motor circuitry.

   The operator may select from several peak scanning schemes. In one mode he may manually position the spectrometer at the beginning of an x-ray peak and
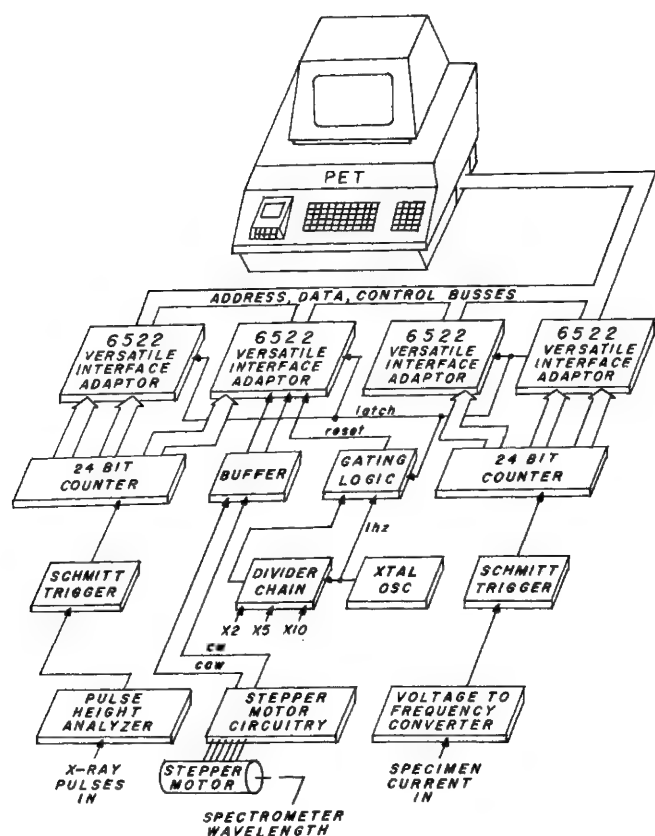
FIG. 1.--Block diagram of system used to count x-ray pulses and specimen current for x-ray spectrometer.

then use the computer to scan over the peak in steps that are any multiple of 1/400 turn of the spectrometer drive shaft, and record x-ray and specimen current counts for each step. Both the wavelength change per step and the number of steps at which data are recorded are set by the operator through the keyboard. Furthermore, the operator can specify that any given x-ray peak be scanned any number of times. For each wavelength scan, mechanical backlash is removed by the process of driving the stepper motor to a position beyond the position for which the data are recorded. In this mode, data for each wavelength position are added to the data recorded from previous scans and the average counts for this position are calculated by the PET at the end of the last scan. This mode of multiple scanning of a given x-ray peak provides signal averaging and better detection limits owing to improved signal-to-background ratio.

In another mode the operator may program the computer to perform peak seeking, for example by a preliminary scan, a polynomial fit of several points near the peak followed by subsequent resetting of the spectrometer to the peak. The first mode is useful in the determination of low-concentration elements; the second mode provides rapid and accurate spectrometer setting for elements whose concentration is greater than a few per cent. In both modes, the only manual operations to be performed by the operator with respect to data collection are the initial setting of the spectrometer position and setting of the counting time per data point.

The design and construction of this data acquisition system for use with an x-ray spectrometer was facilitated by the use of the Pet microcomputer; it provided an easy and inexpensive means of providing spectrometer control and data recording.

References

1. Commodore Business Machines, Inc., 901 California Avenue, Palo Alto, CA 94304.
2. H. D. Peckham, *Hands-on Basic with a PET*, New York: McGraw-Hill, 1979.
3. R. C. Camp, T. A. Smay, and C. J. Triska, *Microprocessor Systems Engineering*, Portland: Matrix Publishers, 1979, 160-174.

ELECTRON MICROPROBE ANALYSIS OF RARE GASES IN THIN METAL FILMS WITH THE USE OF SURROGATE STANDARDS

M. A. Short, Jack Tabock, and D. W. Hoffman

An electron microprobe technique has been devised for the quantitative analysis of the rare gases Ne, Ar, Kr, and Xe entrapped in thin films of eleven metallic elements during cylindrical-post magnetron sputtering.

Studies are in progress on the internal stresses in thin films of Ti, V, Cr, Zr, Nb, Mo, Rh, Gd, Hf, Ta, and W deposited at relatively low temperatures by cylindrical magnetron sputtering.[1-3] The working gases used during deposition included Ne, Ar, Kr, and Xe at pressures generally ranging from 0.1 to 4 Pa. Discharge voltages were generally in the 350-1000V range, depending on the pressure. The substrates used were cleaned, flat, Corning cover-glass wafers. We found a set of critical working gas pressures, which differ for different metals and working gases, below which the internal stresses in the sputtered films were compressive and above which they were tensile. It has been important to ascertain the rare gas contents of the films to determine whether or not the entrapment of the gases is a causative or simply a concurrent process with the inducement of internal stresses in the films, whose thicknesses range from 1000 to 5000Å.

The rare gases have been analyzed in the past by x-ray techniques. In 1961 Levey et al. made semiquantitative measurements of Ar, Kr, and Xe in the surface of samples of Zr, U, and Ag by means of an electron microprobe.[4] In 1963 Castaing examined thin aluminum foil for krypton, also by an electron probe.[5] Hoffmeister and Zuegel,[6] in 1969, determined the argon content of SiO_2 films by conventional wavelength-dispersive x-ray fluorescence analysis; they used a thin film of KCl as a standard, interpolating the argon intensity between the potassium and chlorine fluorescence intensities to give argon concentrations with an estimated accuracy of ±20%. Schwartz and Jones,[7] in 1970, also measured the argon concentration of SiO_2 films by the same technique. Also in 1970, Legrand et al. studied the implantation of argon ions in bulk samples of Al, Ni, and Au with an electron microprobe.[8] The implantation of argon in samples of Al_2O_3, Si, Al, and Cu was examined in 1978 by Hou, DeLavignette, and Art by an energy-dispersive system installed on a transmission electron microscope.[9]

Two problems arise in the quantitative measurement of rare-gas concentrations in thin metal films: the analysis of thin films may be different from the analysis of bulk materials, and conventional standards for rare gases are not available. The first problem is most simply solved by a reduction in the energy of the incident beam of electrons, so that the films may be regarded as bulk material. This solution may be applied only if the incident electrons are sufficiently energetic to excite the rare gases and metals being analyzed. Some excitation voltages are given in Table 1. Appropriate electron energies for the gases and metal films under consideration were calculated from Castaing's equation for the maximum depth Z_m of x-ray production:[10]

$$Z_m = 0.033 \ (V^{1.7} - V_c^{1.7}) \overline{A} / \rho \overline{Z}$$

An accelerating voltage of 7 keV made it possible to consider the thin films as bulk material for all samples. Some maximum depths of x-ray production predicted by Castaing's equation for selected rare gas/metal film combinations are given in Table 1. The energies of the relevant excitation potentials of both rare gases and metals are below 7 keV, a voltage that experiment confirmed to be appropriate (by a comparison of x-ray intensities from films and from corresponding bulk metals). Intensity ratios close to unity were sought and obtained, except for films containing substantial concentrations of gas.

TABLE 1.--Excitation voltages (keV) and maximum depths (Å) of x-ray production in certain substrates.

X rays measured		NeKα	ArKα	KrLα	XeLα	CrKα	MoLα	TaMα
Excitation voltage V_c		0.87	3.20	1.68	4.72	5.99	2.52	1.80
Maximum depth Z_m in substrate of	Cr	2600	3000	2600	1300	600		
	Mo	2000	1500	2000	1000		1700	
	Ta	1300	1000	1300	6000			1200

The problem of rare-gas standards was more complex. The procedure we adopted was based only to a limited extent on previously published work.[4-9] We measured the x-ray intensities of elements adjacent to the gas using convenient compounds, derived the intensities equivalent to 100% of the element by a reverse ZAF procedure, and interpolated linearly to obtain the rare-gas x-ray intentisy. A stable material containing an element with an x-ray emission line close to that of the gas, with a reasonable fluorescence yield, and preferably conducting was subjected to intensity measurement directly after the intensities of the elements adjacent to the rare gas were measured. In some cases the intensity was the same as the compound and element adjacent to the gas. This experimental intensity was then related to that interpolated for the rare gas by a conversion factor. The stable standard, in conjunction with the conversion factor, was then used as a surrogate standard to obtain k ratios for the quantitative analysis of the rare gas in the metal films.

As to the interpolation subsequent to the derivation of x-ray intensities by the above reverse ZAF procedure to obtain the equivalent intensity for the rare gas, the Kα characteristic x-ray intensities were calculated from[11]

$$N_K' = \omega_k [n_k(\text{direct}) + n_k(\text{indirect})] f(\chi)$$

where N_K' = number of K quanta produced per incident electron *and* reduced by the absorption of the quanta to the surface, and

$$n_k(\text{direct}) = 0.6073R(U_0 \ln U_0 - U_0 + 1)/\{Z \ln[0.583(E_0 + E_k)/J]\}$$

$$n_k(\text{indirect}) = 1.38 \times 10^{-6} ZE_k[(r - 1)/r](U_0 \ln U_0 - U_0 + 1)$$

All symbols are defined in the manner customary for electron microprobe analysis.[11] The results for neon and argon and for their adjacent elements showed that within each restricted range of three elements, The Kα intensities varied linearly with the atomic number Z. The x-ray intensities measured experimentally are related to these calculated intensities as modified by spectrometer geometry, crystal efficiency, and detector efficiency (and, in some cases, losses due to detector escape peaks). Changes in spectrometer geometry and crystal and detector efficiency within each Z range are probably small; the effects of escape peaks, particularly in the case of argon, may be more serious. We have assumed, nevertheless, that for the Kα lines of neon and argon a linear interpolation may be made. We have assumed also that a linear interpolation may be made to derive Lα x-ray intensities due to 100% krypton and xenon.

Analysis Procedure for Neon

For the analysis of neon and for the adjacent elements fluorine and sodium, a sealed argon/methane detector and a thallium hydrogen phthalate crystal (TAP) were used. Fluorine and sodium Kα x-ray intensities were measured on a sample of sodium fluoride and the intensities corresponding to pure fluorine and to pure sodium calculated using the reverse ZAF procedure. A linear interpolation gave the Kα x-ray intensity corresponding to pure

neon. Because of the extremely low fluorescence yield of elements iron through gallium (which have Lα line wavelengths in the region of fluorine, neon and sodium Kα lines), sodium in sodium chloride was used as the surrogate standard; we obtained a conversion factor of 2.85 on our microprobe. The exact value of this (and other) conversion factors may be expected to vary from one microprobe to another. This result was used to relate the sodium Kα intensity to that derived for 100% neon.

The neon and metal contents of the prepared films were determined from the sodium surrogate standard and conversion factor, an appropriate metal standard, and a conventional ZAF correction procedure to convert k ratios to neon and metal concentrations. It was assumed that the composition of the neon/metal film was constant throughout the thickness being measured.

Analysis Procedures for Argon, Krypton and Xenon

Argon, krypton, and xenon were analyzed in a manner similar to that described above for neon. The adjacent elements, compounds used, crystals used, surrogate, and surrogate material are given in Table 2. Sealed argon/methane detectors were used throughout.

TABLE 2.--Parameters for the analysis of neon, argon, krypton, and xenon.

Rare gas		Neon	Argon	Krypton	Xenon
X-ray line		Kα	Kα	Lα	Lα
Adjacent	Element	F, Na	Cl, K	Br, Sr	Te, Ba
	Radiation	Kα	Kα	Lα	Lα
	Compound	NaF	NaCl, KBr	KBr, $SrSO_4$	Te, BaF_2
Crystal		TAP	ADP	ADP	LiF
Surrogate	Element	Na	Ag	Br	Sc
	Radiation	Kα	Lα	Lα	Kα
	Compound	NaCl	Ag	KBr	Sc

Two complications arose in the analysis of argon. First, the phosphorus in the crystal used (ADP) has a K absorption edge close to the K radiations of Cl, Ar, and K. Consequently, anomalous dispersion effects were expected to cause a marked change in the relative x-ray intensities as calculated, and were in fact found. The measured intensity of Cl Kα relative to K Kα was substantially lower than that predicted; this effect does not, of course, affect the approximate linearity of the Cl, Ar, and K x-ray intensities as a function of atomic number. Second, K Kα radiation, but not Ar Kα and Cl Kα, produces an escape peak in the argon/methane detector. This escape peak has a very low energy (0.36 keV) and is lost in the system noise. No correction was made for this escape peak, whose intensity was estimated to be about 8% of the main peak, although it was appreciated that this might introduce an error of about 4% (relative) into the argon analysis.

Accuracy

Apart from counting statistics,[12] there were five potential sources of inaccuracy. First, it was assumed that, throughout the thickness of the film being analyzed at 7 keV (Table 1), the composition of the film did not change. Second, a linear interpolation was assumed between the characteristic x-ray intensities of the rare gases and the elements adjacent to them. Third, the escape peak for potassium, which was neglected, will have resulted in some small error in the argon analysis: if the error in the potassium intensity was indeed 8%, then the error in the argon analysis was 4%. Fourth, it was assumed that the spectrometers could be reproducibly reset to the required wavelengths. Fifth, it was assumed that the ZAF corrections procedure was good at 7 keV; several compounds of known composition were analyzed at this energy and good results were obtained by use of the standard ZAF corrections.

Provided the films were homogeneous, we may thus conclude that inaccuracy of the

analyses should not have exceeded about 10% (relative).

Results

Rare gas concentrations determined over a wide range of metal films varied from 0.05 to about 5 *atomic* percent. In general, it was found that the lower the atomic number of the gas the higher was its (atomic) concentration in comparable metal films and the heavier the metal the greater was the rare gas (atomic) concentration. Some results illustrating this finding are shown in Fig. 1.
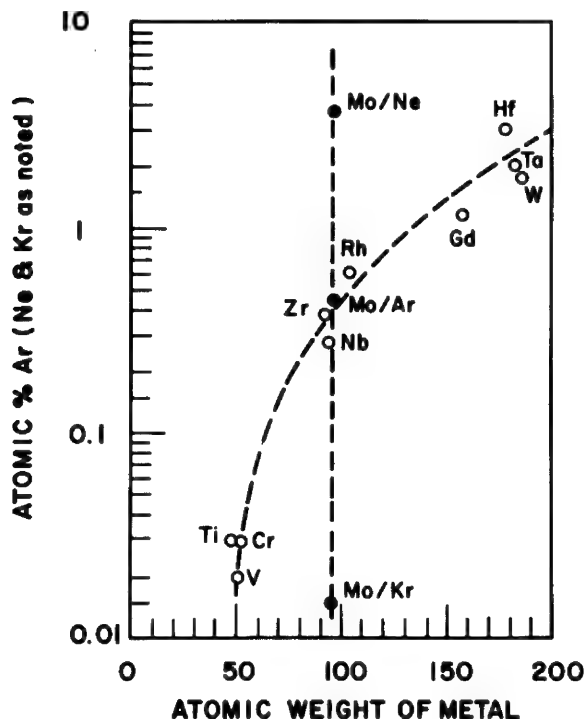
FIG. 1.--Rare-gas concentrations in thin metal films.

It was generally found that the presence of entrapped rare gases correlated with the occurrence of compressive stresses in the metal films, but that the estimated magnitude of the stresses did not change even with substantial changes in gas content. We thus conclude[2,3] that the stresses induced in the metal films are caused by the impingement of energetic rare gas atoms on the metal film during its formation, rather than by the actual incorporation of the rare gases within the metal lattice.

References

1. D. W. Hoffman and J. A. Thornton, "Effects of substrate orientation and rotation on internal stresses in sputtered metal films," *J. Vac. Sci. Technol.* 16: 134, 1979.

2. J. A. Thornton, Jack Tabock, and D. W. Hoffman, "Internal stresses in metallic films deposited by cylindrical magnetron sputtering," *Thin Solid Films* 64: 111, 1979.

3. D. W. Hoffman and J. A. Thornton, "Compressive stress and inert gas in Mo films sputtered from a cylindrical-post magnetron with Ne, Ar, Kr, and Xe," *J. Vac. Sci. Technol.* 17: 1980 (to be published).

4. V. Levy et al., "Contribution à l'étude de la précipitation des gas rares dans les metaux," *Compt. rend.* 252: 876, 1961.

5. R. Castaing, "X-ray microprobe techniques," in H. H. Pattee, V. E. Cosslett and A. Engstrom, Eds., *X-Ray Optics and X-Ray Microanalysis*, 1963, 263, 273.

6. W. Hoffmeister and M. Zuegel, "Determination of the argon content of sputtered SiO$_2$ films by x-ray fluorescence," *Thin Solid Films* 3: 35, 1969.

7. G. C. Schwartz and R. E. Jones, "Argon content of SiO$_2$ films deposited by rf sputtering in argon," *IBM J. Res. Develop.* 14: 52, 1970.

8. C. Legrand et al., "Sur l'emploi de la microsonde électronique pour l'étude de l'implantation des ions," *Compt. rend.* 271: 88, 1970.

9. M. Hou, P. Delavignette, and A. Art, "Detection of implanted ions by x-ray emission analysis in TEM," *Phys. Stat. Sol.* 46: K167, 1978.

10. R. Castaing, "Electron probe microanalysis," in L. Marton and C. Marton, Eds., *Advances in Electronics and Electron Physics*, New York: Academic Press, 1960, vol. 13, 317, 353.

11. M. A. Short, "X-ray intensities from copper-target diffraction tubes," in H. F. McMurdie et al., Eds., *Advances in X-Ray Analysis*, New York: Plenum, 1977, vol. 20, 565.

12. M. A. Short, "Statistical considerations in x-ray fluorescence analysis," in R. W. Gould et al., Eds., *Advances in X-Ray Analysis*, Dubuque, Iowa: Kendall/Hunt Pub. Corp., 1976, vol. 19, 53.

SURFACE CHARACTERIZATION OF CHEMICALLY ETCHED Ti-8Al-1Mo-1Sn AND Ti-13V-11Cr-3Al

A. A. Roche, J. S. Solomon, and W. L. Baun

Because of temperature and weight considerations, Ti and its alloys are used extensively by the aircraft industry. The "super" alpha Ti-8Al-1Mo-1Sn alloy was developed for use in jet engines where a high fracture toughness is required. Ti-13V-11Cr-3Al has good workability and strength properties when properly heat treated. Consequently, it is easily forged and has found use in structural components.

Since Ti and its alloys are subject to environmental damage, surface protection steps are usually required. These steps can involve the use of paint primers or, as in the use of aluminum, anodic oxide protective films. In most cases, as-received alloy sheets are not suitable for immediate priming or other surface-corrosion prevention measures and must undergo some form of cleaning. This process may require only a simple organic-solvent decreasing or a highly reactive chemical etch.

In some cases the performance of surface-protection measures can be related to surface treatments and reasons for a particular level of performance may not be straightforward, but determined indirectly with the use of several analytical tools.

In this work, Ti-8Al-1Mo-1Sn and Ti-13V-11Cr-3Al surfaces were subjected to eight chemical treatments. The topological effects of the treatments were characterized with scanning electron microscopy (SEM). Changes in surface chemistry and elemental distribution were characterized with Auger electron spectroscopy (AES) and positive secondary-ion mass spectrocopy (SIMS).

Experimental

Ti-8Al-1Mo-1Sn and Ti-13V-11Cr-3Al alloys were subjected to the chemical treatments listed in Table 1. After drying, they were analyzed with a Perkin-Elmer Physical Electronics Industries (PHI) model 540-A thin-film analyzer equipped with a single-pass cylindrical mirror analyzer (CMA) with a resolution $\Delta E/E \simeq 0.6\%$. The coaxial electron gun was operated with a 4keV potential at a of beam current 1-5 μA. A peak-to-peak modulation of 7 eV during broad scans (0-2000 eV) and 2 eV for narrow scans (330-530 eV) was applied to the analyzer for phase sensitive detection. Elemental sputter profiles were constructed from digitally recorded and computer processed N(E) data. The ion beam was generated with a PHI model 04-191 sputter ion gun, which was operated with a beam potential of 2 keV and ion current density of approximately 1.9 μA/mm^2 at 10 mA ion gun emission current or 0.5 μA/mm^2 at 3mA ion gun emission current.

The sputtering rate for TiO under the above conditions was 11.5 nm/min with an ion current density of 1.9 μA/mm^2 and 2.8 nm/min with an ion current density of 0.5 μA/mm^2.

SIMS analysis was done with an EAI/1100 quadrupole mass analyzer fitted with a low-resolution double-focusing ion energy filter. The same ion gun used for sputter profiling was used as the primary ion beam source for SIMS. Both He$^+$ and Ar$^+$ were used as primary ion sources. He$^+$ was used to obtain SIMS data from surfaces prior to sputter profiling, since near static (nondestructive) conditions can be achieved with the lighter inert gas. During sputter profile analyses Ar$^+$ was used.

Pieces of the specimens for SEM analysis were coated with about 20-50 nm Au in an ISI-PS-2 sputter coater. All specimens were analyzed with an ISI-60 SEM at a tilt angle of 15°.

Author Roche is at Universal Energy Systems, Dayton, OH 45432; Solomon, at the University of Dayton, Dayton, OH 45432; and Baun, at Wright Aeronautical Laboratories, Wright-Patterson AFB, OH 45433.

TABLE 1.--Surface chemical treatments for titanium and titanium alloys.

CODE	DESCRIPTION	TREATMENT
1	Degrease	Sample slurried in acetone, wiped dry, then ultrasonically cleaned in carbon tetrachloride for 5 minutes.
2	Alkaline	Sample submerged in 0.1N sodium hydroxide, room temperature for 2 minutes. Running tap H_2O for 1 minute, standing deionized H_2O for 5 minutes.
3	HNO_3/HF (fluoro-nitric)	Sample submerged in a solution of 170ml nitric acid, 30ml hydrofluroic acid, 800ml distilled water, room temperature for 2 minutes. Rinse as in #2.
4	$Na_3PO_4/NaF/HF$ (fluoro-phosphate)	Sample submerged in a solution of 50g sodium ortho phosphate, 9g sodium fluoride, 26ml hydrofluoric acid, distilled water to 1 liter, room temperature for 2 minutes. Rinse as in #2.
5	NH_4HF_2 (fluoro-ammonium)	Sample submerged in solution of ammonium bifluoride (10g/liter) room temperature for 2 minutes. Rinse as in #2.
6	H_2SO_4/CrO_3 (sulfo-chromium)	Sample submerged in solution of 300g sulfuric acid, 40g chromium acid, distilled water to 1 liter, room temperature for 2 minutes. Rinse as in #2.
7	$HNO_3/HF/H_2O_2/NH_4F,HF$ (fluoro-nitro-ammonium)	Sample submerged in solution of 80ml nitric acid, 20 ml hydrofluoric acid, 20ml hydrogen peroxide (30%), 10ml ammonium bifluoride (saturated), distilled water 500ml, room temperature for 2 minutes. Rinse as in #2.
8	Hot $NaOH/H_2O_2$ (hot alkaline)	Sample submerged in solution of 20g sodium hydroxide, 20ml hydrogen peroxide (30%), distilled water to 1 liter, 65°C temperature (150 F) for 2 minutes. Rinse as in #2.

Results

Ti-8Al-1Mo-1Sn. Table 2 is a semiquantitative compilation of the elements detected by AES on all the treated Ti-8Al-1Mo-1Sn surfaces. Table 3 summarizes the SIMS data from the same surfaces. All values listed in Tables 2 and 3 are normalized to Ti.

A significant difference between the two techniques is the detectibility of alloying elements. In AES, the major Sn and Ti peaks overlap each other and therefore small amounts of either element in the presence of large amounts of the others cannot be detected with any degree of certainty. This problem does not occur with SIMS: as shown in Table 3, Sn was detected on the as-received surfaces subjected to treatment 2 and 5.

Al was detected on all treated surfaces but neither technique could be used to report reliably the presence of Mo, even after the surface oxide was removed by sputtering. The problem with AES is the overlapping of the most sensitive Mo peak by the Cl and Ar peaks and relatively low sensitivity of other Mo peaks. The SIMS Mo peaks are also subject to overlap by this Ti_2^+ peak and its isotopes.

102

TABLE 2.--AES elemental ID of treated Ti-8Al-1Mo-1Sn.

TREATMENT	ELEMENT IDENTIFICATION										
	Ti (381 eV)	O	C	P	Ca	Na	F	S	Cl	K	Al
1	1	2.3	0.7	x	0.2	x		x	x		x
2	1	2.0	0.6	x	x			x	x		x
3	1	2.3	0.5				x	0.1	x		x
4	1	1.6	0.5	0.1	0.4	0.6	0.7	x	x	x	x
5	1	2.0	0.3	x	x		x	x	x		x
6	1	2.1	0.8	x	x			x	x		x
7	1	2.1	0.5	x	x	x	x	x	x		x
8	1	2.1	0.3		0.2	x		x	x		x

(x APPH RATIO < 0.1)

TABLE 3.--SIMS elemental ID of treated Ti-8Al-1Mo-1Sn.

TREATMENT	m/e / positive ion identification														
	$\frac{16}{O}$	$\frac{19}{F}$	$\frac{23}{Na}$	$\frac{27}{Al}$ C_2H_3	$\frac{35}{Cl}$	$\frac{39}{K}$	$\frac{40}{Ca}$	$\frac{48}{Ti}$	$\frac{59}{AlO_2}$ CaF	$\frac{64}{TiO}$	$\frac{67}{TiF}$	$\frac{86}{TiF_2}$	$\frac{96}{Ti_2}$	$\frac{112}{Ti_2O}$	$\frac{120}{Sn}$
1	x	x	1.9	0.28	x	2.72	0.76	1		0.28			x	x	x
2	x	x	0.8	0.29		0.23	0.29	1	x	0.37			x	x	x
3	x	x	0.9	0.28	x	0.25	x	1		0.22			x	x	
4		0.5	13	0.74		0.12	0.73	1	x	x	0.25	x			
5	x	x	1.6	0.14	x	0.23	0.10	1		0.32			x	x	x
6		x	0.2	0.39		x	0.12	1	x			x	x		
7			0.3	0.26		0.10	x	1		x		x			
8			0.4	0.27	x	0.10	0.76	1		x					

(x VALUE < 0.1)

The Ti$_{LMM}$ Auger peak slopes were nearly identical to TiO$_2$[1] with some subtle differences observed when fluorine was present. The thickness of the surface oxides as determined by Auger sputter profile analysis ranged from approximately 7.8 nm from treatment 8 to 112 nm for treatment 4, compared with approximately 14.6 nm for an untreated surface.

SEM data shows some evidence of selective phase etching from treatments 3, 5, and 7. The fluoro-phosphate treatment produced the most noticeable topographical change. SEM micrographs show the oxide layer produced on this surface to have a "sea shell" like appearance.

Ti-13V-11Cr-3Al. Tables 4 and 5 contain the respective AES and SIMS semiquantitative data obtained from the treated Ti-13V-11Cr-3Al surfaces. As in Tables 2 and 3, the values listed in Tables 4 and 5 are normalized to Ti. Both Tables 4 and 5 show the presence of Ti as well as the three alloying elements on all treated surfaces. The surface

TABLE 4.--AES elemental ID of treated Ti-13V-11Cr-3Al.

TREATMENT	ELEMENT IDENTIFICATION												
	Ti (381 eV)	O	C	P	Ca	Na	F	S	Cl	K	Al	Cr	V
1	1	3.1	1.4	x	0.1	x		0.2	0.3	x	x	x	x
2	1	2.8	1.5	x	0.1	x		x	x		x	x	x
3	1	3.0	1.2		x			x	0.4		x	x	x
4	1	3.1	1.3	x	0.1	x	0.1	x	x		x	x	x
5	1	2.5	0.7					x	x		x	x	x
6	1	2.4	0.8		x	x		x	x		x	x	x
7	1	2.5	0.8		x			0.1	x		x	x	x
8	1	3.5	3.5		0.1	x		x	x		x	x	x

(x APPH RATIO < 0.1)

TABLE 5.--SIMS elemntal ID of treated Ti-13V-11Cr-3Al.

TREATMENT	m/e / positive ion identification													Al/V	Cr/V
	$\frac{16}{O}$	$\frac{19}{F}$	$\frac{23}{Na}$	$\frac{27}{C_2H_3\,Al}$	$\frac{35}{Cl}$	$\frac{39}{K}$	$\frac{40}{Ca}$	$\frac{48}{Ti}$	$\frac{51}{V}$	$\frac{52}{Cr}$	$\frac{64}{TiO}$	$\frac{67}{VO}$	$\frac{68}{CrO}$		
1	x	x	8.2	0.26	x	>9	0.5	1	0.17	0.13	0.15	x		1.8	1.0
2	x	x	0.8	0.22		0.4	0.6	1	0.12	0.13	0.20	x	x	2.1	1.1
3	x	x	0.7	0.21	x	0.4	0.2	1	0.17	0.19	0.18	x	x	1.4	1.2
4	x	x	>3	0.16	x	0.2	0.5	1	0.18	0.49	0.17	x	x	1.0	2.6
5	x	x	0.3	0.16		x	x	1	0.26	0.16	0.19	x	x	0.6	0.6
6	x	x	0.5	0.13		0.1	0.2	1	0.12	0.24	0.23	x	x	1.1	2.0
7	x	x	0.3	0.15	x	0.1	0.2	1	0.19	0.17	0.19	x	x	0.8	0.9
8	x	x	0.9	0.22	x	0.2	0.8	1	0.13	0.35	0.16	x	x	1.8	2.8

(x VALUE < 0.1)

concentration of the alloying elements in all cases was less than the bulk. The surface of the fluoro-phosphate treated panel contained F but no TiF^+ species was detected by SIMS nor did the Ti_{LMM} peak shape differ from that of TiO_2. The oxide layers produced on this alloy were all thinner than that of as received panels. The thickest oxide ($\sim$8 nm) was formed by the sulfo-chromium (6) treatment; the thinnest ($\sim$2.3 nm) was produced by alkaline (2) treatment.

Discussion

The advantage and necessity of using several surface analytical techniques was very evident in this work. For example, the Ti_{LMM} Auger peaks at 418 and 451 eV as well as oxygen at 510 eV and its lower energy plasmons between 450 and 500 eV overlap the major Sn, Cr, and V peaks between 400 and 530 eV and make it difficult to analyze for small amounts of these elements in the presence of Ti and O. Although Cr and V are shown as being detected by AES in Table 4, absolute certainty of their presence was provided by SIMS, since no overlapping problems occur for these elements in this technique.

The detection of Sn by AES is further complicated when Sn is oxidized. Normally the major Sn_{MNN} peak positions are 430 and 437 eV. However, when Sn is oxidized, the peaks shift to a lower energy by 5-6 eV.[2] This shift is toward the Ti_{LMM} peaks and therefore small amounts of Sn do not adequately change AES spectral features, as in the case of V, when both Ti and O are present as major constituents. Again, no overlapping problems exist for the SIMS detection of Sn in the presence of Ti and O.

In some cases, two techniques may not be sufficient. For example, neither AES nor SIMS could verify the presence of Mo. In AES, the most sensitive Mo peaks at 186 and 221 are overlapped by Cl and Ar (in sputtering). Also, the Mo 221eV peak decreases in intensity with respect to the 186 peak when Mo is oxidized.[3] Unlike AES, SIMS can detect molecular species such as those reported in Tables 3 and 5. One of the problems with reporting molecular species is knowing for sure the origin of the species. For example, it is difficult to determine whether a particular species was present on a surface or created during sputtering. Such is the case with TiO^+, $TiOF^+$, and TiF^+ detected on Ti-8Al-1Mo-1Sn subjected to the fluoro-phosphate (4) treatment. In this case, the limited ability of AES to detect chemical state differences was used to determine whether the bonding state of Ti was different on this specimen from one in which fluorine was not detected. The Ti_{LMM} peaks from this surface had subtle differences in their shape compared with nonfluoride-containing surfaces and standard TiO_2. This result is an indication that Ti was in a slightly different bonding state from that in TiO_2. Perhaps it is bound to both O and F as an oxyfluoride. In the case of Ti-13V-11Cr-3Al no $Ti-F^+$ species was observed in the SIMS data and the Ti_{LMM} Auger peak shapes were identical to TiO_2. The Ti_{LMM} peak shapes from the other treated surfaces were also identical to TiO_2.

The SEM was extremely valuable, not only for the characterization of surface topography, but in determining oxide film thicknesses in the determination of sputter rates for Auger sputter profile analysis.

Conclusions

Based on the characterization data presented, the following conclusions are made about the effects of the chemical treatments listed in Table 1 on Ti-8Al-1Mo-1Sn and Ti-13V-11Cr-3Al.

1. No single surface analytical technique can thoroughly characterize Ti alloy surfaces for their elemental, chemical, and physical properties.
2. The effects of a particular chemical treatment may not be the same for each alloy.
3. Chemical treatments 2 through 8 replace the original oxide with a new one containing traces of elemental species common to a particular treatment.
4. The α Ti-8Al-1Mo-1Sn is etched at a faster rate than β by treatments 3, 5, and 7.
5. The oxide produced as Ti-8Al-1Mo-1Sn by the fluoro-phosphate treatment is not TiO_2 but one in which Ti may be chemically bound as an oxyfluoride.

References

1. J. S. Solomon and W. L. Baun, *Surface Science* 51: 228 1975.
2. R. A. Powell, *Applications of Surface Science* 2: 397 1979.
3. M. P. Hooker, J. T. Grant, and T. W. Haas, *J. Vac. Sci. Technol.* 12: 325 1974.

APPLICATION OF AN AUTOMATED MICROPROBE TO THE CHARACTERIZATION OF PROTECTIVE COATINGS ON NICKEL-BASE SUPERALLOYS

G. S. Fritz, K. P. Gumz, and J. M. Walsh

Although nickel-base superalloys possess high strength at the elevated temperatures encountered in gas turbines, they require protection from the oxidation and hot-corrosion effects that persist in these hostile environments. This protection is accomplished by the application of coating systems that have a high volume fraction of a high-temperature, oxidation-resistant phase such as the intermetallic compound NiAl.[1] The electron microprobe has proved to be an extremely important analytical tool in the development and evaluation of these materials. This paper describes an automation system that was developed for a JEOL JXA-50A electron microprobe and emphasizes the application of the system to superalloy coatings research and development.

For an understanding of the chemical and metallurgical processes that occur during the formation and degradation of these complex coating systems, we need detailed quantitative concentration/penetration curves from the superalloy substrate out through the coating. Several automated microprobes have been described at these meetings; however, the emphasis in the system described here is on generating automatically a comprehensive concentration/penetration plot and getting the finished product into the hands of the end user in the shortest possible time.[2,3]

The JXA-50A microprobe is equipped with two high-precision wavelength spectrometers and a programmable Faraday cup for measuring beam current. Automation hardware was designed and built by Tracor Northern. The system employs a PDP 11/34 minicomputer to control X, Y, and Z stage movements, spectrometer angles, crystal selection, and beam current measurements. A four-color Hewlett-Packard digital plotter (7221A) is interfaced to the computer for graphical presentation. The analysis scheme (Fig. 1) allows for a large amount of versatility and efficiency. The operator chooses the number of points to be analyzed, the distance between points, and counting times for the elements. K-ratios or fully ZAF-corrected results are stored on floppy disks and can be easily retrieved for plotting or further processing. Because several small phases are present in these coating systems, one must collect all data at a given analysis location before advancing to the next site, even in cases where crystal flipping is required.

To provide the end user with results in the most meaningful and useful form and in the shortest possible time, particular consideration was given to software development for a comprehensive on-line concentration-vs-penetration plot, a goal readily accomplished with the H-P plotter, which provides an extremely high-quality four-color plot (Fig. 2). This plotting format allows for convenient correlation of microprobe results with metallographic and x-ray mapping techniques routinely used by this laboratory for coating evaluation. Because complex reactions and phase transformations occur during interdiffusion, no attempt at data smoothing was made; the individual data points were simply connected. A logarithmic concentration scale is used so that concentration changes in the lower-weight-percent ranges can be seen clearly. Pen colors and symbols can be selected for easy interpretation of the data. A custom labeling feature is also available that allows one to draw particular attention to specific regions of interest.

These automatically generated concentration/penetration plots result in both cost effectiveness and technology benefits in that coatings research and development engineers can complete their work faster and get a more comprehensive and more easily understood picture of coating/substrate interactions.

References

1. G. W. Goward, "Materials and coatings for gas turbine hot section components," *Proc. Gas Turbine Materials Conf.* 1972, 85-96.
2. H. Ohyi et al., "A new fully automatic electron probe x-ray microanalyzer and its analytical methods," "Phase Map," and "Content Profile," *Proc. EMAG 75* September 1975, 175-178.
3. J. J. McCarthy and F. H. Schamber, "A modular microprobe automation system," *Proc. 8th Intern. Conf. X-ray Optics and 12th MAS Conf.*, 1977, paper 51.
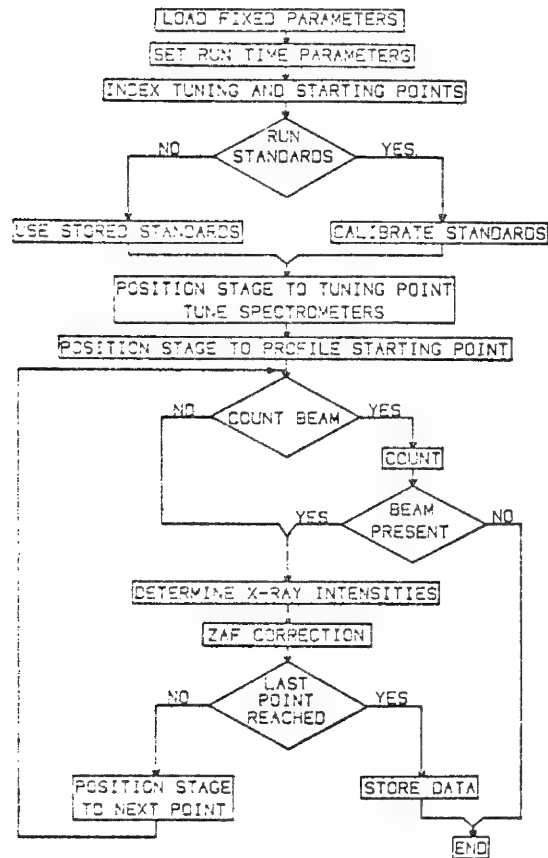
FIG. 1.--Flow diagram shows principles of operation of automated system.

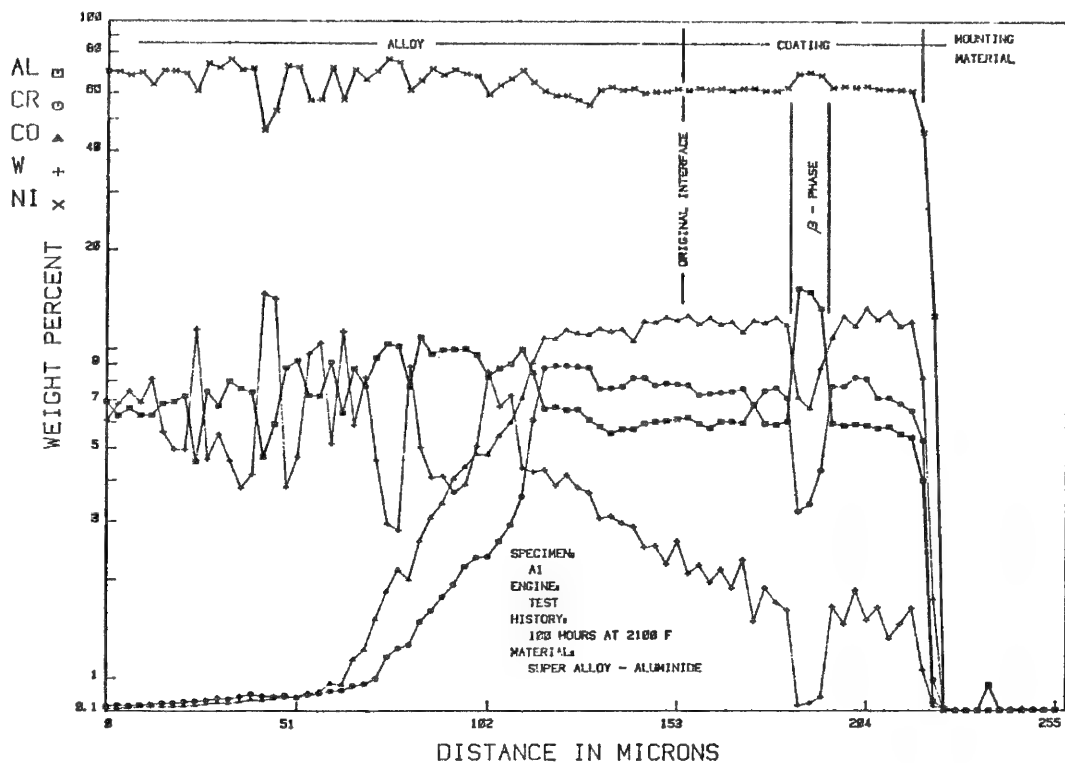

FIG. 2.--Concentration penetration curves from superalloy substrate through protective coating.

AN OVERVIEW OF THE APPLICATIONS OF MICRODROPLET ANALYSIS: PAST, PRESENT, AND FUTURE

Claude Lechene and Ronald Warner

Past

Liquid-droplet analysis is a technique for measuring by electron-probe analysis the con-
centration of all chemical elements above boron within a single fluid volume that can be
as small as 10 pL. The first description of the use of electron-probe analysis on a
dried liquid droplet was by Ingram and Hogben in 1967.[1] The first application of liquid-
droplet analysis was on renal tubular transfer of water and electrolytes in adrenalecto-
mized rats by Cortney, who analyzed samples from 31 animals.[2] Independently, renal tubu-
lar fluid samples collected from 3 rats were analyzed for 6 elements.[3] The subnanoliter
samples were deposited with a calibrated micropipette on the cold surface of a beryllium
block.[4] The techniques of preparation did not prevent the formation of large crystals
(larger than approximately 2 μm), unfitted to reproducible electron-probe analysis. The
obtaining of very small crystals was insured by deposition of the liquid droplet under
oil to avoid evaporation at room temperature and formation of large crystals, washing
the oil in xylene, quenching the preparation, and freeze drying.[5] The technique has
been described in detail.[6]

The basis for quantitative analysis is the preparation of calibration curves from
salt-solution standards that relate characteristic x-ray intensities to chemical element
molarities. Calibration curves are linear and provide excellent reproducibility over
concentration ranges of physiological interest.[6,7] Liquid-droplet analysis has been es-
tablished in several laboratories and modified for energy-dispersive spectrometry,[8,9]
for the analysis of precipitates or organic compounds,[10] or for the analysis of urea.[11]

Electron-probe analysis of a liquid droplet allows analysis of many more chemical
elements in much smaller volume than with any other ultramicroanalytical method.[12,13]
The samples are not destroyed by the analysis and can be reanalyzed for other elements
either immediately or after storage. The practical detectability limit with wavelength-
dispersive spectrometers is of the order of 0.1 mM; i.e., 10^{-15} Moles in a 10 pL sample.
The characteristic x-ray lines are well separated and, at least with wavelength-dispersive
spectrometry, can be identified without ambiguity. Compared to other uses of electron-
probe analysis in biology, quantitative analysis of a liquid droplet is easy, standards
and unknown samples are similar, and results are directly obtained in mM/L.

Present

Liquid-droplet analysis is being applied in numerous fields of physiology in which,
by micromanipulation, one can sample small quantities of the microenvironment of living
cells or tissues. Liquid-droplet analysis can also be applied in situations in which one
has a large volume of samples but where one wishes to analyze for many chemical elements,
for example Na, K, Ca, Mg, Cl, P, or S. Such an analysis, which would necessitate sev-
eral techniques otherwise, could be done by electron-probe analysis for all the elements
on the same sample.

The following examples illustrate the results obtained by liquid-droplet analysis in
various area of biology.

In renal physiology, Le Grimellec et al.[14] performed a segmental analysis and correl-
lative studies of the movement of Na, K, Cl, P, Mg, and Ca in a micropuncture sample col-
lected along the rat nephron. Le Grimellec et al.[15] compared glomerular and artificial
ultrafiltration and found that Ca and to a lesser degree Mg and K concentrations were dif-
ferent in the two modes of ultrafiltration. The authors suggested that the difference

could be due to difficulties in controlling pH, temperature, and pore size during artificial ultrafiltration. Poujeol et al.[16] specified the segment in the nephron responsible for the increase in calcium, magnesium, and phosphate excretion observed after saline expansion in the rat. Agus et al.[17] made laboratory studies of the movement of P and Ca in the kidney. Agus et al.[18] showed a specific role of parathormone to increase calcium reabsorption in the terminal nephron. Studying renal phosphate metabolism, we demonstrated a lack of phosphate secretion in the nephron proximal tubule,[19] distal nephron phosphate reabsorption,[20,21] and distal nephron inhibition of phosphate reabsorption by parathormone.[21] An extensive study of ionic movement along the outer and inner medullary collecting duct is under way.[22]

In reproductive biology electron-probe analysis of liquid droplets brought numerous results in the study of the microenvironment of the egg, of the early embryo, and of the mechanism of fluid accumulation in the blastocyst. The chemical elemental content of human follicular fluid was shown to be similar to blood, with minimal differences.[23] Blastocoele fluid from the mouse was shown to be very dissimilar to mouse serum; higher concentrations of Na, K, Ca, and Mg and lower concentrations of S and P were found in the blastocoelic fluid than in the serum.[24] Fluid accumulation and ion transport in the rabbit blastocysts was found to be ouabain sensitive; the concentration of K in the blastocoele fluid was shown to be maintained predominately by leakage of K from the trophoblast cells into the blastocoele and by ouabain-sensitive transport of K into the trophoblast cells from the blastocoele fluid; exposure of blastocysts to ouabain on the justacoelic, but not the abcoelic, surface of the trophectoderm inhibits blastocoele fluid accumulation.[25]

A very promising field is the study of the microenvironment of the male gamete from the rete testis to the seminiferous tubule and along the different portions of the epididymis.[26]

In auditory physiology analysis of the composition of inner-ear lymphs in cats, lizards, and skates showed the high content in K of the endolymph. Concentration of Cl was higher and Ca and Mg concentrations were lower in endolymph than in perilymph.[27]

In digestive physiology, it was found that in spite of the high bicarbonate concentration of pond water, the water of NaCl absorption along the intestine of *Tilapia grahami* seems to proceed remarkably similar to the case of teleosts in NaCl or seawater solutions.[28]

The function of calcium in sweat secretion was studied in the human eccrine sweat gland.[29] It was found that calcium is an essential requirement for stimulating sweat and that this ion may be a factor in regulating the hypotonicity of sweat.

An interesting application of electron probe analysis of liquid droplets was the fast identification as vanadium of a potent (Na, K)-ATPase inhibitor purified from "Sigma grade" ATP.[30] This finding suggested that vanadate could be an ideal specific regulator of (Na, K)-ATPase.

Electron-probe analysis measures the chemical element content. Several techniques have been developed to analyze various chemical forms. In samples containing protein, in order to differentiate between bound and free forms of an element, an ultrafiltration method of submicroliter sample volume has been developed.[31] Nanoliter volumes can be ultrafiltered by means of a dialysis membrane mounted between two capillaries filled with oil. The sample is introduced in the upper capillary; ultrafiltration is obtained by centrifugation in a microhematocrit centrifuge, and the ultrafiltrate is collected in the pulled extremity of the lower capillary tube. To differentiate between ionic and organic forms of an element, precipitation techniques of qualitative analytical chemistry have been scaled down to be performed on liquid droplets with subsequent analysis of liquid-droplet supernatant or of the microprecipitate after freeze substitution.[10] We have applied such a technique to precipitate the sulfate content of nephron tubular fluid after addition of $BaCl_2$ and thus differentiate between sulfate and organic sulfur. There are experimental situations in which the carbon content of a sample belongs unambiguously to one organic compound. For example, in the study of isosmotic transport in the renal proximal tubule we have measured the raffinose content of standing-droplets experiments simultaneously with the concentration of Na, Cl, K, Ca, Mg, P, and S in picoliter sample volumes. Raffinose was measured by measurement of the carbon characteristic x-ray signal in the sample; standard calibration curves provided a linear relation between raffinose standards concentration and C x-ray signal.[32] Urea could also be measured in the absence of

other organic components by means of the carbon and nitrogen signal; however, the sensitivity would be lower than for raffinose. A method to measure urea by forming an insoluble precipitate containing sulfur has been developed.[11] An interesting feature of the method is that the reagent is added in one manipulation step: it is dissolved in the oil covering the droplet and its partition coefficient between the oil and the water droplet phases is utilized. However, the method is not very sensitive; the lower concentration of urea measurable in a biological sample is approximately 25 mM and does not differentiate from the other sources of sulfur contained in the sample. Overall, we do not think that electron-probe microanalysis of liquid droplets could be used as a general method to measure organic compounds in small sample volumes. We have developed a method based on scaling down the well-developed technique of fluorescence analysis to the measurement of organic compounds in liquid droplet. Microfluorometric analyses are performed on volumes of approximately 20 pL after reactions. The limit of detection for urea is of the order of 10 fmol.[33]

An electron-probe analyzer is a costly investment. Large arrays of data that could necessitate long calculations are provided by analysis of liquid droplets. To use the full capability of the electron probe and to minimize the time required for intermediate calculations we have developed a powerful automated system.[34] A minicomputer is used to set the instrument, control its round-the-clock operation, move the stage, time the spectrometers, collect the data, and perform calculations and statistical analyses. The software program guides the user over the operation of the instrument and the reduction of the data. Simultaneous program execution allows the computer to collect data from the electron probe at the same time the user performs program development on data manipulation. A display terminal facilitates the choice of the operative options and allows for fast and complex interactive calculations with graphics display. A hard-copy unit allows retention of only meaningful informations.

Some special aspects of liquid-droplet preparation and analysis have been described[31,32,35] and will not be expanded upon. The deal particularly with concentrating effects during droplet conservation or manipulation, the manipulation of samples containing protein, the existence of a chloride loss that differs for samples and for standards, the absorption of Mg x rays by Na, and the possible use of a single standard for analysis.

Future

Electron-probe microanalysis of liquid droplets is now a routine method that allows one to analyze a large number of chemical elements in very small biological liquid samples. It can be used with samples collected easily in large volumes and has the advantage of providing the analysis of the chemical-element make-up by a single method. However, its main advantage is in the analysis of very small samples, in the nanoliter or picoliter volume range, as they can be withdrawn by micropuncture techniques during *in vivo* experiments from the microenvironment of cells or from cell vacuoles. It should become an important tool for studying ionic transport phenomena and correlating them with electrical phenomena in well-controlled biological systems.[36,37] Electron-probe analysis can be applied to the search for chemical-element contaminants or inhibitors of biological activity in very small amounts of extracts of an organic compound. Qualitative analysis could be quickly performed on biochemical samples at various stages of a purification.

The sensitivity of the x-ray analytical method could be increased by excitation of the characteristic x-ray emission not with an electron beam but with either a proton beam[38] or with high-energy primary x rays, which would therefore lower the continuum. X-ray analysis of trace elements could likely be developed with such sources of excitation for characteristic x rays.

X-ray analysis of liquid droplets could find applications in hospital clinical laboratories. In patients in shock or in children, one drop of blood could be more than enough to follow the patient state and adjust the solutions to be perfused during intensive care. Adapted equipment, less expensive than research electron probes, could be developed toward this goal. X-ray spectrometry could also be useful in toxicological diagnostics.

Conclusion

X-rays spectrometry analysis of liquid droplets by means of an electron probe, allows biologists to measure many more chemical elements in much smaller volumes than was previously possible. The method has come to be routinely used. It opens new horizons for the study of the chemical-element anatomy of living systems and is expanding to all fields of physiology. It could be used for the analysis of trace elements. It could be developed for clinical applications in intensive care or toxicology.

References

1. M. J. Ingram and C. A. Hogben, "Electrolyte analysis of biological fluid with the electron microprobe," *Anal. Biochem.* 18: 54-57, 1967.

2. M. A. Cortney, "Renal tubular transfer of water and electrolytes in adrenalectomized rats," *Am. J. Physiol.* 216: 589-598, 1969.

3. F. Morel, N. Roinel, and C. LeGrimellec, "Electron-probe analysis of tubular fluid composition," *Nephron* 6: 350-264, 1969.

4. F. Morel and N. Roinel,"Application de la microsonde électronique à l'analyse élementaire quantitative d'echantillons liquides d'un volume inférieur à 10^{-9} l,"

5. C. Lechene, "The use of the electron microprobe to analyze very minute amounts of liquid samples," *Proc. Fifth Nat. Conf. Electron Probe Analysis* (New York), 32A-32C, 1970.

6. C. Lechene, Electron probe microanalysis of picoliter liquid samples, in Theodore Hall, Patrick Echlin, and Rudolf Kaufmann, Eds., *Microprobe Analysis as Applied to Cells and Tissues*, London: Academic Press, 1974, 351-368.

7. N. Roinel et al., "Quantitative analysis of lyophilized solutions: Experimental and theoretical evaluation of the limits of linearity of the calibration curves," *Proc. 13th MASS Conf.*, 1978, 62A-62D.

8. R. Rick, R. M. Horster, A. Dörge, and K. Thurau, "Determination of electrolytes in small biological fluid samples using energy dispersive x-ray microanalysis," *Pflügers Arch.* 369: 95-98, 1977.

9. P. M. Quinton, "Techniques for microdrop analysis of fluids (sweat, saliva, urine) with an energy-dispersive x-ray spectrometer on a scanning electron microscope," *Am. J. Physiol.* 234(3): F255-259, 1978.

10. J. V. Bonventre and C. Lechene, "A method for electron probe microanalysis of organic components in picoliter samples," *Proc. 9th MAS Conf.*, 1974, 8A-8D.

11. R. Beeuwkes, J. M. Amberg, and L. Essandoh, "Urea measurement by x-ray microanalysis in 50 picoliter specimens," *Kidney Int.* 12: 438-442, 1977.

12. C. Lechene and R. R. Warner, "Ultramicroanalysis. X-ray spectrometry by electron probe excitation," *Ann. Rev. Biophysics and Bioengineering* 6: 57-85, 1977.

13. C. Lechene, "Electron probe microanalysis: Its present, its future," *Am. J. Physiol.* 1(5): F391-396, 1977.

14. C. Le Grimellec, N. Roinel, and F. Morel, "Simultaneous Mg, Ca, P, K and Cl analysis in rat tubular fluid: IV. During acute phosphate plasma loading," *Pflügers Arch.* 346: 189-204, 1974.

15. C. Le Grimellec, P. Poujeol, and C. de Rouffignac, "^{3}H-Inulin and electrolyte concentrations in Bowman's capsule in rat kidney: Comparison with artificial ultrafiltration," *Pflügers Arch.* 354: 117-131, 1975.

16. P. Poujeol et al., "Influence of extracellular fluid volume expansion on magnesium, calcium and phosphate handling along the rat nephron," *Pflügers Arch.* 365: 203-211, 1976.

17. Z. S. Agus et al., "Effects of parathyroid hormone on renal tubular reabsorption of calcium, sodium, and phosphate," *Am. J. Physiol.* 224: 1143-1148, 1973.

18. Z. S. Agus, P. J. S. Chiu, and M. Goldberg, "Regulation of urinary calcium excretion in the rat," *Am. J. Physiol.* 232: F545-F549, 1977.

19. R. F. Greger et al., "Absence of significant secretory flux of phosphate in the proximal convoluted tubule," *Am. J. Physiol.* 232(3): F235-238, 1977.

20. F. G. Knox and C. Lechene, "Distal site of action of parathyroid hormone phosphate reabsorption in the thyroparathyroidectomized dog," *Am. J. Physiol.* 229(6): 1556-1560, 1975.

21. E. Pastoriza-Munoz et al., "Effect of parathyroid hormone on phosphate reabsorption in the rat distal convolution," *Am. J. Physiol.* 235(4): F321-F330, 1978.

22. H. H. Bengele, C. Lechene, and E. A. Alexander, "Calcium and magnesium transport along the inner medullary collecting duct of the rat," *Am. J. Physiol.* (in press).

23. A. P. Chong, M. L. Taymor, and C. Lechene, "Electron probe microanalysis of the chemical elemental content of human follicular fluid," *Am. J. Obstet. and Gynec.* 128(2): 209-211, 1977.

24. R. M. Borland et al., "The elemental composition of the environments of the gametes and preimplantation embryo during initiation of pregnancy," *Biol. of Reprod.* 16: 147-157, 1977.

25. J. D. Biggers, R. M. Borland, and C. P. Lechene, "Ouabain-sensitive fluid accumulation and ion transport in rabbit blastocysts," *J. Physiol.* (London) 280: 319-330, 1978.

26. S. Howards, C. Lechene, and R. Vigersky, "The fluid environment of the maturing spermatozoon," in D. Fawcett and J. M. Bedford, Eds., *The Spermatozoon*, Baltimore and Munich: Urban Schwarzenberg, 1979, 35-41.

27. S. K. Peterson et al., "Element composition of inner ear lymphs in cats, lizards, and skates by electron probe microanalysis of liquid samples," *J. Comp. Physiol.* 126: 1-14, 1978.

28. E. Skadhauge, C. P. Lechene, and G. M. O. Maloiy, "Osmoregulation of *Tilapia grahami* in alkaline ponds in East Africa," in B. Lahlou, Ed., *Epithelial Transport in Lower Vertebrates*, London: Cambridge University Press (in press).

29. C. A. Prompt and P. M. Quinton, "Functions of calcium in sweat secretion," *Nature* 272: 171-172, 1978.

30. L. C. Cantley et al., "Vanadate is a potent (Na-K)-ATPase inhibitor found in ATP derived from muscle," *J. Biol. Chem.* 252: 7421-7423, 1977.

31. J. V. Bonventre, K. Blouch, and C. Lechene, "Biological sample preparation for electron probe analysis: Liquid droplets and isolated cells," in M. A. Hayat, Ed., *X-ray Microscopy in Biology*, Baltimore: University Park Press, (in press).

32. C. Lechene and R. Warner, "Electron probe analysis of liquid droplets," in C. Lechene and R. Warner, Eds., *Microbeam Analysis in Biology*, New York: Academic Press, 1979, 279-297.

33. E. A. Mroz and C. Lechene, "Fluorescence analysis of picoliter samples," *Anal. Biochem.* 102: 90-96, 1980.

34. T. Moher and C. Lechene, "Automated electron probe analysis of biological samples: Process control and data reduction by interactive graphic display," *Biosciences Communication* 1: 314-329, 1975.

35. N. Roinel, "Electron microprobe quantitative analysis of lyophilised 10^{-10} l volume samples, *J. Microscop. Biol. Cell.* 22: 261-268, 1975.

36. W. Holt and C. Lechene, "Vasopressin (ADH) decreases the reabsorption of sodium and chloride across the light segment of the cortical collecting tubule (CCT_1) of the rabbit," *Am. Fed. for Clinical Research* 1/1980.

37. W. Hold and C. Lechene, "Vasopressin (ADH) inhibits the reabsorption of calcium and phosphate in the light segment of the cortical collecting tubule (CCT_1) of the rabbit," *Am. Fed. for Clinical Research* 1/1980.

38. P. Horowitz et al., "Elemental analysis of biological specimens in air with a proton microprobe," *Science* 194: 1162-1165, 1976.

TECHNIQUES OF WAVELENGTH-DISPERSIVE SPECTROMETRY WITH EMPHASIS ON ELEMENTAL ANALYSIS OF ULTRAMICROVOLUME SAMPLES

G. A. Quamme and M. Muhlert

The electron microprobe (EMP) offers the unique advantage of rapid and accurate analysis of ultramicrovolume samples where conventional chemical methods are not possible or feasible.[1-5] Detectability limits for EMP analysis are comparatively poor when considered in terms of the minimum amount of an element detected relative to the total sample in a homogenous mixture. However, the ultimate sensitivity is very high considering the actual number of atoms required to produce a detectable signal above background (about 100 ppm or 10^{-16} g). Thus EMP analysis is ideal for analyzing ultrasmall samples of relatively high elemental concentrations. This technique has been extensively applied to investigations of kidney physiology where one routinely collects sample volumes in the nanoliter range from individual nephrons by micropuncture techniques.[6-10]

Typically a micropuncture experiment involves collection of nanoliter volume samples by micropipettes from various renal compartments. The small size relative to the large surface area of the sample volumes dictates that all handling be accomplished under an antiwetting phase, usually paraffin oil, with the use of micromanipulators and stereo microscopes. This condition in itself may lead to unforeseen errors in microdroplet analysis. All of the many methods that have been reported for sample preparation involve placing small volumes (10-100 pL) of samples and standards on a support and freeze-drying to produce geometrically amorphous deposits comparable to each other.[1-10] Electron microprobe analysis includes setting the electron beam to the same diameter as the sample and standard deposits and comparing the x-ray intensities. The x-ray intensity is proportional to the number of atoms present in the sample; thus, the absolute concentration of the liquid volumes can be obtained from the standards of known composition. This method can be applied to any aqueous fluid provided adequate standards are prepared.

The wavelength-dispersive spectrometer (WDS) is the most widely used method of x-ray spectral analysis in the microprobe. The spectrometer consists of a mechanical assembly that positions a diffracting crystal and gas-proportional detector in such a fashion as to allow selective diffraction by the crystal of characteristic wavelengths. (Each element is characterized by its own wavelength spectra.) The advantages of WDS are: (1) high line-to-background ratio as a result of the spectrometer's excellent inherent wavelength resolution (which thus yields low elemental detection limits even in the presence of high x-ray background), a particularly important feature in biological fluids containing important elements of low x-ray yield such as sodium and magnesium; and (2) unambiguous x-ray line identification, which is important in elemental determination of low concentrations in the presence of very high concentrations of other elements, e.g., phosphorus at 1mM versus chloride at 120mM concentrations, which are commonly encountered in biological fluids. A consequence of these properties is the relatively low counting times required for analysis, a significant consideration in that each routine micropuncture experiment may generate over 100 separate deposits. Although the above ultramicroanalytical procedure appears direct and unaffected, several problems are inherent to the analysis of biological fluids. First, as mentioned above, sample handling requires special techniques owing to the extremely small volume proportional to the large surface area, so that surface contact with air, glass, paraffin oil, and solvents becomes very important with regard to elemental contamination and (more important) elemental loss. Second, the nonuniformity of composition of biological samples may unpredictably alter the background absorption parameters. Third, many of the elements of interest in physiology possess low atomic numbers (e.g., sodium) and may be present in relatively low concentrations (e.g., magnesium). Despite these inherent drawbacks x-ray microanalysis has become a major tool in investigation of kidney physiology.

The authors are members of the Faculty of Medicine at the University of British Columiba in Vancouver, B.C., Canada V5Z 1M9.

References

1. M. J. Ingram and C. A. Hogben, "Electrolyte analysis of biological fluid with the electron probe," *Anal. Biochem* 18: 54-57, 1967.

2. F. Morel and N. Roinel, "Application de la microsonde électronique à l'analyse élémentaire quantitative d'échantillons liquide d'un volume inférieur à 10^{-9} l," *J. Chem. Physique* 66: 1084-1091, 1969.

3. C. P. Lechene, "The use of the electron microprobe to analyze very minute amounts of liquid samples," *Proc. Nat. Conf. Electron Probe Anal. 5th New York*, 1970, 32-35.

4. P. M. Quinton, "Techniques for microdrop analysis of fluids (sweat, saliva, urine) with an energy-dispersive x-ray spectrometer on a scanning electron microscope," *Am. J. Physiol.* 233: 255-259, 1978.

5. R. Rick et al., "Determination of electrolytes in small biological fluid samples using energy dispersive x-ray analysis," *Pflügers Archiv* 369: 95-98, 1977.

6. F. Morel, N. Roinel, and C. LeGrimellec, "Electron probe analysis of tubular fluid composition," *Nephron* 6: 350-364, 1969.

7. C. P. Lechene, "Electron probe microanalysis: Its present, its future," *Am. J. Physiol.* 232: 391-396, 1977.

8. Z. S. Agus et al., "Effects of parathyroid hormone on renal tubular reabsorption of calcium, sodium, and phosphate," *Am. J. Physiol.* 224: 1143-1148, 1973.

9. P. C. Fernandez and J. B. Puschett, "Proximal tubular actions of metolazone and chlorothiazide," *Am. J. Physiol.* 225: 954-961, 1973.

10. G. A. Quamme et al., "Magnesium handling in the dog kidney: A micropuncture study," *Pflügers Archiv* 377: 95-99, 1978.

EDS X-RAY ANALYSIS OF LIQUID MICRODROPLETS

P. M. Quinton

In slightly more than a decade, x-ray analysis of liquid microdroplets of volumes of the order of 10^{-11} to 10^{-10} pL has evolved from a possibility put forth by Ingram and Hogben[1] to a well-accepted, standard method of analysis for biological microsamples performed routinely in numerous laboratories.[2-6] Analysis of microdrops with energy-dispersive spectometry (EDS) provides at least two inherent advantages: (1) the acquired spectrum provides simultaneous quantification of all elements present, and (2) the analysis requires relatively minimal beam currents for sample excitation, which reduces potential specimen deterioration owing to beam damage. Two disadvantages inherently associated with EDS are that (1) comparatively low peak-to-background (P/BG) ratios are generated by poorer detector resolution (typically 150 eV at FWHM), and (2) the simultaneous detection of all characteristic peaks requires a well-characterized computer routine for separating overlapping peaks as well as for stripping background from the spectrum.

Despite these limitations, EDS analysis of microdroplets is sufficiently sensitive to be of general use in the quantitation of most fluids of biological origin.[5,7] That is, most of the elements in microsamples of fluid from various segments of the nephron, seminephrous tubules, sweat glands, salivary glands, and other biological fluids are in sufficient concentrations to be accurately determined by EDS x-ray analysis. However, the many laboratories with EDS capabilities make for a wide variety of applications; further characterization of the methodology is needed in order to ascertain the appropriateness of the technique in specific situations. This presentation briefly describes the methodology and considers characteristics of (1) the minimum detectable and minimum determinable limits (MDcL and MDrL, respectively), (2) the reduction of extraneous background by collimation, and (3) the effects of peak overlaps on quantification.

Methods

The methods of specimen preparation and analysis are similar to those described previously.[5] Briefly, one volume of 50% glycerol in water and one volume of fluid sample are deposited together by means of the same constant-volume self-filling pipette onto a colloidin film under water-saturated hexadecane.[8] The samples are supported on a thin film rather than on a solid substrate, which reduces the total background sufficiently so that the MDrL of minor components such as sulfur, phosphate, calcium, or magnesium is below the normal biological range of concentrations. The film is supported by a 60% open 100-mesh nickel grid. After samples of unknowns and standards have been deposited on the film, it is rinsed successively three times in hexane, to remove the oil. The deliquescent nature of the glycerol prevents the samples from dessicating in room atmosphere even after the oil is removed. The samples are then placed inside a small vial and rapidly exposed to a vacuum of about 0.5 μm Hg for a period of 5-10 min. The rate of dessication of particularly deliquescent samples such as $CaCl_2$ or $MgCl_2$ can be substantially enhanced by heating of the samples with an incandescent lamp.

For x-ray analysis, the scanning electron microscope (SEM) is adjusted so that the accelerating voltage gives optimal peak-to-background ratios, i.e., 20 kV.[5] The beam current is adjusted to give a count rate of about 4000 cps with the most concentrated sample. The beam is adjusted in spot mode to a diameter that is slightly larger than the diameter of the largest sample (usually about 50-60 μm). Beam current is usually less than 1 nA. A 30 mm^2 detector collimated to 15 mm^2 (Fig. 1) and mounted at 37° with respect to horizontal provides a beam incidence angle and an x-ray take-off angle of 26.5°.
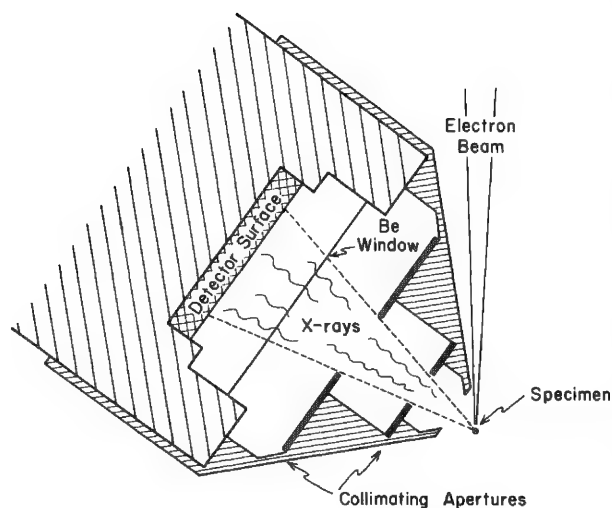
FIG. 1.--Cross section of simple collimator cap for EDS detector tube. Cap is turned and drilled to appropriate dimensions for proper separation of aperture disks, which are cut from sheets of 0.010in. hardened graphite. Relative diameters of the apertures and distances from detector surface determine "focal point" of collimator and "active" surface area of detector.

The pulse processor is set for maximal peak resolution and the peaks of the acquired spectrum are deconvoluted, separated from overlaps, and stripped from background using the multiple-least-squares fitting routine of Schamber.[9]

In the examination of the specific aspects in this study, minimum concentration parameters were characterized by the analysis of solutions of Na_2SO_4 at concentrations of 0, 1.25, 2.5, and 5.0 mM. The effect of the overlap of potassium K-β peak on the calcium K-α peak was examined by analysis of 2.0mM Ca solutions containing potassium at 0, 2.5, 5.0, 10.0, 50.0, and 100mM concentrations. The effects of extraneous background were examined by measurement of the amount of background generated in solutions of sodium chloride at 0, 37.5, 75.0, and 150mM concentrations and by determining background parameters with, and without, the detector collimator.

Results and Discussion

The limit of sensitivity of most counting analyses is determined by the background count rate. The background count in x-ray analysis consists of three components: (1) the background inherent to the sample mass, bremsstrahlung, (2) extraneous bremsstrahlung due to primary and secondary electron interaction with mass not associated with the sample, and (3) background inherent to the electronic noise of the system.[10] In previous work,[5] it was assumed that most biological samples exhibit a mass approximated by that of a solution of 150 mM NaCl, i.e., isotonic saline, or interstitial fluid. Under those conditions, for most elements of biological interest (atomic numbers 11-20), the MDrL ranged from about 0.5 to 1.0 mM depending on counting parameters.

However, several biological fluids such as hypotonic urine, sweat, and saliva occur with mass concentrations smaller than that of isotonic saline, with consequent changes in MDcL. Nonbiological applications such as might be employed in the analysis of environmental waters also call for estimates of MDcL on samples with relatively low mass concentrations. Table 1 shows minimal detectable concentrations of Na and S estimated from varying concentrations of standards. Inspection shows the MDcL is an inverse function of the concentration of the standards used. This function obtains because the normal MDcL calculation assumes that background is a constant, but in the case of microdroplets supported on thin films, the component of background due to sample bremsstrahlung is directly proportional to sample mass. Consequently, as the concentration of the standard decreases, its absolute residual mass decreases, the background signal decreases, and the estimated MDcL decreases.

TABLE 1.--Minimal detectable limit (in mM) for Na and S calculated from data from increasing concentrations of solutions of Na_2SO_4 by use of relation MDcL = $3B^{1/2}C_{st}/P$, where P = total peak counts, B = background counts in ROI, and C_{st} = concentration in standard.

Conc. (mM)	1.25	2.5	5.0	10.0
Na MDcL	-	.142	.170	.197
S MDcL	.041	.061	.087	-

Frequently, a more useful parameter in quantitative analysis is the minimal determinable concentration. In the special case of solutions containing a single solute, the bremsstrahlung component is proportional to the characteristic peak. This relation can be used to estimate the MDrL from calculations of the relative error (RE). The relative error for a single count is given by

$$\%RE = \frac{\sqrt{P + 2B}}{P} \times 100$$

where P is the net counts in the peak and B is the background count under the peak.[11]

The MDrL is arbitrarily determined by the degree of tolerance, i.e., acceptable %RE, in a given analysis. For example, if a relative error of 10% provides acceptable accuracy, we can empirically determine the relation between peak and background for a specific system by analysis of several solutions of different concentrations. (The ratio of the characteristic peak to sample bremsstrahlung is principally a function of the resolution of the detector and size of the region of interest.) Figure 2 hows an example of the linearity and constancy of the bremsstrahlung to sodium peak ratio as a function of increasing concentration of single solute solution of NaCl. With 100 sec total acquisition time, BG/P and the BG intercept for solutions of Na_2So_4 were found to be 0.14 and 1726, respectively. By substitution, the above expression reduces to

$$RE = 0.1 = \frac{\sqrt{P + 0.28P + 1726}}{P}$$

BACKGROUND AND Na PEAK COUNTS
vs. NaCl CONCENTRATION
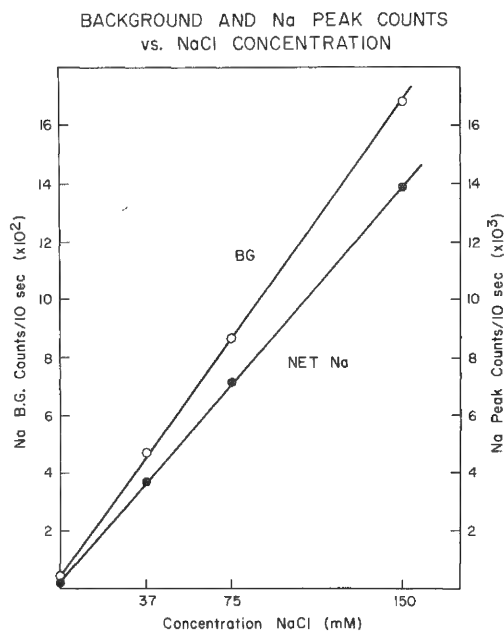
FIG. 2.--Net peak and background x-ray counts generated from increasing concentrations of solutions of NaCl only. Both counts are linear functions of Na concentrations so that P/BG is constant over concentration range. BG may be therefore calculated as a function of P. The y-intercept of BG slope estimates extraneous (nonsample) component of total background.

Solution of this equation for P gives 488 counts, which under these parameters of analysis is about 0.16 mM of Na. That is, with the given system and conditions the minimal concentration that can be determined with an accuracy of ±10% at a confidence level of one standard deviation is slightly less than 0.2 mM Na.

Collimation

As is shown in Table 2, collimation of the detector is extremely important in the reduction of the extraneous component of background due to excitation of bremsstrahlung in nonsample mass. In this system, collimation improved the sodium P/BG ratio by 52% and reduced the Ni signal detected from the grid by more than 80%. Reduction of the detected Ni signal not only reduces the total background, but also improves pulse processing efficiency. Presumably, fewer electrons are scattered by low-mass samples, and the difference between detected Ni signal with, and without, collimation during analysis of these samples is even more striking. Again, collimation reduced the total background signal generated by excitation of film support with no sample present by more than an order of magnitude.

Potassium K-β Effects

Of the elements of principal interest in biological fluids (Na through Ca), significant problems of characteristic peak overlap exist only between the potassium K-β and the calcium K-α lines. Since calcium is of major interest in many experi-

mental settings, it is important to determine the effectiveness of the peak-stripping routine of the computer program used to calculate the peak integrals. To examine this parameter, we analyzed solutions of 2 mM Ca containing increasing concentrations of potassium chloride. Although Fig. 3 suggests that there may be a slight overcorrection for the potassium K-β line, the effects on the calcium line are minimal, if not negligible. The difference between the Ca peak integral at 0.0 mM and 100 mM K was only 6%. This difference would contribute an error of about 0.12 mM to the determination of Ca in the presence of 100 mM K. In general, since both calcium and potassium are normally present in biological fluids at concentrations of less than 10 mM, the error in calcium analysis with this routine should be negligible. However, if ultimate accuracy is required at significantly higher potassium concentrations, appropriate standards should be used.

TABLE 2.--Effects of collimation on background (BG) and Ni peak detection. (See Fig. 1 for details of collimator.)

		Total BG	P/BG	Ni Peak
150 mM NaCl	Collimator	1620	7.73	1.748
	No Collimator	2332	5.08	9,405
Film, no sample	Collimator	36	-	645
	No Collimator	516	-	7,847
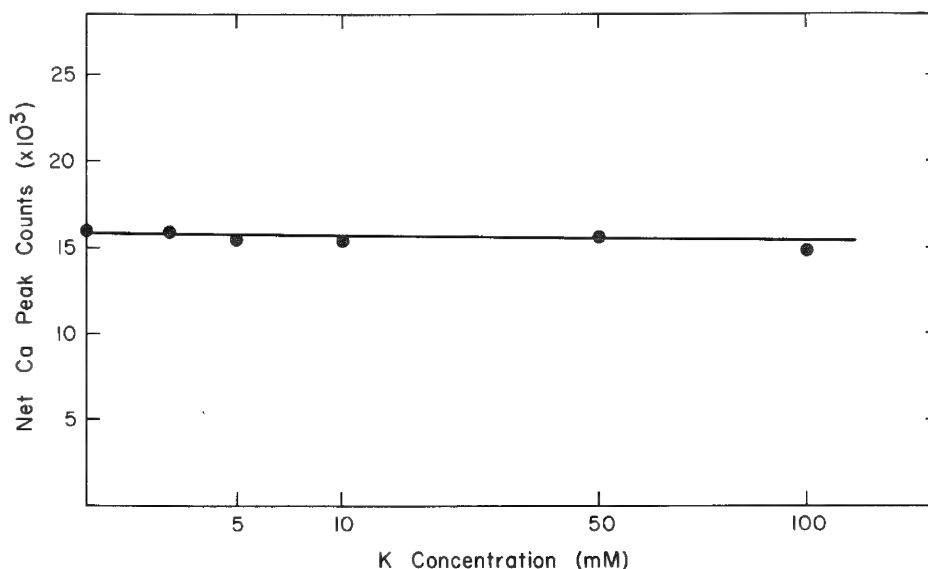
FIG. 3.--Net Ca x rays vs K concentration. In range shown, K-β x-rays of potassium peaks appear to have only minimal effects on Ca K-α peak that are not corrected by peak-separation routine used.

Summary

In general, EDS x-ray analysis is a powerful tool for quantification of liquid microdroplets, and though the ultimate minimal detectable and determinable concentrations are somewhat inferior to those obtainable with other methods, they remain compatible with levels of accuracy and sensitivity needed for most biological and perhaps many other applications. However, to achieve optimal accuracy and sensitivity, it is necessary to select conditions that minimize the detection of extraneous background, i.e. film substrate,

proper acceleration voltage, and detector collimation.

References

1. M. J. Ingram and C. A. M. Hogben, "Electrolyte analysis of biological fluids with the electron microprobe," *Analyt. Biochem.* 18: 54-57, 1967.

2. H. O. Garland et al., "The application of quantitative electron probe microanalysis to renal micropuncture studies in amphibians," *Micron* 4: 164-176, 1973.

3. C. P. Lechene and R. R. Warner, "Electron probe analysis of liquid droplets," in C. P. Lechene and R. R. Warner, Eds, *Microbeam Analysis in Biology,* New York: Academic Press, 1979, 279-299.

4. N. Roinel, "Electron microprobe quantitative analysis of lyophilised 10^{-10}L volume samples," *J. Microsc.* 22: 261-268, 1975.

5. P. M. Quinton, "Ultramicroanalysis of biological fluids with energy dispersive x-ray spectometry," *Micron* 9: 57-69, 1978.

6. G. A. Quame, "Magnesium handling in the dog kidney: A micropuncture study," *Pflügers Arch.* 377: 95-99, 1978.

7. R. Rick et al., "Electron microprobe analysis of electrolytes in picoliter volumes," *Pflügers Arch.* 369: 95-198, 1977.

8. P. M. Quinton, "Construction of pico-nanoliter self-filling volumetric pipettes," *J. Appl. Physiol.* 40: 260-262, 1976.

9. F. Schamber, "A modification of the linear least-squares fitting method which provides continuum suppression," in T. G. Dzubay, Ed., *X-Ray Fluorescence Analyses of Environmental Samples,* Ann Arbor, Mich.: Ann Arbor Science, 1977, 241-257.

10. S. J. B. Reed, *Electron Microprobe Analysis,* London: Cambridge University Press, 1975, 2d ed., p. 145.

11. L. A. Currie, "Limits for qualitative detection and quantitative determination: application to radiochemistry," *Analyt. Chem.* 3: 586-593, 1968.

DETAILS OF THE LIQUID DROPLET TECHNIQUE

R. R. Warner and C. P. Lechene

This paper presents some technical aspects or "nuts and bolts" of the liquid droplet technique.[1,2] We discuss our observations regarding liquid droplet storage and concentrating effects; we present techniques for analyzing samples containing protein; we mention our results regarding differential Cl loss; we point out a potential problem regarding Mg analysis; we compare two techniques for measuring background; we discuss a single-standard analysis; and we present minimum detectable concentrations for the major physiological elements.

Concentrating Effects

Prior to sample processing by the liquid droplet technique, nanoliter (nL) or picoliter (pL) fluid volumes are usually stored under saline-saturated oil to prevent fluid evaporation that would artifactually elevate droplet concentrations. However, these droplets may still concentrate even under freshly prepared saline-saturated oil. We have shown that droplets placed under oil do not concentrate when stored at -80°C.[3] However, even very large droplets concentrate at room temperature, as shown in Fig. 1 for a
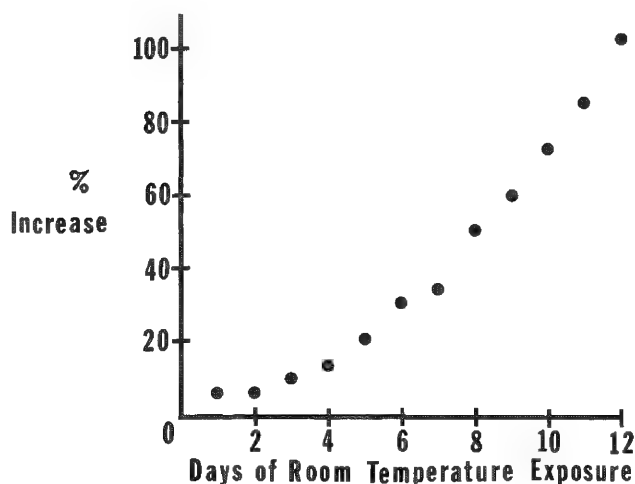
FIG. 1.--Effect of room temperature storage on droplet ^{3}H inulin concentration. A 23nL droplet under oil was kept at room temperature for 6 hr before sampling. The same droplet and procedure were used on subsequent days. The droplet was kept at -80°C between tests. (From Ref. 3.)
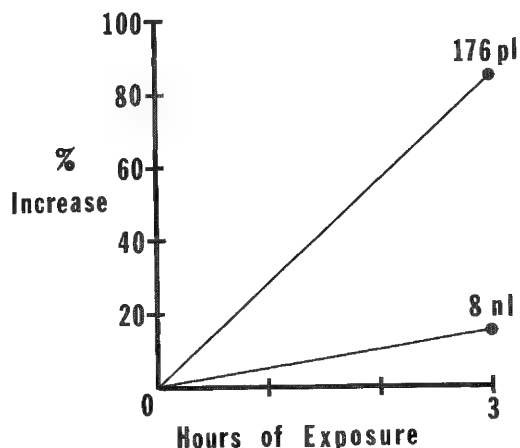
FIG. 2.--Effect of initial droplet volume on change in droplet concentrations after 3 hr under oil at room temperature. Values are the mean change in Na, Cl, K, P, S, Ca, and Mg concentrations. (From Ref. 3.)

23nL droplet.[3] The rate of droplet concentration depends on the initial droplet size (Fig. 2): after a 3 hr exposure to room temperature under freshly water-saturated oil, the mean concentration for all analyzed elements increased nearly two-fold for a 176pL droplet but increased by only 15% for an 8nL droplet.[3]

120

We have investigated the storage of small (picoliter) droplets. Droplets of 79 pL were placed under freshly water-saturated oil, picked up and isolated by oil within individual micropuncture pipettes, and the pipettes stored at -80°C. At intervals over a 2-week period, selected micropipettes were thawed, their contents expelled under freshly water-saturated oil, and aliquots taken for analysis. These droplets concentrated approximately 15% before freezing (Fig. 3), probably due to the waiting period under oil at room temperature; systematic concentration did not subsequently occur at -80°C.

The storage at room temperature of small (198pL) droplets was investigated as follows. Droplets of a 100mM NaCl solution ($[Na]_s$) were placed under freshly water-saturated oil and were then picked up and isolated by oil within individual micropuncture pipettes. At regular intervals a stored droplet was expelled under freshly water-saturated oil and aliquots were taken for analysis and compared with identical aliquots from a large volume of the source solution ($[Na]_c$). The results (Fig. 4) are similar to those
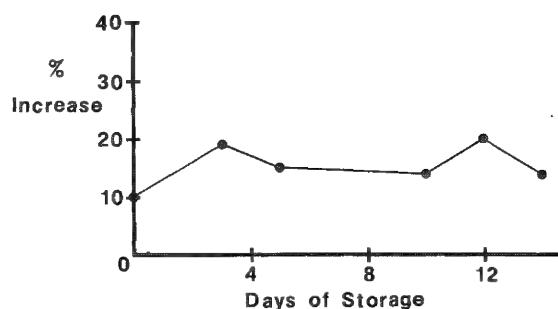
FIG. 3.--Effect of storage at -80°C on 79pL droplets containing H inulin. Droplets were stored within micropuncture pipettes. (From Ref. 3.)

DROPLET CONSERVATION
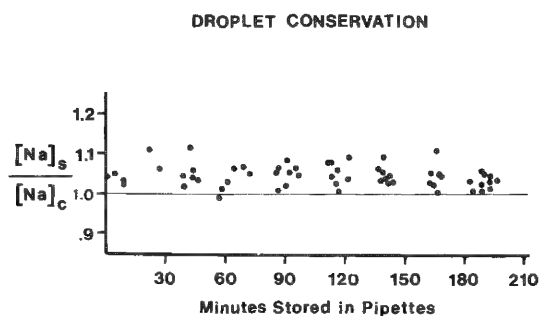
FIG. 4.--Na concentrations from 198pL aliquots of a 100mM NaCl solution ($[Na]_s$) stored in micropipettes at room temperature compared with the Na concentration of a large volume of the same solution kept under oil ($[Na]_c$). Each point represents a single droplet; determinations are from four separate experiments.[4]

obtained with droplets stored at -80°C (described above): droplets do not concentrate within micropipettes when isolated by a small amount of oil, although concentration initially occurs during the droplet transfer steps where exposure to a large volume of oil is unavoidable.[4]

It can be concluded that nanoliter or picoliter volume samples can be safely stored at -80°C for weeks, or within micropuncture pipettes at room temperature for hours. However, it is important to use identical timing for a given set of sample manipulations of droplets at room temperature and to reduce this time as much as possible.

Samples Containing Protein

The presence of protein in fluid samples complicates the liquid-droplet technique in several ways: (1) the protein makes the accurate delivery of fluid from a volumetric pipette more difficult owing to the interaction of the sticky fluid with the glass (in spite of siliconization); (2) high concentrations of protein can absorb soft x-ray emissions, giving erroneously low concentrations when compared with the protein-free standards; and (3) the presence of protein may alter the crystallization pattern of samples versus the pattern in standards and affect their comparison. Analysis of de-proteinated solutions is preferable; submicroliter volumes can be ultrafiltered by use of a single

121

hollow dialysis fiber as the ultrafiltration membrane[3,4]; nanoliter volumes can be ultra-filtered using a dialysis membrane mounted between two capillaries filled with oil.[5] Alternatively, protein-containing solutions can be quantitatively manipulated and ana-lyzed if the protein concentration is less than about 50 g/L, which can be accomplished by sample dilution. For example, plasma samples diluted by 1/2 with distilled water are relatively easy to pipette and give reproducible results that are comparable to macro-analyses of the same samples.[3,6] A disadvantage of the dilution procedure is that unlike in ultrafiltration, the total element amounts rather than free concentrations are measured.

Differential Cl Loss

It has been suggested that the relatively high Cl values found by electron-probe analysis in some biological fluids could be due to a differential loss of Cl in the standards and in the biological fluids containing organic material, and that this effect could be eliminated by the addition of urea to the standards.[7] Our results do not con-firm this suggestion. We compared the chloride concentrations from kidney tubular fluid, plasma, and urine samples measured with respect to the usual salt-solution standards and with respect to the same standards plus urea. We observed only a minimal improvement in our Cl values; the mean difference obtained when using standards containing urea versus standards without urea was -2.08 ± 2.83 mM (N = 136, t = 3.03). This is a negligible de-crease for the chloride concentration.[3]

Absorption of Mg X rays by Na

Although absorption effects in droplets can generally be ignored under most physio-logical situations,[8] that is not true for Mg in the presence of high Na concentrations, such as normally found in plasma samples. Mg X-rays are strongly absorbed by Na; as shown in Fig. 5, with increasing Na concentration the Mg concentration appears to de-crease, although its concentration is constant.[9] At physiological Na levels (150 mM) the Mg signal is attenuated by 18 ± 4% (n = 7); however, at the very low Mg concentrations normally encountered in physiological fluids (0.6 mM), this error can be of the same or-der of magnitude as the precision of the measurement.

Single Standard Analysis

With the liquid droplet technique, droplet x-ray intensities are translated into molar concentrations by means of regression lines based on the analysis of a graded series of salt-solution standards; the curves are not forced through the origin.[1,2] However, a calibration curve could also be obtained by a single (high-concentration) standard with a "regression" line forced through the origin. Tests on a variety of salt solutions in-dicate (Table 1) that electron-probe results based on a single standard are slightly closer to macromeasurements than electron-probe results based on the usual series of salt-solution standards.[3] This single-standard technique would shorten the preparation time involved in the liquid-droplet technique, and could be more accurate in that the re-gression line would not be influenced by the analysis of standards having low concentra-tions where errors are larger.

Background Measurement

With the liquid-droplet technique, background for all samples is customarily measured by analysis of a clear area of the beryllium support without detuning of the spectrometers (off sample, on peak).[2] It could be argued that this procedure is imprecise, and that one should measure the background on the sample by detuning the spectrometers to equidistant points above and below the characteristic line and averaging the two measurements (on sample, off peak). We have compared these two procedures for measuring sample background using paired analysis. Off-peak measurements were made on the standard solution of high-est concentration, thus maximizing possible differences in on-sample vs off-sample back-grounds. As shown in Table 2, we found no significant differences between the on-peak and off-peak backgrounds for Na, Cl, or K, whereas highly significant differences were found for P, S, Ca, and Mg. This result contrasts with a previous study that found essentially

TABLE 1.--Comparison of data reduction by use of customary series of standard solutions (St) and one solution (Os).

	K		Na		Ca		Mg		P	
	St	Os	St	Os	St	Os	St	Os	St	Os
$\Delta\%$[a]	5.79	3.51	2.48	2.21	23.6	0.80	8.7	1.69	27	10.8
SD	8.45	8.95	3.77	2.27	10.5	8.81	9.3	7.97	29.4	20.7
t	1.68	0.88	1.61	1.02	5.51	.20	2.3	0.47	2.25	1.17
N	5		5		6		5			

[a]$\Delta\%$ = (((EP - Macro)/Macro)x100)/N, or the mean of the difference expressed in percentile between electron probe analysis (EP) and macromeasurements (Macro) of different salt solutions, the value for each solution being the mean of 16 measurements.

TABLE 2.--Paired comparison of background determinations measured on-peak and off-peak (N = 10).

	Na	Cl	K	P	S	Ca	Mg
% Difference[a]	0.68	12.6	1.15	-6.61	14.2	-8.43	8.16
t[b]	0.81 NS[c]	1.95 NS[c]	0.39 NS[c]	6.06	3.79	6.11	8.73

[a] % Difference: $\sum\limits^{N} \left(\dfrac{\text{value on peak-value off peak}}{\text{value on peak}} \right) \times 100$

[b]t: Student's t value for null hypothesis (value on peak = value off peak)

[c]NS: Not significant, P > .05; accept null hypothesis.

no differences between the two background determination procedures.[3] Our primary point is that the numerical magnitudes of the differences are small. Although the off-peak analysis may be preferred on theoretical grounds, in practice this procedure would require three measurements on each sample (on peak and above and below peak), which presents difficulties in implementation; either the spectrometers can be tuned and detuned for each sample, or all samples can be analyzed at each spectrometer setting. Retuning of the spectrometers for each sample creates problems in finding the same on-peak spectrometer setting for each sample. Separate runs at each spectrometer setting exacerbates problems of instrument drift. We feel that off-peak analysis may in practice be less precise, and that on-peak background determinations are generally preferable given the small numerical differences between the two procedures.

Minimum Detectable Concentrations

No absolute value can be assigned to the concentration detection limit since this limit varies inversely with analysis time and (as shown by Fig. 6) directly with the pipette size. We have determined minimum detectable concentrations obtained under routine operating conditions (50 sec per sample, 64.7pL samples). Backgrounds were measured on sample, off peak. Determinations were made on samples mounted on the customary beryllium blocks[1,2] as well as mounted on formvar grids[10]; backgrounds were reduced by an order of magnitude with the use of formvar films.[11,12] Minimum detectable concentrations
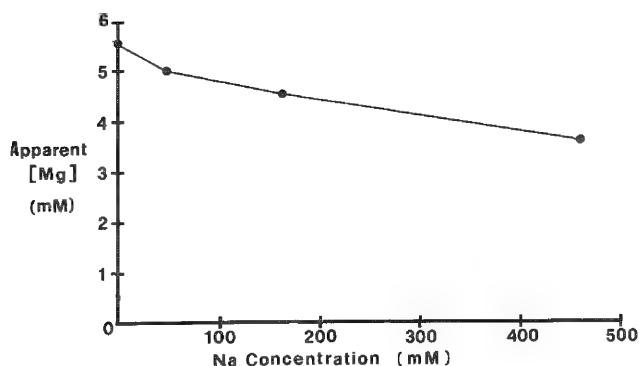
FIG. 5.--Measured attenuation of Mg x rays by Na. At all Na concentrations the true Mg concentration was the same. (From Ref. 9.)
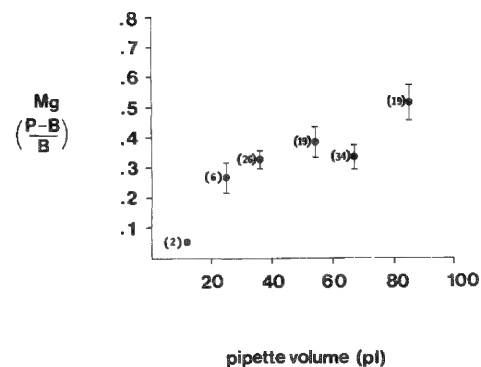
FIG. 6.--Mg P-B/B ratios for a standard solution containing approximately 0.5 mM Mg. Values in parentheses are the number of determinations. Error bars are standard deviations. Determinations are from routine analyses obtained under automated conditions over 1-yr period.

determined from measurements using beryllium blocks or thin films are shown in Table 3. Minimum detectable concentrations obtained under routine operating conditions were calculated to be approximately 0.2 mM with beryllium blocks and 0.1 mM with thin films; however, experimentally we were unsuccessful in accurately measuring 0.1mM concentrations with thin films.[12]

TABLE 3.--Minimum detectable concentrations (mM).

	P	S	Mg	Ca	K	Na	Cl
Block	0.18	0.17	0.22	0.14	0.11	0.28	0.31
Film	0.09	0.09	0.05	0.05	0.05	0.18	0.24

References

1. C. P. Lechene, "The use of the electron microprobe to analyze very minute amounts of liquid samples," *Proc. Fifth Nat. Conf. Electron Probe Analysis* (New York), 1970, 32A-32C.

2. C. P. Lechene, "Electron probe microanalysis of picoliter liquid samples," in T. Hall, P. Echlin and R. Kaufmann, Eds., *Microprobe Analysis as Applied to Cells and Tissues*, New York: Academic Press, 1970, 351-368.

3. C. P. Lechene and R. R. Warner, "Electron probe analysis of liquid droplets," in C. Lechene and R. Warner, Eds., *Microbeam Analysis in Biology*, New York: Academic Press, 1979, 279-298.

4. R. R. Warner and C. P. Lechene, "Analysis of standing droplets in rat proximal tubules" (submitted for publication).

5. J. V. Bonventre, K. Blouch, and C. Lechene, "Biological sample preparation for electron probe analysis: Liquid droplets and isolated cells," in M. A. Hayatt, Ed., *X-ray Microscopy in Biology*, Baltimore: University Park Press, in press.

6. R. M. Borland, J. D. Biggers and C. Lechene, "Studies on the composition and formation of mouse blastocoele fluid using electron probe microanalysis," *Dev. Biol.* 55: 1-8, 1977.

7. N. Roinel, "Electron microprobe quantitative analysis of lyophilised 10^{-10} l volume samples," *J. Microsc. Biol. Cell.* 22: 261-268, 1975.

8. N. Roinel, M. Champigny, L. Meny, and J. Henoc, "Quantitative analysis of lyophilized solutions: Experimental and theoretical evaluation of the limits of linearity of the calibration curves," *Proc. 13th MAS Conf.*, 1978, 62A-62D.

9. R. R. Warner and C. P. Lechene, "Quantitative microprobe analysis in biology," in C. Lechene and R. Warner, Eds., *Microbeam Analysis in Biology*, New York: Academic Press, 1979, 161-170.

10. P. M. Quinton, "Ultramicroanalysis of biological fluids with energy dispersive x-ray spectrometry," *Micron* 9, 57-69, 1978.

11. P. M. Quinton, R. R. Warner, and C. Lechene, "Minimum detectable concentrations with the liquid-droplet technique," in O. E. Newbury, Ed., *Microbeam Analysis 1979*, San Francisco: San Francisco Press, 73-76.

12. R. R. Warner, P. M. Quinton, and C. P. Lechene, "Minimum detectable concentrations with the liquid droplet technique" (submitted for publication).

ANALYSIS OF ORGANIC SOLUTES IN MICRODROPLETS

R. Beeuwkes

Electron-probe x-ray microanalysis of microdroplets has now become routine in many laboratories. When the sample volume is extremely limited (of the order of 10^{-9} L or less) this approach makes experimental studies possible that could not be otherwise considered. However, microdroplet analysis as commonly practiced is restricted to the determination of *elemental* composition, such as sodium or potassium, and can only be applied to the study of organic molecules when those molecules contain characteristic, naturally occurring marker elements. Through the use of specific chemical reactions it may be possible to add an elemental label to a compound of particular interest, or to use the unknown compound to promote the formation or precipitation of a molecule containing a distinctive and quantifiable element. In the course of studies of the renal concentrating mechanism we have found it necessary to develop an analytical technique for the measurement of urea in specimens of 50 pL or smaller. Although the concentration of urea in the droplet is on the order of 100 mM, the absolute quantity involved is only about 5 picomoles. The method employed is based on the precipitation of urea in combination with thioxanthen-9-ol, a sulfur-containing compound. Although this method is specific only for urea, certain features of the analytical approach may be of more general interest.

Analytical Technique

The chemistry of the analytical scheme is shown in Fig. 1. Urea, consisting of carbon, oxygen, hydrogen, and nitrogen, lacks a distinctive elemental label. However, urea is known to react with xanthen-9-ol to form the insoluble complex di(xanthen-9-ol) urea. Replacement of the oxygen in xanthen-9-ol by sulfur at a nonreactive site creates the new compound thioxanthen-9-ol, which, when reacted with urea, yields an insoluble product in which each urea molecule is associated with 2 moles of sulfur. The preparation of these reagents has previously been described in detail.[1]

Specimen droplets are deposited under water-saturated oil onto the surface of slices of polished single crystal silicon (Semiconductor Processing, Inc., Hingham, Mass.). The use of silicon instead of beryllium supports is advantageous because of convenient size and shape, low cost, and absence of toxicity. The x-ray background on such supports is only 2-3 times the very low levels commonly achieved with beryllium. To provide multiple crystallization sites, we apply a very thin coating of dixanthyl-urea crystals (sulfur-free) by spraying a saturated solution onto the silicon surface with a simple atomizer. A single 5 × 24 mm silicon wafer easily holds many hundreds of specimens.

The chemistry requires the establishment of fixed concentrations of acetic acid, methanol, and thioxanthen-9-ol within each 50 pL specimen droplet. This is simply and easily achieved by placing the silicon sample support in oil containing these reagents. Because the reagents are soluble in both oil and water, when reagent-loaded oil comes in contact with an aqueous droplet, reagents diffuse into the droplet until a stable equilibrium, defined by partition coefficients, is reached. Thus no pipetting of reagents is necessary and concentrations in each drop are exactly equal. The amount of reagent in the oil is effectively infinite compared with that removed by the reaction, so that it is essentially impossible to deplete the reagent source. Thus, as the reaction proceeds, thioxanthen-9-ol is precipitated and more diffuses into the droplet so as to maintain the partition equilibrium. The reaction is allowed to go to completion during a period of 60 min at 30°C. Excess reagent is removed by the same principle. The silicon wafer is removed from the reagent-loaded oil and rinsed in pure xylene or isopentane. The water from the
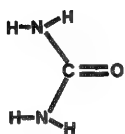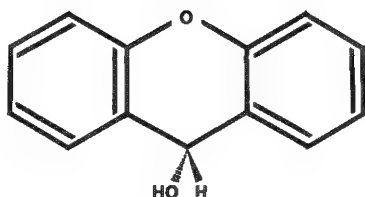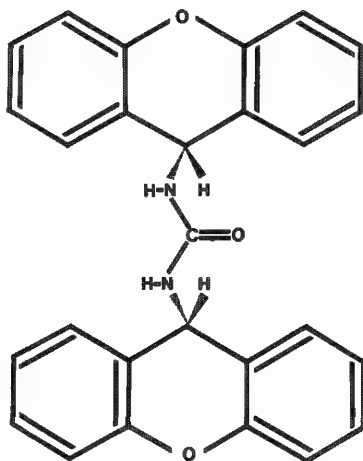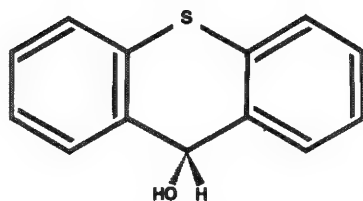
FIG. 1.--Molecular structures of reagents used in microdroplet urea analysis.

droplets is not removed during the rinsing procedure, and it is allowed to dry in air. Freeze-drying is not required since the size of the crystals of urea complex was defined by the reaction conditions. Inorganic solutes such as sodium, potassium, and chloride are not removed from the droplets by the partition processes and remain within the dry residue as very small crystals dispersed within the urea reaction product.

X-ray microanalysis is performed by means of a Cameca MBX instrument. A 20keV, 200nA beam, is defocused to cover the largest specimen spot, typically 70-100 μm in diameter. Crystal spectrometers are used and these are tuned on the reaction product itself. Only 10 sec of counting time is required on each spot, although for better statistics longer counting times may be used. No change in counting rate for any of the elements studied has been observed in repeated counts made during a period of over 100 sec. Background is measured on-peak, off-specimen, and subtracted. A standard curve for urea in a solution also containing sodium, potassium, and chlorine is shown in Fig. 2. The limit of sensitivity is reached at less than 1 picomole of urea.

Discussion

Some features of this technique may be useful in the analysis of other organic compounds. The labeling reagent was developed by the substitution of sulfur for oxygen in a nonfunctional site. Such oxygen molecules are common in organic reagents. Many organic reagents either have appropriate partition coefficients or can be made to have them by substitutions of polar or nonpolar side chains. Such reagents include both acids and bases. Because ionic constituents are neither added nor removed, simultaneous multi-element analysis is possible.

Although the analytic scheme is straightforward, there are many areas of potential difficulty. Most should be obvious to persons familiar with chemical analytic technique and microdroplet analysis. An obvious source of error would be the presence of significant quantities of endogenous sulfur in the solution to be analyzed. Similarly, loss of the unknown compound to the covering oil would lead to serious error. To test for loss of urea we have left unreacted droplets under the covering oil for periods in excess of 2 hr before adding the reagents. No urea loss is observed (Table 1). Other sources of inappropriately increased or decreased sulfur signal may include the continued presence of unreacted reagent due to insufficient washing, or inaccurate spectrometer tuning. Crystal spectrometers must be tuned on a specimen of reaction product itself, so that there is no need to correct for any chemical shift. Reaction conditions must be adjusted so as to obtain uniformly dispersed crystals of very small size. The preseeding technique is of great importance in this respect. The accelerating voltage must be sufficient to excite the full thickness of the precipitate, and the precipitate must be sufficiently thin so that x rays--both of sulfur and of light elements such as sodium--can reach the detector without attenuation. If the dried droplet size is very large, it may exceed the region of best focus for a high-resolution spectrometer. That does not seem to be a problem for spot sizes of the order of 100 μm at a take-off angle of 40°. For increased sensitivity, it has been suggested that precipitates be formed on thin films or beryllium surfaces. In our experience, thin films have proved too fragile for routine use, and beryllium surfaces may be attacked by acid media. Finally,

the solubility of the product in the medium, even though very small, must necessarily result in some product loss. The sensitivity of 10^{-12} mole routinely achieved using the methods described is adequate for the present needs of our laboratory.

The use of x-ray microanalysis for the quantitative estimation of organic solutes in microdroplets is a new and largely unexplored area. Although the technique described here was based upon the adaptation of conventional organic chemical techniques, extensions within the biochemical realm appear feasible. For example, the activity of soluble enzymes might be studied by the precipitation of inorganic phosphate. Adaptations of this approach might be used for co-factor analysis. The histochemical literature contains a wealth of specific reactions resulting in insoluble products, many of which may be adaptable to microdroplet or gelatin film preparations.

References

1. R. Beeuwkes III, J. M. Amberg, and L. Essandoh, "Urea measurement by x-ray microanalysis in 50 picoliter specimens," *Kidney Int.* 12: 438, 1977.

2. R. Beeuwkes III, "Techniques for quantitative organic analysis in microdroplets," *SEM/1979/II*, p. 767.

3. R. Beeuwkes III and S. Rosen, "Renal sodium-potassium adenosine triphosphatase: optical localization and X-ray microanalysis," *J. Histochem. Cytochem.* 23: 828, 1975.
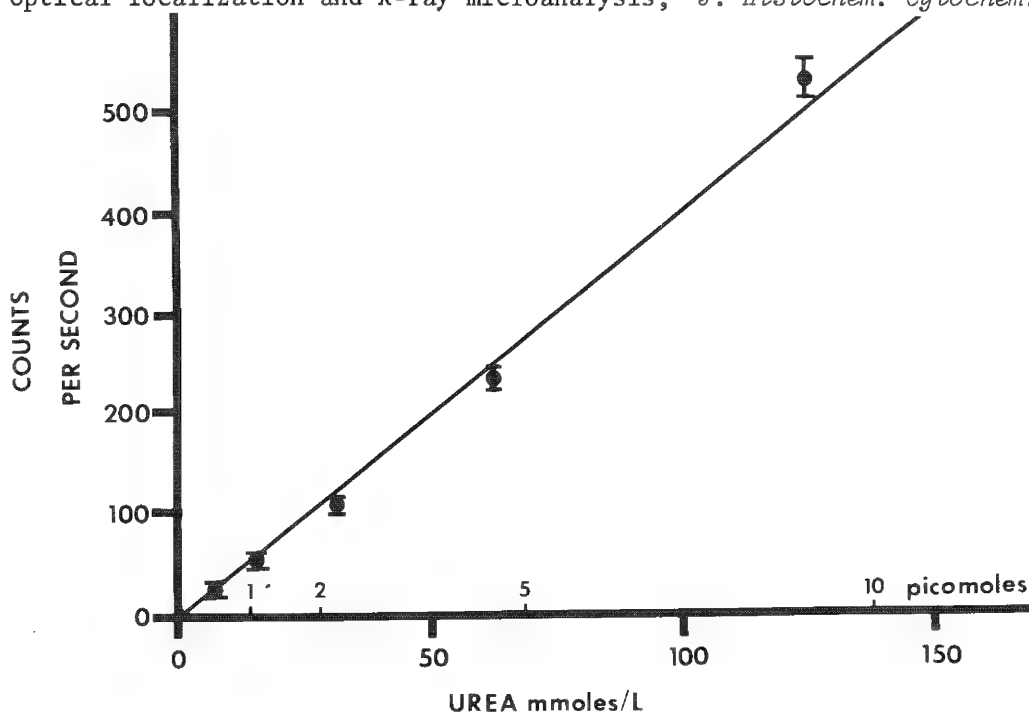
FIG. 2.--Sulfur counting rate observed during x-ray microanalysis of urea reaction products. Each point represents mean ± S.E. of 10 replicate analyses of single standard solution. Picomole scale is based on pipette volume of 48 pL.

TABLE 1.--Counting rates observed on urea specimens after immediate and delayed precipitation. To test for loss of urea, 40pl specimens of each of three standard urea solutions were pipetted under oil 0, 1, and 2 hr before precipitation reaction was begun. Each resulting precipitate was counted for 10 sec; mean ± SD (background subtracted) of counts recorded in each group is shown in Table. No decline in counting rate was observed as function of time.

Urea (mM)	Time delay (hr)		
	0	1	2
50	173 ± 32	161 ± 25	191 ± 21
100	430 ± 28	454 ± 11	464 ± 20
200	985 ± 97	1089 ± 71	1086 ± 65

VARIATIONS IN CHARACTERISTIC SIGNALS OF THE ELEMENTS DURING MICROPROBE ANALYSIS OF DROPLETS: A REVIEW

N. G. Roinel and A. F. Le Roy

The possibility that the characteristic signals which give the measure of droplet content vary with the irradiation time has become clear during the past five years. These variations have been observed by means of both energy-dispersive systems (EDS) and wavelength-dispersive systems (WDS). This paper attempts to summarize the present state of the art.

The first reports about quantitative analysis of droplet content by WDS did not mention variations in counting rates or losses of elements during irradiation.[1-4] They concerned analyses performed at various beam-current densities and accelerating voltages. In the course of 32min irradiation, Morel and Roinel detected no variations in the Na or K counting rates of a mineral solution, at 2×10^{-3} A-cm^{-2} and 20 kV.[2] The same observation was made by Garland et al., who followed Na, Cl, and K counting rates in tubular fluid and plasma samples for 10 min at 3×10^{-3} A-cm^{-2} and 15 kV.[3] Lechêne reported a possible decline in the chlorine counting rate of a mineral solution, for beam current densities above 3.8×10^{-3} A-cm^{-2} at 11 kV, and mentioned that this decline could be avoided by using a lower current density or a higher accelerating voltage.[5] Mg, P, Ca, K, and Na signals from the same standard solution were stable over 13-16min irradiation at 1.5×10^{-2} A-cm^{-2} and 11 kV.

Since 1975 the publication of various observations has shown that droplet analysis was not at all comparable to tissue analysis. Beam damage to tissue sections is manifested by a drop in the continuum radiation, by which the mass of the analyzed area is measured.[6,7] This drop seriously complicates quantitative analysis of thin biological sections. It is generally assumed that the characteristic intensities in tissue sections do not change with time, but this assumption was recently qualified by Hall.[8] The observation that during droplet analysis the characteristic intensities of some elements may, under certain conditions, vary, might seriously undermine the accuracy of an analysis performed under such conditions.

Morgan et al. used an EDS to analyze isoatomic mineral solutions sprayed into droplets 3 μm in diameter.[9] These analyses, in which droplets were covered by an 80kV defocused beam, lasted for 200 s; beam intensity was not measured. These authors determined an "overall sensitivity factor" for several elements; for chlorine, the intensity of the signal was half that expected. This result was attributed to thermal removal of chlorine from the droplets during analysis, as reported for NaCl by Sweatman and Long.[10] Attempts by Morgan et al. to reduce this loss by lowering beam intensity were not successful.

Roinel reported stable Na, Mg, P, Ca, and K counting rates throughout 1000s irradiation with a beam of 4×10^{-3} A-cm^{-2} at 15 kV.[11] As to the chlorine signal, it was observed to be stable in urine, plasma, and tubular fluid samples, but to decrease in the mineral solutions used as standards. The higher the beam current density and the sample mass thickness, the greater the loss in chlorine. This loss appeared to be independent of the beam accelerating voltage value within a range of 12-18 kV. The signals of bromine and iodine originating from pure KBr and KI exhibited a similar decline in counting rates with the irradiation time. The difference as regards signal stability between mineral and biological fluids was attributed to the presence of organic compounds in the latter, since addition of urea to the mineral solutions resulted in stable counting rates. In another investigation, it was found that the loss in chlorine depended on the accompanying cation, and that the sulfur signal from sulfate droplets decreased with time, but was stable when it originated from aminoacids such as methionine and cysteine.[12]

Like Morgan et al., Marshall used isoatomic mineral solution droplets sprayed onto film-covered grids to calibrate an EDS.[13] These analyses were performed at 100 kV with

Author Roinel is at the Department of Biology/LPPC, Saclay Center for Nuclear Studies, B.P. 2, F-91190 Gif-sur-Yvette, France; author Le Roy, at BEIDRS, National Institutes of Health, Bethesda, MD 20014.

a current density of 1 to 2×10^{-2} A-cm^{-2}. The duration of the measurement was not mentioned. Fifty to 80% losses of chlorine were also observed, depending on whether the film coating was Al or C. Those losses were not reduced when the measurements were performed at -180°C. A further observation that droplets sprayed onto cold grids lost 90% of their chlorine signal led Marshall to suppose that the drying rate was important in restricting chlorine losses. The quicker the drying, the smaller the crystals composing the droplet and the smaller the loss of chlorine. Furthermore, as this loss was smaller for films coated with aluminum than with carbon, Marshall concluded that the thermal conductivity of aluminum-coated films was better.

Unlike other groups, Rick et al. mentioned no chlorine loss with an EDS at a beam-current density of 6×10^{-6} A-cm^{-2} at 25 kV.[14] Also with an EDS, but with an 0.5nA beam scanning 80×80 μm^2 at 20 kV, Quinton reported no loss in KCl for 50 min of irradiation.[15,16] On the other hand, when H$_2$SO$_4$ was added to NaCl, the chlorine loss observed was equal to the amount of acid added and was abolished by the addition of a base such as LiOH. Quinton explained the loss by the formation of volatile HCl, which is impossible in the presence of a base.

Lechêne and Warner reported that the chlorine concentration measured with the electron microprobe dropped as the calcium concentration in the sample rose.[17] A correction equation was calculated, relating the real chlorine concentration to the value measured and to the calcium concentration in the sample and in the standard solution. The chlorine loss was thus explained by the simultaneous formation of Ca(OH)$_2$ and volatile HCl.

Roinel et al. reported several kinetic curves for Cl and S signals from various pure and mixed salts. The variations in counting rates were followed for 1200 s with beam-current densities of 2-9×10^{-3} A-cm^{-2} at 15 kV.[18] Depending on the salt, the kinetics and direction of the variation (increase or decrease) varied considerably. Cation signals were reported to vary concomittantly, but to a lesser extent. Le Roy and Roinel studied the influence of two parameters--beam current density and sample mass thickness-- on the kinetics of chlorine losses from KCl and NaCl.[19] The accelerating voltage was kept constant at 15 kV. With a computer, the curve for the Cl counting rate, expressed as a percentage of the initial value, was fitted to the sum of two negative exponentials. Such curves were sometimes preceded by a plateau, whose duration was negatively correlated with beam current density. This density had a greater effect on the exponential periods than the sample mass thickness. Table 1 summarizes the observations concerning chlorine losses.

It is thus widely recognized that, during droplet analysis by electron microprobe, the characteristic signals of many elements in addition to chlorine may vary with time, especially in the mineral solutions used as standards. The observations reported here have not yet been substantiated by coherent explanations. Despite the difficulty of comparing results, owing to variations in experimental conditions, the present findings clearly indicate the role of major factors such as the thermal conductivity properties of the sample, and the formation of volatile compounds. Independently of an explanation which would connect all those observations, the users of the microdroplet technique must bear in mind that depending on their conditions of analysis, signal instability can occur for any element in any solution, and that accurate analysis requires prior checking of signal stability.

References

1. M. J. Ingram and C. A. Hogben, "Electrolyte analysis of biological fluids with the electron microprobe," *Anal. Chem.* 18: 54, 1967.

2. F. Morel and N. Roinel, "Application de la microsonde électronique à l'analyse élémentaire quantitative d'échantillons liquides d'un volume inférieur à 10^{-9} L," *J. Chim. Phys.* 66: 1084, 1969.

3. C. Lechêne, "The use of the electron microprobe to analyze very minute amounts of liquid samples," *Proc. 9th MAS Conf.*, 1970, 32.

4. H. O. Garland, T. C. Hopkins, I. W. Henderson, C. W. Haworth, and I. Chester-Jones, "The application of quantitative electron probe microanalysis to renal micropuncture studies in amphibians," *Micron* 4: 164, 1973.

5. C. Lechêne, "Electron probe microanalysis of picoliter liquid samples," in T. Hall, P. Echlin and R. Kaufmann, Eds., *Microprobe Analysis as Applied to Cells and Tissues*, London: Academic Press, 1974, 351.

TABLE 1.--Losses in chlorine for various samples and analytical conditions.

Authors	Sample	kV	A/cm^2	Irrad. (sec)	EDS or WDS	Observations	Explanation
Morgan & al.,[9] 1975	Mixture of mineral salts	80		200	EDS	50% loss	Thermal removal
Roinel,[11] 1975	Mineral salts	15	0.002 -0.01	1000	WDS	Loss depending on A/cm^2 & sample mass thickness	
	Plasma, urine, & tubular fluid	15	0.004	1000	WDS	No loss	Loss prevented by organic compounds
Marshall,[13] 1977	Mixture of mineral salts	100	0.01		EDS	50-80% loss	
Rick & al.,[14] 1977	KCl	25	6 × 10^{-6}		EDS	No loss	
Quinton,[15,16] 1978	KCl	20	0.5 nA scanning 80 × 80 μm	3000	EDS	No loss	
	NaCl + H$_2$SO$_4$	20	-"-		EDS	Loss equal to H$^+$	Formation of volatile HCl
Lechêne & Warner,[17] 1979	NaCl + CaCl$_2$				WDS	Loss dependent on Ca	Formation of Ca(OH)$_2$↓ + HCl↑
Leroy & Roinel,[19] 1980	NaCl KCl	15	0.001 -0.015	1200	WDS	Loss of 5-75% Cl as a function of A/cm^2 Presence of a plateau of variable duration before loss, depending on A/cm^2	

6. K. Stenn and G. F. Bahr, "Specimen damage caused by the beam of the transmission electron microscope, a correlative reconsideration," *J. Ultrastruct. Res.* 31: 526, 1970.

7. T. A. Hall and B. L. Gupta, "Beam-induced loss of organic mass under electron microprobe conditions," *J. Microscop.* (London) 100: 177, 1974.

8. T. A. Hall, "Biological x-ray microanalysis," *J. Microscop.* (London) 117: 145, 1979.

9. A. J. Morgan, T. W. Davies, and D. A. Erasmus, "Analysis of droplets from iso-atomic solutions as a means of calibrating a transmission electron analytical microscope (TEAM)," *J. Microsc.* (London) 104: 271, 1975.

10. T. R. Sweatman and J. V. P. Long, "Quantitative electron probe microanalysis of rock-forming minerals," *J. Petrol.* 10: 332, 1969.

11. N. Roinel, "Electron microprobe quantitative analysis of lyophilized 10^{-10} L volume samples," *J. Microscop.* (Paris) 22: 261, 1975.

12. N. Roinel, "Elementary quantitative analysis of lyophilized 10^{-10} L volume solutions," in G. W. Bailey, Ed., *35th Ann. EMSA Proc.*, 1977, 362.

13. A. T. Marshall, "Iso-atomic droplets as models for the investigation of parameters affecting x-ray microanalysis of biological specimens," *Micron* 8: 193, 1977.

14. R. Rick, M. Horster, A. Dörge, and K. Thurau, "Determination of electrolytes in small biological fluid samples using energy dispersive x-ray microanalysis," *Pflügers Arch.* 369: 95, 1977.

15.   P. Quinton, "SEM-EDS x-ray analysis of fluids," *SEM/1978/II*, 391.

16.   P. M. Quinton, "Ultramicroanalysis of biological fluids with energy dispersive x-ray spectrometry," *Micron* 9: 57, 1978.

17.   C. Lechêne and R. Warner, "Electron probe analysis of liquid droplet," in C. Lechêne and R. Warner, Eds., *Microbeam Analysis in Biology*, New York: Academic Press, 1979, 279.

18.   N. Roinel, L. Meny, and J. Henoc, "Accuracy of electron microprobe analysis of biological fluids: Choice of standard solutions and range of linearity of the calibration curves," *NBS Special Report 533*, 1979.

19.   A. Leroy and N. Roinel, "Quantitative analysis of lyophilized solutions: Loss of elements during the irradiation time as a function of sample current density and mass thickness," *9th Intern. Conf. X-ray Optics and Microanalysis*, 1980 (in preparation).

SIMPLE QUANTITATIVE ENERGY-DISPERSIVE ANALYSIS OF EXOTIC MINERALS: ANALYSIS OF SYNROC BY POCKET CALCULATOR

N. G. Ware

The SYNROC method of disposal of nuclear reactor waste material involves the synthesis of a mineral assemblage which is capable of holding all the radioactive elements in crystal lattices for long periods of time.[1] Such an assemblage consists of perovskite ($CaTiO_3$), zirconolite ($CaTi_2ZrO_7$), and a mineral with the hollandite structure ($BaAl_2Ti_6O_{16}$). Development of this technique requires extensive use of microbeam analysis. The partitioning between the various phases of elements such as strontium, cesium, uranium, and the rare earths must be measured by microanalysis of experimental charges; solid solutions within the principal minerals must be determined accurately and extraneous phases, sometimes not described previously, must be analyzed. In addition, much microprobe time is required for research into alpha-particle damage of naturally occurring minerals and investigations of alternative mineral assemblages.[2]

Such work poses severe problems for the microanalyst. The crystal size in subsolidus experimental charges rarely exceeds 10 μm, the combined x-ray spectra of the constituent elements are very complicated, and the feedback time between microprobe and experimental petrology laboratories must be kept to a minimum.

The sequential "simplex" or PIBS (peak integration with background subtraction) method of energy-dispersive electron-beam analysis has proved successful for the analysis of common rock-forming minerals where the errors in calculation of continuum intensity and estimation of peak overlap are tolerable.[3-5] This paper indicates how the technique may be extended to provide serviceable data reduction of spectra containing severely overlapping peaks and continuum formed by high atomic number matrices.

Data Handling Considerations

An advantage of using the PIBS method is that an on-line computer is not essential for obtaining good quantitative energy-dispersive analyses. Indeed, a small electronic calculator is all that is required for some applications where good standards are available. The first step in the data reduction is the integration of the contents of the energy channels covering the full-width half-maxima (FWHM) of the relevant x-ray peaks. This procedure results in a small set of numbers and may be done by hard-wired multichannel analyzer. However, some early models lack the facility for integrating overlapping groups of channels and, in SYNROC mineralogy, there are several cases of mutually overlapping FWHMs. Nevertheless, an on-line computer has many uses and rapid data reduction is possible by the PIBS method even when interpretative languages like BASIC and FOCAL are used.

Continuum Subtraction

The contribution of bremsstrahlung to the integrated count in a FWHM is estimated by measurement of the x-ray intensity in parts of the spectrum known to be free of peaks and interpolation by application of predetermined empirical ratios corrected for absorption and backscattering. Omission of the backscattering correction results in a negligible error when one is analyzing samples such as silicates, where the mean atomic number is low and uniform, but the correction must be included for the variable high atomic number phases found in SYNROC.[6] Correcting the continuum ratios for absorption and backscattering requires very little extra computing effort as both corrections must be included anyway in the ZAF routine.[4] Such corrections are impractical when the simplified pocket

calculator approach is used but good results are obtainable nevertheless on the basis of carefully selected standards. For example, the limit of detection of uranium in zircono- lite is 0.08% by the full correction procedure and 0.1% by the simplified method.

Peak Overlap

Energy dispersive spectra composed entirely of K lines are readily resolved. Mutual Kα overlap at low energies is of the order of only 1% and although Kβ/Kα overlap may reach 13% of the parent peak, the spectrum may be stripped sequentially starting at the lowest energy. However, in other spectra mutual Lα overlap can exceed 50% and SYNROC spectra contain the notorious BaLα/TiKα overlap which is about 90%. Nevertheless, simple algebraic solutions can give quite good results. If A and B are the FWHM intensities of two mutually overlapping peaks, I_a and I_b the measured uncorrected intensities at the FWHM, and a_b and b_a the overlap ratios of A on B and of B on A, then two simultaneous equations may be written the solutions of which are

$$A = (I_a - I_b b_a)/P$$

$$B = (I_b - I_a a_b)/P$$

where $P = (1 - a_b b_a)$. The solution for FWHM intensity C in the case of three simultane- ously overlapping peaks is more complicated but still simple enough to calculate without invoking statistical or matrix computer library subroutines:

$$C = [I_c(1 - a_b b_a) - I_a(a_c - a_b b_c) - I_b(b_c - a_c b_a)]/Q$$

where

$$Q = (1 - b_c c_b - a_c c_a - a_b b_a + a_c c_b b_a + a_b b_c c_a).$$

By means of these equations the simultaneously overlapping Sr, Y, and Zr or Y, Zr, and Nb L-lines and the mutually overlapping U and Th M-lines all may be resolved. The smaller the denominator P or Q in the above equations, the larger is the error in calcu- lating the peak intensity. The large error in the resolution of Ba and Ti may be reduced by an additional measurement, of the intensities of the Kβ and Lβ lines, which leads to four equations with two unknowns that may be solved by conventional statistical proce- dures. Repeated measurements on a standard hollandite show that an adequate precision may be obtained by this method (Table 1).

Table 2 shows the steps necessary for the "pocket calculator" computation of a na- turally occurring zirconolite. Once the calibration factors have been determined and ZAF correction coefficients calculated, such a calculation may be performed "manually" within the time required for the measurement of the next spectrum.

TABLE 1.--Mean and standard deviation of 50 analyses of synthetic $BaAl_2Ti_6O_{16}$.

	wt.%	σ	theoretical composition
TiO_2	66.1	1.2	65.25
Al_2O_3	13.7	0.2	13.88
BaO	20.4	0.6	20.87
Total	100.2		100.00

TABLE 2.--Simplified analysis of natural zirconolite.

Line	FWHM-Channels	Counts	Background	Overlap	wt.%	W.D. Analysis
Mg Kα	60- 66	9793	9574	0	0.1	0.13
Zr Lα	99-107	104949	10941	3893	27.0	27.3
Nb Lα	105-113	66366	10473	46413	2.9	3.1
Background	128-134	7273	7273	0	-	-
Th Mα	147-155	9819	8463	179	0.6	0.58
U Mα	156-164	9558	8322	681	0.3	0.31
Ca Kα	181-188	41592	6317	0	11.1	12.9
Ti Kα	222-229	57464	4322	0	21.2	21.5
Nd Lα	257-265	5679	4562	50	0.4	0.43
Fe Kα	316-324	8640	3370	46	3.8	3.9
Background	380-388	2160	2160	0	0	-
Ta Lα	403-411	2043	2029	0	<.1	0.04

References

1. A. E. Ringwood et al., "Immobilization of high level nuclear reactor wastes in SYNROC," *Nature* 278: 219-223, 1979.

2. A. E. Ringwood et al., "The effects of radiation damage on SYNROC," in *Scientific Basis for Nuclear Waste Management*, vol. 2, New York: Plenum Press, 1980 (in press).

3. C. E. Fiori et al., "An on-line correction procedure for quantitative electron probe microanalysis with a Si(Li) detector," *Proc. 10th MAS Conf.*, 1975, 20A-20G.

4. N. G. Ware, "Computer programs and calibration with the PIBS technique for quantitative electronprobe analysis using a lithium drifted silicon detector," submitted to *Computers and Geoscience*.

5. S. J. B. Reed and N. G. Ware, "Quantitative electron microprobe analysis of silicates using energy-dispersive X-ray spectrometry," *J. Petrol.* 16(3): 499-519, 1975.

6. D. G. W. Smith et al., "The atomic number dependence of the x-ray continuum intensity and the practical calculation of background in energy dispersive electron microprobe analysis, *X-ray Spectrom.* 4: 149-156, 1975.

APPLICATION OF SCANNING ELECTRON MICROSCOPY TO THE CANADIAN RADIOACTIVE WASTE DISPOSAL PROGRAM

P. J. Chernis, D. A. Walker, and A. G. Plant

In the development of the Canadian program for the disposal of radioactive waste, a research project is under way to determine whether or not hard rock formations (granite plutons) within the Precambrian Shield possess the requisite structural and petrological characteristics to serve as repository sites.[1,2] As a contribution to this project, we are concerned with the development of methods to measure microcrack content, rock fabric parameters, and related properties of drill core as a basis for the interpretation of rock properties derived from electrical resistivity, porosity, and other measurements. The application of the scanning electron microscope (SEM) to the study of microcracks and pores in rocks was first described by Timur et al.[3] The importance of careful sample preparation of polished rock samples for these studies was recognized by Brace and co-workers who used an ion miller to remove a surface layer containing microcracks enhanced and/or induced by the cutting and polishing processes.[4,5] We have adapted and further developed this procedure to the preparation of doubly ion-milled polished thin sections, and have adopted video tape recording (VTR) as the mode of image recording and routine sample examination.

Sample Preparation

The high-quality polished thin sections of granites and other rock samples are prepared from drill core by the following procedure. Small tablets, $2 \times 2 \times 0.3$ cm, are cut from the core by a thin blade saw. As sawn-induced microcracks can extend about 30 μm into a surface, one of the larger surfaces of the tablet is ground and polished to remove any of these artifacts. This surface is then ion-milled for 15 hr by a Technics MIM 4C ion miller to remove any effects induced during the polishing stage. This intentional overmilling produces a surface with an exaggerated topography to provide for improved bonding of the tablet to a glass slide. After the ion-milled surface of the tablet is bonded to a frosted glass slide by means of cold setting epoxy, the tablet is ground and polished until a section with a thickness of about 100 μm is produced, about triple the thickness of a conventional petrographic section. This polished surface is then ion-milled to remove debris and surface damage produced by the mechanical preparation methods. The ion milling reduces the thickness of the section by 10-15 μm and allows investigation of pristine surfaces of the rock sample. Milling time is limited to between 8 and 12 hr to avoid production of an over-exaggerated topography with milling-induced hummocks. Bridges (Fig. 1d) resembling those seen by Brace et al.[4] remain intact, and indicate that the process produces a polished thin section that is entirely free of mechanical damage features.

In preparation for subsequent SEM examination, the thin sections are coated with 50 Å of Au-Pd in a Technics Hummer V sputtering unit. This thin film of Au-Pd does not hinder any further optical microscopy that may be necessary, whereas the more commonly used film of 200-400 Å applied by others would mask most details.[5,6] Moreover, the 50Å Au-Pd layer is sufficient to provide the advantage of a higher secondary electron emission compared to that of carbon, necessary for high magnification imaging, and yet thin enough that neither Au nor Pd x-ray peaks are observed in energy-dispersive spectra.

Sample Observation

Mosaics of color photomicrographs with a magnification of 30× are used for prelimi-
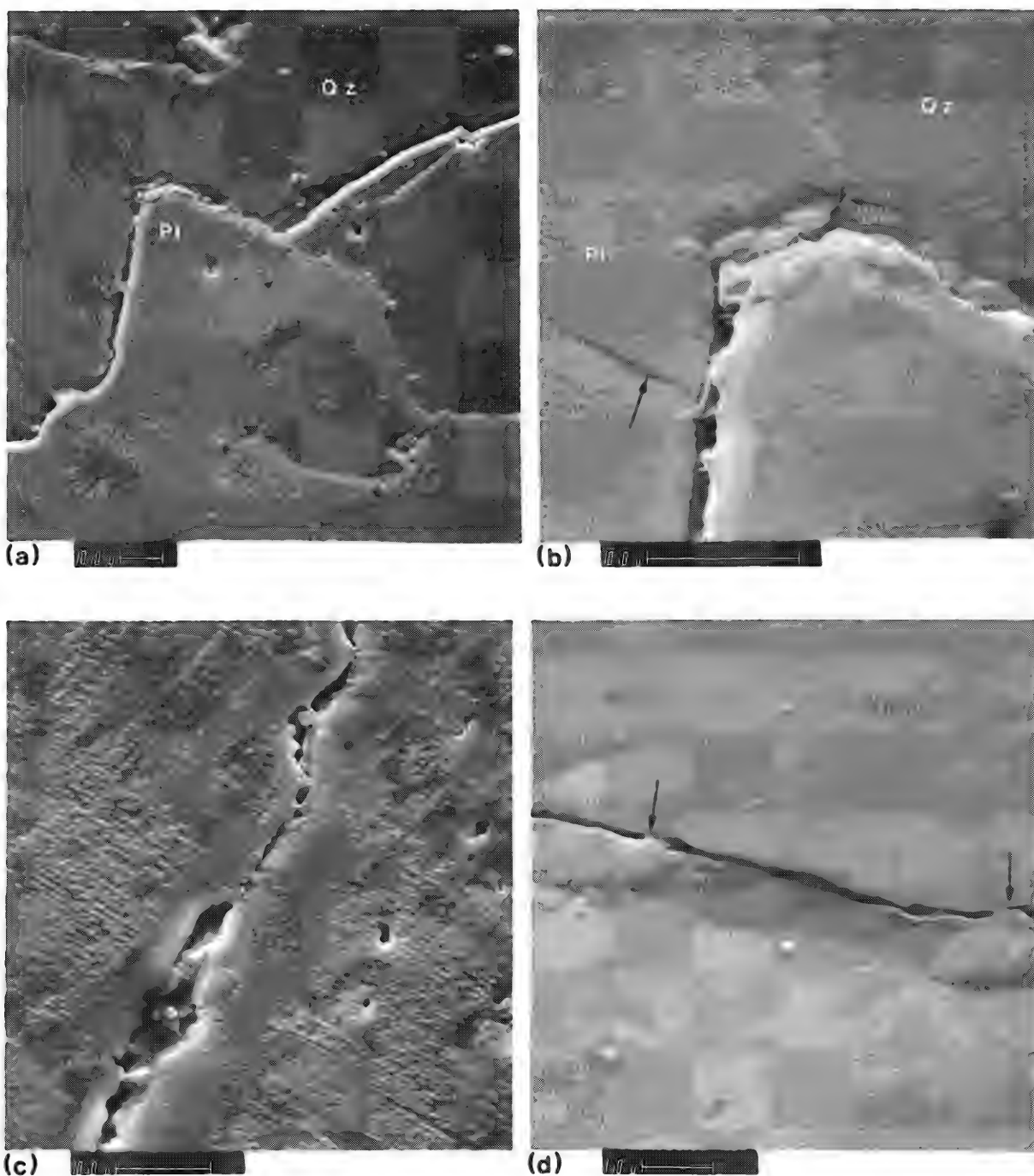
FIG. 1.--(a) Transgranular microcrack crossing plagioclase grain Pl has followed grain boundary for 20 μm before passing into quartz Qz. (b) Detail from (a) showing fine, short intergranular microcrack (arrow) along grain boundary between quartz Qz and plagioclase Pl, and narrow intragranular (cleavage) microcracks in plagioclase (arrow). (c) Intragranular microcrack in microcline. Note irregular sizes and shapes of pores along microcrack, and bridges and infilling material within. Characteristic tartan twinning of microcline is seen as patterned milling hummocks. (d) Intergranular microcrack along a quartz-quartz grain boundary is characterized by narrow aperture with fine bridges (arrows).

nary optical observations of the thin sections prior to SEM observation when they are used to identify and locate areas for detailed study of any microcracks. These mosaics illustrate the entire area of the section (4 cm^2) and allow a more representative selection of microcracks than is possible with a mosaic covering only a small area and composed of low magnification SEM photomicrographs.[6] The microcracks are classified as being intergranular, intragranular, or transgranular (Fig. 1), and each type may be related to physical properties such as porosity and permeability. Following the method described by Underwood,[7] parallel traverses are used to collect data on aperture and density for each type of microcrack for use in comparisons of calculated porosity and permeability with laboratory measurements. An energy-dispersive spectrometer is used to confirm the optical identification of mineral grains and for subsequent analysis of bridging and infilling materials.

Image Recording

High-resolution videotape recording equipment (Sony Model VO2610) has been selected over photographic recording for routine examination of the thin sections for reasons of expediency and cost, without any substantial sacrifice of image quality. In our system, the SEM image is transferred to the VTR via a video storage unit incorporated into an ETEC Autoscan SEM. This mode of recording is preferred to video recording at normal television rates as it permits considerably higher magnifications and lower noise levels. Images are routinely stored at magnifications up to 30 000×, which may be increased to 120 000× by use of a zoom control on the video storage unit. Considering the size of our video monitor (12 in.), the resultant magnification may be up to 240 000×. Microcracks of 50-100 Å can be resolved with this procedure. The VTR system has a number of advantages over the use of a photographic recording medium. Over 150 images, each lasting 10 sec, may be stored on a 1-hr video cassette, at a quarter of the cost of the equivalent amount of Polaroid film. In addition, the speed of videotape recording compared to that of photographic recording allows three to four times the number of images to be recorded per session. Combined with this increased efficiency of VTR for image storage and analysis, the use of the polished thin sections is providing a greater understanding of the relationship between the physical properties of a rock and its microcrack characteristics.

References

1. J. Boulton, Ed., *Management of Radioactive Fuel Wastes: The Canadian Disposal Program*, Atomic Energy of Canada Limited, AECL-6314, 1978.

2. J. S. Scott, "EMR Program for geological disposal of high-level radioactive wastes," *Geol. Surv. Can.* Paper 79-10: 13, 1979.

3. A. Timur, W. B. Hempkins, and R. M. Weinbrandt, "Scanning electron microscope study of pore systems in rocks," *J. Geophys. Res.* 76: 4932, 1971.

4. W. F. Brace et al., "Cracks and pores: A closer look," *Science* 178: 162, 1972.

5. E. S. Sprunt and W. F. Brace, "Direct observation of microcavities in crystalline rocks," *Int. J. Rock Mech. Min. Sci.* 11: 139, 1974.

6. M. L. Batzle and G. Simmons, "Microfactures in rocks from two geothermal areas," *Earth Planet. Sci. Lett.* 30: 71, 1976.

7. E. E. Underwood, *Quantitative Stereology*, Reading, Mass.: Addison Wesley, 1970.

CRYOGENIC ELIMINATION OF SODIUM LOSS IN GLASSES DURING EPMA ANALYSIS

C. H. Nielsen and Haraldur Sigurdsson

A problem often encountered in the quantitative microprobe analysis of hydrous and rhyolitic synthetic and natural glasses is the time dependent loss of Na Kα, and to a lesser extent K Kα, x-ray intensity with exposure to the beam.[1-4] This phenomenon clearly prohibits the precise chemical characterization of the glass due to the continuously changing alkali metal concentration. The increased application of the electron probe microanalyzer (EPMA) to radioactive waste encapsulation as well as geologic materials has further emphasized the problem of alkali loss. We describe here two methods which deal with the loss of *sodium* during analysis. One approach eliminates the problem by a cryogenic technique; the other predicts the initial concentration by fitting the decay curve.

This depletion of alkali metal ions from the glass can be most simply described by a model suggested in 1962 by Lineweaver.[5] The first step in the model requires that incident electrons ionize the alkali metal by splitting it from one of the bridging oxygens. Next, as the beam heats the glass above a certain temperature the alkali metal ion becomes mobile and diffuses out of the excited volume towards a space-charge layer created by the beam several microns beneath the surface. This migration of the more mobile species out of the region where x rays are generated accounts for the loss of alkali counts during analysis. Hence, the effect is more pronounced for Na because it has a higher diffusivity than K in most glasses.[6] Furthermore, the thermal character of the process explains what has been observed in some materials and labeled as an *incubation period*.[7] This is a nearly flat region in the beginning of the decay curve, which probably represents the time required for the sample to attain the temperature necessary for the alkali diffusion.

It is this incubation period that is most likely the key to the solution of the problem. It has been shown that the incubation period can be shortened by increasing the initial specimen temperature.[7] According to Lineweaver's model this relation could be explained by the suggestion that the alkali metal ion reaches its diffusion temperature more rapidly. The obvious question is whether the reverse is true: if one were to reduce the initial specimen temperature, would the incubation period increase? Furthermore, can one lengthen the incubation period enough to allow a reasonable analysis of the sample?

Methods

Rhyolitic glass fragments (KN-18) containing 5.68% Na_2O and 4.39% K_2O and ranging in size from 20 to 200 μm in diameter were mounted in a small brass disk with epoxy, polished, and coated with approximately 200 Å of carbon. The loss of sodium from the rhyolitic glass during electron bombardment was monitored both at 25°C under vacuum, and under cryogenic conditions. A cryogenic cold-finger cooled the sample through a copper braid to a final temperature of -100°C in a specimen chamber under vacuum of 5×10^{-6} Torr. During cooling the rate of sodium loss was monitored every 10°C for 60 sec. Counts were automatically accumulated in 2sec intervals from samples exposed to a focused, 0.02μA, 15 kV electron beam. The EPMA (JEOL JXA-50A) was standardized by means of basaltic glass VG-2 and synthetic mineral 85% diopside--15% jadeite. The standards were mounted in the brass disk with the unknowns so that the standardization could be checked without any need to warm the sample. Quantitative EPMA analyses were performed on unexposed samples of known composition at a temperature of -100°C, with counting times of 30 sec per element. Corrections were made on line with a Bence-Albee routine supplied by Krisel Control.

The authors are with JEOL Electron Optics Division, II Dearborn Rd., Peabody, MA 01960.

Results

The decay curves of Na and K x-ray intensities at room temperature are presented in Fig. 1. The dramatic slope of the Na curve illustrates the severity of the problem of alkali loss which reduces the initial count rate by 50% within the first 10 sec of exposure to the beam. The shape of the sodium curve looks nearly exponential and seems to reach a steady state condition after approximately 45 sec. Observed loss of potassium counts is much less and nearly linear. Note also that no incubation period is present for the Na curve.
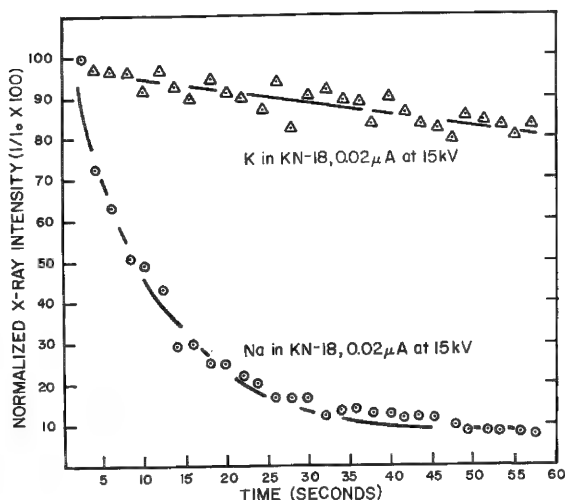

FIG. 1.--Sodium and potassium loss from natural rhyolitic glass during electron microprobe analysis under normal operating conditions.
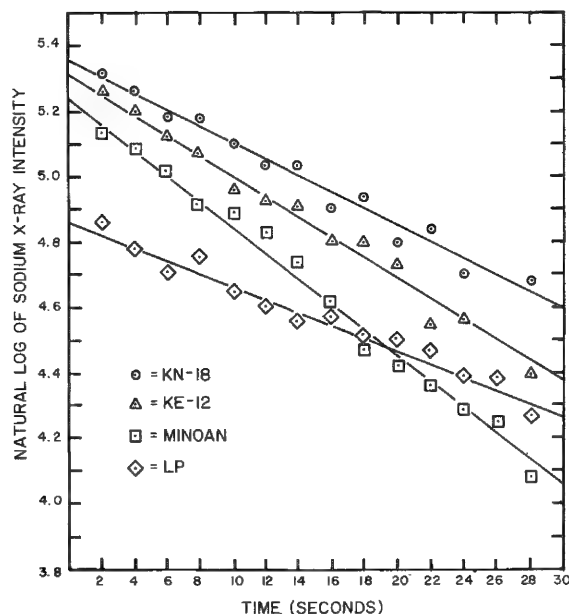
FIG. 2.--Sodium decay plots for four natural rhyolitic glasses, plotted as natural logarithm of x-ray intensity vs time.

A. *Empirical Correction Method*. As noted above, the shape of the alkali metal decay curves appear to obey some functional relationship with time. The function which most closely fits the decline of sodium intensity was empirically determined to be a simple exponential. Hence, a straight-line relationship should be obtained if the natural logarithm of the intensity data is plotted vs time, as illustrated in Fig. 2 for several cases. One can use this approximation to estimate the initial alkali concentration from the decay curve by performing a least-squares fit and then determining the intensity intercept on the semi-log plot and converting to concentration.

A computer-based automation system was used to standardize for sodium, collect sodium counts at 2sec intervals, store the data for the decay curve, plot the log of intensity versus time, and perform the statistical analysis. Sodium standards that are stable under the beam, such as 85% diopside--15% jadeite, were used to calibrate the system. To test the routine, several materials of known composition that experienced sodium depletion were analyzed. Table 1 lists the "true" sodium values together with those obtained by our empirical method. The values reported represent the average and standard deviation of 25 measurements. The standard deviations of sodium concentrations measured by the empirical decay curve method are in all cases well within experimental error of the accepted Na_2O concentration.

B. *Cryogenic Correction Method*. In the empirical method described above the sodium concentration is measured while the sample undergoes a dynamic compositional change. However, to determine the absolute alkali content, the sample must be analyzed under stable conditions. To this end cryogenic experiments were performed to suppress the sodium depletion. A natural rhyolitic glass sample (KN-18) was cooled to a final tempera-

TABLE 1.--Empirical determination of sodium in rhyolitic glasses under normal operating conditions (0.02 µA beam current, 15 kV accelerating voltage).

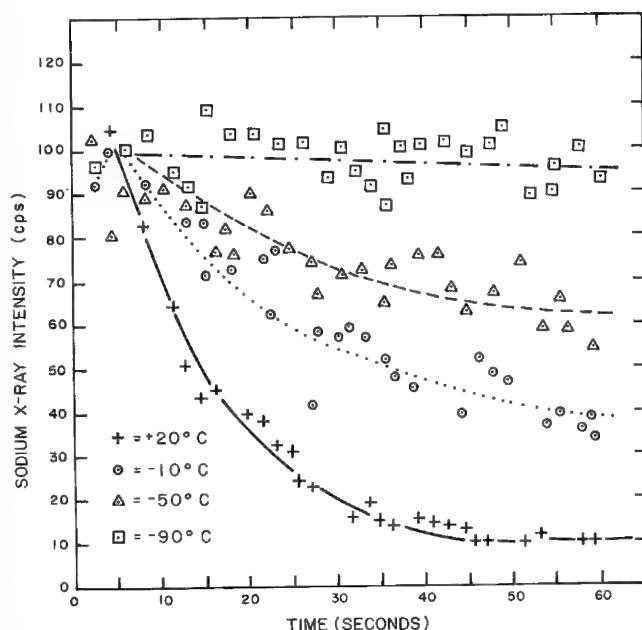| Sample	Accepted Na_2O concentration	Measured Na_2O concentration	Relative % error
KN-18	5.68*	5.53+0.25	2.68%
KE-12	5.40*	5.34+0.30	1.12%
LP	3.22*	3.32+0.18	3.06%
Minoan Tephra	5.11	4.98+0.27	2.57%

*X-ray fluorescence analysis.[8]

FIG. 3.--The effect of sample temperature on sodium loss from a rhyolitic glass (KN-18) during electron bombardment. Cryogenic coding of sample mount to -90°C suppresses alkali diffusion in glass and permits direct quantitative analysis.

ture of -110°C at a rate of 1°C/min, during which a series of 60sec decay curves were accumulated at 10°C intervals. Results of this experiment are presented as a series of decay curves in Fig. 3. The bottom curve, collected at 20°C, has the highest slope and levels off within 40 sec. The 10°C curve shows a marked reduction in the diffusion rate and does not level off within the 60sec observation. Other data collected at lower temperatures yielded decay curves with decreasing slopes. At approximately -90°C the concentration remained stable, within experimental error, for the entire 60sec observation. Cooling to the lowest attainable temperatures of -110°C produced results similar to those obtained at -90°C.

The results indicate that at a sample temperature of -90°C sodium is stable in the glass for at least 60 sec and therefore quantitative determination should be possible. Quantitative microprobe analyses were performed on several samples to test the method. Calibration of the system was made at -110°C by use of known standards. Two samples of known composition (KN-18 and LP) were analyzed under the beam conditions stated above. The average of 10 analyses of each sample is given in Table 2, along with the accepted values. The low standard deviations and percentage errors demonstrate that the precision and accuracy of these analyses are as good as those of glass samples which do not experience alkali depletion.

Conclusions

The severe loss of sodium counts during microprobe analysis of silicate glasses can be corrected for or avoided. First, the migration of sodium due to heating under the electron beam can be arrested by cooling of the sample to -90°C during analysis. However, this cryogenic method involves longer analysis time and special preparation techniques. A more rapid routine of estimating the sodium concentration has been therefore developed. This empirical technique estimates initial sodium concentration by the rate of decay in sodium counts during continuous electron bombardment of the sample and routinely gives accurate data.

TABLE 2.--Microprobe analysis of rhyolitic glasses under cryogenic conditions (-110°C).

Oxide	KN-18 Accepted Composition*	KN-18 This work	LP Accepted Composition*	LP This work
SiO_2	74.6	75.0(.25)**	76.49	76.9(.30)**
Al_2O_3	10.53	10.67(.06)	12.59	12.50(.10)
FeO^*	3.45	3.52(.08)	1.05	1.09(.05)
MgO	0.01	0.02(.01)	0.06	0.05(.01)
CaO	0.15	0.17(.01)	0.31	0.33(.03)
Na_2O	5.68	5.47(.09)	4.34	4.28(.10)
K_2O	4.39	4.25(.06)	4.59	4.50(.10)
TiO_2	0.18	0.20(.02)	0.10	0.10(.01)
P_2O_5	0.01	–	0.01	–
MnO	0.06	0.05(.01)	0.06	0.06(.01)
Total	99.06	99.35	99.60	99.81

*X-ray fluorescence analysis.[8]

**One standard deviation, based on ten measurements.

References

1. R. T. Heiz, "Phase relations of basalts in their melting ranges at PCH_2O = 5kb, Part II: Melt compositions," *J. Petrol.* 17: 139, 1976.

2. I. Kushiro, "Effect on the composition of magmas formed at high pressures," *J. Petrol.* 13: 311, 1972.

3. B. O. Mysen and I. Kishiro, "Compositional variations of coexisting phases with degree of melting of peridotite in the upper mantle," *Am. Mineral.* 61: 843, 1977.

4. N. D. Watkins et al., "Volume and extent of the Minoan Tephra from Santorini volcano: New evidence from deep-sea sediment cores," *Nature* 271: 122, 1978.

5. J. L. Lineweaver, "Oxygen outgassing caused by electron bombardment of glass," *J. Appl. Phys.* 34: 1786, 1962.

6. M. Magaritz and A. W. Hofman, "Diffusion of Sr, Ba and Na in Obsidian," *Geochim. Cosmo Acta* 42: 595, 1978.

7. L. F. Vassamillet and V. E. Caldwell, "Electron-probe microanalysis of alkali metals in glass," *J. Appl. Phys.* 40: 1637, 1969.

8. S. A. Malik, D. A. Bunsgaard, and R. McDonald, personal communication.

APPLICATIONS OF SCANNING ELECTRON MICROSCOPY (SEM) TO THE STUDY OF PHOSPHATE ROCKS

M. M. Soroczak and R. M. Scheib

At TVA, phosphate rock (PR) characterization has been extended to apply SEM/energy dispersive x-ray analysis (EDX) methods to resolve submicroscopic features relating to cementation and distribution of accessory minerals. This study reflects the utility of SEM/EDX to extend conventional mineral characterizations to this important commercial mineral. They are used to elucidate physical relationships of minerals in problem ores as a guide to recovery and utilization of marginal-quality phosphate resources.

These examples from TVA's extensive PR collection, grouped according to their consolidated or unconsolidated texture as defined by McClellan and Gremillion,[1] dramatize the varying textural conditions of minerals in these ores. They demonstrate the differences in the nature and bonding of the impurity phases and explain why apatite recovery techniques cannot be generalized but must be tailored for each ore.

Sample preparation for the PR in this study is as follows. The rocks are fractured and representative pieces 5-25 mm across are mounted, by means of a mixture of epoxy and silver dag, to expose fresh fracture surfaces. Also, some unconsolidated PR are water-washed to remove the fines and leave the grain surfaces exposed. These grains are mounted with double adhesive tape. Loose particles are blown away with compressed gas and the mounted rock pieces are coated with carbon in an evaporator.

From Unconsolidated Phosphate Rock

The unconsolidated PR discussed here contain apatite mainly as aggregates of pelletal grains, intraclasts, and/or phosphatized fossils[2] loosely held in a matrix of quartz; and carbonates and/or clays (Fig. 1a).

In central and south Florida PR, clays often fill the voids within the matrix of phosphate grains. The smoothness of casts formed when grains are removed from the matrix reveals the weak bonding between the clays and the grains (Fig. 1b).

In a south Florida ore, apatite and quartz grains are loosely cemented by carbonates (mainly dolomite) and clays (mainly attapulgite and montomorillonite). Attapulgite is a fiber-shaped clay and montmorillonite can range from "nebulous film-like assemblages" to individual small particles.[3] The attapulgite fibers cling to the surface of the carbonate rhombs and interlock with the montmorillonite to form a supporting mat (Fig. 2a-b).

The carbonate rhombs, most of which are eroded, range from 2 to 30 μm in diameter. The rhombs were separated from the sample for EDX analysis because the chemical constituents of the clays on the surfaces interfered with *in situ* analysis. The EDX spectra of both intact and eroded rhombs were identical with those of a standard dolomite crushed to a similar size. The ratio of magnesium to calcium was lower for the rough surfaces of the eroded rhombs and the broken pieces of dolomite than for the smooth surfaces of each. Since the same piece of dolomite had been crushed to give both smooth and rough surfaces, the lower ratio was caused by topography.

SEM micrographs show that the clays are the actual bonding minerals in these samples, which suggests that the apatite grains could be liberated from the matrix by water washing to facilitate flotation treatments to recover phosphate and remove the quartz.

In a rock from Sardinata (Colombia), most of the phosphate pellets had patchy surface areas covered with silica gel (Fig. 3). This intimate association of silica with the apatite makes separation during beneficiation difficult. This same ore contained wavellite as the product of postdepositional weathering of the apatite, silica, and clays (Fig. 4). Recrystallized apatite could be seen in the matrix (Fig. 5a) and in cavities within the pellets (Fig. 5b).
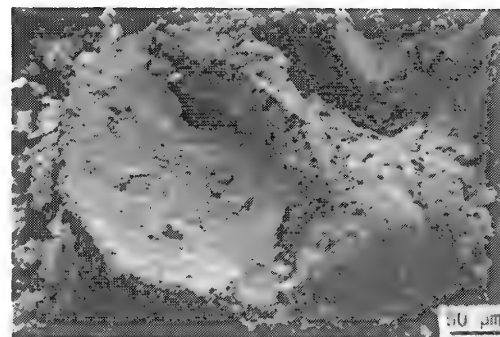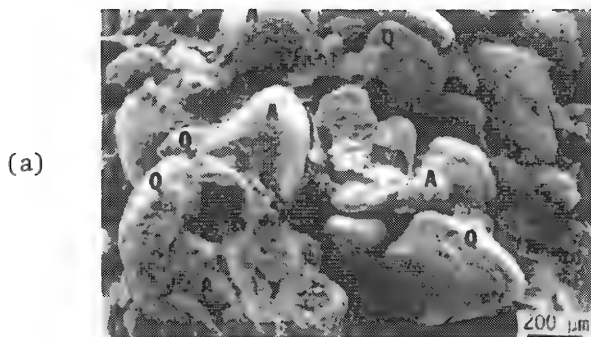
FIG. 1.--Unconsolidated phosphate rock. (a) apatite (A) and quartz (Q) in clay matrix; (b) clay cast left by removal of large grain during fracturing.

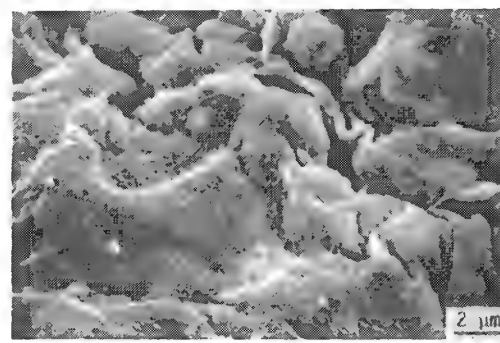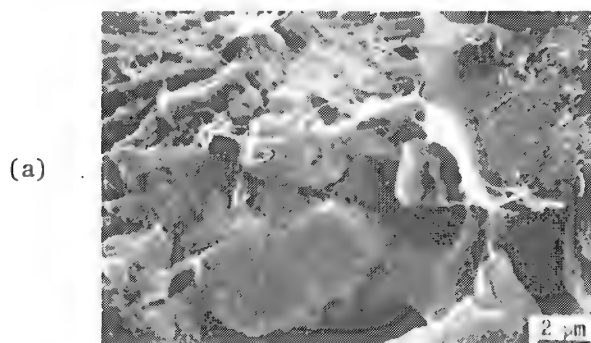FIG. 2.--(a) attapulgite attached to carbonates; (b) mat of attapulgite and montmorillonite over carbonates.
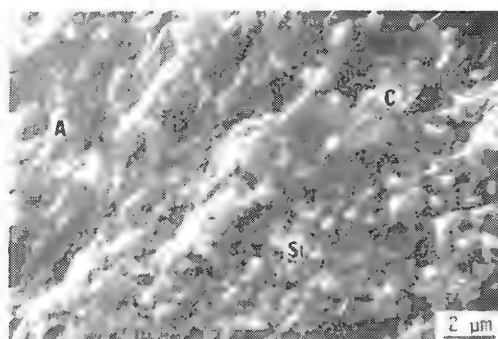

FIG. 3.--Patchy silica gel (Si) and clay (c) on surface of apatite pellet.
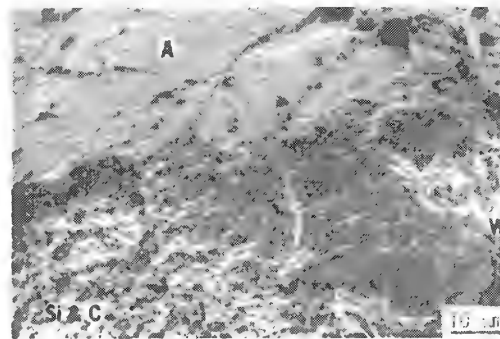
FIG. 4.--Apatite and silica gel-clay mixture weathering to form bladed crystals of wavellite (W).
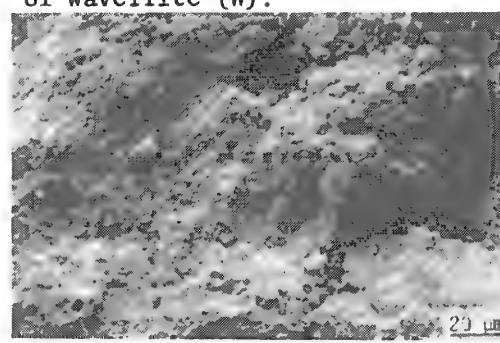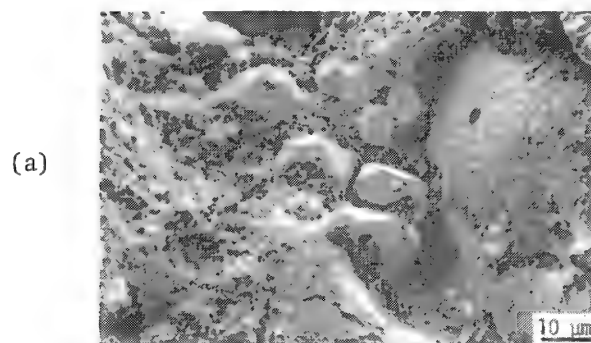

FIG. 5.--(a) equant hexagonal prisms of recrystallized apatite; (b) cluster of recrystallized apatite formed in internal cavity of apatite pellet.

An unconsolidated rock from Machtesh (Israel) shows recrystallized apatite as secondary overgrowths on micro-oolites of primary sedimentary apatite (Fig. 6a). Sometimes the primary apatite is leached and leaves the secondary overgrowths (Fig. 6b). Riggs tentatively interprets a similar feature in Florida phosphate as the result of burrowing or encrusting protozoans.[4]

Examples from Consolidated Rocks

Consolidated PR have a compact texture (Fig. 7). In these examples, the apatite is cemented by silica and silicates or carbonates. The textural features of consolidated phosphate rocks are poorly defined in comparison with those of unconsolidated PR, but element maps can be used to locate minerals. Significant areas can then be investigated at higher magnifications.

Since both apatite and quartz are hexagonal minerals, EDX analysis is necessary for mineral identification when the crystallites are small or only partially exposed. Intimate association of very small crystals (Fig. 8) makes it difficult to determine which mineral is acting as the cementing agent. Such associations present problems in liberating all the apatite during beneficiation.

Successively higher magnifications for element maps clarified the relationship of apatite and quartz in a siliceous PR from Queensland (Australia). Element maps of both silicon and phosphorus confirmed relationships that were suspected because of crystal morphologies (Fig. 9). In this example, both the primary and secondary apatite are finer grained than the quartz.

In PR from Queensland, element mapping was used to distinguish apatite from the calcite matrix and to locate minor concentrations of quartz (Fig. 10). Banded overgrowth encasing a phosphatized fossil is seen in this ore (Fig. 11a-b). EDX analysis shows that the band of dense material contains 60% less phosphorus than either the pellet or the outer band.

References

1. G. H. McClellan and L. R. Gremillion, "Evaluation of phosphatic raw materials," *The Role of Phosphorus in Agriculture,* Madison, Wis.: ASA-CSSA-SSSA, chap. 3 (in press).
2. S. R. Riggs, "Petrology of the tertiary phosphorite system of Florida," *Econ. Geol.* 74: 195-220, 1979.
3. R. E. Grim, *Clay Mineralogy,* New York: McGraw-Hill, 1968, 2 ed., pp. 174, 177.
4. Riggs, *op. cit.* (Ref. 2).
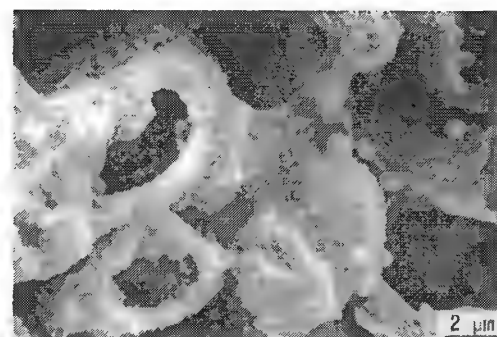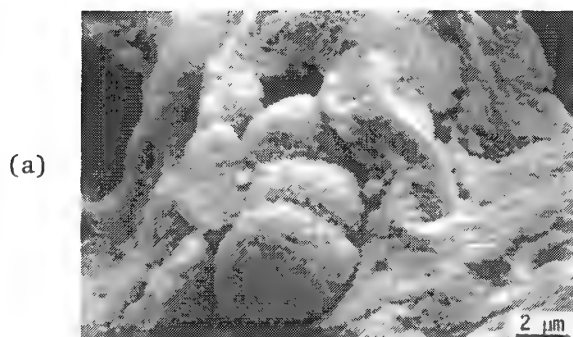
FIG. 6.--(a) recrystallized apatite as secondary overgrowth on micro-oolites of primary apatite; (b) micro-oolites of primary apatite leached, leaving secondary apatite shell.
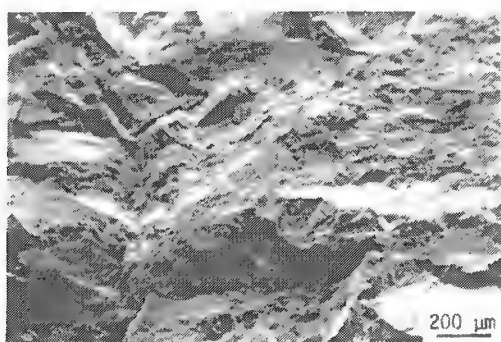
FIG. 7.--Consolidated phosphate rock.
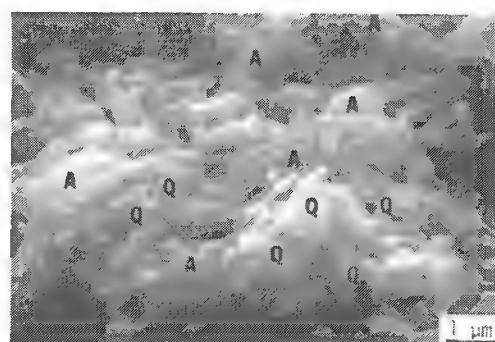
FIG. 8.--Crystallites of apatite and quartz in intimate association.
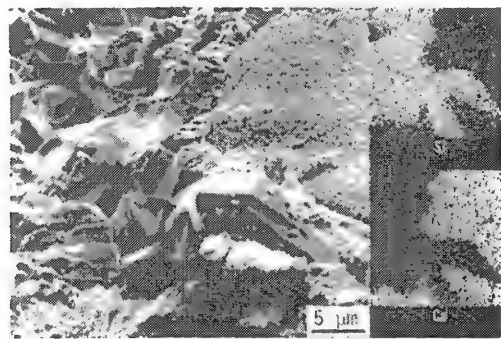
FIG. 9.--Fine-grained apatite surrounded by secondary apatite in quartz matrix. EDX element maps.
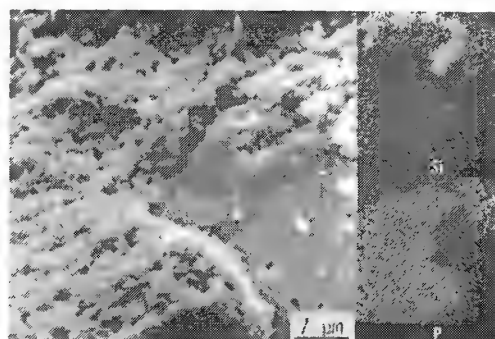
FIG. 10.--Apatite in calcite matrix with minor concentration of quartz. EDX element maps.
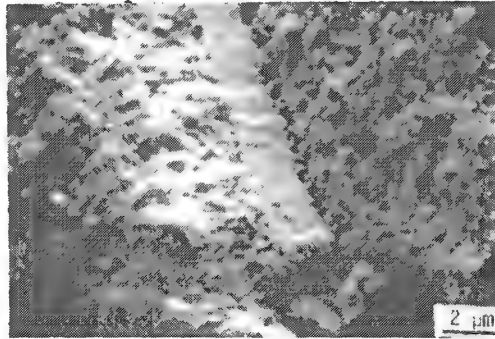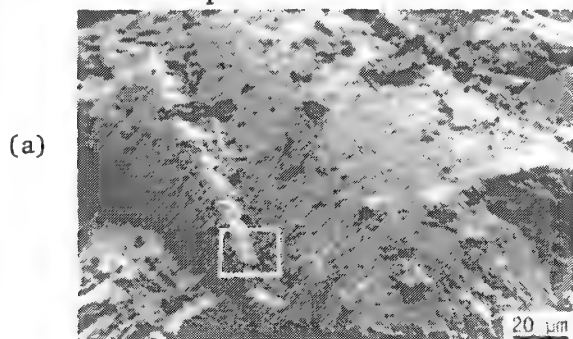
FIG. 11.--(a) banded overgrowths encasing phosphatized fossil; (b) inner band from (a) differs in density and composition from fossil or outer band.

146

A NEW IMPROVED STANDARD FOR ELECTRON PROBE DETERMINATION OF ORGANIC SULFUR IN FOSSIL FUELS

L. A. Harris, R. Raymond Jr., and R. Gooley

Electron probe microanalysis (EPM) has important advantages over conventional methods of analysis for organic sulfur in coal: analysis by EPM is done directly, which avoids problems associated with calculating organic sulfur content by difference; and organic sulfur contents of individual macerals can be measured *in situ* in a sample. A major problem with this technique has been finding a suitable sulfur standard. We have recently prepared a petroleum coke and have found it to be a suitable standard.

Background

Matrix effects caused by major differences in composition, structure, and density between organic and inorganic compounds make inorganic minerals (e.g., pyrite) undesirable as standards. Sutherland reported on EPM studies of organic sulfur in coal using pyrite (FeS_2) as a sulfur standard.[1] He used a common data reduction algorithm for matrix (ZAF) corrections, then multiplied by an additional factor to correct for differences in observed x-ray intensities caused by extreme differences in composition between the standard and samples. Initial standardization to derive the correction factor for the particular instrument and conditions used was time consuming, but once achieved, Sutherland suggested that analytical time for analysis of organic sulfur could be less than 1 hr.

Raymond and Gooley reported on organic sulfur contents of various maceral types in coals, determined by EPM using small (75-200μm dia.), sulfur-bearing carbon beads as a standard.[2] The beads were originally prepared at the Los Alamos Scientific Laboratory for use in nuclear fuel cells. They contain 4.1 wt.% sulfur, are stable under electron bombardment, and eliminate the undesirable matrix effects common to inorganic minerals. The beads were useful in studies involving relative organic sulfur contents of various maceral types, but slight chemical inhomogeneities among beads made development of a better standard desirable.

Organic sulfur contents of coals are typically less than 2 wt.%, and rarely above 4 wt.%. Therefore, an ideal organic sulfur standard for EPM would be a hydrocarbon that contains about 4 wt.% sulfur. We examined a polysulfone resin ($C_{27}H_{22}SO_4$, 9.28 wt.% S) for its potential as a sulfur standard. Though chemically homogeneous, it is sensitive to electron bombardment, as are most organic compounds, and visibly degrades under the electron beam. Avoiding this degradation requires constant sample movement during standardization. We therefore continued our search for a better sulfur standard.

Petroleum Coke: A Good Standard

Petroleum coke, derived from thermal treatment of petroleum pitch, is chemically homogeneous and quite stable during electron bombardment. Petroleum pitch is a thick bituminous substance produced by destructive distillation of petroleum. Petroleum coke is produced by thermal decomposition of the pitch. Chemical analyses of the pitch before coking gave 92 wt.% C, 3.9 wt.% S, 2 wt.% H, and 0.009 wt.% ash. Petroleum pitch typically contains less than 1% mineral matter.

We converted the petroleum pitch into coke in a batch autoclave by heating it to 300°C for a few hours, raising the temperature to 375°C for 5 hr, and finally heating at 500°C for 24 hr. Loss of volatile constituents was minimized by constant refluxing during the

coking process. Chemical compositions of cokes produced by this process vary little from those of the starting pitches. This process essentially duplicates that of a delayed coking oven.

We prepared a polished section of the product coke; a photomicrograph is shown in Fig. 1. Note the lamellar structure of the coke (anisotropic in polarized light) and the large void which is partially filled with a "second phase." The "second phase" is a plastic material that solidified after the coke formed. Its composition is similar to the coke, but the sulfur content may be as much as 1.5 wt.% higher.
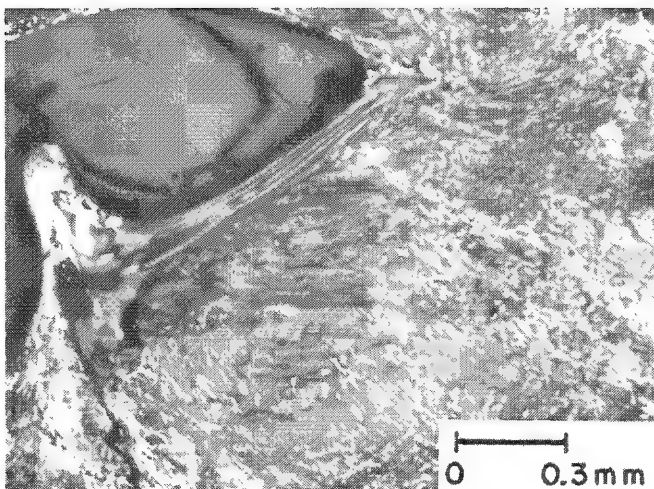
FIG. 1.--Polarized, reflected-light microphotograph of the product coke. Note the lamellar structure of the coke, the large pore, and the second phase material partially filling the pore.

To remove the "second phase" we crushed the coke and boiled it overnight in quinoline. The product was then washed thoroughly in alcohol and air dried. The above is a standard method for removing unreacted phases from cokes and does not affect the sulfur in the remaining single-phase coke. Analyses made on a Leco sulfur analyzer showed the single-phase coke to contain 3.56 ± 0.04 wt.% sulfur.

Using the petroleum coke as its own standard we analyzed 100 random areas of the sample as a homogeneity check, ignoring the lamellar structure of the coke. Using a t-statistics approach, we determined that seven standardization repeats ensure a standardization value of 3.56 ± 0.10 wt.% at the 95% confidence level.

Discussion

In this paper we report on petroleum coke that is stable under an electron beam and contains a uniform sulfur content; hence it is a suitable standard for analysis of organic sulfur content of coal. It should be as applicable for analysis of organic sulfur in other fossil fuels. This standard is available for distribution and may be obtained from any of the authors.

References

1. J. K. Sutherland, "Determination of organic sulphur in coal by microprobe," *Fuel* 54: 132, 1975.
2. R. Raymond Jr. and R. Gooley, "A new standard for electron microanalysis of organic sulfur in coal," in *Trans. 8th Intern. Congress on X-ray Optics and Microanalysis*, Princeton, N. J.: Science Press, 1979.

STATISTICAL VALIDITY FOR ELECTRON PROBE MICROANALYSIS OF ORGANIC SULFUR IN COAL

R. Raymond Jr., T. D. Davies, and R. C. Hagan

In 1978 Raymond and Gooley[1] reported on a procedure for determination of organic sulfur content of coal by electron probe microanalysis (EPM). Because vitrinite is the dominant maceral type in most coals and generally has an intermediate sulfur composition between exinites and inertinites, they showed that the organic sulfur content of a coal could be calculated from the organic sulfur content of vitrinite in that coal. Questions were raised concerning the number of vitrinite grains needed for analysis in order to achieve a good representation. The purpose of this paper is to show that analyzing relatively few vitrinite grains provides data representative of the organic sulfur content of the entire vitrinite population.

Analysis

We analyzed vitrinite from four seams representing a wide range of geographic settings, apparent rank, and total sulfur content (Table 1). We also considered operator bias and used two investigators with no prior experience in coal petrography and two investigators with very little EPM experience.

TABLE 1.--Variability of the four coals analyzed. (Samples and analyses listed below courtesy of The Pennsylvania State University Coal Section.)

Sample	Seam	State	Apparent Rank	Sulfur wt.% (DAF)
PSOC 164	Tebo	Missouri	hvBb	9.37
PSOC 193	Ohio #5	Ohio	sub C	1.02
PSOC 506	Upper Sunnyside	Utah	hvAb	0.69
PSOC 1012	Lower Kittanning	Pennsylvania	low vol	2.81

The organic constituents of coal, such as vitrinite, are commonly identified by reflected-light oil-immersion microscopy. We identified vitrinite points of analysis for the first half of our samples by this method. The time-consuming disadvantage of oil-immersion identification is that photomosaics must be prepared. For the second half of our analyses vitrinite grains were located in the EPM after the samples had been carbon coated. In this case we used morphology and texture of the grains, rather than reflectance, to identify vitrinite.

All samples were analyzed both with and without the aid of photomosaics. In each case investigators analyzed 100 vitrinite grains for organic sulfur content. We used an energy-dispersive spectrometer and multiple-wavelength spectrometers to insure that no sulfur attributable to sulfide or sulfate minerals was measured as organic sulfur.

The results for 2000 analyses are summarized in Table 2. Using the t-statistic approach, we calculated for each run the number of analyses η necessary to give a desired maximum variability ρ relative to the true mean μ defined by 100 analyses. This was calculated in all cases at the 95% confidence level as seen below:

$$Pr\{\mu - \rho\mu \leq \bar{x} \leq \mu + \rho\mu\} = 0.95$$

where $\bar{x}$ is the sample mean determined by n analyses.

TABLE 2.--Summary of vitrinite analyses by individual investigators both with and without photomosaics: μ = the true mean defined by 100 analyses, S = the sample standard deviation, and n = the number of analyses necessary to give a desired maximum variability of 0.1 μ at the 95% confidence level.

Investigator	Sample	w/Mosaic	w/o Mosaic	μ	S	n
1	PSOC 1012	X		1.12	0.12	7
2	PSOC 1012	X		1.13	0.13	8
3	PSOC 1012	X		1.12	0.12	7
4	PSOC 1012	X		1.13	0.14	9
1	PSOC 1012		X	1.09	0.14	9
2	PSOC 1012		X	1.13	0.12	7
3	PSOC 1012		X	1.13	0.12	7
4	PSOC 1012		X	1.11	0.12	7
1	PSOC 506	X		0.86	0.07	6
2	PSOC 506	X		0.83	0.07	6
3	PSOC 506	X		0.87	0.06	5
1	PSOC 506		X	0.84	0.06	5
2	PSOC 506		X	0.84	0.07	6
3	PSOC 506		X	0.85	0.06	5
2	PSOC 193	X		1.35	0.19	11
3	PSOC 193	X		1.42	0.22	12
1	PSOC 193		X	1.30	0.20	12
3	PSOC 193		X	1.39	0.19	10
2	PSOC 164	X		3.95	0.65	13
3	PSOC 164		X	4.00	0.68	14

The number of analyses n necessary to achieve a maximum variability of 0.1μ (that is, ρ = 0.1) has also been listed in Table 2 for the four coals we studied. For example, sample PSOC 1012 requires between 7 and 9 analyses to achieve the desired mean value; sample PSOC 164 requires between 13 and 14 analyses.

Discussion

Most coals contain less than 2.00 wt.% organic sulfur. Therefore, for most coals we expect to achieve a maximum variability from the true mean of less than 0.20 wt.% if we analyze 15 vitrinite grains. The variability decreases for coals containing lower concentrations of organic sulfur. If a greater statistical accuracy is desired when coals with higher contents of organic sulfur are analyzed, it may be achieved by additional analyses.

Neither operator experience nor variation in coal composition and rank appeared to bias the results. Organic sulfur content, which reflects the depositional environment of the basin in which the coal was deposited,[2] appears to affect the number of measurements required to produce statistically valid data. This result is due to higher sample standard deviations, which result from a history of more than one period of organic sulfur emplacement in the coals. Fifteen vitrinite analyses per coal sample take such variations into account.

Analyses performed without photomosaics provide data that are as statistically valid as those obtained with photomosaics. Without the need to produce a photomosaic, the organic sulfur content of vitrinite from a coal may be measured in less than 10 min. The potential therefore exists to achieve very rapid, multiple organic sulfur analyses, which in turn will allow for rapid, detailed measurements of variations in organic sulfur content occurring across coal seams.

References

1. R. Raymond Jr. and R. Gooley, "A review of organic sulfur analysis in coal and a new procedure," in O. Johari, Ed., *Scanning Electron Microscopy*, Chicago: SEM Inc., 1978, vol. 1, p. 93-107.

2. R. Raymond Jr., "Correlating organic sulfur in coal to depositional environments by electron probe microanalysis," *Compte rendu IX. Intern. Cong. Carboniferous Stratigraphy and Geology* (in press).

•

QUANTITATIVE ION MICROPROBE ANALYSIS OF Mg, Fe SILICATES

Ian Steele, Richard Hervig, and Ian Hutcheon

The common rock-forming minerals olivine $[(Mg,Fe)_2SiO_4]$ and low-Ca pyroxene $[(Mg,Fe)SiO_3]$ show a near-binary compositional series between the Mg and Fe end members. This report describes our progress toward development of an accurate ion-probe analysis technique based on a suite of well-documented standards. We previously[1] reported systematics of secondary ion (SI) intensities for major elements in olivine and now present similar data for major elements in low-Ca pyroxene and for minor elements in both minerals. These data reveal consistent relationships between sample composition and SI intensity and thus permit routine analysis of unknowns by comparison to standards. Detailed examination should provide insight into the mechanisms of SI generation and allow development of a general theoretical correction procedure.

Samples and Experimental Conditions

The olivine suite used in our previous study[1] was expanded to include a set of Mg-rich olivines from kimberlites; in addition, 16 low-Ca pyroxenes were selected whose compositions span the natural range of Mg-Fe substitution. Initial electron microprobe analyses were made with a 30μm-diameter beam to provide reference compositional data on areas suitable for ion-probe analysis. An AEI IM-20 ion microprobe was operated under the following conditions: 20keV, 10na $^{16}O^-$ mass-analyzed primary beam focused to about 30μm diameter; sample chamber at $< 5 \times 10^{-8}$ torr with sample region cooled to liquid N_2 temperature; pulse counting of SI by means of an electron multiplier; computer-controlled magnet switching; high (M/ΔM > 3000) or low (about 300) mass resolution as required.

Results

SI intensities for low-Ca pyroxene mimic those of olivine when the SI intensity ratio $Mg^+/(Mg^+ + Fe^+)$ (normalized to 100% isotopes) is plotted against the known $Mg/(Mg + Fe)$ atomic ratio of the sample (Fig. 1). However, the K value $\{K = [A(1 - B)]/[(1 - A)B]$ where $B = Mg^+/(Mg^+ + Fe^+)$ in SI yield and $A = Mg/(Mg + Fe)$ in target$\}$ is about 0.40 for olivine and about 0.55 for low-Ca pyroxene. The cause of this difference is suggested in Fig. 2 where the Mg^+ and Fe^+ SI fraction $[Mg^+$ or $Fe^+/(Mg^+ + Fe^+ + Si^+)]$ is plotted vs the Mg and Fe target atom fraction [atomic Mg or Fe/(Mg + Fe + Si)]. The Mg^+ SI curve is identical for olivine and pyroxene, but the Fe^+ SI curve is distinctly different. Apparently, the higher Si content of pyroxene causes a greater Fe^+ SI yield from pyroxene relative to olivine but has no effect on the Mg^+ SI yield. The simple relation shown in Fig. 1 allows determination of major element atomic ratios by reference to one standard. Repeated determinations over a 1-yr period gave identical curves for olivine indicating that K is independent of slight changes in instrumental conditions for our ion probe.

SI intensity data were obtained for Ca, Ti, Cr, Al, and Mn in low-Ca pyroxene and for Ca, Ti, Al, Cr, and Na in olivine. Results for Al, Mn, Ca, and Na are shown in Figs. 3-6 plotted against the respective atomic concentration based on electron-probe measurements. All trace elements measured in both olivine and low-Ca pyroxene exhibit a simple linear relationship between SI intensity and atomic concentration. Scatter of individual data points about a correlation line is in all cases easily attributable to a combination of electron-probe measurement error [which can be large for low concentrations, e.g., Na in olivine (Fig. 6)], ion-probe statistical error, and sample inhomogeneity. Data for elements analyzed at high (Ca; Cr and Ti, not illustrated) and low mass resolution show
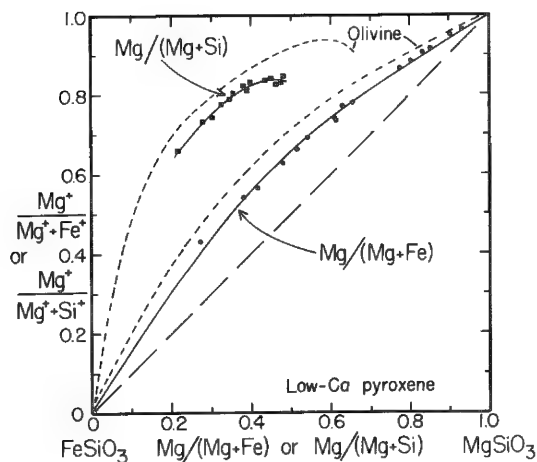
FIG. 1.--SI intensity ratios [Mg$^+$ or Fe$^+$/(Mg$^+$ + Fe$^+$)] vs atomic ratios [Mg or Fe/(Mg + Fe)] in sample. Dashed lines show olivine trend given in Ref. 1. Solid lines are eye-fit to low-Ca pyroxene data.

FIG. 2.--SI intensity ratio [Mg$^+$ or Fe$^+$/(Mg$^+$ + Fe$^+$ + Si$^+$)] vs atomic ratio [Mg or Fe/(Mg + Fe + Si)] in sample. For Mg, olivine and pyroxene data plot on single curve; for Fe, on different curves.

FIG. 3.--SI intensity data for ^{27}Al vs atomic Al in sample for low-Ca pyroxene. Line gives approximate fit.
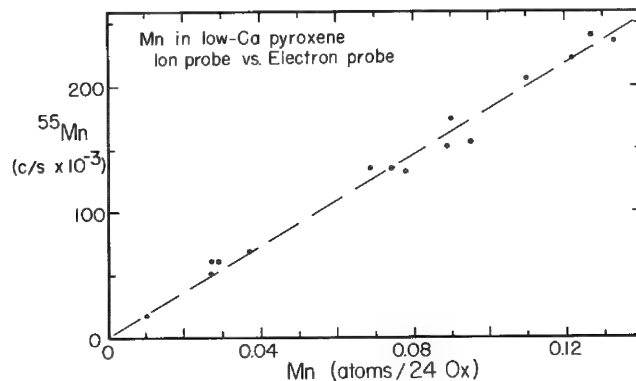
FIG. 4.--SI intensity data for ^{55}Mn vs atomic Mn in sample for low-Ca pyroxene. Line gives approximate fit.

FIG. 5.--SI intensity data for ^{40}Ca vs wt.% CaO in sample for olivines from kimberlite suite. CaO is proportional to atomic Ca for narrow range of major element variation. Inserts show details of electron and ion probe peaks.
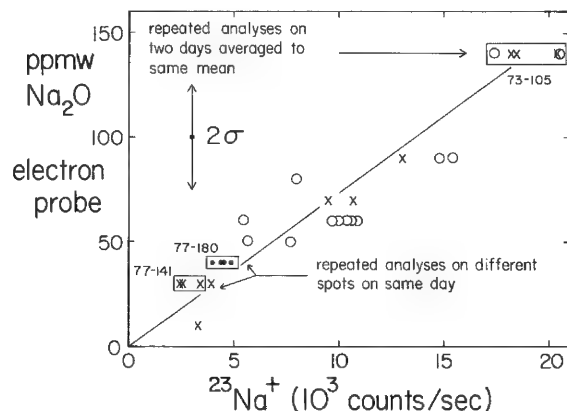
FIG. 6.--SI intensity data for ^{23}Na vs wt.% Na$_2$O for kimberlite olivines. Scatter is due mainly to electron-probe error at these low concentrations.

152

equally good correlations with low scatter.

Conclusions

Several important conclusions can be drawn from this study, although it remains to be seen whether they will be applicable to all SI data. First, the linear relation between SI intensity and atomic concentration for minor elements ($\leq$ 3 wt.% of the oxide) is not affected by the variation of major elements in the olivine or low-Ca pyroxene. This behavior may be a general feature of SI yields which, if true, would greatly simplify quantitative analysis since reference to a single, well-documented standard would be sufficient for determination of minor elements. A similar linear relationship for minor elements has also been found for Fe and Mg in natural plagioclases[2] [(Na,Ca)(Al,Si)$_2$Si$_2$O$_8$]. However, Reed et al[3] have observed a dependence of the Ni$^+$/Fe$^+$ SI intensity ratio on the Mg/Fe ratio in olivine, but it is not clear whether Ni or Fe is the nonlinear species in their study. Finally, normalizing SI count rates to a major element SI count rate is inadequate for quantitative elemental analysis unless the major element SI intensity is linear with composition or the major element composition among samples is constant.

References

1. I. Steele and I. Hutcheon, "Ion probe analysis of natural olivine: Secondary ion intensity variation and systematics for a simple binary silicate," *Microbeam Analysis-- 1979*, San Francisco: San Francisco Press, 1979, 338.

2. I. M. Steele, I. D. Hutcheon, and J. V. Smith, "Ion microprobe analysis of plagioclase feldspar for major, minor and trace elements," *Proc. 8th Int. Conf. X-ray Optics and Microanalysis*, Boston, Mass., 1977 (in press).

3. S. J. B. Reed, E. R. D. Scott, and J. V. P. Long, "Ion microprobe analysis of olivine in pallasite meteorites for nickel," *Earth Plan. Sci. Lett.* 43: 5-12, 1979.

EFFECT OF INCIDENT BEAM CONVERGENCE ON QUANTITATIVE ELECTRON ENERGY LOSS SPECTROSCOPY

D. C. Joy, D. M. Maher, and R. G. Farrow

High spatial resolution microanalysis by electron energy loss spectroscopy requires a focused, convergent incident electron beam. This convergence modifies the distribution of the inelastically scattered electrons, and consequently the efficiency with which these electrons can be collected given a particular acceptance angle β into the spectrometer. A correction to account for this effect is thus required if accurate quantitation is to be performed.

For a perfectly collimated incident beam of electrons with an energy E_0, the inelastically scattered electrons of energy loss E have a scattering distribution $I(E,\beta)$ at some scattering angle β given by

$$\frac{I(E,\beta)}{I(E,0)} = \frac{1}{\beta^2 + \theta_E^2} \tag{1}$$

where $\theta_E = E/2E_0$.[1] If the incident beam has a convergence semi-angle of α_0, then Eq. (1) takes the form

$$\frac{I(E,\beta)}{I(E,0)} = \int_0^{\alpha_0} \frac{I(\alpha)\alpha\,d\alpha}{(\beta - \alpha)^2 + \theta_E^2} \tag{2}$$

where $I(\alpha)$ represents the appropriately normalized distribution of intensity within the incident cone of illumination.[2] Figure 1 shows the form of the scattering distribution
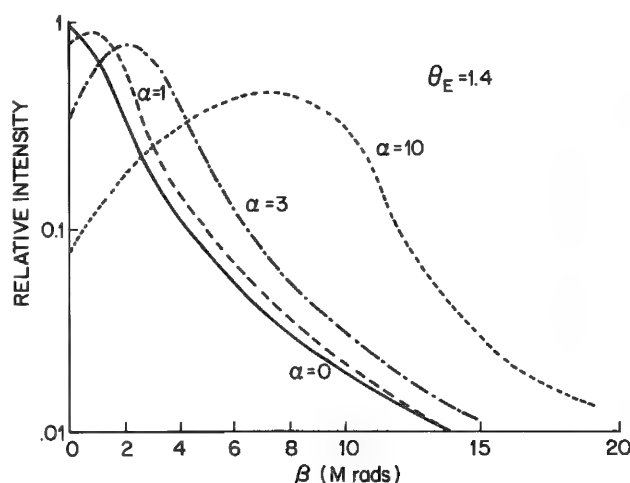

FIG. 1.--Relative scattering intensity distributions for α = 0, 1, 3, and 10 m.rad at θ_E = 1.4 m.rad.
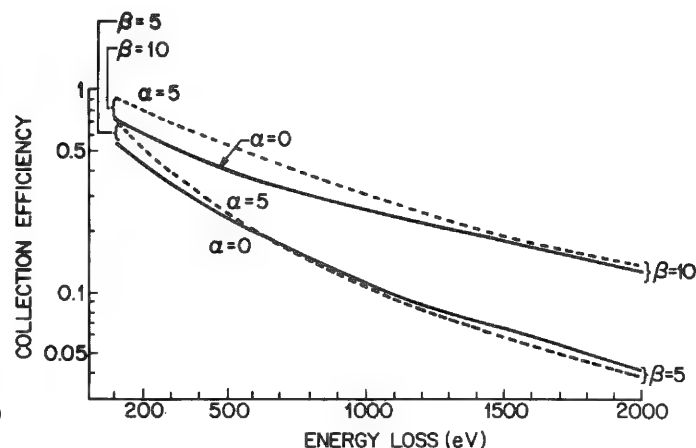
FIG. 2.--Comparison of collection efficiencies for electrons of varying energy loss assuming α_0 = 5 m.rad (dotted lines) and α_0 = 0 (solid lines) for β = 5 and 10 m.rad.

The authors are with Bell Laboratories, Murray Hill, NJ 07974.
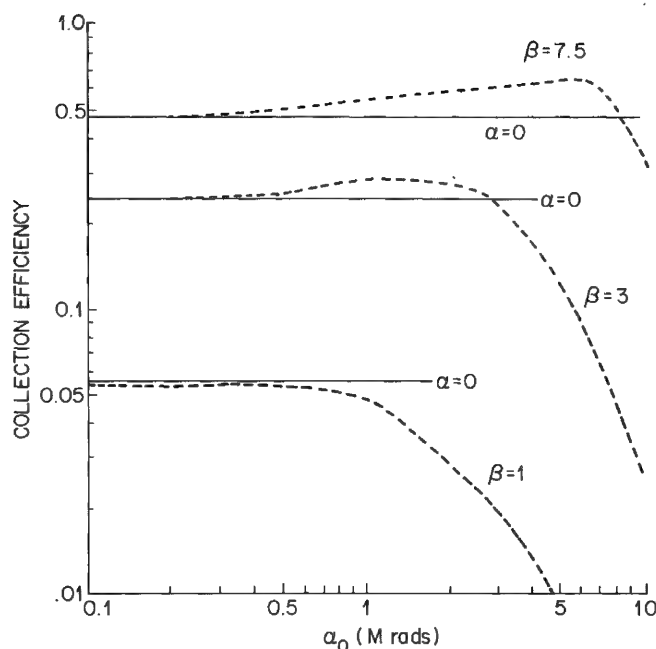
FIG. 3.--Collection efficiencies at $\alpha_0 = 0$ (solid lines) for $\beta = 5$ and 10 m.rad.
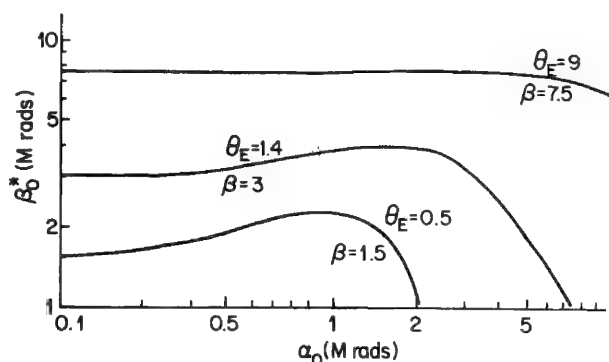
FIG. 4.--The effective collection aperture β_0^* as a function of α_0 for three typical operating situations.

for the case where $\theta_E = 1.4$ m.rad--the carbon K-edge (E = 284 eV) at $E_0 = 100$ keV--and $\alpha_0 = 0, 1, 3,$ and 10 m.rad calculated from numerical integration of Eq. (2). We assume that $I(\alpha)$ is constant for $\alpha \leq \alpha_0$, and zero for $\alpha > \alpha_0$, but the actual form of $I(\alpha)$ does not greatly affect the shape of $I(E,\beta)$. A comparison of the profiles with the $\alpha_0 = 0$ curve shows that the effect of the incident convergence is to broaden the angular distribution and to shift the direction of maximum scattering intensity away from $\beta = 0$.

The fraction $\eta_{\alpha,\beta}$ of the inelastically scattered electrons collected at energy loss E by a spectrometer accepting a semi-angle of β_0 is then

$$
\eta_{\alpha,\beta} = \frac{\displaystyle\int_0^{\beta_0}\int_0^{\alpha_0} \frac{I(\alpha)\alpha\beta d\alpha d\beta}{(\beta-\alpha)^2 + \theta_E^2}}{\displaystyle\int_0^{\theta}\int_0^{\alpha_0} \frac{I(\alpha)\alpha\beta d\alpha d\beta}{(\beta-\alpha)^2 + \theta_E^2}}
\tag{3}
$$

where θ is the maximum scattering angle. For the case $\alpha_0 = 0$, θ is taken to be $\sqrt{2\theta_E}$. Here, since the extremal incident ray is at an angle α_0 to the optic axis, θ must therefore be taken as $(\alpha_0 + \sqrt{2\theta_E})$. Equation (3) can again be rapidly evaluated by numerical integration, and Fig. 2 shows computed values of $\eta_{\alpha,\beta}$ plotted as a function of energy loss, at $E_0 = 100$ keV, for two cases: $\alpha_0 = \beta_0 = 5$ m.rad and $\alpha_0 = 5$, $\beta_0 = 10$ m.rad. For comparison the predicted collection efficiency $\eta_{0,\beta}$, for $\alpha_0 = 0$ is shown as dotted lines for $\beta_0 = 5$ and 10 m.rad; $\eta_{0,\beta}$ is calculated from Eq. (1) and an analogous form of Eq. (3), with $\theta = \sqrt{2\theta_E}$ to give

$$
\eta_{0,\beta} = \frac{\ln(1 + \beta^2/\theta_E^2)}{\ln(2/\theta_E)}
\tag{4}
$$

It is seen that for a range of values of energy loss (i.e., θ_E) the collection efficiency is actually higher than that predicted by the simple theory. That is more evident in Fig. 3, where we have plotted $\eta_{\alpha,\beta}$ as a function of α_0, assuming again $\theta_E = 1.4$ m.rads, for three values of β_0. For $\beta_0 = 1$ m.rad (i.e., $\beta_0 < \theta_E$), the efficiency is always less than that predicted for $\alpha = 0$, and falls rapidly for $\alpha_0 > \beta_0 = 3$ and 7.5 m.rad (i.e., $\beta_0 > \theta_E$), $\eta_{\alpha,\beta}$ rises to a peak as α_0 is increased, before falling once $\alpha_0 > \beta_0$. The effect of the convolution of the scattering and the convergence can thus be to "focus" more electrons into the spectrometer, under some conditions, than the simple theory would predict.

For the electron optical conditions most frequently used in a 100keV TEM/STEM system fitted with an energy analyzer, where $\alpha_0 \approx 0.5$-3 m.rad and $\beta_0 \approx 1$-5 m.rad, the "error" introduced by the beam convergence is seen to be quite small, typically only 30% at worst. For some fortuitous combinations of conditions the error can be essentially zero,

and thus in many cases a quantitation performed with convergent illumination but on the assumption that $\alpha_0 = 0$ gives acceptably accurate results. But for the purposes of accurate quantitation, under all operating conditions an effective angle of acceptance, β_0^* can be defined such that

$$\frac{\ln(1 + \beta_0^{*2}/\theta_E^2)}{\ln(2/\theta_E)} = \eta_{\alpha,\beta} \tag{4}$$

where $\eta_{\alpha,\beta}$ is calculated from Eq. (3). This effective aperture β_0^* can then be used in the calculation of the partial ionization cross sections required for quantitation.[3] Figure 4 plots values of β_0^* as a function of α_0 for three assumed sets of experimental conditions such as might be used to quantitate the beryllium K-edge ($E = 110$ eV, $E_0 = 100$ keV, $\beta_0 = 1.5$ m.rad), the carbon K-edge ($E = 284$ eV, $E_0 = 100$ keV, $\beta_0 = 3$ m.rad) and the silicon K-edge ($E = 1834$ eV, $E_0 = 100$ keV, $\beta_0 = 7.5$ m.rad). As expected for $\alpha_0 \to 0$, $\beta_0^* \to \beta_0^* \to \beta_0$, but particularly for small θ_E values, the deviation of β_0^* from β_0 can be substantial. The calculation of β_0^* can be incorporated directly into an interactive energy loss quantitation program such as SPECTRE.[4] With a PDP-11/03 computer the computation time is only 5-10 sec.

References

1. D. C. Joy, J. Hren, J. Goldstein, and D. Joy, Eds., *Introduction to Analytical Electron Microscopy,* New York: Plenum Press, 1979, 223.

2. See, for example, M. Isaacson, "All you wanted to know about ELS," *Proc. 11th Ann. SEM Symposium,* 1978, 1, 763.

3. D. C. Joy, R. F. Egerton, and D. M. Maher, "Progress in the quantitation of energy loss spectra," *Proc. 12th Ann. SEM Symposium,* 1979, 2, 817.

4. D. C. Joy, R. F. Egerton, D. M. Maher, and P. Mochel (to be published). Listings of SPECTRE are available from D. C. Joy.

MONTE CARLO SIMULATION APPROACH TO QUANTITATIVE ELECTRON MICROPROBE ANALYSIS OF TERNARY ALLOY THIN FILMS

Carl Pihl and Serge Cvikevich

In the quantitative electron microprobe analysis of multicomponent thin films, conventional ZAF correction techniques cannot be used when the mass thickness of the film to be analyzed becomes so small that the film can no longer be considered semi-infinite.

For the analysis of ternary alloy films we have used a Monte Carlo simulation approach developed by Kyser and Murata.[1,2] In our previous work we demonstrated the applicability of this Monte Carlo approach to quantitative analysis of binary Ti-W and Ta-W thin films.[3] The theoretical basis for the single-scattering Monte Carlo simulation approach to quantitative electron microprobe analysis is well documented in the above-mentioned references as well as in the proceedings of a workshop held at the National Bureau of Standards in October 1975.[4] Therefore, we will not repeat the detailed theoretical considerations that form both the physical basis of the Monte Carlo simulation of the electron scattering process and the physics of electron-solid interactions which lead to the generation of the x-ray fluorescence of interest.

The Kyser-Murata Monte Carlo simulation approach to quantitative electron microprobe analysis requires the generation of a database for the system in question. This database contains sets of simulated calibration curves of k ratio vs mass thickness obtained for a number of compositions chosen from the ternary system to be analyzed. In this Monte Carlo simulation approach, the k ratio for a particular element is the ratio of intensities, for the selected x-ray fluorescence line, emitted from a thin film compared to a pure semi-infinite standard. Experimentally obtained k ratios are used as input into the previously generated database. An iterative technique is then used to arrive at a unique solution that is a composition triplet in the database for which the three experimental k ratios lead to the same value of mass thickness.

Experimental Samples

Two sets of thin films were prepared for analysis by Monte Carlo simulation. The first set consisted of three compositions from the Au-Pd-Cu ternary system, and the second set was represented by two compositions from the Pt-W-Cr ternary. The Au-Pd-Cu films were prepared by vapor deposition of pure Cu, Pd, and Au films deposited in sequence on a silicon substrate covered by a 1000Å film of thermal oxide. The film thickness of each individual layer was measured by double-beam interferometry after each deposition. The ternary films were obtained by homogenization for 1 hr at 600°C in a double-jacketed helium furnace. Quantitative nuclear backscattering analysis was performed on these films before and after homogenization. Films representing each of the three compositions were prepared in thicknesses of approximately 300 and 2000Å. The Pt-W-Cr films were prepared by sputtering from an alloy target. Again, films of two thicknesses (approximately 300 and 1500 Å) were prepared for each of the two compositions. These films were also quantitatively analyzed by nuclear backscattering.

Data Analysis

This work is an extension of previous studies which have been limited to binary systems.[3] Several stages of iteration and interpolation are used in the data analysis procedure.

Initially the objective is to generate by simulation a number of sets of theoretical calibration curves of k ratio vs mass thickness ρt. Each curve in the set corresponds to

an appropriate element concentration in the chosen composition. For each element standard, the simulation procedure generates x-ray intensity and absorption corrections, which are combined with corresponding values, for each element, obtained from a thin-film simulation for a range of ρt values. The k ratio calibration curves are obtained from these calculations. The simulation assumes that all elements in the thin film are known, and thus the sum of weight fractions is equal to 1. Following a prior strategy, initial stages of simulation use only 100 electron trajectories for each composition.[3] Figure 1 shows a set of curves generated for the ternary composition containing 0.3 copper, 0.3 paladium and 0.4 gold (weight fraction). A range of composition sets may be chosen so as to survey the entire ternary system and are stored as a data base for continued use. The analysis of a given thin-film system requires experimentally measured k ratios for input. Table 1 shows the analysis procedure in terms of sample input data for the ternary Cu-Pd-Au. A set of measured k ratios is used to scan each composition set in the previously stored data base. This results in a set of calculated ρt values for each composition set. These values are computed by interpolation (or extrapolation) of the simulated data based on the input k ratios. A mean ρt and standard deviation of the mean (least square fit) are computed for each set. The unique solution of film thickness and composition to satisfy the measured k ratios occurs when all ρt values are equal. In practice, the initial estimate of the composition is taken for the set having the lowest standard deviation. In this example the initial estimate is 0.3, 0.3 and 0.4 weight fractions for Cu-Pd-Au (Fig. 1). Refinements are also shown in Table 1, where intermediate compositions are simulated and compared to the input k ratios. Final refinements of composition are done with simulations using a larger number (1000 or more) of electron trajectories. Figure 2 shows an example of a refinement using 1000 electron trajectories.

TABLE 1.--Example of data base scan for one set of measured k ratios. (*Refined compositions not in original data base; **refinement based on 1000 electron trajectories.)

Calculated ρt			$\overline{\rho t}$	σ	Composition (Weight Fraction)		
Cu	Pd	Au			Cu	Pd	Au
0.099	0.329	2.465	0.964	0.753	0.600	0.300	0.100
0.096	1.632	0.417	0.715	0.467	0.600	0.100	0.300
.	.	.	.	.	.	.	.
.	.	.	.	.	.	.	.
.	.	.	.	.	.	.	.
.	.	.	.	.	.	.	.
0.198	0.241	0.306	0.249	0.031	0.318	0.348	0.334*
0.242	0.368	0.239	0.283	0.042	0.300	0.300	0.400
0.242	0.233	0.265	0.246	0.009	0.295	0.350	0.355*
0.266	0.255	0.257	0.260	0.003	0.295	0.350	0.355**
0.314	0.244	0.281	0.280	0.020	0.282	0.356	0.362*
.	.	.	.	.	.	.	.
.	.	.	.	.	.	.	.
.	.	.	.	.	.	.	.
.	.	.	.	.	.	.	.
0.654	0.160	0.366	0.393	0.143	0.200	0.500	0.300
6.358	0.122	0.371	2.284	2.038	0.100	0.600	0.300
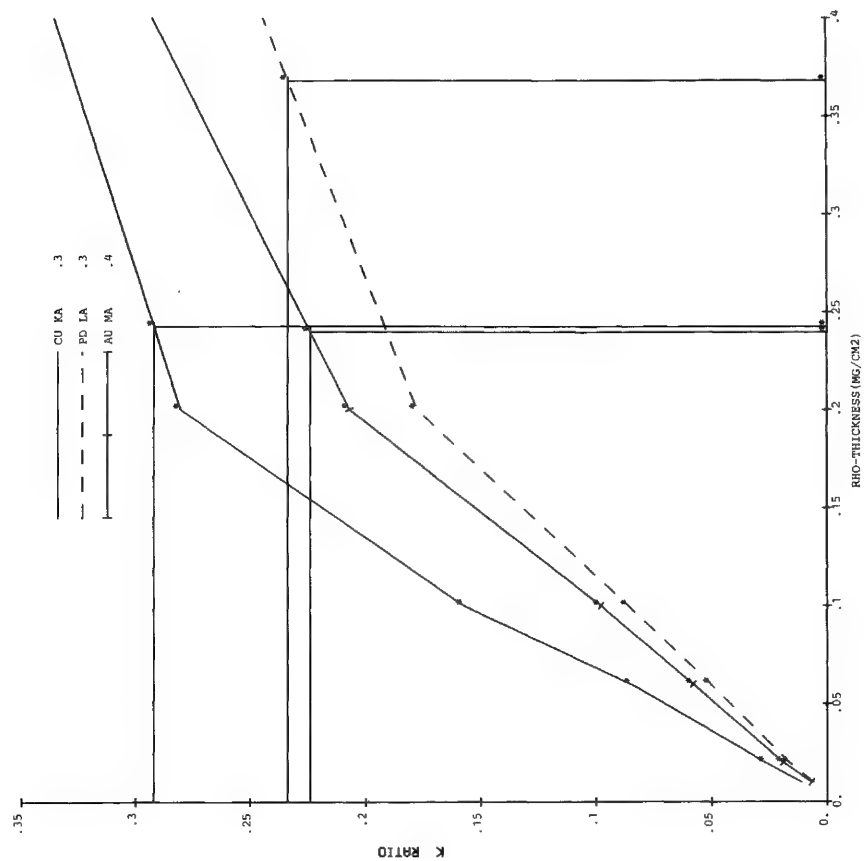
FIG. 1.--Simulated k ratio vs mass thickness for Cu, Pd, and Au, based on 100 electron trajectories. Example of initial estimate of composition, based on measured k ratios.
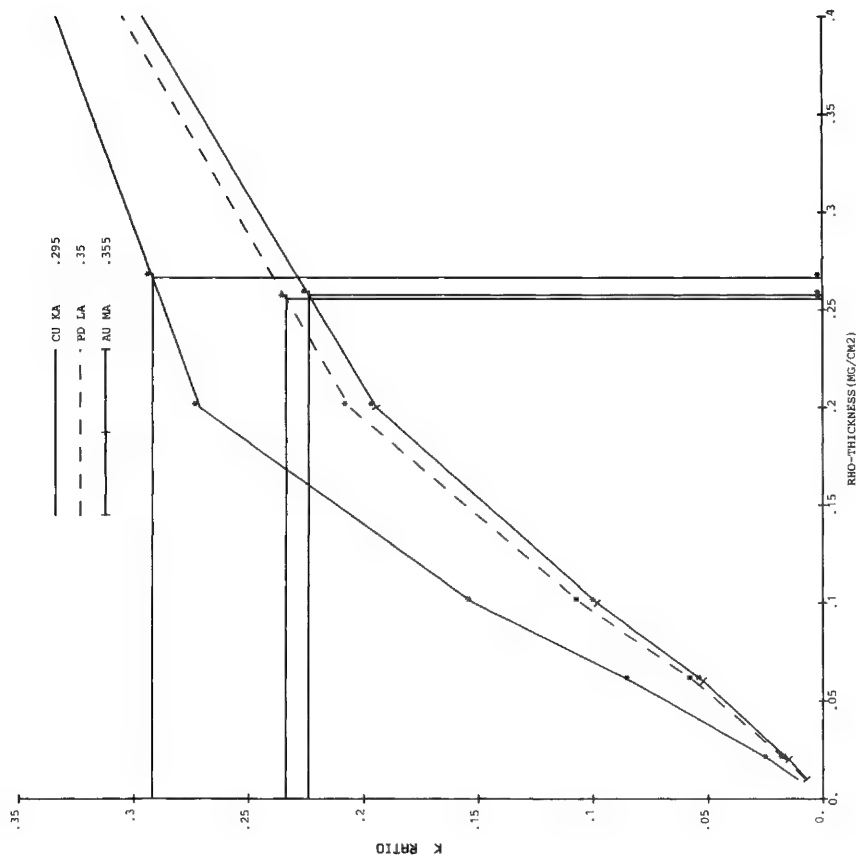
FIG. 2.--Simulated k ratio vs mass thickness for Cu, Pd, and Au, based on 1000 electron trajectories. Example of refinement in composition analysis based on measured k ratios.

159

Summary

The above procedure gives a rapid and economical initial estimate of the composition of films containing multiple elements. The data base remains available for future work and is valuable where little is known about a given sample. Any refinement is made using a limited range of compositions centered around the initial estimate combined with a larger number of electron trajectories.

At present the k ratio simulation is done using an IBM System/370 model 168 computer. Computing costs are directly related to the number of electron trajectories used. The traditional high cost of Monte Carlo simulation is significantly reduced by the ability to make survey scans of a data base prepared by the use of a moderate number of electron trajectories.

References

1. D. F. Kyser and K. Murata, "Quantitative electron microprobe analysis of thin films with Monte Carlo calculations," *Proc. 8th MAS Conf.*, 1973, 28.

2. D. F. Kyser and K. Murata, "Quantitative electron microprobe analysis of thin films on substrates," *IBM J. Res. and Dev.* 18: 352, 1974.

3. S. Cvikevich and C. Pihl, "Application of the Monte Carlo simulation to quantitative electron microprobe analysis of refractory thin films," *Proc. 12th MAS Conf.* 1977, 116.

4. K. F. J. Heinrich, D. E. Newbury, and H. Yakowitz, Eds., *Use of Monte Carlo Calculations in Electron Probe Microanalysis and Scanning Electron Microscopy*, NBS Special Pub. 460, 1976.

A STUDY OF TYPE-II MAGNETIC CONTRAST BY MONTE CARLO SIMULATION

Takashi Ikuta, Eizi Sugata, and Ryuichi Shimizu

Type II magnetic contrast was first observed by Philibert and Tixier.[1] At present it is well confirmed by both experiment and theory that this contrast results from the alteration of electron trajectories in magnetic domains of opposite magnetization. As shown in Fig. 1, the alteration of the trajectory due to the action of the Lorentz force results in the change of the backscattering yield corresponding to the individual domain in the sample. A typical observation of the magnetic domains in Fe-3%Si single crystal samples is shown in Fig. 2.

$$\vec{F} = -\frac{e}{c}(\vec{v} \times \vec{B})$$
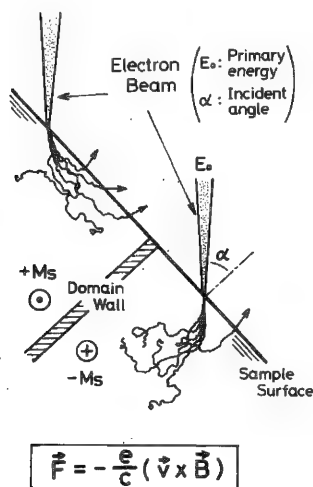
FIG. 1.--Schematic illustration of trajectories of incident electrons around 180° magnetic domain wall. Ms is saturation magnetization in the domain.
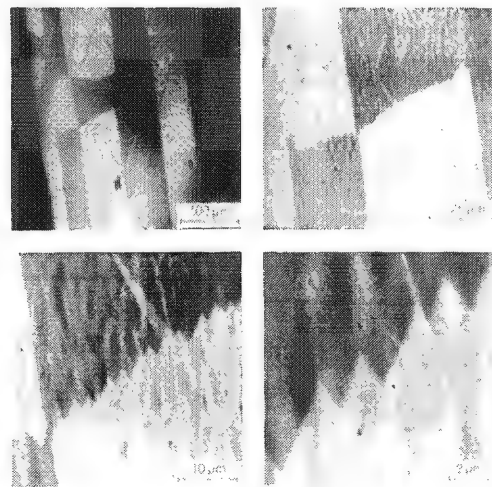
FIG. 2.--Example of observed zig-zag magnetic domains in Fe-3%Si single crystal sample in different magnifications at zero bias field. Incident angle α and incident energy E_0 of the electron beam are 60° and 45 keV, respectively.

The quantitative analysis of this type magnetic contrast has been successfully achieved by several workers using Monte Carlo simulation for both the magnitude of the contrast and its dependence on the incident energy of the electron beam.[2,3] However, it seems that a more detailed analysis, especially with the resolution of this contrast, has not been well established so far.

The present paper describes the result of the Monte Carlo simulation for both the magnitude and the resolution of Type II magnetic contrast. In addition to this result an analysis of the magnetic domain wall image that is observed under the condition of the disappearance for the normal domain contrast is also described.

Monte Carlo Simulation

In the present simulation, the single-scattering approach and continuous slowing down approximation (Bethe's energy-loss formula) are used. The procedure of this simulation is almost the same as those described in the previous paper except for an additional pro-

Authors Ikuta and Sugata are with the Department of Applied Electronic Engineering, Osaka Electro-Communication University, Neyagawa, Osaka, Japan; Shimizu is with the Department of Applied Physics, Osaka University, Suita, Osaka 572, Japan.

gram for the contribution of the Lorentz force.[4] The contribution of the Lorentz force,
$F = -(e/c)(v \times B)$, where v is the velocity of the electron and B is the magnetic flux
density, can be easily taken into consideration as exchanging the original free straight
flight of the electron by the arc in the computer program. The width of the magnetic do-
main boundary (domain wall) is neglected since the width is usually less than 1000 Å.
The magnetic flux density B is given $4\pi Ms$ (where Ms is the saturation magnetization of
the sample) for flux closure domains which are usually formed in the magnetic materials
of cubic anisotropy.

The simulation has been applied for an Fe sample ($4\pi Ms$ = 21 600 G, cubic anisotropy)
when the incident beam angle (which is defined as the angle between the beam and the
sample normal) is $\alpha = 60°$.

Results and Discussions

To obtain the resolution of the magnetic domain contrast, the position of the inci-
dent beam was altered around the domain boundary (180° domain wall) in the simulation.
In Fig. 3(a) and (b), the results of the simulation are shown at the incident beam energy
of 45 and 30 keV, respectively. From these figures, an asymmetrical relation between the
contrast and the beam position is found: the point of neutrality in contrast is not the
position of the 180° domain wall. It is also concluded that the resolution of Type II
magnetic domain contrast is decreased with the increase of the incident beam energy,
whereas the profile of each resolution curve is almost the same expect for the scales in
both the magnitude of the contrast and the beam position.
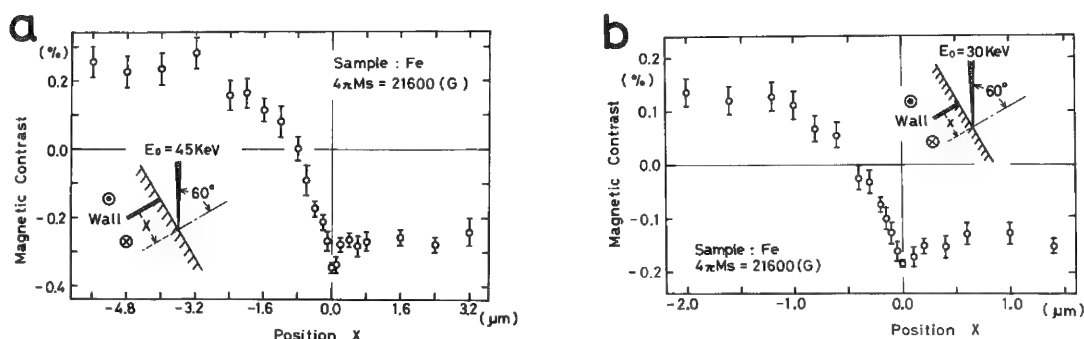
FIG. 3.--Magnetic domain contrast as function of beam position: (a) beam energy of 45 keV;
(b) 30 keV. 180° domain wall is assumed.

As to the backscattered electron image, it is well known that the resolution is
fairly improved by detection of low-loss electrons or forward-scattering electrons as
a signal. According to the similarity of the signal detection, improvement of the reso-
lution is also expected for the Type II magnetic contrast. For this expectation, magnet-
ic contrast due to the backscattered electrons has been also simulated under the condi-
tion of selected angle detection. These results are shown in Fig. 4 at a beam energy of
30 keV. These figures clearly show that the resolution of the Type II magnetic contrast
is improved by detection of the forward-scattering electrons, as well as for the back-
scattered electron image.

On the basis of the theoretical treatment, it is clear that the disappearance of the
magnetic-domain contrast takes place when the magnetization in the domain becomes paral-
lel to the plane of incidence. In this case, however, another magnetic contrast of black
or white line shape can be observed just on the 180° domain walls.[5] The origin of this
magnetic domain wall contrast is considered to be the deflection of the drifted electrons
on either side of the 180° domain wall. When the incident point of the electron beam is
positioned on the 180° domain wall, we can expect that increasing or decreasing of the
backscattering yield will depend on the direction of opposite magnetization in each do-
main on either side of the 180° domain wall. The analysis of this domain wall contrast
is also achieved by use of the present simulation. In Fig. 5(a), the results for both
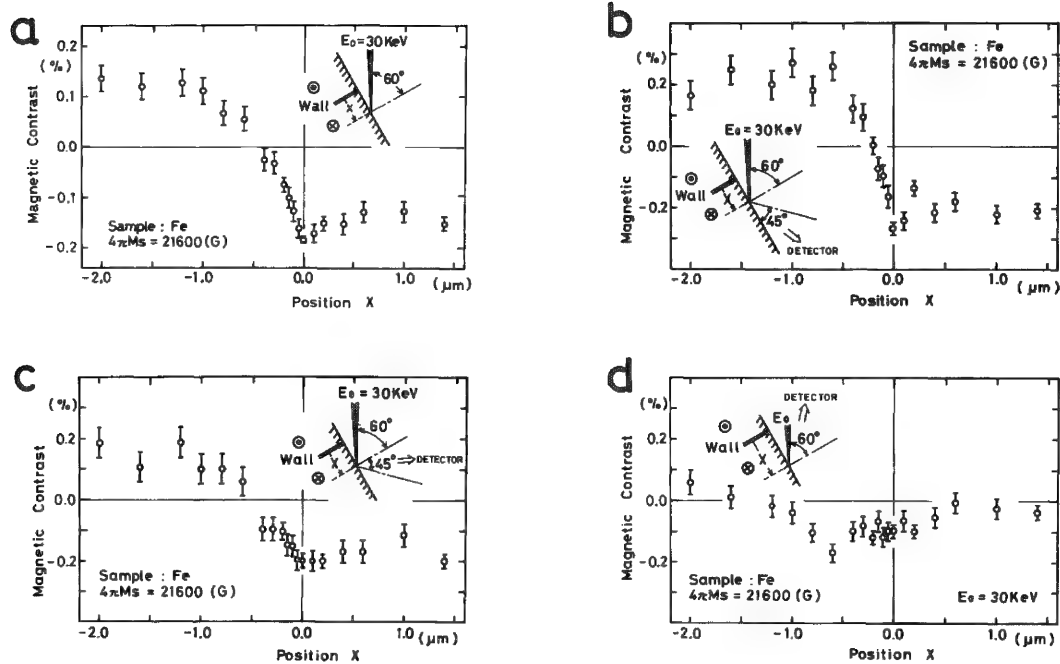
FIG. 4.--Magnetic domain contrast as function of beam position at beam energy of 30 keV: (a) full angle detection; (b)-(d): selected angle detection for backscattered electrons.

the magnitude and the resolution of the wall contrast are shown. In addition to these results, wall contrast under the selected angle detection of the backscattered electron is also shown in Fig. 5(b)-(d). Not only the normal magnetic contrast, but the resolution of the domain wall contrast is improved by detection of forward scattering electrons. It is however concluded that the magnitude of the domain wall contrast due to the backward-scattering electrons is comparable to that due to the forward-scattering electrons, which is not true for the normal magnetic domain contrast.
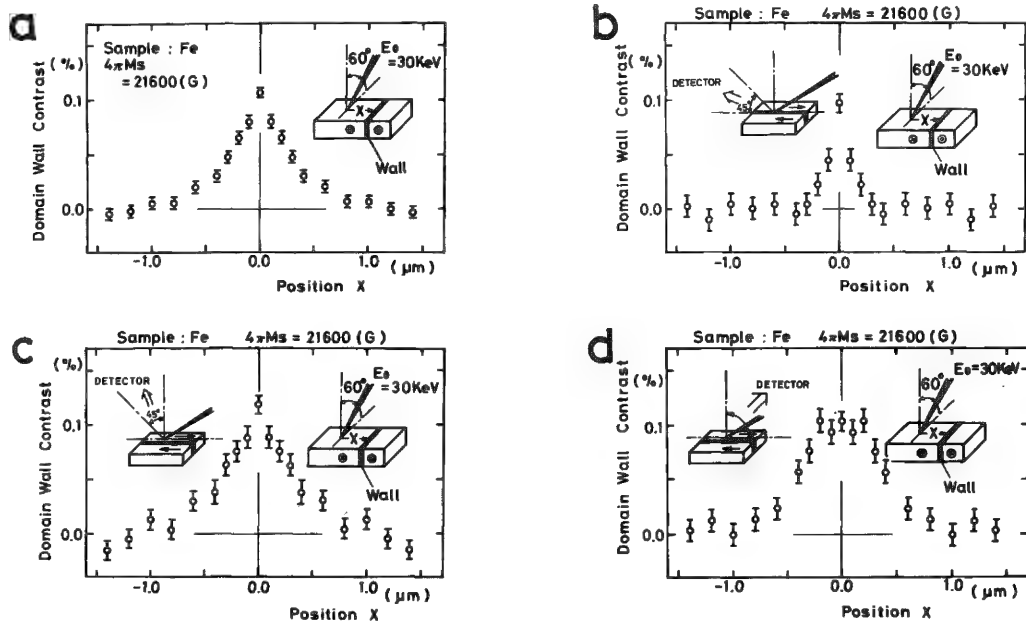
FIG. 5.--Magnetic domain wall contrast as function of beam position at beam energy of 30 keV: (a) full angle detection; (b)-(d) selected angle detection for backscattered electron.

163

References

1. J. Philibert and R. Tixier, "Effects of crystal contrast in scanning electron microscopy" (in French), *Micron* 1: 174, 1969.

2. D. E. Newbury et al., "Monte Carlo calculations of magnetic contrast from cubic materials in the scanning electron microscope," *Appl. Phys. Lett.* 23: 488, 1973.

3. T. Ikuta and R. Shimizu, "Magnetic domain contrast from ferromagnetic materials in the scanning electron microscope," *Phys. Stat. Sol. (a)* 23: 605, 1974.

4. R. Shimizu et al., "High contrast observation of magnetic domain with high voltage SEM," *Japan J. Appl. Phys.* 15: 967, 1976.

5. T. Yamamoto and K. Tsuno, "Unusual magnetic contrast of domain images obtained in the reflective mode of scanning electron microscopy," *Phil. Mag.* 34: 479, 1976.

AN INDIRECT METHOD FOR DETERMINING MASS THICKNESS FOR ABSORPTION CORRECTIONS IN THE MICROANALYSIS OF THIN FOILS

P. J. Statham and M. D. Ball

If intensities I_A and I_B are observed for the characteristic x rays of elements A and B, then for many thin specimens the concentrations of these elements can be determined by the simple intensity ratio technique described by Cliff and Lorimer[1]:

$$\frac{C_A}{C_B} = k_{AB} \frac{I_A}{I_B} \tag{1}$$

where the "k-factor" k_{AB} is a constant for the particular x-ray lines from elements A and B. However, for certain specimens, preferential absorption within the thin-film matrix alters intensity ratios so an absorption correction is necessary. At the accelerat-voltages used for transmission microscopy, there is very little loss of energy for electrons passing through the foil and it is usually a good approximation to assume that the ionization distribution is uniform throughout the thickness of the specimen. If the top and bottom surfaces are parallel then the observed intensity for an x-ray peak is given by

$$I_A' = I_A \frac{1 - \exp(-\mu_A \rho t \operatorname{cosec} \psi)}{\mu_A \rho t \operatorname{cosec} \psi} \tag{2}$$

where $\mu_A (\mathrm{cm}^2 \mathrm{g}^{-1})$ is the mass absorption coefficient of the specimen for x rays from element A, $\rho (\mathrm{g\text{-}cm}^{-3})$ is the specimen density, $t(\mathrm{cm})$ the thickness, and ψ is the take-off angle for x rays. The correction of I_A' to obtain I_A for use in Eq. (1) assumes a knowledge of ρ, t, and ψ, as well as specimen composition. Although ψ can be measured and successive estimates of composition improved by iteration, there are distinct problems in determining the mass thickness ρt. The density of the specimen can be estimated from the known density of a similar specimen but direct measurement of specimen thickness poses some problems[2] and, if nothing else, is a tedious procedure. Thus, it is desirable to have an indirect method which enables ρt to be determined from x-ray intensity values. One of the advantages of working with intensity ratios is insensitivity to beam-current variations; if this advantage is to be retained one cannot use methods that rely on absolute measurements of either characteristic line[2] or x-ray continuum intensity.[3] Two intensity-ratio methods have been briefly described by Morris et al.[4] The first uses the observed ratio of K to L intensity for a given element to deduce the absorption path length and is suitable provided both peaks are visible in the spectrum (usually for atomic numbers > 27). The second is more general but requires spectra to be acquired at different tilt angles. This "multigeometry" approach will now be described in detail.

The Multigeometry Method

When a specimen is tilted, the generated intensity I_A varies in proportion to sec θ, where θ is the angle of tilt; and the absorption correction alters because of the change in x-ray take-off-angle ψ (Eq. 2). If beam current is controllable then the product $\mu_A \rho t$ can be determined by observation of I_A' at different geometries; for example, a first-order expansion of Eq. (2) suggests that $\mu_A \rho t$ can be calculated from a plot of $(I_A'/\sec \theta)$ v cosec ψ. As mentioned above, it is more convenient if beam-current control is not required; and if μ_A and μ_B are known then it should be possible to deduce ρt from the variation in the

---

Author Statham is employed at Link Systems Limited, Halifax Road, High Wycombe, Bucks., England HP12 3SE; author Ball, at Alcan Laboratories Limited, Southam Road, Banbury, Oxon., England.

ratio I_A'/I_B' for various geometries. A more general approach considers the effect of absorption on all the elemental peaks simultaneously; if the correct choice is made for a value of ρt, then the normalized set of concentrations obtained from Eqs. (1) and (2) should be the same at all tilt angles.

The multigeometry technique can now be formalized as follows. First, consider the sum

$$X_m^2 = \sum_{i=1}^{NSP} (C_{mi} - \overline{C}_m)^2/\sigma_m^2 \tag{3}$$

where C_{mi} is corrected concentration for element m, $\overline{C}_m$ is the average corrected concentration for NSP spectra obtained at various geometries, and σ_m is the standard deviation expected from spectrum counting statistics. A good choice for ρt would give an absorption correction that tends to minimize X_m^2. When all NEL elements are considered, the problem reduces to finding that value of ρt which, when used in an absorption correction, minimizes the sum

$$X^2 = \sum_{m=1}^{NEL} X_m^2 \tag{4}$$

From an initial estimate of ρt, several methods could be used to search for the minimum X^2; in this work, a simple stepwise search was used, where the step size was halved at each reversal of the search direction.

X^2 should approximately follow a "chi-square" distribution with η_d = NSP.NEL - NSP - NEL degrees of freedom. Thus X^2/η_d should take values distributed about 1.0. The change in ρt which causes X^2/η_d to increase by 1 from its minimum value can be interpreted as the likely statistical error in ρt.[5] If absorption is severe, the X^2 surface is steep-walled with a well-defined minimum and yields a small relative error in ρt. If absorption is slight, spectra obtained at different geometries differ by very little, so that ρt is imprecise; however, it is the absorption correction that is of prime concern and inaccuracies in ρt are irrelevant if absorption is negligible.

When one is acquiring spectra, the aim is to choose geometries which give the widest variation in absorption path length. When only two elements are present at least three spectra have to be recorded to obtain a statistical estimate of ρt. Acquisition of more spectra helps in averaging out any inaccuracies in measurements of specimen geometry, and statistical accuracy is always improved if more counts are recorded; a reasonable procedure is to record three spectra with equal counting times at geometries that give approximately equal steps in absorption path length.

Experimental Results

Results were obtained with a JEOL TEMSCAN 120C, modified to reduce the "hole count" to an insignificant level. Spectra were recorded with a LINK SYSTEMS 860 analyzer incorporating a LINK 2010 pulse processor and KEVEX detector. At each specimen point, three spectra were acquired, each containing between 50K and 200K counts in the 0-20keV energy region. Since the tilt direction was not in the same plane as the x-ray detector, we calculated ψ (Eq. 1), taking into account detector azimuth (α, measured at 47.97°), elevation (E, zero for this instrument), and tilt angle Θ, from the formula

$$\mathrm{cosec}\ \psi = \frac{1}{\sin \Theta \cos \alpha \cos E + \cos \Theta \sin E} \tag{5}$$

Absorption coefficients tabulated by Heinrich[6] were used and k_{AB} values were derived from empirical results obtained by Morris[7] and Cliff and Lorimer[1]; note that the "k factors" referred to in Tables 1 and 2 apply to the sum of $K\alpha$ and $K\beta$ peak areas.

The specimens were prepared from alloys of aluminum and certain heavier metals and contained several large intermetallic constituents. Those selected for microanalysis

were about 10 μm or larger and extended through the thickness of the foil. All samples were jet-electropolished at room temperature in a mixture of 70% perchloric acid, 20% ethanol, and 10% glycerol. (Although the Fe-Al was freshly prepared, the Zr and Ti samples were stored for more than a month before they were analyzed.) In such materials, the absorption of AlK radiation is significant in all but the thinnest of regions, which is reflected in the difference between the results obtained with a simple "k-factor" correction and the results obtained with a correction including absorption effects (Tables 1 and 2).

TABLE 1.--Results for thin Fe/Al specimen with k_{AlSi} = 1.29, k_{FeSi} = 1.18. Composition of $FeAl_3$ is 59.2 wt.% Al, 40.8 wt.% Fe. Tilts of 20°, 30°, and 40° were used for each point.

	Apparent Composition (30° tilt) No absorp. correction %	Absorption corrected composition %	Calculated mass thickness at zero tilt $(x10^{-7}g - cm^{-2})$
Point 1	Al 59.88 Fe 40.12	Al 59.81 Fe 40.19	0 ± 20
Point 2	Al 56.72 Fe 43.28	Al 59.21 Fe 40.80	390 ± 70
Point 3	Al 48.34 Fe 51.55	Al 56.40 Fe 43.60	1280 ± 50

TABLE 2.--Results for thin Zr/Al specimen with k_{AlSi} = 1.29, k_{ZrSi} = 3.114 (ZrK lines used). Composition of $ZrAl_3$ is 47.01 wt.% Al, 52.99 wt.% Zr. For point 1, tilts of 25°, 35°, and 45° were used; for point 2, 35°, 40°, and 50°.

	Apparent Composition (35° tilt) No absorp. correction %	Absorption corrected composition %	Calculated mass thickness at zero tilt $(x10^{-7}g - cm^{-2})$
Point 1	Al 37.00 Zr 63.00	Al 46.48 Zr 53.52	2400 ± 700
Point 2	Al 38.42 Zr 61.58	Al 47.97 Zr 52.03	2800 ± 700

The standard mounting in the TEMSCAN 120C traps the specimen between two blocks of carbon which tend to cause obstruction; the electron beam may be prevented from reaching the specimen at high tilt angles and the emitted x-rays may be prevented from reaching the detector at low tilt angles. The Fe-Al results in Table 1 were therefore obtained from a specimen fixed to the top surface of a single drilled carbon support block. However, it is inconvenient to have to stick the specimen on the block; in this position the geometry may not be well defined. The Zr-Al results in Table 2 were obtained with the specimen firmly clamped in the standard holder; in this case, a range of tilts from 25° to 45° could be used if specimen points were chosen well away from the edge of the sample.

For the Fe-Al results, tilts from 20° to 40° gave a variation in cosec ψ from 4.37 to 2.32. As shown in Table 1, the corrected composition in the first two cases is close to that calculated from the formula $FeAl_3$, which is the expected composition for these intermetallics. Even in the third case, on a thicker region of the specimen, the predicted composition is considerably closer to the expected result than is that calculated without an absorption correction. In Table 2, the Zr-Al results display a similar degree of success despite a large absorption correction for AlK x rays. However, experiments on a Ti-Al alloy specimen were not nearly so successful: the multigeometry method repeatedly predicted aluminium concentrations which were much higher than the 62.7% expected from the formulae $TiAl_3$ and even when, in one case, the thickness was measured at 0.35 μm by parallax of contamination spots, a conventional absorption correction predicted 68.1% Al (with k_{AlSi} = 1.29, k_{TiAl} = 1.03). The observation of a substantial increase in the Al/Ti intensity ratio in very thin regions of this specimen does suggest some chemical inhomogeneity but at the time of writing, we have not fully resolved these discrepancies.

Conclusion

The results indicate that for normal specimen thicknesses ($< 10^{-4}$ g-cm^{-2}) a good absorption correction is achieved by the "multigeometry" method and even in very thick regions, results still approach the true composition. The major source of error lies in accurate determination of sample geometry. Even if the specimen stage permits the sample to be mounted and tilted to a known degree, the sample itself may be buckled so that the holder position does not reflect the true surface tilt. Furthermore, the specimen may be wedge-shaped in section and consequently the variation in absorption path length with tilt differs from that calculated for plane-parallel surfaces. However, these problems are identical to those faced when specimen thickness is determined by measurement of parallax between contamination spots; and the present method has the advantage that sample density ρ need not be known.

References

1. G. Cliff and G. W. Lorimer, "The quantitative analysis of thin specimens," *J. Microscopy* 103: 203-207, 1975.
2. G. Love, M. G. C. Cox, and V. D. Scott, in D. L. Misell, Ed., "Foil thickness measurement in transmission electron microscopy," *Proc. EMAG 1977*, London: Inst. Phys. Conf. Ser. No. 36, 1977, 347-350.
3. B. L. Gupta, T. A. Hall, and R. B. Moreton, "Electron probe x-ray microanalysis" in *Transport of Ions and Water in Animals*, London: Academic Press, 1977, 83-143.
4. P. L. Morris, M. D. Ball, and P. J. Statham, "The correction of thin foil microanalysis data for X-ray absorption effects," *Proc. EMAG 1977*, London: Inst. Phys. Conf. Ser. No. 52, 1980, 413-416.
5. P. R. Bevington, "Data reduction and error analysis for the physical sciences," New York: McGraw-Hill, 1969, chap. 11.
6. K. F. J. Heinrich, "X-ray absorption uncertainty," in *The Electron Microprobe*, New York: Wiley, 1966, 296-377.
7. P. L. Morris, "Quantitative thin-foil x-ray analysis of inorganic materials," Alcan Laboratories Technical File R-79/24, 1979.

APPLICATION OF ANALYTICAL ELECTRON MICROSCOPY TO THE STUDY OF INTERGRANULAR CORROSION IN 304 STAINLESS STEEL

C. S. Pande and R. L. Sabatini

The technique of analytical electron microscopy in a scanning transmission electron microscope fitted with an energy-dispersive X-ray spectrometer is used to measure the chromium depletion in sensitized 304 stainless steel *along* the grain boundaries. It is shown that such measurements could be misleading unless care is taken to choose the regions on the grain boundaries properly for such analysis.

Intergranular corrosion in sensitized stainless steel is supposed to be caused by the precipitation of chromium iron carbide $[(Fe,Cr)_{23}C_6]$ at the grain boundaries, with a concomitant depletion of chromium in and around the grain boundaries, to the levels below that required for protection against corrosion.[1,2] With the advent of the analytical electron microscope the first direct evidence in support of this theory was obtained by Pande et al.,[3] and independently by Rao and Lifshin.[4] These authors measured the chromium concentration *across* the grain boundary, and showed that the chromium concentration dropped drastically adjacent to grain boundaries in sensitized specimens. The results reported in this paper refer to measurements made *along* and adjacent to grain boundaries instead of across them.

Experimental Set-up

The experiments were performed on a JEOL 100C electron microscope with scanning and energy-dispersive attachments. When the scanning electron beam was made stationary it acted as an electron probe and the x rays generated were detected by an NSI Si(Li) detector mounted on the electron microscope column. In order to improve the spatial resolution and yet obtain sufficient counts, it was necessary to optimize various parameters, such as the accelerating voltage of the electrons (120 kV), the detector area (30 mm^2), the beam size (about 30Å), a constant counting time (30 sec), and specimen tilt of 40°. For further details see Refs. 3 and 5.

The following three improvements on the previous procedure[3] were introduced. (1) The beam size was reduced to the smallest possible in our instrument for a 250µm condenser aperture. The reason for this step was the following. It has been noted previously[3] that the depleted zone along the grain boundaries is only of the order of 1000 Å. Therefore, it is critical that the spatial resolution of the measurement be as good as possible. The spatial resolution could be of course improved by a reduction in specimen thickness. However, it was found that in specimens less than 1000 Å thick, the Fe/Cr concentration ratio is a function of specimen thickness even when no such variation exists in the bulk.[5] The only other alternative for improving the spatial resolution is to reduce the beam size. In our experiments the beam size was about 30 Å; according to Romig and Goldstein[6] that would give us a spatial resolution of 220-380 Å for foils of thickness 1000-1500 Å. (2) The spurious copper peak was virtually eliminated in the 304 stainless steel spectra by use of a modified graphite-holder and an aperture over the specimen stage. This modification is important because it is known that the spurious copper signal enhances the chromium and iron peaks of the stainless steel spectra by fluorescence.[7] (3) Specimen drift was minimized by the use of the modified graphite holder in which the specimen is clamped by screws, instead of being held together only by friction.

Results

Figure 1 shows the grain boundary in a 304 stainless steel specimen used for analysis. The specimen has been 'sensitized' by being heated at 600°C for 24 hr. The measured concentrations of chromium, iron, and nickel for the various points indicated in
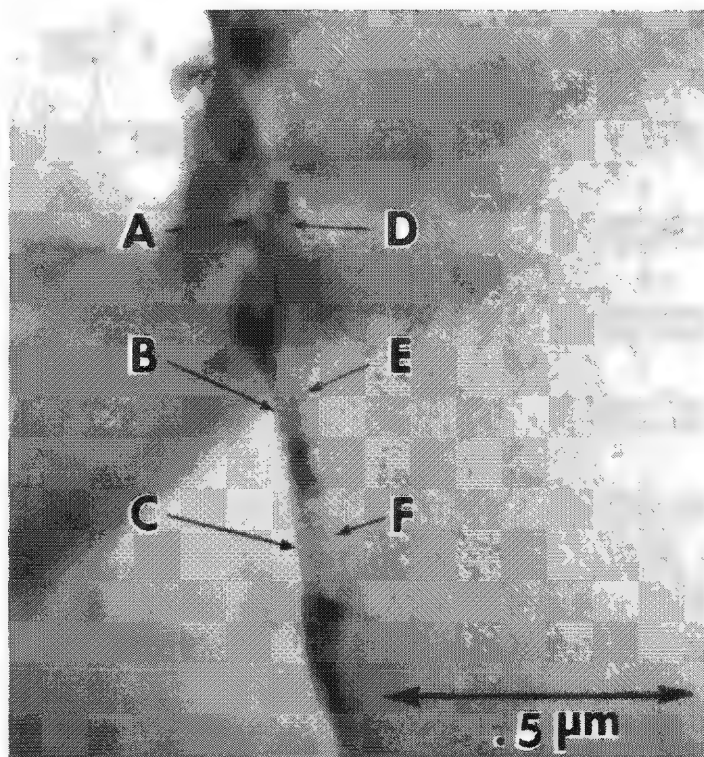
FIG. 1.--Scanning transmission electron micrograph showing precipitates along grain boundary in sensitized type 304 stainless steel specimen. Letters indicate various points of analysis along grain boundary (Table 1).

FIG. 2.--Transmission electron micrograph of the same area as in Fig. 1 with grain boundary tilted 45° along an axis parallel to grain boundary direction. Contamination marks indicate regions that were analyzed.

Fig. 1 are given in Table 1. The concentrations have been measured both for points on and adjacent to the grain boundary (about 300 Å from the grain boundary). A point on or adjacent to the grain boundary may or may not show a depletion in chromium. The reason for this result becomes clear when the grain boundary is tilted 45° along an axis parallel to the grain boundary direction (Fig. 2). It can be seen that some of the measured regions may have in part overlapped the precipitates on the boundary, especially where the number of such precipitates per unit grain boundary area is relatively high. In such cases, although the depletion of Cr near these precipitates may even be higher, the actual measurements may not reveal such a depletion. Table 2 shows results of the concentration measurements along the grain boundary in another 'sensitized' specimen at the points shown in Fig. 3. The Cr value never falls below 15%, as compared with the 14% measured in the previous grain boundary, although the number of precipitates is higher. In some cases the Cr values measured along the grain boundary are higher than those in the matrix, which shows that the analyzed region contains a precipitate.

A careful selection of the areas of analysis is therefore necessary before such results may be used to interpret a chromium depletion as a function of the angle of misorientation, or the heat treatment in this material.
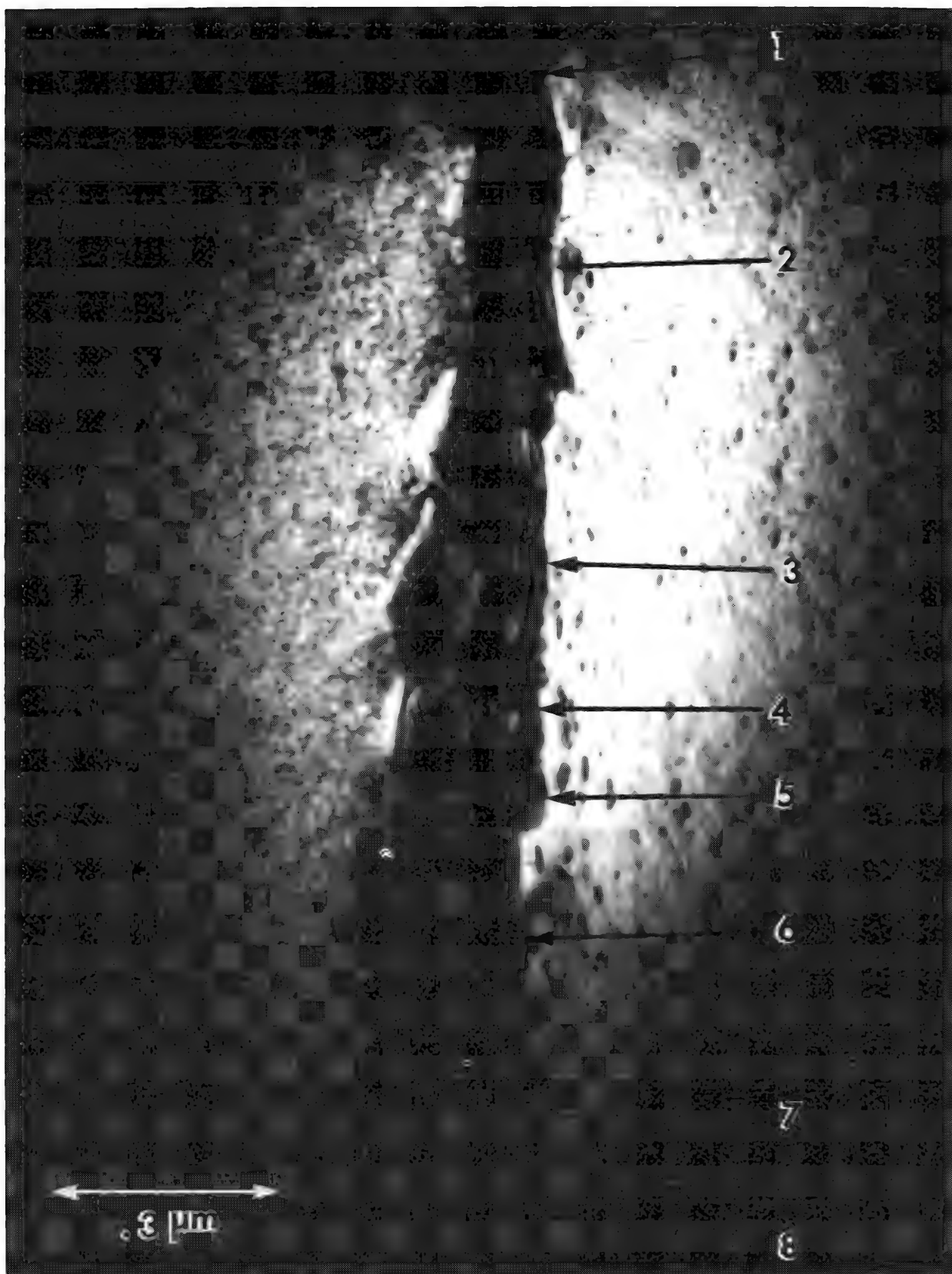
FIG. 3.--TEM micrograph of another sensitized Type 304 stainless-steel specimen along which 8 points were analyzed before tilting (Table 2). Depending on region selected for analysis, one might actually be exciting x rays from a small precipitate somewhere in plane of grain boundary.

TABLE 1.--Results of microanalysis along grain boundary in Fig. 1.

Point	Cr	Fe	Ni
A	.144 ± .020	.726 ± .010	.105 ± .053
B	.172 ± .019	.708 ± .011	.095 ± .057
C	.160 ± .019	.716 ± .010	.099 ± .054
D	.142 ± .020	.736 ± .010	.097 ± .056
E	.160 ± .019	.720 ± .010	.094 ± .057
F	.186 ± .018	.700 ± .011	.090 ± .058

TABLE 2.--Results of microanalysis along grain boundary in Fig. 3.

Points along the grain boundary	Cr	Fe	Ni
1	.198 ± .014	.684 ± .008	.093 ± .018
2	.180 ± .015	.704 ± .008	.091 ± .019
3	.153 ± .021	.719 ± .010	.103 ± .023
4	.175 ± .017	.702 ± .009	.097 ± .020
5	.174 ± .018	.705 ± .009	.096 ± .021
6	.273 ± .012	.628 ± .008	.074 ± .020
7	.149 ± .025	.736 ± .012	.089 ± .028
8	.174 ± .025	.702 ± .013	.099 ± .029

References

1. E. C. Bain, R. H. Aborn, and J. J. B. Rutherford, "The nature and prevention of intergranular corrosion in austenitic stainless steel," *Trans. Am. Soc. Metals* 21: 481, 1933.

2. R. L. Cowan and C. S. Tedmon Jr., "Intergranular corrosion of iron, nickel, and chromium alloys," *Advances in Corrosion Sci. and Tech.* 3: 293, 1973.

3. C. S. Pande et al., "Direct evidence of chromium depletion near the grain boundaries in sensitized stainless steels," *Scripta Metallurgica* 11: 681, 1977.

4. P. Rao and E. Lifshin, "Microchemical analysis in sensitized austenitic stainless steel," *Proc. 12th MAS Conf.*, 1977, 118.

5. R. L. Sabatini and C. S. Pande, "A comparison of procedures for quantitative x-ray analysis in thin films," *Proc. 14th MAS Conf.*, 1979, 129.

6. A. D. Romig Jr. and J. I. Goldstein, "Detectability limit and spatial resolution in STEM x-ray analysis: Application to Fe-Ni alloys," *Proc. 14th MAS Conf.*, 1979, 124.

7. N. J. Zaluzec, "Fluorescence by uncollimated radiation: Local sources," in J. J. Hren, J. I. Goldstein, and D. C. Joy, Eds., *Introduction to Analytical Electron Microscopy*, New York: Plenum Press, 1979, 128.

CALCULATIONS OF ELECTRON BEAM SPREADING IN COMPOSITE THIN FOIL TARGETS

D. E. Newbury and R. L. Myklebust

From the beginning of the recent surge of interest in the technique of analytical electron microscopy (AEM), the determination of the spatial resolution of analysis has been one of several key problems under investigation.[1-4] Goldstein et al. have provided a simple model to describe the interaction volume produced by elastic scattering of the beam electrons in the foil.[1] This model has the advantage that a straightforward mathematical expression can be written that describes the broadening as a function of foil and beam parameters. Other authors have devised Monte Carlo electron trajectory simulations to estimate the beam broadening.[3,4] Conveniently, these more elaborate simulations have confirmed that the simple model provides a good estimate of beam broadening, at least for thin foils where multiple scattering is minimized. The Monte Carlo methods have provided the capability for exploring the multiple scattering regime, as well as for studying interesting sample geometries, e.g., tilted foils, structure within foils, etc.

Recently, an experiment was reported by Hall and Vander Sande in which the measured beam broadening was apparently much less, by an order of magnitude or more, than that predicted by the simple model, and by extension, the Monte Carlo simulation as well.[5] Hall and Vander Sande studied the x-ray signal response measured as a 2.5nm beam was scanned across an iron-enriched grain boundary in MgO, where the iron-rich region had a width of less than 10 nm. These authors claimed that their results revealed such serious discrepancies as to suggest "a need to carefully examine the assumptions underlying the Monte Carlo calculations for 100 kV electrons."[5] We shall demonstrate in this paper that (1) the apparent discrepancy observed by Hall and Vander Sande results from an incorrect application of the simple model; (2) the existing Monte Carlo methods are adequate to describe their experiment; and (3) inadequate consideration of beam spreading can lead to severe errors in concentrations calculated by conventional AEM methods.

Extension of Simple Model to Consider Structure

The simple model for beam spreading approximates the interaction volume as a cone of constant x-ray generation with an altitude equal to one-half the foil thickness t and with a base diameter given by

$$b = 625(\rho/A)^{0.5}(Z/E)\ t^{1.5} \quad (cm) \tag{1}$$

where ρ is the density (g/cm^3), A is the atomic weight (g), Z is the atomic number, E is the incident beam energy (keV), and the foil thickness t is in cm. In their experiment, Hall and Vander Sande compared the full width, half maximum in their measured profiles with the value of b given by Eq. (1).

The experimental situation is illustrated schematically in Fig. 1 for a foil 338 nm thick (b = 53 nm). If we assume an iron-enriched slab thickness of 10 nm, it is apparent that the slab represents only a small fraction of the interaction cone. The value of the broadening given by Eq. (1) should not be compared directly with the width of the signal profile generated at the boundary, since most of the electrons in the cone are not interacting in the slab. To compare the simple model with the experiment more realistically, we must calculate the signal response when a cone is moved through a slab. Fortunately, for the case of a slab formed by parallel planes intersecting a cone, we can derive a function for the area of the hyperbola created by the intersection of each boundary plane with the cone:

$$A_{Hyp} = (tb/4)(1 - F^2)^{0.5} - (tb/4)\ F^2\ \ln\{[1 + (1 - F^2)^{0.5}]/F\} \tag{2}$$

The authors are with the Microanalysis Group, Center for Analytical Chemistry, National Bureau of Standards, Washington, DC 20234.

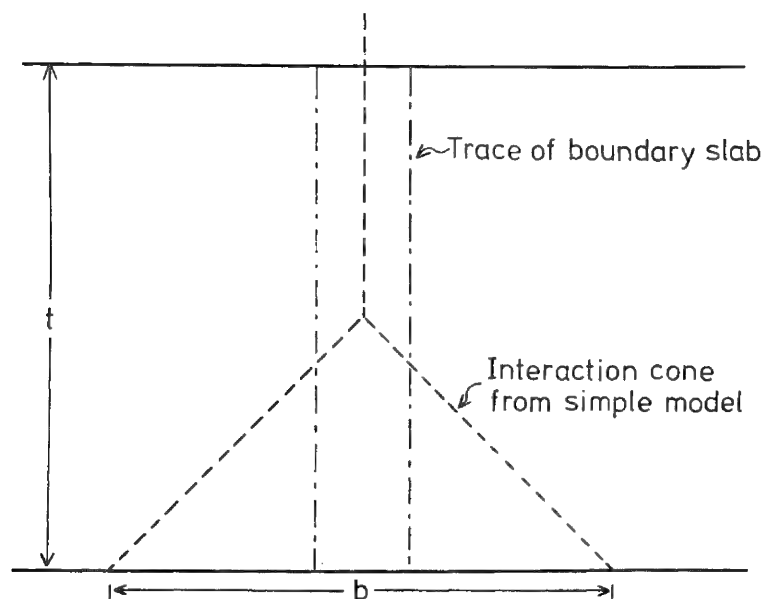FIG. 1.--Schematic illustration of simple model for beam spreading in thin foil. Approximate relationship of slab intersecting cone in thick foil.
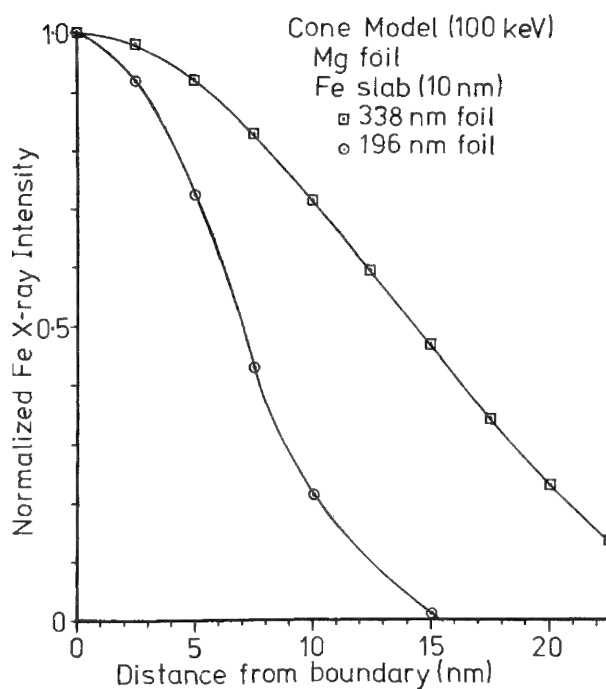

FIG. 2.--X-ray intensity profile across slab calculated with simple model extended through Eq. (2).
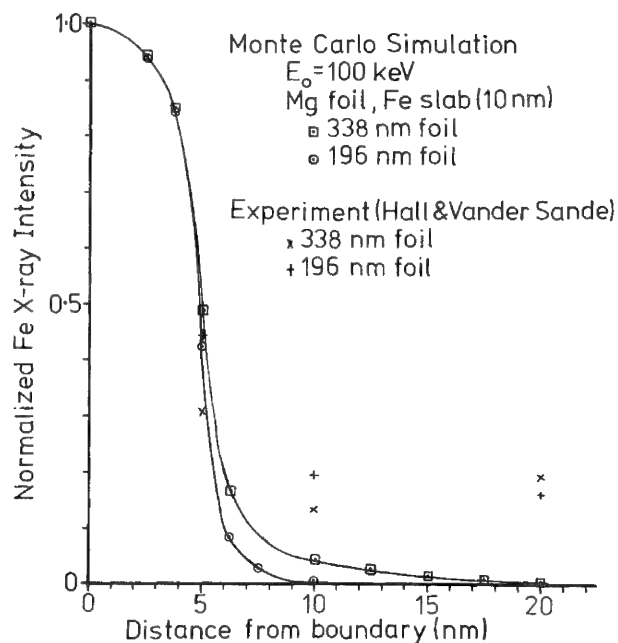

FIG. 3.--X-ray intensity profiles calculated by Monte Carlo electron trajectory simulation for 2.5nm beam scanned across 10nm-thick slab of iron in magnesium foil.

174

where t is the foil thickness, b is the broadening given by Eq. (1), and $F = r/(b/2)$, the fraction of the radius of the cone intersected by the plane.[6] Equation (2) can be integrated numerically between any two values of F to find the volume of the slab within the cone, and this volume can be used to calculate the predicted signal response function when the beam crosses the slab (Fig. 2). The signal response curves have been normalized to the maximum value of the signal observed when the beam is in the center of the boundary. The response curve is found to be sharply peaked, with a FWHM of 12 nm for a 196nm foil and 280nm for a 338nm foil. These values are about 50% of the full value of the broadening. The response curves are still substantially wider than those observed experimentally by Hall and Vander Sande.[5]

From Monte Carlo calculations, it is clear that the electron trajectory density is not a constant in the interaction volume in thin foils.[3,4] To predict the signal response across the boundary accurately, we must take this trajectory distribution into account by employing a detailed single-scattering Monte Carlo calculation, appropriately modified to consider the presence of a slab. For the present calculations, the extreme case of a slab of pure iron in a magnesium film was taken. Inclusion of the oxygen component would reduce the scattering and further sharpen the profiles. The signal response curves thus calculated (Fig. 3) are substantially narrower than those calculated with the simple cone model, with a FWHM of 10 nm for the 338nm foil and 9 nm for the 196nm foil. The data of Hall and Vander Sande, replotted in the normalized form in Fig. 3, agree quite well with the Monte Carlo calculations. Note also that the Monte Carlo calculations show that the profiles do not differ very much with increasing thickness, as observed in the experiment. It therefore appears that the Monte Carlo simulation with its present theoretical basis is quite capable of describing the Hall and Vander Sande experiment.

Close examination of Fig. 1 suggests that it is appropriate to reconsider the Hall and Vander Sande experiment with regard to their assignment of a concentration axis to the results by the use of the Cliff-Lorimer sensitivity factor method. This method can only provide an accurate result if the structure being measured is (1) completely contained within the interaction volume and (2) is homogeneous. For the case illustrated in Fig. 1, that is clearly not the case. With Eq. (2), we can roughly estimate the size of the error that beam spreading can introduce. If the 10nm slab were actually pure iron, beam spreading would cause the apparent concentration to be reduced to 70% for the 196nm foil and to 35% for the 338nm foil. That a sharp drop in the maximum apparent concentration as a function of foil thickness is seen in the results of Hall and Vander Sande confirms the seriousness of ignoring this effect. Ignoring the effect of beam broadening can lead to significant errors in the analysis of fine structures such as boundaries and small inclusions. This is a case where careful application of the Monte Carlo technique will be necessary to deconvolute the complex interaction of the distribution of the signal being measured with the true distribution of the analyte of interest in the sample. The simple model for beam spreading can provide an estimate of the sample dimension below which the concentration derived from the sensitivity factor method becomes suspect.

References

1. J. I. Goldstein et al., "Quantitative x-ray analysis in the electron microscope," in O. Johari, Ed., *Scanning Electron Microscopy*, Chicago: IITRI, 1977, 315-324.

2. J. I. Goldstein, "Principles of thin film x-ray microanalysis," in J. J. Hren, J. I. Goldstein, and D. C. Joy, Eds., *Introduction to Analytical Electron Microscopy*, New York: Plenum, 1979, 83-120.

3. D. E. Newbury and R. L. Myklebust, "Monte Carlo electron trajectory simulation of beam spreading in thin foil targets," *Ultramicroscopy* 3: 391-395, 1979.

4. D. F. Kyser, "Monte Carlo simulation in analytical electron microscopy," in J. J. Hren, J. I. Goldstein, and D. C. Joy, Eds., *Introduction to Analytical Electron Microscopy*, New York: Plenum, 1979, 199-221.

5. E. L. Hall and J. B. Vander Sande, "The effect of sample thickness on high resolution composition profiles in dedicated STEM," *Proc. 37th Ann. EMSA Meeting*, Baton Rouge: Claiters, 1979, 474-475.

6. The derivation of this equation is somewhat lengthy; to our surprise it was not given in any of a dozen general mathematics texts or specific treatises on the conic section. The full derivation will be given in a subsequent journal paper.

EL
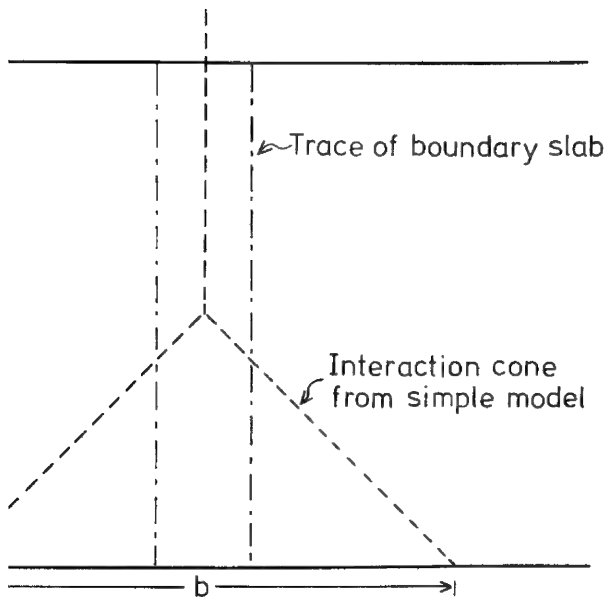
—Trace of boundary slab

Interaction cone
from simple model

b

:ion of simple model for beam spreading in thin foil.   Approx-
.ntersecting cone in thick foil.

el (100 keV)

(10 nm)
ım foil
ım foil

Monte Carlo Simulation
E_o = 100 keV
Mg foil, Fe slab (10 nm)
□ 338 nm foil
⊙ 196 nm foil

Experiment (Hall & Vander Sande)
x 338 nm foil
+ 196 nm foil

Normalized Fe X-ray Intensity

Distance from boundary (nm)

15   20
y (nm)
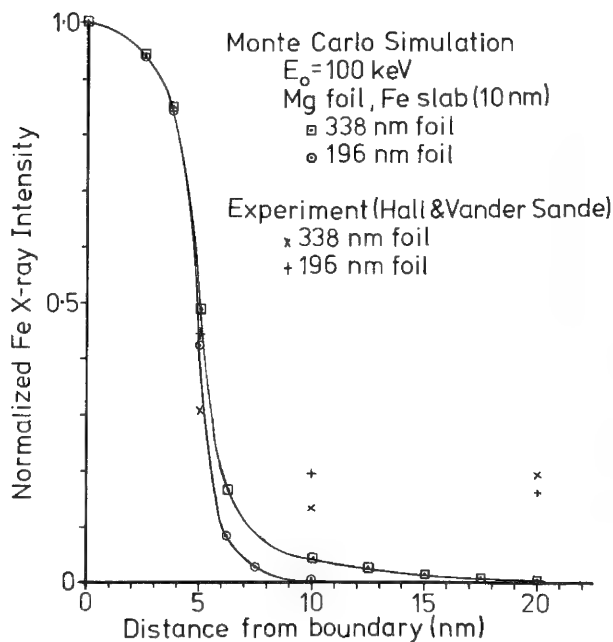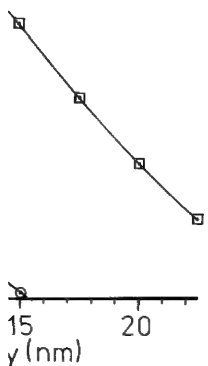
file across slab
extended

FIG. 3.--X-ray intensity profiles calcul-
ated by Monte Carlo electron trajectory
simulation for 2.5nm beam scanned across
10nm-thick slab of iron in magnesium foil.

aw materials, and the growing emphasis
of the occurrence of nonmetallic in-
ıe production of steel.   In addition,
reduce their deleterious effects has
ɔr in quest of an alternate, perhaps
ls in material properties.
lusions is the manganese sulfide in-
room temperature, but at the tempera-
ırticles are quite ductile and elon-
ɔn as well as the volume fraction of
ɔaring on the degree to which mechani-
rmation characteristics could be linked

:hese sulphides to be homogeneous and
laries or internal structure. Uncon-
ɔvious notions on the structure of the
)lid state phenomena occur; and that
complete without consideration of

)t and a uniaxially hot deformed bar
:o disks, and thinned by impingement

ɔ, conventional TEM, and STEM revealed
The as-cast inclusions all had a nu-
glassy matrix. There were disloca-
.dification or from the thermal and
ʾain boundaries occasionally occurred
:erminating at dislocation tangles at

100Å
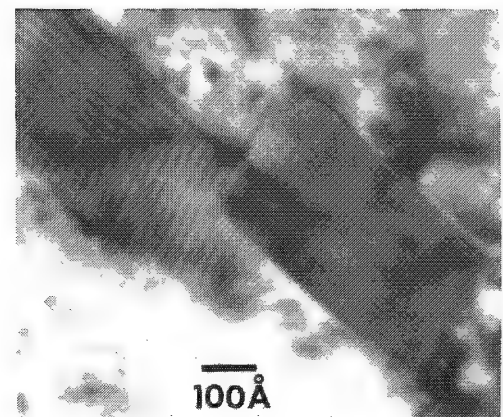
2.--Precipitates on dislocation in MnS
sion.

1 7ᴸ

Inclusions in hot-deformed steel revealed dense polygonized dislocation arrays, low-angle boundaries, deformation twins, and 500Å precipitates on dislocations. Weak beam images confirmed that lattice strain was relieved by the formation of the precipitates, which suggests that they formed during cooling of a dislocation rich supersaturated solid solution.

Since such a wide variety of potent hardening mechanisms appear to be operating in these inclusions, studies of inclusion deformation cannot be complete without consideration of these mechanisms.

20Å
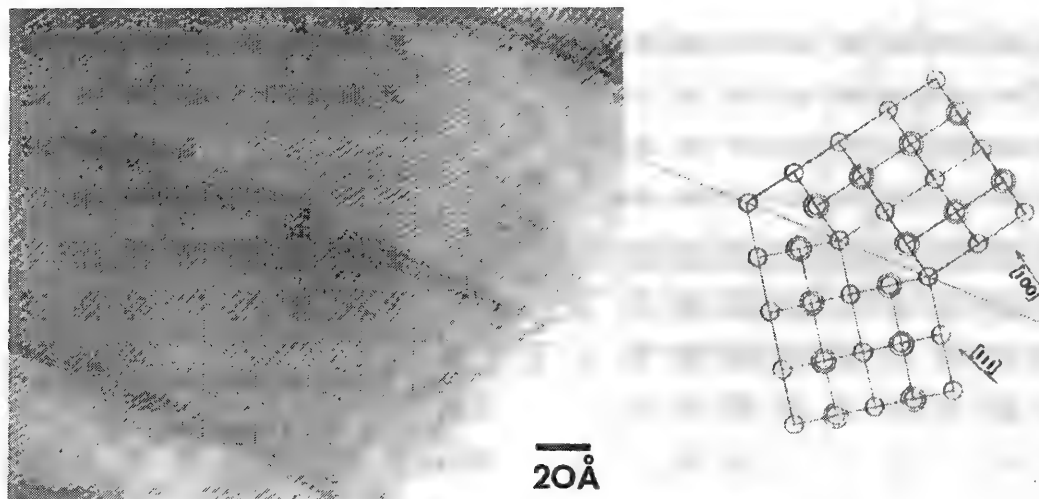
FIG. 3.--Lattice fringe image of (200) and (111) planes in adjacent twins with diagram of (110) planes to show twinning mechanism.

FIG. 4.--STEM image of MnS inclusing showing its nucleus at thin edge; and x-ray spectra from nucleus and MnS of inclusion, obtained after JEM 100-CX was "cleaned up." Iron peak is certainly from inclusion nucleus, not iron matrix.

ION MICROPROBE, ION MICROSCOPE, AND LASER MICROPROBE MASS ANALYSIS OF PARTICULATES

David S. Simons

The mass spectrometer offers several important advantages for elemental analysis of solids. Among these are high sensitivity owing to pulse-counting ion detection and the absence of a continuum background, detectability of all elements including those of low atomic number that are not observable by x-ray spectroscopies, and the capability of detecting and measuring the abundance of each isotope of a given element.
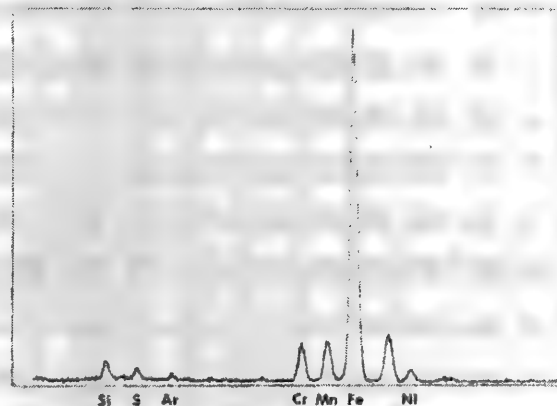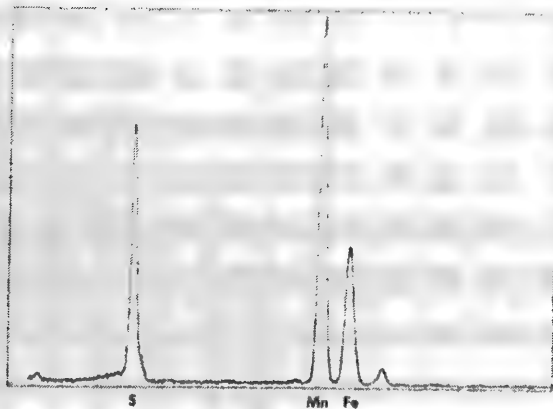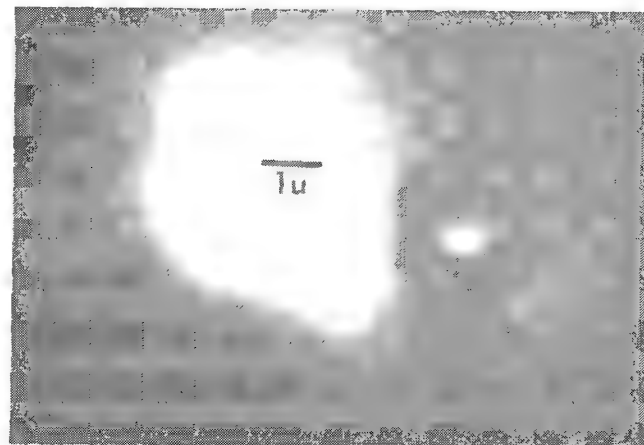
Mass spectrometry is especially attractive for the analysis of individual particulates where the quantity of material available for analysis is severely limited. Ideally, the source of ions for this application should be confined to the individual particle in order to minimize spectral interferences from the mounting medium. Two ionization processes lend themselves readily to localized analysis--sputtering by an ion beam and vaporization by a laser beam. Instruments have been constructed that make use of each of these processes.

The instruments based on ion sputtering are divided into two categories. The *ion microprobe* uses a sputtering ion beam with a minimum diameter of approximately 2 μm to achieve a localized analysis. The *ion microscope*, on the other hand, generally uses a considerably larger sputtering ion beam diameter of 100-300 μm. The sputtered ions are mass-filtered through a mass spectrometer that preserves their spatial relationship, and localization of the area from which ions are accepted can be limited to a diameter of approximately 2 μm with the use of an appropriate aperture at an image plane.

The *laser microprobe* uses a pulsed laser beam that can be focused to approximately 0.5 μm to vaporize a small volume of material. At sufficient energy density a portion of the evaporated material will be ionized. Since the ionization event is localized in time, a time-of-flight mass spectrometer is the logical choice for measuring the mass spectrum with high efficiency.

These three types of instruments have been investigated for their capability to analyze individual particulates.[1] The ion microprobe used in this study was the Applied Research Laboratories Ion Microprobe Mass Analyzer (IMMA),[2] the ion microscope was the CAMECA Instruments IMS-3F Ion Microanalyzer,[3] and the laser microprobe was the Leybold-Heraeus LAMMA 500 Laser Microprobe Mass Analyzer.[4] Samples used for the evaluation were microchips and microspheres of research glasses manufactured at NBS.[5] For the ion-beam instruments, the samples were dispersed on 1cm-diameter high-purity gold disks. For the laser microprobe they were dispersed on formvar-coated 3mm-diameter TEM grids. The size range of the glass particles was 1-15 μm.

An example of comparative data from the three instruments is shown in Table 1. In this case the samples were spheres of a glass containing 80% PbO and 20% SiO_2 by weight. The Pb and Si ion signals were measured from several particles of different sizes to determine the relative sensitivity of the two elements and its variability from particle to particle. The table indicates that the relative sensitivity differs by less than a factor of 2 among the three instruments in this case. The relative standard deviation (RSD) of the sensitivity ratio is highest for the laser microprobe. This result reflects a lack of reproducibility of ionization conditions among particles of different size as well as insufficient data density of two or three data points per mass peak when a wide mass range is recorded.

TABLE 1.--Lead - silicon sensitivity ratios from K227 microspheres.

	Ion Microprobe	Ion Microscope	Laser Microprobe
No. of particles	10	5	8
S_{Pb}/S_{Si}	2.13	3.44	2.67
R.S.D. (%)	16	7	80

TABLE 2.--Isotopic ratios of lead from K227 microspheres.

	Ion Microprobe	Ion Microscope	Laser Microprobe	Natural Lead
No. of particles	10	6	13[*]	
206/208	0.461	0.511	0.53	0.461
R.S.D. (%)	0.6	3.4	15.4	
207/208	0.412	0.451	0.47	0.422
R.S.D. (%)	0.2	3.7	9.6	
206/207	1.098	1.140	1.15	1.093
R.S.D. (%)	1.0	0.4	7.8	

[*] 4 particles for 206/208 and 207/208

Table 2 indicates the capability of the three instruments to measure isotopic ratios of Pb in these same microspheres. The higher precision of the ion microprobe measurements is attributable to an electrostatic peak-switching system that allows isotope ratio measurements to be taken without changing the magnetic-field setting of the mass spectrometer. The relatively low precision of the laser microprobe is a result of the 8-bit resolution of the transient recorder that is used to measure and store the mass spectrum in 256 discrete levels. This characteristic also restricts the dynamic range of signals that can be measured in one spectrum and sets a practical limit of about 10:1 on the magnitude of an isotopic ratio that can be measured with the laser microprobe. The ion microscope produces well-defined trapezoidal peaks that vary in intensity by less than 0.2% over the flat portion of the peak top. One would therefore expect the precision between particles to be less than 1%, but that is not the case. A computer-controlled cyclic mass scan is used to generate the isotope ratios. Improvements in interparticle precision may occur through the use of a different software routine that minimizes the effect of magnetic hysteresis.

The true isotopic ratios of the Pb in these particles has not been measured, but the best estimate for naturally occurring Pb is shown in Table 2.[6] Any bias in the measurement of the ratios in the particles could be corrected by comparison with a standard of known Pb isotopic composition. A future project will be the production of lead silicate microspheres using isotopically characterized Pb as a starting material.

Table 3 summarizes some of the special features of each of the three instruments as applied to particulate analysis. It is apparent that no single instrument is the best choice for all situations. The ion microprobe can measure isotope ratios with high precision. The ion microscope has a variety of features that give it great versatility to

handle different analytical problems, for example the ability to screen a field of particles for a particular element by use of the ion-imaging mode of operation. Finally, the laser microprobe can acquire full mass spectra from many particles at a very rapid rate, and is the easiest instrument to use for the analysis of very small particles.

TABLE 3.--Special features of three instruments for particle analysis.

Instrument	Special Features
Ion microprobe	High precision isotopic ratios
Ion microscope	Rapid ion imaging of a particle field Faraday cup or electron multiplier detector High abundance sensitivity spectrometer Molecular ion rejection by energy offset High mass resolution
Laser microprobe	High resolution optical microscope Rapid analysis (30-60 particles/hr.)

References

1. Certain commercial instruments are identified in this paper so that the experimental procedure can be adequately specified. In no case does such identification imply NBS recommendation or endorsement, nor does it imply that the material or equipment identified is necessarily the best available for the purpose.
2. H. Liebl, "Ion microprobe mass analyzer," *J. Appl. Phys.* 38: 5277, 1967.
3. J. M. Rouberol et al., "A new secondary ion emission microanalyzer," *Proc. 12th MAS Conf.*, 1977, 133.
4. R. Wechsung et al., "LAMMA: A new laser microprobe mass analyzer," *SEM/I/1978*, 611.
5. J. A. Small et al., "The production and characterization of glass fibers and spheres for microanalysis," *ibid.*, 445.
6. E. J. Catanzaro et al., "Absolute isotopic abundance ratios of common, equal-atom, and radiogenic lead isotopic standards," *J. Res. NBS* 72A: 261, 1968.

THREE-DIMENSIONAL SIMS ANALYSIS BY IMAGE DEPTH PROFILING

A. J. Patkin, B. K. Furman, and G. H. Morrison

The feasibility of three-dimensional analysis of solids is demonstrated. Secondary Ion Mass Spectrometry (SIMS) is combined with a real-time digital image acquisition system and computer processing to allow display of concentration distribution in the x, y, and z directions.

Three-dimensional information may be obtained by SIMS in two ways. In the first, a series of areas in a grid-like pattern on a sample can be monitored for secondary-ion intensity with an ion microprobe. Repetition of this procedure several times while the primary ion beam sputters away the sample surface yields a depth profile. The resulting spatial information may then be displayed with depth of analysis in an appropriate manner. This method suffers from being time consuming. A single image of only 64 × 64 picture element (pixel) resolution requires 4096 separate positionings of a mechanical or electronic aperture. These repositionings must be done with precise x-y reproducibility to produce a depth profile, and may be subject to uncorrected variations in primary-ion beam intensity and detector sensitivity between areas during the course of this multi-area profile. The second method of obtaining three-dimensional information from SIMS, and the one described here, is by use of an ion microscope. The detection area no longer needs to be moved over the sample surface to generate an image, since the entire image is present simultaneously, which increases the speed of analysis and eliminates the pixel-to-pixel variations in instrumental parameters associated with the use of an ion microprobe.

The ion microscope is a unique surface analytical tool combining ion sputtering, mass filtering, and ion optics to provide a spatially resolved mass analysis of the surface of a solid.[1] The resultant ion image of up to 250μm diameter field-of-view with a 1μm point-to-point resolution contains over 50 000 elements of information. The intensity of each element is proportional to the number of secondary ions of a specific mass sputtered from a particular point on the sample's surface.

The system described here permits direct viewing of ion images on a television monitor as well as on-line digitization for storage or real-time computer processing. By correlation of these images with depth profiling, three-dimensional information can be readily obtained.

Experimental

Previously, multi-element depth profiles were acquired by integration of elemental signals of a preselected, mechanically apertured area of the sample, as with an ion microprobe. The current work uses electronic aperturing of the secondary-ion image, so that multi-area, multi-element depth profile analysis is made possible.

The present system consists of a CAMECA IMS-300 Ion Microscope interfaced to a PDP-11/20 computer. Image acquisition is performed by a QUANTEX QX-26 ISIT low light-level TV camera, which produces a 6-bit/pixel image of 256 × 256 pixel area. The video image may then either be displayed directly on a high-resolution TV monitor, or digitized in real time by a GRINNELL GMR-27 digital image processor[2] at a rate of 30 frames/sec. The GRINNELL is also capable of real-time image integration and averaging.

Electronic aperturing of the image is done by superposition of computer-generated rectangles on the displayed images, which are positioned under potentiometer control, to define rectangular subimages. These subimages may range in area from one pixel ($\sim$ 1 μm^2) to the entire image. Several subimages may be defined in this manner. The image is then profiled through the sample. The areas within the rectangles are simultaneously averaged, recorded, and displayed in a graphical format similar to that commonly used for display of

multi-element SIMS profiles.

Image display may be either 8 bits (256 levels) of black and white, or 12 bits (4096 levels) of color. Since the human eye can only distinguish among a few dozen gray levels at any one time, whereas it can distinguish among several thousand different hues and intensities of color,[3] pseudo-color display can convey much more information to the human eye than black and white.

Ion images recorded at several depths in the sample are converted to two-dimensional elemental concentration maps by means of ion implant standards.[4] The conversion procedure produces a series of concentration images at several depths for a net three-dimensional concentration characterization of the sample.

Previously it has been impossible to record simultaneous depth profiles of noncontiguous areas or to characterize three-dimensionally the elemental distribution of a sample by SIMS or any other technique. Image depth profiling achieves both.

References

1. G. H. Morrison and G. Slodzian, "Ion microscopy," *Anal. Chem.* 47: 32A, 1975.

2. B. K. Furman and G. H. Morrison, "Direct digitization for quantification in ion microscopy," *1980 Pittsburgh Conf. on Anal. Chem. and Applied Spec.*, Atlantic City, N.J., 1980, paper 607.

3. O. Sheppard, *Am. J. Optom.* 46: 735, 1969.

4. D. P. Leta and G. H. Morrison, "Ion implantation for in-situ quantitative ion microprobe analysis," *Anal. Chem.* 52: 277, 1980.

SOME EXPERIMENTAL PROBLEMS IN THE RAMAN ANALYSIS OF MICROSAMPLES

J. J. Blaha and E. S. Etz

The Raman microprobe, developed at the National Bureau of Standards (NBS), has been shown to be an effective tool for the analysis of microsamples. Through the interpretation of the Raman spectra obtained from these samples, the molecular components and the matrix of those components in the sample can be identified. Many applications to the study of microsamples have been made with both the NBS instrument and the commercially available MOLE (Molecular Optics Laser Examiner).[1]

Several experimental difficulties in the spectroscopic analysis of microscopic samples have been encountered; their resolution is of importance for successful analysis. Two of these difficulties (heating of a sample by the laser beam and the chemical reaction of some atmospheric particles exposed to ambient conditions) are discussed below.

Heating of samples by the laser beam can cause noticeable changes in the Raman spectrum and can lead to phase transitions, compositional modifications, or even destruction of the particle. The simplest approaches to preventing heating in particles are to decrease the laser power on the sample and/or change the excitation wavelength from the laser. To demonstrate this point, Fig. 1 shows the first Raman spectra from microparticles (single $0.8 \times 30\mu m$ fibers) of croconate blue (see figure for molecular description). The top spectrum was obtained with the 514.5nm (green) line of an argon/krypton ion laser. At the irradiance level used (1.6 kW/cm^2, 5 mW output power), the spectrum shows an increasing luminescent background in the region from 400 to 2000 cm^{-1}, indicative of heating in the sample. The particle was destroyed during the course of the measurement. As croconate blue has its absorption maximum at 590 nm, we used the 647.1nm (red) line, where much less absorption was expected. Under the same irradiance conditions, this Raman spectrum (middle) shows a weaker Raman spectrum and a somewhat increased background, probably indicative of particle heating in much the same manner as observed for the particle exposed to the green line. Thus, analysis with the 647.1nm line is impossible at this irradiance. The bottom spectrum in the series is of a third particle exposed to green radiation but the power level of the laser has been reduced to 1 mW. A good Raman spectrum can be obtained under these conditions and a slightly increased background, perhaps indicative of a lowe degree of heating, is observed. However, when the laser output power is very low, power fluctuations are observed, which are manifested in the spectrum background. An optical filter can be used to keep the power on the particle low to prevent heating and maintain a high, well-regulated laser output to prevent modulations. The measurements are preliminary and indicate the care that must be used in choosing measurement conditions. Studies are being conducted to measure the effects of varying power levels with other wavelengths in the analysis of particles.

Chemical reactions of microsamples also complicate the analysis. Some materials require special handling to yield a Raman spectrum. An example is presented for nitrosyl sulfuric acid (NOHSO$_4$). This material is suspected of being a component of the stratosphere. However, it is extremely difficult to handle owing to the rapidity of decomposition to NO$_2$ and H$_2$SO$_4$ when exposed to ambient air. Figure 2 presents the Raman spectra of samples of nitrosyl sulfuric acid from a 10% solution of NOHSO$_4$ in sulfuric acid encased in a sealed capillary tube and from a crustal of NOHSO$_4$ coated with a film of paraffin wax. These were laboratory samples studied to determine how to handle and analyze NOHSO$_4$ when collected from stratospheric aerosols.

The Raman spectrum of solid NOHSO$_4$ (top spectrum) is characterized primarily by the very strong feature at 2273 cm^{-1} associated with the N-O stretching motion and by the features at 420, 578, 1035, and 1173 cm^{-1} that are associated with the HSO$_4^-$ motions of the molecule and by the lattice features in the region below 250 cm^{-1}. The Raman spectrum of NOHSO$_4$ in the solution of H$_2$SO$_4$ is characterized by the N-O stretch near 2273 cm^{-1}. The other features are overshadowed by the strong sulfuric acid bands , which are indicated by an S in the lower spectrum. A number of other bands are observed in the

The authors are with the Microanalysis Group of the Center for Analytical Chemistry of the National Measurement Laboratory, National Bureau of Standards, Washington, DC 20234.
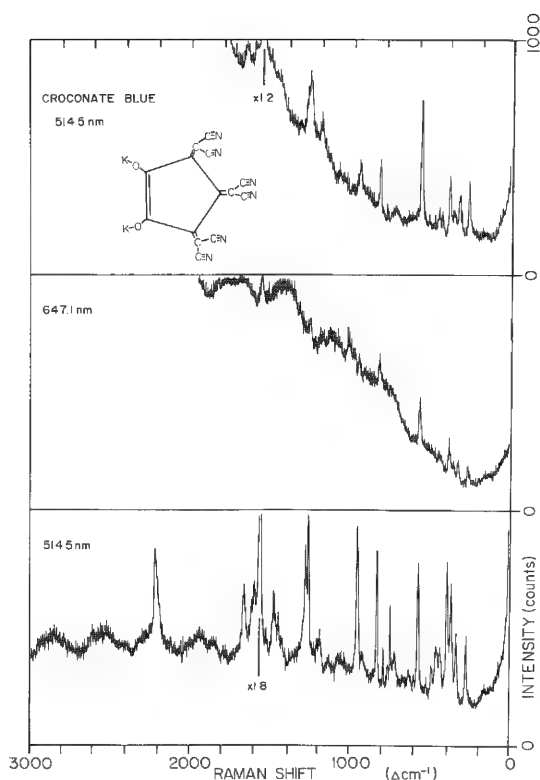
FIG. 1.--Raman microprobe spectra of croconate blue. Wavelength is indicated. Top and middle spectra: 5 mW power at sample; 20 μm beam spot; 3.0 sec time constant; bottom spectrum: 1 mW power at sample; 20 μm beam spot; 6.0 sec time constant.
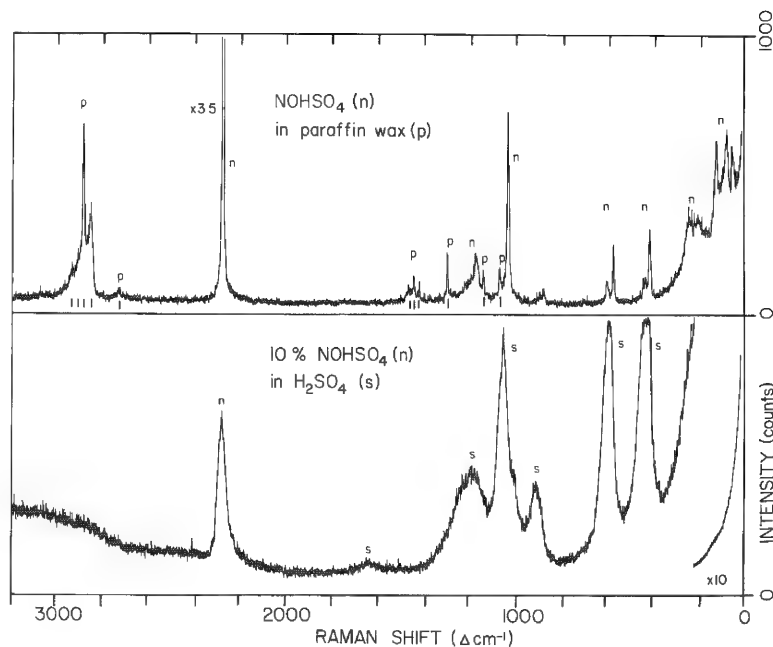
FIG. 2.--Raman microprobe spectra of nitrosyl sulfuric acid. Top: crystal of $NOHSO_4$ coated with a thin film of paraffin wax; bottom: solution of 10% $NOHSO_4$ in H_2SO_4 sealed in a capillary tube.

top spectrum. These bands arise from the paraffin wax used to protect the sample. The paraffin bands are indicated by lines below the spectrum. When $NOHSO_4$ reacts with water the strong feature at 2273 cm^{-1} disappears and only the bands associated with sulfuric acid remain. Studies on samples collected in the statosphere are being conducted.

Coating samples with such materials as a thin layer of paraffin wax prohibits the interaction of ambient air with the particle and thus preserves its integrity. Other materials are being investgated as possible coating agents. These materials must be transparent to allow spectroscopic analysis and yet not interact with the particles.

References

1. W. C. Cunningham, E. S. Etz, and W. H. Zoller, "Raman microprobe characterization of South Pole aerosol," *Microbeam Analysis--1979*, San Francisco: San Francisco Press, 1979, 148; P. Dhamelincourt, "Developments and applications of the MOLE laser Raman microprobe," *ibid.*, p. 155; F. Adar, M. J. Mitchell, and J. N. Ramsey, "Raman microanalysis of SiO source materials by means of MOLE," *ibid.*, p. 165; F. S. Casciani and E. S. Etz, "Raman microprobe study of biological mineralization in situ: enamel of the rat incisor," *ibid.*, p. 169; E. S. Etz and J. J. Blaha, "Investigations into the critical measurement aspects of Raman microprobe analysis," *ibid.*, p. 173; D. O. Landon, "The development of instrumentation for microparticle analysis by Raman spectroscopy," *ibid.*, p. 185.

CHARACTERIZATION OF THIN FILMS THROUGH FINE FEATURES OF SOFT X-RAY EMISSION SPECTRA

M. J. Romand, R. Bador, A. A. Roche, and M. Charbonnier

In the past few years powerful new physical techniques have become available for solid-surface characterization. However most are too sophisticated to be in common use. Moreover, only a few can provide clear information on chemical combinations, with the line shapes serving as fingerprints of surface molecular environments. The prime purpose of the present work is to demonstrate that *low-energy electron-induced X-ray spectrometry (LEEIXS)*[1-3] can be a simple and useful method for obtaining such information in a large number of surface analytical situations. The results presented here deal with LEEIXS study of various thin films grown on metal or alloy substrates.

Experimental Set-up

The instrument used is a wavelength-dispersive x-ray spectrometer equipped with a cold-cathode device as excitation source. This open tube runs in the primary vacuum of the spectrometer. Soft x-ray spectra are registered with a flow-proportional counter mounted with a polypropylene window approximately 0.5 μm thick and filled with a 10%CH_4-90%Ar mixture at a pressure of 760 torr. The beam accelerating voltage varies from 0.5 to 5 keV and the current, from 0.5 to 2 mA. Voltage and current are stabilized by an automatic pressure regulator and are digitally controlled during the measurements. Other features of the experimental set-up (such as flat analyzing crystals) are standard.

The low penetration depth of impinging electrons into samples and consequently the low x-ray excitation depth makes of LEEIXS a surface analysis method.

Results

Figure 1 shows the $TiL_{2,3}$ emission band from an oxide anodically grown on a titanium substrate. This spectrum is obtained with 2.5keV electrons so that x rays come from a depth of about 800 Å. A clinochlore crystal (2d = 28.393 Å) is used for dispersing the relevant long-wavelength radiations. This spectrum can be compared to corresponding bands of Ti, TiO, and TiO_2. The spectra of the different titanium suboxides present intermediary chemical shifts and A/B peak ratios.[4] The corresponding changes in fine structure can therefore be employed for characterizing the anodic film. Indeed comparison between (b) and (d) spectra provides strong support for attributing a TiO_2 form to the outer part of the passivation oxide. This interpretation corroborates a similar one drawn from fine features of the O K emission band.[3]

Figure 2 shows the VL_3 emission bands from a Ti-6 Al-4 V alloy and an oxide anodically grown on this substrate. These spectra are obtained with 2.5keV electrons; the relevant radiation is dispersed with a RbAP crystal (2d = 26.118 Å). These emission bands can be compared to those of pure vanadium and V_2O_5. In contrast to V_2O_5, the V_2O_4 and V_2O_3 spectra[5] exhibit a A/B peak ratio respectively equal to about unity and largely less than unity. As can be seen from a comparison of the A/B peak ratios from (b) and (d) spectra, the VL_3 emission band from the anodic film looks very much like that obtained from V_2O_5.

In addition, owing to the sensitivity of LEEIXS, molecular information can be deduced from spectra of certain impurities incorporated into thin layers. For example the Kβ - Kβ' spectrum of phosphorus obtained with a germanium crystal is reproduced in Fig. 3; in this case the sample is a 600Å Al_2O_3 anodic film containing 0.4 μg.cm^{-2} of phosphorus. This impurity is incorporated from the electrolyte in the form of phosphate anions as it is demonstrated by the presence of the Kβ' emission band.

Investigations are continuing in our laboratory but it is quite apparent from these preliminary results that soft x-ray band spectroscopy by means of LEEIXS can be an ex-

Authors Romand, Roche, and Charbonnier are with the Department of Applied Chemistry, CNRS--ERA 500, Univ. Claude Bernard--Lyon I, 69622 Villeurbanne, France; Bador is with the Biophysics Laboratory of the Pharmaceutical Sciences Unit at the same university.

tremely valuable technique for probing the electronic structure of materials and more especially for developing practical studies in surface characterization.
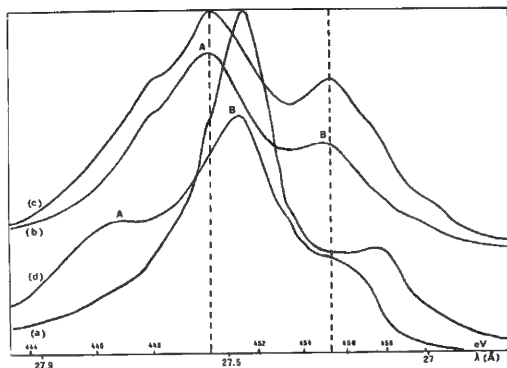
FIG. 1.--TiL$_{2,3}$ emission band from (a) metal, (b) TiO$_2$, (c) TiO, and (d) titanium anodic oxide.
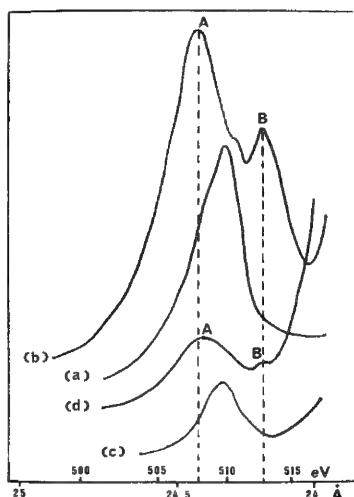
FIG. 2.--VL$_3$ emission band from (a) metal, (b) V$_2$O$_5$, (c) Ti-6Al-4V alloy, and (d) Ti-6Al-4V alloy anodic oxide.
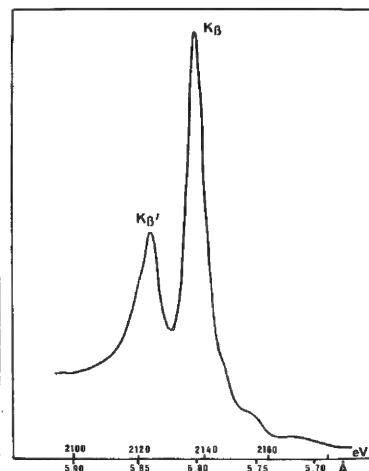
FIG. 3.--Kβ - Kβ' emission spectra of phosphorus impurity in Al$_2$O$_3$ anodic oxide.

References

1. M. Romand et al., "Utilisation de sources à cathode froide pour la caractérisation des surfaces," *J. Microsc. Spectrosc. Electron.* 2: 627, 1977.

2. R. Bador et al., "Analyse de films minces et ultra-minces: Perspectives nouvelles en spectrométrie d'émission de rayons X," *Spectrochimica Acta* 33B: 437, 1978.

3. A. Roche et al., "Etudes comparatives de couches superficielles à l'aide de techniques spectrométriques d'émission X et de rétrodiffusion d'ions," *J. Microsc. Spectrosc. Electron.* 4: 351, 1979.

4. D. W. Fischer and W. L. Baun, "Band structure and the titanium L$_{2,3}$ x-ray emission and absorption spectra from pure metal, oxides, nitride, carbide, and boride," *J. Appl. Phys.* 39: 4757, 1968.

5. D. W. Fischer, "Molecular-orbital interpretation of the soft-X-ray L$_{2,3}$ emission and absorption spectra from some titanium and vanadium compounds," *J. Appl. Phys.* 41: 3561, 1970.

ALPHA PARTICLE INDUCED X-RAY ANALYSIS OF ALUMINUM OXIDE FILM THICKNESS

J. L. Bomback and R. G. Musket

Alpha particle induced x-ray emission measurements were used to determine oxide film thicknesses on anodized high-purity aluminum. Two methods, one based on a thin-film oxide standard and the other on a bulk oxide standard, gave nearly identical results. These x-ray analyses, combined with direct thickness measurements by transmission electron microscopy (TEM), gave a measure of the anodized film densities.

Aluminum and its alloys are being used increasingly in automotive applications to reduce vehicle weight and achieve improved fuel economy. Analysis of the composition and thickness of thin oxide films on these materials is important to the development of processes to fabricate them into engineering components. For example, the ability to weld or braze aluminum alloys to themselves or to other materials critically depends on the composition, structure, and thickness of the oxide films present on the surfaces to be joined.

Alpha particle induced x-ray analysis has been demonstrated to be a useful nondestructive technique for the quantitative determination of oxide film thicknesses on several materials in the film thickness range of several atomic layers up to several micrometers.[1] The K-shell x-ray production cross section for oxygen by 5.8MeV alpha particles is one of the highest of all the elements. The mass absorption coefficient of O Kα x rays in alumina[2] allows roughly 50% x-ray transmission through 5000 Å of alumina. Consequently, alpha particle induced x-ray emission measurements can provide a rapid determination of oxide film thickness in the regime encountered on commercial materials.

Experimental

A series of aluminum oxide films were grown by anodization on 7/8in.-diameter circular disks punched from a 0.04m.-thick high-purity (99.99%) aluminum sheet. The disks first were polished mechanically and then electrolytically and then stored in a dessicator for 10 days prior to anodization. The procedure of Brock and Wood[3] was followed to obtain predicted aluminum oxide thickness t of 12 Å/V of anodization potential. Films with nominal thicknesses of 50, 100, 200, 400, and 800 Å were prepared and assigned sample numbers 1 through 5, respectively.

TABLE 1.--Oxide film thicknesses measured by transmission electron miscropy. (Nominal thickness assumed 12 Å/V.)

Sample number	Anodization voltage	Thickness (Å)	
		Nominal	Actual
1	4.17	50	144 ± 16
2	8.33	100	ND
3	16.67	200	321 ± 25
4	33.33	400	558 ± 90
5	66.67	800	1076 ± 85

*Assumed 12A per volt.

Segments were cut with a shear from the 7/8in. disks for TEM thickness measurements. Thin sections of the films and substrates were prepared by diamond knife ultramicrotomy of these segments. The sections were examined in a Siemens 102 TEM whose magnification was calibrated with the 15.06Å 6H SiC lattice plane image.

The alpha particle-induced x-ray measurements were made with a Kevex ALPHA-X system, which uses a radioactive curium-244 source (5.8MeV alpha particles) and a windowless Si(Li) detector to monitor the resultant x-ray spectra. The x-ray take-off angle was 90°. Two oxygen standards were used: a thick, high-purity sapphire (Al_2O_3) single crystal and a thermally grown silicon oxide film of known thickness on a silicon substrate. Although the x-ray spectrometer monitors all elements simultaneously, only the oxygen Kα data were used in the analyses.

Results and Discussion

Several thin sections were cut from each of the five samples and examined in the TEM. The oxide films were free of porosity and were fairly uniform in thickness from point to point on a given sample, except for sample 2 which was quite variable in the region of the microtomed sections. A micrograph of a film cross section of sample 5 is shown in Fig. 1. The thickness measurements are plotted in Fig. 2. There is a nearly linear relationship between thickness t and the anodic potential V:

$$t(\text{Å}) = 73 + 14.9V \tag{1}$$
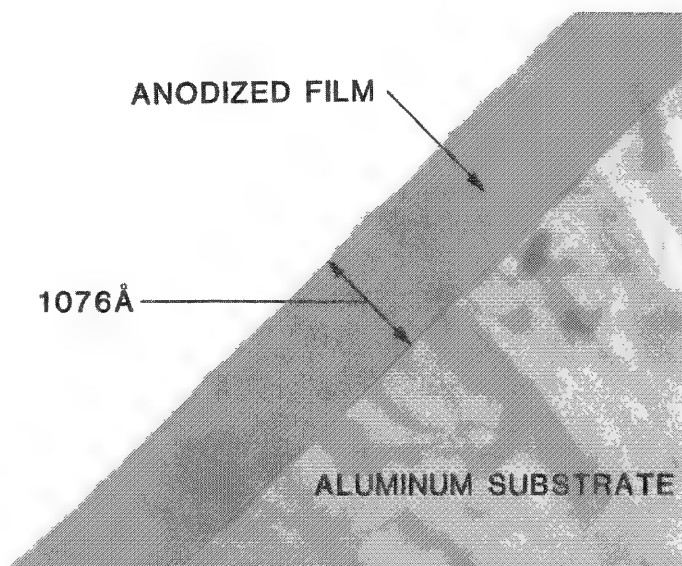
FIG. 1.--Oxide film cross section prepared by diamond knife microtomy, sample 5.
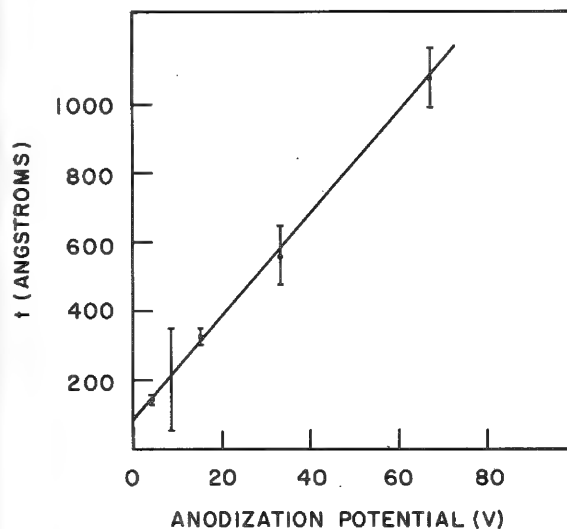
FIG. 2.--Oxide film thickness t, measured by TEM as a function of anodization potential.

The conversion factor of 14.9 Å/V is slightly higher than that given by Brock and Wood,[3] and the substrates apparently started with a 73Å film which was "transparent" to the anodization process.

The x-ray spectra from the thinnest and thickest films (samples 1 and 5, respectively) are shown in Fig. 3. Also shown are spectra from the two standard materials: the thermally grown silicon oxide film of known mass thickness and the bulk sapphire (Al_2O_3) single crystal. The integrated intensities from the films and standards are listed in Table 2.

Two methods were used to determine the oxide film mass thickness. In the first, the *oxygen* mass thicknesses L_0 were calculated by[4]

$$L_0(\text{g oxygen/cm}^2) = -\ (\rho/\mu)\ln[1 - 2.35 \times 10^{-6}(\mu/\rho)k_{\text{film standard}}] \tag{2}$$

188

TABLE 2.--X-ray intensity measurements.

| Sample | Analysis time | Number of analyses | Average O Kα integral | | Average background corrected O Kα integral/600 sec |
			Gross	Background corrected	
1	5000	2	27 644	9 477	1 137
2	1800	1	12 060	5 517	1 839
3	1200	3	10 255	5 663	2 831
4	600	1	8 007	5 383	5 383
5	600	3	12 977	10 516	10 516
Sapphire	600	1	96 000	91 315	91 315
Silicon oxide film	1800	1	9 580	5 280	1 760

where $\mu/\rho = 8144$ is the mass absorption coefficient of O Kα in silicon oxide[2] expressed in terms of (cm^2/g *oxygen*) and $k_{Film\ standard}$ is the ratio of background corrected O Kα intensity from the anodized film to that from the thermally grown silicon oxide standard. The latter was known to have 2.37 µg *oxygen*/cm^2.[5] If it is assumed that the anodized films are homogeneous stoichiometric Al_2O_3, their mass thicknesses are given by

$$\rho t(g^2\ \text{oxide/cm}^2) = L_0/C_0^{Al_2O_3} \tag{3}$$

where $C_0^{Al_2O_3} = 0.47$ is the weight fraction of oxygen in alumina. The k-ratios based on the silicon oxide film standard and the corresponding mass thickness are given in Table 3.

TABLE 3.--The k-ratios and mass thickness.

| Sample | Silicon oxide film standard | | Sapphire bulk standard | |
	k-ratio	$\rho t(\mu g/cm^2)$	k-ratio	$\rho t(\mu g/cm^2)$
1	0.6460	3.23	0.0125	3.28
2	1.045	5.28	0.0201	5.30
3	1.609	8.17	0.0310	8.22
4	3.059	15.8	0.0589	15.8
5	5.975	31.7	0.1152	31.9

In the alternate method, based on the pure Al_2O_3 bulk standard, it was assumed that the distribution in depth of O Kα x-ray production is constant beneath the surface through depths from which these x rays can escape and that alpha particle scattering back through the surface is negligible. The k-ratio ($I_{0K\alpha}^{Film} / I_{0K\alpha}^{Bulk}$) is then given by

$$k = \frac{A \int_0^{\rho t} \exp[-(\mu/\rho)\ z]\ d\rho z}{A \int_0^{\infty} \exp[-(\mu/\rho)\rho z]\ d\rho z} \tag{4}$$

$$= 1 - \exp[-(\mu/\rho)\rho t] \tag{5}$$

where $\mu/\rho = 3833\ cm^2/g$ is the mass absorption coefficient of O Kα in Al_2O_3[2] and A is a constant that incorporates factors such as the detector efficiency, detection solid angle, and fluorescence yield. These factors are the same for the standard and unknown and therefore cancel. The mass thickness of the oxide is then given by

189
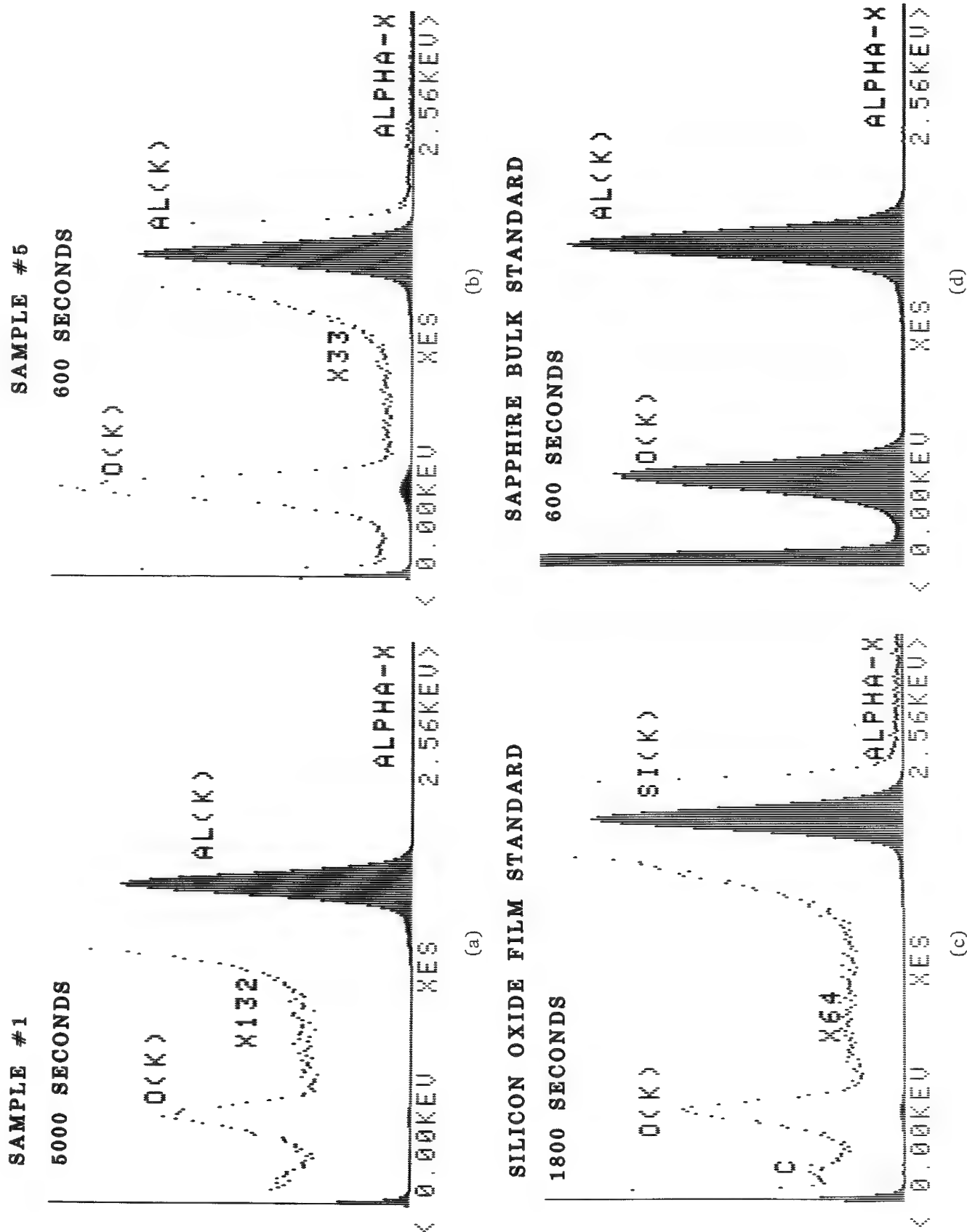
FIG. 3.--ALPHA-X spectra: (a) thickest and (b) thinnest oxide film, and (c) thin-film and (d) bulk standards.

$$\rho t(g\ oxide/cm^2) = -\ (\rho/\mu)\ln(1 - k_{Bulk\ standard}) \qquad (6)$$

Mass thicknesses for the oxide films were calculated and are also listed in Table 3.

Figure 4 is a plot of the film mass thicknesses ($\mu g/cm^2$) for the two sets of calculations versus the film thicknesses measured by TEM. The TEM value of 197A for sample 2 was calculated from Eq. (2) since a reliable film-thickness measurement was not made. The solid line is a linear least-squares fit to the data. The slope gives a film density $\rho = 3.05\ g/cm^3$. This value is lower than the range (3.5-$3.9\ g/cm^3$) of handbook values for Al_2O_3 but within the range for aluminum oxide films prepared by anodization.[6] That the line in Fig. 4 does not pass exactly through the origin may be due to the higher density (by a factor of two) of the anodized films compared with that of the thin oxide films on the substrate prior to anodization; however, unknown errors in the TEM measurements may also be significant.

FIG. 4.--Oxide film mass thicknesses ρt determined by ALPHA-X as a function of TEM linear thickness measurements: (□) based on silicon oxide thin film standard, (o) based on sapphire standard.

Conclusions

Alpha particle induced x-ray emission studies have been shown to provide excellent agreement between the mass thickness results obtained with a thin film silicon oxide standard and those obtained with a bulk sapphire standard. Combining the results with TEM thicknesses measurements on microtomed film cross sections yielded a density of $3.05\ g/cm^3$ for the oxide films grown by the particular anodization process. Evidence for a less dense film prior to anodization was consistent with the initial film being transparent to the anodization.

References

1. R. G. Musket, "Thin layer analysis with alpha-induced x-ray emission," *Research/Development* 28(10): 26, 1977.

2. W. J. Veigele, "Photon cross sections from 0.1 keV to 1 MeV for Elements Z = 1 to Z = 94," *Atomic Data Tables* 5: 51-111, 1973.

3. A. J. Brock and G. C. Wood, "Hydroxl ion and proton mobility during anodic oxidation of aluminum," *Electrochemica Acta* 12: 395-412, 1967.

4. R. G. Musket and W. Bauer, "Oxide-thickness determination by proton-induced x-ray fluorescence," *J. Appl. Phys.* 43: 4786-4792, 1972.

5. A. Lurio, IBM Research Laboratories, Yorktown Heights, N. Y., private communication.

6. S. Tajima, "Anodic oxidation of aluminum," *Adv. Corrosion Sci. & Tech.* 1: 336, 1971.

RAPID QUANTITATIVE ANALYSIS OF INDIVIDUAL MICROPARTICLES USING THE α- FACTOR APPROACH

J. T. Armstrong

A rapid semi-empirical correction method enabling the quantitative analysis of individual microparticles is described. Initial results indicate that this new correction method yields corrected analyses of accuracy comparable with those obtained by use of full ZAF particle corrections.

Theoretical equations have been developed that correct for atomic number, absorption, and fluorescence effects in unpolished particles of given size and shape.[1] These Armstrong-Buseck corrections enable the accurate quantitative electron microprobe analysis of individual microparticles.[2,3]

The use of the Armstrong-Buseck particle analysis method is limited by the extensive computational time needed for the numerical integrations used in the correction procedure. Corrections employed for a typical particle analysis, by means of the original BASIC language correction program of Armstrong,[2] require approximately 10 sec of CPU time on a moderate speed computer (Univac 1110) and well over 10 min of real time on a typical minicomputer.

In an attempt to enable a faster means of implementing the Armstrong-Buseck correction method, I have explored the development of particle "α-factors" similar to those employed by Ziebold and Ogilvie for thick polished binary alloys,[4] and by Bence and Albee for thick polished silicate and oxide specimens.[5,6] Initial results indicate that particle α-matrices can be successfully used in a simple and accurate correction procedure.

Development of the Analytical Expression

The α-factor approach is based upon two assumptions.

1. In binary systems, AB, there is a simple hyperbolic relation between relative concentration, C_{AB}^A, and relative intensity, K_{AB}^A, such that

$$\frac{1 - K_{AB}^A}{K_{AB}^A} = \alpha_{AB}^A \, \frac{1 - C_{AB}^A}{C_{AB}^A} \tag{1}$$

or

$$C_{AB}^A / K_{AB}^A = \alpha_{AB}^A + (1 - \alpha_{AB}^A) C_{AB}^A \tag{2}$$

where α_{AB}^A, the α-factor, is a constant for the AB binary. (K_{AB}^A is the ratio of the background-subtracted, deadtime-corrected, x-ray line intensity for the specimen in the binary to that for the pure A element or oxide end member; C_{AB}^A is expressed as an element weight fraction for an alloy system and as an oxide weight fraction for an oxide system.)

2. The relation between relative intensity and relative concentration in a multicomponent system ABC...n can be determined by a linear combination of α-factors determined for the different binary systems, so that
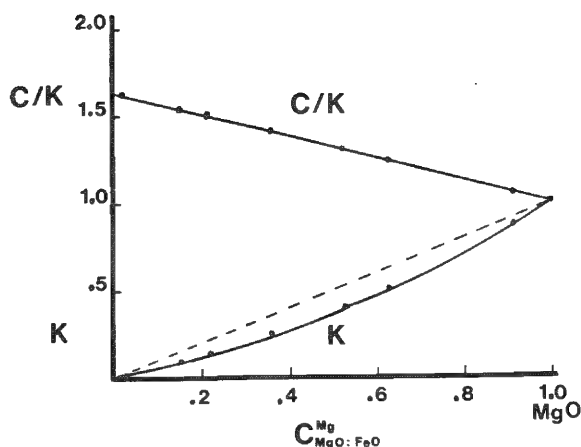
FIG. 1.--Plot of relative intensity K vs relative concentration C, and C/K vs C for Mg in tetragonal prism particles of mass diameter 1 mg/cm^2. Binary oxide system is MgO: FeO; accelerating potential is 15 keV; takeoff angle is 40°.
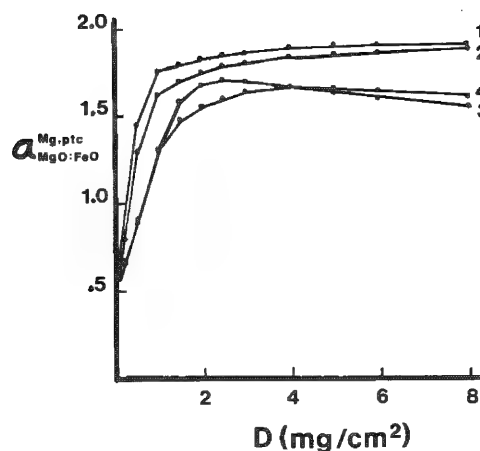
FIG. 3.--Plot of Mg α-factors vs mass diameter (mg/cm^2) for rectangular prism (1), tetragonal prism (2), triangular prism (3), and square pyramid (4) particles. Binary system is MgO:FeO.
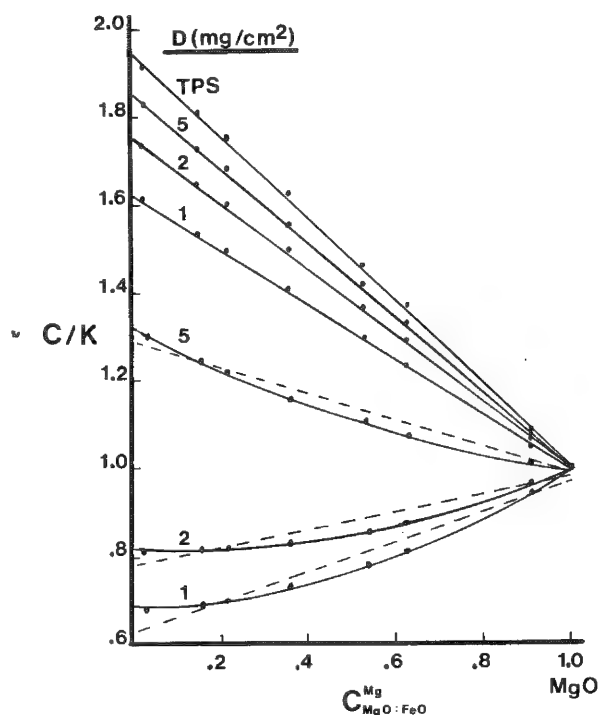
FIG. 2.--Plot of C/K vs C for Mg in thick polished specimen and in tetragonal prism particles of various mass diameters (mg/cm^2). Binary system is MgO:FeO.
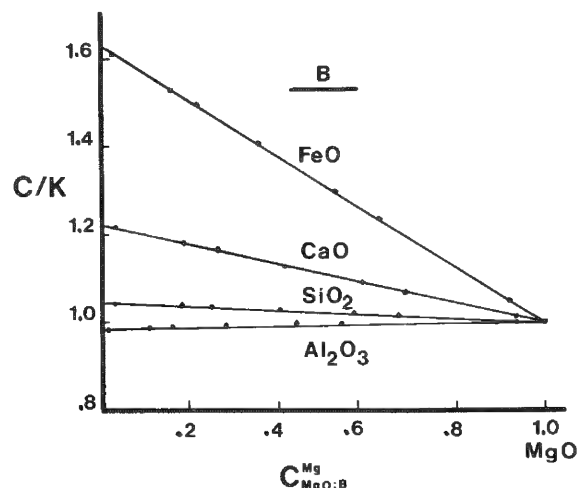
FIG. 4.--Plot of C/K vs C for Mg in tetragonal prism particles of mass diameter 1 mg/cm^2 for various binary oxide systems.

FIG. 5.--Plot of C/K vs C for various elements in tetragonal prism particles of mass diameter 1 mg/cm^2 for binary oxide systems containing MgO.

194

$$\beta^A_{ABC...n} = C^A_{ABC...n}/K^A_{ABC...n} = \frac{C^A_{ABC...n}\alpha^A_{AA} + C^B_{ABC...n}\alpha^a_{AB} + \cdots + C^n_{ABC...n}\alpha^A_{An}}{C^A_{ABC...n} + C^B_{ABC...n} + \cdots + C^n_{ABC...n}} \quad (3)$$

For a particle system, $K^{A,ptc}_{AB}$ and $K^{A,ptc}_{ABC...n}$ correspond to the ratio of the net intensity of the x-ray line of element A in a particle of a given size and shape in the binary or multicomponent system to the net intensity for a particle of the same size and shape having the end member composition. If the a-factor approach is applicable to particulate specimens, $a^{A,ptc}_{AB}$ must be a constant for particles of a given size and shape in a binary system. However, the value of $a^{A,ptc}_{AB}$ in a given binary may be different for different particle sizes and shapes.

Simulations

Simulations were performed to determine whether the two assumptions of the a-factor approach are applicable to systems involving individual, unpolished microparticles. From the correction equations of Armstrong and Buseck, relative intensities were calculated for given particle compositions, sizes, and shapes in the quinary oxide system $MgO-Al_2O_3$-SiO_2-CaO-FeO. The compositions chosen were the pure end members and the 20:1, 3:1, 2:1, 1:1, 1:2, 1:3, and 1:20 oxide proportions for each binary pair. The simulations were performed for an accelerating potential of 15 keV and a spectrometer take-off angle of $40°$.

Mass diameters used in the simulations were 0.1, 0.2, 0.5, 1, 1.5, 2, 2.5, 3, 4, 5, 6, and 8 mg/cm^2. (1 mg/cm^2 is equivalent to a diameter of 10 μm for a density of 1 g/cm^3.) The geometric models used in the simulations, in addition to the thick polished specimen, were the rectangular prism, the tetragonal prism, the triangular prism, and the square pyramid. (See Armstrong and Buseck[1] for the description of these models.) The particle thickness was set equal to the diameter for the first two models, and to half the diameter for the second two models. The whole particle was assumed to be bombarded with electrons from the primary beam.

Intensities relative to a thick polished specimen of the same composition were calculated for each particle model, at each diameter, for each of the binary compositions. The results were processed to yield particle intensities relative to the pure oxide particle of the same size and shape and to the pure oxide thick polished specimen (per incident electron striking the sample). Relative intensities for thick polished specimens were calculated both by the algorithms of Armstrong and Buseck and by a modified version of the ZAF-based FRAME correction program of Yakowitz et al.[7]

The a-factors were determined by a least squares fit to a straight line of $C^A_{AB}/K^{A,ptc}_{AB}$ vs C^A_{AB} for each of the compositions simulated for a given bin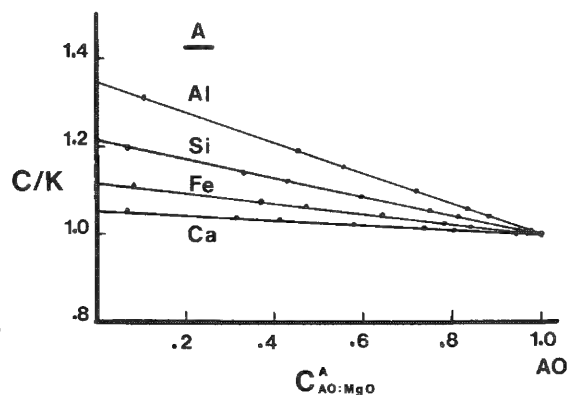ary system, particle diameter, and particle geometry (Eq. 2). The a-factor was set equal to the average of the y-intercept and 1 minus the slope of the least-squares fit. The correlation coefficient was used as a test of the constancy of the a-factor for the binary system.

Results of Simulations

Figure 1 shows the relation between relative x-ray intensity and relative concentration for a typical particle binary system--Mg in the binary MgO-FeO for tetragonal prism particles of mass diameter 1.0 mg/cm^2. As can be seen in the figure, there is indeed a simple hyperbolic relationship between C and K, and thus a linear relation between C/K and C. The least-squares fit of C/K vs C yields a slope of -0.635 and a y-intercept of 1.632 for an a-factor of 1.633. The correlation coefficient for the least squares fit is 0.99993.

The linearity between C/K and C shown in Fig. 1 is typical for Mg in the MgO-FeO system, as can be seen in Fig. 2, which presents data for thick polished specimens and for tetragonal prism particles of all of the diameters used in the simulations for this binary. For diameters of 1.0 mg/cm^2 or greater, the correlation coefficients of the least-squares fits are 0.9996 or better. The fits for diameters from 0.1 to 0.5 mg/cm^2 are not quite as good, with correlation coefficients ranging from 0.947 to 0.989; however, they are still quite adequate.

It was typical in all the simulations that the poorest fits occurred for the smallest particle diameters where the absorption correction was minimal and electron transmission was the major factor affecting x-ray intensity. Even in these cases, the calculated value of C/K for a given C from the least-squares fit did not differ from the simulated value by more than 5% relative.

The dependence of the calculated $a_{MgO:FeO}^{Mg,ptc}$ on particle size and shape can be seen in Fig. 3. As is obvious in the figure, there is a large variation of the a-factor with the various sizes and shapes. The a-factor depends more on particle size than on particle shape for small particles, and more on shape than size for large particles.

The linear relation between C/K and C for particles of a given size and shape holds for all the binary pairs tested in these simulations. The fits for 1 mg/cm^2 diameter tetragonal prism particles in all binary systems with MgO as a member are shown in Figs. 4 and 5. The a-factors for particles of this shape and size in the quinary system are given in Table 1 and compared with the a-factors for thick polished specimens. Since there is less absorption in small particles than there is in thick polished specimens, the a-factors for the light, heavily absorbed elements are considerably less for the particles than they are for the thick polished specimens.

The fits for all particle binary pairs in the quinary system are comparable with those for thick polished specimens. In most cases the correlation coefficients for the particle fits are greater than 0.99. Thus, the first assumption of the a-factor approach--the linear relation between C/K and C in a binary--appears valid for particle systems.

The ultimate test of the validity of the a-factor approach is, of course, its ability to relate relative intensity to relative concentration in multicomponent systems. In particle analysis, it is desirable to employ thick polished specimens, rather than individual particles, as standards. It is therefore useful to define a modified $\beta_{ABC...n}^{'A,ptc}$:

$$\beta_{ABC...n}^{'A,ptc} = C_{ABC...n}^{A}/K_{ABC...n}^{'A,ptc} \tag{4}$$

where $K_{ABC...n}^{'A,ptc}$ is the intensity, per incident electron striking the sample, of the x-ray line of element A in a particle of given size and shape in a multicomponent system relative to the intensity of a *thick polished specimen* having the end member composition. Thus,

$$K_{ABC...n}^{'A,ptc} = K_{ABC...n}^{A,ptc} \cdot k_A \tag{5}$$

where k_A is the ratio of the intensity of the end member particle to that of the end member thick polished specimen, per incident electron (the k_A factor defined in Armstrong and Buseck[1]). Combination of (3) and (5) yields

$$\beta_{ABC...n}^{'A,ptc} = \frac{C_{ABC...n}^{A}a_{AA}^{A,ptc} + C_{ABC...n}^{B}a_{AB}^{A,ptc} + \cdots + C_{ABC...n}^{n}a_{An}^{A,ptc}}{k_A (C_{ABC...n}^{A} + C_{ABC...n}^{B} + \cdots + C_{ABC...n}^{n})} \tag{6}$$

From the simulation procedures of Armstrong and Buseck,[1] a matrix of k_A values for each end member composition, at each particle size and shape, can be calculated. Table 2 lists the appropriate k_A values for the a-factor matrix given in Table 1.

To test the validity of the a-factor approach in a multicomponent system, the following simulations were performed. $K_{ABC...n}^{'A,ptc}$ values were calculated for particles of various sizes and shapes having the composition of MgFeSiO$_4$ (olivine). Using these K-factors as a first estimate of $C_{ABC...n}^{A}$, and taking the appropriate values from Tables 1 and 2, one may solve Eq. (6) for a first estimate of $\beta_{ABC...n}^{'A,ptc}$. A second estimate of $C_{ABC...n}^{A}$ is then calculated from the relation

$$C_{ABC...n}^{A} = \beta_{ABC...n}^{'A,ptc} \cdot K_{ABC...n}^{'A,ptc} \tag{7}$$

196

TABLE 1.--a-factors for thick polished specimens (TPS) and tetragonal prism particles of mass diameter 1 mg/cm^2 (Ptc) in quinary oxide system.

			a-factor matrix, TPS		
A \ B	MgO	Al$_2$O$_3$	SiO$_2$	CaO	FeO
Mg	1	1.01	1.09	1.32	1.95
Al	1.74	1	1.02	1.16	1.57
Si	1.44	1.50	1	1.06	1.29
Ca	1.07	1.07	1.09	1	.94
Fe	1.12	1.11	1.13	1.12	1

			a-factor matrix, Ptc		
A \ B	MgO	Al$_2$O$_3$	SiO$_2$	CaO	FeO
Mg	1	.98	1.04	1.22	1.63
Al	1.35	1	1.00	1.11	1.37
Si	1.21	1.23	1	1.04	1.17
Ca	1.05	1.04	1.07	1	.93
Fe	1.12	1.11	1.13	1.11	1

TABLE 2.--k_A factors for pure oxide tetragonal prism particles of mass diameter 1 mg/cm^2.

A	k_A
Mg	1.19
Al	1.14
Si	1.10
Ca	1.01
Fe	1.00

TABLE 3.--Results of a-factor calculations of compositions (in oxide wt. %) of MgFeSiO$_4$ tetragonal prism (A) and square pyramid (B) particles of various mass diameters (mg/cm^2).

MgFeSiO$_4$		Oxide weight percent		
Diam.	Model	MgO	SiO$_2$	FeO
0.2	A	24.5	35.0	40.5
	B	24.7	35.0	40.3
1.5	A	23.6	34.7	41.7
	B	23.6	34.8	41.7
2.0	A	23.6	34.8	41.6
	B	23.6	35.0	41.4
3.0	A	24.4	34.5	41.2
	B	23.5	34.9	41.5
4.0	A	23.5	34.8	41.7
	B	23.4	34.9	41.7
6.0	A	23.4	34.8	41.7
	B	23.3	34.8	41.8
Actual		23.4	34.9	41.7

The new values of concentration are then used to calculate new estimates of β' and the cycle is repeated until convergence is obtained.

Since in real particle analysis the electron beam or scanned area is larger than the particle cross section, the relation between the number of electrons striking the particle and those striking the standard is unknown, and the results for the concentration must be normalized. In these simulations, no more than three iterations were required in any case before the normalized concentrations converged to differences of less than 0.1 wt. %.

Table 3 lists representative results of these simulated analyses. The errors produced by using the α-factor method are minimal; that is, both the simplified α-factor approach and the full Armstrong-Buseck method yield approximately the same results. The largest errors produced in the simulations are less than 6%, and the typical errors are less than 1% relative. These results indicate that concentration-weighted combinations of α-factors can be successfully used to relate intensities to concentrations in multi-component particle systems. Thus, both criteria for the application of the α-factor method to quantitative particle analysis appear to be met.

Discussion

The α-factor approach appears to be an accurate and quick method of implementing the Armstrong-Buseck particle corrections. Unlike the case of the thick polished specimens for which there is only one α-matrix for a given accelerating potential and take off angle, a series of α-factor matrices are required for the various particle sizes and shapes encountered in analysis.

As seen in Fig. 3, the variation of the α-factor with particle size is regular, and linear interpolation between α-factor matrices of different diameters is possible. Access to a high-speed computer is required for the initial compilation of α-factor matrices. Matrices for a given, limited number of particle sizes and shapes can be calculated and stored on a fast-retrieval data-storage device, such as a floppy disk. Once that is done, the interpolation of matrices and α-factor corrections can be executed very quickly with a small minicomputer system.

We are at present completing the computer programs to calculate and compile particle α-factor matrices and are acquiring a series of such matrices. Programs to implement these matrices in particle analysis are available.

References

1. J. T. Armstrong and P. R. Buseck, "Quantitative chemical analysis of individual microparticles using the electron microprobe," *Anal. Chem.* 47: 2178, 1975.

2. J. T. Armstrong, *Quantitative Electron Microprobe Analysis of Airborne Particulate Material*, Ph.D. Thesis, Arizona State University, Ann Arbor, Mich.: Microfilms International, 1978.

3. J. T. Armstrong, "Methods of quantitative analysis of individual microparticles with electron beam instruments," *SEM/1978/I*, 455.

4. T. O. Ziebold and R. E. Ogilvie, "An empirical method for electron microanalysis," *Anal. Chem.* 36: 322, 1964.

5. A. E. Bence and A. L. Albee, "Empirical correction factors for the electron microanalysis of silicates and oxides," *J. Geol.* 76: 382, 1968.

6. A. L. Albee and L. Ray, "Correction factors for electron probe microanalysis of silicates, oxides, carbonates, phosphates, and sulfates," *Anal. Chem.* 42: 408, 1970.

7. H. Yakowitz, R. L. Myklebust, and K. F. J. Heinrich, *FRAME: An On-line Correction Procedure for Quantitative Electron Probe Microanalysis*, NBS Tech. Note 796, 1973.

TERRESTRIAL AND EXTRATERRESTRIAL POLLUTION IN THE STRATOSPHERE

D. E. Brownlee

The stratosphere is an unusual terrestrial environment that contains a rather exotic mixture of sulfuric acid aerosols, sapphires, and meteorites. The submicron regime is dominated by sulfate aerosols[1] of terrestrial origin, but the size range above 5 μm is composed primarily of materials from sources above the atmosphere.[2] Large terrestrial particles are exceedingly rare owing to high sedimentation rates, of the order of a kilometer per day, and the general lack of mechanisms for vertical transport of large particles above the tropopause. Large particles are injected from the troposphere into the stratosphere, but only during transient events such as thunderstorms, volcanic eruptions, and nuclear explosions. Most of the large stratospheric particles are either aluminum oxide or particles of extraterrestrial origin. The aluminum oxide particles are rocket exhaust produced by oxidation of aluminum powder used as a fuel additive in solid fuel boosters. The cosmic particles are interplanetary debris produced by gradual disintegration of comets and asteroids.

Over the past decade we have collected and analyzed 3-50μm stratospheric particles in an attempt to obtain samples of comets. The spatial density of 10μm particles is only about 10^{-3} m^{-3}, so that collection methods were required to sample huge volumes of air and produce only minor levels of contamination. Our successful collection schemes used inertial impaction from a high-velocity air stream onto very clean oil-coated collection plates. At first we made collections from balloons at 34 km using a large hydrazine-fueled air pump. The balloon experiments collected the first interplanetary particles, but now collections are made exclusively by routine aircraft sampling. The aircraft collections offer the advantage of a large number of collection hours per year. Collections are made at 20 km by means of a collector mounted under the wing of a NASA U-2 aircraft flown by Ames Research Center. The collector was built by G. V. Ferry and Neil Farlow at Ames to collect submicron stratospheric aerosols. For large particles it was modified to accept a 33cm^2 impactor plate. During collection the plate is placed in the ambient air stream with the surface normal to the air flow. When not collecting the surface is shielded in a cannister to prevent contamination. Each collection surface is rammed through ambient air for a cumulative time of 40 hr at 200 ms^{-1} before return to the laboratory for analysis. To prevent particle bounce off the collection surfaces are coated with 20μm films of 5×10^5 centistokes silicone oil. All handling and preparation of the collection surfaces are done in a class 100 laminar flow cleanroom with specially designed tools and techniques.

In the laboratory particles are located on the collection surfaces by means of an optical stereo microscope, and they are individually removed by tapered glass fibers held with a micromanipulator. The particles are next mounted on a drum-like mount consisting of a nuclepore filter glued to an electropolished stainless-steel ring. The particles are placed on a grid-like pattern produced by evaporating Pd through a mask overlay. After a sample drum is loaded with 48 particles it is placed on a fritted glass disk saturated with hexane (Fig. 1). The hexane wicks up through the nuclepore and washes the oil from the particles without moving them from their original positions. The particles are then coated with Pd and examined in the SEM. Routine analysis involves imaging and quantitative EDX analysis using the Armstrong-Buseck ZAF correction procedures for particles.[3]

In the initial SEM screening the particles are classified and the extraterrestrial particles are distinguished from rocket debris and aircraft or cleanroom contaminants. One third of the particles picked off are identifiable as cosmic on the basis of their

elemental compositions. Most of the particles have unfractionated elemental abundances similar to those in the Sun and primitive meteorites. Typical weight percent abundances are the following: 10%--Fe, Mg, Si; 5%--C, S; 1%--Na, Al, Ca, Ni; 0.1%--Cr, Mn, Ti. Following SEM work, the particles are subjected to a diverse array of studies depending on the particle type. These studies involve many laboratories and use techniques such as x-ray diffraction, use of a small diameter vacuum camera, neutron activation of individual particles,[4] rare gas analysis,[5,6] cosmic-ray ray track studies, Mg and Ca isotopic analysis,[7] IR measurements, light scattering, and Auger spectroscopy. Of increasing importance is TEM analysis of individual components of single particles. This technique requires first crushing the particle between slides (Fig. 2) and then mounting the debris on carbon films using either plastic replica techniques or floating the carbon film off the slide onto water. With sequential crushing on different slides, it is possible to take a single 10^{-9}g particle and mount it in the center squares of a half-dozen TEM grids.
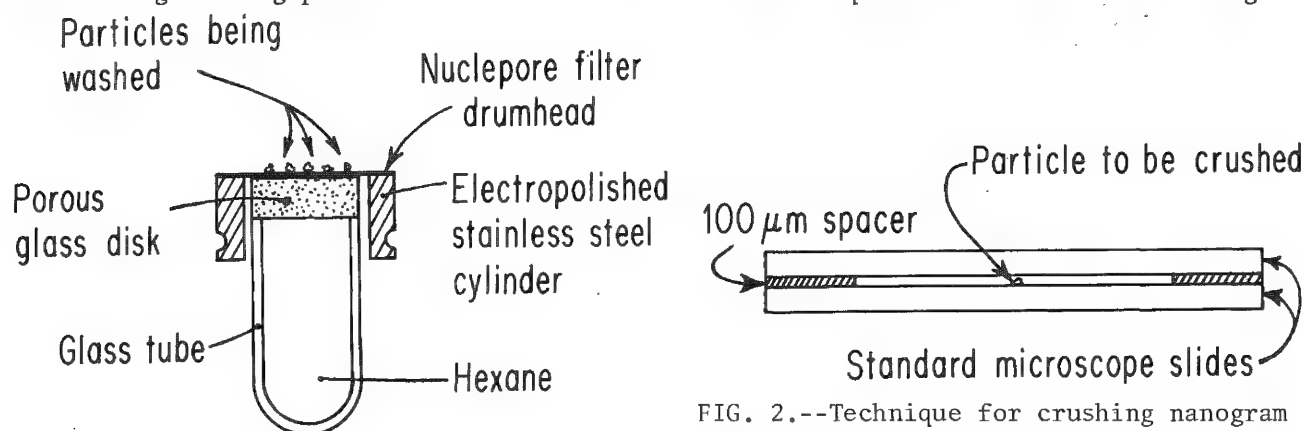
FIG. 1.--Apparatus for batch cleaning of silicone oil from particles mounted on nucleopore filter.

FIG. 2.--Technique for crushing nanogram particles prior to TEM analysis: particle is located in scribed circle on bottom slide and is crushed and ground by pressure on center of top slide.

The initial surprise of the work on large stratospheric particles was the finding of large numbers of transparent aluminum oxide spheres.[8] The spheres are usually colorless and quite round, and have smooth surfaces without adhering debris. The larger spheres are usually polycrystalline and grain boundaries produce a brain-like pattern on the sphere surfaces. At 3μm size the aluminum particles outnumber cosmic particles ten to one, but the size distribution is steep, and for sizes above 8 μm, cosmic particles are dominant. The stratospheric aluminum oxide spheres are identical to those collected in the plume of a Titan III missile.[9] The stratospheric concentration of spheres is fairly constant and apparently is maintained in quasi-equilibrium by injection of fresh particles from solid-fuel rockets, mainly the Titan III.

Analysis of 400 extraterrestrial particles collected in the stratosphere indicates that most are produced by gentle fragmentation of only a few meteoroid types. The particles are similar to primitive carbonaceous chondrite meteorites in respect to elemental composition. However, typical particles differ from all known meteorite types in the morphology and composition of individual constituent grains. The most common particles are aggregates of grains ranging in size from less than 50Å to microns (Figs. 3-5). Optically the particles are black even for sizes below 5 μm. In the SEM typical constituent grains appear to be about 0.3 μm but TEM analysis of crushed aggregates shows that many of the submicron grains are themselves aggregates of very small crystallites and amorphous grains.[10,11] Often the aggregates are highly porous and fragile. Micron-sized grains in the aggregates are usually olivine, enstatite, pyrrhotite, or pentlandite. Most of the submicron grains are silicates of nonstoichiometric compositions with Mg, Fe, and Si as major elements.

In addition to fine-grained aggregates of solar abundance materials, cosmic particles are also found that consist of single mineral grains ranging in size up to 50 μm. Gener-
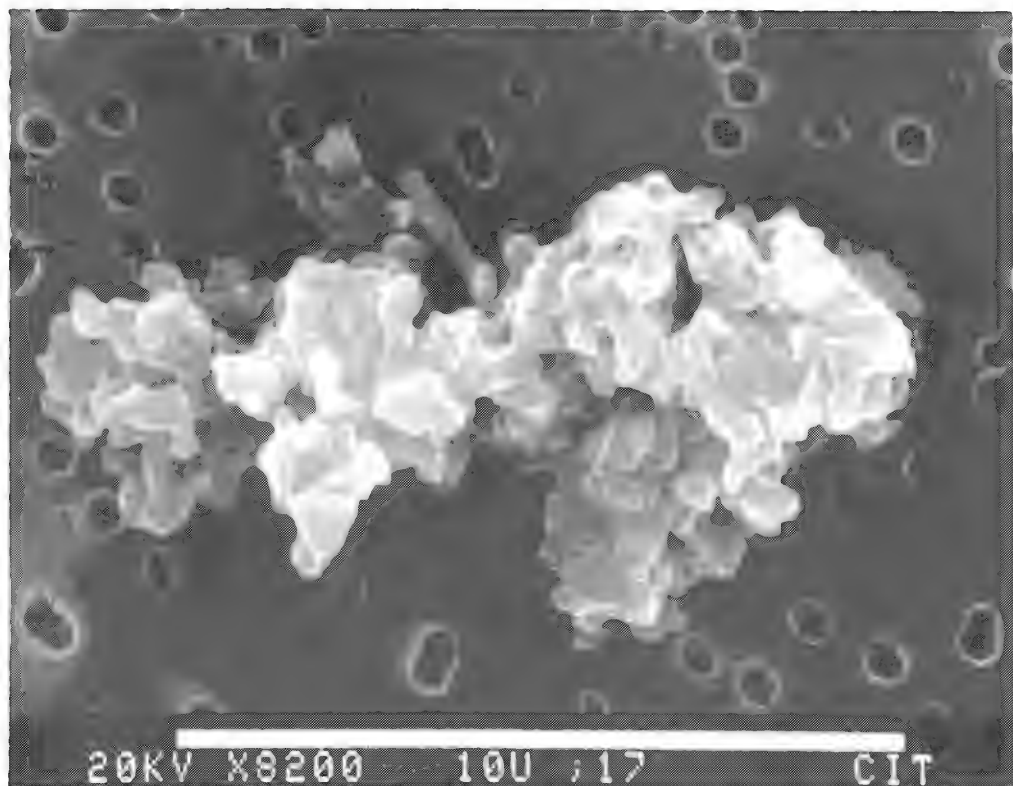
FIG. 3.--Typical extraterrestrial particle collected in stratosphere: bulk composition is similar to that of Sun for rock-forming elements; shaped grain is enstatite crystal.
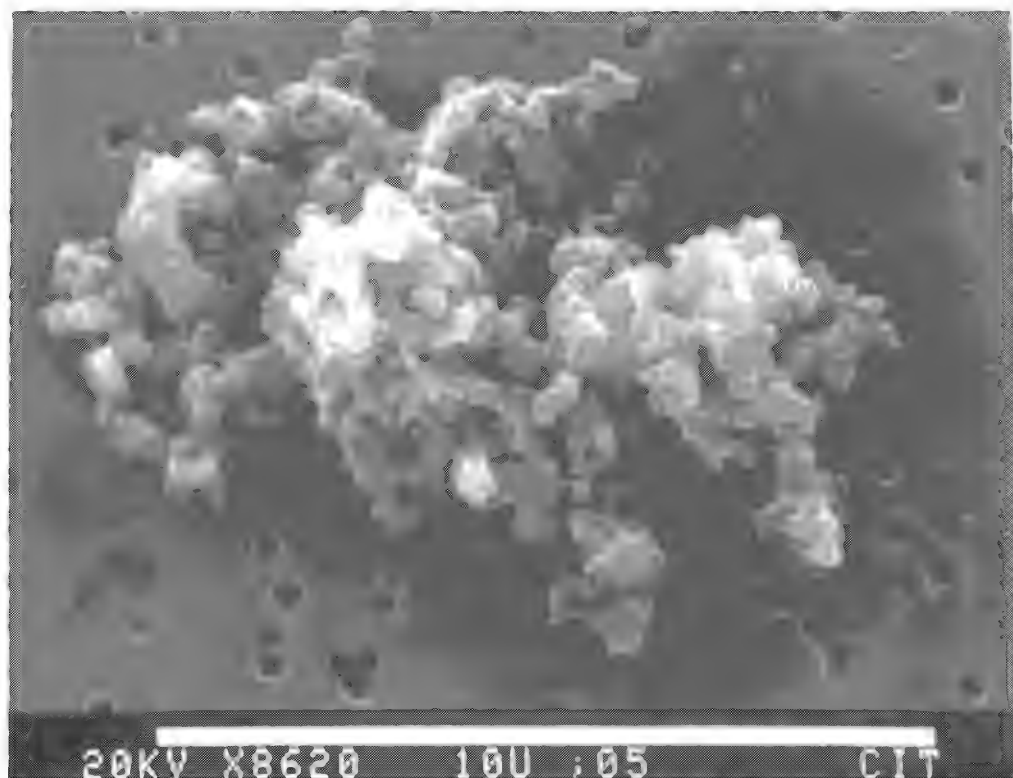
FIG. 4.--Cosmic aggregate particle similar to that in Fig. 3.

201

ally these particles are olivine, pyroxene, FeS, or FeNi metal. Particles of calcite and phosphate are occasionally found. The particles composed of single large grains are often coated with a black fine-grained material identical to the fine-grained "solar composition" particles. It is clear that the large grains were at one time embedded in a fine-grained matrix material similar to the aggregate particles.
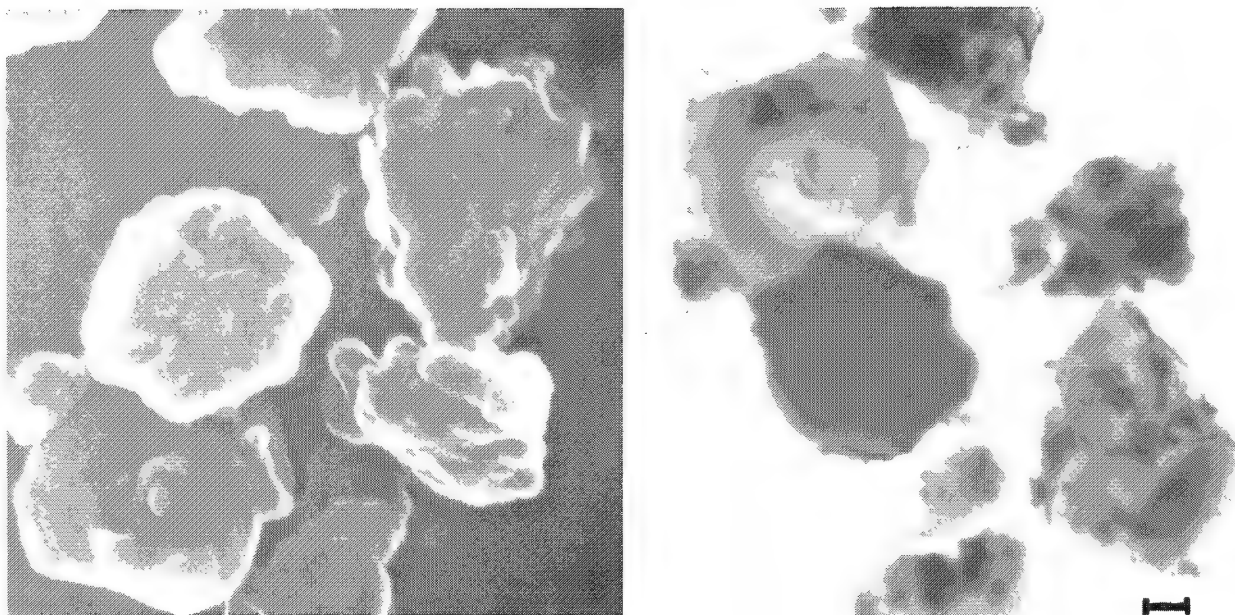
FIG. 5.--STEM (left) and SEM (right) pair of images of grains from crushed cosmic aggregate particle: prints are mirror images, dark grain in STEM is sulfide, others are silicates; some grains are single minerals, others are composites. Scale bar = 0.1 μm.

The study of large stratospheric particles has shown that the composition of stratospheric particulates is strongly size dependent. The submicron size range is dominated by "sulfate aerosol," but for sizes in the approximate range 1-10 μm most of the particles are transparent aluminum oxide spheres from solid-fuel rockets. For sizes larger than 10 μm most of the particles are extraterrestrial. The cosmic particles have primitive compositions, are fragile, and differ in important ways from the strong materials that survive atmospheric entry in large enough chunks to be found on land as meteorites. The cosmic particles are believed to be samples of interplanetary dust released from comets over the past 10 000 yr.

References

1. R. D. Cadle and G. W. Grams, "Stratospheric aerosols and their optical properties," *Rev. Geophys. Space Physics* 13: 475, 1975.
2. D. E. Brownlee, "Microparticle studies by sampling techniques," in J. A. M. Mc Donnell, Ed., *Cosmic Dust*, Chichester: Wiley, 1978, 295.
3. J. T. Armstrong and P. R. Buseck, "Qualitative chemical analysis of individual microparticles using the electron microprobe: Theoretical," *Annal. Chem.* 47: 2178, 1975.
4. R. Ganapathy and D. E. Brownlee, "Trace element analysis of individual interplanetary dust particles by neutron activation," *Science* 206: 1075, 1979
5. R. S. Rajan et al., "Detection of ^{4}He in stratospheric particles gives evidence of extraterrestrial origin," *Nature* 267: 133, 1977.
6. B. Hudson et al., "Rare gases in Brownlee particles: Proof of extraterrestrial origin," Lunar and Planetary Science XI (in press, 1980).
7. T. Esat et al., "Mg isotopic composition of interplanetary dust," *Science* 206: 190, 1979.
8. D. E. Brownlee, G. V. Ferry, and D. A. Tomandl, "Stratospheric aluminum oxide," *Science* 191: 1270, 1976.
9. G. V. Ferry and H. Y. Lem, "Particulates in solid fuel rocket exhaust," *EOS* 56: 1123, 1974.

THE CHEMICAL COMPOSITION OF INDIVIDUAL SUBMICRON SULFATE PARTICLES FROM AN AEROSOL NEAR A POWER PLANT

G. D. Aden and P. R. Buseck

The particulate emissions collected 70 km downwind of the Navaho coal-fired power plant in northern Arizona have been studied by the quantitative analysis of individual particles. The major submicron species are sodium sulfate and soot. A few of the smallest sulfate particles appear to have a silicate core. Rough size and volume distributions of the particles have been determined from SEM photographs. The sodium sulfate particles are abundant and distinctive and thus appear to be a good tracer for the detection of the long-range transport of emissions from the Navaho coal-fired power plant.

Introduction

Coal combustion plays a major role in the production of electricity in the USA and is a large source of particulates, including sulfates in the atmosphere. There have been extensive studies of the particulates formed during coal combustion and of the fate of the trace elements contained in the coal.[1] Recently there has been a major effort to understand the nature and fate of the sulfur species emitted, which have been linked with visibility reduction and adverse health effects.[2] Bulk chemical analyses of sized fractions have shown the size ranges in which the particulate sulfates are concentrated,[3] but only a few chemical species have been identified.[4,5]

To further understanding of the chemistry of the particulates released during coal combustion, the individual submicron particles collected in the plume of the Navaho coal-fired power plant have been studied. This plant is the largest in Arizona, with a full-load capacity of 2250 MW. Its three combustion units burn mostly low-sulfur western coal and are each outfitted with electrostatic precipitators.[6] By a procedure developed for an analytical scanning electron microscope (SEM) with energy-dispersive spectrometer (EDS), individual submicron particles have been imaged and chemically analyzed, qualitatively for all elements from Na to U and quantitatively for elements found in the particles. These data reveal substantial numbers of particles whose major chemical species are sodium and sulfur with atomic proportions of 2:1, respectively. Such emissions have not been previously described in power-plant plumes.

Sample Collection, Preparation, and Analysis

Samples were collected by means of 47mm serial nuclepore sampling heads[7] fitted with 12.0, 3.0, and 0.4µm nuclepore filters. Sample collection times varied from 15 min to 2 hr at a constant flow rate of 13 lpm. In all cases mass loadings on the filters were low enough so that particles were sufficiently dispersed to preclude reactions between particles and allow individual particle analysis. Samples were collected both within and outside of the emission plume; SO_2 levels monitored in the area were used to detect the presence of the plume. The presence or absence of fly ash spheres on the sample stages was used as an independent confirmation of whether or not a sample was from the plume or background. In all cases, these two methods agreed so that we believe the plume definition was adequate.

For the analyses, two 0.5cm squares were cut from each nuclepore filter and directly mounted to a carbon stub by a thin film of colloidal graphite between the filter and stub. One square was coated with gold-palladium for imaging, size analysis, and qualitative chemical analyses; the other square was coated with carbon and used for quantitative analyses.

A size distribution of particles on each filter was determined by measuring the particle sizes from a series of SEM photographs ranging in magnification from 200 to 30 000×.

A volume distribution was also calculated from the size measurements. These data were plotted in the manner described by Whitby[8] (Fig. 1), to permit comparisons with other studies.
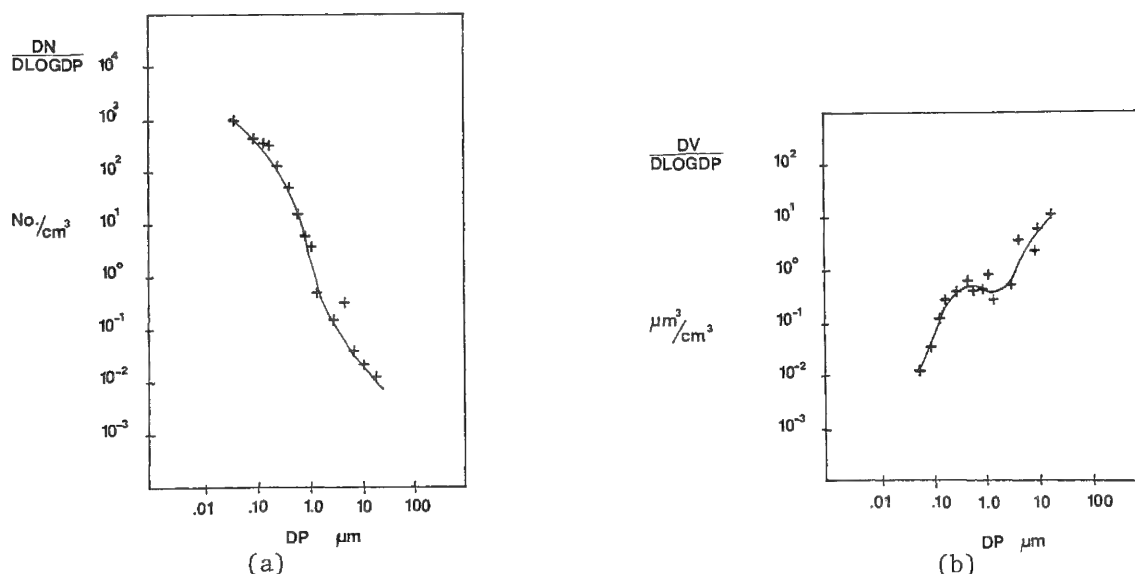
FIG. 1.--(a) Number size distribution for downwind sample taken in power-plant plume vs particle diameter DP; (b) volume distribution calculated from same data.

All samples for quantitative analysis in the SEM were run at a current of 4.0×10^{-10} amp, which allowed reasonable counting rates (2500 cps on quartz) and yet enabled imaging of particles as small as 0.1 μm. Thick polished samples of albite ($NaAlSi_3O_8$) and troilite (FeS) were used for the sodium and sulfur standards.

Data from the quantitative SEM/EDS individual particle analyses were reduced by procedures developed for minicomputers combining new theory[9] with portions of algorithms referenced and described previously.[10,11] We confirmed the accuracy of the analyses of individual particles by grinding crystals of reagent grade Na_2SO_4 to submicron size in a boron carbide mill and then analyzing them in the same manner as the aerosol samples.

Table 1 shows the results of the analyses of 20 standard particles ranging in size from 0.3 to 3.0 μm. It can be seen that the error in the analyses is well within the limits needed to identify the ratio of Na to S as 2:1 and thus the particles as Na_2SO_4 rather than $NaHSO_4$. However, this type of analysis does not allow sulfate to be distinguished from sulfite. With this limitation in mind, all samples will be treated as sulfate.

TABLE 1.--Average analysis of 20 standard Na_2SO_4 particles in the size range 0.3-3.0 μm; tσ is the precision at the 95% confidence level. Wt. % and errors relative to $NaHSO_4$ are presented for comparison.

Element	Average wt. %	tσ	true wt. % calc. as Na_2SO_4	% rel. error	true wt. % calc. as $NaHSO_4$	% rel. error
Na	33.6	(3.8)	32.4	+ 3.7	19.3	+ 74
S	21.9	(2.1)	22.6	- 3.1	26.9	- 19
O	44.5*	(-)	45.1	- 1.4	53.8	- 17

*Oxygen calculated by stoichiometry, Na_2O and SO_3 assumed.

204

Results

Qualitative analyses of several hundred particles in the 0.1-0.5μm size fraction show that the major species contain only sodium and sulfur (Fig. 2). A few of the smaller particles also show a small Si peak (Fig. 3). Quantitative analyses of many
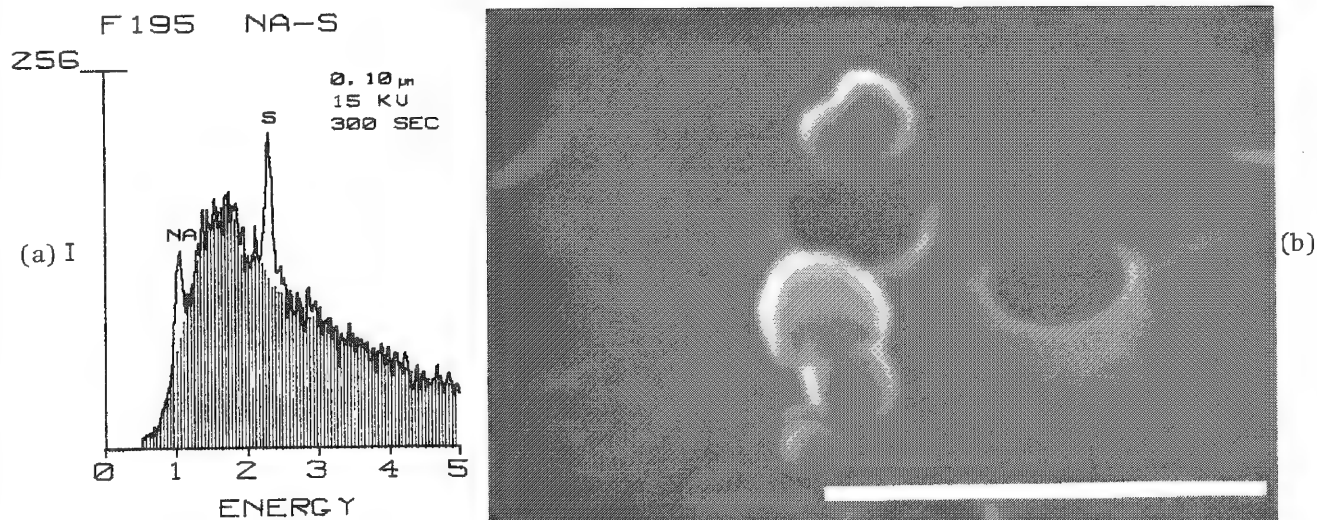
FIG. 2.--(a) Spectrum of 0.1μm sodium sulfate particle: shaded area shows calculated background; there were no visible peaks beyond 5 keV; (b) image of sodium and sulfur containing particles. (Scale bar is 1.0 μm).

particles at random in several $20 \times 20\mu m^2$ samples of filter showed that 90% have a Na to S ratio of 2:1 (Table 2). The remaining particles are agglomerates that gave no visible peaks in the x-ray spectrum. These particles are very stable within the electron beam, which precludes ammonium sulfate; they have the morphology of soot and are therefore presumably carbonaceous material (Fig. 4).

TABLE 2.--Average analysis of 30 aerosol particles in the size range 0.1-0.5 μm.

Element	Average wt. %	tσ	true wt. % calc. as Na_2SO_4	% rel. error
Na	32.8	(3.8)	32.4	+ 1.2
S	22.3	(1.8)	22.6	- 1.3
O	44.8*	(-)	45.1	- 0.7

* oxygen calculated by stoichiometry

The volume distribution calculated from the plume samples (Fig. 1b) shows a small peak centered in the diameter range Whitby has described as accumulation mode aerosol.[8] This peak is very small when compared with the volume distributions calculated by others for power plant plumes,[12] probably because of the amount of dilution of primary particulates that has taken place by the time the plume reached our collectors. It would also seem to indicate that not much secondary growth of particles from smaller size ranges into this intermediate range had taken place yet.
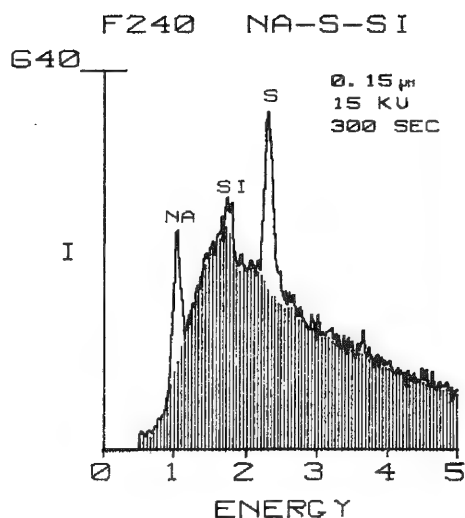
FIG. 3.--Spectrum of 0.15µm sodium
sulfate particle showing evidence
of silicate core.
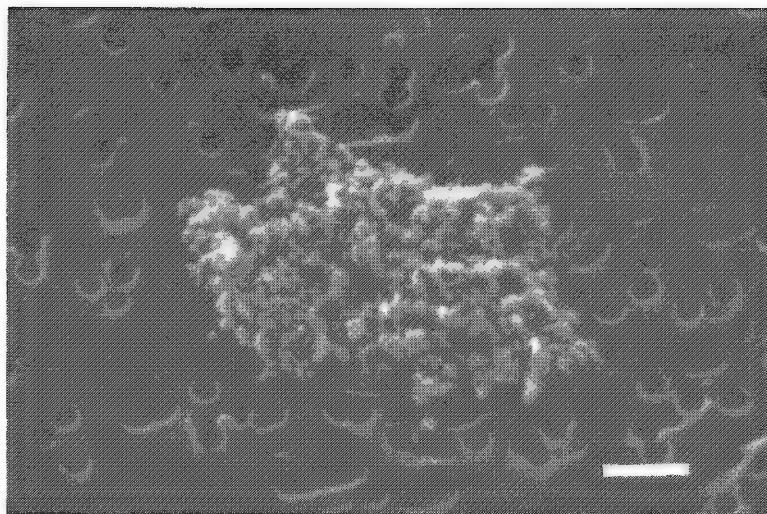
FIG. 4.--SEM image of soot particles. (Scale bar
is 1.0 µm).

Conclusions

A major sodium sulfate phase has been identified in the submicron emissions of a
large coal-fired power plant. The presence of a Si peak in some of the sodium sulfate
particles may indicate that they were formed around a fly ash core. The intensity of
this peak would suggest that the core is less than 0.05 µm in size, but the data are
limited and therefore not conclusive.

Quantitative analysis of the individual particles indicates that the great majority
of submicron particles 0.1 to 0.5 µm in diameter are Na_2SO_4. It is curious and of some
concern that sodium sulfate particles have not been described previously as an emission
from coal-fired power plants and yet we have observed them in such abundance. Sodium
sulfates have been postulated as an artifact of sample collection from the reaction of
sodium chloride particles with sulfuric acid mist.[5,13] However, in this case no NaCl
particles were observed in the background samples (~0 SO_2 levels) and no sodium sulfate
particles have been observed on our control blanks. Small numbers of Na_2SO_4 are observed
in the background samples at about a 10-fold reduction in numbers when compared to the
plume samples. These are presumably particles emitted earlier that have not yet been re-
moved from the atmosphere. Sodium sulfite and bisulfate can be produced if the flue gas
is scrubbed by the Wellman-Power gas process[14] but not in the size range described and
certainly not in this case, as these gases are not scrubbed before being released.

The source for the sodium sulfates would seem to be by primary production during
coal combustion. Na_2SO_4 is known to be a major source of corrosion in coal-fired boil-
ers and presumably is also available to escape through the electrostatic precipitators
and up the stacks. It is not known why studies of power plants by mass-balance calcula-
tions have not described the sodium loss, but that may be due to the fact that even though
the numbers of particles are large, the actual mass associated with the particles is small.

The sodium sulfate particles have not been observed as emissions from other sources
in Arizona in this size range. However, large numbers of these particles are emitted
from the Navaho power plant. These facts, combined with the distinctive chemistry, mor-
phology, and size range of the particles, makes them a prime candidate for use in the
long-range tracing of coal-fired plumes.

References

1. R. C. Flagan and S. K. Friedlander, "Particle formation in pulverized coal com-
bustion: A review," in R. T. Shaw, Ed., *Recent Developments in Aerosol Science,* New York:
Wiley, 1978, pp. 25-60.

2.   National Research Council, *Sulfur Oxides*, Washington, D.C.: National Academy of Sciences, 1979.

3.   S. V. Herring, R. C. Flagan, and S. K. Friedlander, "A new low pressure impactor: Determination of the size distribution of aerosol sulfur compounds," Extended Abstracts Div. of Environ. Chem., Amer. Chem. Soc. Meet., 1977, 108.

4.   W. E. Wilson et al., "Sulfates in the atmosphere: A progress report on Project MISTT," EPA-60017-77-021. Research Triangle Park, N.C.: U.S. Environmental Protection Agency, 1977.

5.   P. D. E. Biggins and R. M. Harrison, "Characterization and classification of atmospheric sulfates," *J. Air Poll. Conf. Assoc.* 29:838, 1979.

6.   "A Southwest power plant saga," *Environ. Sci. Technol.* 10:532, 1976.

7.   R. D. Parker et al., "A two stage respirable aerosol sample using nuclepore filters in series," *Atmos. Environ.* 11: 617, 1977.

8.   K. T. Whitby, "The physical characteristics of sulfur aerosols," *Atmos. Environ.* 12:135, 1978.

9.   G. D. Aden and P. R. Buseck, in preparation.

10.   G. D. Aden and P. R. Buseck, "Rapid quantitative analysis of individual particles by energy dispersive spectrometry, *Microbeam Analysis--1979*, San Francisco: San Francisco Press, 1979, 254-258.

11.   J. T. Armstrong and P. R. Buseck, "Quantitative chemical analysis of individual microparticles using the electron microprobe: Theoretical," *Anal. Chem.* 47:2178, 1975.

12.   B. K. Cantrell and K. T. Whitby, "Aerosol size distributions and aerosol volume formation for a coal-fired power plant plume," *Atmos. Environ.* 12:323, 1978.

13.   J. H. Seinfeld, *Air Pollution: Physical and Chemical Fundamentals*. New York: McGraw-Hill, 1975, p. 57.

14.   H. C. Perkins, *Air Pollution*, New York: McGraw-Hill, 1974, p. 280.

15.   W. T. Reid, *External Corrosion and Deposits: Boilers and Gas Turbines*, New York: American Elsevier, 1971.

FIBROUS PARTICLES FROM A COPPER SMELTER AEROSOL

J. P. Bradley and P. R. Buseck

Recent studies of aerosol released from an Arizona copper smelter have indicated substantial concentrations of fibrous particles within the $< 10^4 Å$ size range. Although x-ray energy-dispersive analysis (EDS) yielded little information on their compositions, wavelength-dispersive analysis (WDS) has shown that carbon is a major constituent of the fibers. Subsequently, high-resolution transmission electron microscopy (HRTEM) was utilized to obtain lattice images from single particles. The measured fringe spacings obtained from some fibers are consistent with those of graphite. Other fibrous particles and particle agglomerates are seen to consist of single crystals joined together to form dendritic particle agglomerates. These particles contain elements of low atomic number and, as a result, their chemistry has not been fully characterized.

There are seven copper smelters in Arizona. Together they account for more than 50% of the copper produced in the USA by pyrometallurgical smelting.[1,2] It has been estimated that these smelters release about 40 000 tons of particulate material into the atmosphere every year.[3] Such large quantities of emitted debris pose the possibility of a health hazard to the population within the fallout region of the particulates. On the other hand, it is possible that the emissions do not produce serious health effects. Clearly, before any reliable conclusions can be reached regarding the environmental impact of these particles in the aerosol it is necessary to understand both bulk properties and individual particle characteristics including sizes, morphologies, and chemical compositions.

The bulk chemistry of particulates released from the Arizona copper smelters has recently been investigated.[4,5] However, little is known about the characteristics of individual component particles. We have initiated a study of particle emissions from a southern Arizona copper smelter and have encountered some unusual and distinctive fibrous particles in the smelter plume. They range in length from $10^3 - 10^4$ Å and have very distinctive morphologies. They occur in three forms: (a) single unbranched particles up to 10^4 Å in length, (b) four particles joined together in a tetrahedral arrangement, or (c) dendritic particle agglomerates formed by the linking together of several tetrahedra (Fig 1).

Collection Procedures

Samples were recovered over a six-month period from various locations within the valley surrounding the smelter. Most were collected at one of the eight emission monitoring stations built and maintained by the smelter personnel. Sampling episodes were timed to coincide with high SO_2 levels and/or when the plume had visibly descended over a station. Portable sampling equipment was also used during times of plume migration and for sampling at greater distances from the source. In addition, direct sampling of the plume was achieved by the use of a light aircraft. Particles were collected by vacuum filtration directly onto nucleopore substrates and TEM grids. Samples for light element analysis were collected with an Anderson cascade impactor onto aluminum substrates.

Analytical Techniques

Analyses were performed with an analytical scanning electron microscope (JEOL-JSM 35) with crystal spectrometer and Princeton Gamma Tech x-ray energy analyzer. In general the most common fibrous material found in aerosols is asbestos, a group of silicate minerals. Therefore preliminary investigations were confined to elements common to that group. However, EDS analysis shows no silicon signal, nor that of any other element except for minor
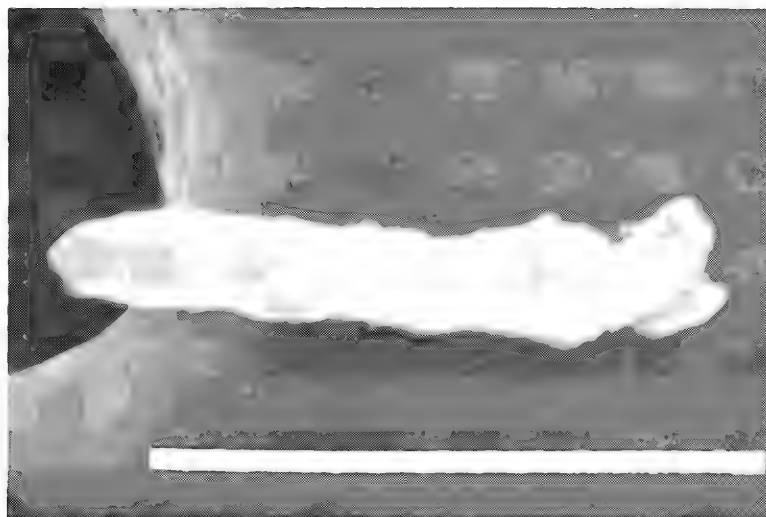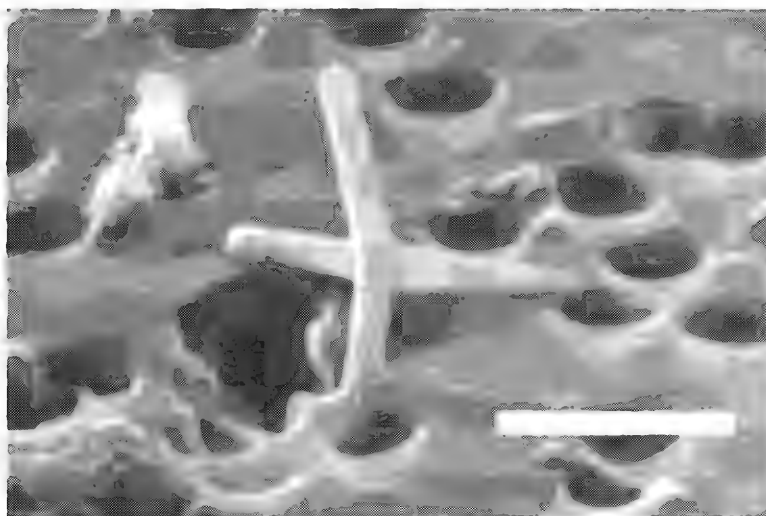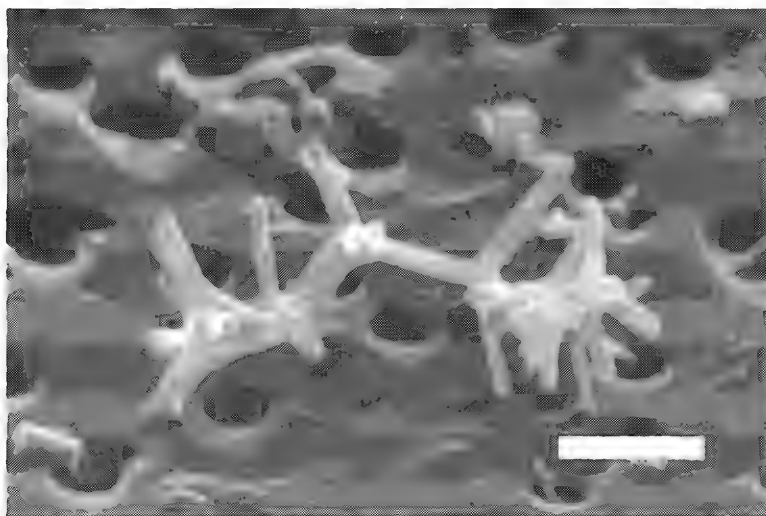
FIG. 1.--Three fibrous particle morphologies: (a) single fibers, (b) tetrahedra, (c) dendritic agglomerates. (Scale bars, 10^4 Å.)

sulfur which may be present on the particles as a surficial sulfate compound (Fig. 2).[6,7] In order to test for light elements, particles collected directly onto aluminum substrates were analyzed with the crystal spectrometer. Although the signals were weak and thus yielded a low peak-to-background ratio, the results suggest that both the single fibers and the fiber agglomerates contain carbon as a major constituent. (Since the smelter furnaces at this location are fired by coal and/or natural gas, this finding is not unexpected. In fact, carbonaceous particles, chiefly in the form of "soot," make up a substantial proportion of the respirable size range).

HRTEM was employed to obtain high-resolution images of single fibers (Fig. 3). The measured fringe spacings (3.4 Å) suggest that some of the particles are graphite fibers. Images obtained from particle agglomerates show single crystals joined together to form tetrahedra and dendritic structures. Electron diffraction and energy loss spectroscopy are being used currently to elucidate both the structures and chemical compositions of these particles.
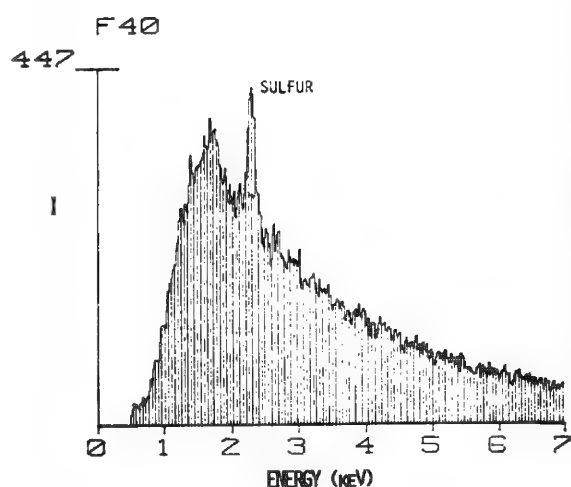
FIG. 2.--X-ray energy-dispersive spectrum of a fibrous particle agglomerate showing only minor sulfur, possibly present as a surficial sulfate.
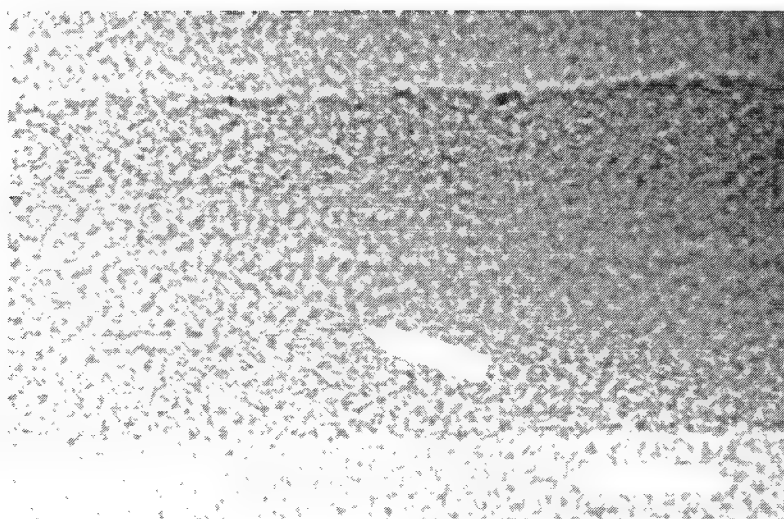
FIG. 3.--High-resolution transmission electron micrograph of a single fibrous particle. (Arrow shows 3.4Å fringe spacings. Scale bar = 100 Å.)

References

1. Arizona Department of Health Services, *First Annual Report on Arizona Copper Smelter Air Pollution Control Technology*, State of Arizona, 1977.
2. Arizona Department of Health Services, *Second Annual Report on Arizona Copper Smelter Air Pollution Control Technology*, State of Arizona, 1978.
3. Arizona Department of Health Services, *Particulate Monitoring Network Data:1971*, State of Arizona, 1972.
4. M. S. Germani et al., "Fractionation of elements during copper smelting," *Envir. Sci. Tech.*, in press.
5. M. Small et al., "An airborne plume study of emissions from the processing of copper ores in southeastern Arizona," *Envir. Sci. Tech.*, in press.
6. T. Novakov et al., "Sulfates as pollution particulates: Catalytic formation of carbon (soot) particles," *Science* 186: 259, 1974.
7. P. A. Russel, "Carbonaceous particulates in the atmosphere: Illumination by electron microscopy," in T. Novakov, Ed., *Proc. Carbonaceous Particles in the Atmosphere*, 1979.

APPLICATION OF INDIVIDUAL PARTICLE QUANTITATIVE ANALYSIS IN THE DETERMINATION OF AMBIENT AND SOURCE AEROSOL HETEROGENEITY

J. T. Armstrong and P. R. Buseck

A useful summary of individual particle quantitative analyses for air pollution samples is the determination of the degree of particle heterogeneity. The particle-heterogeneity level can provide valuable information regarding particle sources and formation mechanisms, and is applied in this paper to the characterization of suspended mineral material in an urban environment.

The quantitative analysis of individual airborne particles can provide important information regarding the nature, sources, and mechanisms of formation and modification of pollutant aerosols.[1,2] A serious problem in the analysis of individual particles, however, is how to summarize the many disparate particle compositions and relate them in any meaningful way to the bulk aerosol.

One approach of particle-data summarization is to characterize the typical compositions of particles from various sources and, by mass balance calculations, to relate them to the aerosol bulk composition. Such mass balance calculations require analysis of a large number of particles before accurate "typical" source particle compositions can be attained, and become impractical when the bulk aerosol is very heterogeneous.

Another means of aerosol characterization by individual particle analysis is the determination of the degree of particle heterogeneity. An aerosol emitted from a given source is composed either of particles of similar composition or of particles of different compositions. The degree of this particle heterogeneity can be an indicator of the mechanism of particle formation or modification, and can, in certain instances, act as a fingerprint of the particle source.

The determination of particle heterogeneity is a simple operation, but it requires individual particle *quantitative* analysis and cannot be inferred by bulk analysis and individual particle *qualitative* analysis alone. To determine the degree of particle heterogeneity, one simply performs quantitative analyses on a representative number of particles from the particular set to be studied (e.g., from a size fraction of particles of a given aerosol source). The mean $\bar{x}$ and standard deviation σ of the various element weight fractions are then determined. By dividing the standard deviation by the mean, one obtains a measure of the level of particle heterogeneity $\sigma/\bar{x}$. The larger the value of $\sigma/\bar{x}$, the greater the particle heterogeneity for that element in the aerosol. To determine whether a representative group of particles has been analyzed, the mean particle analysis can be compared to the measured bulk analysis.

We have employed particle heterogeneity determinations in the characterization of silicate and other mineral particles found in ambient air samples from the Phoenix, Arizona, metropolitan area. We have found that particle heterogeneity determinations are useful both in understanding the nature of mineral particle formation in the Phoenix aerosol and in distinguishing between some natural and anthropogenic mineral particle sources.

Methods of Collection and Analysis

Ambient and source particle samples were collected in conventional low-volume and cascade-impactor air samplers. Source samples were collected in close proximity and downwind from the source emission. The particles were transferred to graphite planchets, carbon coated, and analyzed with a Cameca MS-46 electron microprobe. The quantitative analy-

TABLE 1.--Mean element weight percents $\bar{x}$, and levels of heterogeneity $\sigma/\bar{x}$, for (A) coarse 5-7µm diameter, (B) medium 2-5µm diameter, (C) small 0.5-2µm diameter mineral particles from Phoenix ambient air sample.

	(A) Coarse		(B) Medium		(C) Fine	
	$\bar{x}$	$\sigma/\bar{x}$	$\bar{x}$	$\sigma/\bar{x}$	$\bar{x}$	$\sigma/\bar{x}$
Na	4.3	0.6	1.0	1.9	0.8	2.8
K	3.1	0.8	2.8	1.2	0.6	1.9
Ca	4.2	0.7	12.4	1.8	13.2	2.0
Mg	2.4	0.7	1.4	0.7	0.6	1.6
Fe	5.2	0.7	11.1	1.7	13.6	1.9
Al	9.8	0.5	7.7	0.7	6.1	1.4
Si	25.4	0.2	21.1	0.6	22.2	0.8
Ti	-	-	-	-	0.1	3.8
Cl	0.7	0.8	-	-	-	-
O	45.0	-	42.5	-	42.7	-

TABLE 2.--Mean element weight percents $\bar{x}$, and levels of heterogeneity $\sigma/\bar{x}$, for coarse 5-20µm diameter mineral particles from (A) natural dust air sample in South Phoenix, (B) emissions from rock-crushing operation near location (A).

	Site A (Ambient)		Site B (Source)	
	$\bar{x}$	$\sigma/\bar{x}$	$\bar{x}$	$\sigma/\bar{x}$
Na	1.7	1.3	1.4	1.7
K	2.0	0.4	2.8	1.7
Ca	9.0	1.3	4.6	2.1
Mg	2.5	0.5	1.7	3.4
Fe	5.5	0.6	0.4	1.7
Al	8.6	0.4	7.6	0.8
Si	23.9	0.3	33.0	0.2
Ti	0.5	2.3	-	-
Cl	-	-	0.1	4.8
O	45.2	-	48.5	-

sis and particle correction procedures of Armstrong and Buseck[3,4] were employed. The means and standard deviations of the analyses for particles in given size fractions were determined. The number of particles necessary to yield representative mean mineral particle compositions varied from sample to sample and ranged from as few as 20 in homogeneous samples to more than 100 in heterogeneous samples.

Results

Table 1 shows typical values of selected mean element weight fractions and levels of heterogeneity for various sized fractions of a natural dust aerosol collected in the Phoenix, Arizona, metropolitan area. There are distinct differences among fractions of various sizes both in the average composition and in the degree of particle heterogeneity. (The former could have been determined by bulk analysis of the sized fractions, but the latter could not have been so determined.)

As can be seen in Table 1, the large particles are more homogeneous in composition ($\sigma/\bar{x}$ is smaller) than the small particles. The individual particle analysis results indicate that the large particles do not correspond to any simple monominerallic composition, where-as a number of the small particles were of simple monominerallic composition (such as quartz and calcite).

A possible explanation for the above results is that the dominant components of both coarse and fine particles are fine-grained mineral weathering products. Whereas some of the fine particles are composed of single grains, most of the large particles are agglomerates of many grains of the weathering products. These large particle agglomerates could be simple surface-abrasion products of natural rock weathering. Thus, the large particle agglomerates could be assumed to be more uniform in composition than the smaller grains.

Large silicate particles are commonly found to be fairly homogeneous in composition in Phoenix-area natural dust samples. However, the large particle fraction of silicate dust from anthropogenic sources can be quite heterogeneous. Table 2 shows the results of heterogeneity determinations for the large particle

fraction of two dust samples from south Phoenix. The first is a natural dust sample; the second, a sample of emissions from a rock-crushing operation not far from the first location.

Although the mean particle compositions of the two samples are similar (except for Fe), the heterogeneity levels are quite different. The emissions from the rock-crushing operation are much more heterogeneous than the natural dust sample. Individual particle analyses show that several of the particles from the rock-crushing operations are monominerallic--plagioclase, mica, quartz, etc.

In rock crushing, unweathered rock interiors are exposed and ground up. Such unweathered portions are much coarser-grained than the weathering products on the rock surface. Crushing of unweathered rock portions can be expected to produce quantities of monominerallic particles and thus a heterogeneous aerosol. Therefore, the degree of particle heterogeneity can possibly be used as an index of the "freshness" of source material and as an indicator of the aerosol's possible origin.

Conclusion

Particle heterogeneity levels are very easy to determine when individual particle quantitative analyses are performed. As is shown in the examples above, the heterogeneity levels can, in some instances, provide some interesting and valuable information regarding the nature of ambient and source aerosols.

References

1. J. T. Armstrong and P. R. Buseck, "Applications in air pollution research of quantitative analysis of individual microparticles with electron beam instruments," in P. A. Russell and A. E. Hutchings, Eds., *Electron Microscopy and X-ray Applications to Environmental and Occupational Health Analyses*, Ann Arbor: Ann Arbor Press, 1978, 211.

2. J. T. Armstrong and P. R. Buseck, "The chemical composition, morphology, and surface properties of individual airborne microparticles," in S. Kasuga et al., Eds., *Proc. 4th Inter. Clean Air Conference*, Tokyo: JUAPPA, 1977, 617.

3. J. T. Armstrong and P. R. Buseck, "Quantitative chemical analysis of individual microparticles using the electron microprobe: Theoretical," *Anal. Chem.* 47: 2178, 1975.

4. J. T. Armstrong, "Methods of quantitative analysis of individual microparticles with electron beam instruments," *SEM/1978*, 1: 455.

ELEMENTAL ANALYSIS OF AERODYNAMICALLY SEPARATED RESPIRABLE FLY ASH PARTICLES

P. B. DeNee and R. L. Carpenter

Characterization of the fly ash particles emitted from fluidized bed coal combustion is of interest to those concerned with the inhaled dose to man represented by these particles. Since the parent coal combusted in the fluidized bed combustor (FBC) is heterogeneous, we expected the fly ash particles to vary considerably in their composition. This result was borne out by our data. Methods of chemical analysis such as atomic absorption, neutron activation analysis, x-ray fluorescence, electron spectroscopy for chemical analysis and spark source mass spectrometry result in an average composition for the fly ash rather than the composition of individual particles. It is important to determine the composition of individual particles and to determine whether the chemical composition changes with the aerodynamic diameter D_{ae} of the particles because such factors may influence the toxicity of the fly ash. We have determined the composition of individual respirable fly ash particles of four aerodynamic sizes.

Methods

The aerosol particles were collected from an experimental atmospheric pressure fluidized bed combustor burning Montana Rosebud coal with a dolomitic limestone bed. They were collected by means of a Lovelace aerosol particle separator (LAPS) device[1] that separates the particles as a function of aerodynamic diameter and collects them on a stainless steel foil. Copper transmission electron grids with Formvar-carbon substrates were attached to the foil at various positions along its length. Four foil positions were selected (10, 20, 30, and 40 cm, measured from the beginning of the foil) in order to collect particles of various aerodynamic sizes. These positions correspond to aerodynamic diameters D_{ae} of 2.7, 1.7, 1.2, and 0.7 µm, respectively. The samples were collected for 38 min at a sample flow rate of 300 cm^3/min at the FBC stack breech. Up to 50 particles were chosen for analysis from each size class.

The analysis was performed by means of a JEOL JSM 35 scanning electron microscope. The beam voltage was 25 kV and the beam current was about 10 na. Each grid was mounted separately in a carbon grid holder (PELCO 1653, made by Ted Pella, Inc., Tustin, Calif.). The grid was tilted at 45° (measured from the beam normal) towards the X-ray detector. The X-ray detector was a lithium drifted silicon detector, Kevex Model 78, with a detection area of 30 mm^2. The elemental analysis was performed by means of an x-ray analyzer, Kevex Model 5100. Nine elements were selected for analysis (Mg, Al, Si, P, S, K, Ca, Ti, and Fe) because they represent the most common inorganic elements in the parent fuel and bed material. A grid square was chosen at random and particles were chosen from the middle of the grid square. The x-ray spectra were first collected for 100 sec and the background was then subtracted from these spectra in accordance with a background normalization procedure developed by Kevex.

Results

Table 1 is a compilation of the average composition of the fly ash particles in each of four size classes. The mean, median, and range of concentration for each of the nine elements are included for each size class. The results from two different samples are included, D_{ae} = 2.7 µm. Also included in Table 1 are the compositions of the parent coal, the limestone, and the used bed material. For ease of comparison, the concentrations of all nine elements were normalized so that their sum was 100%.

TABLE 1.--Composition of fly ash vs particle size.

Particle size, D_{ae} (μm)	Particles analyzed (n)		Percent concentration* of the nine elements									Ratio S/Ca
			Mg	Al	Si	P	S	K	Ca	Ti	Fe	
2.7	50	Mean	7.9	25	23	0.7	6.1	1.3	29	1.7	6.1	0.2
		Median	6.5	24	23	0	2.7	0.7	25	0.7	2.3	
		Range+(U)	28	52	66	19	35	7.9	76	22	73	
		Range (L)	0‡	4.8	0	0	0	0	1.0	0	0	
2.7	15	Mean	7.8	28	21	2.1	2.5	0.7	29	0.6	8.2	0.1
		Median	6.4	24	19	0	1.1	0	27	0	0.8	
		Range (U)	21	62	63	24	8.7	4.6	66	2.8	89	
		Range (L)	0	7.2	0.6	0	0	0	2.7	0	0	
1.7	39	Mean	1.3	16	8.5	0	3.8	1.7	44	2.1	23	0.1
		Median	0	13	0	0	0	0	49	0	11	
		Range (U)	15	56	100	0	23	20	100	18	94	
		Range (L)	0	0	0	0	0	0	0	0	0	
1.2	16	Mean	18	23	9.4	1.8	13	0.9	30	1.3	2.5	0.4
		Median	19	18	3.3	1.8	11	0.4	33	0.2	1.1	
		Range (U)	40	100	32	4.0	32	5.1	50	5.7	9.5	
		Range (L)	0	6.8	0	0	0	0	0	0	0	
0.7	9	Mean	13	24	19	0.5	12	0.8	18	0.2	13	0.6
		Median	12	18	5.1	0	6.4	0	16	0	1.4	
		Range (U)	34	50	44	1.9	35	4.5	39	1.2	100	
		Range (L)	0	0	0	0	0	0	0	0	0	
Parent Coal Montana Rosebud[2]			2.9	21	39	0.1	6.6	1.4	21	0.8	7.5	0.3
Parent Coal Montana Rosebud[3]			4.5	19	41	0.7	6.7	1.1	16	1.0	8.7	0.4
Dolomitic Limestone			3.1	4.3	12	0	0	0	80	0	1.3	0
Spent Bed Material[3]			2.7	8.2	22	0.2	5.6	1.6	52	0.6	5.7	0.1

*Concentration was normalized to 100% for the nine elements.

+U = upper limit of range; L = lower limit of range.

‡A zero value indicates the element could not be detected.

Figure 1 is a plot of the frequency of particles containing an element vs the concentration of the element (weight % plotted in 10% increments) for a sample of particles with D_{ae} = 2.7 μm. The mean concentration ± 1 standard deviation for all the particles of this size range is included on each plot. Calcium, aluminum, and silicon were present in the largest quantities in the majority of the particles in this size range.

Discussion

Comparison of mean and median elemental concentrations allows deductions to be made about the distribution of elements among the particles. The mean values of the elemental composition within a particle size range correlated with the elemental composition measurements on milligram size samples. The median values for the elemental concentrations are indicative of the analysis of individual particles. If the mean and median are not equal, it means that the distribution is skewed. In a majority of the analyses, the mean
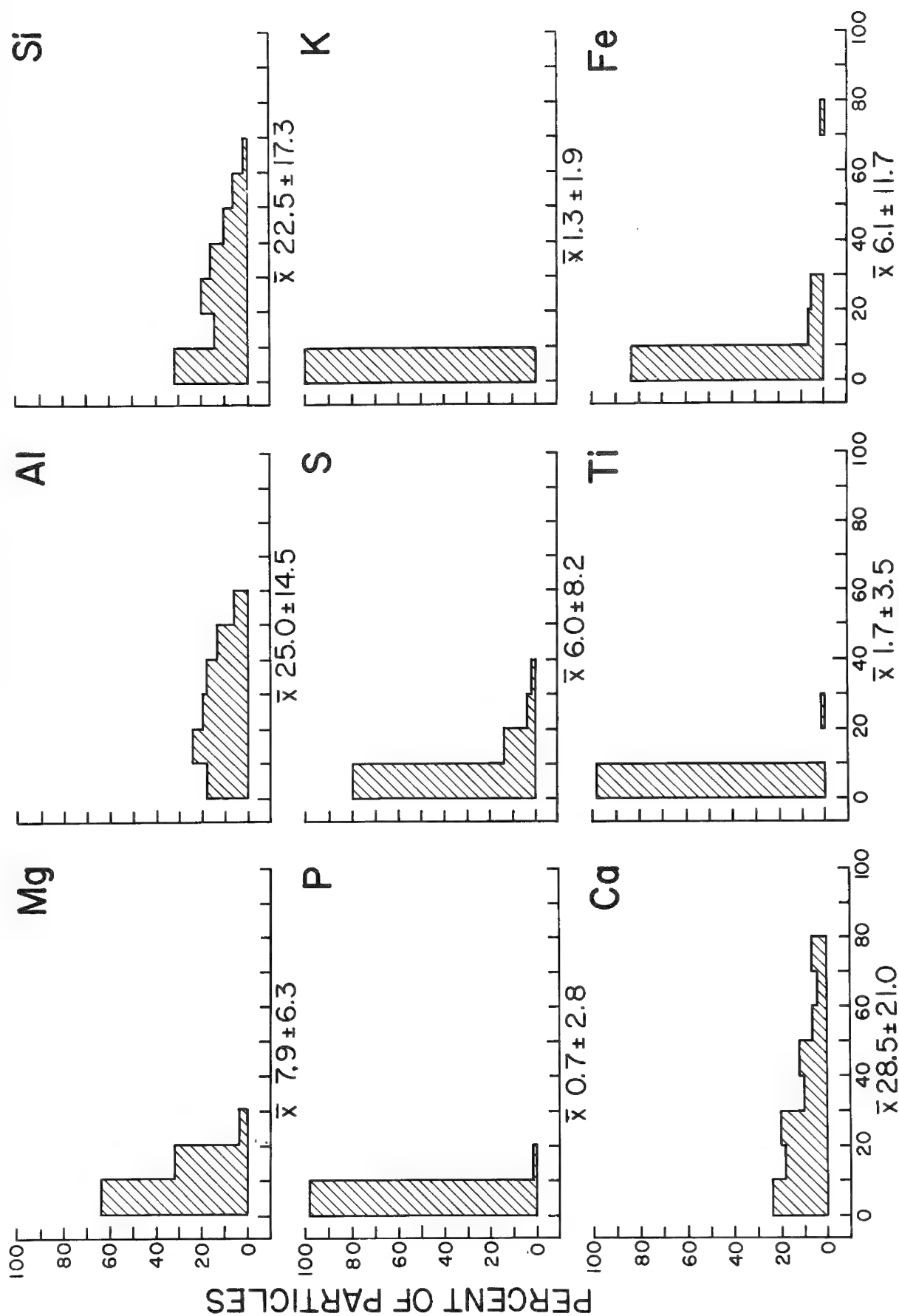
FIG. 1.--Plot of percentage of particles (D_{ae} = 2.7 μm) containing Mg, Al, Si, S, K, P, Ca, Ti, and Fe vs concentration in each particle of element (weight % plotted in 10% increments).

value was greater than or equal to the median value. The median value for several elements was below the detection limit; the mean values ranged from 0.2 to 8.5%. This result implies that these particular elements were detectable in fewer than half of the particles. In addition, there were a few particles that contained only one element, e.g., Al, Si, Ca, or Fe. The large range of elemental composition for many of the particle classes (from 0 to 100 %) strongly indicates a large degree of heterogeneity within the samples as shown in Fig. 1. In addition, although there was great variability in the composition of the particles within a single size group, there appeared to be a trend toward the smaller particles containing a larger percentage of magnesium, sulfur, and iron, but a smaller percentage of calcium and titanium than the larger particles. Although it is difficult to obtain statistically significant analyses because of the large standard deviations and ranges, several trends are apparent.

First, there is reasonable agreement between the composition of the parent coal and the 2.7μm size fraction, except for Si, Mg, and Ca. This observation would suggest that the large particles are a combination of the coal minerals and the limestone. The increased presence of Mg in the large-size fraction many result from the larger errors present in the analysis of low atomic number material by energy-dispersive x-ray analysis.

Second, the S/Ca ratio increases as particle size decreases. Sulfur increased, Ca decreased. This observation suggests that the smaller Ca particles are more effective for trapping the sulfur. Although S was seen in some of the Ca-containing particles, it was not detected in all the particles.

Third, the amount of Si in the fly ash is less than in the parent coal, more than in the limestone, and about the same as in the spent-bed material. In contrast, the amount of Al in the fly ash is about the same as in the parent coal but more than in either the limestone or spent-bed material. This observation would suggest that since the parent coal contains both silica and aluminosilicates, the silica may be trapped in the bed material but the aluminosilicates may be released with the fly ash. This possibility is being investigated further.

Finally, our examination of the major element composition of FBC fly ash shows considerable particle-to-particle variation for all aerodynamic size ranges.

References

1. R. L. Carpenter et al., "Respirable aerosols from fluidized bed coal combustion: II. Physical characteristics of fly ash," *Environmental Science and Technology*, 1980 (in press).

2. H. J. Gluskoter et al., "Trace elements in coal: Occurence and distribution," Illinois State Geological Survey Circular 499, 1977. (Available from the Illinois State Geological Survey, Urbana, IL 61801.)

3. M. H. Mazza et al., "Mineral characterization of fluidized-bed combustion aerosol ash: Montana Rosebud sub-bituminous coal," Department of Energy Report MERC/TPR-78/1, 1978. (Available from the National Technical Information Service, U.S. Department of Commerce, Springfield, VA 22151.)

IMPROVEMENT IN ASBESTOS ANALYSES USING MICRODIFFRACTION

D. R. Beaman and H. M. Baker

It is shown that microdiffraction provides a better means of identifying chrysotile fibers than selected-area electron diffraction. The accuracy in the measurement of fiber concentrations in relatively unclean samples is highest when the fiber identification is based on morphology, microdiffraction, and elemental intensity ratios.

If the proposed Environmental Protection Agency guidelines[1] concerning the asbestos content of ambient water are used to set limitations for waste water effluents, the accuracy of the analysis methods based on transmission electron microscopy[2-5] must be improved. The problem is most severe when an effluent with high solids and low chrysotile content is analyzed. In such cases the detection limits are high, each detected chrysotile fiber may correspond to 1 to 10 million fibers per liter, and only a few fibers are observed in an analysis requiring 8-12 hr. Under such circumstances the interim method proposed by the EPA[5] is subject to significant error because the chrysotile fibers are identified only on the basis of their morphology and selected-area electron diffraction (SAED) patterns. Although chrysotile morphology is distinctive, it is not entirely unique and is often compromised or obscured by other solids in the sample.[2] A group of ten investigators counted chrysotile fibers on a series of electron photomicrographs with the results shown in Table I. The samples were all 50% NaOH and clean when compared with a typical effluent sample. The broad range in counted fibers illustrates the difficulties with morphological identification. Chrysotile and the clay minerals halloysite and polygorskite have been shown to have similar morphologies.[6]

TABLE 1.--Counting of chrysotile fibers in a series of electron micrographs. Range column shows minimum and maximum number of fibers counted by 10 different investigators.[7]

Sample	Number of photo-micrographs	Number of fibers			Relative standard deviation (%)
		Range	Mean	$\pm 1 \sigma$	
A	16	7-73	24	19	79
B	22	62-121	87	18	21
C	18	43-66	54	8	15

SAED of chrysotile fibrils is even less reliable. In earlier work it was found that less than 15% of the chrysotile fibrils in a clean water standard provided positive SAED patterns, and the percentage providing positive SAED patterns only reached 50% when there were 4 fibrils in a fiber.[2,8,9] Other investigators have encountered similar difficulties. Ampian reported that positive identification using SAED could be made only from carefully indexed pat erns yielding accurate lattice parameters.[10] Ross found SAED patterns of asbestos minerals difficult to obtain and interpret; 200 keV was required for distinct patterns.[11] Biles and Emerson reported that most chrysotile fibers in beer did not give identifiable patterns.[12] On the other hand, Samudra reported that 99% of the chrysotile fibers in the size range of 20-120 nm (diameter) provided good patterns.[13] Feldman found in four samples of the same reference solution (chrysotile in filtered distilled water) that 68% (58-84% range) of all fibers were diffracting, but that only 47% (36-66% range) of the fibers with lengths below 0.4 μm were diffracting.[14] In a recent ASTM study of a filtered water sample spiked with chrysotile, the percentage of chrysotile fibers identified on the basis of SAED varied from 5 to 70% and averaged 30% for ten independent laboratories. The results would be far worse for an effluent sample in which

many fibers would be coated or in close proximity to other crystalline solids.

There are several reasons for the difficulties and variations encountered with SAED identification. A major problem is the lack of a consistent classification scheme. Some investigators require fully indexed diffraction patterns for positive identification.[10,15] This requirement is impractical in an analysis that requires 8-12 hr even when identification is based on visual inspection of the diffraction pattern on the fluorescent screen; it is also usually unnecessary in the case of chrysotile where the SAED pattern is distinctive. Some patterns are similar to chrysotile,[6,9] but any uncertainties can generally be resolved by means of an elemental spectrum from an energy dispersive spectrometer.[2,16] The chrysotile pattern is streaked in alternate layer lines, has a characteristic layer line spacing, and exhibits distinctive reflections, e.g., in the second and fourth rows from center. If the positive identification of a fiber were based on the presence of all these features, only a small fraction of chrysotile fibers would be counted.[2,8] The problem is that many patterns are initially incomplete and others fade within 30 sec to such an extent as to be unidentifiable. This is an electron beam-induced degradation due to dehydroxylization[10] and carbon contamination. Under such conditions an analyst, discouraged by poor diffraction patterns, may relax the criteria for positive SAED identification and classify as positive all fibers providing any indication of crystallinity. In a chrysotile standard where only 10% of the fibrils gave positive SAED patterns, 40-70% gave indications of crystallinity.[2,8] In the extreme case the analyst tires of poor patterns and begins classifying fibers on the basis of morphology only. Reliance on crystallinity and/or morphology alone leads to highly inaccurate results and, in the case of an effluent, can result in the detection of large quantities of asbestos where none is present. These problems, coupled with differences in instruments[2] and the presence of fiber coatings or interfering crystalline solids, make SAED identification relatively unreliable.

The quality of the analyses can be improved if individual fibers are subjected to elemental analysis by means of an energy-dispersive spectrometer (EDS). In modern instruments with large solid angles ($30mm^2$ detector surface and 15mm specimen-to-crystal distance) the Mg/Si ratio of a fibril can be acquired in under 30 sec. Basing the fiber identification on the combination of morphology, SAED, and EDS can minimize the ambiguities associated with each individual mode. With this approach interlaboratory reproducibility has been better than 20%.[8]

The diffraction portion of the identification can be improved by use of the microdiffraction mode rather than SAED. Microdiffraction was performed on chrysotile standards in the JEOL 100CX and the Philips EM400T analytical transmission electron microscopes. The former was a diffusion-pumped system subjected to rigorous cleaning procedures and the latter had an ion-pumped column. Twelve fibrils that did not provide good SAED patterns were successively examined in the microdiffraction mode and a positive pattern was obtained on each (Fig. 1). In another experiment forty consecutive fibrils gave positive microdiffraction patterns. The patterns were stable and did not fade within the time required to establish diffraction conditions. In two experiments on pattern stability the pattern did not fade in 20 min, a significant improvement over SAED that allows electron diffraction to be effectively utilized in the routine analysis of chrysotile asbestos in water and air samples. In relatively clean water samples, such as tap water and many lakes, an accurate analysis should be possible by the EPA interim method[5] with SAED replaced by microdiffraction. In relatively unclean waters, such as waste-water effluents and many river samples, where a few fibers lead to a large concentration and the fibers may be compromised by coatings and other interfering materials, the identification should be based on morphology, the Mg/Si ratio determined by EDS, and the microdiffraction pattern. When this approach is used in conjunction with a sample-preparation technique in which fiber losses are minimized (carbon-coated Nuclepore),[3,9] improved accuracy and interlaboratory reproducibility should be possible.

Microdiffraction (μ-diffraction) has been referred to as microbeam diffraction,[17,18] focused-beam Riecke technique,[19] or focused-aperture microdiffraction.[20] The image and diffraction patterns are formed in the normal manner, but the sample is illuminated with a fine beam of electrons. The fine parallel beam of electrons is formed by a strongly excited first condenser lens and a small (typically 20μm) second condenser aperture. The second condenser is focused to provide the minimum spot diameter. The diffraction pattern
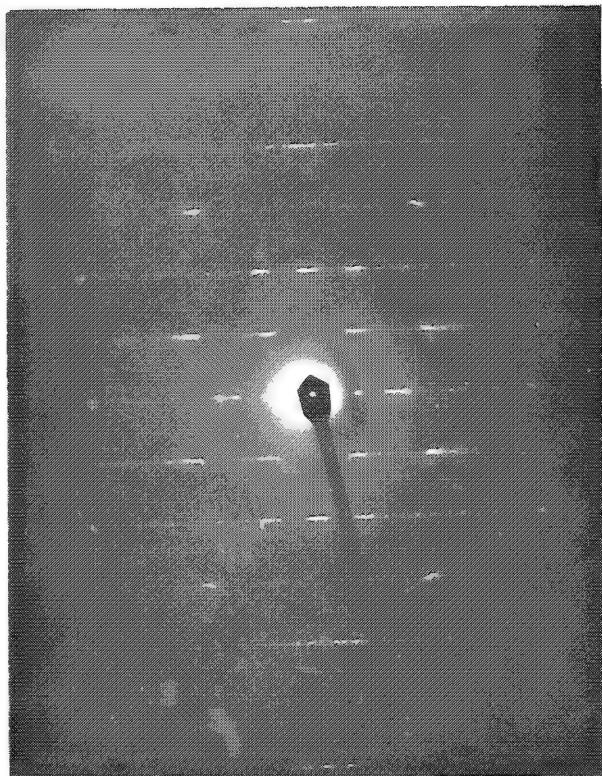
FIG. 1.--Microdiffraction pattern from a chrysotile fibril obtained in a JEOL 100CX instrument at 100 kV.

is formed on the back focal plane of the objective lens, magnified (intermediate lens), and projected (projection lens), as in conventional diffraction. Microdiffraction differs from SAED in that the small second condenser aperture defines the analysis area rather than the field-limiting aperture used in SAED.

In SAED the field-limiting aperture and the spherical aberation of the objective lens limit the minimum analysis diameter to 0.5-1 μm. In microdiffraction the beam diameter at the sample defines the diffraction analysis diameter, which can be as small as 40 nm.

References

1. *Asbestos: Ambient Water Quality Criteria,* Document No. 297-917, Criteria and Standards Division, Office of Water Planning and Standards, U.S. Environmental Protection Agency, Washington, DC, 1979.

2. D. R. Beaman and D. M. File, *Anal. Chem.* 48: 101, 1976.

3. P. M. Cook et al., *Proc. Intern. Conf. Environmental Sensing and Assessment,* Sec. 34-1, IEEE, Las Vegas, 1976.

4. J. R. Millette, in I. M. Asher and P. P. McGrath, Eds., *Electron Microscopy of Microfibers,* Proceedings of the First FDA (Office of Science) Summer Symposium, 1976, 85.

5. C. H. Anderson and J. M. Long, *Preliminary Interim Procedure for Fibrous Asbestos,* U.S. Environmental Protection Agency, Athens, GA., 1978.

6. J. R. Millette et al., *SEM/1979/I,* 579.

7. *Summary Report III of the Asbestos Methods Task Force,* New Orleans: Chlorine Institute Products Analysis and Specifications Committee, Analytical Procedures Subcommittee (H. Bohmer, Chairman), 1980.

8. D. R. Beaman and H. J. Walker, in C. C. Gravatt, P. D. Lafleur, and K. F. J. Heinrich, Eds., *Workshop on Asbestos: Definitions and Measurement Methods,* National Bureau of Standards Special Publication 506, 1978, 249.

9. D. R. Beaman and H. J. Walker, in Ref. 4, p. 98.

10. S. G. Ampian, *ibid.,* p. 12.

11. M. Ross, *ibid.,* p. 34.

12. B. Biles and T. R. Emerson, *Nature* 219: 93, 1968.

13. A. V. Samudra, *SEM/1977/I,* 385.

14. R. S. Feldman, EPA, Cincinnati, Ohio, private communication, 1979.

15. R. J. Lee, J. S. Lally, and R. M. Fisher, in Ref. 8, p. 387.

16. D. R. Beaman, in T. Y. Toribara, J. R. Coleman, B. E. Dahneke, and I. Feldman, *Environmental Pollutants,* New York: Plenum Press, 1977, 255.

17. E. S. Sherman and E. L. Thomas, *J. Mat. Sci.* 14: 1109, 1979.

18. *JEOL News* 15E: 20, 1977.

19. M. N. Thompson, Philips Electron Optics Bulletin, EM-110: 31, 1977.

20. J. B. Warren, in J. J. Hren, J. I. Goldstein, and D. C. Joy, Eds., *Introduction to Analytical Electron Microscopy,* New York: Plenum Press, 1979, 369.

ELECTROSTATIC DEFLECTION SYSTEM FOR USE WITH AN ELECTRON ENERGY LOSS SPECTROMETER

C. E. Fiori, C. C. Gibson, and R. D. Leapman

An electrostatic deflection system is described that can be placed between the magnet and analyzing slit of an electron energy loss spectrometer and has the advantage of providing a fast, essentially flicker-free display for the energy loss spectrum. This display can greatly simplify spectrometer alignment, which often involves the optimization of several instrumental parameters; it allows the effect of a change in any adjustment control to be seen immediately. The deflection system can be easily and independently addressed by a computer; we discuss how it might be used to sample the energy loss spectrum just above and just below a core edge to give energy-selected imaging. The spectrum is normally recorded by ramping of the magnetic prism excitation, which could also be used for alignment.[1,2] However, a rapid scan in the coil current is not as easily achieved as a fast ramp of the potential across electrostatic plates. Moreover, the use of an electrostatic system excludes the possibility of hysteresis effects that could be present in the magnet ramp.

Our instrument consists of a 200keV hitachi H700H electron microscope with a STEM attachment combined with a magnetic sector spectrometer. Although certain features of our system are specific to this machine, the general principle of the electrostatic deflection plates could be utilized in other instruments. Figure 1 shows a schematic diagram of the electron microscope and spectrometer with the electrostatic plates situated after the exit polepiece face of the magnetic sector. It is found that a potential of ±150 V applied to the plates, which are 1.8 cm in length and 7 cm from the slits, and are separated by 0.5 cm, offsets the spectrum by about ±150 eV of energy loss. A commercial high-speed 300V operational amplifier (Analog Devices 171) is used to drive the plates.

FIG. 1.--Electron microscope and spectrometer with electrostatic deflection plates.

Use of Plates for Alignment

A nearly flicker-free display of the energy loss spectrum is obtained as follows. A 1024-channel digital voltage ramp is applied to the 300V operational amplifier that drives the plates in synchronism with a similar voltage applied to the x axis of a display oscilloscope. The total scan range can be adjusted from 0 to 300 V. The y axis of the display is obtained by use of a high speed digital ratemeter to count and display individual pulses from a scintillator-photomultiplier at each of the 1024 channels.

In our instrument the spectrometer is operated in the STEM mode where the excitation voltage of the objective lens is high but constant and the condenser lens focuses the probe on the sample. Only the inter-
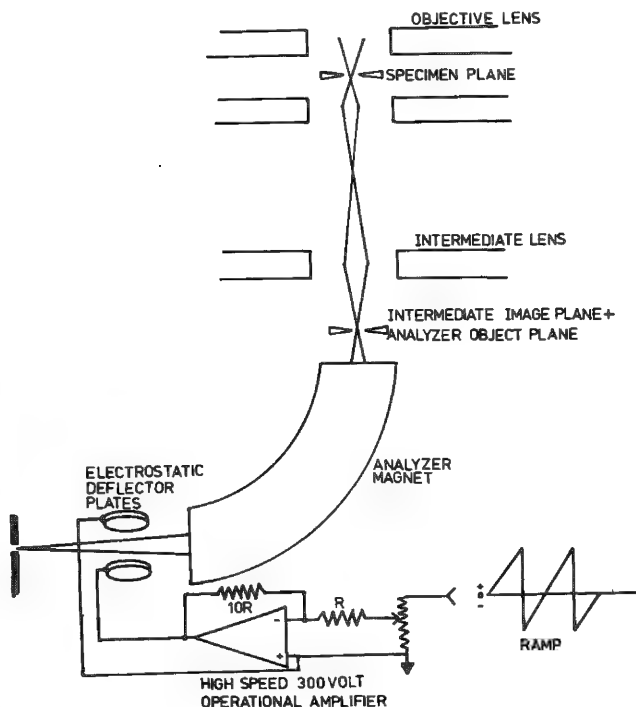
mediate is used as a postspecimen lens to couple the scattered electrons into the spectrometer; the selected area aperture serves to limit these demagnified angles to about 1 mrad (or about 10 mrad from the sample). Alignment by means of the deflection plates proceeds as follows. The sample is removed after the STEM conditions have been established and the analyzing slit is closed down so that the intrinsic spectrometer resolution may be optimized. A voltage ramp is applied to the plates and the electron intensity is scanned across the slit. The strength of the intermediate lens is adjusted until the zero-loss (incident beam) width as observed on the display oscilloscope is minimum. This setting corresponds to the intermediate lens crossover being in the object plane of the spectrometer and is a critical adjustment. The position of the analyzing slit in a plane normal to the exit axis of the spectrometer is then varied and the zero-loss intensity maximum is brought back to the x-axis center of the display oscilloscope by an offset to the magnet excitation. This process is repeated until the zero loss width is minimum. After this alignment the analyzing slit width is increased to obtain a larger signal until an appropriate resolution is reached. The total spectrometer response is the convolution of the intrinsic resolution with the slit function; these components add approximately quadratically.
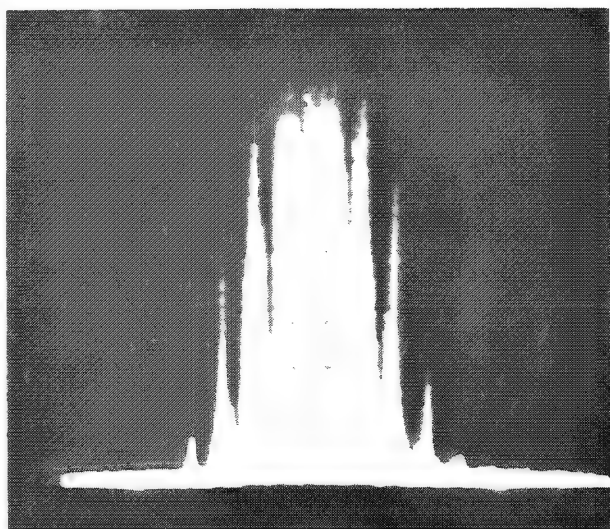

FIG. 2.--Zero-loss (direct-beam) intensity modulated by ac magnetic fields in vicinity of spectrometer; width of peak is about 4 eV.

The deflection plates are also very convenient for observing effects of ac fields. Figure 2 shows the zero-loss (direct beam) intensity as observed on the display oscilloscope. The counting time is 17 msec per channel. A series of spikes spaced at intervals of 1/60 sec are evident; they arise from stray ac fields in the vicinity of the spectrometer. Ac fields are well known to have a deleterious effect on the energy resolution (which is in this case limited to about 3 eV).[1,3] Magnetic shielding can be effective in reducing or eliminating these fields. Alternatively, the effects of fields may be cancelled if a variable-amplitude and phase-correction current is passed through the prism windings or other coils mounted near the prism for this purpose.

Selected-energy Imaging

We may carry out energy-selected imaging by choosing a characteristic signal in a given band of the energy loss spectrum and forming an image with it. In particular, it has been shown that elemental maps can be formed with electrons that have given rise to inner shell ionization.[4-7] Several difficulties have emerged in these experiments. First, a large background intensity usually precedes the inner-shell edges arising from excitation of other electrons in the sample. The contrast in the image formed from electrons after the edge is therefore generally low. Moreover, the spectrum is very thickness-dependent because of plural scattering, and artifacts often tend to occur from local fluctuations in thickness. A better procedure is to subtract the background intensity I_b underlying the edge at each pixel in the image.[8] The STEM is well suited for doing that since the signal can be easily recorded digitally and fed directly into a computer for processing.[9] The procedure for background subtraction is quite well established and a power law $I_b \propto E^{-r}$ can be used where E is the energy loss and r is a constant usually lying between 3 and 4 depending on the sample and collection angle.[10]

Ideally, to observe the spectrum near a given core edge we would wish to use multiple detectors.[8] However, there are practical difficulties with this scheme owing to small detector separations required for typical spectrometer dispersions of a few microns per electron volt. The electrostatic plates offer a convenient method of scanning the spectrum past a core edge. A voltage across the plates can be accurately set and controlled by a computer after the edge is first selected by offsetting of the magnetic prism exci-

tation. Typically several channels below the edge energy (two or more) at each pixel should be selected and a least-squares fit to the power law extrapolation made.[8] This value can then be subtracted from the intensity above the edge measured at one or more channels. After the spectrum has been counted at the appropriate channels the computer can move the probe to a different pixel and recommence counting. Each channel in the spectrum and each pixel is independently addressable.

We have estimated times required to form a core-loss image with our instrument, which is intended for biological work, with neglect of radiation damage or mass loss effects. The heated tungsten filament source provides a current $J \simeq 10^{-10}$ A, measured with a Faraday cup, focused into a probe diameter of 5-10 nm, which defines the pixel size.

The count rate dN/dE of scattered electrons which have been analyzed by the spectrometer and have lost energy E through core level excitation is given in terms of the cross section per unit energy loss $d\sigma_X(\alpha)/dE$ where α is the maximum scattering angle collected from the sample (in our case about 10 mrad),

$$dN/dE = Jn_X t[d\sigma_X(\alpha)/dE] \tag{1}$$

Here n_X is the number density of atoms of type X in the microarea. Let us consider a biological sample of thickness 100 nm which contains mainly carbon with about 10 atomic percent of a fluorine tracer. This is the type of sample studied by Costa et al.[11] in work on fluorinated serotonin, where energy-selected images were recorded at the fluorine K edge. Putting in a value for the cross section just above threshold (686 eV) for excitation of the fluorine K shell,[12] $d\sigma_X/dE \simeq 10^{-9}$ nm^2/eV, we estimate a count rate of 400 sec^{-1} eV^{-1} from Eq. (1). The signal/background ratio will typically only be a few per cent (or less than 1% for smaller concentrations), so that we are required to count for about 1 sec in a 1eV channel or 0.1 sec in a 10eV channel. To carry out energy-selected imaging we therefore need between 1 and 10 sec per pixel. This result suggests that it would only be reasonable to image a limited field of, say, 30 × 30 pixels at the most, by means of an instrument with a standard tungsten filament source. Larger images could be obtained with a brighter field emission source capable of providing about 10 nA of probe current. For core edges at lower energies (such as the L_{23} edges of P, Cl, and Ca, which are also important elements biologically), cross sections and hence count rates can be higher by more than an order of magnitude. Shorter counting times might also be achieved if a parallel detection rather than serial detection of the spectrum were employed. Our estimates indicate that a useful approach may be to obtain elemental distributions from lines in the sample rather than from areas. This approach would take much less time and the resulting information might be superposed on a STEM image to give comparable information.

In conclusion, it is anticipated that electrostatic deflection plates will be useful for performing this type of analysis as well as for initial alignment of the spectrometer.

References

1. R. F. Egerton, "A simple electron spectrometer for energy analysis in the transmission electron microscope," *Ultramicroscopy* 3: 39, 1978.
2. D. C. Joy, "Principles of electron energy loss spectroscopy," in: *Analytical Electron Microscopy*, New York: Plenum, 1979, 223.
3. D. B. Wittry, "Electron energy loss spectrometer for a transmission electron microscope," *J. Phys. D* 2: 1957, 1969.
4. C. Colliex and B. Jouffrey, "Contribution à l'étude des pertes d'énergie dues a l'excitation des niveaux profonds," *C. R. Acad. Sci.* 270: 144, 1970.
5. R. F. Egerton and M. J. Whelan, "High resolution microanalysis of light elements by electron energy loss spectroscopy," *Proc. 8th Intern. Congr. on EM* (Canberra) 1: 384, 1974.
6. P. Ottensmeyer, "Energy filtration and energy analysis in fixed beam transmission electron microscopy," *Proc. 37th EMSA Meeting*, 1979, 380.
7. J. Hainfeld and M. Isaacson, "The use of electron energy loss spectroscopy for studying membrane architecture," *Ultramicroscopy* 3: 87, 1978.

8. C. Jeanguillaume, P. Trebbia, and C. Colliex, "About the use of electron energy loss spectroscopy for chemical mapping of thin foils at high spatial resolution," *Ultramicroscopy* 3: 237, 1978.

9. C. J. Wilson et al., "Differentiated energy loss spectroscopy in STEM," *Developments in Electron Microscopy and Analysis,* London: Inst. Phys. 36: 365, 1977.

10. R. F. Egerton, "Inelastic scattering of 80 keV electrons in amorphous carbon," *Phil. Mag.* 31: 199, 1975.

11. J. L. Costa et al., "Subcellular localization of fluorinated serotonin in human platelets by electron energy loss spectroscopy," *Proc. 35th EMSA Meeting,* 1977, 238.

12. R. D. Leapman, P. Rez, and D. F. Mayers, "K, L, and M shell generalized oscillator strengths and ionization cross sections for fast electron collisions," *J. Chem. Phys.* 72: 1232, 1980.

Microcharacterization of Semiconductor Materials

SILICON IMPATT DIODES: A FAILURE ANALYSIS BY ELECTRON PROBE MICROANALYSIS AND SCANNING ELECTRON MICROSCOPY

T. D. Kirkendall and J. C. Hannsen

COMSAT Laboratories has designed and built an all-solid-state centimeter-wave beacon that incorporates impact avalanche transit-time (IMPATT) diodes, which has been successfully operating on COMSTAR domestic communications satellites D1, D2, and D3.[1] The purpose of the beacon experiment is to measure propagation parameters such as attenuation and depolarization at 19 and 28 GHz. These frequencies will be used by commercial communications satellites in the future to augment the crowded bands at 4 and 6 GHz now used for virtually all domestic and international satellite communications. Both the 19 and 28GHz beacon amplifiers were designed with silicon IMPATT diodes. This design represents the first nonmilitary use of IMPATT diodes as spaceborne solid-state power amplifiers. To qualify the IMPATT diodes for space use, an intensive microanalytical effort was combined with accelerated life test studies to insure reliability.[2] Electron probe microanalysis (EPMA) and scanning electron microscopy (SEM) were used (a) to select proper chemical etching techniques for the production of the desired edge profile, (b) to characterize early diode failures due to copper diffusion through the palladium barrier, and (c) to identify the source of a carbonaceous contaminant which was causing junction shorts. An ARL EMX/SM electron probe was used to obtain all the results reported here, including the secondary-electron images.

Construction and Failure Modes

The IMPATT diode is operated with a reverse-biased p-n junction. Amplification is based on the combination of avalanche breakdown and the negative resistance caused by a 180° phase difference between the applied rf voltage and the current. The time delay inherent in the build-up of the avalanche current and the motion of carriers through the drift zone is the cause of the phase shift. Two types of silicon IMPATTs were used in the beacon (Fig. 1.) The regular profile of n^+np^+ on a diamond heat sink[3] was used at both 19 and 28 GHz; the complementary profile of p^+pn^+ on a copper heat sink was used for applications at 28 GHz only.

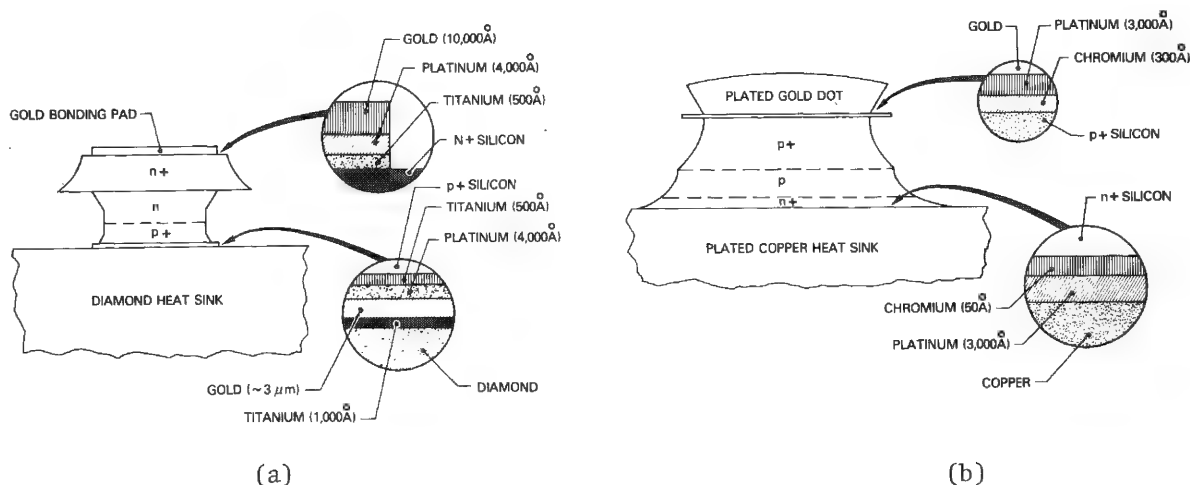(a)   (b)

FIG. 1.--IMPATT diode cross sections, courtesy of P. Fleming: (a) regular device section, (b) complementary device section.

The authors are with COMSAT Laboratories, Communications Satellite Corp., Box 115, Clarksburg, MD 20734.

The failure of an IMPATT diode is invariably catastrophic,[4,5] Typically there is a runaway condition of the high avalanche current which can become localized because of a defect in construction or some irregularity in the electric field. A local hot spot can develop in the junction causing the silicon to alloy with metals used in the contacts or the heat sink. A typical efficiency for a silicon IMPATT is 10%; therefore, 90% of the input power is dissipated as heat in a 1μm-thick region of high field.

The operating temperature at the junction of these diodes in the beacon application is between 135 and 185°C. Therefore, two important considerations in the design and construction of a reliable IMPATT diode are a heat sink with a low thermal impedance and a dense, pinhole-free barrier metal in the contacts to avoid possible diffusion of Au or Cu to the semiconductor surface. It is also important to exclude any polar or mobile contaminants such as moisture from the IMPATT diode package in order to avoid electrical leakage at the perimeter of the Si mesa. By its very nature, the IMPATT operates with high surface fields and is one of the few silicon devices which is neither passivated nor otherwise protected from the possible deleterious effects of surface contaminants.

Failure Analysis

At the time it was chosen for use in the centimeter-wave beacon, the IMPATT diode was an unproven device in terms of reliability. During the accelerated life tests, few troubles were experienced with the regular profile diodes, which employed the platinum barrier layer and Au-plated diamond heat sink. Failures of devices of this design were limited to inadvertent voltage spikes and overheating caused by mishandling. Figure 2 shows an example of the resultant Au-Si alloy formation at the perimeter of the Si mesa of a 28GHz diode which was voltage/current overstressed. A section of the Pt/Au saucer used to bond the diode to the Au-plated diamond heat sink was also consumed in the alloy formation. By using a chemical etchant (5 parts HNO_3: 20 HAc: 3HF) to dissolve the Si selectively, we found that the bulk of the alloy was actually hidden behind the edge of the mesa, i.e., in the Si.

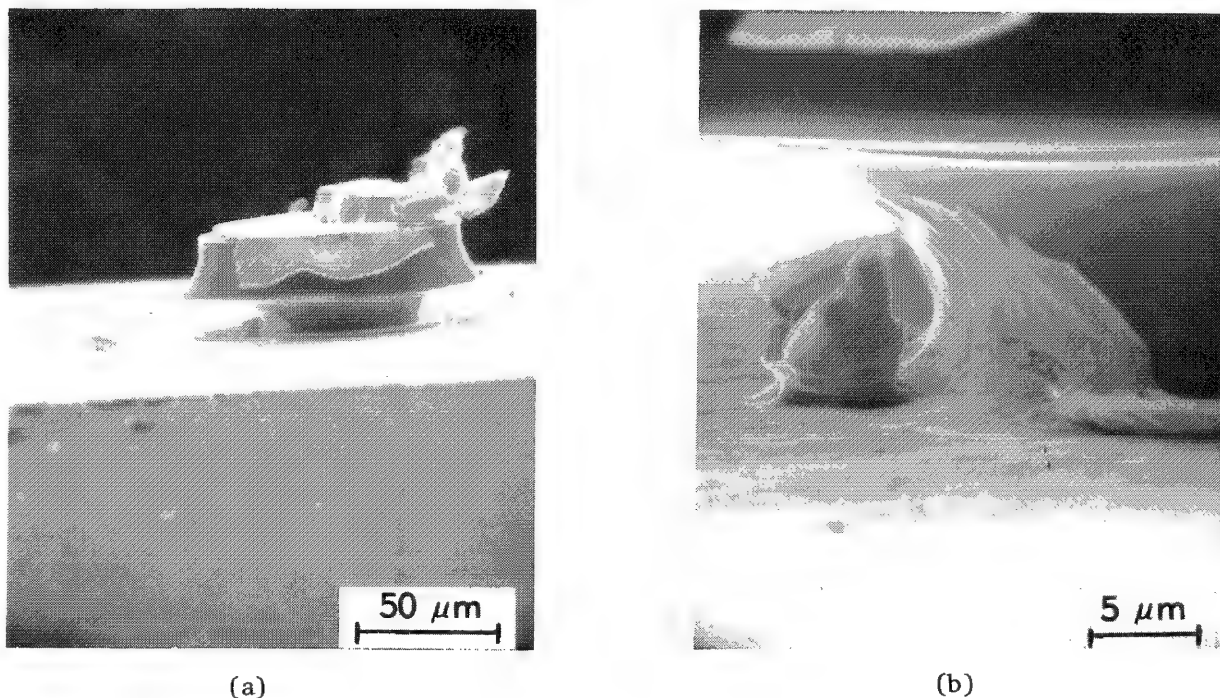| (a) | (b) |

FIG. 2.--Example of failure in 28GHz regular profile Si IMPATT: (a) side view of diode on diamond heat sink; (b) close-up of failure site.

Problems with the 28GHz copper-plated heat-sink IMPATTs were varied. Close cooperation with the manufacturer in the early phases of development resulted in the identification and correction of several shortcomings of materials selection and processing. For

instance, it was discovered that the chemicals used to etch through the copper heat sink of early diodes had a fixing effect on the dot of photoresist that had been put on each diode for protection. The chemically hardened photoresist did not always yield to normal cleaning solvents and thus could remain on the diode as a thin, conformal, organic film. Separation of the diodes with a scribing technique (rather than by acid etching) eliminated the need for the troublesome photoresist.

Another problem involved the metals system used in the contacts. When Au and Cu are used in Si device construction, a thin barrier metal is inserted between these metals and the silicon to retard diffusion. Palladium was originally chosen for the barrier in the diodes made with Au-plated Cu heat sink. The adequacy of Pd as a barrier was tested by a simple screening test: the diode was exposed at the wafer or chip stage to forming gas at 450°C for 1 hr. Use of a test temperature above the Au-Si eutectic melting point (370°C) makes it possible to judge the comparative effectiveness of chip processing and metallization. Diodes made with palladium and with platinum barriers were tested, but only those with platinum (4000 Å thick) survived the test. SEM and electron probe analysis of the shorted palladium barrier diodes showed extensive penetration of the barrier by a resultant alloy product containing silicon, copper, and gold. All diodes selected for the beacon program were therefore made with platinum barriers.

The most difficult problem with failures of the IMPATTs was the inexplicable occurrence of alloy spikes in carefully handled diodes after hundreds of hours of operation. Two kinds of alloy spikes were observed: a stitch-like bridge of metal at the perimeter of the Si mesa, and a bulk spike completely out of sight within the Si. The stitch failure (Fig. 3) appears to have punctured holes at each end in the p and n$^+$ regions of the silicon. Also, with the top metal contact removed from the p$^+$ silicon, one can see additional alloy material which has erupted at the top of the mesa. By selective etching away of the silicon, a bulk spike about 1 μm in diameter was discovered hidden just inside the edge of the mesa.

(a)

(b)
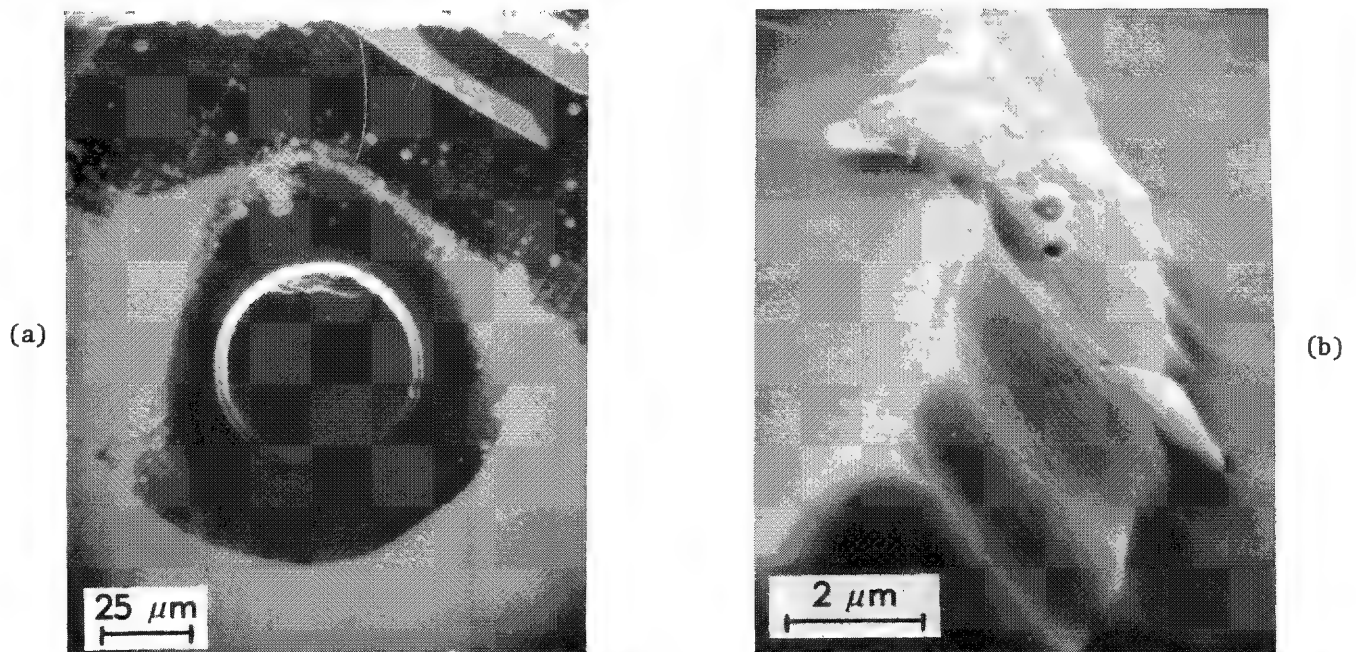
FIG. 3.--Stitch-type failure in 28GHz complementary profile Si IMPATT: (a) top view of diode on Cu heat sink, (b) close-up of failure site seen at 1 o'clock position in (a).

An example of this bulk-spike failure mode is shown in Fig. 4. The columnar structure consists of an Au-Si alloy which was observed only after etching away of all the Si. The alloy joins the top and bottom contacts and seems to replicate, in frozen form, the path and shape of the high-current spike that caused it.

The evidence of IMPATT failure is sometimes less obvious and the cause is not so clear. The only abnormal feature on one failed diode was the presence of a very thin

231

(few hundred angstroms thick) disk of copper on the top of the Si mesa. This artifact became visible after the top metal contact was removed. The significance of the Cu disk was revealed only after the removal of the silicon by reactive-plasma etching with CF_4 gas. The thin copper disk was joined to the heat sink by several thin Cu filaments. Beneath this artifact, there had been a breach of the platinum barrier on the heat sink; this hole was attributed to a defect in plating (Fig. 5). This diode, one of those originally qualified for flight, had been operated for 580 hr at $T_j = 180°C$ before failure occurred.

(a)

(b)

10 μm

2 μm

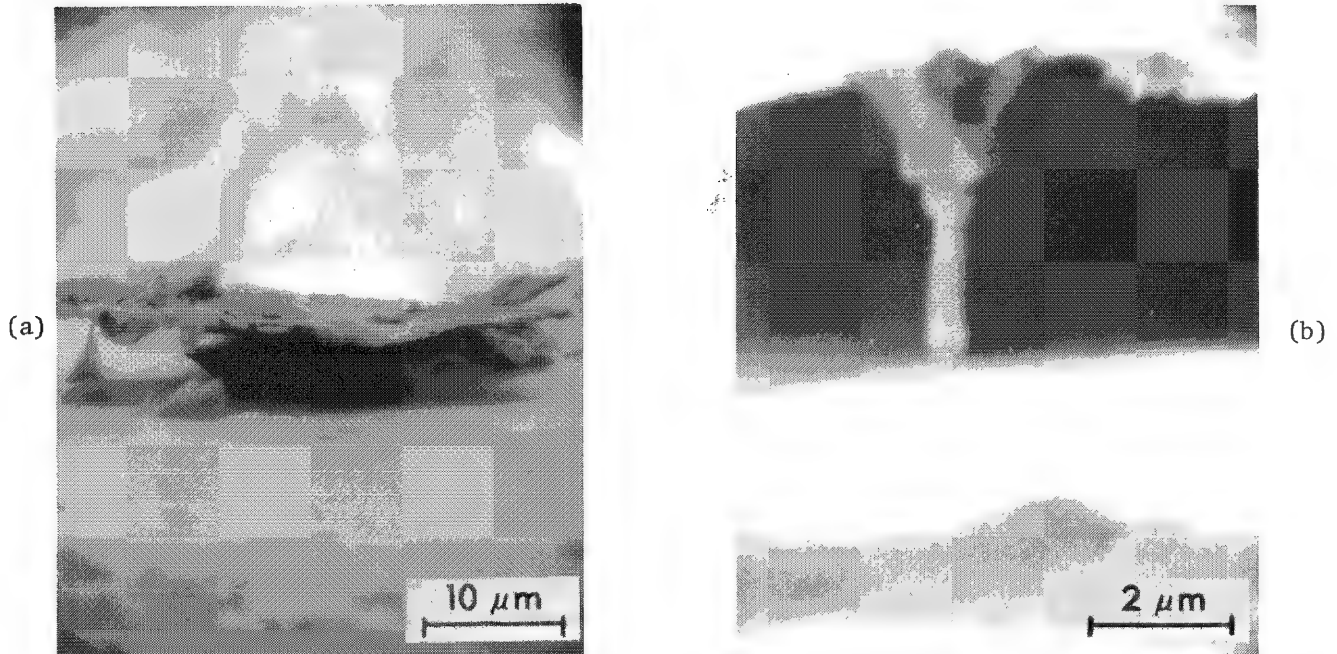FIG. 4.--Bulk-spike failure in 28GHz complementary profile Si IMPATT: (a) side view after chemical etching away of Si, (b) close-up BSE of Au-Si spike.

The final example of the microanalysis of IMPATT diode failure mechanisms is selected to show the importance of avoiding surface contamination of the junction of an unpassivated device such as the IMPATT. Several premature and unexplained diode failures were pinpointed during this program as the result of a surface contamination by a small amount of an organic material inadvertently trapped in the devices during fabrication. The plating bath used to fabricate the Cu heat sink incorporated a proprietary organic brightening agent; a small amount of this organic complex was entrained in the plated Cu and thus sealed into the package as part of the diode. During diode operation certain products of the organic complex containing C, O, and S were slowly released from the Cu. The residue of this organic material appeared as a film a few hundred Ångstroms thick on the perimeter of the junction of the diode.

The mesa of a contaminated diode with the top contact removed is shown in the SE, Si, C, and O x-ray images of Fig. 6. The contaminant has an affinity for silicon and shows higher concentrations there than on the platinum layer associated with the heat sink. Because it had been protected by the original plated contact, the top of the Si mesa is relatively free of the carbonaceous material. On the p region (the annular dark ring in Fig. 6), there was less residue. This feature was typical of contaminated diodes and could be attributed to a lower sticking coefficient for the organic agent on p-doped Si owing to higher local temperature or to an unattractive surface potential. The identification of the residue and the location of its source led to a stringent test for electrical leakage under reverse bias, a test that was used for the selection of diodes free of contaminant effects.

FIG. 5.--Complementary IMPATT diode failure caused by Cu Diffusion: (a) Top view with top contact removed to show thin Cu disk, (b) same view as (a) after CF₄ plasma removal of Si, (c) magnified view of the breach in the Pt barrier beneath the Cu disk.
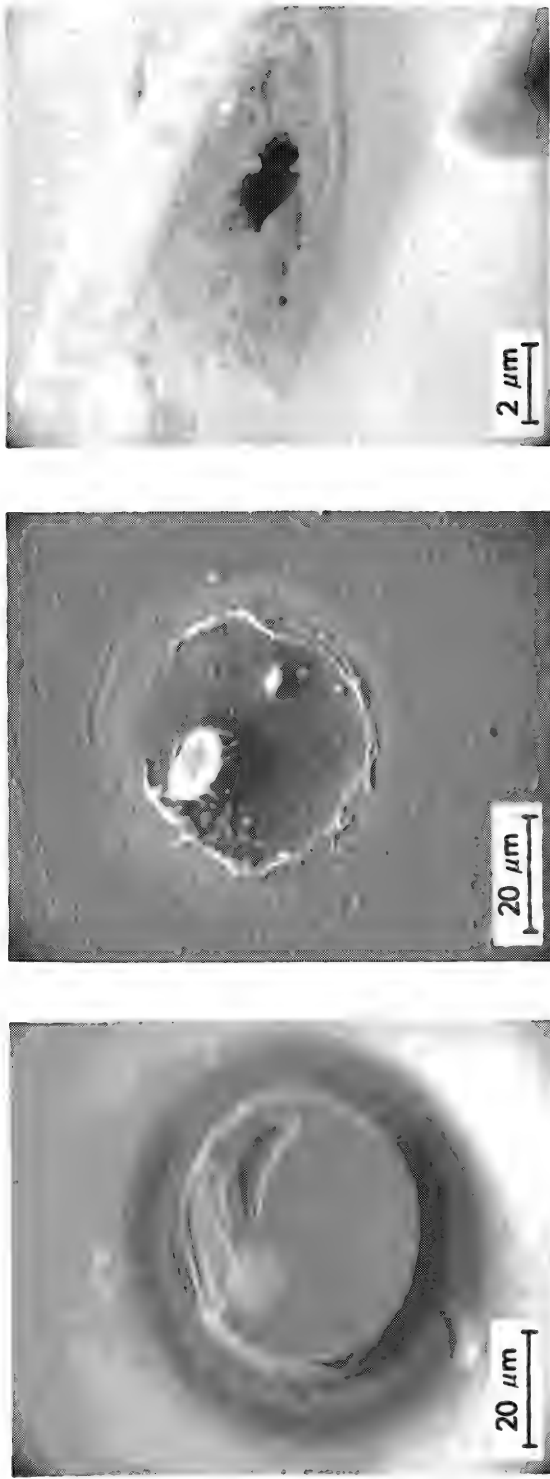
FIG. 6.--Evidence of contamination of IMPATT by organic complex volatilized from brightening agent trapped in Cu-plated heat sink: (a) SE top view with top contact removed, (b) $Si_{K\alpha}$, (c) $C_{K\alpha}$, (d) $O_{K\alpha}$.

233
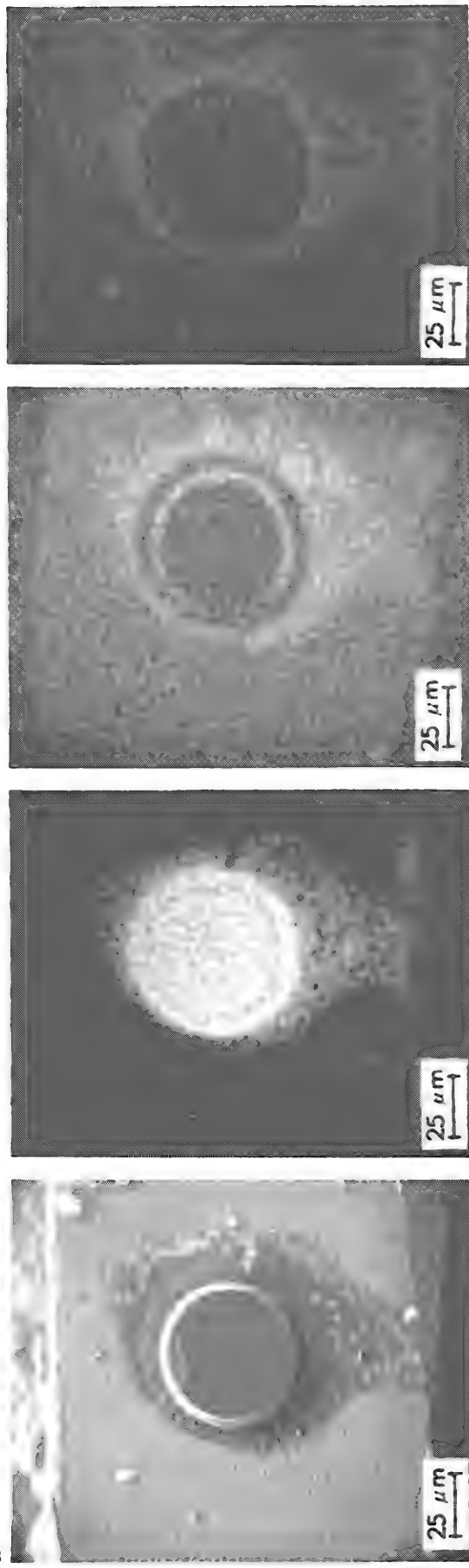
Conclusion

Three 19 and 28GHz beacon transmitters were built with a total of 24 Si IMPATT diodes. During the qualification phase of the program, which included accelerated life tests at junction temperatures of 300-370°C, EPMA/SEM techniques were used to characterize the failure of more than 40 diodes. The failure analysis results were effectively used to improve construction and testing methods. The original requirements of the mission dictated a mean time to failure for the IMPATTs of 4×10^5 hr (46 yr); however, the results of accelerated life tests on screened and burned-in devices show a projected life of more than 1×10^7 hr (over 1100 yr).[2] The first beacon was launched in May 1976 followed by one each in July 1976 and June 1978. There have been no failures of the 24 IMPATTs as of January 1980 after an accumulated life of 53 300 hr or a total of 1.3×10^6 device hours.

References

1. W. J. Getsinger, "Centimeter wave beacon transmitter design," *COMSAT Tech. Rev.* 7(No. 1): 109, 1977.

2. P. Koskos, P. Fleming, and J. Reynolds, "Reliable IMPATT diodes for the COMSTAR centimeter wave beacon," *COMSAT Tech. Rev.* 7(No. 2): 577, 1977.

3. H. Nagao and S. Katayama, "Silicon IMPATT diode device incorporating a diamond heat sink," *NEC Research and Development*, N35, p. 67, October 1974.

4. H. M. Olsen, "Thermal runaway of IMPATT diode," *IEEE Trans.* ED-22: 165, 1975.

5. H. M. Olsen, "A mechanism for catastrophic failure of avalanche diodes," *IEEE Trans.* ED-22: 842, 1975.

RAMAN, PHOTOLUMINESCENCE, AND CATHODOLUMINESCENCE APPLIED TO MICROCHARACTERIZATION OF S/C DEVICE MATERIALS

J. N. Ramsey

As miniaturization has proceeded in the semiconductor industry, it has been necessary to push analytical techniques to provide analysis and characterization information from progressively smaller analytical volumes in smaller (trace) quantities. Many small-area and shallow-depth techniques are used. (Examples were covered in the workshop session.) Some materials can still be difficult: boron carbide, boron nitride, lithium fluoride, etc., would be difficult for small-area analysis by electron microprobe because the x-ray emission wavelengths are so long. Optical spectroscopic techniques with a small beam are thus very attractive. At present the techniques are laser-through-a-microscope and e-beam excitation with either Raman scattering or luminescence as output. Raman scattering is related to the vibrational modes of the molecule as seen in infrared and thus "sees" molecular structure. Luminescence, in the sense used in the paper, occurs in ionic materials as the loss of energy of an electron in dropping to lower energy levels is transformed into radiant energy. Thus luminescence "sees" the electron band gap, trap, and defect energies, which are related to crystal structure, lattice parameter, temperature, stress, impurities, damage, etc. The Raman and photoluminescence (PL) in this paper has been done on a comparatively new instrument, the Molecular Optical Laser Examiner (MOLE) manufactured by Jobin Yvon of France and distributed by Instruments SA, Metuchen, N.J. This instrument has a lateral resolution of 1-2 μm and has been described in the literature.[1] (Small-area Raman was the subject of a symposium at the 1979 MAS meeting in San Antonio, Tex.) The cathodoluminescence (CL) has been done on an ARL Electron Microprobe, following Knisely, Laabs and Faisel,[2] and the results have previously been reported.[3,4] Usually, the lateral resolution is 3-5 μm.

Boron Nitride

Figure 1 shows the Raman spectra of a six 9's, hot-pressed disk of boron nitride. The primary peak at 1365 cm^{-1} agrees with the 1370cm^{-1} peak in the literature[5] (which is the only peak mentioned). Figures 2 and 3 show PL and CL, respectively; the CL spectra are of two different areas on the specimen. Although this BN is not likely to have local variations, it gives a fingerprint capability in about 1 μm (Raman and PL) to 5 mm (CL) to allow small-area characterization.
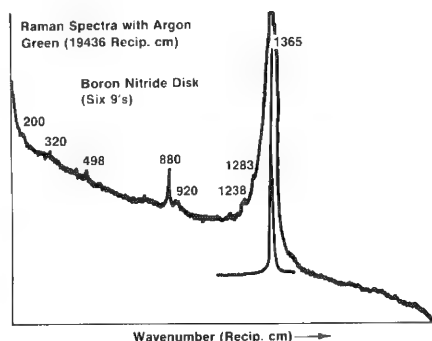

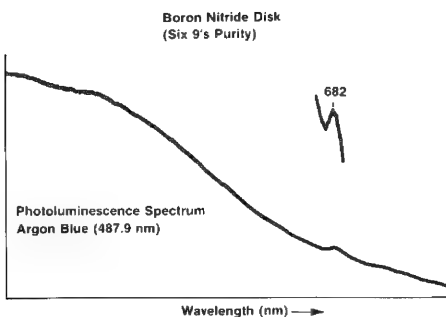FIG. 1.--Boron nitride disk: Raman spectrum with argon green (19 436 cm^{-1}).

FIG. 2.--Boron nitride disk: Photoluminescence spectrum with argon blue (487.9 nm).
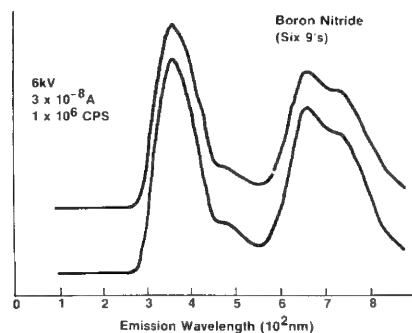
FIG. 3.--Boron nitride disk: Cathodoluminescence at 6 kV, 3×10^{-8} A, and 1×10^6 cps.

The author is at IBM's East Fishkill Facility, Hopewell Junction, NY 12533.

Magnesium Oxide

MgO crystalline source material for evaporated films has been examined by the three techniques mentioned. Figure 4 shows the Raman spectrum, which is weak and has only broad peaks at about 470, 550, 630, and 1175 cm^{-1}, none of which agrees with Ross.[5]

Figure 5 shows the sample to have a sharp impurity luminescence at 697 nm by photoluminescence using the argon blue laser line. Optical emission analysis showed 10 ppm Cr and 50 ppm Fe as the only transition elements present. There is extensive literature showing that Cr is responsible for the peak at about 700 nm,[6] and for a broad band about 800 nm,[7] and higher.[8] Figure 6 shows the cathodoluminescence spectra of the MgO material and the broad band between 700 and 800 nm is probably due to the Cr, or O^{2-} interstitials.[9] The other emission peaks are ~180 nm from the band gap[10], the 420-440 nm peak from Mg^{2+} interstitials[9] and possibly point defects due to oxygen vacancies,[11] and the ~500 nm peak probably due to the Fe^{2+}, which causes an absorption peak at 469 nm.[12] (By the Stokes Rule of fluorescence the absorbing wavelength is smaller than the emitting wavelength.)
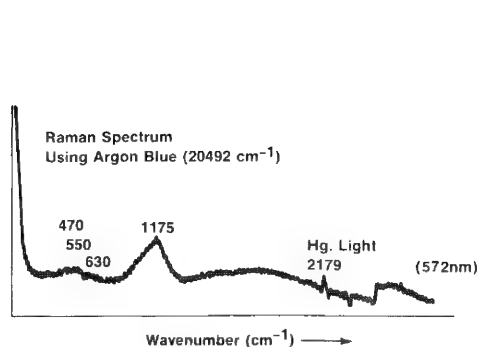

FIG. 4.--Magnesium oxide single crystal: Raman spectrum with argon blue (20 492 cm^{-1}).
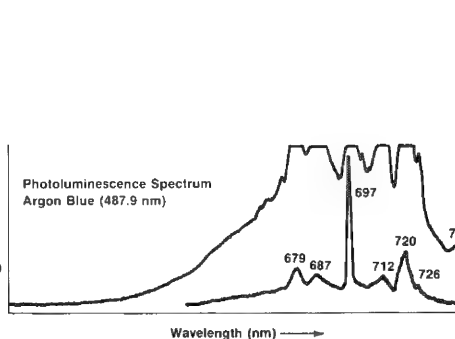
FIG. 5.--Magnesium oxide single crystal: Photoluminescence spectrum with argon blue (487.9 nm).
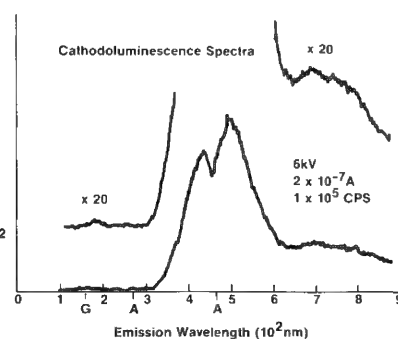
FIG. 6.--Magnesium oxide single crystal: Cathodoluminescence at 6 kV, 2 $\times 10^{-7}$ A, and 3 $\times 10^4$ cps.

Alpha and Mu Cordierite

Alpha and Mu cordierites are magnesium aluminum silicate crystalline phases which can precipitate from various complex ceramic or mineral systems. Although the cordierites are listed as having identical composition, they have different crystal structures according to the ASTM cards. As the crystals are usually smaller than x-ray spatial resolutions (even with the 10 μm measured with a Rigaku Denki Microdiffractometer) and their compositions would not be differentiated by an electron probe microanalyzer, another small-area characterization technique would be helpful. Figure 7 shows the Raman spectra of both α and μ cordierite: the α has several peaks, with one at 565 cm^{-1} predominating, whereas the μ shows no real peaks,[13] with just hints at 185 cm^{-1}, 200 cm^{-1}, and something around 350 cm^{-1} even though the gain and noise level are comparable. Thus, marked differences exist between the two phases. Figure 8 shows the photoluminescence for both α and μ cordierite. The main feature in PL is a sharp doublet at 694-695 nm, which looks like an impurity level similar to the Cr^{3+} in Al_2O_3. Optical emission showed about 2000 ppm Fe. There are variations in the smaller peaks between α and μ, with the most prominent being the 686-688nm peak in the α: the variations would allow identification and mapping of α vs μ crystallites larger than 1-2 μm. Figure 9 shows the cathodoluminescence, and the poorer resolution CL spectra do not reveal differences between α and μ but do reveal the impurity luminescence rising out of the broad CL peaks.

Zinc Sulfide

Figure 10 shows the Raman spectrum of a chemical-vapor-deposited (CVD) sample of zinc sulfide. The dominant peak, 349 cm^{-1}, is the Longitudinal Optical[14]; the 272 cm^{-1} peak is the Transverse Optical.[14] The remainder of the peaks (all Raman and not photoluminescence) have not yet been accounted for. Figure 11 shows the cathodoluminescence spectra

236
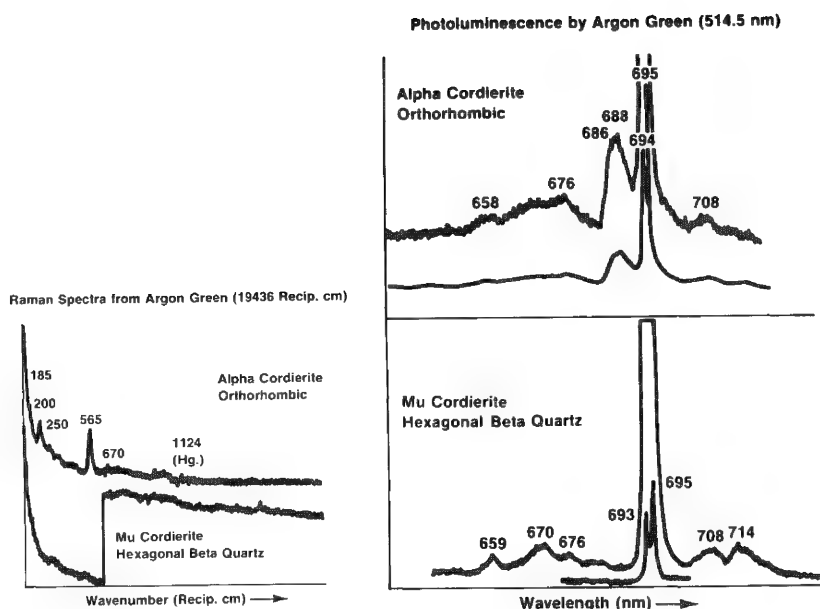
FIG. 7.--Alpha and Mu cordierite: Raman spectra with argon green (19 436 cm^{-1}).

FIG. 8.--Alpha and Mu cordierite: Photoluminescence spectra with argon green (514.5 nm).
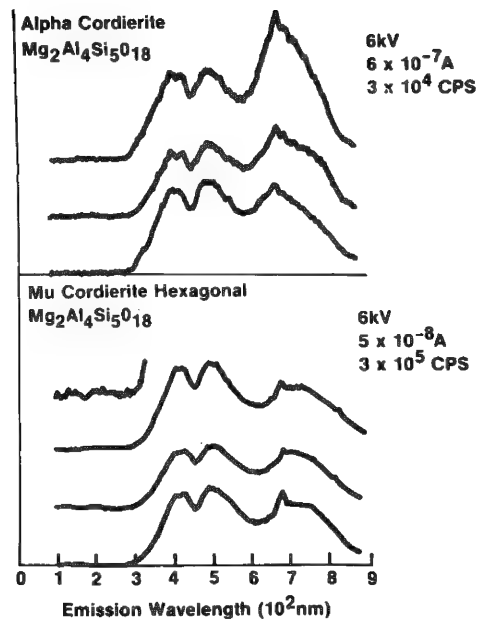
FIG. 9.--Alpha and Mu cordierite: Cathodoluminescence spectra at Alpha 6 kV, 6 × 10^{-7} A, and 3 × 10^4 cps; and Mu 6 kV, 5 × 10^{-8} A, and 3 × 10^5 cps.

of two locations of the specimen in which the band gap (~325 nm) and, probably, an impurity luminescence (~660 nm) are seen clearly in one location but not the other: thus local inhomogeneities on a 3-5μm level can be located for further analysis. Careful mapping by cathodoluminescence should allow study by photoluminescence with its higher resolution.

The application of these techniques to thin ZnS films will be given elsewhere.[15]
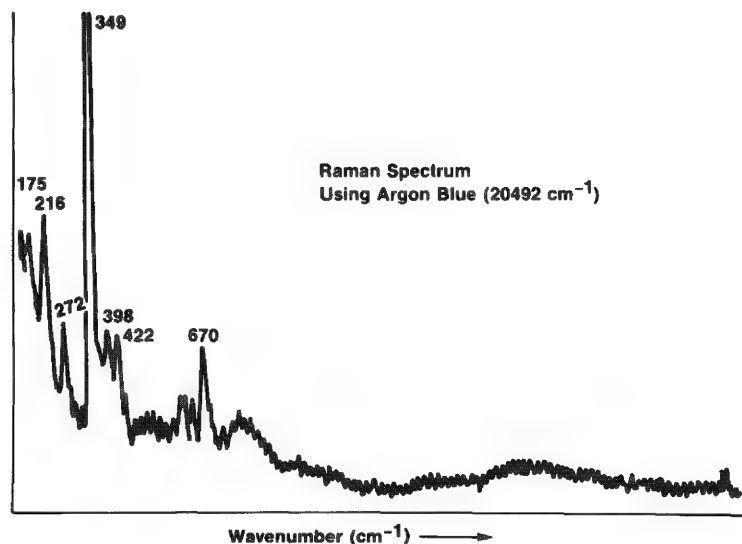
FIG. 10.--Zinc sulfide (CVD): Raman spectrum with argon blue (20 492 cm^{-1}).
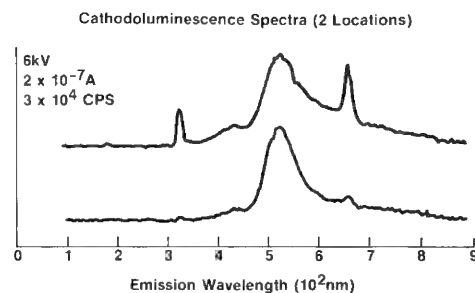
FIG. 11.--Zinc sulfide (CVD): Cathodoluminescence spectra at 6 kV, 2 × 10^{-7} A, and 3 × 10^4 cps.

Conclusion

Raman, photoluminescence, and cathodoluminescence provide complementary small-area analytical techniques that can offer unique capabilities in some materials. In addition, though previously mentioned, Raman provides unique organic small-area analysis because no other technique exists.

References

1. M. Delhaye and P. Dhamelincourt, "Raman microprobe and microscope with laser excitation," *J. Raman Spectroscopy* 3: 33-43, 1975.

2. R. N. Knisely, F. C. Laabs, and V. A. Fassel, "Analysis of rare earth materials by cathodoluminescence spectra excited in an electron microbrope," *Analy. Chem.* 41: 50, 1969.

3. J. N. Ramsey and M. J. Mitchell, "Cathodoluminescence studies of various aluminas at low kV," Late News Paper, *Proc. 11th MAS Conf.*, 1976.

4. M. J. Mitchell and J. N. Ramsey, "Difficulties of interpreting cathodoluminescence spectra," *Proc. 8th Intern. Conf. X-ray Optics & Microanal. & 12th MAS Conf.*, 1977, p. 123.

5. S. D. Ross, *Inorganic IR and Raman Spectra*, New York: McGraw-Hill, 1972, Chap. 4.

6. F. Castelli and L. E. Forster, "Fluorescence and phosphorescence in MgO:Cr," *Phys. Rev.* B11: 920, 1975.

7. A. Boyrivent and E. Duval, "Broad-band luminescence in MgO:Cr^{3+}: Relaxed level and emission process," *J. Phys. Chem.* 11: 439, 1978.

8. M. O. Henry, J. P. Larkin, and G. F. Imbusch, "Nature of the broad band luminescence center in MgO:Cr^{3+}," *Phys. Rev.* B13: 1893, 1976.

9. V. N. Rozhanskii et al., "Local loss of stoichiometry caused by plastic deformation of an MgO crystal," *Sov. Phys. Sol. State* 19: 1159, 1977.

10. W. D. Kingery, *Introduction to Ceramics*, New York: Wiley, 1975, 2d ed.

11. Y. Chen et al., "Luminescence in deformed MgO, CaO and SrO," *Phil. Mag.* 32: 99, 1975.

12. K. W. Blazey, "Optical absorption of MgO:Fe," *J. Phys. Chem. Solids* 38: 371, 1977.

13. The problem of little or no Raman from complex structures is mentioned briefly by White in chap. 13 of C. Karr, Ed., *IR and Raman Spectroscopy of Lunar and Terrestrial Minerals*, New York: Academic Press, 1975. ("Actinolite....Instead of the rich spectrum that might be expected from the large number of atoms in the unit cell, only a few weak bands are observed...it appears likely that a degree of mixed site substitution is responsible for the weak spectrum...similar in sheet silicates....")

14. G. R. Wilkenson, "Raman spectra of ionic covalent and metallic crystals," in Anderson, Ed., *The Raman Effect*, New York: Dekker, 1973, Chap. 11.

15. J. N. Ramsey, "Characterization of II-VI compound thin films by small area Raman, photoluminescence and cathodoluminescence," submitted to *IXth ICXOM*, The Hague, 1980.

TRACE-LEVEL MICROANALYSIS OF CARBON AND OXYGEN IN ELECTRONIC MATERIALS BY Cs BOMBARDMENT SIMS

V. R. Deline, R. J. Blattner, and C. A. Evans Jr.

This paper discusses the use of Cs^+ ion bombardment for the analysis of C and O in semiconductor materials. With ion-implanted standards, the residual vacuum is shown to limit the analysis to the 4-6ppm-at. regime in silicon and 0.2-2 ppm-at. in GaAs. The use of the SIMS technique for the analysis of C and O is demonstrated by the analysis of amorphous SiH_x layers typical of those being studied for photovoltaic solar-cell applications.

The trace microanalysis of gaseous or interstitial impurities, particularly C and O, is difficult because analytical techniques with good elemental specificity tend to have poor sensitivity at trace levels, whereas techniques with good sensitivity suffer from the ubiquitous occurrence of these elements, i.e., contamination during the analysis. Unintentional incorporation of these elements during materials preparation also makes these impurity elements important in the context of contemporary materials science, e.g., thin-film phenomena, epitaxy, interfaces, etc. Consequently, the analytical process must be carefully examined with regard to

1. extraneous contamination of the material between the time of preparation and sample introduction into the analytical system;
2. indirect contamination during analysis from the ambient environment of the sample, which is typically either a blanket of inert gas or vacuum; and
3. direct sample contamination in ion-beam analytical systems (such as secondary ion mass spectrometry) via impurities in the probing beam itself.

Secondary ion mass spectrometry (SIMS) is the most sensitive of the modern surface analysis techniques, but is susceptible to all three forms of contamination mentioned above: sample handling, adsorption from the residual vacuum, and implantation by the primary beam.

The intrinsic sensitivity of SIMS arises from three sources. First, if we consider a typical analytical volume composed of an analyzed area of 100×100 μm at a sputtering rate of 10 Å/sec, the number of atoms sputtered in 1 sec is about 5×10^{11}. If an impurity is present at the 1ppm level, then 5×10^5 atoms of that trace element are sputtered every second and constitute a *potentially* large number of atoms for the generation of an analytical signal. Thus, the *conversion* of those atoms into positive and negative ions, as well as the *collection* and *transmission* of the ions in a mass spectrometer, becomes central to realizing the potential of SIMS for trace analysis at the microanalytical level. The realization of high secondary-ion yields (positive or negative ions) requires the use of oxygen and cesium ion bombardment, respectively.[1,2] Only by use of these reactive species can ion yields of 10^{-1} to 10^{-4} be routinely obtained and 5×10^4 to 50 secondary ions per second produced for a 1ppm impurity. These secondary ions are ejected from the surface over a wide angle of emission and with a large initial kinetic energy, which requires specialized ion optics for efficient collection and analysis of the ions with transmissions of 1-10% and so allows the detection of 10^3 ions for an element at the ppm level. This is indeed the case for C and O if Cs^+ ion bombardment/negative-ion spectroscopy is used, but as with most techniques, it is plagued by the unintentional introduction of these elements during the analysis from sources other than the sample. Thus, detection limits are not in general a function of signal availability, but rather are controlled by "backgrounds" resulting from the various external sources of C and O. Most important among these sources is incorporation from the residual vacuum.

Three important factors must be considered in assessing the impact of vacuum on a

given analysis: (a) the partial pressures of active species in the residual gas (carbon and oxygen containing for our purposes), (b) the sticking probabilities of those species on the sample, and (c) the attainable sputtering rate. If we assume that a monolayer of a species forms in 1 sec when that species is present in the residual vacuum at 1×10^{-6} Torr, then with a unit sticking probability, we can calculate the fraction of analytical signal arising from the residual vacuum during a SIMS analysis. For either carbon or oxygen, 0.1 monolayer will form in 1 sec if the sticking probability is 0.1. If the partial pressure of the active species is 10^{-9} Torr, the corresponding coverage is 10^{-4} monolayer/sec. Therefore, if we employ a sputtering rate of 10 monolayers/sec (approximately 30 Å/sec or nearly 0.2 μm/min), then we can expect a contribution of that atom from the residual vacuum of approximately 10 ppm equivalent concentration. It is perhaps fortuitous that the negative-ion spectroscopy needed to realize high secondary-ion yields for C and O also requires the use of Cs ion bombardment, which allows the use of sputtering rates concomitant with the above assumptions. The purpose of this study is to evaluate the possibility of obtaining ppm (or better) detection limits for C and O in semiconductor materials such as Si or GaAs.

Experimental

The samples used to evaluate sensitivity and background were either ion-implanted GaAs or Si, which provide a known concentration at the peak of the ion implant and permit a determination of background levels where C and O were known a priori not to be present at the levels detected. Float-zone Si was used with expected oxygen concentrations in the 10^{15} at.cm^{-3} region and C in the 10^{16} at.cm^{-3} region.[3] Several thin films were prepared in order to demonstrate the depth profiling capabilities of the SIMS technique for C and O incorporated during materials preparation. One difficulty encountered in this study concerned obtaining samples with a known amount of the species of interest. However, it was possible to obtain some information based on literature values, solubility, and other work.

The instrument used for this study was the CAMECA IMS-3f ion microanalyzer,[4] equipped with a General Ionex Model 133 Cesium Ion Source.[5] The sample-chamber vacuum system has been modified by the replacement of the turbomolecular pump, supplied with the basic instrument, with a vacuum "T" accomodating a recirculating He refrigerator with dual cryo-panels and a 20L/sec ion pump. Samples for the evaluation were mounted in the instrument vacuum system followed by a bake of the sample chamber at approximately 80°C for an extended period.

Results

Figure 1(a) shows the depth profile for a 100keV, 1×10^{16} at.cm^{-2} oxygen implant into float-zone Si. The peak concentration can be calculated to be 4×10^{20} at.cm^{-3} from which a background level of 3×10^{17} at.cm^{-3} can be determined. Figure 1(b) shows a similar profile for a C implant made at 100 keV to a dose of 1×10^{16} at.cm^{-2} producing a peak concentration of 7×10^{20} at.cm^{-3} and a background of 2×10^{17} at.cm^{-3}. Similar profiles were obtained for H and N, which provided background limits of approximately 8 and 10 ppm, respectively. Comparable studies in GaAs produced backgrounds of 1×10^{17} at.cm^{-3} for O and 1×10^{16} at.cm^{-3} for C. Although the exact C and O content of this particular GaAs sample was not known, various materials prepared by different growth techniques were examined, each of which should produce differing amounts of residual C and O contamination. No variations in observed background levels could be detected, regardless of how the GaAs was grown. Examination of MBE, VPE, and LPE layers did reveal higher C and O levels in the epitaxial layer than in the bulk GaAs substrates, which indicates contamination during layer growth.

A comparison of the background levels obtained for the Si and GaAs samples provides information on both the samples and the analytical technique itself. Somewhat surprising is the fact that the O background is identical in both Si and GaAs. These materials are known to have an oxygen concentration almost an order of magnitude lower than was found for the analytical background. Thus, the oxygen introduced by the analysis is most likely coming from the residual vacuum. For a constant sputtering rate and at the same vacuum level, both materials gave the same background during the two different analyses, so that
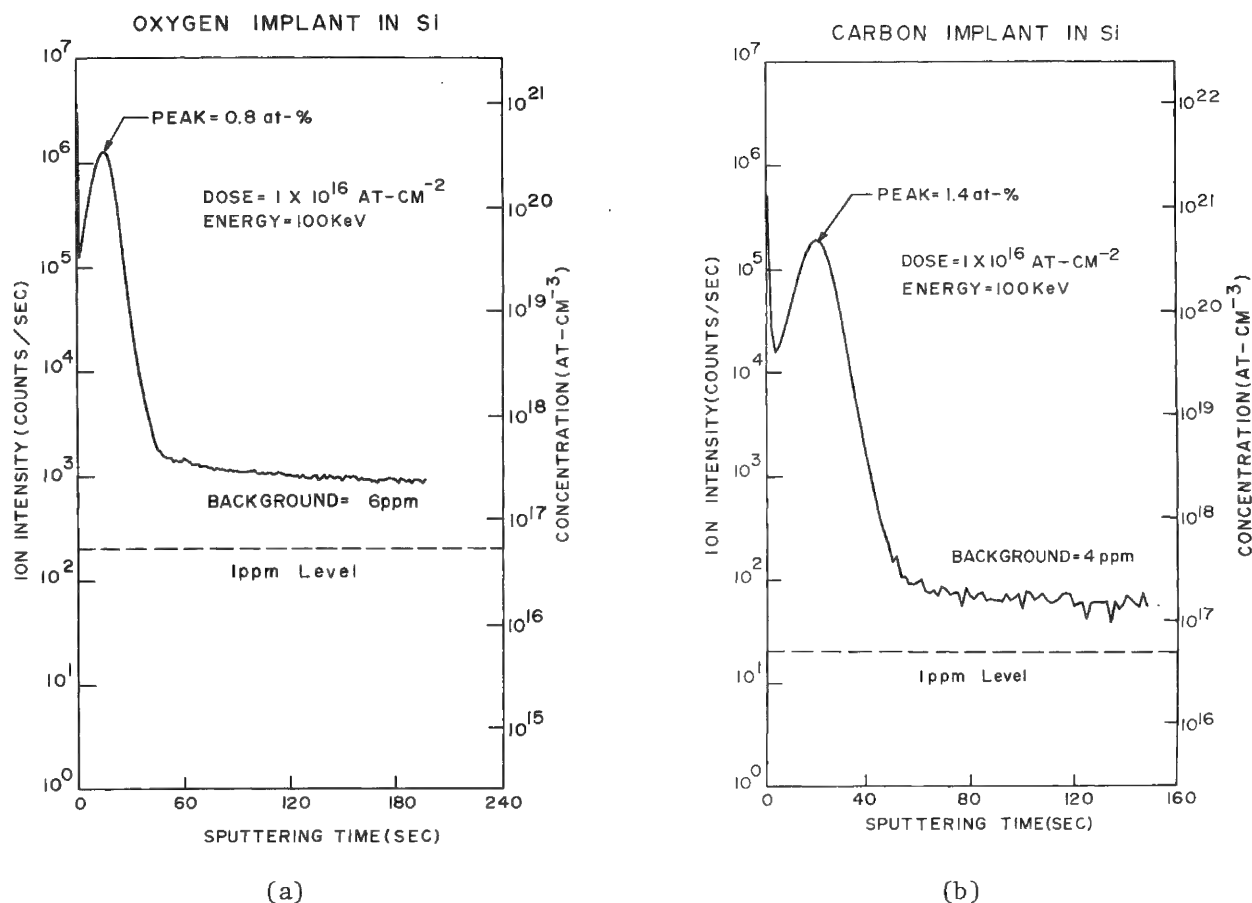
FIG. 1.--(a) Depth profile of oxygen ion implant into float-zone silicon from Cs^+ ion-bombardment/negative-ion spectroscopy on the CAMECA IMS-3f ion microanalyzer at sample chamber pressure of about 2×10^{-8} Torr; (b) the same for sample with carbon implant.

one may assume that under these experimental conditions, the sticking coefficient of oxygen from the active oxygen-bearing species must be nominally the same for both Si and GaAs. This result is rather surprising, since studies of oxygen ion emission as a function of partial pressure of O_2 suggest that oxygen does not stick to clean GaAs surfaces until the partial pressure is above 10^{-5} Torr.[7,10,11] However, these referenced studies all employed Ar^+ ion bombardment. Our results then suggest that the "stickiness" of the surface is controlled not by the substrate material, but by the presence of Cs in and around the near-surface region of the sample. Therefore, oxygen-bearing species can adsorb onto the Cs atom sites and so yield a background somewhat independent of the intrinsic properties of the material. The situation for carbon seems to differ in that the C background for GaAs is much lower than that for the float-zone Si (1×10^{16} vs 2×10^{17} at.cm^{-3}). Based on the above discussion, this finding would suggest that the partial pressure of carbon-bearing species in the residual vacuum is such that the vacuum contribution to the background is below 10^{16}, and thus the measured carbon signal of 10^{17} at.cm^{-3} for silicon is probably real.

Figure 3 illustrates how these established background levels (and hence detection limits) for carbon and oxygen can be used to determine the presence of these impurities in a contamination situation. The figure shows a multi-element depth profile for a bi-layer of SiH_x on a stainless-steel substrate. This type of structure is typical of materials being developed for low-cost solar-cell applications.[12] The amorphous silicon is deposited from silane in the presence of H_2 by reaction in a glow discharge. The role of hydrogen is to stabilize the amorphous state by saturating "dangling bonds" in the material. Since epitaxy is not required, the layers can be deposited on low-cost substrates.

AMORPHOUS SILICON

undoped | P-doped | stainless steel

- Si
- H
- O
- C
- P
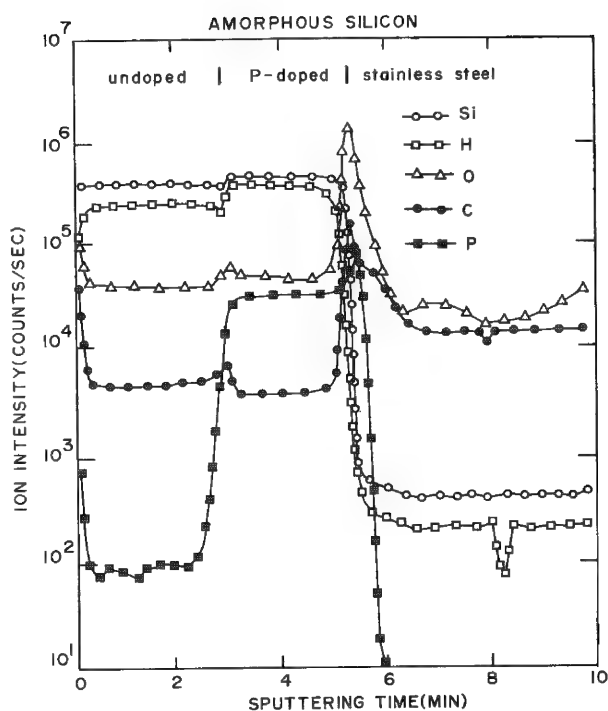
FIG. 2.--Depth profile of amorphous SiH_x bilayer on stainless steel (taken under experimental conditions similar to those used for Fig. 1), which shows incorporated carbon and oxygen contamination during film deposition and phosphorus doping profile taken at high mass-resolving power.

This profile shows that deposition of the two layers containing differing amounts of hydrogen and phosphorus also contain differing amounts of carbon and oxygen. The changes in the deposition conditions from the phosphorus-doped to the undoped layer also causes changes in the incorporation rate of C and O. It is interesting to note that these deposition changes cause the carbon content to increase but they decrease the amount of oxygen incorporation.

Conclusions

This study has shown that carbon and oxygen detection limits in the low $10^{17} at.-cm^{-3}$ range in Si and GaAs can be obtained with the CAMECA IMS-3f ion microanalyzer by Cs^+ ion bombardment. The major limitation in the analysis is not signal availability, but background levels related to the residual vacuum of the instrument. Furthermore, under Cs ion bombardment, it appears that the presence of Cs dominates the behavior of the sticking probability, which gives rise to backgrounds somewhat independent of matrix material. Finally, based on measured signal levels, signal-limited detectabilities of the order of 1-10 ppb should be obtainable if vacua in the range of $10^{-12}-10^{-13}$ Torr could be achieved in the instrument.

References

1. H. A. Storms, J. D. Stein, and K. F. Brown, *Anal. Chem.* 40: 1399, 1977.

2. P. Williams et al., *Anal. Chem.* 49: 1399, 1977.

3. H. M. Kiaw, *Semiconductor International* 2(No. 8): 71-82, 1979.

4. CAMECA Instruments Inc., Stamford, Conn.

5. General Ionex Corp., Newburyport, Mass.

6. R. Wilson, Hughes Research Laboratories, Malibu, Calif., private communication.

7. C. Magee, RCA Laboratories, Princeton, N.J.,private communication.

8. T. Magee, Advanced Research and Applications Corp., Sunnyvale, Calif., private communication.

9. R. Reynolds, Defense Advanced Research and Projects Agency, Washington, D.C., private communication.

10. K. Wittmack, in *Inelastic Ion-surface Collisions*, New York: Academic Press, 1977, 153-199.

11. A. M. Huber et al., *J. Appl. Phys.* 50: 4022, 1979.

12. D. E. Carlson, *Proc. Photovoltaics Advanced R & D Annual Rev. Mtg.*, Denver, Colo., 1979, 113-119.

CHARACTERIZATION AND ORIGIN OF MICROCRACKS IN A SEMICONDUCTOR PASSIVATION GLASS

H. A. Freeman and K. W. Michael

Examination of defective integrated circuits encapsulated with molding compound was part of a cooperative effort to assist manufacturers of electronic devices in defining the cause of device failures. Concurrent with the more widespread use of the scanning electron microprobe (SEMP) in semiconductor failure analysis, a Cameca MBX instrument was employed to expand upon information obtained by optical microscopy.[1] This particular study was originally started to investigate a suspected corrosion mechanism of failure in devices encapsulated with molding compound. Such modes of failure have been described, particularly as they are produced by moisture and bias testing.[2] In this instance, there was no evidence of a corrosion type of failure. However, the study did define cracks in the passivation glass which were responsible for electrical failure in the test environment. It was also established that the cracks formed during fabrication of the device prior to etching of windows for the wire-bonding step.

The devices were Metal Oxide Semiconductors (MOS) used in the construction of computer circuitry. The devices were protected with a layer of passivation glass approximately 1 μm thick. Initial studies were made on devices encapsulated with two types of Dow Corning molding compounds. Standard transfer molding and cure schedules were employed. Devices from the same wafer lot, available in ceramic packages, were also opened and examined. The encapsulated devices failed after exposure to autoclave conditions of 96 hr at 121°C and 15 psig steam.

Chip Preparation

The devices were mechanically exposed for observation by a process of drilling around the periphery of the chip and gently lifting off the molding compound. Previous experience with this type of study had demonstrated the inadvisability of using solvents or acids to expose the chip since substantial modification of the surface may result. Mechanical extraction of the chip was followed by application of an evaporated film of carbon, about 200Å thick, to the surface. The coating was essential to enhance surface detail during initial optical microscopical studies of the passivation glass by Nomarski interference contrast techniques. The carbon also provided better secondary electron image generation and minimized charging in the SEMP.

Results

The optical Nomarski examination technique revealed a random network of numerous intersecting fractures across the entire surface of the passivation glass. Further examination with the secondary electron mode of imaging in the SEMP readily defined these cracks at higher magnification. The morphology was accentuated by Y-deflection image processing (Figs. 1 and 2). Since the cracks were well developed on the integrated circuits from the ceramic packages as well as on those from both molding compound compositions, it became evident that the molding compound was not responsible for these defects. A further explanation of the origin of the cracks was sought.

Continued examination of the cracks in the SEMP revealed that they abruptly changed to shallow U-shaped channels within the windows of the bonding pads and aluminized test sites (Fig. 3). The channels were uniformly about 4 μm wide and substantially less than 1 μm deep. The cracks were found to be continuous with these channels, often completely crossing the aluminization and appearing again as cracks within the glass on the other side. Similar channels were found on bonding pads of the integrated circuit from the ceramic package (Fig. 4). Centrally located within each channel also appeared a crack which was continuous with that in the passivation glass at each end of the channel (Fig. 5).

The authors are with the Dow Corning Corporation in Midland, MI 48640.
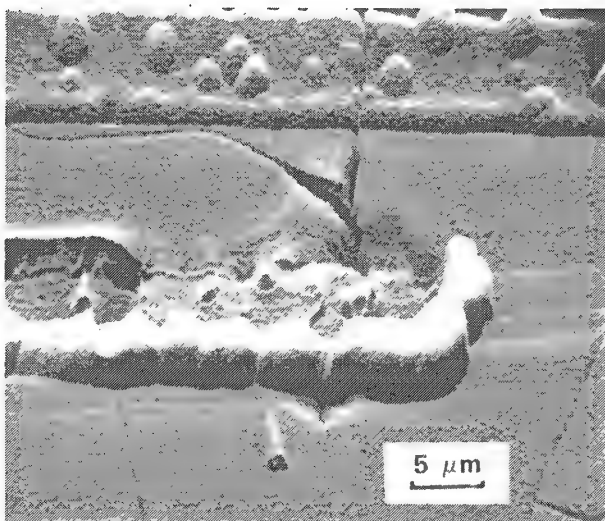
FIG. 1.--Microcracks in semiconductor
passivation glass. Secondary-electron
image, Y deflection.
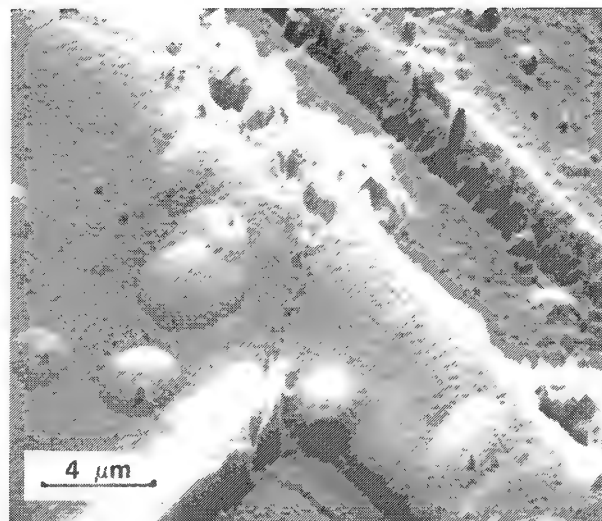
FIG. 2.--Microcracks related to topogra-
phic configuration of semiconductor sur-
face. Secondary-electron image, Y deflec-
tion.
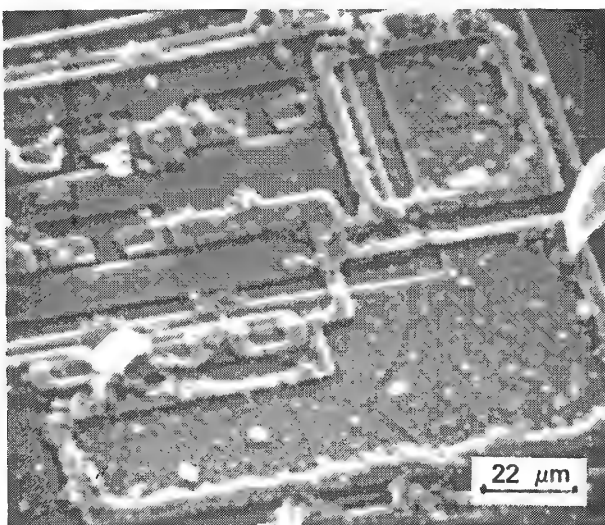
FIG. 3.--Etch channels developed in test
site areas. Secondary-electron image.
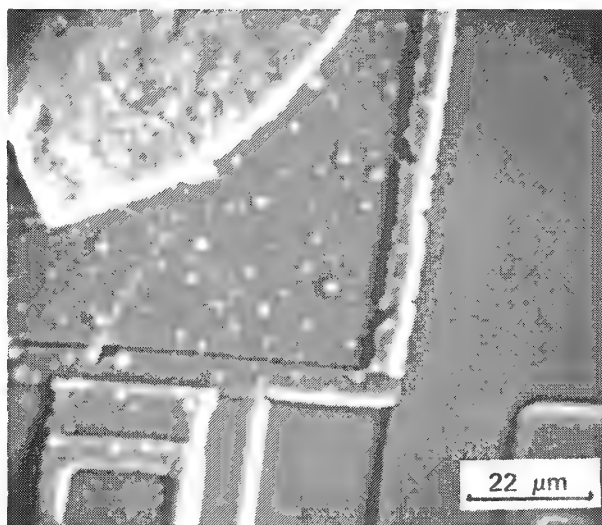
FIG. 4.--Etch channels on bonding pad of
integrated circuit from ceramic package.
Microcracks, as at arrows, continue across
passivation glass. Secondary-electron
image.

Mechanical separation of molding compound from the chip often caused the gold wire
bonds to be pulled free of the integrated circuit. Examination of these bond areas in
the SEMP showed that the channels progressed under the wire bonds. Intersecting bands
of remnant gold alloy were visible as fillings of the shallow channels in the aluminum
substrate (Fig. 6). Energy-dispersive x-ray analysis in the SEMP of these channel fill-
ings verified the alloy composition.

Interpretation

The microscopical findings were significant since they unequivocally related the chan-
nels on exposed aluminization with cracks in the passivation glass. Moreover, the
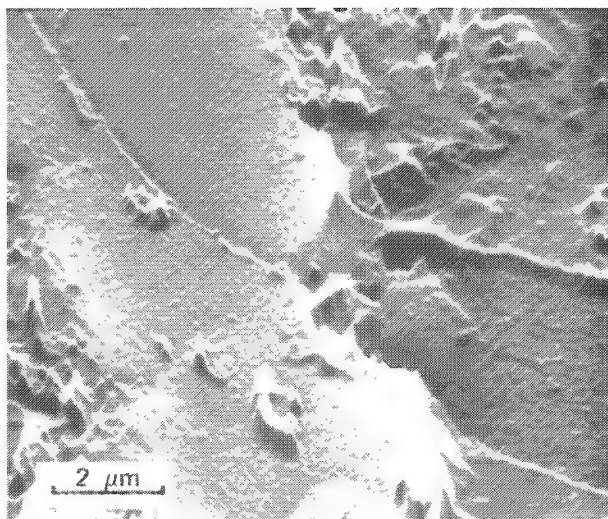
FIG. 5.--Microcrack in passivation glass, at arrow, is continuous with medial crack in etch channel at margin of bonding pad. Secondary-electron image, Y deflection.
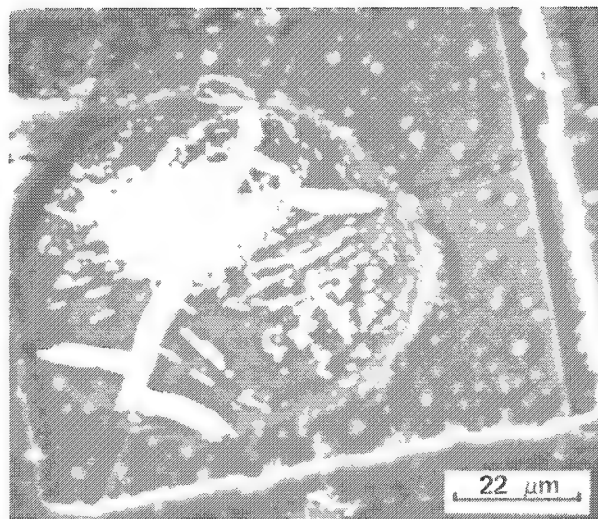
FIG. 6.--Branched gold alloy occupying etch channels within confines of wire bond area. Note continuation of channels across adjacent aluminization. Secondary-electron image.

branched gold-filled channels that were beneath the wire bonds showed that the channels had formed before emplacement of the bonds. The morphology suggested that the cracks developed upon cooling of the passivation glass following its application. In the subsequent etchant step, acid penetrated the cracks over the bonding pads and test sites, causing attack of the aluminization and formation of U-shaped channels. Aluminization under cracks in other parts of the circuitry was protected from attack by the overlying photoresist resin. Complete dissolution of glass over the bonding pads left channels in the aluminization that became filled with gold in the subsequent wire bonding step. Failure of the encapsulated devices during autoclave testing was attributed to water vapor penetrating the cracks in the passivation which changed operating characteristics of the devices. The findings from this study made possible a better understanding of these defects and assisted in the manufacturer's efforts to correct the problem.

References

1. D. P. Nicolas, "Role of SEM in microcircuit failure analysis," O. Johari, Ed., *SEM/1974*, Part IV, 956-962.
2. S. P. Sim and R. W. Lawson, "The influence of plastic encapsulants and passivation layers on the corrosion of thin aluminum films subjected to humidity stress," 17th Annual International Reliability Physics Symposium, Presentation of Abstracts, IEEE Reliability Group, San Francisco, p. 4.3-1, 1979.

ELECTRON MICROPROBE ANALYSIS OF ELECTROLYTES IN EPITHELIAL TISSUES

Roger Rick, Adolf Dörge, F. X. Beck, June Mason, and Klaus Thurau

During recent years an increasing number of laboratories have employed electron microprobe analysis for biological specimen such as fluid samples, isolated cells, biological hard and soft tissues. This paper is confined to the analysis of diffusable elements in epithelial tissues on a cellular and subcellular scale. The limitations of the method, which result mainly from problems of specimen preparation, irradiation damage, and quantitation, are discussed and analyses of the intraepithelial electrolyte concentrations in frog skin and rat kidney are reported.

EDS Analysis of Thin Freeze-dried Cryosections

We prepared 1μm-thick freeze-dried cryosections by shock-freezing small pieces of fresh tissue in propane or isopentane/propane mixtures at -190°C, cryosectioning at -100°C in a cryoultramicrotome (Reichert), and afterwards freeze-drying at 10^{-6} Torr and -80°C. The analysis of the sections was performed in a scanning electron microscope (Cambridge) to which an energy-dispersive x-ray detector (Link) had been attached. The acceleration voltage was 17 kV and the probe current was 0.2-0.5 nA. Quantification of the cellular electrolyte concentration in mmole/kg wet weight was achieved by direct comparison of the characteristic x-ray peaks in the cell with those of an internal albumin standard. The discrimination between characteristic radiations and background was performed with the aid of a computer program. Details of the method have been described earlier.[1-3]

It is generally accepted that 'physical fixation' by rapid freezing of the tissue is the only way to keep readily diffusible elements such as Na, K, and Ca in place. However, owing to ice crystal formation during freezing inevitably some dislocations of electrolytes and distortions of the tissue structure occur. Under optimal freezing conditions, measurements on a cellular scale can be performed in a region extending up to 50 μm from the freezing surface.

The attainable spatial resolution power of electron microprobe analysis is mainly a function of section thickness and acceleration voltage. In 1μm-thick sections at 17 kV a lateral resolution of 0.5 μm was obtained for diffusable elements such as Na and K. In principle, an improvement of the spatial resolution power can be expected from the use of even thinner sections.

The use of freeze-dried sections offers the advantage that the specimen can be analyzed and stored at room temperature. Furthermore, compared to analysis in the frozen-hydrated state, freeze-dried tissue sections allow a much better electron optical visualization and, since almost 80% of the mass is removed during drying, a much better signal-to-noise ratio in the x-ray analysis can be achieved. On the other hand, freeze-drying may lead to some shrinkage of biological soft tissues; and in extracellular tissue compartments that contain almost no biological matrix, such as the lumen of kidney tubules, the electrolytes may be dislocated during drying.

Electron microprobe analysis of biological specimen is complicated by the sensitivity of organic materials to electron bombardment. At current densities used in the present study (0.2-0.5 nA/μm^2), mass loss during irradiation appears to affect only constituents of the biological matrix, whereas electrolytes such as Na, Cl, and K are stable. Furthermore, the formation of a contamination layer at the site of analysis is negligibly small.

The current dose administered to the specimen can be drastically reduced by the use of an energy-dispersive x-ray detector (EDS) owing to its high detection sensitivity. At 30mm^2 surface area of the detector and 7mm distance between detector and specimen, a solid angle of 0.6 steradian, equal to a detection efficiency of almost 5%, was obtained.

On the other hand, owing to the low peak-to-background ratios of an energy-dispersive system and the low x-ray yield obtained from a thin biological specimen, all extraneous radiations must be carefully eliminated. This goal can be achieved if the section is supported only by a thin collodion film, with a specimen stage of low background properties and shielding of the detector against stray radiations. At 17kV acceleration voltage only about 10% of the Bremsstrahlung does not originate from the specimen itself and no extraneous signals were detected for the characteristic radiations of Na, P, S, and K.[4] At higher acceleration voltages, the contribution of spurious signals is more pronounced, since the x-ray yield of the section decreases and the excitation of solid parts of the specimen chamber increases. Furthermore, the high-energy electrons can penetrate the Be-entrance window of the detector. Figure 1 demonstrates that for most biologically relevant elements optimal peak-to-background ratios (P/B) are obtained in the range of acceleration voltage between 15 and 23 kV.
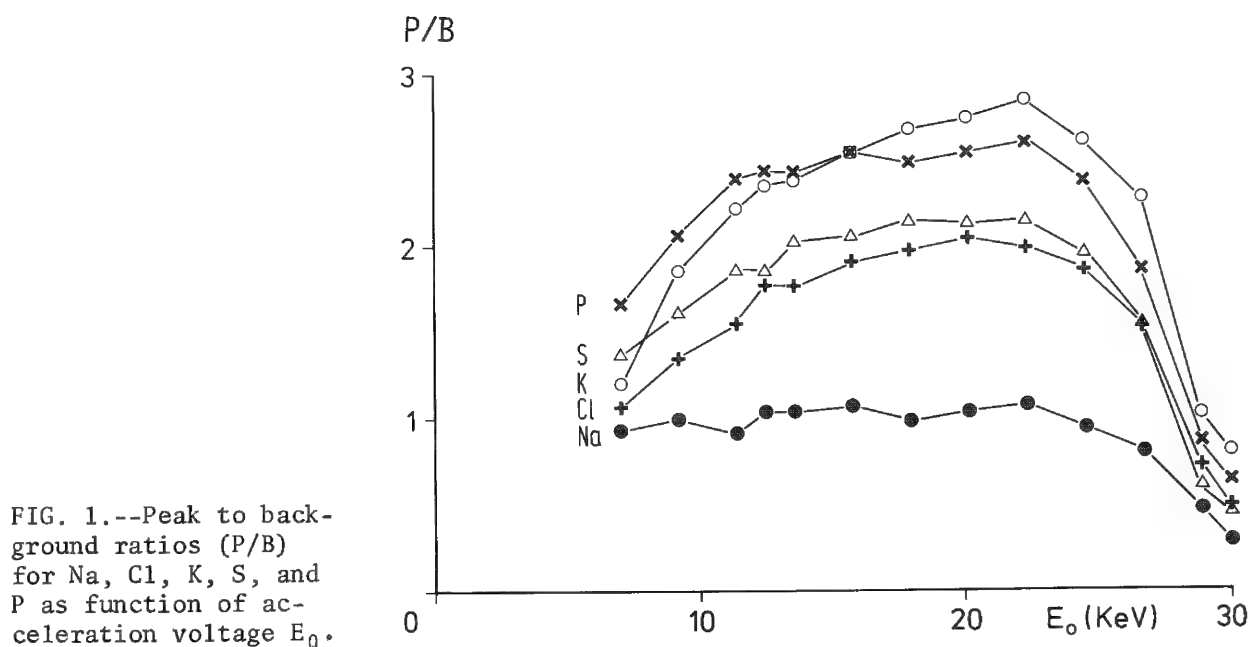
FIG. 1.--Peak to background ratios (P/B) for Na, Cl, K, S, and P as function of acceleration voltage E_0.

The use of thin sections greatly simplifies the quantification, since x-ray absorption, secondary fluorescence, and deceleration of the electrons within the specimen can be neglected. Thus, under constant experimental conditions the recorded x-ray intensities depend only on the respective element concentration. For all elements from Na trough Ca linear calibration curves were obtained in the full biologically relevant concentration range. Quantification of the cellular element concentration is achieved by comparison of the element characteristic peaks in the cells with those of an internal standard. The albumin standard layer is produced by immersion of the specimen immediately prior to shock-freezing in a solution of known element composition containing 20g% bovine albumin. The evaluation of the EDS spectra is performed by means of a computer program. In a single measurement, peaks corresponding to 0.4 mmole/kg w.w. of K or 2 mmole/kg w.w. of Na can be detected.

Electrolyte Concentrations in Frog Skin and Rat Kidney Epithelial Cells

Table 1 lists the cellular concentrations of Na and K in frog skin epithelium obtained by this method with those obtained by chemical analysis. Compared to chemical or radiochemical analysis of whole skin or isolated epithelium, the present values for Na are much lower and those for K are much higher. On the other hand, the electron microprobe analysis is in good agreement with chemical analysis of isolated epithelial

cells, which have been jet-washed in Na-free solutions in order to reduce the amount of adherent extracellular Na. The discrepancy between chemical and electron microprobe data can be attributed to an underestimation of the extracellular space in the chemical analysis.[5]

TABLE 1.--Cellular Na and K concentrations of frog skin epithelium. a = Rick et al.[5]; b = Nagel and Dörge[6]; c = Aceves and Erlij[7]; d = Zylber et al.[8]

	Na	K
	mmole/kg wet weight	
electron microprobe analysis[a]	9.4	118.4
chemical analysis		
- whole skin[b]	82.7	54.9
- isolated epithelium[c]	20.6	110.7
- isolated epithelial cells[d]	12.1	109.1
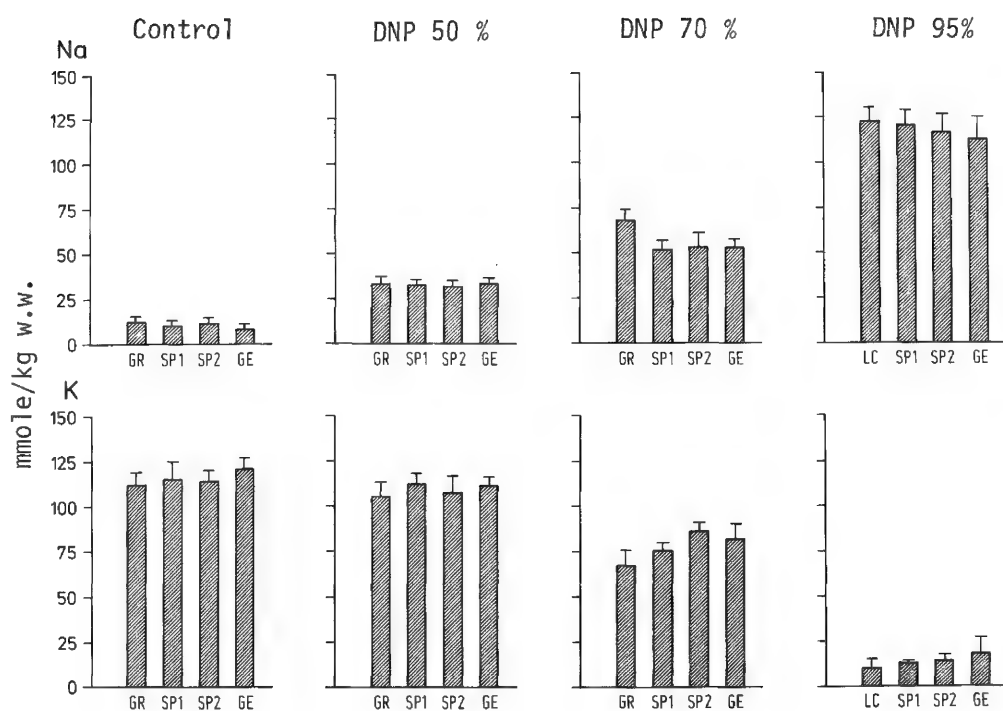
FIG. 2.--Na and K concentrations in the several epithelial layers of frog skin in control and when short-circuit current was reduced by 50%, 70% or 95% following application of 10^{-4}M 2-4-dinitrophenol (DNP). GR = granular layer; SP1, SP2 = superficial and deeper spiny layer; GE = germinal layers; under DNP 95% the granular layer was found to be transformed into light cells (LC).

No significant differences were detected between nuclear and cytoplasmic concentrations of Na and K. Figure 2 shows the Na and K concentrations of granular, superficial, and deeper spiny and germinal cells that form the several living epithelial cell layers of the frog skin epithelium. Under control conditions--both sides of the skin bathed in normal frog Ringer's solution, transepithelial potential difference short-circuited--the Na concentration in all layers is low and the K concentration is high. After inhibition

of the active transepithelial Na transport by 2-4-dinitrophenol, the Na concentrations in all layers are increased, whereas the K concentrations show an almost equivalent drop. A similar Na/K exchange was also observed when the Na/K pump was inhibited by ouabain.[*] It could also be demonstrated that the Na increase after ouabain is due to an Na influx from the outside bathing solution. When we blocked the Na influx--either by rendering the outer membrane impermeable to Na by amiloride or by using a Na-free outer bathing solution--the effect of ouabain was completely abolished. Furthermore, when the Na influx from the outside was stimulated, as with novobiocin or argininvaso-pressin, the Na concentrations in all epithelial layers were found to be increased. In contrast, after the Na influx from the outer bathing solution was reduced by the addition of amiloride, the Na concentrations in all layers dropped.

According to these results all living epithelial layers are involved in transepithel-ial Na transport. It can also be concluded that the various epithelial cells are connected via low resistance pathways for Na and form a syncytial Na transport compartment. However, a few epithelial cell types are not contained in the syncytial Na transport compartment: the gland cells, the mitochondria-rich cells, and the cornified cells.[5]

Electron microprobe analysis of cortical rat kidney revealed characteristic differences between proximal and distal tubular cells.[9] As shown in Table 2, the cellular concentrations of Na and Cl were significantly higher in the proximal tubule, whereas the K concentrations were virtually identical. Further functional differences between proximal and distal tubular cells could be detected during acute renal ischemia.[10] Following 20 min of renal ischemia the Na, Cl, and K concentrations of proximal tubular cells were drastically changed at 93, 53, and 65 mmole/kg w.w., respectively, whereas the concentrations of distal tubular cells were only slightly changed at 18, 29, and 146 mmole/kg w.w., respectively. However, after 60 min of ischemia only minor differences in the proximal and distal values could be detected. The Na, Cl, and K concentrations were 112, 66, and 42 for the proximal tubule and 77, 48, and 89 mmole/kg w.w. for the distal tubule, respectively. After reflow of blood was permitted the electrolyte concentrations returned within 60 min to values not significantly different from controls.

TABLE 2.--Cellular Na, Cl, and K concentrations of proximal and distal tubular cells of cortical rat kidney.

	Na	Cl	K
	mmole/kg wet weight		
proximal tubule	19.6	22.8	144.4
distal tubule	11.4	12.5	143.3

References

1. A. Dörge et al., "Preparation of freeze-dried cryosections for quantitative x-ray microanalysis of electrolytes in biological soft tissues," *Pflügers Arch.* 373: 85, 1978.
2. R. Rick et al., "Quantification of electrolytes in freeze-dried cryosections by electron microprobe analysis," *SEM/1978/II;* 619.

*The cardiac glycoside *ouabain* is known to inhibt the Na pump almost completely.

3. R. Bauer and R. Rick, "Computer analysis of x-ray spectra (EDS) from thin biological specimens," *X-ray Spectrom.* 7: 63, 1978.

4. R. Rick et al., "Quantitative determination of cellular electrolyte concentrations in thin freeze-dried cryosections using energy-dispersive X-ray microanalysis," in C. P. Lechene and R. R. Warner, Eds., *Microbeam Analysis in Biology*, New York: Academic Press, 1979, p. 517.

5. R. Rick et al., "Electron microprobe analysis of frog skin epithelium: Evidence for a syncytial sodium transport compartment," *J. Membrane Biol.* 39: 313, 1978.

6. W. Nagel and A. Dörge, "A study of the different sodium compartments and the transepithelial sodium fluxes of the frog skin with the use of ouabain," *Pflügers Arch.* 324: 267, 1971.

7. J. Aceves and D. Erlij, "Sodium transport across the isolated epithelium of the frog skin," *J. Physiol.* 212: 195, 1971.

8. E. A. Zylber et al., "Ion and water balance in isolated epithelial cells of the abdominal skin of the frog Leptodactylus ocellatus," *J. Membrane Biol.* 13: 199, 1973.

9. F. Beck et al., "Electron microprobe analysis of intracellular elements in the rat kidney," *Kidney Int.* (in press).

10. J. Mason et al., "The intracellular electrolyte composition following renal ischaemia" (submitted for publication).

ANALYTICAL CONSIDERATIONS FOR ASSESSING THE EFFECTS OF MASS LOSS IN BIOLOGICAL MATERIALS

J. W. Edie

A major limitation in the quantitative microanalysis of biological specimens is the destructive action of the electron beam on the low density specimens. These electron beam-specimen interactions result in varying characteristic and continuum count rates for the duration of mass loss from the specimen and these variations impose severe restrictions on the validity of quantitative results.[1,2]

The irradiation effects for biologically significant materials occur for electron doses of 10^{-11} to 10^{-9} C-μm^{-2} under normal operating conditions. It is not uncommon in focused beam analyses to supply doses in excess of 10^{-6} C-μm^{-2} to acquire statistically significant data when determining the low elemental contents that are typical of biological materials. Analytical considerations for acquiring the data within an electron dose of 10^{-10} C-μm^{-2} are presented in Fig. 1. The time of analysis is shown versus probe diameter for a range of beam currents. Instrumental limitations in operating conditions are indicated by dashed lines for a tungsten gun (W), a LaB$_6$ gun (LB), and a field-emission gun (FE). Typical operating conditions for microanalysis would exist within the shaded area. For these conditions, the specimen alterations resulting from electron irradiation would occur within a small fraction of a second. It would be necessary to increase the probe diameter to 100 μm before the count rate variations could be readily monitored.
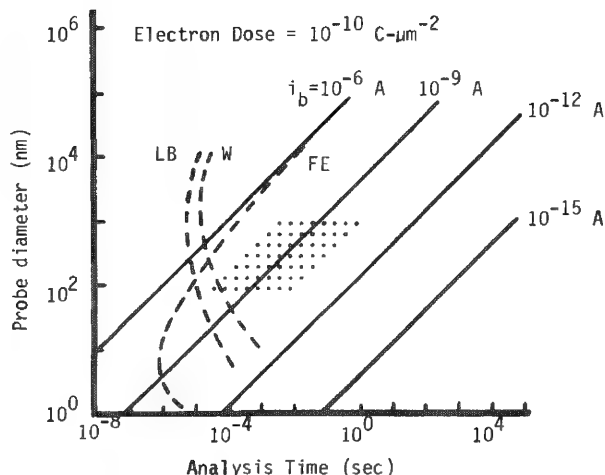
FIG. 1.--Probe diameter vs time of analysis for an accumulated electron dose of 10^{-10} C-μm^{-2} at beam currents of 10^{-6}, 10^{-9}, 10^{-12}, and 10^{-15} A. Dashed lines represent instrumental limitations for tungsten gun (W), LaB$_6$ gun (LB), and field-emission gun (FE). Typical operating conditions for microanalysis fall within shaded area.

The effects of electron beam-specimen interactions must be known before reliable quantitation is possible in biological specimens. For focused-beam analyses, this requirement means that specimen damage must be prolonged to doses $\geq 10^{-6}$ C-μm^{-2}. The operating parameters for a 10^{-6} C-μm^{-2} dose may be read from Fig. 1 if the analysis time scale is moved four powers of ten to the left. Count-rate variations could then be monitored since they occur over reasonable time intervals and appropriate corrections to the data become feasible.

Cooling the specimen to cryogenic temperatures is frequently suggested to reduce beam damage.[3,4] Mass loss has been observed to reduce with specimen temperature, but several laboratories have observed erratic count rates and inconsistent mass losses under microanalytical conditions at these reduced temperatures. Unless special apparatus is available, it is possible the analysis conditions are adversely impaired by condensation, beam charging, and thermal effects that negate the potential advantage gained in reduced mass loss at cryogenic temperatures.

Assuming mass loss is primarily a thermal

The author is with the Dows Institute for Dental Research, University of Iowa, Iowa City, IA 52242.

phenomenon, maintaining the temperature of the specimen through the application of an Al film should prolong the duration of mass loss.[5] Friskney and Haworth[6] have reported approximate algebraic solutions to the temperature of a thick, low-conductivity specimen under an Al coating. These solutions were used to predict maximum specimen surface temperatures in the analysis of tooth dentine under an Al coating of varying thicknesses. Table 1 lists these temperatures for an absorbed power of 10^{-3} W and a beam radius of 1 μm. The calculations assume the thermal conductivity of dentine is 10^{-3} $W-cm^{-1}-°C^{-1}$, the thermal conductivity of Al is 2 $W-cm^{-1}-°C^{-1}$, the depth of penetration is 1 μm, and the distance within the specimen necessary to attain ambient temperature from the excitation point is 1 mm. A 1 μm Al coating should reduce the specimen temperature to at most a few degrees above ambient temperature and mass losses resulting from heating should be correspondingly minimized.

TABLE 1.--Maximum dentine surface temperature under various Al film thicknesses.

Al film thickness (nm)	Temperature (°C)
0	2387
10	320
100	36
1000	4

FIG. 2.--Calcium count rate variations versus electron dose as recorded from human tooth dentine coated with 20, 100, 500, and 1000nm Al film thicknesses. Accelerating voltage, 12 kV; total absorbed power, 10^{-3} W. Count rates increase about 25% for each Al film thickness.
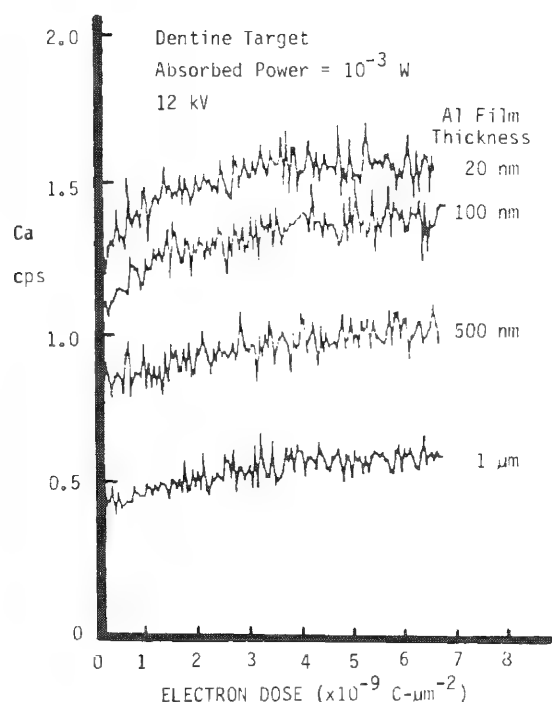
A polished, longitudinally sectioned molar was coated with Al to thicknesses of 20, 100, 500 and 1000 nm. The Ca count rate as a function of electron dose at 12kV accelerating voltage and total absorbed power of 10^{-3} W is displayed in Fig. 2. The Ca count rates decrease with film thickness owing to energy losses within the Al coating. The electron range within the dentine most closely approximates that assumed in Table 1 for the 1 μm Al film thickness. The apparent increase in electron dose necessary to produce the count rate variation in the 1 μm Al coated dentine may be a thermal phenomenon or it may reflect the decreased current actually reaching the dentine through the Al film.

Application of the thicker Al films yields no obvious benefit, since the slight prolongation of the mass loss is more than offset by the reduced characteristic x-ray count rate and absorption of long-wavelength x rays. There are also difficulties in interpretation for x-ray spatial resolutions approaching 1 μm. The temperature of the specimen appeared to be greatly reduced during analysis since contamination was not visible after prolonged irradiation of the 1 μm Al film, but was very pronounced for the thinner Al films. However, it is not known whether the temperatures listed in Table 1 were actually attained.

The mass loss resulting from electron irradiation forms as "gas" bubbles beneath the Al films. The gas is believed to consist of the organic elements and H_2, O_2, and CO_2 gases.[7] The above results suggest the ejection of these light-element components of the dentine is not strongly temperature dependent. "Knock-on" losses due to elastic inter-

actions become more probable as the binding energy of light elements in the specimen decrease[8] and this may contribute to the observed mass losses.

There is no apparent simple solution to the mass loss problem in biological microanalysis. The problems are compounded for the more volatile soft tissues, which impose more stringent analysis requirements due to low elemental contents. Electron irradiation at low accelerating voltages is incapable of removing the heavy apatite crystals from mineralized tissues, but several of the biologically significant light elements have been observed to be removed from other organic materials. The use of thin sections at cryogenic temperatures and of higher accelerating voltages are frequently recommended for soft-tissue analysis. The local heating within thin sectioned organic specimens as a result of electron bombardment may easily exceed hundreds of degrees unless coatings up to 1 μm Al are applied or absorbed powers less than 10^{-5} W are used with thinner coats. These conditions imply that either submicron quantitative analyses are not feasible or that analysis times ranging to hours would be necessary to acquire satisfactory data.

References

1. T. A. Hall, "Biological x-ray microanalysis," *J. Microscopy* 117: 145, 1979.
2. J. W. Edie and P. L. Glick, "Irradiation effects in the electron microprobe quantitation of mineralized tissues," *J. Microscopy* 117: 285, 1979.
3. R. M. Glaeser and K. A. Taylor, "Radiation damage relative to transmission electron microscopy of biological specimens at low temperature: A review," *J. Microscopy* 112: 127, 1978.
4. P. Echlin and A. J. Sauberman, "Preparation of biological specimens for x-ray microanalysis," *SEM/77/I*, Chicago, Ill.: IIT Research Institute, 1977, 621.
5. G. S. Almasi et al., "A heat flow problem in electron-beam microprobe analysis," *J. Appl. Phys.* 36: 1848, 1965.
6. C. A. Friskney and C. W. Haworth, "Heat-flow problems in electron-probe microanalysis," *J. Appl. Phys.* 38: 3796, 1967.
7. J. W. Edie and P. L. Glick, "Electron irradiation products from organic materials and implications for microanalysis of biological sections," *Microbeam Analysis--1979*, San Francisco: San Francisco Press, 1979, 81.
8. M. S. Isaacson, "Specimen damage in the electron microscope," in M. A. Hayat, Ed., *Principles and Techniques of Electron Microscopy*, New York: Van Nostrand-Reinhold, 1977, vol. 7, p. 1.

ELECTRON-PROBE MICROANALYSIS OF TRANSPORTING TISSUES: DUCKLING ERYTHROCYTES AND SALT-SECRETING EPITHELIUM

S. B. Andrews, J. E. Mazurkiewicz, and R. G. Kirk

The salt glands of marine birds, including the domestic duck, are capable of secreting a hypertonic sodium chloride solution that can approach six times the osmolarity of the plasma when the animals are salt-loaded.[1] The transport mechanism(s) of the principal cells of this gland are of considerable interest,[2,3] and a knowledge of the cellular elec-trolyte concentration is crucial to an understanding of this process. However, the diver-cells of this gland is of considerable interest,[2,3] and a knowledge of the cellular elec-trolyte concentrations is crucial to an understanding of this process. However, the diver-sity of cell types and complex cellylar organization of the glandylar tubules complicate the study of this tissue by conventional methods. In contrast, the superficial supra-analysis of the blood and salt glands of normal and salt-stressed ducklings.

Experimental Methods

Nine-day old ducklings, *Anas platyrhynchos*, were either maintained for an additional six days on an *ad libitum* supply of duck mash and fresh water (unstressed) or switched to a 1% saline solution for drinking (stressed) prior to sacrifice by decapitation. The salt glands were rapidly excised and plunged into supercooled Freon 22 (-160°C) for freezing. Thin cryosections (ca 130 nm thick after drying) were cut from the natural face of the gland at -105°C by means of a Sorvall MT-2B microtome equipped with an FTS cryokit. The sections were mounted on 100-mesh copper grids covered with a carbon film (ca 45 nm), and subsequently freeze-dried essentially as described by Somlyo et al.[4] Samples of packed pellets of red blood cells in plasma (obtained from an aliquot of whole blood collected from the same animal) were quench-frozen, sectioned, and freeze-dried as described. The remainder of the blood was used for flame photometric measurements of Na and K concentra-tions of red cells and plasma, and for gravimetric determination of dry-mass content.

Energy-dispersive (EDS) X-ray spectra were obtained by means of an ETEC Autoscan elec-tron microscope equipped with a Kevex 7000 series X-ray spectrometer interfaced to a DEC PDP 11V03-L computer. X-ray acquisition conditions were: 30kV accelerating voltage; 1.0nA beam current; 100s (livetime) analysis time; $\geq 0.2\mu m^2$ analyzed area; and ambient tempera-ture specimen stage. The extraction of quantitative data from raw EDS spectra was carried out by the multiple least-squares fitting method,[5] essentially as described by Shuman et al.[6] In addition to corrections for systems background and grid-generated x-rays, the calculated continuum was also corrected for contamination (which was < 5% in the worst case) and support contributions, as will be described in detail. To obtain elemental con-centrations from x-ray intensities, both the continuum normalization method[7] and the in-ternal standard approach[8] were employed. In favorable cases, both methods can be shown to give self-consistent results, as discussed below.

Results

Erythrocytes. The nucleated red blood cells of the duck are of interest because of the general and unresolved issue of ion compartmentalization in the nucleus of such cells, and also because of the possibility that the composition of the red cells may reflect the salt load of the plasma in a stressed bird. In this study, the red cells also serve a methodological purpose, since they can be used to test the accuracy of x-ray derived con-

FIG. 1.--Transmission EM image of freeze-dried cryosection of duckling erythrocytes, ×11 000. Bar, 1 μm.
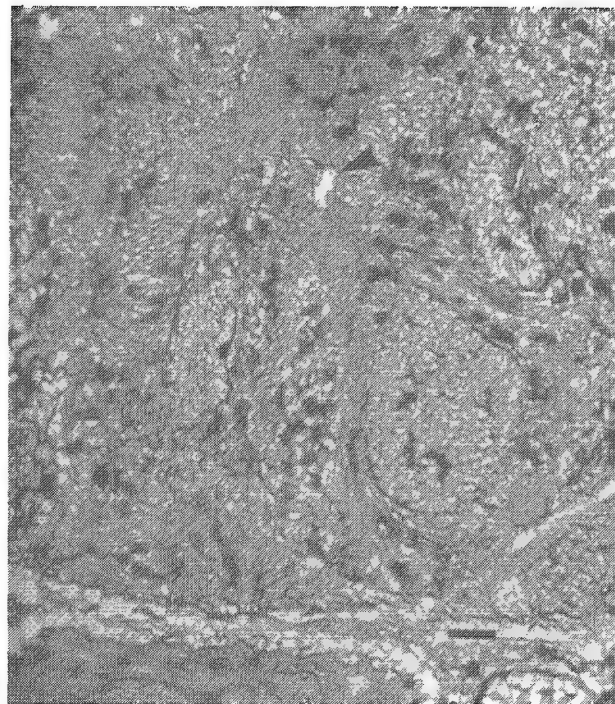
FIG. 2.--Transmission EM image of a freeze-dried cryosection of salt gland tubule from salt-stressed duckling. Tubule lumen is indicated by arrowhead, ×6600. Bar, 1 μm:

TABLE 1.--Calculation of potassium concentration and dry-mass fractions of normal duckling erythrocytes.

	X-ray Counts		K Concentration			Dry wt fraction
	I_K	I_C	$C_K'(dry)$	$C_K(dry)$	$C_K(wet)$	
				mmol/kg		g/100 g
Red Blood Cells						
EPMA						
Nucleus	5875	2492	436±15	439±14	190±5	43±1
Cytoplasm	2559	2273	211± 7	211± 7	83±2	39±1
Total				247	100	40.0
Chemical Analysis				252	100±4	39.7±0.4

Data are the weighted average ± SEM for the paired analysis of nucleus/cytoplasm for 10 red cells. Symbols are defined in the text. The weighted average of the ratio $I_K(nuc)/I_K(cyto)$ was 2.29 ± 0.10 (SEM); for the continuum, the ratio $I_C(nuc)/I_C(cyto)$ was 1.10 ± 0.03 (SEM). The volume-fraction of the nucleus was 0.158 ± 0.014.

centrations and tissue mass estimates.

As a two-compartment system, the wet-weight concentrations in these cells are uniquely determined by the characteristic x-ray intensity ratios, the overall cell concentration per liter packed cells (by chemical analysis), and the volume-fraction of the nuclear compartment (by morphometric estimate). The following equations illustrate the general relationships.

$$C_{X,T}(\text{wet}) = V_N C_{X,N}(\text{wet}) + V_C C_{X,C}(\text{wet})$$

$$C_{X,N}(\text{wet}) = (I_{X,N}/I_{X,C}) C_{X,C}(\text{wet})$$

$$V_N = 1 - V_C$$

where V = volume-fraction, C = concentration in mmol/kg, and I = X-ray counts. The element (or continuum) and cell compartment are indicated in subscripts and the state of hydration is specified in parentheses. An example of this calculation is given in Table 1; Fig. 1 illustrates typical cryosection morphology. The chemical data in Table 1 are in agreement with literature values.[9] For K, the ratio $I_{K,N}/I_{K,C}$ (column 1) specifies the concentration $C_K(\text{wet})$ given in column 5. A similar calculation for the dry-weight fraction (column 6) follows from the ratio of continuum intensities (column 2). The dry-weight concentration in column 4, $C_K(\text{dry})$ (calculated as column 5 divided by column 6), equals the dry-weight concentration in column 3, $C_K'(\text{dry})$ (calculated from peak/continuum ratios, i.e., column 1 divided by column 2), only if there is no significant absolute error in the estimation of tissue-derived continuum. The good correlation between dry-weight concentration calculated by these two independent methods indicates that under these experimental conditions tissue dry mass can be approximated from continuum intensities with a useful degree of accuracy.

Using the strategy outlined above we determined the wet-weight concentration for all elements analyzed in unstressed duckling erythrocytes (Table 2). The results indicate a dramatic localization of K and P in the nuclei of these cells. Conversely, Cl was moderately elevated in the cytoplasm and Fe was detected only in this compartment. Cellular Na levels were too low to quantitate, in agreement with a chemical measurement of $C_{Na,T}(\text{wet})$ = 4.8 mmol/L packed cells. These results are consistent with elemental distributions reported by Jones et al.[10] for chick embryo erythrocytes.

TABLE 2.--Elemental concentrations of duckling erythrocytes and salt-gland epithelial cells.

	No. of Analyses	Na	P	Cl	K	Dry wt fraction
		mmol/kg wet wt				g/100 g
Red Blood Cells						
Nucleus	10	-*	385±13	64±3	190±5	43±1
Cytoplasm	10	-*	67±3	72±3	83±2	39±1
Salt Gland Epithelium						
Nucleus	14	9±3	108±2	33±1	113±2	19±1
Apical Cytoplasm	9	11±4	121±3	30±2	108±3	24±1

Data are the weighted average ± SEM.   *Values not significantly different from 0.

Elemental concentrations were also determined for stressed duckling erythrocytes by both chemical and microprobe methods. No major differences in electrolyte concentrations between stressed and unstressed red cells were found, although plasma Na was elevated to 170 mM in the stressed bird (compared with 155 mM in the normal duckling). High plasma

Na has previously been reported in the salt-stressed herring gull.[11]

Salt Gland Epithelium. The example of a cryosectioned tubule of stressed salt gland shown in Fig. 2 illustrates the preservation of the characteristic morphology of the tubule lumen and the basal and lateral cell interdigitations. Further, ice damage is reasonable for a tissue of relatively high water content. (For examples of salt gland morphology as seen in conventional sections, Ref. 12 should be consulted.)

We have found that elemental peak/continuum ratios, and therefore dry weight concentrations, can be obtained from these preparations with good reproducibility. However, this information alone is not sufficient, since, as in other transporting epithelia, a measure of the local water content is indispensable for inferring the physiological relevance of the results. Therefore, a variation of the internal standard proportionation method[8,13] has been adopted.

In the intertubular microvasculature of a cryosection of salt gland, it is generally possible to find several well-preserved erythrocytes. Since the elemental concentrations and dry-mass content of these cells are known from EPMA and chemical analysis of the blood of the same animal, the *in situ* red cells serve as well-defined internal standards. This approach was used to calculate the results given in Table 2 for the epithelial cells; data for the cytoplasm are specifically confined to the apical region of the cells where the probe could be unequivocally located on the cytoplasm of a single cell (e.g., above and below the lumen in Fig. 2). The values in Table 2 are statistically inferior to dry-weight concentrations calculated from peak/continuum ratios; however, the need to express the results in physiologically useful units dictates the choice of wet-weight concentrations.

These results indicate a relatively uniform distribution of electrolytes between nuclear and apical cytoplasmic compartments. When the data are converted to mmol/L cell water, the cellular concentrations of Na (10-15 mM), K (140 mM) and Cl (40 mM) are suggestive of a prototypical epithelial cell. In comparison to chemical determinations of intracellular ion concentration in avian salt glands,[11,14,15] EPMA results indicate a significantly lower cellular Na and higher K. However, the microprobe data were obtained from one specific morphological region of the cytoplasm, and it cannot be assumed that these values are representative of the cell cytoplasm as a whole. Moreover, it is well recognized[2] that the enzymatic and ultrastructural specializations related to salt transport are localized in the basolateral domains of this cell, and that these are the regions that respond developmentally and physiologically to salt loading. It will be therefore of interest to obtain electrolyte concentrations from the basal and lateral cytoplasm, in order to determine whether local ion levels reflect the specialized function of this region of the cell.

References

1. K. Schmidt-Nielsen, *Circulation* 21: 955, 1960.
2. S. A. Ernst and J. W. Mills, *J. Cell Biol.* 75: 74, 1977.
3. R. A. Ellis, C. C. Goertemiller Jr., and D. L. Stetson, *Nature* 268: 555, 1977.
4. A. V. Somlyo, H. Shuman, and A. P. Somlyo, *J. Cell Biol.* 74: 828, 1977.
5. F. H. Schamber, in T. G. Dzubay, Ed., *X-ray Fluorescence Analysis of Environmental Samples*, Ann Arbor, Mich.: Ann Arbor Science Publishers, 1977, 241.
6. H. Shuman, A. V. Somlyo, and A. P. Somlyo, *Ultramicroscopy* 1: 317, 1976.
7. T. A. Hall, in G. Oster, Ed., *Physical Techniques in Biological Research*, New York: Academic Press, 1971, 2nd ed., vol. 1A, p. 157.
8. A. Dörge et al., *Pflügers Arch.* 373: 85, 1978.
9. W. F. Schmidt III and T. J. McManus, *J. Gen. Physiol.* 70: 59, 1977.
10. R. T. Jones et al., *J. Cell Sci.* 35: 67, 1979.
11. B. Schmidt-Nielsen, *Am. J. Physiol.* 230: 514, 1976.
12. S. A. Ernst and R. A. Ellis, *J. Cell Biol.* 40: 305, 1969.
13. T. C. Appleton and P. F. Newell, *Nature* 266: 854, 1977.
14. M. R. Hokin, *J. Gen. Physiol.* 50: 2197, 1967.
15. M. Peaker, *J. Physiol.* (London) 213: 399, 1971.

CALCIUM AND MAGNESIUM COMPARTMENTALIZATION IN SKELETAL MUSCLE: ELECTRON PROBE X-RAY MICROANALYSIS

L. M. Popescu, W. C. de Bruijn, Ilie Diculescu, and W. T. Daems

Muscle fibers from frog sartorius were "prefixed" with K oxalate, to immobilize Ca and Mg in situ, then fixed in glutaraldehyde, postfixed or not in osmium, dehydrated, and embedded in Epon. The normal intracellular concentrations of elements, deduced from earlier bulk chemical analyses, were preserved in such oxalate-treated muscle fibers. Electron probe analysis showed that the sarcoplasmic reticulum (SR), mitochondria, and nuclei contained concentrations of Ca and Mg in excess of cytoplasmic levels. The results also suggest that Na, Cl, P and S are compartmentalized inside the muscle fibers. All analytical values are given in mmol/kg dry wt. ± SEM.

In the context of the existing data, Somlyo et al. very recently reported some unexpected results.[1-3] They used dry cryosections of striated muscle for electron-probe analysis and found that the SR was the only intracellular Ca-accumulating structure. In addition, their findings suggested that Mg, Na, Cl, K, P, and S are not compartmentalized in striated muscle fibers.

As an alternative approach to freezing, we tried Ca and Mg immobilization with oxalate. The proper use of the oxalate anion for Ca trapping in living cells was recently reviewed;[4] the oxalate anion, in concentrations higher than 10 mM, can immobilize not only Ca but also Mg in muscle fibers.[5]

A preliminary report of some of our results has been presented.[6]

Material and Methods

Muscle strips from frog sartorius (*Rana pipiens*; winter frogs) were equilibrated for 30 min at room temperature in Ringer's solution. The composition of Ringer's solution in mM was: NaCl, 116; $CaCl_2$, 1.8; KCl, 2.0; $NaHCO_3$, 2.38; NaH_2PO_4, 0.087; glucose, 11.0; pH = 7.2 and osmolarity of 250 mosmol/kg H_2O.

Oxalate Treatment of Muscle Fibers. Muscle strips were incubated for 10 min in a high-K oxalate (40mM) medium that produced initially a K-contracture followed by gradual relaxation.[7] Then muscle strips under relaxation were fixed for 1 hr in 2.5% glutaraldehyde in 0.1M cacodylate buffer, pH = 7.4, briefly rinsed in the same buffer, and *occasionally* postfixed in OsO_4. After being rapidly dehydrated through graded ethanols, the specimens were cleared in propylene oxide and embedded in Epon. Each aqueous solution was saturated with oxalate; Ca and Mg were not added to any of the solutions used. Although these solutions were nominally Ca- and Mg-free, as expected, they contained traces of Ca and Mg. Atomic absorption measurements showed that Ca and Mg contaminations in the glutaraldehyde fixative and in ethanol solutions were in the range of 10^{-5} M.

Electron-probe X-ray Microanalysis was done on a Philips 400 high-vacuum transmission electron microscope equipped with scanning polepieces and x-ray stray aperture. EDAX Si(Li) x-ray detector (30 mm^2, detector perpendicular to the specimen rod) was interfaced with the analyzer and EDIT/NOVA computer. The extraneous signals and the associated low background were obtained by collecting the spectrum generated with the electron beam passing through an empty grid hole and subtracted by computer routine. We confirm the finding of an extraneous and variable Si peak without biological significance, previously reported by Somlyo et al.[1]

All the analytical values were obtained on *unstained thin sections* of about 100 nm.

The sections were cut on a LKB ultrotome and mounted on copper grids. To convert the x-ray spectra to elemental concentrations (mmol/kg dry wt.), we used the method suggested by Shuman et al.[8] Since Somlyo's group used the same method,[1-3] the possibility of an immediate comparison of results is obvious.

Results

The *Ultrastructure* of oxalate-treated muscle fibers is virtually of the same quality as that observed in usual specimens of striated muscle. The characteristic features of striated-muscle fine structure were easily recognized (Figs. 1 and 2). Electron-opaque precipitates were found in the SR and mitochondria, as previously reported.[9]
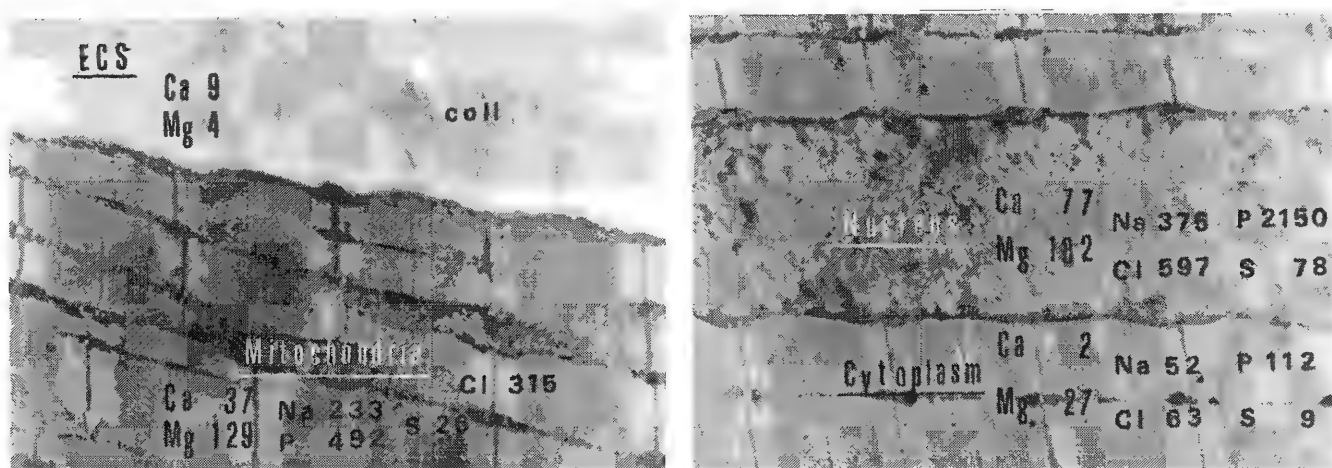
FIG. 1.--Frog sartorius. Oxalate-treated muscle fiber: ×15 000. Elemental concentrations (mmol/kg dry wt.) found by electron-probe analysis are imprinted. ECS = extracellular space; coll = collagen fibrils. The cytoplasmic elemental concentrations were measured over I bands. Cl concentrations were deduced after the subtraction of Epon Cl-counts.
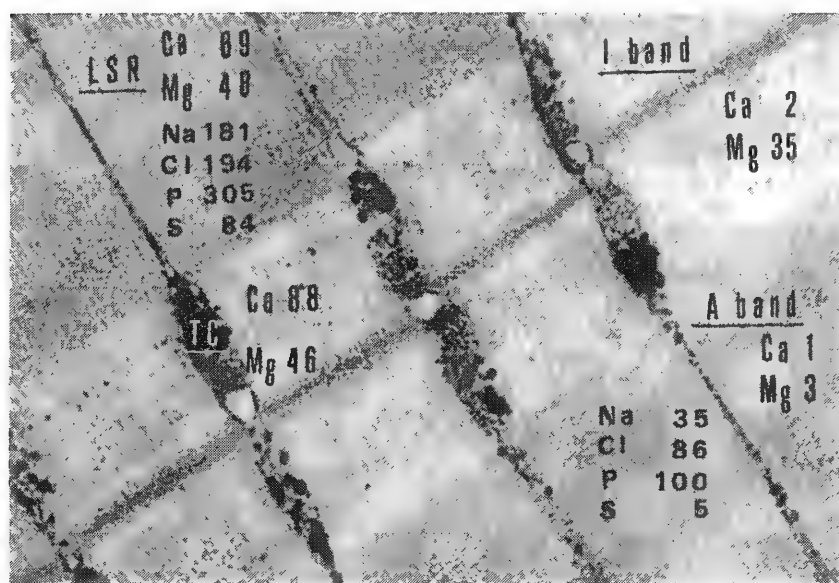

FIG. 2.--Frog sartorius. Oxalate-treated muscle fiber. Higher magnification: ×75 000. Elemental concentrations (mmol/kg dry wt.) found by electron probe analysis are imprinted. LSR = longitudinal SR; TC = terminal cisternae.

Control of Ca and Mg Immobilization by Oxalate Treatment. The total amount of Ca and Mg contained in muscle strips was measured by atomic absorption spectrophotometry (Pye-Unicam SP 90). After oxalate treatment (before fixation in glutaraldehyde) muscle strips contained 12 ± 3.0 mmol Ca/kg dry wt. and 41 ± 14.1 mmol Mg/kg dry wt. After dehydration (before embedding in Epon) muscle strips contained 9 ± 0.5 mmol Ca/kg dry wt. and 44 ± 6.5 mmol Mg/kg dry wt. These data show that there is no significant modification of Ca and Mg content in oxalate-treated muscle strips during preparation for electron-probe x-ray microanalysis. For functional test we used caffeine, which is well known to produce a vigorous contraction of striated muscle fibers as a result of Ca mobilization from intracellular stores, mainly the SR.[10] Caffeine (5 mM) was unable to produce a contraction in muscle fibers treated with oxalate. Therefore, it seems reasonable to believe that Ca ions were indeed immobilized *in situ* by precipitation with oxalate.

Mean intracellular concentrations of elements were determined to establish whether or not the "normal" concentrations (deduced from earlier bulk chemical measurements) were kept in oxalate-treated and conventionally processed specimens. Analyses were done over 2 parallel sarcomeres or across 5 adjacent sacomeres with needle-shaped probe. The average intracellular concentrations were: Ca, 16 ± 3; Mg, 39 ± 12; Na, 127 ± 56; P, 230 ± 40; S, 46 ± 13.

Ca and Mg distribution was determined by small-spot analyses, and is shown in Table 1. A typical x-ray spectrum from the analyses of the terminal cisternae of SR is given in Fig. 3.

TABLE 1.--Ca and Mg concentrations measured by electron probe analysis on thin sections of oxalate-treated frog sartorius muscle.

Frog sartorius muscle	Concentration (mmol/kg dry wt.)	
	Ca	Mg
Extracellular space	11 ± 2.2	6 ± 5.4
Cytoplasm		
I band	3 ± 1.3	53 ± 18.8
A band	1 ± 0.4	4 ± 2.1
Sarcoplasmic reticulum		
Terminal cisternae	97 ± 20.9	48 ± 9.0
Longitudinal tubules	76 ± 15.4	54 ± 13.4
Mitochondria	49 ± 31.6	134 ± 8.6
Nuclei		
Euchromatin	85 ± 33.8	145 ± 69.3
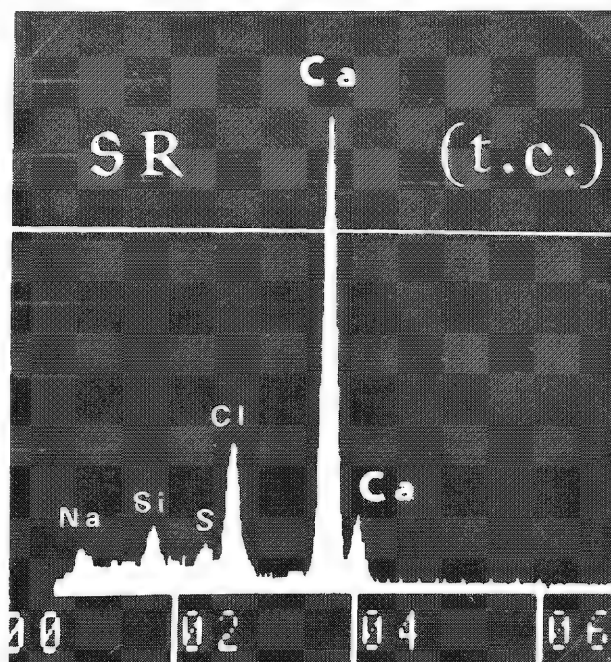
FIG. 3.--X-ray spectrum over a terminal cisterna of SR from oxalate-treated, glutaraldehyde-fixed and Epon-embedded muscle fiber. No osmium postfixation was used.

Discussion

Electron-probe analysis measures the *total* amount of a given element, irrespective of being ionized or not, free or bound.

Mean intracellular concentrations of elements measured on thin sections of oxalate-treated, glutaraldehyde-fixed and Epon-embedded skeletal muscle fibers were in concordance with numerous "bulk" chemical determinations reported previously and with the values given by Somlyo et al., who used dry cryosections (Table 2). This concordance is particularly valuable when frog-to-frog and fiber-to-fiber variations or differences in the incubation times and in the composition of physiologic saline solutions used (Ringer's solutions) are

261

considered. In addition, the total Ca and Mg concentrations measured chemically in the same muscles used for the electron-probe analysis were in good agreement (within the inherent error) with the electron-probe results. Thus, we are able to contend that the concentrations of elements are preserved in oxalate-treated muscle fibers despite the conventional processing for electron microscopy.

TABLE 2.--Average concentrations of elements in frog skeletal muscle. Comparison between results obtained by electron-probe analysis and earlier bulk chemical analyses. We used thin sections of oxalate-treated muscle; Somlyo et al. freeze-dried sections. "Somlyo's group" results were calculated from Table 1 of Ref. 1. Only determinations on muscle fibers from winter frogs (marked A and B in that Table 1) were taken into account because we used winter frogs, too. Ca concentration was not reported in Ref. 1.

Element	Average concentration of elements (mmol/kg dry wt.) in frog skeletal muscle		
	Electron probe analysis		Chemical analyses
	Our results	Somlyo's group	Others
Ca	16 ± 3		10 Henrotte & Cosmos, 1959; Winegrad, 1965; Bianchi, 1968; 13 Fenn, 1936; Conway, 1945; Gilbert & Fenn, 1957; 15 Cloetta et al., 1942; 20 Sorokina & Kholodova, 1970;
Mg	39 ± 12	52 ± 13	35 Bianchi, 1968; 41 Fenn, 1936; 45 Cloetta et al., 1942; Gilbert & McGann, 55 Conway, 1945; 1958;
Na	127 ± 56	81 ± 34	80 Steinbach, 1962; Riordan et al., 1972; 100 Adrian, 1956; Hodgkin & Horowitz, 1959; 115 Conway, 1945; 120 Sorokina & Kholodova, 1970; 125 Fenn, 1936;
P	230 ± 40	294 ± 44	200 Barany, 1973 235 Diem & Lentner, 1968;

Ca Compartmentalization. No significant difference was found between Ca accumulation in the terminal cisternae and longitudinal tubules of the *SR*, as earlier low-resolution autoradiographic or qualitative cytochemical studies suggested.[10] The average Ca concentration of the SR, measured in situ by electron probe analysis was 85 ± 18.9. This Ca accumulation corresponds to 15-25 mmol Ca/liter of SR in living muscle, and is virtually identical with that expected from in vitro biochemical studies of Ca uptake by purified microsomes isolated from the frog skeletal muscle.[10]

In vitro Ca accumulation by *mitochondria* is well documented.[11] Qualitative cytochemical studies showed in situ Ca accumulation by mitochondria of frog skeletal muscle.[9] We confirm the ability of muscle mitochondria to accumulate Ca in situ: 49 ± 31 mmol/kg dry wt. However, the high SEM suggests a significant heterogeneity of the mitochondrial population in muscle fibers.

In contrast to mitochondria, little or no attention has been paid to *nuclei* as Ca-accumulating sites. Our results show that Ca concentration inside the nuclei is comparable with that of the SR. A Ca-ATP-ase located in the nuclear envelope, as in smooth

muscle,[4] might perform Ca transport from the cytoplasm against a large concentration gradient. Nevertheless, a (considerable) part of nuclear Ca could be bound to chromatin.

Electron-probe analysis of oxalate-treated *smooth muscle* cells provided direct evidence for Ca compartmentalization, as suggested previously.[4,7,12] The measured Ca concentrations (mmol/kg dry wt.) were about 100 in the SR and mitochondria, and about 60 inside the nucleus, significantly higher than in cytoplasm.[13] These analytical values are in good agreement (within statistical error) with Ca concentrations determined in subcellular components of skeletal muscle. Somlyo et al. used dry cryosections for electron-probe analysis of smooth muscle and did not find any Ca accumulation in mitochondria or nucleus, but reported high Ca sequestration (255 ± 7 mmol/kg dry wt.) in some electron-opaque granules scattered in cytoplasm and presumably located in the SR.[14]

Mg Compartmentalization. We believe that the Mg concentration measured over A bands represents a more accurate estimate of cytoplasmic Mg-concentration, because of the well-known Mg binding by thin filaments in I bands (Table 1). Thus, our results show Mg accumulation in the *SR*. Mg concentration in the terminal cisternae and longitudinal tubules was not significantly different. The average Mg concentration of the SR is 51 ± 7.1 mmol/kg dry wt. Although Somlyo et al.[1] found 40 ± 5.9 mmol Mg/kg dry wt. in the terminal cisternae, they concluded that the SR did not accumulate Mg, because they measured the cytoplasmic Mg concentration (39 ± 5.2) immediately adjacent to terminal cisternae (at the level of I bands), where Mg is tightly bound to thin filaments.

The high concentrations of Mg found by us in *mitochondria* and *nuclei* are expected, when the variety of functions ascribed to mitochondrial Mg or the role of Mg in the control of chromatin aggregation are taken into account.

In conclusion, the oxalate treatment of muscle fibers, for Ca and Mg immobilization, followed by usual fixation, dehydration, embedding, and sectioning, is an alternative (but simple, quick, and inexpensive) approach to the use of dry cryosections to measure the intracellular Ca and Mg distribution. However, a priori, each experimental approach, either "chemical fixation" of Ca and Mg with oxalate or physical fixation by freezing could produce artifacts. We have to consider that the similar findings obtained by methods that are as different as they could be would represent the intracellular truth.

References

1. A. V. Somlyo, H. Shuman, and A. P. Somlyo, "Elemental distribution in striated muscle and the effects of hypertonicity," *J. Cell Biol*. 74: 828, 1977.

2. A. V. Somlyo, H. Shuman, and A. P. Somlyo, "Composition of sarcoplasmic reticulum in situ by electron probe X-ray microanalysis," *Nature* 268: 556, 1977.

3. H. Gonzales-Serratos et al., "Composition of vacuoles and sarcoplasmic reticulum in fatigued muscle: Electron probe analysis," *Proc. Natl. Acad. Sci. U.S.A.* 75: 1329, 1978.

4. L. M. Popescu, "Cytochemical study of the intracellular calcium distribution in smooth muscle," in R. Casteels et al., Eds., *Excitation-Contraction Coupling in Smooth Muscle*, Amsterdam: Elsevier/North-Holland Biomedical Press, 1977, 13.

5. R. J. Podolsky, T. Hall, and S. L. Hatchett, "Identification of oxalate precipitates in striated muscle fibers," *J. Cell Biol*. 44: 699, 1970.

6. L. M. Popescu, W. C. deBruijn, and I. Diculescu, "Electron probe microanalysis of skeletal muscle fibers under relaxation," in *Proc. 7th Europ. Conf. Muscle and Motility*, Warsaw: Nencki, 1978, 38.

7. L. M. Popescu and I. Diculescu, "Calcium in smooth muscle sarcoplasmic reticulum in situ: Conventional and x-ray analytical electron microscopy," *J. Cell Biol*. 67: 911, 1975.

8. H. Shuman, A. V. Somlyo, and A. P. Somlyo, "Quantitative electron probe microanalysis of biological thin sections: methods and validity," *Ultramicroscopy* 1: 317, 1976.

9. I. Diculescu and L. M. Popescu, "Electron microscopic demonstration of calcium in mitochondria of the frog skeletal muscle in situ," *Exptl. Cell Res.* 82: 152, 1973.

10. M. Endo, "Calcium release from the sacroplasmic reticulum," *Physiol. Rev.* 57: 71, 1977.

11. F. L. Bygrave, "Mitochondrial calcium transport," *Curr. Topics Bioenerg.* 6: 259, 1977.

12. L. M. Popescu et al., "Ultrastructural distribution of calcium in smooth muscle cells of the guinea-pig taenia coli," *Cell Tiss. Res.* 154: 357, 1974.

13. L. M. Popescu et al., "Intracellular distribution of calcium in smooth muscle: Facts and artifacts," *Morphology and Embryology* (in press).

14. A. P. Somlyo, A. V. Somlyo, and H. Shuman, "Electron probe analysis of vascular smooth muscle," *J. Cell Biol.* 81: 316, 1979.

X-RAY ANALYSIS OF FROZEN HYDRATED TISSUE SECTIONS BY MEANS OF A SCANNING ELECTRON MICROSCOPE

A. J. Saubermann, Reinier Beeuwkes III, R. E. Bulger, and Patrick Echlin

X-ray microanalysis of frozen hydrated tissue sections permits direct quantitative analysis of diffusible elements in defined cellular quantitative analysis of diffusible elements in defined cellular compartments. Because the sections are hydrated, elemental concentration can be defined as wet weight mass fractions. Use of these techniques also permits determination of water fraction in those cellular compartments. Absolute quantitative standardization can be established through direct analysis of frozen hydrated and then dried sections of independently measured standard solutions of elements with a probable error of less than 10%. Fundamental to application of these techniques are, first, a reliable method for cryosectioning, and second, a specimen support and transfer system that permits hydrated sections to be transferred to the scanning electron microscope (SEM) cold stage for examination and analysis without contamination or water loss and without introduction of extraneous x radiation.

Cryosectioning

Cryosectioning must produce smooth, relatively thin, flat tissue sections. Frozen sections nominally 0.5 μm thick are thin enough to permit the Hall analytical method to be used and to show reasonable morphology with scanning transmission electron microscopy (STEM) imaging at 30 keV.[1] Such sections are thick enough to provide sufficient characteristic x-ray intensity for energy-dispersive analysis with reasonable counting rates at a reasonably small probe current. Frozen biological tissue appears to behave similarly to brittle metals during cutting, which makes cyrosectioning fundamentally different from plastic or paraffin section cutting. During metal cutting operations internal stress is created at the cutting tool edge; the concentration of these stresses causes the chip to shear from the material and flow along the chip-tool interface. This separation occurs through plastic deformation or through fracturing depending on the ductility of the metal. If fracturing occurs, discontinuous chips are formed. If plastic deformation occurs, a continuous chip is formed. As the angle between the top of the tool and the face of the workpiece is narrowed, chip deformation in the shear zone is reduced. Such conditions promote continuous-chip formation. These metal cutting principles were applied to cryosectioning through the use of a new cryosectioning system mounted on a Sorvall Porter-Blum (MT-2) microtome. This system included (1) large cryochamber, (2) continuous-flow, constant-temperature cooling system, (3) three-point holder, (4) transfer port, and (5) razorblade knife holder fitted with an antiroll plate (Fig. 1). The brittleness of frozen hydrated biological tissue depends on its composition, structure, and temperature. The major controllable factor appears to be temperature.[2] Continuous-chip formation generally begins at approximately -50°C, and the entire section becomes a continuous chip by -30°C. More morphological information is obtained with continuous chips than with discontinuous chips. Furthermore, the origin of the x-ray signal is generally better defined in a continuous chip. The effective cutting temperature depends on both chamber temperature, which defines the initial temperature of the block face, and the heat introduced during sectioning. The temperature rise in the section and in the workpiece varies primarily with composition of the tissue block, the rate of cutting, and type of chip formed. Thus, as the sectioning temperature became colder the total amount of heat introduced increases
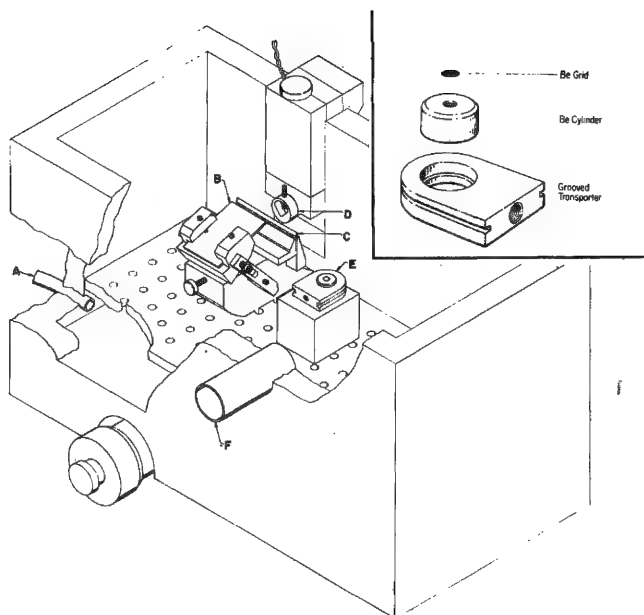
FIG. 1.--Schematic of equilibrium of
cryosectioning system: continuous-flow,
constant-temperature, nitrogen-cooled
system through inlet A; razorblade
knife holder C equipped with glass anti-
roll plate B; specimen held in three-
point hold system D; frozen section placed
in specimen holder E (detail in insert);
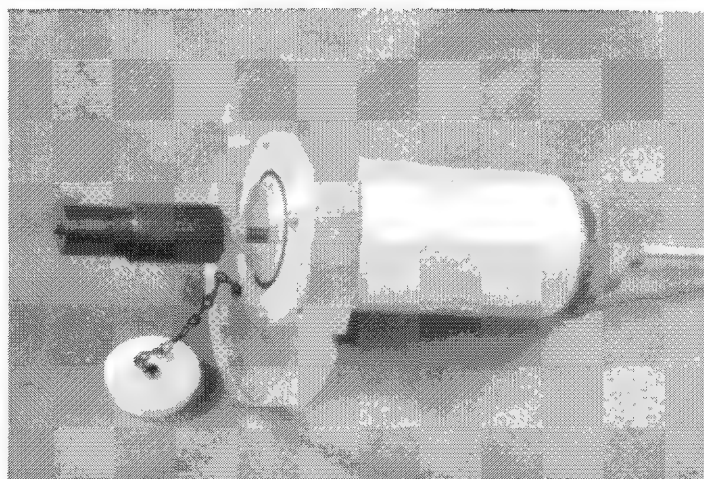transfer of sections from the chamber is
through port F.

FIG. 2.--Sealable transfer system with heat
sink in extended position; Delrin cylinder with
transparent vacuum flange can be sealed with
small attached plug.

markedly. However, as heat input is ap-
parently independent of section thickness,
potential temperature rise varies inversely
with section mass. Consequently, thick sec-
tions probably do not rise in temperature as
much during cutting as thin sections. We
have observed that thick sections generally
cannot be cut so as to form continuous chips
at temperatures below -80°C unless heat in-
put is raised by cutting at faster speeds.[2]

Section Handling and Transfer

After sectioning the tissue section was
picked up from the knife edge by means of a
cold eyelash and placed directly on a nylon-
covered Be holder that had been previously
coated with carbon (Fig. 1). This holder was
precooled (-155°C) to reduce the likelihood
of drying occuring to the tissue section
prior to transfer. The use of a 75-mesh Be
grid beneath the nylon film markedly reduced
the thermoresistivity of the nylon film, and
avoided an unacceptably large extraneous x-
ray background. The support system for the
grid was also machined from Be (Fig. 1). For
ease of handling, mechanical and thermal in-
terfacing between the specimen holders and
the microscope cold stage was provided by
means of a Be grooved transporter (Fig. 1).
This system provided a closed, frost-free en-
vironment for this transporter and a massive
heat sink to minimize temperature rise. This
system maintains specimens colder than -155°C
during transfer (Fig. 2). Because the Delrin
tube was backfilled by cold dry nitrogen from
the microtome chamber, frost accumula-
tion during transfer was found to be
negligible. Transfer was accomplished
through an intermediate airlock pump-
down system. The microscope cold
stage was designed to incorporate an
anticontamination system. At stage
temperatures below -150°C the rate of
ice sublimation from sections was so
slow as to be undetectable.

Compartment Identification and Analysis

The identification of compartments
in fully hydrated tissue sections was
difficult. Secondary-electron images
provided some morphological information
when differential shearing planes oc-
cured in different tissue compartments.
Transmitted electron images had little
contrast (Fig. 3). Thin, frozen hy-
drated sections showed morphology,
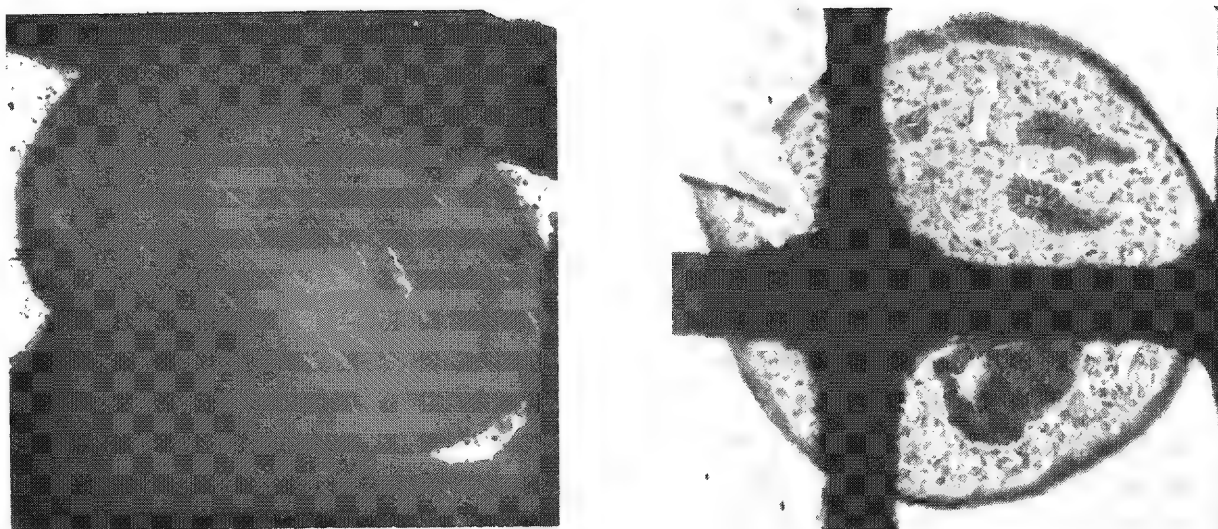which was not visible in equally hy-

266

FIG. 3.--STEM micrographs of rat renal papillae sections 0.5 μm thick: (a) frozen hydrated, with no morphological information; (b) frozen dried, with distinct morphological compartments. (Grid spacing about 300 μm.)

drated thicker sections viewed simultaneously. Although good contrast was seen in dried sections, the presence of a STEM image did not necessarily indicate dehydration. However, the presence of visible ice-crystal damage artifacts, either in the STEM or secondary image, was invariably an indication of water loss. X-ray mapping techniques were employed to assist in compartment identification in hydrated sections.[3,4] Phosphorus maps proved valuable for studies of renal papillae.[3,4] Such a map corresponded roughly to the application of a nuclear stain. STEM images of dried frozen sections showed clearly identifiable cellular structures (Fig. 3). For analysis the Hall method of quantitative analysis was employed; this method determines relative mass fractions (R-value) from the ratio of characteristic counts to continuum. Continuum counts were recorded from within the energy range of 4.60 through 6.00 keV. Background radiation was subtracted from the spectrum by means of a "top hat" digital bandpass filter technique.[5] Application of this function was done on line by use of a relatively simple interactive Fortran program on a PDP-11/03 computer. Corrections for extraneous or escape peaks were unnecessary since there were no extraneous characteristic x-rays or escape peaks in the spectrum. The weight fraction of water in specimens analyzed was calculated by two general methods. The first was based on the proportionality between continuum and total mass, which is in turn based on the relative consistency of the average atomic numbers and biological tissue. The second method was based on the change in weight fraction (R-value) of an element normally present in the section. Standard curves for P, S, Cl, K, and Ca were prepared by addition of 2 g of PVP (40 000 MW) to 8 cc of standard solutions of NaCl, KSCN, KH_2PO_4, $CaCl_2$. Frozen droplets of these solutions were sectioned at -40°C and analyzed in the frozen hydrated state, after which they were dried in the microscope by a raise the stage temperature to -50°C for 45 min. The stage was then recooled to -175°C and the sections reanalyzed. The relative mass fractions (R-values) of these sections were found to be linear functions of the independently measured absolute weight fractions (Fig. 4). Water fraction as measured by the ratio of hydrated R-value to dried R-value was found to be within 4% of that determined gravimetrically. Calculation of water fraction from contiuum ratio was less accurate than the R-value method.

Summary

X-ray analysis of defined tissue compartments in frozen hydrated specimens showed distinct and characteristic patterns of elemental distribution (Table 1). Similar patterns can be observed in sections after drying. Peak to background ratios in hydrated sections
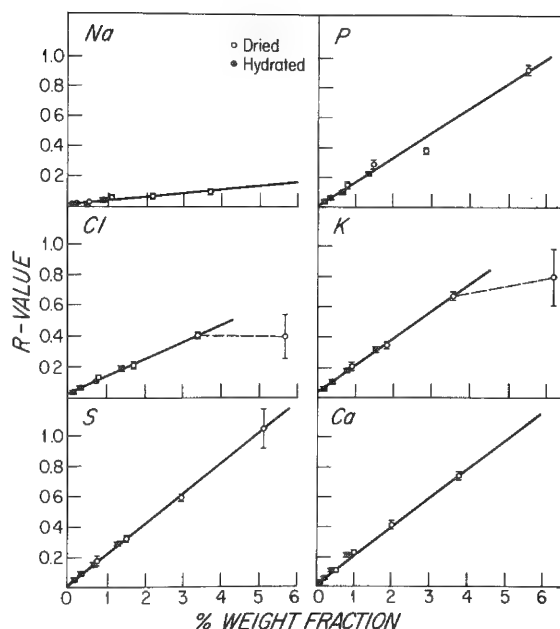
FIG. 4.--Standard curves obtained during X-ray microanalysis of frozen hydrated (closed circles) and frozen dried (open circles) sections cut from frozen droplets of standard solutions. Each point represents mean of six determinations ± standard deviation. In physiologic range R-value for each element increased as linear function of measured weight fraction (Na, R = 0.9332; Cl, R = 0.9934; S, R = 0.9979; R, R = 0.9811: K, R = 0.9972; Ca, R = 0.9961).

are sufficient for qualitative and quantitative analysis. Comparison of the relative mass fractions in the hydrated state with those in the dried state from the same compartment permit quantitation of the water fraction present in that compartment. The overall performance of this method is within 10% of expected. Considering the small size of the analytical compartment this should permit wide use of this exciting analytical approach to direct analysis of intracellular elemental compartments.

References

1. T. C. Hall, H. C. Anderson, and T. Appleton, "The use of thin specimens for x-ray microanalysis in biology," *J. Microsc.* (Oxford) 99: 177-182, 1973.

2. A. J. Saubermann, W. D. Riley, and R. Beeuwkes, "Cutting work in thick section cryomicrotomy," *J. Microsc.* (Oxford) 111: 39-49, 1977.

3. A. J. Saubermann et al., "Definition of tissue compartments in renal papilla by direct x-ray microanalysis of frozen specimens," *Kidney Int.* 14: 779, 1978.

4. R. Beeuwkes, A. J. Saubermann, and R. E. Bulger, "Determination of solute and H_2O of renal papilla cells by x-ray microanalysis of frozen hydrated sections," *Kidney Int.* 16: 805, 1979.

5. P. J. Statham, "Quantitative chemical analysis with EDS systems," *Proc. 13th MAS Conf.*, 1978.

TABLE 1.--Elemental concentration (mM/kg wet wt.) measured by x-ray microanalysis in rat renal papillary compartments.[4]

Compartment	(N)	%H_2O	K	P	S	Na	Cl
Collecting Duct Cells	(36)	57 ± 6	156 ± 54	252 ± 20	29 ± 6	344 ± 127	331 ± 108
Papillary Epithelial Cells	(33)	60 ± 11	141 ± 36	242 ± 54	39 ± 16	287 ± 105	318 ± 79
Interstitial Cells	(36)	60 ± 7	79 ± 16	145 ± 26	26 ± 7	898 ± 194	725 ± 140
Interstitium	(30)	77 ± 2	42 ± 8	39 ± 16	27 ± 9	590 ± 119	445 ± 115

ULTRASTRUCTURAL EXAMINATION OF UNSTAINED BALB/3T3 CELLS BY SOFT X-RAY CONTACT MICROSCOPY

N. Baturay-Smith and R. Feder

Cell cultures provide valuable experimental tools for many biological disciplines, including toxicology, genetics, cytology, most extensively virology, and recently chemical carcinogenesis. The efficacy of cell-culture techniques in these areas relies, at least in initial analyses, on morphological variations. Recent advances in oncological research have been utilizing cell cultures with increasing success to study effects of compounds found in the environment that may cause or contribute to the cause of chemically induced cancers.

When cell cultures, most notably mouse and hamster cells, are exposed to chemicals such as the polycyclic aromatic hydrocarbon benzo(a)pyrene, a radical alteration in colonial and individual characteristics occurs. Cellular alterations of malignant cells result in populations that, in contrast to normal cells, do not appear to recognize or influence each other. This alteration may ultimately comprise a significant component of the invasion mechanisms shown by tumor cells, including their entry into vascular channels and subsequent transport through normal tissue boundaries.[1] The behavioral differences observed between transformed and normal cells may be due to a redistribution of cytoskeletal microtubules.[2]

Detection of changes that take place early in the transformation process would indeed be of considerable value in these types of studies. It is the early changes that have been most difficult to visualize. Scanning electron microscopic (SEM) techniques have been used to detect cytoskeletal microtubular changes in cells that have rather well-defined morphological transformation markers.[2] What is needed at this stage, therefore, is a new technique that offers high resolution by which cellular fine structure can be visualized.

It appears that a new technique--soft x-ray contact microscopy (SXCM)--may offer a new way to image intact cells at resolutions approaching 4 to 30 nm.[3] The cultures imaged in this study appear to have the clarity of structure necessary for observations of early ultrastructural modifications of cells treated with carcinogens. Therefore, based on these preliminary studies with Balb/3T3 mouse cells, a new method for imaging cell cultures at high resolution with few artifacts may be afforded by SXCM.

Materials and Methods

Confluent Balb/3T3 cell cultures (American Type Culture Collection, Rockville, Md.; CCL#163) were removed from 75cm^2 Corning polystyrene flasks by treatment with 0.25% trypsin. The cell suspension was centrifuged at 1000 rpm. Following resuspension in Minimum Essential Medium, Eagle, supplemented with 10% newborn calf serum (GIBCO; Grand Island, N.Y.), 10^5 cells were seeded onto 60mm Falcon plastic Petri dishes containing sterile silicon nitride windows. The cultures were then incubated at 37°C in a humid, 5% CO$_2$, 95% air atmosphere. Following 5 days of incubation, windows were removed, fixed with 3% gluteraldehyde in 0.1 M Hepes buffer, dehydrated with ethanol, and air dried.[4]

Specimens on silicon nitride windows were exposed for 18 hr to carbon Kα soft x rays emitted from a stationary target source. A silicon wafer, uniformly coated with photoresist (1μm polymethylmethacrylate or PMMA) was placed against the silicon nitride windows to form a sandwich with the specimen. This arrangement affords imaging onto the photoresist-coated wafer and leaves the cells intact on the original specimen. Thus, the

soft x rays penetrate the silicon nitride window and are differentially absorbed by the cells. The underlying photoresist is exposed in the areas where the x rays penetrate the specimen, causing chain scissons in the PMMA. The dense areas of the specimen do not permit x-ray exposure of the underlying photoresist.[5,6]

Following exposure, the photoresist was chemically developed in a 1:5 mixture of iso-propanol and isobutyl ketone, respectively, for 3 min and observed through a Leitz interference contrast microscope with Nomarski optics. Prior to SEM examination, the developed contact replicas of the cells were sputter coated with AuPd by means of a Denton 505 system. Scanning images were taken on a JOEL 35 SEM at an accelerating voltage of 25 Kv, 45° tilt.

Results and Discussion

Figures 1 and 2 were photographed with an interference microscope. Phase differences that result from small differences in the refractive index and thickness of various parts of the cells afford higher contrast than either phase contrast or the usual light-microscopic techniques. These variations in phase make specimens appear stained.

Figure 1 is the original colony of 3T3 cells grown on a silicon nitride window. The nucleus appears fairly well defined in most cells, with several, often vaguely outlined, nucleoli present. Cytoplasmic detail seems to be lacking and cell-cell contact regions are also absent or not clearly discernible. The slightly darker area F, is the "frame" of the window and the lighter area W is the window itself.

Figure 2 is the replica on the photoresist-coated wafer, following exposure to soft x rays, and is also a mirro image of Fig. 1. No image was formed in the region of the frame that did not permit x-ray transmission; the frame F appears blank and only the area W that permitted transmission of x rays has a contact replica of the cells.

Because the specimens remain intact on the original window, following exposure to x rays, the question of transference of specimen from original window to photoresist coated wafer is eliminated.

Figure 3 is an SEM of two adjacent cells that appear on the replica. Many intracellular details are now evident. These intracellular inclusions may represent sites of accumulations of higher atomic number in the cytoplasm. The outline of the nucleus is clearly defined and appears to have a higher relief than the surrounding membrane, probably owing to a combination of dense collections of materials, as well as materials with higher atomic numbers. The highest areas are perhaps due to the absorption of incident x rays by the thickness of the materials present. Contrast formation with soft x rays is not due to the presence of stains, but depends solely on the differential absorption of soft x rays and subsequent differential exposure of the underlying photoresist.[6]

In Fig. 4, the two dense areas D seen in Fig. 3 appear at this higher magnification to be an incorporation of exogenous material by the cell. However, further controlled studies are required to clarify and define this observation. Figures 4 and 5 show microfilamentous cytoplasmic extensions X that are also apparent in the areas of cell-cell contact, and may be areas of cellular communication. If that is so, these areas may be responsible for the intercellular behavior exhibited by normal and transformed cells. Microfilaments M are clearly defined in Figs. 3 and 4, and demonstrate the cytoskeletal elements involved in defining cell morphology.

Conclusions

Soft x-ray contact microscopy appears to be an effective new technique for viewing intact cells at high resolution. This method allows visualization of detailed ultrastructural events achieved by differential absorption of soft x rays resulting in an atomic number related topographic image revealing intracellular detail. Staining and sectioning artifacts are avoided and the original specimen following exposure remains intact and undamaged, which is also an important consideration as the x-ray exposure time and solvent developing time may be varied to allow further detailed delineation of intracellular structures as well as any surface changes due to experimental conditions.

With the advent of available synchrotron exposure time, it will be possible in the future to examine hydrated, viable cells at high x-ray doses and short exposure times.
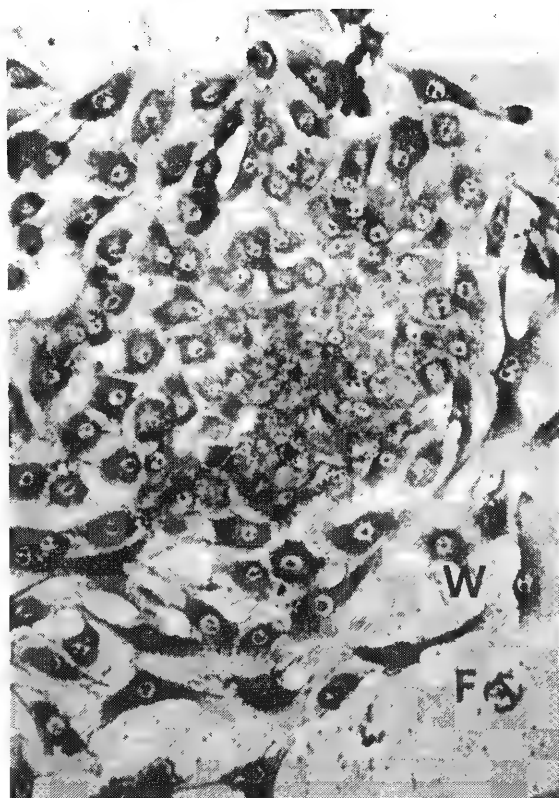
FIG. 1.--Interference micrograph (100×) of Balb/3T3 cells grown on silicon nitride windows. Original specimen following exposure to soft x rays.

FIG. 2.--Interference micrograph (100×) of cell replica on photoresist-coated silicon wafer following exposure of original specimen to soft x rays.

FIG. 3.--SEM (800×, 45° tilt) of two adjacent cells (replica). Note higher relief of membrane around nucleus N and nucleoli NU.

F - FRAME

W - WINDOW

D - DENSE AREA

N - NUCLEUS

NU- NUCLEOLI

X - CYTOPLASMIC EXTENSIONS

M - CYTOSKELETAL MICROTUBULES

↢ - BACKGROUND/CELL REPLICA INTERFACE

271
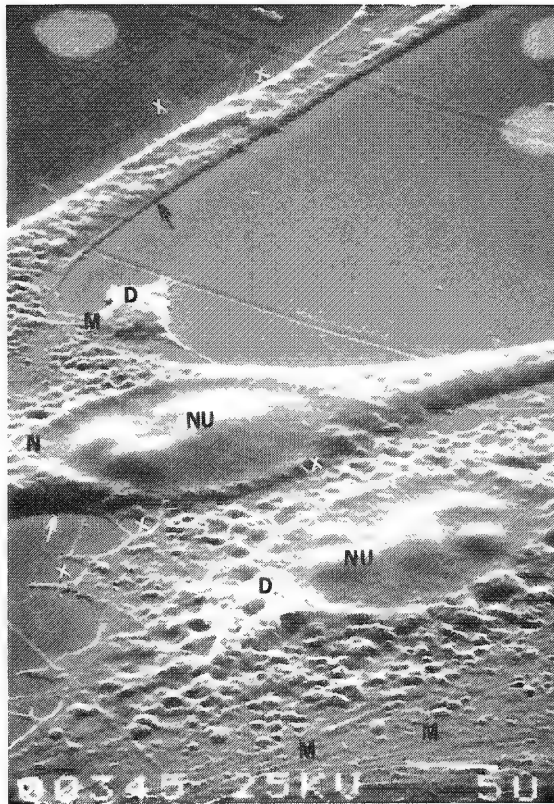
FIG. 4.--SEM (2500×, 45° tilt) of two ad-
jacent cells in replica of Fig. 3 showing
cytoskeletal events (M and X). Dense
areas that may represent phagocytized
material also seen more clearly (D). Note
well-defined background/cell interface
(arrows).
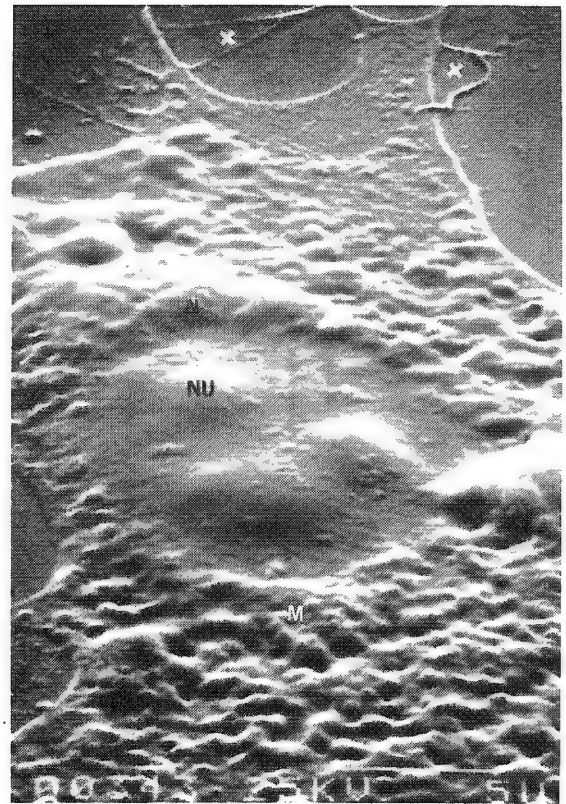
FIG. 5.--SEM (5000×, 45° tilt) of cyto-
plasmic extensions (X), readily seen in
this replica at higher magnification.

References

1. R. O. Hynes "Role of surface alterations in cell transformation," *Cell* 1: 147, 1974.

2. M. M. Burger, "A difference in the architecture of the surface membrane of normal and virally transformed cells," *Proc. Nat. Acad. Sci.* 62: 994, 1969.

3. R. Feder et al., "High-resolution soft x-ray microscopy," *Science* 197: 259, 1977.

4. E. C. Pirtle and J. E. Gallagher, "An air dry method for preparation of cell culture monolayers on cover slips for scanning electron microscopy," *Tissue Culture Assoc. Manual* (Procedure No. 53361) 2: 165, 1976.

5. J. McGowan et al., "High resolution microchemical analysis using soft x-ray lithographic techniques," *J. Cell Bio.* 80: 732, 1979.

6. B. Panessa-Warren and J. Warren, "Determining biological fine structure by differential absorption of soft x-rays," *Annal. N.Y. Acad. Sci.* 1: 1980.

MICROANALYSIS OF THE ELEMENTAL DISTRIBUTION OF URINARY CALCULI

B. E. McConville

Urinary calculi (kidney and bladder stones) have been examined by means of the scanning electron microscope (SEM) with accompanying x-ray microanalysis and proton-induced x-ray emission spectroscopy (PIXE). The complementary techniques show considerable promise for the study of urinary calculi and some interesting correlations have been achieved.

Because of the frequent occurrence of urinary calculus formation and the resultant morbidity, more information regarding the pathogenesis of the disease is urgently required.[1] Most people have, apparently, the conditions within themselves for stone growth but it is still unknown why they actually nucleate in any one person.[2] Study of the stone composition and structure is of prime importance from the therapeutic and prophylactic viewpoint.[3] Furthermore, it seems inescapable that the composition of the stone's nucleus or nidus must bear a fundamental relationship to causation and it is understood that this nucleating process may be caused by trace amounts of 'foreign bodies.'[4] Since these trace amounts have been hitherto undetectable by so called 'ordinary' chemical analysis, the more sensitive techniques of SEM with accompanying x-ray microanalysis and PIXE have been employed. The PIXE technique has been developed as a method for quantitative analysis of biological material for trace and minor elements.[5]

Experimental Procedure

Calculi sections were evaporated with gold or carbon and analyzed in a Cambridge S4 SEM, which was equipped with an energy-dispersive x-ray analysis system for routine simultaneous elemental analysis of each specimen.

Birmingham Radiation Centre's Dynamitron (Fig. 1), which is a 3MV high-current Cockcroft-Walton accelerator, was used to produce a beam of protons incident upon calculi sections; Fig. 2 shows a schematic diagram of the target assembly. The characteristic x-ray yield is proportional to the elemental concentration seen by the proton beam in the region of the stone through which the beam has passed. The yield varies linearly with trace concentrations (less than about 500 ppm). The x rays produced were determined by means of a Si(Li) detector on line to a computer; peak recognition was obtained directly.

Results

Since space does not permit a large presentation of results, an interesting illustration of the complementary techniques is shown here. A calculus supplied as a so-called 'pure' uric acid stone by University College, London, was analyzed on the SEM and the nuclear region was found to exhibit a degree of epitaxy (Fig. 3). Epitaxy is the growth mechanism of one crystal on the face of another and is believed to be one of the possible growth mechanisms of urinary calculi.[6] However, from the x-ray analysis of this area of stone, and indeed across all sections of the stone, no unexpected trace elements were found. The same stone analyzed by PIXE was found to contain trace amounts of sulfur, chlorine, potassium, calcium, and iron (Fig. 4).

Detailed ultrastructural analysis by the electron microscope has demonstrated mechanisms of stone growth in many calculi, which has been of particular significance in the nuclear regions. The x-ray microanalysis technique, whose sensitivity is of the order of 0.5%, has been augmented in many analyses by the sensitivity of the PIXE technique, when the limits of determination are in parts per million. These low levels of trace elements have been undetectable by previous methods of stone analysis. The full potential of the techniques has not yet been realized but it is expected that further detailed analyses will lead to a better understanding of the pathogenesis of stone formation.

The author is in the Department of Physics of the University of Birmingham, England, B15 2TT.

References

1. J. Grieve and P. M. Zarembski, *Urinary Calculi*, White Plains, N.Y.: Karger, 1973, 231-236.

2. R. W. Marshall et al., *Symp. on Vesical Calculus*, Bangkok: World Health Organization, 1972, pp. 192-198.

3. E. L. Prien and E. P. Prien Jr., "Composition and structure of urinary stones," *Amer. J. Med.* 45: 654-672, 1968.

4. B. E. McConville, "Investigations using autoradiographic analysis of urinary calculi," *Brit. J. of Urology*, in press.

5. N. A. Dyson and A. E. Simpson, "Measurement of lead and other elements in biological materials by PIXE," *Proc. Analyt. Div. Chem. Soc.* 13(7): 198-201, 1976.

6. G. H. Nancollas, *Urolthiasis Research*, New York: Plenum, 1976, pp. 5-25.
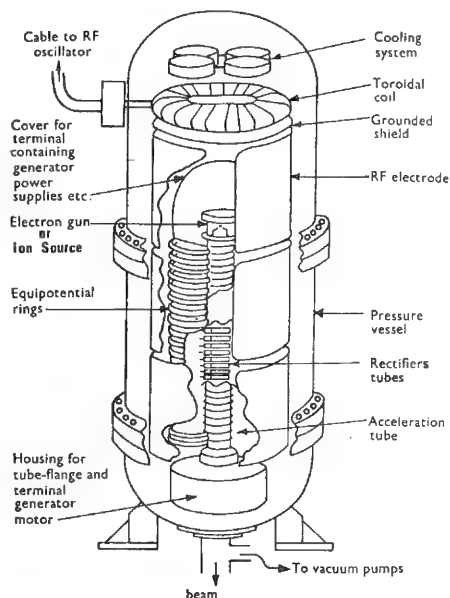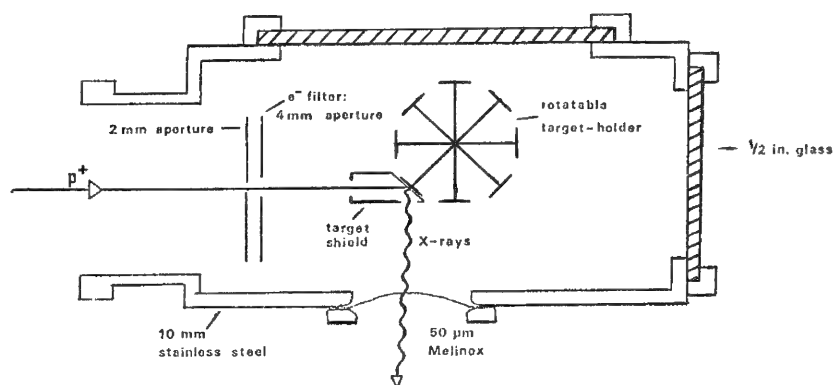
FIG. 1.--Dynamitron accelerator.

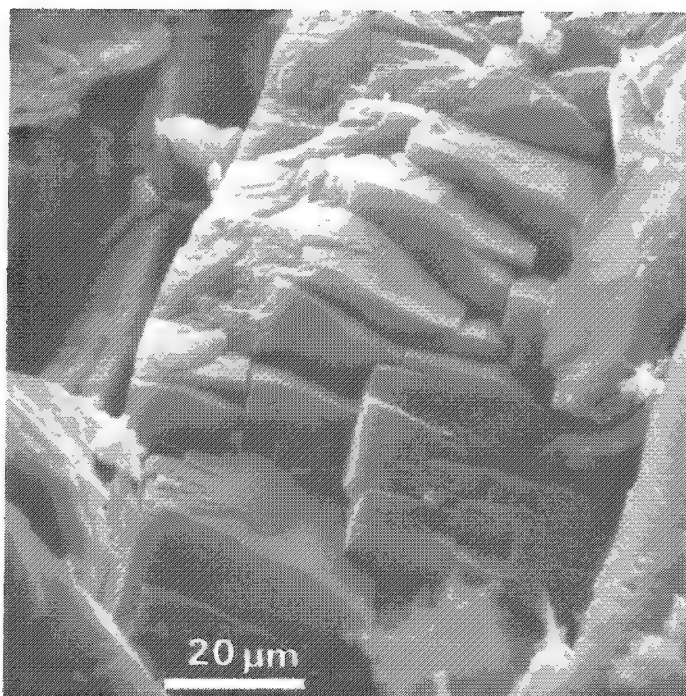FIG. 2.--Schematic diagram of target assembly used in PIXE.
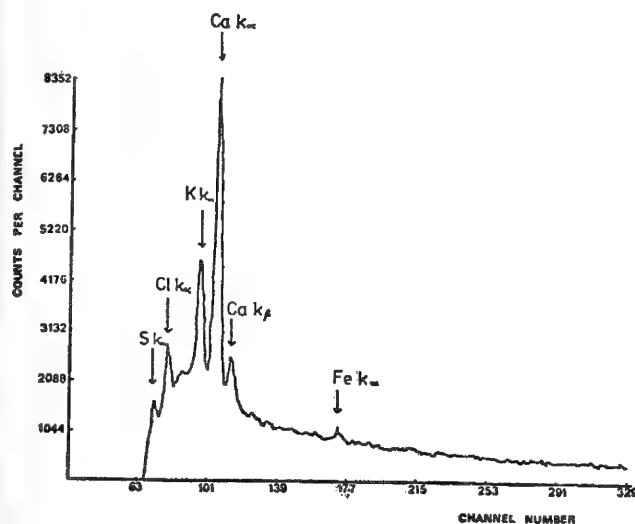

FIG. 3.--Electron micrograph of uric acid calculus.

FIG. 4.--Proton-induced x-ray spectra of uric acid calculus.

ELECTRON ENERGY-LOSS ANALYSIS AND ITS BIOLOGICAL APPLICATIONS WITH SPECIAL
REFERENCE TO MUSCLE

Henry Shuman, A. V. Somlyo, and A. P. Somlyo

Electron energy-loss analysis (EELS) is currently evolving as a practical technique for
the characterization of biological materials[1-6] through the following three major ap-
proaches: (1) elemental analysis based on the measurement of absorption edges due to
core shell excitations;[7-9] (2) detection of chemical bonding states and nearest-neighbor
relationships revealed in the low (0-10eV) energy loss region of the spectrum and the
near absorption edge and extended edge (EXELFS) fine structure[1,4,5,8,10]; and (3) imag-
ing of compositional contrast through elemental or molecular mapping at, respectively,
the absorption edges[1,5,12,13] or fine structure features.[10] The potential for single-
atom discrimination through EELS has been anticipated.[11] Electron energy loss analysis,
for the present, is complementary to energy-dispersive electron probe analysis (EDS) in
biology. However, EDS provides only atomic (elemental), but not molecular (nearest-
neighbor) information, does not detect elements of $Z < 11$ (except with windowless detec-
tors), and is also more limited than EELS in geometric detection efficiency and by the
relatively low fluorescence yields of low-Z materials. Furthermore, the computerized
fitting routines required for separation of overlapping peaks that occur in biological
x-ray spectra, such as the overlap of the K and Ca K lines, are not readily adapted for
x-ray mapping and reduce the sensitivity of Ca measurements in the presence of physio-
logical concentrations of potassium.[14,15] In view of the importance of calcium as a reg-
ulator of muscle contraction and our interest in this system,[15,16] we have began to ex-
plore the use of EELS for the detection of Ca through its L-edge spectrum. In addition,
we also present preliminary observations on L-edge fine structure observed with EELS.

Experimental Arrangement

The spectrometer used for these experiments[17] is a second-order aberration-corrected
magnetic prism, and is mounted on a Philips field-emission-gun-equipped EM400. The elec-
trons are detected with a CaF(Eu) scintillator and photomultiplier, and the signal is
digitized with a Teledyne 4707 voltage-to-frequency converter. The magnet ramp generator
and a 50 MHz counter for the converter output were built onto a Unibus interface card for
a PDP 11/34 computer. The 11/34 is further used for data storage and manipulation.

Elemental Analysis

The detection and quantitation of calcium, as mentioned earlier, is an important prob-
lem in determining the mechanism of excitation-contraction coupling and contractile acti-
vation in muscle. Although EDS x-ray analysis has provided useful information on calcium
concentrations in muscle, low collection efficiency and Ca Kα overlap with the K-Kβ peak
can make this analysis difficult. Preliminary measurements with EELS indicate a substan-
tial improvement for Ca detection. Figure 1 shows an EELS and an EDS spectrum of, respec-
tively, the Ca K edge and the Kαβ x-ray peak taken simultaneously from an evaporated film
of CaO. The EELS Ca spectrum was taken with 20eV resolution to increase the signal. The
estimated number of electrons and the number of x rays in the two spectra are approximately
equal. Figure 2 shows the EELS spectrum of the Ca L_2 and L_3 edges and an EDS spectrum
taken from the same area of a CaO film. The scale of the EELS spectrum was compressed by
a factor of 512, otherwise the spectra were acquired under identical conditions (total
time and probe parameters). The minimum detectable mass of Ca is clearly lowest for the
EELS Ca $L_{2,3}$ edge measurement, whereas the Ca K edge and Ca K x-ray peak have roughly

equivalent minimum detection masses in fair agreement with previous calculations.[1] For trace elemental measurements, as in biological specimens, the minimum detectable concentration is a more important parameter. EELS and EDS measurements were performed on the terminal cisternae of frog striated muscle. Many previous EDS spectra have been taken for this system and its calcium concentration is well known.[15,16] The specimens were ultrathin cryosections of rapidly frozen bundles of frog semitendinosus muscles. Detailed description of preparatory techniques have been published.[18] EELS spectra were taken from a 400Å spot at the center of a frog T.C. and again from a neighboring region of cytoplasm, known to contain very little Ca. The spectra were scaled to match in the energy loss region preceding the Ca $L_{2,3}$ edges and subtracted. The resulting spectrum is shown in Fig. 3. The number of electrons detected in a 46eV region under the edge is estimated to be $S = 0.41 \times 10^6$ electrons; the number of electrons in the same region of the unsubtracted TC spectrum was $S + B = 20.0 \times 10^6$ electrons. The signal-to-noise ratio for the EELS spectrum can be estimated to be

$$S/N = S/(S + B)^{1/2} \simeq 90$$
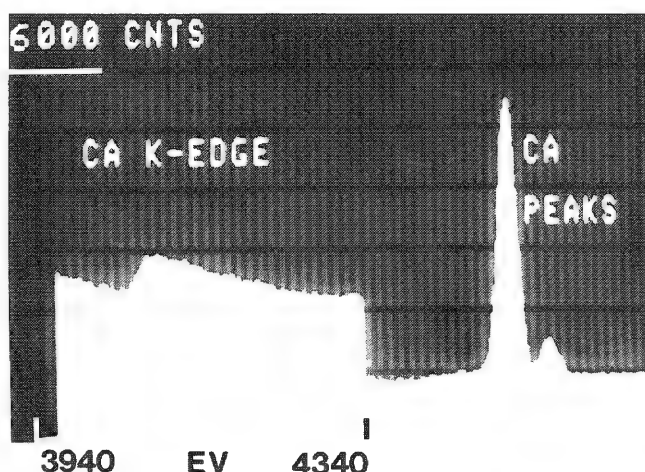
FIG. 1.--Ca K edge and Ca Kα,β peak from evaporated CaO film, taken simultaneously in 100 sec. EELS spectrum shows the energy loss region 3940 < E < 4340 eV and was taken with a half acceptance angle referred to specimen of β ≃ 125 mrad, and 20 eV resolution.
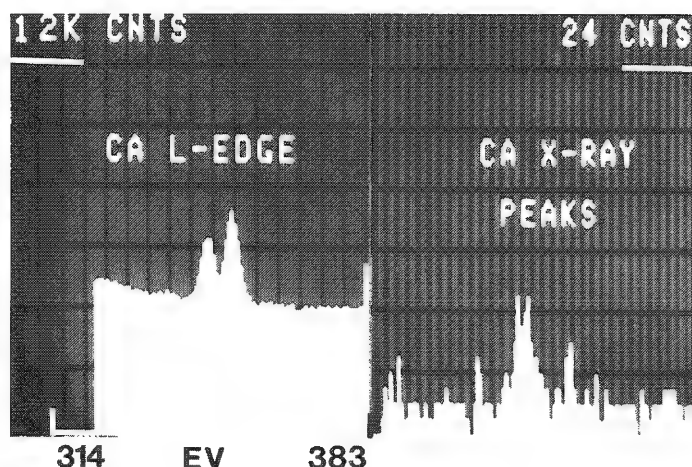
FIG. 2.--Ca L edge and Ca Kα,β peaks from CaO film taken from the same area, each for 250 sec. The EELS spectrum covers the energy loss region 323 < E < 383 eV at ≃ 2 eV resolution and β = 17 mrad.

The x-ray-determined concentration and estimated standard deviation σ_c of Ca in this T.C. was obtained from the EDS spectrum to be

$$[Ca] = 120 \text{ mmol/kg dry wt. } \pm 4.6 \text{ (x ray)}$$

so that for the EELS measurement, if we assume[9] σ_c (EELS) = $[Ca]/(S/N)_{EELS}$,

$$[Ca] = 120 \text{ mmol/kg } \pm 1.3 \text{ (EELS)}$$

For calcium, at least, the EELS has a 3 times smaller error and consequently a 3 times smaller MDC. If the 128 channels of EELS spectra had been collected in parallel rather than serially, the MDC could be reduced by a further factor of $(128)^{1/2} \simeq 11$, or for 95% confidence limits

$$Ca \text{ MDC} \simeq 0.23 \text{ mmol/kg}$$
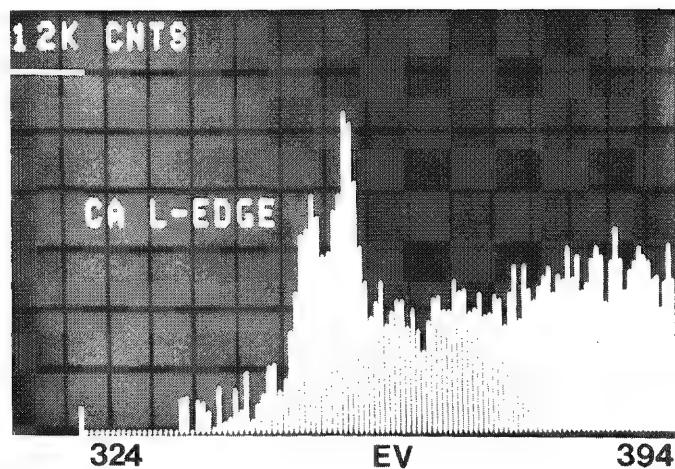
FIG. 3.--Background subtracted EELS spectrum from terminal cisterna in freeze-dried, ultrathin cryosection of frog semitendinosus muscle taken in 100 sec, for the energy region 333-393 eV with β = 8 mrad.

Similar measurements were performed for the P concentration of the cytoplasm of frog semitendinosus muscle. EDS and EELS spectra of, respectively, the phosphorus K peaks and the K-edge (2145eV) energy loss were obtained simultaneously. The EELS spectrum was taken with an energy resolution of 20 eV and $\beta \simeq 125$ mrad. A subsequent EELS spectrum of extracellular space of approximately equivalent mass thickness and known to contain a minimal amount of P was used to subtract the cytoplasm background. The number of electrons detected in a 240eV region under the P K-edge was estimated to be $S = 0.10 \times 10^6$ electrons; the number of electrons in the same region of unsubstracted cytoplasm was $S + B = 5.6 \times 10^6$ electrons or

$$S/N = 42$$

The x-ray-determined concentration of cytoplasmic phosphorus and error were

$$[P] = 212 \text{ mmol/kg dry wt. } \pm 5.9 \text{ (x ray)}$$

so that for EELS the concentration would be

$$[P] = 212 \text{ mmol/kg } \pm 5.0 \text{ (EELS)}$$

Fine Structure

The ability to distinguish chemically different atomic species, or to determine molecular composition on a microscopic scale is perhaps the most exciting potential of EELS. Figure 4 shows two superimposed EELS spectra of the sulfur L_{23} edge at $\simeq 165$eV energy loss. The dotted spectrum was obtained from thin crystals of elemental sulfur deposited from ethyl alcohol solution, whereas the solid spectrum is for crystals of Na_2SO_4. The L-edge of pure sulfur is broad, as expected from theoretical prediction for atomic sulfur, whereas the edge for the sulfate has three strong peaks presumably due to the four coordinated oxygen atoms. The phosphorus L edge shows a similar effect. Figure 5 shows the P $L_{2,3}$ edge at $\simeq 132$eV energy loss for a thin film of phosphoric acid. The multipeak structure is again presumably due to the coordinated oxygens.

Conclusion

For elemental analysis of low concentrations of calcium in thin sections of muscle, electron energy-loss spectrometry of L-edge losses is more sensitive than energy-dispersive x-ray analysis, even when the EELS data are collected with the information waste associated with serial collection. With parallel collection of EELS spectra, the predicted minimum detectable concentration of calcium is 0.23 mmol/kg for a 250sec collection and for a cryosection $\simeq 1000$Å thick ($\simeq 2.5 \times 10^{-6}$ gram/cm^2 dry). For thicker sections the shape of the background near the carbon K-edge becomes thickness sensitive, which makes accurate background subtraction far more difficult. Even this difficulty may be overcome with the deconvolution of multiple scattering effects.[19]

Quantitation from the K-edge losses of the elements Na to Ca is not as severely affected by thickness dependent variations in background. Our preliminary results with the P K-edge spectra agree with the prediction (1) that EELS in the serial collection mode is as efficient for P analysis as EDS.
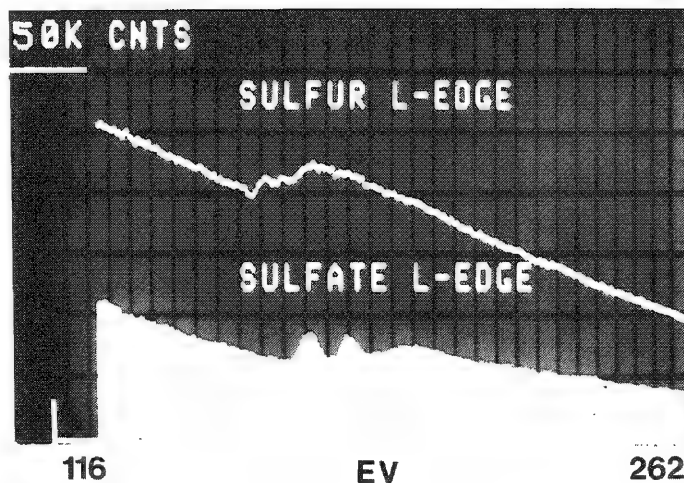
FIG. 4.--EELS spectra of sulfur (dotted line) and sulfate (Na_2SO_4) over energy region 125-262 eV with β = 8 mrad. The carbon support film background was subtracted in both cases.
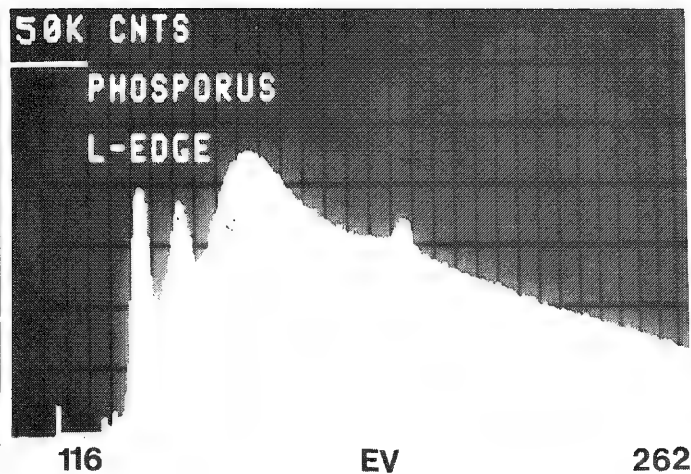
FIG. 5.--Phosphate (H_3PO_4) L_{23} edge at 132 eV and L_1 edge at 189 eV. Spectra were collected for 100 sec, at β = 8 mrad.

Measurements of the carbon K-edge for various nucleotide bases showed dramatic variations of near edge fine structure (1). The P and S $L_{2,3}$-edges for the phosphate and sulfate ligands also show fine structure. It is almost certain, however, that in order to measure L-edge fine structure, multiple scattering effects must be eliminated with deconvolution procedures[19] or by use of ultrathin sections.

References

1. M. Isaacson and D. Johnson, "The microanalysis of light elements using transmitted energy loss electrons," *Ultramicroscopy* 1: 33, 1975.
2. C. Colliex and P. Trebbia, "Quantitation and detection limits in electron energy loss spectroscopy (EELS) of thin biological sections," in C. P. Lechene and R. R. Warner, Eds., *Microbeam Analysis in Biology*, New York: Academic Press, 1979, p. 65.
3. M. S. Isaacson and A. V. Crewe, "Electron microscopy," *Ann. Rev. Biophys. and Bioengn.* 4: 165, 1975.
4. D. E. Johnson, "Energy loss spectrometry for biological research," in J. J. Hren, J. I. Goldstein, D. C. Joy, Eds., *Introduction to Analytical Electron Microscopy*, New York: Plenum Press, 1979, p. 245.
5. D. C. Joy and D. M. Maher, "Inner-shell electron spectroscopy for microanalysis," *Science* 206: 162, 1979.
6. P. L. Fejes, Ed., *Proceedings of a Specialist Workshop in Analytical Electron Microscopy*, Ithaca, N.Y.: Cornell University, 1978.
7. R. F. Egerton, "Formulae for light-element microanalysis by electron energy-loss spectrometry," *Ultramicroscopy* 3: 243, 1978.
8. R. D. Leapman, "Energy loss spectroscopy of core excitations and quantitative microanalysis," *Ultramicroscopy* 3: 413, 1979.
9. D. M. Maher, "Elemental analysis using inner-shell excitations: A microanalytical technique for materials characterization," in J. J. Hren, J. I. Goldstein, and D. C. Joy, Eds., *Introduction to Analytical Electron Microscopy*, New York: Plenum Press, 1979, p. 259.
10. J. Hainfeld and M. Isaacson, "The use of electron energy loss spectroscopy for studying membrane architecture: A preliminary report," *Ultramicroscopy* 3: 87, 1978.
11. M. Isaacson and M. Utlant, "On the chemical identification of individual atoms," *Proc. 37th EMSA Mtg.*, 1979, 524.

12.   G. T. Simon and F. P. Ottensmeyer, "Phosphorus containing cellular components as evidenced by energy loss electron microscopy," *37th EMSA Mtg.*, 1979, 510.

13.   S. W. Hui et al., "Intracellular localization of the sugar analog 6-fluorogalactose by electron energy-loss spectroscopic mapping," *37th EMSA Mtg.*, 1979, 512.

14.   H. Shuman, A. V. Somlyo, and A. P. Somlyo, "Quantitative electron probe microanalysis of biological thin sections: methods and validity," *Ultramicroscopy* 1: 317, 1976.

15.   A. V. Somlyo, A. V., H. Shuman, and A. P. Somlyo, "Elemental distribution in striated muscle and effects of hypertonicity: electron probe analysis of cryo sections," *J. Cell Biol.* 74: 828, 1977.

16.   H. Gonzalez-Serratos et al., "The composition of vacuoles and sarcoplasmic reticulum in fatigued muscle: Electron probe analysis," *Proc. Natl. Acad. Sci.* 75: 1329, 1978.

17.   H. Shuman, "Correction of the second order aberrations of uniform field magnetic sectors," *Ultramicroscopy*, in press.

18.   A. V. Somlyo and J. Silcox, "Cryoultramicrotomy for electron probe analysis," in C. Lechene and R. Warner, Eds., *Microbeam Analysis in Biology*, New York: Academic Press, 1979, p. 535.

19.   A. B. Ray, "Deconvolution of multiple scattering effects from core level electron energy loss spectra," *37th EMSA Mtg.*, 1979, 522.

ELECTRON SPECTROSCOPIC IMAGING AND ELECTRON ENERGY LOSS SPECTROSCOPY: HIGH-RESOLUTION MICROANALYSIS OF BIOLOGICAL SPECIMENS

F. P. Ottensmeyer, D. P. Bazett-Jones, and K. M. Adamson-Sharpe

The elemental analysis of specimens in the electron microscope has to the present generally been carried out by means of a focused electron probe coupled to an x-ray detector. Minimum sensitivities of 10^{-19} g and spatial resolutions of 5 nm have been estimated for this technique, though practical values of about 5×10^{-19} g and 50 nm have had to be accepted owing to physicostatistical limitations.[1,2]

A technique complementary to x-ray microanalysis is the use of the information carried by the electrons that have originally caused the x-ray excitation in the specimen: electron energy-loss spectroscopy along with electron spectroscopic imaging. In this technique electrons that have passed through the specimen are first dispersed to form a high-resolution energy spectrum, generally by means of a magnetic spectrometer. The spectral information is then analyzed directly, or the signal from a specifically chosen part of the spectrum is passed on to form an image. The technique is not new; it was developed and examined in part for metallurgical use by Castaing, one of the early workers in microprobe analysis.[3]

The analysis can be carred out with a scanning system, in which case it is very similar in operation to x-ray microanalysis, except that energy-loss spectra are recorded, or raster images are produced with the signal at a preselected energy loss.[4] Alternatively, an imaging spectrometer in a fixed-beam electron microscope can produce spectra of localized regions or display images filtered simultaneously over their entire extent at a selected energy loss.[3,5-7]

We have built such an imaging spectrometer into a Siemens Elmiskop 102 and examined its capabilities on several demonstrative biological specimens. The spectrum of a thin layer of hematin (Fig. 1) shows a 3eV loss in the low energy region, corresponding to the 400nm molecular absorption of the porphyrin ring structure in the visible region.
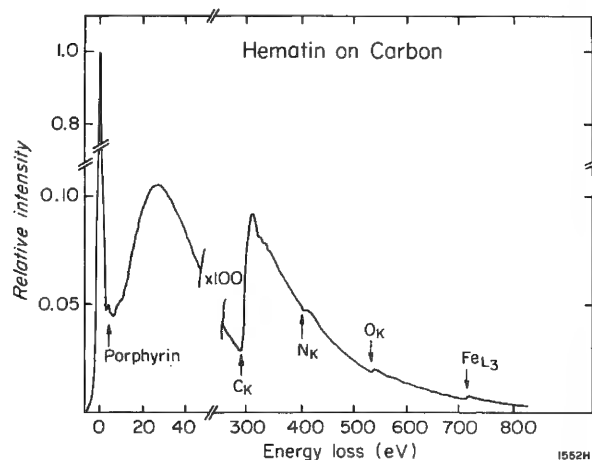

FIG. 1.--Electron energy-loss spectrum of thin film of hematin on thin carbon foil.
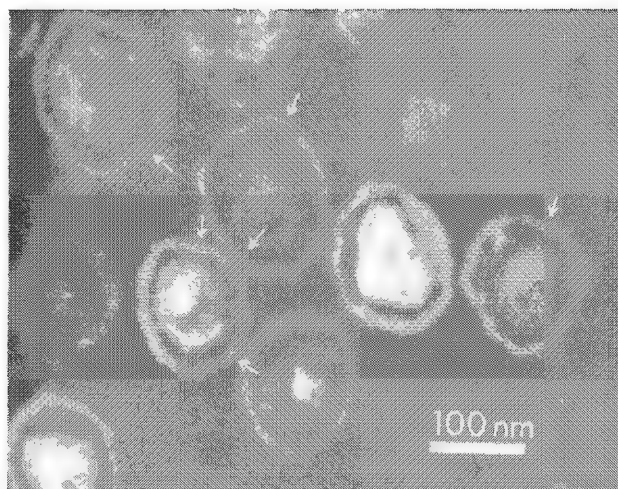

FIG. 2.--Electron-spectroscopic image of thin section of unstained purified concentrated murine leukemia virus taken with energy loss of 150 ± 7 eV.

Further out the strong carbon K-absorption, due both to the porphyrin molecule and the supporting carbon film, is followed by the K-edges of nitrogen and oxygen and the L-edge of iron, which identifies the atoms in hematin except for hydrogen.

Figure 2 shows an electron-spectroscopic image of a section of unstained murine leukemia virus taken with an energy loss of 150 ± 7 eV, an energy just above the phosphorus L-edge at 128 eV. Spatial resolution of the energy loss selected image is so good that the phospholipid-containing bilayer of the membrane of the virus is well resolved in portions where the membrane is sufficiently perpendicular to the membrane. Analysis of densitometer traces of thirty resolved bilayers indicated that one-third of them showed peaks with a full width at half height that was less than 0.5 nm; the separation between the peaks was around 5.0 nm.

The electron energy-loss spectrum, except for the low-energy region, is basically an electron distribution that decreases continuously with energy. Superposed on this continuum are stepwise increases in intensity at positions corresponding to the electron absorption edges of the atomic elements in the specimen (Fig. 1). An electron-spectroscopic image (ESI) with an energy loss just above the phosphorus L-edge, such as Fig. 2, is therefore not an elemental map of the chosen element, but contains structural information from the continuum as well. To obtain a measure of the contribution of this continuum, one must take a reference ESI with an energy loss just below the chosen absorption edge. The difference between the two ESIs then constitutes the desired elemental map. This process is demonstrated for ESIs of unstained nucleosomes taken above and below the phosphorus L-edge at 128 eV (Fig. 3). The images were digitized, aligned by computer-assisted crosscorrelation, normalized in the background region, and subtracted. The resulting phosphorus distributions, corresponding to the DNA distribution within the nucleosome, is shown in Figs. 3(c) and 3(g). Corresponding sketches of the interpretation of the coiling of DNA, consistent with the conformation suggested by Finch et al., are shown in Figs. 3(d) and 3(h), respectively.[8]
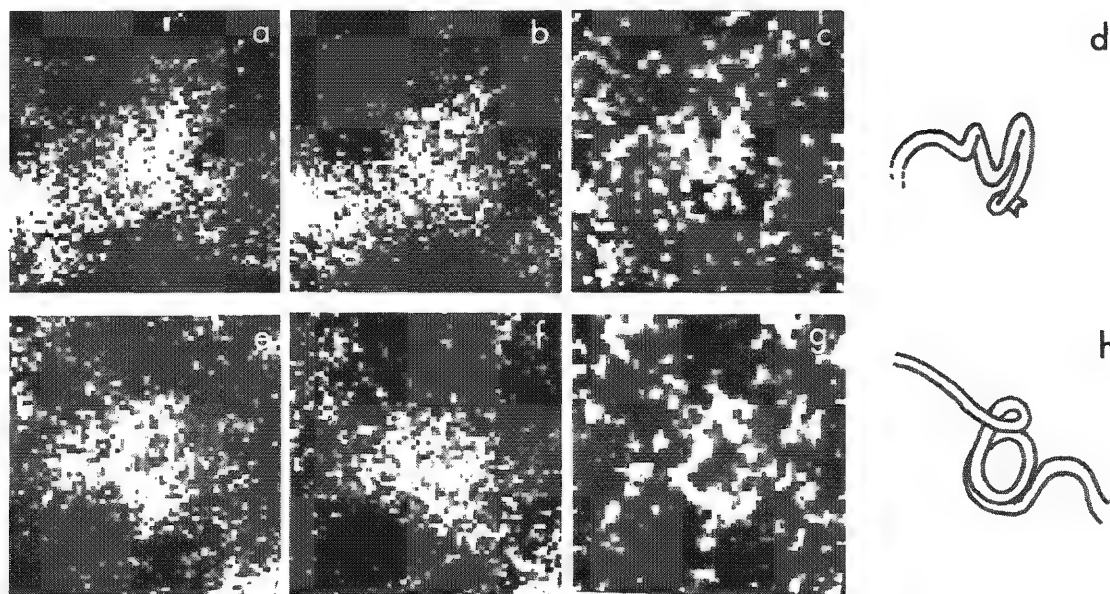
FIG. 3.--Elemental mapping of phosphorus in calf thymus nucleosomes by numerical subtraction of digitized electron spectroscopic images taken at 155 ± 7 eV (a and e), 105 ± 7 eV (b and f). Net phosphorus images (c and g). Interpretation of DNA coiling (d and h). Total size 40 nm.

Quantitative analysis of similarly obtained phosphorus distributions from images of the membranes of the murine leukemia virus shown in Fig. 2 indicated that a mass of phosphorus of 7×10^{-21} g had been detected in a single layer of membrane 5.0 nm long (length of densitometer slit referred to specimen) in a section thickness of 30 nm.

Thus, electron energy-loss spectrometry coupled with electron spectroscopic imaging appears to be a rather useful microanalytical technique for biological specimens, with superb spatial resolution and detection sensitivity. It complements x-ray microanalysis, since its strongest signals are obtained at lower energies, corresponding to absorptions from light elements such as boron, carbon, nitrogen, oxygen, phosphorus, sulfur, or calcium.

Although spatial resolution, sensitivity in electron spectroscopic imaging, and electron spectral analysis of specimens consisting of light elements were demonstrated here by means of a fixed-beam instrument, a high-resolution transmission scanning microscope with electron-energy analyzer should produce similar results. Nevertheless, conventional fixed-beam imaging, lack of contamination problems, and, at present, the rather larger number of picture points of photographic recording compared with the number of lines per image in scanning may be cited as advantages of the fixed-beam system. In both systems, however, energy-selected images are produced by high-energy electrons scattered in a forward direction. Therefore, elemental maps with high spatial resolution can be produced even in specimens that contain small elemental signals immediately adjacent to large concentrations of the same element, a particularly difficult case in x-ray microanalysis.

References

1. H. Shuman and A. P. Somlyo, "Electron probe x-ray analysis of single ferritin molecules," *Proc. Natl. Acad. Sci. USA* 73: 1196, 1976.

2. J. I. Goldstein, "Principles of thin film x-ray microanalysis," in J. J. Hren, J. I. Goldstein, and D. C. Joy, Eds., *Introduction to Analytical Electron Microscopy*, New York: Plenum Press, 1979, p. 83.

3. R. Castaing and L. Henry, "Filtrage magnétique des vitesses en microscopie électronique," *C. r. Acad. Sci. Paris* 255: 76, 1962.

4. J. A. Costa et al., "Fluorinated molecule as a tracer: Difluoreserotonin in human platelets mapped by electron energy-loss spectroscopy," *Science* 200: 537, 1978.

5. R. M. Kenkleman and F. P. Ottensmeyer, "An energy filter for biological electron microscopy," *J. Microsc.* 102: 79, 1973.

6. R. F. Edgerton et al., "Modification of a transmission electron microscope to give energy-filtered images and diffraction patterns, and electron energy loss spectra," *J. Phys. E.* 8: 1033, 1975.

7. Y. Kihn et al., "Application du filtrage en énergie des électrons à l'observation des objets épais en microscopie électronique," *J. Microsc. Spectrosc. Electron.* 1: 363, 1976.

8. J. T. Finch et al., "Structure of nucleosome core particles of chromatin," *Nature* 269: 29, 1977.

LOCALIZATION AND QUANTITATION OF SODIUM, POTASSIUM, AND CALCIUM IN GALACTOSE-INDUCED CATARACTS IN RATS BY SECONDARY-ION MASS SPECTROMETRY (SIMS)

M. S. Burns and D. M. File

Cataract was induced in young Sprague-Dawley rats by a diet of 3% d-galactose. The cataract progressively developed from cystic, water-cleft spaces at the equator and spread both anteriorly and posteriorly in the subcapsular cortex until at 15-16 days a dense nuclear opacity occurred. Localization and quantitation of ions was followed separately in cortical and nuclear areas by secondary-ion mass spectrometry (SIMS) of freeze-dried lenses.

A homogenous distribution of sodium, potassium, and calcium in normal lenses was visualized with ion images. Rubidium was also present and distributed homogeneously. Local variations in Na, K, and Ca were present in cataractous lenses.

Quantitation by ion counting showed a rapid loss of K from the cataractous lens cortex that plataued at ca Day 15 of feeding. The loss of K was dependent upon cataract development in a localized area. Na values in the cortex rose dramatically from Day 6 to Day 17 without an indication of saturation. In the nucleus, Na increased rapidly in the same time period but exhibited a shallower gradient beginning at ca Day 15. Ca in the cortex remained normal until approximately Day 14 when it rose to 5 times the normal value. Nuclear Ca values rose sooner but reached the same final concentration as the cortex (ca 4 mmoles/kg). Values of Na, K, and Ca were variable within cataractous areas, especially during early cataract development.

The data are consonant with a spatially progressive disruption of lens cell membrane activities responsible for Na, K, and Ca balance in the normal lens.

PROTON-INDUCED AND X-RAY INDUCED FLUORESCENCE ANALYSIS OF SCOLIOTIC TISSUE

B. J. Panessa-Warren, H. W. Kraner, K. W. Jones, and L. S. Weiss

Adolescent idiopathic scoliosis is characterized by a curvature or asymmetry of the spine which may become progressively more severe, with clinical symptoms appearing just prior to, or during, puberty. The incidence for scoliosis in the 12-14 age group has been reported as high as 10%, with more than 80% of the cases occurring in females.[1] Although pathologic changes exist in muscles from both sides of the spinal curvature, and "no statistically significant side differences have been reported," morphologic changes suggest that the concave side is the most affected.[2] This paper reports our preliminary data on the elemental composition of individual muscle fibers derived from convex, concave, and gluteal muscle, and erythrocytes from scoliotic and normal patients, analyzed by proton-induced x-ray emission (PIXE) and x-ray fluorescence spectroscopy (XRF). A new type of specimen holder was designed for this study that offers low x-ray background, minimal absorption, and maintenance of a moist environment around the specimen.

Methods

The muscle fibers used in this study were obtained from residual muscle tissue removed during surgery to correct curvature of the spine. Small samples (8 × 4 mm) of paraspinal muscle tissue (from a female of 18 with idiopathic scoliosis), was removed on the convex and concave sides of the spine at the apex of the curvature during corrective surgery. A specimen from the gluteus maximus was also removed for analysis. After excision, the tissue was immediately fixed in 3% glutaraldehyde in 0.1 M cacodylic buffer (pH 7.4) at room temperature for 3 hr. The fixative was then removed and replaced with fresh fixative and the specimens were stored in fresh fixative for 3 days at 4°C.

We separated individual muscle fibers by dissecting away the outer layers of muscle tissue that had come in contact with the scalpel during surgery. Wooden and glass dissection instruments were used to prevent metal contamination of the muscle fibers. The isolated muscle fibers were washed in buffer and placed on a formvar film stretched across a 25mm-diameter hole of a lucite frame (Fig. 1).

Lucite frames 30 × 30 × 1 mm were washed several times in glass-distilled, deionized water. A formvar film (40-70nm thick) was placed across the lucite frame, and stretched across the central circular opening in a uniform sheet. The muscle fibers, which had been placed in the center of this formvar diaphragm with some fresh buffer, were covered with an equally thin sheet of formvar, forming a formvar sandwich that sealed the fibers within a marginal bubble of buffer (Fig. 1b and c). Two muscle fibers from the gluteus maximus, and two sets of muscle fibers from convex and concave paraspinal muscles, were analyzed in this way.

The muscle fibers were scanned with a proton microprobe[3,4] in air using 2.5MeV protons to stimulate characteristic x rays from elements within the sample. The x rays were detected with a high-resolution Si(Li) energy-dispersive spectrometer placed about 1 cm from the sample, which was itself placed 2 mm (or less) from the emergent port of the Van de Graaff accelerator (Fig. 1c). The beam spot available in this mode is about 25 μm and scans of the fibers were made at about 0.1mm intervals along the fibers. Energy and concentration calibrations were carried out by means of commercially available trace ele-

ment standards in a representative matrix. Data analysis was carried out by standard computer integration of spectral areas. Unfortunately an anomolously high x-ray background was present in addition to copious arsenic characteristic x rays from the buffer, and little information above 8 keV (Z > 29) could be obtained by the scans. However, the samples remained intact and viable, albeit somewhat dehydrated--a problem discussed below.
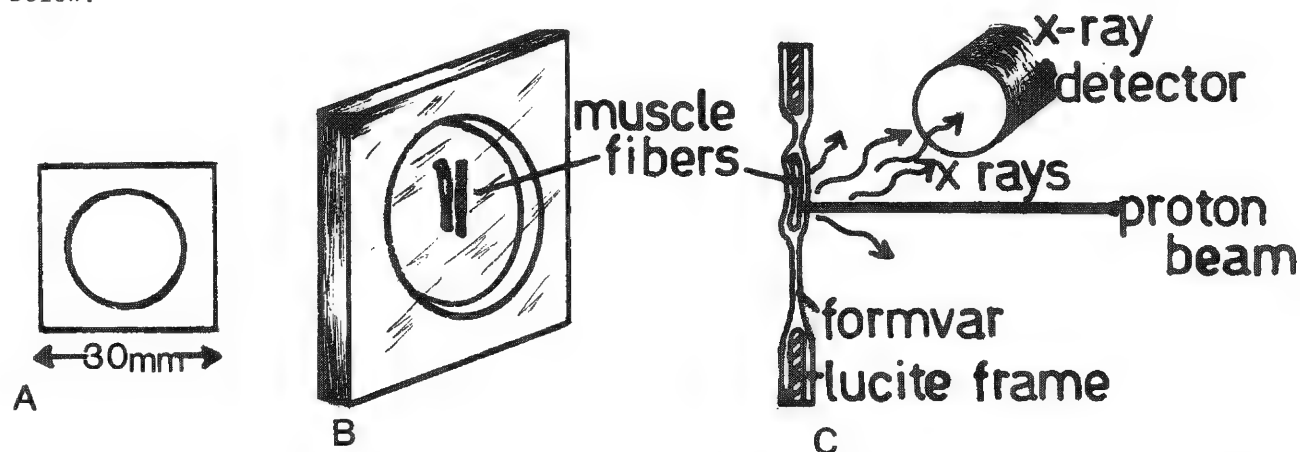
FIG. 1.--A lucite frame (A) with a circular opening (35mm diam.) is covered with thin formvar film. Muscle fibers are placed in center of formvar window (B) and coated with another layer of formvar. Trapped buffer accumulates around muscle fibers and keeps them moist throughout proton beam excitation (C).

The samples were then irradiated by a broad, uniform beam of protons in vacuum in a standard PIXE system having somewhat greater elemental sensitivity (down to a few parts per million for many elements), particularly for lighter elements (Z < 26). The samples were also studied by XRF with a hardened, filtered x-ray beam from an x-ray tube-Si(Li) detector system. This XRF system is complementary to the PIXE system in that its sensitivity emphasizes elements with Z > 26.

Since adolescent idiopathic scoliosis is believed to have a genetic as well as environmental etiology,[1] it appears feasible to assume that the genetic defect may express itself in tissues of the body other than the musculoskeletal system. To determine whether any unusual electrolytes could be found in the blood of scoliotic patients, clotted, heparinized, and glutaraldehyde fixed (1.5% in 0.1M cacodylic buffer) preparations of whole blood were placed on formvar-lucite frames and analyzed by PIXE and XRF. Initial trials demonstrated that fixation increased the elemental background and did not preserve sufficient sample integrity to warrant its use. Subsequent blood samples were collected with, and without heparin, and centrifuged in hematocrit capillary tubes to separate the erythrocytes from leukocytes and serum. A 2-5 µg aliquot of blood was smeared onto the formvar (90nm thick) window, and all samples were analyzed for about 20 min by PIXE and about 60 min by XRF. Twenty-one blood samples were surveyed, with donors ranging from 12 to 34 yr.

Results and Discussion

By XRF analysis, Yarom et al.[5] reported somewhat high copper and zinc concentrations in freeze-dried thick sections of scoliotic muscle, when compared to normal specimens. He notes that convex muscle reveals somewhat higher calcium levels than the concave paraspinal tissue, and significantly less calcium than observed in glutei.

The spectra we observed from hydrated muscle fibers analyzed by PIXE and XRF show no significant variations in calcium, phosphorus, zinc, or copper x-ray events emitted from convex, concave, or glutei muscle fibers. However, the muscle fibers from the concave sample reveal spectra with small selenium (Se) K_α (11.21 keV) and K_β (12.49 keV) x-ray events. Initially it was not possible to distinguish the Se signals from the arsenic (As) K_α (10.54 keV) and K_β (11.72 keV) x-ray events produced by the cacodylate buffer.

FIG. 2.--Proton-induced x-ray emission (PIXE) spectra of isolated muscle fibers routinely show presence of Se in fibers taken from concave paraspinal musculature (a), and total lack of Se in fibers from glutei . (b).

(a)
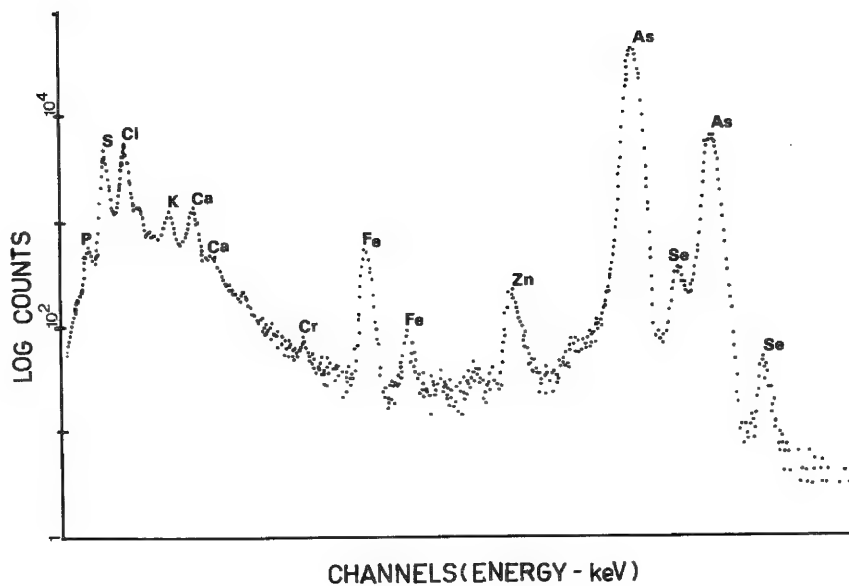
(b)
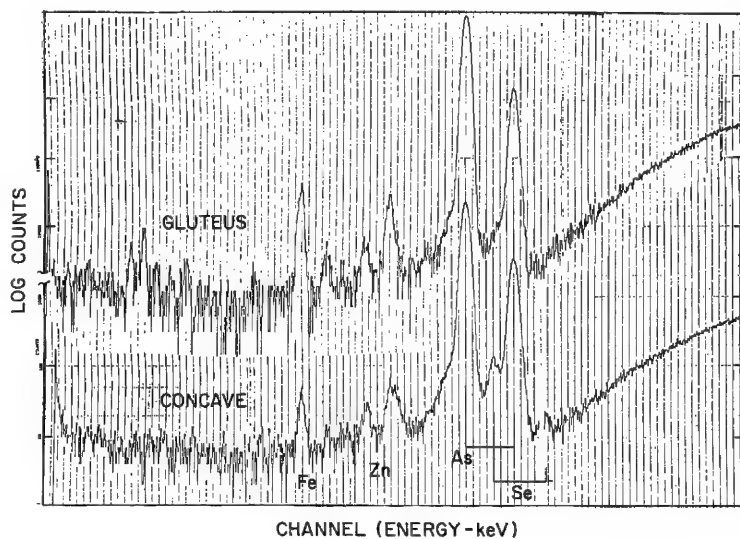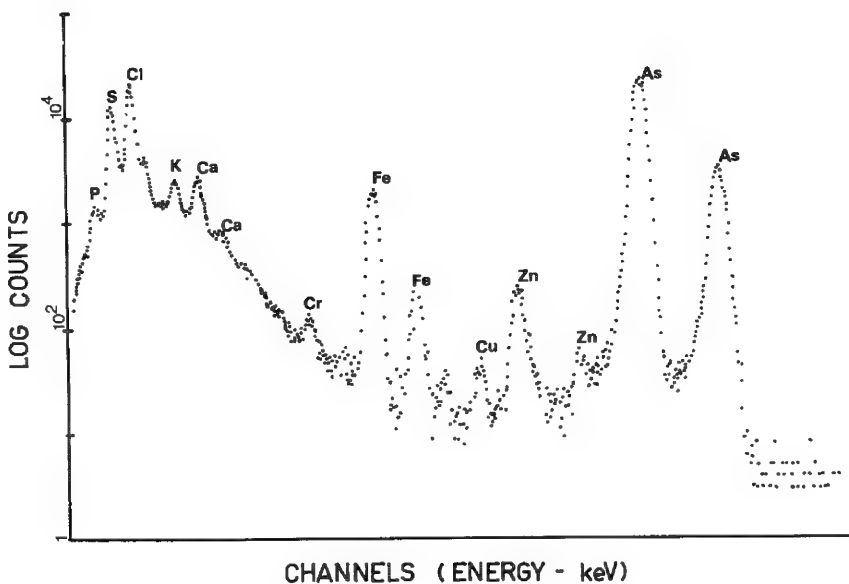
FIG. 3.--X-ray induced fluorescence spectra (XRF) also show presence of Se in concave paraspinal muscle fibers and lack of Se in gluteal fibers.

By reseting the gain to maximize Se signal above background using PIXE, we observed the Se. XRF spectroscopy supports the PIXE data and reveals no Se signal from gluteal muscle fibers, and significant Se signal from concave, and to a lesser extent, convex muscle fibers (Figs. 2 and 3). After 2 days of observation, the muscle fibers became desiccated owing to the presence of minute pores in the formvar. We later learned that one can prevent porosity by using only anhydrous ethylene dichloride to dissolve the formvar, thereby eliminating water vapor contamination. Subsequent experiments with rabbit muscle fibers demonstrated that the wet chambers can be maintained for 3-5 days. We were also able to introduce polyethylene catheter tubing (1. 5mm bore) into the chambers to provide a constant flow of oxygenated Ringer's solution to the tissue.

X-ray spectra from most of the scoliotic erythrocyte samples show significant Se signal, whereas the spectra from normal samples show none. Non-heparinized samples show significantly greater Se content than heparainized identical specimens. It is unfortunate that some of the pathological blood samples could not be included in the tabulated results owing to the possibility of undiagnosed blood dyscrasias and possible endocrinopathies. Further studies will have to be done with a known sample population to eliminate these variables.

Conclusions

Additional work must be done to determine conclusively whether the presence of Se in concave muscle (and to some extent convex) from patients with idiopathic scoliosis is universally observed. The fact that no Se is found in gluteal muscle fibers, and is found in not only the paraspinal muscle fibers adjacent to the curvature of the spine, but also associated with the red blood cells of affected patients, strongly suggests that Se may be a marker element for idiopathic scoliosis. It is too soon to speculate whether Se is a byproduct of abnormal neuromuscular function, or whether its presence may be the genetic expression of altered enzyme or transport systems.

In conclusion, it appears that PIXE and XRF analysis offer a very direct and sensitive means of detecting trace elements in intact muscle fibers. Furthermore, experience with these techniques indicates possible accuracies of 10-20% at about 10ppm trace levels. Ideally the tissue should not be fixed, but quench-frozen in liquid nitrogen and examined frozen by PIXE or freeze-dried by XRF, to avoid exogenous elemental contamination and reduce the background. The proton μ-beam has the efficiency and sensitivity to detect small amounts of endogenous elements in biological samples with accuracy comparable with XRF. Because samples can be elementally analyzed as intact structures at atmospheric pressure and in a wet cell, the proton microprobe has a marked advantage as a biological research tool.

References

1. P. R. Harrington, "The etiology of idiopathic scoliosis," *Clinical Orthopaedics and Related Research* 126: 17, 1977.

2. R. Yarom and G. Robin, "Studies on spinal and peripheral muscles from patients with scoliosis," *Spine* 4: 12, 1979.

3. R. E. Shroy, H. W. Kraner, and K. W. Jones, "Proton microprobe with windowless-exit port," *NIM* 157: 163, 1978.

4. P. Horowitz and L. Grodzins, "Scanning proton-induced x-ray microspectrometer in an atmospheric environment," *Science* 189: 795, 1975.

5. R. Yarom, G. C. Robin, and R. Gorodetsky, "X-ray fluorescence analysis of muscles in scoliosis," *Spine* 3: 142, 1978.

Eighteen Years of Secondary Ion Mass Spectrometry: A Bibliography of SIMS, 1958-1975

Shaiw-Yih Yin

Introduction--by D.B. Wittry

In recent years, the technique of secondary ion mass spectrometry (SIMS) has attracted increasing interest because of its extremely high sensitivity for elemental detection and because of its capabilities for local analysis and for ion microscopy. At least nine commercial instruments for this analytical technique have been developed and many investigations have been made concerning sputtering phenomena that influence the quantitative and qualitative aspects of SIMS. Two international conferences and two U.S.-Japan seminars on SIMS have been held during the past 5 years.

In this bibliography, the author has included publications on instrumentation, applications and theory of SIMS. In addition, many references are included that technically are not a part of the SIMS literature but provide information that is essential in interpreting the data obtained with SIMS. An index has been included for convenience in locating references concerned with a particular aspect of SIMS or on sputtering phenomena related to SIMS.

It is expected that this bibliography will be a valuable aid not only for researchers presently engaged in SIMS investigations but also for new researchers in this field. Hopefully, another bibliography covering the later years of SIMS will be published in the next volume of these proceedings. In this next bibliography, corrections or additions to the present bibliography will be included. (Please send any corrections or suggestions for additions for 1958-1975 to D. B. Wittry, VHE 602, University of Southern California, Los Angeles, CA 90007).

INDEX

Applications

Biology: (1966): 17; (1969): 11; (1970): 18; (1972): 70, 71; (1974): 81.

Geology: (1967): 10; (1970): 5; (1973): 39, 54; (1974): 33, 35, 56, 57, 67; (1975): 121.

Metallurgy: (1960): 6; (1961): 3; (1962): 9, 12, 13; (1963): 4; (1964): 4; (1965): 2; (1966): 6, 18, 20; (1967): 15; (1968): 7; (1969): 19; (1970): 7, 8, 16, 24, 29; (1971): 2, 14, 34; (1972): 11, 12, 13, 26, 41, 55, 59, 62; (1973): 1, 11, 12, 22, 49, 60, 76, 80, 82; (1974): 7, 8, 10, 11, 16, 44, 47, 60, 61, 68, 73, 76, 78, 80, 85, 100, 104, 106, 111, 121; (1975): 10, 27, 40, 55, 56, 62, 66, 73, 74, 83, 84, 85, 94, 97, 100, 103, 107, 116.

Solid State Electronics: (1963): 1; (1966): 1; (1971): 6, 31; (1972): 15, 25, 38, 39, 49, 58, 60, 64, 72, 77; (1973): 9, 19, 27, 29, 34, 38, 40, 41, 46, 51, 53, 59, 72, 81, 83; (1974): 1, 13, 19, 26, 34, 39, 43, 70, 74, 75, 114; (1975): 6, 15, 22, 23, 25, 26, 42, 43, 44, 53, 60, 61, 64, 71, 72, 76, 79, 80, 93, 96.

Miscellaneous: (1960): 3; (1961): 6; (1962): 6; (1963): 8, 9; (1964): 2, 3, 6, 7; (1965): 6, 7, 8, 10; (1966): 12, 13, 22; (1967): 2, 6; (1968): 6, 9, 19, 28; (1969): 28, 33; (1970): 9, 15, 20, 30; (1971): 5, 10, 11, 12, 15, 20, 21, 24, 26, 28, 29, 40, 44, 45, 50, 55; (1972): 4, 7, 8, 10, 23, 28, 32, 33, 35, 35, 37, 56, 57; (1973): 10, 26, 28, 33, 36, 37, 43, 47, 50, 61, 63, 71, 74, 77, 78, 84; (1974): 9, 16, 23, 24, 25, 32, 38, 89, 96, 101, 112, 113, 117; (1975): 3, 7, 8, 14, 31, 36, 37, 39, 48, 49, 65, 67, 89, 105, 106, 113, 114.

Quantitative Analysis

Proposed Models and Their Experimental Evaluation: (1968): 10; (1970): 6; (1971): 3, 30; (1972): 67; (1973): 3, 44, 45, 68, 69; (1974): 2, 20 82, 86, 116; (1975): 29, 45, 59, 92, 97, 120.

Empirical Methods: (1972): 3; (1974): 58, 63, 82, 91, 115; (1975): 35, 78, 110, 111.

Specimen Charging Problems and Soutions: (1966): 13; (1969): 2; (1971): 57.

Author Shaiw-Yih Yin is in the Department of Materials Science at the University of Southern California. D. B. Wittry who suggested this work and served as an advisor during the preparation of the bibliography is in the Departments of Materials Science and Electrical Engineering at the University of Southern California. Support by the National Science Foundation is gratefully acknowledged.

General Discussion of Problems in Quantitative Analysis: (1973): 5, 7, 17, 24, 25; (1974): 20, 64, 83, 84, 99, 103; (1975): 41, 99, 112.

Instrumentation

General Description of SIMS Instruments: (1966): 16, 21; (1967): 7; (1968): 21, 22; (1969): 10, 14, 20, 23: (1970): 25, 28; (1971): 8, 35, 39, 42, 53, 54, 59; (1972): 1, 2, 40, 52, 54, 65, 74, 76; (1973): 48, 52, 56, 70, 86; (1974): 12, 48, 52, 53, 55, 62, 93, 109, 118; (1975): 2, 3, 5, 13, 16, 82, 87, 104.

Ion Optics of SIMS Instruments: (1967): 16; (1969): 10; (1971): 36, 56; (1972): 53; (1973): 64, 67; (1974): 45, 95.

Mass Spectrometers for SIMS Instruments: (1968): 25, 29; (1969): 10; (1970): 31; (1971): 9, 49; (1972): 66; (1973): 64, 67; (1974): 36, 51, 54, 59; (1975): 87.

Ion Sources for SIMS Instruments: (1961): 13; (1962): 2; (1963): 6; (1964): 9, 10, 12, 13; (1965): 12; (1967): 13, 18; (1968): 17; (1969): 32; (1970): 11, 17, 26; (1971): 13; (1972): 31, 63, 73; (1973): 42, 65; (1974): 30; (1975): 38, 63, 81, 103.

Detectors for SIMS Instruments: (1960): 5; (1969): 6; (1971): 52; (1972): 50, 75.

Computers Used for Data Analysis: (1974): 21; (1975): 86, 101.

Miscellaneous: (1959): 1; (1970): 27; (1971): 18, 43, 48; (1972): 21; (1973): 75; (1974): 66, 102; (1975): 17, 52, 91.

Sputtering Pheonomena Important in SIMS

Chemical and Matrix Effects on Ion Yields: (1966): 19; (1971): 16; (1973): 16, 21; (1974): 87; (1975): 47, 58, 89.

Effects of Reactive Gases on Sputtering Rates or on Ion Yields: (1968): 1; (1970): 1; (1971): 1; (1972): 63; (1973): 14; (1975): 57.

Energy and Angular Distributions of Sputtered Ions: (1960): 8, 9; (1966): 6, 10; (1967): 1, 12; (1968): 2, 8, 15, 16, 18; (1969): 19, 21; (1972): 27, 48; (1973): 4, 20, 57, 87; (1974): 46, 77; (1975): 28, 50, 75.

Monte-Carlo Calculations of the Sputtering Process: (1969): 13; (1972): 14, 43; (1973): 35; (1974): 41, 42; (1975): 46, 90, 98.

Secondary Ion Yields: (1959): 2; (1960): 2; (1961): 1, 2; (1962): 4, 8, 9, 12; (1963): 1; (1964): 4, 14; (1966): 2; (1968): 3; (1969): 4, 18; (1970): 2, 3, 14; (1971): 27, (1972): 9, 17, 45, 46, 47; (1973): 1, 15, 18, 23; (1974): 4, 58, 65, 92; (1975): 1, 9, 75, 85, 117, 119.

Sputtering Mechanisms and Sputtering Effects: (1958): 1; (1959): 3, 4; (1960): 1, 4, 7, 11, 12; (1961): 2, 4, 7, 8, 9, 10, 11, 12, 14; (1962): 1, 3, 5, 7, 10, 11; (1963): 2, 3, 5, 7, 10, 11, 12; (1964): 1, 5, 8, 11; (1965): 1, 3, 4, 9, 11; (1966): 8, 9, 14, 15; (1967): 3, 4, 8, 9, 11, 12, 17, 19, 20; (1968): 4, 5, 11, 12, 13, 14, 20, 24, 26, 27; (1969): 3, 5, 7, 8, 9, 12, 15, 16, 17, 22, 25, 26, 27, 29, 30, 31; (1970): 4, 10, 12, 13, 21, 22, 23, 32; (1971): 4, 7, 17, 19, 25, 41, 46; (1972): 5, 6, 19, 20, 24, 29, 34, 44, 51, 69; (1973): 13, 79; (1974): 97, 107, 108; (1975): 12, 32, 54, 108, 118.

Surface Topography of Sputtered Targets: (1969): 24, 30; (1971): 22, 58; (1972): 18; (1973): 2, 6, 62, 73, 85; (1974): 6, 40, 90, 94, 105, 119; (1975): 30, 31, 51.

SIMS Compared with or Used with Other Surface Analytical Techniques

(1971): 29, 37, 38, 51; (1972): 11, 58, 59, 60; (1973): 11, 55, 58, 59; (1974): 3, 5, 15, 17, 18, 22, 29, 31, 49, 50, 60, 68, 69, 71, 72, 79, 88, 110; (1975): 4, 11, 21, 24, 33, 68.

Review and General Papers

(1961): 5; (1966): 3, 4, 5, 7, 11; (1967): 14; (1968): 23; (1970): 19; (1971): 23, 26, 32, 33, 47; (1972): 1, 2, 22, 30, 42; (1973): 8, 30, 31, 32; (1974): 27, 28, 37, 120; (1975): 18, 19, 20, 34, 69, 70, 77, 109.

1958

1. Honig, R.E., "Sputtering of Surfaces by Positive Ion Beams of Low Energy", J. Appl. Phys., 29, 549 (1958).

1959

1. Bernard, R., Goutte, R., and Guillaud, C., "Use of an Image Converter in Emission Microscopy with Negative Ions', J. Phys. Radium., 20, 981 (1959).
2. Bradley, R. C., "Secondary Positive Ion Emission from Metal Surface", J. Appl. Phys., 30, 1 (1959).
3. Wehner, G., "Influence of the Angle of Incidence on Sputtering Yields", J. Appl. Phys., 30, 1762 (1959).
4. Wehner, G.K., "Velocities of Sputtered Atoms", Phys. Rev., 114, 1270 (1959).

1960

1. Arifov, U.A., and Khadzhimykhamedov, Kh.Kh.,"On the Question of the Neutralization of Fast Positive Ion on the Surface of a Metal", Izv. Ahad. Nauk SSSR, Ser. Fiz., 24, 705 (1960).
2. Bradley, R.C., Arking, A., and Beers, D.S., "Secondary Positive Ion-Emission from Platinum", J. Chem. Phys., 33, 764 (1960).
3. Castaing, R., Jouffrey, B., et Slodzian, G., "Sur les Possibilites d'Analyse Locale d'un Echantillon par Utilisation de son Emission Ionique Secondaire", Academie des Sciences, 22, 1010 (1960).
4. Cunningham, R.L., Haymann, P., Lecomte, C., Moore, W.J., and Trillat, J.J., "Etching of Surfaces with 8-KeV Argon Ions", J. Appl. Phys., 31, 839 (1960).
5. Daly, N.R., "Scintillation Type Mass Spectrometer Ion Detector", Rev. Sci. Instrum., 31, 264 (1960).
6. Fogel', Y.M., Slabospitskii, R.P., and Karnaukhov, I.M., "Mass Spectrometer Investigation of Secondary Positive and Negative Ionic Emission, Excited by the Bombardment of a Molybdenum Surface by Positive Ions", Zh. Tekh. Fiz., 30, 824 (1960).
7. Rol, P.K., Fluit, J.M., and Kistemaker, J., "Theoretical Aspects of Cathode Sputtering in the Energy Range of 5-25 KeV", Physica, 26, 1009 (1960).
8. Stanton, H.E., "On the Yield and Energy Distribution of Secondary Positive Ions from Metal Surfaces (Energy Burst)", J. Appl. Phys., 31, 678 (1960).
9. Veksler, V.I., "Energy Distribution of Sputtered and Scattered Ions in the Bombardment of Tantalum and Molybdenum by Positive Cesium Ions", Sov. Phys. JETP, 11, 235 (1960).
10. Wehner, G.K., and Rosenburg, D., "Angular Distribution of Sputtered Material", J. Appl. Phys., 31, 177 (1960).
11. Yonts, O.C., Normand, C.E., and Harrison, D.E., Jr., "High-Energy Sputtering", J. Appl. Phys., 31, 447 (1960).
12. Yurasova, V.E., Pleshivlsev, N.V., and Orfanov, I.V., "Directed Emission of Particles from a Copper Single Crystal Sputtered by Bombardment with Ions up to 50 KeV Energy", Sov. Phys. JETP, 37, 689 (1960).

1961

1. Batanov, G.M., "Secondary Ion (Ion-Ion) Emission from Single Crystals of Sodium Chloride Under Bombardment by Lithium Ions", Sov. Phys. Solid State, 3, 471 (1961).
2. Colligon, J.S., "Ion Bombardment of Metal Surfaces", Vacuum, 11, 272 (1961).
3. Fogel' Ya.M., Slabospitskil, R.P., and Karnaukhov, I.M., "Mass-Spectrometer Investigation of Secondary Positive and Negative Ion Emission Resulting from the Bombardment of an Mo Surface by Positive Ions", Sov. Phys. Tech. Phys., 5, 777 (1961).
4. Harrison, D.E., Jr., "Determination of the Maximum Lattice--Chain Energy from Sputtering Yield Curves," J. Appl. Phys., 32, 924 (1961).
5. Honig, R.E., "Mass Spectrometric Studies of Solid Surfaces", Advances in Mass Spectrometry, Vol. 2. R.M. Elliott, Ed., (Oxford: Pergamon Press Ltd. 1961), p. 25.
6. Honig, R.E., "The Sputtering of Silicon Carbide by Positive Ion Bombardment", Proc. of the 5th Int. Conf. on Ionization Phenomena in Gases, Munich, W. Germany, 28 Aug.-1 Sept. 1961. H. Maecker Ed., (Amsterdam: North Holland Publishing Company 1962), p. 106.
7. Kopitzki, K., and Stier, H.E., "The Mean Velocity of Particles Emitted During Cathodic Sputtering of Metals", Z. Naturforsch, 16A, 1257 (1961).
8. Lindhard, J., and Scharff, M., "Energy Dissipation by Ions in the KeV Region", Phys. Rev., 124, 128 (1961).
9. Magnuson, G.D., Meckel, B.B., and Harkins, P.A., "Etch Effects from Oblique-Incidence Ion Bombardment", J. Appl. Phys., 32, 369 (1961).
10. Molchanov, V.A., Tel'kovskii, V.G., and Chicherov, V.M., "Anisotropy of Cathodic Sputtering of Single Crystals", Sov. Phys. Dokl, 6, 223 (1961).
11. Stein, R.P., and Hurlbut, F.C., "Angular Distribution of Sputtered Potassium Atoms", Phys. Rev., 123, 790 (1961).
12. Thompson, M.W., "A Theory of High-Energy Sputtering Based on Focused Collision Sequences", Proc. of the 5th Int. Conf. on Ionization Phenomena in Gases, Munich, W. Germany, 28 Aug.-1 Sept. 1961. H. Maecker Ed., (Amsterdam: North Holland Publishing Company 1962), p. 85.

13. Von Ardenne, M., "Duoplasmatron as an Ion or Electron Injector of Extremely High Emission Current Density", Exper. Tech. Phys., 9, 227 (1961).
14. Yurasova, V.E., and Sirotenko, I.G., "Cathode Sputtering of Single Crystalline Spheres", Zh. Eksper. Teor. Fiz., 41, 1359 (1961).

1962

1. Arifov, U.A., Flyants, N.N., and Ayukhanov, A.Kh., "On Certain Properties of Secondary Ion-Neutral-Particle Emission", Dokl. Akad. Nauk SSSR, 142, 1265 (1962).
2. Becherer, R., Gautherin, G., and Septier, A., "Effect of Magnetic Field Topography on the Properties of a Source of Duoplasmatron Type", J. Phys. Radium, 23, Suppl. No. 6, 121A (1962).
3. Bernard, R., Goutte, R., Guillaud, C., and Javelas, R., "Mechanism of Secondary Ion Emission from a Metallic Surface", 5th Int. Congr. on Electron Microscopy, Philadelphia, 29 Aug. - 5 Sept. 1962. Vol. 1 Non-Biology, S.S. Breese Jr. Ed., (New York and London: Academic Press 1962) Paper C-7.
4. Bradley, R.C., and Ruedl, E., "Ions Sputtered from Copper", J. Appl. Phys., 33, 880 (1962).
5. Carter, G., Collingon, J.S., and Leck, J.H., "Ion Sorption in the Presence of Sputtering", Proc. Phys. Soc., 79, Pt. 2, 299 (1962).
6. Castaing, R., and Slodzian, G., "Optique Corpusculaire-Premiers Essais de Microanalyse par Émission Ionique Secondaire", C.R. Acad. Sci., 255, 1893 (1962).
7. Kopitzki, K., and Stier, H.E., "Average Kinetic Energy of Particles Ejected From Metals During Cathode Sputtering", Z. Naturforsch, 17A, 346 (1962).
8. Krohn, V.E., Jr., "Emission of Negative Ions from Metal Surfaces Bombarded by Positive Cesium Ions", J. Appl. Phys., 33, 3523 (1962).
9. Panin, B.V., "Secondary-Ion Emission from Metals Under the Action of Ions with Energies Between 10 and 100 keV", Sov. Phys. JETP, 14, 1 (1962).
10. Panin, B.V., "Interaction Between Medium Energy (10-100keV) Atomic Particles and Solid Bodies (Energy Spectra of Secondary Ions)", Sov. Phys. JETP, 15, 215 (1962).
11. Ruedl, E., and Bradley, R.C., "Vaporization of Impurities in Copper, Including Those Introduced by Ion Bombardment", J. Phys. Chem. Solids, 23, 885 (1962).
12. Walther, V., and Hintenberger, H., "Positive Secondary Ion Emission from Graphite, Copper, and Gold by Bombardment with Rare-Gas Ions at Energies Between 100 and 30000 eV", Z. Naturforsch, 17A, 1034 (1962).
13. White, F.A., Sheffield, J.C., and Rouke, F.M., "Isotopic Abundance Determination of Copper by Sputtering", J. Appl. Phys., 33, 2915 (1962).

1963

1. Abroyan, I.A., and Lavrov, V.P., "Secondary Emission of Dielectrics and Semiconductors when Bombarded with Potassium Ions", Sov. Phys. Solid State, 4, 2382 (1963).
2. Anderson, G.S., Wehner, G.K., and Olin, H.J., "Temperature Dependence of Ejection Patterns in Ge Sputtering", J. Appl. Phys., 34, 3492 (1963).
3. Fluit, J.M., Rol, P.K., and Kistemaker, J., "Angular Dependent Sputtering of Copper Crystals", J. Appl. Phys., 34, 690 (1963).
4. Fogel', Ya.M., Slabospitskii, R.P., and Slavnyi, A.A., "Mass-Spectrometric Investigation of the Secondary Ionic Emission when Platinum is Bombarded by Argon Ions", Radiotechnika I Elektronika, 8, 684 (1963).
5. Haneman, D., and Chung, M.F., "Hillocks on Sputtered Ge Surfaces", J. Appl. Phys., 34, 2488 (1963).
6. Lieble, H.J., and Herzog, R.F.K., "Sputtering Ion Source for Solids", J. Appl. Phys., 34, 2893 (1963).
7. Lindhard, J., Scharff, M., and Schiøtt, H.E., "Range Concepts and Heavy Ion Ranges", Mat. Fys. Medd. Dan. Vid. Selski., 33, No. 14, 1 (1963).
8. Smith, A.J., Cambey, L.A., and Marshall, D.J., "Mass Analysis of Sputtered Particles", J. Appl. Phys., 34, 2489 (1963).
9. Walther, V., and Hintenberger, H., "Study of the Emission of Positive Secondary Ions and the Reflection of Inert Gases by Solid Surfaces", Z. Naturforsch, 18A, 843 (1963).
10. Wehner, G.K., and Stuart, R.V., "Velocity Distribution of Sputtered Atoms", CR VI Conf. Int. Phenomenes d'Ionisation dans les Gaz (Paris: S.E.R.M.A. 1963), 2, p. 49.
11. Weijsenfeld, C.H., "Average Energy and Yield of Sputtered Atoms", CR VI Conf. Int. Phenomenas d'Ionization dans les Gaz (Paris: S.E.R.M.A. 1963), 2, p. 43.
12. Wolsky, S.P., "Sputtering Mechanisms", 1963 Transactions of the Tenth Nat. Vacuum Symposium of the American Vacuum Society (New York: Macmillan 1963) p. 309.

1964

1. Anderson, G.S., and Wehner, G.K., "Temperature Dependence of Ejection Patterns in Ge, Si, InSb, and InAs Sputtering", Surf. Sci., 2, 367 (1964).
2. Fogel', Ya.M., Nadykto, B.T., Rybaiko, V.F., Slabospitskil, R.P., Korobchanskaya, I.E., and Shvachko, V.I., "A New Method for Studying Heterogeneous Catalytic Reactions", Kinetics and Catalysis, 5, 127 (1964).
3. Kirchner, F., and Benninghoven, A., "Mass Spectrometric Investigations of the Energy Distribution of Sputtered Particles", Phys. Lett., 8, 193 (1964).
4. McHugh, J.A., and Sheffield, J.C., "Secondary Positive Ion Emission from a Tantalum Surface", J. Appl. Phys., 35, 512 (1964).
5. Odintsov, D.D., "Sputtering of Single Crystals as a Function of the Direction of Incidence of the Particles", Bull. Acad. Sci. USSR, Phys. Ser., 28, 1333 (1964).

6. Slodzian, G., "A Study of a Method of Local Chemical and Isotopic Analysis by Secondary Ion Emission", Ann. Phys., 9, 591 (1964).
7. Smith, A.J., Marshall, D.J., Cambey, L.A., and Michael, J., "Mass Spectrometer for the Study of Sputtering", Vacuum, 14, 263 (1964).
8. Smith, H.P., Jr., "Effect of Collision Focusing on Monocrystalline Sputtering Yield Theory", J. Appl. Phys., 35, 2522 (1964).
9. Smith, H.P., Jr., "Comment on "Sputtering Ion Source for Solids", J. Appl. Phys., 35, 3067 (1964).
10. Sreenivasan, T., and Carter, G., "Characteristics of a Los Energy Ion Source", J. Electronics Control, 17, 159 (1964).
11. Stuart, R.V., and Wehner, G.K., "Energy Distribution of Sputtered Cu Atoms", J. Appl. Phys., 35, 1819 (1964).
12. Tawara, H., "Some Characteristics of a Duoplasmatron Ion Source", Japan. J. Appl. Phys., 3, 342 (1964).
13. Tawara, H., Suganomata, S., and Suematsu, S., "A Compact Duoplasmatron Ion Source Using a Ferrite Permanent Magnet", Nucl. Instrum. Methods, 31, 353 (1964).
14. Von Beske, H.E., "Positive Secondary Ionic Yield from 21 Elements", Z. Naturforsch, 19A, 1627 (1964).

1965

1. Benninghoven, A., "Concerning the Energy Distribution of Particles Produced in Cathode Sputtering Processes", Ann. Phys., 15, 113 (1965).
2. Charkovskii, E.F., and Ptitsyn, G.V., "The Use of the Positive Surface Ionization Effect in the Investigation of Cathode Sputtering of Metals", Zh. Tekh. Fiz., 34, 2194 (1965).
3. Cheney, K.B., and Pitkin, E.T., "Sputtering at Acute Incidence", J. Appl. Phys., 36, 3542 (1965).
4. Cooper, C.B., and Comas, J., "Angular Distribution of Sublimed and Sputtered Particles from Ag Single Crystals", J. Appl. Phys., 36, 2891 (1965).
5. Darwin, H.W., and Felenbok, P., "Data for Plasmas in Local Thermodynamic Equilibrium", (Paris: Garthier-Villars 1965).
6. Kasten, R., and Slodzian, G., "A Microanalysis Method Employing Secondary Ion Emission", Radio Engng. Electronic Phys., 10, 291 (1965).
7. Long, J.V.P., "A Theoretical Assessment of the Possibility of Selected-Area Mass-Spectrometric Analysis Using a Focused Ion Beam", Brit. J. Appl. Phys., 16, 1277 (1965).
8. McHugh, J.A., and Sheffield, J.C., "Mass Analysis of Subnanogram Quantities of Iodine", Anal. Chem., 37, 1099 (1965).
9. Nelson, R.S., "An Investigation of Thermal Spikes by Studying the High Energy Sputtering of Metals at Elevated Temperatures", Phil. Mag., 11, 291 (1965).
10. Rafal'son, A.E., "The Quadrupole Mass-Analyser and its Application to Chemical and Isotopic Analysis", Sov. Phys. Tech. Phys., 10, 1 (1965).
11. Stein, R.P., Malakhof, V., and Smith, H.P., Jr., "Angular Distributions of Argon-Sputtered Lithium", J. Appl. Phys., 36, 1504 (1965).
12. Vincent, G., and Warnecke, R.J., "Development and Construction of Ion Sources of the Duoplasmatron Type", Ann. Radioelect., 20, 101 (1965).

1966

1. Abroyan, I.A., Lavrov, V.P., and Titov, A.I., "Secondary Emission of Germanium Under Bombardment by Potassium Ions Along Various Crystallographic Directions", Sov. Phys. Solid State, 7, 2557 (1966).
2. Abroyan, I.A., Lavrov, V.P., and Fedorova, I.G., "Angular Dependence of the Secondary Emission Coefficients for a KBr Single Crystal Bombarded with Potassium", Sov. Phys. Solid State, 7, 2954 (1966).
3. Bernheim, M., and Castaing, R., "Micro-Usinage par Bombardment Ionique", Le Vide N° special A.V.I. SEM, p. 3 (1966).
4. Castaing, R., et Slodzian, G., "Microanalyse par Émission Ionique Secondaire", Advances in Mass Spectrometry, Vol. 3, W.L. Mead Ed., (London: The Institute of Petroleum 1966) p. 91.
5. Castaing, R., "Quelques Progrès Récents dans l'Application de l'Optique Corpusculaire à la Microanalyse", X-Ray Optics and Microanalysis, R. Castaing, P. Deschamps and J. Philibert Ed., (Paris: Hermann 1966) p. 48.
6. Castaing, R., and Hannequin, J.F., "Sur l'Analyse des Alliages par Émission Ionique Secondaire", X-Ray Optics and Microanalysis, R. Castaing, P. Deschamps and J. Philibert Ed., (Paris: Hermann 1966) p. 64.
7. Collins, T.L. Jr., and McHugh, J.A., "Sputtering Analyses with a Cascade Mass Spectrometer", Advances in Mass Spectrometry, Vol. 3, W.L. Mead Ed., (London: The Institute of Petroleum 1966) p. 169.
8. Colombie, N., Fagot, B., and Fert, C., "Distribution of Sputtered Atoms from Monocrystalline Germanium Targets", C.R. Acad. Sci. B, 263, 822 (1966).
9. Green, J.B., Thomas Olson, N., and Smith, H.P., Jr., "Yield and Angular Distribution of Cesium-Sputtered Molybdenum", J. Appl. Phys., 37, 4699 (1966).
10. Hennequinn, J.F., "Energy and Angular Distribution of Secondary Ion Emission I. Experimental Apparatus", Rev. Phys. Appl., 1, 273 (1966).
11. Honig, R.E., "Analysis of Solids by Mass Spectrometry", Advances in Mass Spectrometry, Vol. 3, W.L. Mead Ed., (London: The Institute of Petroleum 1966) p. 101.
12. Horn, H.R.F., and Warbichler, P., "Beobachtung von Gitterdefekten auf Einkristalloberflächen mit dem Ionenmikroskop", Electron Microscopy, R. Uyeda Ed., (Tokyo: Maruzen Co. Ltd. 1966) p. 549.
13. Kaminshy, M., "Mass Spectrometric Studies of the Species of Particles Leaving a Monocrystalline Target in a Charged or Uncharged State Under High Energy Ion Bombardment", Advances in Mass Spectrometry, W.L. Mead Ed., (London: The Institute of Petroleum 1966) p. 69.
14. Kelly, J.C., and Peterson, M.C.E., "Focusons in Potassium Chloride", Phys. Lett., 22, 295 (1966).
15. Lehmann, C. and Sigmund, P., "On the Mechanism of Sputtering", Phys. Status Solidi 16, 507 (1966).

16. McCracken, G.M., Maple, J.H.C., and Watson, H.H.H., "30 KeV Ion Bombardment Apparatus for Study of Interaction of Light Ions with Surfaces", Rev. Sci. Instrum., 37, 860 (1966).
17. Sasaki, N., Watanabe, M., Goto, T., and Someya, T., "Observation of Element Distribution in Biological Tissues Using Ion Microscope", Electron Microscopy, R. Uyeda Ed., (Tokyo: Maruzen Co., Ltd. 1966) p. 219.
18. Shvachko, V.I., Nadykto, B.T., Fogel', Ya.M., Vasyutinskii, B.M., and Kartmazov, G.N., "Application of the Method of Secondary Ion-Ion Emission to the Study of the Interaction of Oxygen with a Niobium Surface", Sov. Phys. Solid State, 7, 1572 (1966).
19. Slodzian, G., and Hennequin, J.F., "Sur l'Émission Ionique Secondaire des Métaux en Présence d'Oxygène", C.R. Acad. Sci. B, 263, 1246 (1966).
20. Tomita, H., and Takahaski, N., "Observation of Precipitation with an Ion Bombardment Type Secondary Electron Emission Microscope", Electron Microscopy, R. Uyeda Ed., (Tokyo: Maruzen Co. Ltd. 1966) p. 227.
21. Uchikawa, Y., Kojima, M., Maruse, S., and Sakaki, Y., "The Emission Microscope of the Ion Bombardment Type", Electron Microscopy, R. Uyeda Ed., (Tokyo: Maruzen Co. Ltd. 1966) p. 225.
22. Werner, H.W., "Mass Spectrometer Analysis of a Solid Surface", Philips Tech. Rev., 27, 344 (1966).

1967

1. Benninghoven, A., "Studies of The Spectrum and Initial Energies of Negative Secondary Ions", Z. Phys., 199, 141 (1967).
2. Beske, H.E., "Investigations of the Emission of Positive Secondary Ions From Solid Targets. Practicability of the Ion-Bombardment Ion-Source in Mass Spectroscopy", Z. Naturforsch, 22A, 459 (1967).
3. Brandt, W., and Laubert, R., "Unified Sputtering Theory", Nucl. Instrum. Methods, 47, 201 (1967).
4. Chapman, G.E., and Kelly, J.C., "The Angular Distribution of Atoms Sputtered from Monocrystalline Gold", Austral. J. Phys., 20, 283 (1967).
5. Comas, J., and Cooper, C.B., "Mass-Spectrometric Study of Sputtering of Single Crystals of GaAs by Low-Energy A Ions", J. Appl. Phys., 38, 2956 (1967).
6. Deines, P., Eskew, T.J., and Herzog, L.F., "New Method for the Production of Ions From Nonconductors for Analysis by Solid-Source Mass Spectrography", Appl. Spectrosc., 21, 28 (1967).
7. Drummond, I.W., and Long, J.V.P., "Scanning Ion Microscopy and Ion Beam Micromachining", Nature, 215, 950 (1967).
8. Fogel', Ya.M., "Secondary Ion Emission", Sov. Phys. Usp., 10, 17 (1967).
9. Francken, L., Art, A., and Goche, O., "Sputtering of a Gold Hemispherical Single Crystal", Phil. Mag., Ser. 8, 15, 673 (1967).
10. Gradsztajn, E., Salome, M., Yaniv, A., and Bernas, R., "Isotopic Analysis of Lithium in the Holbrook Meteorite and in Terrestial Samples with a Sputtering Ion Source Mass Spectrometer", Earth Plan. Sci. Lett., 3, 387 (1967).
11. Hulpke, E., and Schlier, C., "The Velocity Distribution of Sputtered Potassium", Z. Phys., 207, 294 (1967).
12. Kirchner, F., and Klein, H.J., "New Measurements of the Energy Distribution of Cathode Sputtered Ions and Its Significance for the Understanding of the Sputtering Process", Z. Naturforsch, 22A, 577 (1967).
13. Lejeune, C., and Prangere, F., "Study of the Variation of Pressures in an Ion Source of Duoplasmatron Type as a Function of the Discharge Parameters", C.R. Acad. Sci. B, 264, 1075 (1967).
14. Liebl, H., "Ion Microprobe Mass Analyzer", J. Appl. Phys., 38, 5277 (1967).
15. McHugh, J.A., and Sheffield, J.C., "Mass Spectrometric Determination of Beryllium at the Sub-Nanogram Level", Anal. Chem., 39, 377 (1967).
16. Renskaya, I.V., Kushnir, Yu.M., and Bordovskii, G.A., "Ion-Optical Apparatus for Producing Ion Probes", Exper. Tech., No. 1, 143 (1967).
17. Schroeer, J.M., "Excitation and Ionization of Atoms at a Surface", Bull. Am. Phys. Soc., 12, 137 (1967).
18. Valot, C., "Properties of the Ion Sources Duoplasmatron", Rev. Gen. Elect., 70, 1283 (1967).
19. Weijsenfeld, C.H., "Yield, Energy and Angular Distributions of Sputtered Atoms", Philips Res. Rep. Suppl., No. 2, 1 (1967).
20. Yurasova, Y.Ye., and Bukhanov, V.M., "Dependence of Single-Crystal Sputtering Intensity in the Directions of Dense Packing on Angle of Incidence of the Ions", Radiotekhnika I Elektronika, 12, 1853 (1967).

1968

1. Andersen, C.A., and Liebl, H.J., "Analysis by Bombardment with Chemically Reactive Ions", US Patent No. 3508045, 12 July 1968.
2. Arifov, U.A., and Aliev, A.A., "Angular and Energy Distribution of Secondary Ions as a Result of Bombarding a Target with Ions at Grazing Angles", Sov. Phys. Dokl., 13, 431 (1968).
3. Blaise, G., et Slodzian, G., "Émission Ionique Secondaire des Métaux de la Première Série de Transition", C.R. Acad. Sci. B, 266, 1525 (1968).
4. Carter, G., and Colligon, J.S., Ion Bombardment of Solids, (London: Heinmann Educational Books, Ltd., 1968) viii + 446 pp.
5. Comas, J., and Cooper, C.B., "Ejection Patterns in Low-Energy Sputtering of GaAs and GaP Crystals", J. Appl. Phys., 39, 5736 (1968).
6. Contamin, P., and Slodzian, G., "Oxygen Isotopic Concentration Gradient Determination with the Cameca Ion Mass Analyzer", Appl. Phys. Lett., 13, 416 (1968).
7. Cox, B., and Pemsler, J.P., "Diffusion of Oxygen in Growing Zirconia Films", J. Nucl. Mat., 28, 73 (1968).

8. De Wames, R.E., Hall, W.F., and Lehman, G.W., "Mass Dependence of the Angular Distribution of Charged-Particle Emission from Crystals" Transition to the Classical Limit", Phys. Rev., 174, 392 (1968).

9. Dillon, A.F., Lehrle, R.S., Robb, J.C., and Thomas, D.W., "Positive Ion Emission from Polymers under Ion Impact", Advances in Mass Spectrometry, Vol. 4, E.E. Kendrick Ed., (London: The Institute of Petroleum 1968) p. 477.

10. Dresser, M.J., "The Saha-Langmuir Equation and its Application", J. Appl. Phys., 39, 338 (1968).

11. Evdokimov, I.N., and Molchanov, V.A., "The Dependence of the Sputtering Ratio of Polycrystalline Metals on the Angle of Ion Incidence on the Target", Canad. J. Phys., 46, 779 (1968).

12. Farmery, B.W., and Thompson, M.W., "III. Energy Spectra for Copper", Phil. Mag., Ser. 8, 18, 415 (1968).

13. Formann, E., Viehböck, F.P., and Wotke, H., "The Angular Distribution of Scattered and Sputtered 40-KeV Particles on Polycrystalline Targets", Canad. J. Phys., 46, 753 (1968).

14. Gurmin, B.M., Martynenko, T.P., and Ryzhov, Yu.A., "Mechanism of the Sputtering of Solids", Fiz. Tver. Tela, 10, 411 (1968).

15. Hennequin, J.J., "Energy and Angular Distributions of the Secondary Ion II. Nature and Energy Distribution of the Secondary Ions", J. Phys., 29, 655 (1968).

16. Hennequin, J.F., "Energy and Angular Distribution of Secondary Ion Emission III. Angular Distribution and Ion Yield", J. Phys., 29, 957 (1968).

17. Hill, A.R., "Uses of Fine Focused Ion Beams with High Current Density", Nature, 218, 202 (1968).

18. Jurela, Z., and Perovic, B., "Mass and Energy Analysis of Positive Ions Emitted by Heavy Ions in the KeV Energy Region", Canad. J. Phys., 46, 773 (1968).

19. Kozlov, V.F., Pistryak, V.M., and Fogel', Ya.M., "Possibility of Application of Secondary Ion-Ion Emission in Investigation of Volume Processes in Solids", Fiz. Tver. Tela, 10, 3713 (1968).

20. Nelson, R.S., and von Jan, R., "The Role of Focusing Collisions in Sputtering", Canad. J. Phys., 46, 747 (1968).

21. Robinson, C.F., Liebl, H.J., and Andersen, C.A., "New Developments in the Ion Microprobe Mass Analyzer", Proc. 3rd National Conf. on Electron Microprobe Analysis. Chicago, IL, July 1968, Paper No. 26.

22. Rouberol, J.M., Guernet, J., Deschamps, P., Dagnot, J.P., Guyon de La Berge, J.M., and Judson, C.M., "A Secondary Ion Emission Microanalyzer", Proc. 3rd Nat. Conf. on Electron Microprobe Analysis, Chicago, IL, July 1968, Paper No. 28.

23. Rouberol, J.M., Guernet, J., Deschamps, P., Dagnot, J.P. and Guyon de la Berge, J.M., "Microanalyseur par Émission Ionique Secondaire", 5th Int. Congr. on X-Ray and Microanalysis, Tubingen, W. Germany. Sept. 1968. G. Möllenstedt and K.H. Gaukler Ed., (Berlin, Heidelberg, New York: Springer-Verlag 1969) p. 311.

24. Schulz, F., and Sizmann, R., "Sputtering Pattern Distortions on Plane and Cylindrical Collectors. Deposit Structure of Aluminium Pattern Between 100 and 560°K", Phil. Mag., Ser. 8, 18, 269 (1968).

25. Thompson, M.W., Farmery, B.W., and Newson, P.A., "I. A Mechanical Spectrometer for Analysing the Energy Distribution of Sputtered Atoms of Copper or Gold", Phil. Mag., Ser. 8, 18, 361 (1968).

26. Thompson, M.W., "II. The Energy Spectrum of Ejected Atoms During the High Energy Sputtering of Gold", Phil. Mag., Ser. 8, 18, 377 (1968).

27. Von Jan, R., and Nelson, R.S., "The Role of Focusing Collisions in Sputtering", Phil. Mag., Ser. 8, 17, 1017 (1968).

28. Werner, H.W., "Investigation of Solids by Means of an Ion-bombardment Mass Spectrometer", Developments in Applied Spectroscopy, Chicago, IL., 13-17, 239 (1968).

29. White, F.A., Mass Spectrometry in Science and Technology, (New York: John Wiley and Sons, Inc. 1968) xvi + 352 pp.

1969

1. Andersen, C.A., "Progress in Analytic Methods for the Ion Microprobe Mass Analyzer", Int. J. Mass Spectrom. Ion Phys., 2, 61 (1969).

2. Andersen, C.A., Roden, H.J., and Robinson, C.F., "Negative Ion Bombardment of Insulators to Alleviate Surface Charge up", J. Appl. Phys., 40, 3419 (1969).

3. Andersen, H.H., "The Dependence of Sputtering Efficiency on Energy and Angle of Incidence", Atomic Collision Phenomena in Solids, Brighton, Sussex, England, Sept. 1969. (Amsterdam, Netherlands: North-Holland 1970), p. 300.

4. Benninghoven, A., "The Emission of Negative Secondary Ions from Compounds with Complex Anions", Z. Naturforsch, 24A, 859 (1969).

5. Benninghoven, A., "Zum Mechanismus der Ionenbildung und Ionenemission bei der Festkörperzerstäubung", Z. Physik, 220, 159 (1969).

6. Collins, R.D., "The Use of Electron Multipliers in Mass Spectrometry", Vacuum, 19, 105 (1969).

7. Cunningham, R.L., and Ng-Yelim, J., "The Application of the Deviation Thoery to Patterns Obtained from Faceted Surfaces of Face-Centred Cubic Metals", Atomic Collision Phenomena in Solids, Brighton, Sussex, England, Sept. 1969. (Amsterdam, Netherlands: North Holand 1970) p. 290.

8. Firsov, O.B., "On the Dependence of Target Sputtering on the Angle of Incidence of Bombarding Particles", Atomic Collision Phenomena in Solids, Brighton, Sussex, England, Sept. 1969. (Amsterdam, Netherlands: North Holland 1970) p. 301.

9. Firsov, O.B., "Dependence of Sputtering of a Target on the Angle of Incidence of the Bombarding Particles", Sov. Phys. Dokl., 14, 1092 (1970).

10. Gall', R.N., "Ion-Optical System of an Energy-Focusing Mass Spectrometer for Microimpurity Analysis", Sov. Phys. Tech. Phys., 14, 263 (1969).

11. Galle, P., Blaise, G., and Slodzian, G., "Study of Distribution of Diffusible Ions in Biological Tissues Using a Secondary Ion Emission Micro-Analyzer", Proc. 4th Nat. Conf. on Electron Microprobe Analysis, Pasadena, CA. July 1969. Paper No. 36.

12. Gurmin, B.M., Ryzhov, Y.A., and Shkarban, I.I., "Angular Distribution of Atoms Sputtered from Polycrystalline Targets by Inert-Gas Ions", Bull, Acad. Sci. USSR. Phys. Ser., 33, 816 (1969).
13. Harrison, D.E., "Additional Information on 'Computer Simulation of Sputtering'", J. Appl. Phys., 40, 3870 (1969).
14. Heinrich, K.F.J., "Electron and Ion Microprobe Analysis", Record of the 10th Symposium on Electron, Ion, and Laser Beam Technology, Gaithersburg, MD, USA, May 1969. (San Francisco, CA: San Francisco Press Inc. 1969) p. 345.
15. Hennequin, J.F., Blaise, G., and Slodzian, G., "The Origin of Multi-Charged Secondary Ions, Produced by the Ionic Bombardment of a Metal", C.R. Acad. Sci B, 268, 1507 (1969).
16. Hofer, W.O., and Sizmann, R., "Sputtering Emission Patterns of Zinc-Single Crystals", Atomic Collision Phenomena in Solids, Brighton, Sussex, England, Sept. 1969. (Amsterdam, Netherlands: North Holland 1970) p. 298.
17. Joyes, P., "Theoretical Investigation of Secondary Ion Emission", J. Phys., 30, 365 (1969).
18. Jurela, Z., "The Yield of Positive and Negative Ions of Metallic and Semiconductor Targets Bombarded by Ar$^+$ Ions of 40 keV Energy", Atomic Collision Phenomena in Solids, Brighton, Sussex, England, Sept. 1969. (Amsterdam, Netherlands: North Holland 1970) p. 339.
19. Jurela, Z., "Mass and Energy Analysis of Negative Ions Emitted from Al, Mn, Co, Ta and Au Targets by 40 keV A$^+$ Ions", 9th Int. Conf. on Phenomena in Ionized Gases, Bucharest, Rumania. Sept. 1969. (Bucharest, Rumania: Editura Akademiei Republicii Socialistic Romania 1969) p. 89.
20. Lewis, R., and Cambey, A., "Imaging Properties of the Secondary Ion Emission Microanalyzer", Proc. 4th Nat. Conf. on Electron Microprobe Analysis, Pasadena, CA, July 1969. Paper No. 18.
21. MacDonald, R.J., Dennis, E., and Zwangobani, E., "Sputtering Studies with Selected Targets. A. Ejection Patterns from Diamond Type Semiconductors. B. Energy Spectra of Ions Sputtered from Cu". Atomic Collision Phenomena in Solids, Brighton, Sussex, England, Sept. 1969. (Amsterdam, Netherlands: North Holland 1970), p. 307.
22. MacDonald, R.J., "Temperature Dependence of the Sputtered Ejection Pattern from Ge (100) Surfaces", Phys. Lett., 29A, 256 (1969).
23. Nishimura, H., and Okano, J., "An Ion Microprobe Analyzer", Japan. J. Appl. Phys., 8, 1335 (1969).
24. Nobes, M.J., Colligon, J.S., and Carter, G., "The Equilibrium Topography of Sputtered Amorphous Solids", J. Mat. Sci., 4, 730 (1969).
25. Robinson, M.T., "Sputtering Experiments with 1-5 keV Ar$^+$ Ions. Displacement of Ejection Pattern Spots", J. Appl. Phys., 40, 4932 (1969).
26. Rybalko, V.F., Kolot, V.Y., and Fogel', Ya.M., "On Sputtering Probability of Secondary Tungsten Oxide Ions with Ar$^+$ Ions", Ukrayin Fiz. Zh., 14, 913 (1969).
27. Sigmund, P., "Theory of Sputtering. I. Sputtering Yield of Amorphous and Polycrystalline Targets", Phys. Rev., 184, 383 (1969).
28. Socha, A.J., "Analysis of Thin Films Utilizing Mass Spectrometric Techniques", J. Vac. Sci. Technol. 6, 901 (1969).
29. Stuart, R.V., Wehner, G.K., and Anderson, G.S., "Energy Distribution of Atoms Sputtered from Polycrystalline Metals", J. Appl. Phys., 40, 803 (1969).
30. Van Veen, A., and Fluit, J.M., "Low Energy Sputtering: Angular Distribution and Surface Roughness", Atomic Collision Phenomena in Solids, Brighton, Sussex, England, Sept. 1969. (Amsterdam, Netherlands: North Holland 1970) p. 246.
31. Van Wijngaarden, A., Reuther, E., and Bradford, J.N., "Directional Effects of Sputtering a Single Gold Crystal Under Bombardment by Heavy Ions", Canad. J. Phys., 47, 411 (1969).
32. Wells, N., and Hanley, P.R., "Inert Gas Ion Beams from a Duoplasmatron Ion Source", IEEE Trans. Nuclear Sci. ns-16, No. 3, 43 (1969)
33. Werner, H.W., "Investigation of Solids by means of an Ion-Bombardment Mass Spectrometer", Developments in Applied Spectroscopy, Vol. 7A, E.L. Grove, Ed., (New York: Plenum Press 1969), p. 239.

1970

1. Abdullaeva, M.K., and Ayukhanov, A.Kh., "Negative Sputtering of the Ions of Cu and Ag and Au Targets During Bombardment by Positive Cs$^+$ Ions", Radiotekhnika I Electronika, 15, 1263 (1970).
2. Adylov, A.A., Vekslev, V.I., and Reznik, A.K., "Secondary Emissions of Mo$^+$ Ions During Bombardment of Molybdenum with Alkali Metal Ions", Sov. Phys. Solid State, 11, 1441 (1970).
3. Adylov, A.A., Veksler, V.I., and Reznik, A.W., "Secondary Emission of W$^+$ Ions in the Bombardment of Tungsten by Ions of Alkali Metals", Dokl. Akad. Nauk Uz SSr, No1 12, 19 (1970).
4. Agranovich, V.M., Kapusta, O.I., Lebedev, S.Ya., and Semenov, L.P., "Angular Distributions of Sputtering Products of InSb Single Crystals Bombarded with Fast Argon Ions", Sov. Phys. Solid State, 11, 2280 (1970).
5. Andersen, C.A., Hinthorne, J.R., and Fredriksson, K., "Ion Microprobe Analysis of Lunar Material from Apollo 11", Proc. of the Apollo 11 Lunar Science Conf., Houston, Texas, Jan. 1970. (A.A. Levinson Ed., Vol. 1, Minerology and Petrology, New York: Pergamon Press 1970) p. 159.
6. Andersen, C.A., "Analytic Methods for the Ion Microprobe Mass Analyzer Part II", Int. J. Mass Spectrom. Ion Phys., 3, 413 (1970).
7. Bassville, Ph., and Astrue, J., "Exemples d'Utilisation de 1'Analyseur Metallographique Quantitatif Cameca", Microscopie Électronique, P. Favard Ed., Vol. 1, (Paris: Société Francaise de Microscopie Électronique 1970) p. 277.
8. Benninghoven, A., "Observing Surface Oxidation of Molybdenum with the Static Method of Secondary Ion Mass Spectroscopy", Chem. Phys. Lett., 6, 626 (1970).
9. Benninghoven, A., "Die Analyse Monomolekularer Festkörpenokerflächenshichter mit Hilf der Sekundarionenemission", Z. Phys., 230, 403 (1970).

10. Bukhanov, V.M., Odintsov, D.D., and Yurasova, V.E., "Dependence of the Sputtering Along the Dense Packing Directions on the Angle of Incidence of Ions", Fiz. Tver. Tela, 12, 2425 (1970).
11. Cuiti, P., "A Study of Ion Beams Produced by a Duoplasmatron Ion Source", Nucl. Instrum. Methods, 79, 55 (1970).
12. Dubinskii, V.E., and Lebedev, S.Ya., "Angular Distribution Characteristics of Particles Sputtered by Bombardment of Single Crystals with Ions", Fiz. Tver. Tela 12, 1906 (1970).
13. Dubinskii, V.E., and Lebedev, S.Ya., "Fine Structure in the Angular Distriubtions Obtained in the Sputtering of Single Crystals", Fiz. Tver. Tela 12, 2295 (1970).
14. Efremenkova, V.M., Bunin, I.G., Karpuzov, D.S., Pavlichenko, A.A., and Yurasova, V.E., "Surface Structure, Sputtering and Scattering of Ions from $A^{II}B^{VI}$ Single Crystals", Microscopie Électronique, P. Favard Ed., Vol, 1, (Paris: Sociéte Francaise de Microscopie Électronique 1970) p. 249.
15. Evans, C.A., Jr., and Pemsler, J.P., "Analysis of Thin Films by Ion Microrpobe Mass Spectrometry", Anal. Chem., 42, 1060 (1970).
16. Evans, C.A., Jr., "Ion Microrpobe Mass Spectrometric Determination of Oxygen in Copper", Anal. Chem., 42, 1130 (1970).
17. Fitch, R.K., Mulvey, T., Thatcher, W.J., and McIlraith, A.H., "A New Type of Ion Source", J. Phys. D, 3, 1399 (1970).
18. Galle, P., Blaise, G., and Slodzian, G., "Etude de la Distribution des Ions Diffusibles dans les Tissns au Moyen de l'Analyseur à Émission Ionique Secondaire", Microscopie Électronique, P. Favard Ed., Vol. 1, (Paris: Sociéte Francaise de Microscopie Électronique 1970) p. 489.
19. Hollerbach, J.M., "Ion Probe Mass Spectrometer: Concentrations and Diffusion Profiling", Proc. 5th Nat. Conf. on Electron Probe Analysis, New York, N.Y., July 1970, Paper No. 41.
20. Jurela, Z., "Mass Analysis of Positive and Negative Secondary Ions Emitted from NaCl and KCl Bombarded by 40 KeV Ions", Contributed papers of the 5th Yugoslav Symposium and Summer School on the Physics of Ionized Gases. Herceg-Novi, Yugoslavia, July 1970. (Ljubljana, Yugoslavia: Inst. 'J. Stefan 1970) p. 67.
21. Kapusta, O.I., Lebedev, S.Ya., and Omel'yanovskaya, N.M., "Angular and Temperature Dependences of the Secondary Emission of InSb Single Crystals Bombarded with Argon Ions", Sov. Phys. Solid State, 12, 781 (1970).
22. MacDonald, R.J., "Sputtered Atom Ejection Patterns from (100) Ge Surfaces", Phil. Mag., 21, 519 (1970).
23. MacDonald, R.J., "Sputtered Atom Ejection Patterns from Ge", Rad. Eff., 3, 131 (1970).
24. Quataert, D., and Coen-Porisini, F., "Utilization of the Ion Analyser for the Study of Oxygen Diffusion in Solids and Its Application to Zirconium", J. Nucl. Mat., 36, 20 (1970).
25. Reed, R.I., and Robertson, D.H., "Mass Spectrometry--Selected Topics", Appl. Spectrosc., 24, 175 (1970).
26. Rouberol, J.H. and Dagnot, J.P., "Adaptation of an Ion Source of the Duoplasmatron Type to the Ionic Analyser of Castaing and Slodzian", Microscopie Électronique, P. Favard Ed., Vol. 1, (Paris: Sociéte Francaise de Microscopie Électronique 1970) p. 267.
27. Rudenauer, F.G., "180° Homogeneous Field Electromagnets with Optimized Current Transmission", Nucl. Instrum. Methods, 88, 93 (1970).
28. Suurmeijer, E.P.Th.M., Boers, A.L., and Begemann, S.H.A., "A New Approach to Measure Ion Reflection and Secondary Ion Emission During Ion Bombardment of Atomically Clean and Smooth Monocrystalline Metal Surfaces", Surf. Sci., 20, 424 (1970).
29. Vasil'ev, M.A., Ivashchenko, Yu.N., and Cherepin, V.T., "Influence of Composition and Structure of Fe-C Alloys on Discharge of Positive Ions During Atomization by Ionic Bombardment", Akad. Nuak. UKSSR. Metallofiz. No. 32, 143 (1970).
30. Vasil'ev, M.A., Ivashchenko, Yu.N., and Cherepin, V.T., "Mass-Spectrometric Investigation of Ion Emission Produced During Bombardment of Materials by Argon Ions", Akad. Nauk. UKSSR. Metallofiz., No. 32, 148 (1970).
31. Vasil'ev, M.A., Ivashchenko, Yu.N., and Cherepin, V.T., "Use of an MI-1305 Mass Spectrometer to Study the Secondary Ion Emission of Solids", Instrum. & Exp. Tech., No. 2, 523 (1970).
32. Veksler, V.I., "Energy Spectra of the Products of Cathodic Sputtering in Bombardment of Metals with Light Ions", Fiz. Tver. Tela, 12, 1682 (1970).

1971

1. Abdulaeva, M.K., and Ayokhanov, A.Kh., "Negative Ion Sputtering of Cu and Ag by Cs^{+} Ion Bombardment", Bull. Acad. Sci. USSR. Phys. Ser., 35, 371 (1971).
2. Abramenkov, A.D., Slezov, V.V., Tanatarov, L.V., and Fogel', Ya.M., "Investigation of Surface Diffusion of Copper Atoms on Molybdenum by the Secondary Ion-Ion Emission Method", Sov. Phys. Solid State, 12, 2365 (1971).
3. Andersen, C.A., "Quantitative Theory of Sputtered Ion Mass Analysis", Proc. 6th Nat. Conf. on Electron Probe Analysis, Pittsburgh, Penn., July, 1971, Paper No. 8.
4. Andersen, H.H., "The Dependence of Sputtering Efficiency on Ion Energy and Angle of Incidence", Rad. Eff., 7, 179 (1971).
5. Aoki, S., Fujiwara, M., Yano, M., Hirano, T., Nakajima, Y., Kondo, T., and Tamura, H., "The Ion Microanalyzer for Routine Analysis", Proc. 6th Int. Conf. on X-Ray Optics and Microanalysis, Osaka, Japan, Sept. 1971, G. Shinoda, K. Kohra and T. Ichinokawa Ed., (Tokyo, Japan: University of Tokyo Press 1972) p. 439.
6. Arifov, U.A., Flynants, N.N., and Rakhimov, R.R., "Secondary Emission of Dielectric and Semiconductor Films Bombarded by Na and K Ions and Atoms", Bull. Acad. Sci. USSR, Phys. Ser., 35, 228 (1971).
7. Arnold, G.W., and Whan, R.E., "Preferential Etching of Ion-Bombarded GaAs", Rad. Eff., 7, 109 (1971).
8. Bayard, M., "Ion Probe", Microscope, 19, 425 (1971).
9. Benninghoven, A., and Loebach, E., "Tandem Mass Spectrometer for Secondary Ion Studies", Rev. Sci. Instrum., 42, 49 (1971).

10. Benninghoven, A., "Mass Spectrometric Analysis of Monomolecular Layers of Solids by Secondary Ion Emission", <u>Advances in Mass Spectrometry</u>, Vol. 5, A. Quayle Ed., (London: The Institute of Petroleum 1971) p. 444.

11. Benninghoven, A., "Beobachtung von Oberflächenreaktionen mit der Statischen Methode der Sekundärionen-Massenspektroskopie. I. die Methode", Surf. Sci., 28, 541 (1971).

12. Benninghoven, A., and Storp, S., "Analysis of Interfaces and Volume of Thin Films by Secondary Ion Mass Spectroscopy", Z. Angrew. Phys., 31, 31 (1971).

13. Beske, H.E., and Holybrecher, H., "A Cryopumped Ion-Bombardment Ion Source for the Trace Analysis of Solids", Int. J. Mass Spectrom. Ion Phys., 7, 111 (1971).

14. Blaise, G., and Slodzian, G., "Secondary Ion Emission of Transition Elements in Dilute Solutions of Alloys: Influence of Localized Electronic States", C.R. Acad. Sci. B, 273, 357 (1971).

15. Blanchard, B., Hilleret, N., and Monnier, J., "Analysis of Thin Silica Films by Secondary Ion Emission", Mat. Res. Bull., 6, 1283 (1971).

16. Brochard, D., and Slodzian, G., "Secondary Ion Emission of Copper-Aluminum Alloys in the Presence of Oxygen", J. Phys., 32, 185 (1971).

17. Brusilovsky, B.A., and Mochanov, V.A., "Dependence of the Anisotropy of the Secondary Ion-Electron Emission Coefficient upon Ion Energy", Rad. Eff., 8, 71 (1971).

18. Bryce, P., Richards, J., and Kelly, J.C., "The Electrostatic Deflection of Sputtered Ions by the Incident Sputtering Beam", J. Phys. C, 4, 263 (1971).

19. Bukhanov, V.M., Odintsov, D.D., and Yurasova, V.E., "Dependence of the Sputtering Along the Dense Packing Directions on the Angle of Incidence of Ions", Sov. Phys. Solid State, 12, 1937 (1971).

20. Campbell, A.B., III, "Mass Spectrometer Study of Potassium Bromide Sputtering and Ion Emission", Univ. Delaware, Newark, USA Thesis, 89 pp.

21. Campbell, A.B., and Cooper, C.B., "Mass Spectrometric Method of Detection of Negative Ions from the Target Surface During Low Energy Sputtering", J. Phys. E, 4, 876 (1971).

22. Carter, G., Colligon, J.S., and Nobes, M.J., "The Equilibrium Topography of Sputtered Amorphous Solids II", J. Mat. Sci., 6, 115 (1971).

23. Castaing, R., "Recent Progress in Secondary Ion Microanalysis", Proc. 6th Int. Conf. on X-Ray Optics and Microanalysis, Osaka, Japan, Sept. 1971. G. Shinoda, K. Kohra and T. Ichinokawa Ed. (Tokyo, Japan: University of Tokyo Press 1972) p. 399.

24. Castaing, R., and Hennequin, J.F., "Secondary Ion Emission From Solid Surfaces", <u>Advances in Mass Spectrometry</u>, Vol. 5, A. Quayle Ed., (London: The Institute of Petroleum 1971) p. 419.

25. Chandderton, L.T., Johansen, A., and Sarholt-Kristensen, L., "A New Structure in <110> Spots on Sputtered Ejection Patterns from Single Crystals of Gold", Phys. Scripta, 3, 233 (1971).

26. Cherepin, V., "Mass Spectrometric Measurements of the Secondary Ion Emission of Alloys as an Analytical Tool", <u>Advances in Mass Spectrometry</u>, Vol. 5, A. Quayle Ed., (London: The Institute of Petroleum 1971) p. 448.

27. Chida, K., Kaneko, K., Iwata, K., and Sakai, M., "Secondary Ion Emission from Metal Surface in Collision of 30 KeV Ar+ Ions", Mass Spectrosc., 19, 49 (1971).

28. Conley, D.K., "Surface Chemistry Characterization of Alumina Ceramic Substrates by Ion Microprobe Mass Analysis", Proc. 6th Nat. Conf. on Electron Probe Analysis, Pittsburgh, Penn., July, 1971. Paper No. 9.

29. Crawford, C.R., "Surface Analysis Using Simultaneous Electron and Ion Bombardment", 10th Nat. Meeting of the Society for Applied Spectroscopy, St. Louis MO, USA, Oct. 1971 (New York, USA: Soc. Applied Spectroscopy 1971) p. 70.

30. Croset, M., "A Study of Quantitative Microanalysis by Secondary Ion Emission", Revue Tech. Thomson-CSF, 3, 19 (1971).

31. DiLorenzo, J.V., and Marcus, R.B., "An Ion Microanalyzer Analysis of Impurities in Homoepitaxial n or n+ Films of GaAs", 10th Nat. Meeting of the Society for Applied Spectroscopy, St. Louis, MO., USA, Oct. 1971. (New York: Soc. Applied Spectroscopy 1971) p. 10.

32. Evans, C.A. Jr., "Analytical Applications of an Ion Microprobe Mass Spectrometer-Negative Ion Spectroscopy", <u>Advances in Mass Spectrometry</u>, Vol. 5, A. Quayle Ed., (London: The Institute of Petroleum 1971) p. 436.

33. Honig, R.E., "Selected Topics in Instrumentation--A Review", <u>Advances in Mass Spectrometry</u>, Vol. 5, A. Quayle Ed., (London: The Institute of Petroleum 1971) p. 249.

34. Joyes, P., "Alterations in the Secondary Emission of Molecular Ions from Noble Metals", J. Phys. Chem. Solids, 32, 1269 (1971).

35. Klemm, D.D., "State of Development of the Ion Microprobe for the Investigation of Solid Substances", Exp. Tech. Phys., 19, 467 (1971).

36. Leleyter, M., and Slodzian, G., "A Study of Second Order Aberrations in an Ion Microanalyser and Other Systems Used for the Filtering of Broadened Images", Revue Phys. Appl., 6, 65 (1971).

37. Liebl, H., " A Combined Ion and Electron Microprobe", <u>Advances in Mass Spectrometry</u>, Vol. 5, A. Quayle Ed., (London: The Institute of Petroleum 1971) p. 433.

38. Liebl, H., "Design of a Combined Ion and Electron Microprobe Apparatus", Int. J. Mass Spectrom. Ion Phys., 6, 401 (1971).

39. Maifet, Yu.P., and Cherepin, V.T., "Ion Mass-Spectral Microscope", Instrum. & Exp. Tech. 14, 1587 (1971).

40. Nakamura, K., Aoki, S., Tamura, H., and Doi, H., "A New Technique for Analyzing Insulating Materials by Means of the Ion Microanalyzer", Proc. 6th Int. Conf. on X-Ray Optics and Microanalysis, Osaka, Japan, Sept. 1971. G. Shinoda, K. Kohra and T. Ichinokawa Ed., (Tokyo, Japan: University of Tokyo Press 1972) p. 447.

41. Nelson, R.S., "Randomisation of Crystal Structure within Energetic Collision Cascades Revealed by the Sputtering of Au Single Crystals During Ion Bombardment", Rad. Eff., 7, 263 (1971).

42. Nicholson, J.B., "The Ion Microprobe Mass Analyser", 10th Nat. Meeting of the Society for Applied Spectroscopy, St. Louis, MO., Oct. 1971. (New York: Soc. Applied Spectroscopy 1971) p. 69.

43. Nishimura, H., Fujiwara, T., and Okanao, J., "Improvement of Detectable Limit of an Ion Probe Mass Spectrometer", Mass Spectrosc., 19, 205 (1971).
44. Nishimura, H., and Okano, J., "Isotopic Ratio of Lithium in Chondrite Measured by an Ion Probe Mass Spectrometer", Japan. J. Appl. Phys., 10, 1613 (1971).
45. Nishimura, H., Fujiwara, T., and Okano, J., "Element and Isotope Analysis with the Ion Probe Mass Spectrometer", Proc. 6th Int. Conf. on X-Ray Optics and Microanalysis, Osaka, Japan, Sept. 1971, G. Shinoda, K. Kohra and T. Ichinokawa Ed., (Tokyo, Japan: University of Tokyo Press 1972) p. 431.
46. Paletto, S., Bignon, C., Goutte, R., and Guillaud, C., "Demonstration by Velocity Analysis of a Double Origin of Secondary Ions O⁻ Emitted from a Metal Target", C.R. Acad. Sci. B, 272 1307 (1971).
47. Rouberol, J.M., Basseville, P., and Lenoir, J.P., "Recent Improvements in the Ion Analyzer and Typical Examples of Applications", Proc. 6th Int. Conf. on X-Ray Optics and Microanalysis, Osaka, Japan, Sept. 1971, G. Shinoda, K. Kohra and T. Ichinokawa Ed., (Tokyo, Japan: University of Tokyo Press 1972) p. 409.
48. Rudenauer, F.G., "Some Basic Considerations Concerning the Sensitivity of Sputter Ion Mass Spectrometers", Int. J. Mass Spectrom. Ion Phys., 6, 309 (1971).
49. Rudenauer, F.G., "Die Trennscharfe von Homogenen und Inhomogenen Magnetischen Sektorfeldern bei Optimaler Stromtransmission", Int. J. Mass Spectrom. Ion Phys., 6, 325 (1971).
50. Socha, A.J., "Analysis of Surfaces Utilizing Sputtering Ion Source Instruments", Surf. Sci., 25, 147 (1971).
51. Stärk, M., Mollenstedt, G., and Gaukler, K.H., "Mass Spectrometry of Ions Emitted from a Small Area under Electron Bombardment and Comparison with Ion Bombardment", Proc. 6th Int. Conf. on X-Ray Optics and Microanalysis, Osaka, Japan, Sept. 1971, G. Shinoda, K. Kohra and T. Ichinokawa Ed., (Tokyo, Japan: University of Tokyo Press 1972) p. 15.
52. Summers, A.J., Freeman, N.J., and Daly, N.R., "Application of an Energy Selective Detector to the Sputtering Analysis of Solid", Rev. Sci. Instrum., 42, 1353 (1971).
53. Suurmeijer, E.P.Th.M., and Boers, A.L., "Instrumentation for the Study of Ion Reflection and Secondary Ion Emission upon Ion Bombardment of Atomically Clean and Smooth Monocrystalline Metal Surfaces", J. Phys. E, 4, 663 (1971).
54. Tamura, H., Kondo, T., and Hirano, T., "The Scanning Ion Microscope and Its Application", Proc. 6th Int. Conf. on X-Ray Optics and Microanalysis, Osaka, Japan, Sept. 1971, G. Shinoda, K. Kohra and T. Ichinokawa Ed., (Tokyo, Japan: University of Tokyo Press 1972) p. 423.
55. Tamura, H., Kondo, T., and Doi, H. "Analysis of Thin Films by Ion Microprobe Mass Analyser", Advances in Mass Spectrometry, Vol. 5, A. Quayle Ed., (London: The Institute of Petroleum 1971) p. 441.
56. Tamura, H., Kondo, T., and Doi, H., "A New Secondary Ion Extractor with Pierce Electrode", Japan J. Appl. Phys., 10, 1482 (1971).
57. Vance, W., "Surface Charging of Insulators by Ion Irradiation", J. Appl. Phys., 42, 5430 (1971).
58. Wehner, G.K., and Hajicek, D.J., "Cone Formation on Metal Targets During Sputtering", J. Appl. Phys., 42, 1145 (1971).
59. Whatley, T.A., Slack, C.B., and Davidson, E., "Performance Evaluation of an Ion Microprobe", Proc. 6th Int. Conf. on X-Ray Optics and Microanalysis, Osaka, Japan, Sept. 1971, G. Shinoda, K. Kohra and T. Ichinokawa Ed., (Tokyo, Japan: University of Tokyo Press 1972) p. 417.

1972

1. Andersen, C.A., Hinthorne, J.R., Robinson, C.F., and Hosoi, K., "Microanalysis with the Ion Microprobe Mass Analyzer", Shimadzu Rev., 29, 75 (1972).
2. Andersen, C.A., and Hinthorne, J.R., "Ion Microprobe Mass Analyzer", Science, 175, 853 (1972).
3. Andersen, C.A., and Hinthorne, J.R., "CARISMA a Quantitative Correction Procedure for the Ion Microprobe Mass Analyzer", Proc. 7th Nat. Conf. on Electron Probe Analysis, San Francisco, CA, July 1972. Paper No. 39.
4. Ayukhanov, A.Kh., and Besedina, Ye.A., "The Possibility of Determining the Potential of a Surface and Structure of a Continuous Current by Bombardment with Ions of Thin Dielectric Films", Radio Eng. & Electron. Phys., 17, 1331 (1972).
5. Bach, H., "Sputtering Yields and Specific Energy-Losses of Noble Gas-Ions of 5.6 keV at SiO_2 Glass", Z. Naturforsch, 27A, 333 (1972).
6. Bach, H., "Zur Winkelabhängigkeit Abtragraten und der Spezifischen Energieverlurte von 5.6-keV-Edelgasionen an Gläsern", Int. J. Mass Spectrom. Ion Phys., 9, 247 (1972).
7. Bayard, M.A., "Ion Microprobe Analysis of Small Particles", Proc. 7th Nat. Conf. on Electron Probe Analysis, San Francisco, CA, July 1972. Paper No. 37.
8. Begemann, S.H.A., and Boers, A.L., "Surface Composition and Structure Analysis with a One-Apparatus Ion Probe Technique", Surf. Sci., 32, 607 (1972).
9. Benninghoven, A., and Mueller, A., "Secondary Ion Yields near 1 for some Chemical Compounds", Phys. Lett., 40A, 169 (1972).
10. Benninghoven, A., and Loebach, E., "Analysis of Monomolecular Layers of Solids by the Static Method of Secondary Ion Mass Spectroscopy (SIMS)", J. Radioanal. Chem., 12, 95 (1972).
11. Benninghoven, A., Loebach, E., and Treitz, N., "Simultaneous SIMS, EID and Flash-Filament Investigations of the Interaction of Gases with a Tungsten Surface", J. Vac. Sci. Technol., 9, 600 (1972).
12. Benninghoven, A., and Muller, A., "Investigation of the Surface Oxidation of Metals in the Sub-Monolayer and Monolayer Range with the Static Method of Secondary Ion Mass Spectrometry", Thin Solid Films, 12, 439 (1972).
13. Berkey, E., Sweeney, G.G., and Hickam, W.M., "Sodium Corrosion and Mass Analysis with an Ion Probe Mass Spectrometer", Nucl. Technol., 16, 263 (1972).
14. Bespalova, N.S., and Gurvich, L.G., "Computer Simulation of Ejection of Atoms from Surface Layers of a Crystal", Sov. Phys. Dokl., 17, 123 (1972).

15. Blanchard, B., Hilleret, N., and Quoirin, J.B., "Application of Ionic Microanalysis to the Determination of Boron Depth Profiles in Silicon and Silica", J. Radioanal. Chem., 12, 85 (1972).
16. Blewer, R.S., and Guthrie, J.W., "Means of Obtaining Uniform Sputtering in an Ion Microprobe", Surf. Sci., 32, 743 (1972).
17. Campbell, A.B., III, and Cooper, C.B., "Mass Spectrometric Study of Sputtering of KB by Low-Energy Ar^+ and Xe^+ Ions", J. Appl. Phys., 43, 863 (1972).
18. Catana, C., Colligon, J.S., and Carter, G., "The Equilibrium Topography of Sputtered Amorphous Solids III. Computer Simulation", J. Mat. Sci., 7, 467 (1972).
19. Chadderton, L.T., Johansen, A., Sarholt-Kristensen, L., Steenstrup, S., and Wohlenberg, T., "A Contribution to Sputtered Ejection Patterns from Collision Sequences in Atomic Cascades: Firm Evidence From Channeling Experiments", Rad. Eff., 13, 75 (1972).
20. Chapman, G.E., Farmery, B.W., Thompson, M.W., and Wilson, I.H., "The Energy Distribution of Sputtered Atoms from Gold", Rad. Eff., 13, 121 (1972).
21. Cherepin, V.T., and Maifet, Yu. P., "Ion-Electron Image Converter", Sov. Phys. Tech. Phys., 17, 766 (1972).
22. Coburn, J.W., and Kay, E., "Surface Analysis Today", Rev./Dev., 23, No. 12, 37 (1972).
23. Combasson, J.L., Bernard, J., Guernet, G., Hilleret, N., and Bruel, M., "Physical Profile Measurements in Insulating Layers Using the Ion Analyser", Ion Implantation in Semiconductors and Other Materials, B.L. Crowder Ed., (New York: Plenum Press 1972) p. 285.
24. Cowell, G.K., and Smith, H.P., Jr., "Measurement of Sputtered-Particle Velocity Spectra", J. Appl. Phys., 43, 412 (1972).
25. Croset, M., "Quantitative Analysis of Boron Profiles in Silicon Using Ion Microprobe Mass Spectrometry", J. Radioanal. Chem., 12, 69 (1972).
26. Croset, M., and Velasco, G., "Study of the Competitive Diffusion at 525°C of Nitrogen and Oxygen in Sputtered β-Tantalum Films", J. Vac. Sci. Technol., 9, 165 (1972).
27. Dennis, E., and MacDonald, R.J., "The Energy Spectra of Sputtered Ions", Rad. Eff., 13, 243 (1972).
28. Dorsey, G.A., Jr., "Anodic Oxide Hydration Measured by Ion Probe Mass Spectrometry", J. Electrochem. Soc., 119, 1227 (1972).
29. Elich, J.J.PH., Roosendaal, H.E., and Onderdelinded, D., "Precision Measurements on the Angular and Temperature Dependence of Sputtering", Rad. Eff., 14, 93 (1972).
30. Evans, C.A., Jr., "Secondary Ion Mass Analysis: A Technique for Three-Dimensional Characterization", Anal. Chem., 44, 67A (1972).
31. Evans, C.A., Jr., and Hendricks, C.D., "An Electrohydrodynamic Ion Source for the Mass Spectrometry of Liquids", Rev. Sci. Instrum., 43, 1527 (1972).
32. Feldman, C., and Satkiewica, F.G., "The Study of Amorphous and Crystalline Silicon Thin Films by Sputter-Ion Source Mass Spectrometry", Thin Solid Films, 12, 217 (1972).
33. Fogel', Ya.M., "Ion-Ion Emission-A New Tool for Mass-Spectrometric Investigations of Processes on the Surface and in the Bulk of Solids", Int. J. Mass Spectrom. Ion Phys., 9, 109 (1972).
34. Furukawa, S., and Ishiwara, H., "Range Distribution Theory Based on Energy Distribution of Implanted Ions", J. Appl. Phys., 43, 1268 (1972).
35. Guthrie, J.W., and Blewer, R.S., "Improved 'Tuning' of Ion Microprobe Using Scandium Thin Film Target", Rev. Sci. Instrum., 43, 654 (1972).
36. Habraken, L., Leroy, V., and Servais, J.P., "Possibilities of the Ion Microprobe in Surface Analysis", Electron and Ion Beam Science and Technology 5th Int. Conf., Houston, Tex, USA, May 1972. (Princeton, N.J., USA: Electrochemical Soc. Inc. 1972) p. 196.
37. Hernandez, R., Lanusse, P., Slodzian, G., and Vidal, G., "Mass Spectrography with Secondary Ion Emission Source", Rech. Aerosp., No. 6, 313 (1972).
38. Hofker, W.K., Werner, H.W., Oostoek, D.P., and de Grefte, H.A.M., "Experimental Analysis of Concentration Profiles of Boron Implanted in Silicon", Ion Implantation in Semiconductors and Other Materials, B.L. Crowder Ed., (New York: Plenum Press 1972) p. 133.
39. Huber, A.M., and Moulin, M., "Use of the Ion Microanalyzer for the Characterization of Bulk and Epitaxial Silicon and Gallium Arsenide", J. Radioanal. Chem., 12, 75 (1972).
40. Huber, W.K., Selhofer, H., and Benninghoven, A., "An Analytical System for Secondary Ion Mass Spectrometry in Ultra High Vacuum", J. Vacuum Sci. Technol., 9, 482 (1972).
41. Huber, W.K., and Lobach, E., "Analysis of Stainless Steel Surfaces by Secondary Ion Mass Spectroscopy (SIMS)", Vacuum, 22, 605 (1972).
42. Hurley, R.E., "Ion-Beam Technology", Stud. Q. J. Inst. Electr. Eng., 42, 114 (1972).
43. Ishitani, T., Shimizu, R., and Murata, K., "Monte Carlo Simulation on the Behavior of Energetic Ions in Polyatomic Targets", Phys. Status Solidi B, 50, 681 (1972).
44. Joyes, P., and Toulouse, G., "Thoery of the Ionization Probability for an Atom Crossing a Metal-Vacuum Surface", Phys. Lett. 39A, 267 (1972).
45. Joyes, P., and Leleyter, M., "On the Secondary Emission of Molecular Li^+ Ions from a Lithium Target", C.R. Acad. Sci. B, 274, 751 (1972).
46. Joyes, P., "Influence of Asymmetrical Correlations in the Secondary Emission of Solid Compounds", J. Phys. C, 5, 2192 (1972).
47. Jurela, Z., "Comparison of Secondary Ion Yields from Conducting, Semiconducting and Nonconducting Targets Bombarded with 40 KeV Argon Ions", Rad. Eff., 13, 167 (1972).
48. Jurela, Z., "Energy Distribution and Mean Energy of Secondary Ions from Polycrystalline Targets", 6th Yugoslav Symposium on Physics of Ionized Gases, Split, Yugoslavia, July 1972 (Belgrade, Yugoslavia: Inst. of Phys. 1972) p. 115.
49. Krautle, H., and Kalbitzer, "Ion Implanted Silicon-Metal Systems $Si_{1-x}M_x$", Ion Implantation in Semiconductors and Other Materials, B.L. Crowder Ed., (New York: Plenum Press 1972) p. 585.
50. Krohn, V.E., and Ringo, G.R., "Secondary-Ion Collection System for an Ion Microprobe Analyzer of High Mass Resolution", Rev. Sci. Instrum., 43, 1771 (1972).
51. Kushner, R.A., McCaughan, D.V., and Murphy, V.T., "Ion Mobilization by Ion Bombardment", Proc. 7th Nat. Conf. on Electron Probe Analysis, San Francisco, CA, July 1972. Paper No. 29.

52. Liebl, H., "Ion Microprobe Analysers", Messtecknik, 80, 358 (1972).
53. Liebl, H., "A Coaxial Combined Electrostatic Objective and Anode Lens for Microprobe Mass Analysers", Vacuum, 22, 619 (1972).
54. Liebl, H., and Iwanaga, M., "Ion Microprobe Mass Analyzer", Shimadzu Rev., 29, 83 (1972).
55. Maifet, Yu,P., and Cherepin, V.T,, "Ionic Mass Spectroscope (and Metallurgical Applications)", Metallofizika, Kiev, 40, 109 (1972).
56. Maul, J., Schulz, F., and Wittmaack, K., "Determination of Implantation Profiles in Solids by Secondary Ion Mass Spectrometry", Phys. Lett., 41A, 177 (1972).
57. McHugh, J.A., and Stevens, J.F., "Elemental Analysis of Single Micrometer Size Airborne Particles by Ion Microprobe Mass Spectrometry", Anal. Chem., 44, 2187 (1972).
58. Monnier, J., Hilleret, H., Ligeon, E., and Quoirin, J.B., "The Use of Secondary Ionic Emission and Nuclear Reations to Determine the Parameters in the Manufacture of a Planar Transistor", J. Radioanal. Chem., 12, 353 (1972).
59. Morabito, J.M., Minetti, R.H., and Lewis, R.L., "Secondary Ion Emission and Auger Spectroscopy for the Surface and In-Depth Analysis of Sputtered Tantalum Thin Films", Proc. 7th Nat. Conf. on Electron Probe Analysis, San Francisco, CA, July 1972. Paper No. 38.
60. Morabito, J.M., and Tsai, J.C., "In-Depth Profiles of Phosphorus Ion-Implanted Silicon by Auger Spectroscopy and Secondary Ion Emission", Surf. Sci., 33, 422 (1972).
61. Nakamura, K., Aoki, S., Nakajima, Y., Doi, H., and Tamura, H., "A New Analytical Technique for Insulating Materials by Means of an Ion Microanalyzer", Mass Spectrosc., 20, 1 (1972).
62. Pawel, R.E., Pemsler, J.P., and Evans, C.A., Jr., "Impurity Distributions in Anodic Films on Tantalum", J. Electrochem. Soc., 119, 24 (1972).
63. Perron, C., and Baril, M., "A Simple Cs$^+$ Ion Source for Ion Sputtering Studies", Revue Phys. Appl., 7, 21 (1972).
64. Poole, D.M., "Identification of Copper Precipitation in Single Crystal Silicon Using the Cameca Ion Analyzer", J. Mat. Sci., 7, 1348 (1972).
65. Rouberol, J.M., Basserville, Ph., and Lenoir, J.P., "Recent Improvements of the Ion Analyzer and Typical Examples", J. Radioanal. Chem., 12, 59 (1972).
66. Rudenauer, F.G., "A Comparison Between Quadrupole and Magnetic Spectrometers for Use in SIM", Vacuum, 22, 609 (1972).
67. Schroeer, J.M., "Quantitative Analysis and the Yield of Ions in a Mass Spectrometer with Sputter Ion Source", Vacuum, 22, 603 (1972).
68. Sigmund, P., "Collision Theory of Displacement Damage, Ion Ranges, and Sputtering", Revue Roum. Phys., 17, 823 (1972).
69. Teodorescu, I.A., and Vasiliu, F., "Influence of the Incidence Angle on Iron and Copper Surface Microtopography Induced bye Ion Bombardment", Rad. Eff. 15, 101 (1972).
70. Tousimis, A.J., "Secondary Ion Microanalysis of Biological Tissues", Proc. 7th Nat. Conf. on Electron Probe Analysis, San Francisco, CA, July 1972. Paper No. 45.
71. Tousimis, A.J., "Mineral Localization During Bone Formation: Secondary Ion and Electron Probe Microanalyses", Proc. 30th Ann. Meeting Electron Microscopy Soc. of America, Los Angeles, CA, Aug. 1972. C. J. Arceneaux Ed., (Baton Rouge, Louisiana: Claitor's Publishing Division 1972) p. 20.
72. Tsai, J.C.C., Morabito, J.M., and Lewis, R.K., "Arsenic Implanted and Implanted-Diffused Profiles in Silicon Using Secondary Ion Emission and Differential Resistance", Ion Implantation in Semiconductors and other Materials, B.L. Crowder Ed., (New York: Plenum Press 1972) p. 87.
73. Ueda, Y., and Okano, J., "Sputtering Mass Spectrometer with Cesium Primary Ion Source", Mass Spectrosc., 20, 185 (1972).
74. Werner, H.W., "Instrumental Aspects of Secondary Ion Mass Spectrometry and Secondary Ion Imaging Mass Spectrometry", Vacuum, 22, 613 (1972).
75. Werner, H.W., de Goefte, H.A.M., and Berg, J.V.D., "The Measurement of Small Ion Currents with the Aid of Photo Multipliers", Int. J. Mass Spectrom. Ion Phys., 8, 459 (1972).
76. Whatley, T.A., Slack, C.B., Davidson, E., and Iwanaga, M,, "Performance Evaluation of an Ion Microprobe", Shimadzu Rev., 29, 67 (1972).
77. Wittmaack, K., Maul, J., and Schulz, F., "Energy Dependence and Annealing Behavior of Boron Range Distribution in Silicon", Ion Implantation in Semiconductors and Other Materials, B.L. Crowder Ed., (New York: Plenum Press 1972) p. 119.

1973

1. Abdullayeva, M.K., and Ayukhanov, A.K,, "Determination of the Negative Ion Yield of Copper Sputtered by Cesium Ions", Rad. Eff., 19, 225 (1973).
2. Aithen, D., Goodhew, P.J., and Waldron, N.B., "Helium Bubble Formation and Migration in Niobium", Nature, 244, 15 (1973).
3. Andersen, C.A., and Hinthorne, J.R., "Thermodynamic Approach to the Quantitative Interpretation of Sputtered Ion Mass Spectra", Anal. Chem., 45, 1421 (1973).
4. Arifov, U.A., Gruich, D.D., Ermakov, G.E., Parilis, E.S., Turayev, N,Y., and Umarov, F.F., "Accomodation Coefficients for Low-Energy Ions on Metal Surfaces", Rad. Eff., 19, 219 (1973).
5. Bakale, D.K., Colby, B.M., Evans, C.A, Jr,, and Woodhouse, J.B., "Reduction of Spectral Interferences in Ion Probe Mass Spectrometry", Proc. 8th Nat. Conf. on Electron Probe Analysis, New Orleans, Louisiana, August 1973, Paper No. 7.
6. Barber, D.J., Frank, F.C., Moss, M., Steeds, J.W., and Tsong, I.S.T., "Prediction of Ion-Bombarded Surface Topographies Using Frank's Kinematic Theory of Crystal Dissolution", J, Mat. Sci,, 8, 1030 (1973).
7. Bayard, M., and McCrone, W.C., "Inter-Element Effects in the Ion Probe", Proc. 8th Nat. Conf. on Electron Probe Analysis, New Orlenas, Louisiana, Aug. 1973, Paper No. 11.
8. Benninghoven, A., "New Developments in the Surface Analysis of Solids", Appl. Phys., 1, 3 (1973).
9. Benninghoven, A, and Storp, S., "Study of Silicon-Oxygen Interaction with the Statical Method of Secondary Ion Mass Spectroscopy (SIMS)", Appl. Phys, Lett., 22, 170 (1973).

10. Benninghoven, A., "Surface Investigation of Solids by the Statical Method of Secondary Ion Mass Spectroscopy (SIMS)", Surf. Sci., 35, 427 (1973).
11. Benninghoven, A., Loebach, E., Plog, C,, and Treitz, N., "Simultaneous SIMS and EID Investigation on the Interaction of Oxygen with a W(100) Surface", Surf. Sci,, 39, 397 (1973).
12. Benninghoven, A., and Muller, A., "Investigation of Surface Reactions by the Static Method of Secondary Ion Mass Spectrometry; II. The Oxidation of Chromium in the Monolayer Range", Surf. Sci., 39, 416 (1973).
13. Bernheim, M., Blaise, G., and Slodzian, G., "Sur la Formation Retardée a l'Extérieur d'une Cible Soumise à un Bombardement Ionique", Int. J. Mass Spectrom. Ion Phys., 10, 293 (1973).
14. Bernheim, M., and Slodzian, G., "Effect of Oxygen on the Sputtering of Aluminium Targets Bombarded with Argon Ions", Int. J. Mass Spectrom. Ion. Phys., 12, 93 (1973).
15. Bernheim, M., "Influence of Channelling on Secondary Ion Emission Yields", Rad. Eff., 18, 231 (1973).
16. Bernheim, M., and Slodzian, G., "Influence de la Chimisorption de l'Oxygène et l'Azote sur l'Émission Ionique Seconaire d'Échantillons Monocristallins de Nickel et d'Alliage Nickel-Chrome", Surf. Sci., 40, 169 (1973).
17. Bernheim, M., Roques-Carmes, C., and Slodzian, G., "Influence of Directional Effects on Quantitative Analysis by Secondary Ion Emission", C.R. Acad. Sci. B, 277, 643 (1973).
18. Bhattacharya, R.S., and Karmohapatro, S.B., "Libration of Positive Ions From Silver Single Crystals under Heavy-Ion Bombardment", Nucl. Instrum. Methods, 109, 191 (1973).
19. Bibik, V.F., Borziak, P.G., Yatsenko, A.F., Nakhodkin, N.G. and Zykov, G.A., "Localization and Composition of Impurity Clusters in Silicon and Their Influences on its Emission Properties", Phys. Status Solidi A, 16, 151 (1973).
20. Blaise, G., and Slodzian, G., "Distributions Energetiques des Ions Secondaires", Rev. Phys. Appl., 8, 105 (1973).
21. Blaise, G., and Slodzian, G., "Effets Comparés de l'Oxygène sur l'Émission Ionique et le Potentiel de Surface des Métaus", Surf. Sci., 40, 708 (1973).
22. Blaise, G., "Seondary Ion Emission of Alloys in Relations with Their Electronic Structure", Rad. Eff., 18, 235 (1973).
23. Blaise, G., et Slodzian, G., "Influence des Processus d'Échange Électronique Atome-Métal sur la Production des Ions Secondaires Lents", Rev. Phys. Appl., 8, 247 (1973).
24. Castaing, R., "Secondary Ion Microanalysis - Crystalline and Temperature Effects", Proc. 8th Nat. Conf. on Electron Probe Analysis, New Orleans, Louisiana, Aug. 1973, Paper No. 1.
25. Colby, B.N., and Evans, C.A. Jr., "Spectral Interferences in Secondary Ion Mass Spectrometry", Appl. Spectrosc., 27, 274 (1973).
26. Colby, J.W., "Failure Analysis Using the Ion Microprobe", Proc. 11th Ann. Reliability Phys. Conf., Las Vegas, Nev., April 1973. (New York: IEEE 1973) p. 194.
27. Colby, J.W., "Application of the Ion Microprobe to Semiconductor Problems", Proc. 8th Nat. Conf. on Electron Probe Analysis, New Orleans, Louisiana, Aug. 1973, Paper No. 6
28. Devant, G., "New Results Obtained with a Surface Analysis Technique Secondary Ion Mass Spectrometry", Vide, 28, 204 (1973).
29. Dobrott, R.D., Schwettmann, F.N., and Prince, J.L., "Determination of Ion-Implanted Dopant Distribution in Semiconductors by Ion Microanalysis", Proc. 8th Nat. Conf. on Electron Probe Analysis, New Orleans, Louisiana, Aug. 1973, Paper No. 10.
30. Evans, C.A., Jr., "Secondary Ion Mass Spectrometry - The Ion Probe", (Tutorial Session), Proc. 8th National Conf. on Electron Probe Analysis, New Orleans, Louisiana, Aug. 1973, p. 29.
31. Evans, C.A., Jr., Colby, B.N., and Kearns, G.L., "Workshop on Surface Analysis and Secondary Ion Mass Analysis", Anal. Chem., 45, 398A (1973).
32. Evans, C.A., Jr., "Ion Probe Mass Spectrometry: Overview", Thin Solid Films, 19, 11 (1973).
33. Gentry, R.V., Cristy, S.S., McLanughlin, J.F., and McHugh, J.A., "Ion Microprobe Confirmation of Pb Isotope Ratios and Search for Isomer Precursors in Polonium Radichaloes", Nature, 244, 282 (1973).
34. Gerber, R.M., and Dzimianski, J.W., "Use of an Ion Microprobe in Semiconductor Failure Analysis", J. Vac. Sci. Technol., 10, 1072 (1973).
35. Harrison, D. Jr., Moore, W.L. Jr., and Holcombe, H.T., "Computer Simulation of Sputtering", Rad. Eff., 17, 167 (1973).
36. Heinrich, K.F.J., and Myklebust, R.L., "Characterization of Layered Materials with the Ion Microprobe", Proc. 8th Nat. Conf. on Electron Probe Analysis, New Orleans, Louisiana, Aug. 1973, Paper No. 4.
37. Hernandez, R., Vidal, G., and Lanusse, P., "Surface Chemical Analysis by Secondary Ion Mass Spectrography", Vide, 28, 58 (1973).
38. Hernandez, R., Vidal, G., Lanusse, P., and Slodzian, G., "Surface Analysis of Ion Implantations by Secondary Emission Mass Spectrography", Mem. Sci. Rev. Metall., 70, 47 (1973).
39. Hinthorne, J.R., and Andersen, C.A., "Geological Applications of the Ion Microrpobe Mass Analyzer", Proc. 8th Nat. Conf. on Electron Probe Analysis, New Orleans, Louisiana, Aug. 1973, Paper No. 9.
40. Hofker, W.K., Werner, H.W., Oosthoek, D.P., and de Grefte, H.A.M., "Influence of Annealing on the Concentration Profiles of Boron Implantations in Silicon", Appl. Phys., 2, 265 (1973).
41. Hofker, W.K., Werner, H.W., Oosthoek, D.P., and de Grefte, H.A.M., "Profiles of Boron Implantations in Silicon Measured by Secondary Ion Mass Spectrometry", Rad. Eff., 17, 83 (1973).
42. Ishitani, T., and Shimizu, R., "An Ion Beam Apparatus in the Range of KeV-Energies", Japan. J. Appl. Phys., 12, 926 (1973).
43. Johnson, C.E., "Application of Electron and Ion Microprobe Techniques to the Study of Nuclear Fuels", Proc. 8th National Conf. on Electron Probe Analysis, New Orleans, Louisiana, Aug. 1973, Paper No. 68.
44. Joyes, P., "Theoretical Models in Secondary Ionic Emission", Rad, Eff., 19, 235 (1973).
45. Jurela, Z., "The Application of Nonequilibrium Surface Ionization to the Emission of Secondary Ions", Int. J. Mass Spectrom. Ion Phys., 12, 33 (1973).
46. Kachare, A.H., Spitzer, W.G., Kahan, A., Euler, F.K. and Whatley, T.A., "Ion-Implanted Nitrogen in Gallium Arsenide", J. Appl. Phys., 44, 4393 (1973).

47. Kusao, K., Nakamura, N., and Konishi, F., "Study of Properties of the Secondary Ions by an Ion Bombardment Mass Spectrograph", Mass Spectrosc., 21, 53 (1973).
48. Lane, W.C. and Yew, N.C., "Ion Analysis in the SEM", Scanning Electron Microscopy, Vol. 1, Om Johari and I. Corvin Ed., (Chicago, IL: ITT Research Institute 1973) p, 81.
49. Laurent, R., and Slodzian, G., "Influence of Temperature on the Secondary Ion Emission of a Monocrystalline Aluminium Target", Rad. Eff., 19, 181 (1973).
50. Leleyter, M., and Joyes, P., "Secondary Emission of Molecular Ions from Light-Element Targets", Rad. Eff., 18, 105 (1973),
51. Lewis, R.K., Morabito, J.M., and Tsai, J.C.C., "Primary Oxygen Ion Implantation Effects on Depth Profiles by Secondary Ion Emission Mass Spectrometry", Appl. Phys. Lett., 23, 260 (1973).
52. Liebl, H., "Microbeam Probe Apparatus," U.S. Patent No. 358970, May 10, 1973,
53. Litovchenko, V.G., Marchenko, R.I., and Romanova, G.F., "Application of Secondary Ion Emission Technique for the Analysis of Si-SiO$_2$ Structures", Poluprovodn. Tekh. & Mikroelektron, 11, 20 (1973).
54. Lovering, J.F., "Ion Microprobe Mass Analyser (IMMA) Ultimate Weapon for the Geochemist?", Comments Earth Sci. Geophys., 3, 153 (1973).
55. Mayer, J.W., and Turos, A., "Comparison of Surface Layer Analysis Techniques", Thin Solid Films, 19, 1 (1973).
56. McCaughan, D.V., Sloane, R.H., and Geddes, J., "An Apparatus for Study of Secondary Ions from Ion Bombardment of a Metal Surface", Rev. Sci. Instrum., 44, 605 (1973).
57. Miyagawa, S., "Energy Spectrum of Na$^+$ Ions Sputtered from NaCl Crystals", J. Appl. Phys., 44, 5617 (1973).
58. Morabito, J.M., "Three-Dimensional Elemental Analysis with Auger Electron Spectroscopy and Secondary Ion Mass Spectrometry", J. Electrochem. Soc., 121, 110C (1973).
59. Morabito, J.M., and Rand, M.J., "An Investigation of Three-Component Diffusion (Platinum, Phosphorus, Silicon) by Sputtering Auger and Secondary Ion Emission Techniques", Proc. 8th Nat. Conf. on Electron Probe Analysis, New Orleans, Louisiana, Aug. 1973, Paper No. 8.
60. Morabito, J.M., and Lewis, R.K., "Secondary Ion Emission for Surface and In-Depth Analysis of Tantalum Thin Films", Anal. Chem., 45, 869 (1973).
61. Muller, A., and Benninghoven, A., "Investigation of Surface Reactions by the Static Method of Secondary Ion Mass Spectrometry", Surf. Sci., 39, 427 (1973).
62. Nelson, R.S., and Mazey, D.J., "Surface Damage and Topography Changes Produced During Sputtering", Rad. Eff., 18, 127 (1973).
63. Paletto, S., Perdrix, M., Goutte, R., and Guilland, G., "Study of the Mechanism of the Negative Secondary Ionic Emission by Selective Superficial Oxidation and adsorption", Surf. Sci., 35, 473 (1973).
64. Pichlmayer, F., und Rudenauer, F.G., "Uber die Dynamische Empfindlichkeit von Quadrupol - Massenspektrometern", Vakuum-Technik, 22, 1 (1973)
65. Potosky, J.C., and Wittry, D.B., "Study of a Duoplasmatron With a Quadrupole Mass Spectrometer", Proc. 8th Nat. Conf. on Electron Probe Analysis, New Orleans, Louisiana, Aug. 1973, Paper No. 2.
66. Remond, G., "Exemples d'Edentification et de Localization des Elements Entraces dans des mineraux. Liminescents (Cassiterites) a l'Aide de l'Analyseus Ionique", Bull. Soc. fr. Minearl Cristallogr., 96, 183 (1973)
67. Rudenauer, F.G., "A Comparison Between Quadrupole and Magnetic Mass Spectrometers for Use in SIM", Vacuum, 22, 609 (1973).
68. Schroeer, J.M., Rhodin, T.N., and Bradley, R.C., "A Quantum-Mechanical Model for the Ionization and Excitation of Atoms during Sputtering", Surf. Sci., 34, 571 (1973).
69. Schroeer, J.M., "Calculation from First Principles of the Yield of Ions and Excited Neutral Atoms Sputtered from Metal Surfaces", Surf. Sci., 35, 485 (1973).
70. Schubert, R., and Tracy, J.C., "A Simple, Inexpensive SIMS Apparatus", Rev. Sci. Instrum., 44, 487 (1973).
71. Schulz, F., Wittmaack, K., and Maul, J., "Implications in the Use of Secondary Ion Mass Spectrometry to Investigate Impurity Concentration Profiles in Solids", Rad. Eff., 18, 211 (1973).
72. Schwarz, G., Trapp, M., Schimko, R., Butzke, G., and Rogge, K., "Concentration Profiles of Implanted Boron Ions in Silicon from Measurements with the Ion Microprobe", Phys. Status Solidi A, 17, 653 (1973).
73. Sigmund, P., "A Mechanism of Surface Micro-Roughening by Ion Bombardment", J. Mat. Sci., 8, 1545 (1973).
74. Sroubek, Z., "Measurement of Depth Profiles and Surface Concentrations of Impurities Using the SIMS Method", Merici Systemy a Jejich Pouziti EMISCON 73, Brno, Czechoslovakia, Oct. 1973, (Brno, Czechoslovakia: CSTV House of Technics 1974) p, 311.
75. Sroubek, Z., "Velocity Filtering for Secondary Ion Quadrupole Mass Spectrometer", Rev. Sci. Instrum., 44, 1403 (1973).
76. Stomrs, H.A., "Relative Secondary Ion Yeilds as Functions of Sputter Depth in Stainless Steel", The Pittsburgh Conference on Analytical Chemistry and Applied Spectroscopy, Cleveland, March, 1973, Paper No. 134.
77. Storms, H.A., and Tichy, W., "Probing Concentration Zero", Chemistry, 46, No. 3, 6 (1973).
78. Takagi, S., and Yamaguchi, G., "Characterization of Ceramics with the Applied Ion Probe Mass Analyzer", Yogyo-Kyokai-Shi, 81, 459 (1973).
79. Tsong, I.S.T., and Barber, D.J., "Review: Sputtering Mechanisms for Amorphous and Polycrystalline Solids", J. Mat. Sci., 8, 123 (1973).
80. Vasilev, M.A., Ivashchenko, Yu.I., and Cherepin, V.T., "Mass-Spectrographic Study of Secondary Ion Emission in Metallic Alloys", Metallofizika, 45, 91 (1973).
81. Werner, H.W., "Profiles of Boron Implantations in Silicon Measured by Secondary Ion Mass Spectrometry", Rad. Eff., 17, 83 (1973).
82. Werner, H.W., De Grefte, H.A.M., and Van Den Berg, J., "Application of Characteristic Secondary Ion Mass Spectra to a Depth Analysis of Copper Oxide on Copper", Rad. Eff., 18, 269 (1973).

83. Werner, H.W., "Influence of Annealing on the Concentration Profiles of Boron Implantations in Silicon", Appl. Phys., $\underline{2}$, 265 (1973).
84. Werner, H.W., and de Grefte, H.A.M., "Investigation of Surface Layers by SIMS and SIIMS", Surf. Sci., $\underline{35}$, 458 (1973).
85. Wilson, I.H., "The Topography of Sputtered Semiconductors", Rad. Eff., $\underline{18}$, 95 (1973).
86. Wittmaack, K., Maul, J., and Schulz, F.A., " A Low Background Secondary Ion Mass Spectrometer with Quadrupole Analyser", Int. J. Mass Spectrom. Ion Phys., $\underline{11}$, 23 (1973).
87. Yurasova, V.E., Sysoev, A.A., Samsonov, G.A., Bukhanov, V.M., Nevzorova, L.N., and Shelyakin, L.B., "Spatial and Energy Distributions of Secondary Ions Produced by Ion Bombardment of Single Crystals", Rad. Eff., $\underline{20}$, 89 (1973).

1974

1. Akkerman, A.F., and Akkerman, S.A., "Calculation of the Spatial Distribution of Defects and of the Profiles of Implanted Atoms in Silicon Irradiated with Boron Ions up to 100 KeV Energy", Sov. Phys. Semicond., $\underline{8}$, 629 (1974).
2. Andersen, C.A., "A Critical Discussion of the Local Thermal Equilibrium Model for the Quantitative Correction of Sputtered Ion Intensities", (Workshop), Proc. SIMS and IMMA, Gaithersburg, MD, USA, Sept. 1974, (Washington, D.C.: Nat. Bureau Standards 1975) p. 79.
3. Auwerter, M., "The Analysis of Solid Surfaces and Thin Films by Secondary Ion Mass Spectrometry and Auger Electron Spectroscopy", Vac. News, $\underline{5}$, 3 (1974).
4. Bach, H., Kitzmann, I., and Schroder, H., "Sputtering Yields and Specific Energy Losses of Ar^+ Ions with Energies From 5 to 30 KeV at SiO_2", Rad. Eff., $\underline{21}$, 31 (1974).
5. Banner, A.E., and Stimpson, B.P., "A Combined Ion Probe/Spark Source Analysis System", Vacuum, $\underline{24}$, 511 (1974).
6. Barber, D.J., "The Sputtering of Solids and the Creation of Surface Microstructure", Vacuum, $\underline{24}$, 469 (1974).
7. Benninghoven, A., Plog, C., and Treitz, N., "Measurements of Relative Secondary Ion Yields from Oxidized Tungsten (100) under Bombardment by Ions with Different Masses and Energies", Int. J. Mass Spectrom. Ion Phys., $\underline{13}$, 415 (1974).
8. Benninghoven, A., and Wiedmann, L., "Investigation of Surface Reactions by the Static Method of Secondary Ion Mass Spectrometry: IV. The Oxidation of Magnesium, Strontium, and Barium in the Monolayer Range", Surf. Sci., $\underline{41}$, 483 (1974).
9. Bernheim, M., and Slodzian, G., "Une Tentative Pour Supprimer les Effets de Reseau en Émission Ionique Secondaire et Ameliorer l'Analyse Quantitative", Trans. 7th Int. Conf. on X-Ray Optics and Microanalysis, Moskow-Kiev, July 1974, X-Ray Optics and Microanalysis, I. Borovsky and N. Komyak Ed., (Leningrad, USSR: Mashinostrocnie 1976) p. 254.
10. Blaise, G., and Slodzian, G., "Evolution of the Secondary Ion Yield of Alloys with the Nature of Solute Atoms. I. Experimental Results", J. Phys., $\underline{35}$, 237 (1974).
11. Blaise, G., and Slodzian, G., "Evolution of the Secondary Ion Yield of Alloys with the Nature of Solute Atoms. II. Interpretation", J. Phys., $\underline{35}$, 243 (1974).
12. Blattner, R.J., Baker, J., and Evans, C.A. Jr., "Simple Ion Probe Attachment for Existing Mass Spectrometers", Anal. Chem., $\underline{46}$, 2171 (1974).
13. Blood, P., Dearnaley, G., and Wilkins, M.A., "The Depth Distribution of Phosphorus Ions Implanted Into Silion Crystals", Rad. Eff., $\underline{21}$, 245 (1974).
14. Bokharey, S.Z., "A SIMS Apparatus for the Study of Carbon Monoxide Absorbed on Tungsten", Vacuum, $\underline{24}$, 519 (1974).
15. Bradley, J.G., Jerome, D.Y., and Evans, C.A., "A Comparison of Mass Spectra from Three Ion Probes", (Workshop), Proc. SIMS and IMMA, Gaithersburg, MD., USA, Sept. 1974, (Washington, D.C.: Nat. Bureau Standards 1975) p. 69.
16. Brongersma, H.H., Meijer, F., and Werner, H.W., "Surface Analysis, Methods of Studying the Outer Atomic Layers of Solids", Philips Technical Review, $\underline{34}$, 357 (1974).
17. Buhl, R., Huber, W.K., and Lobach, E., "The Combination of SIMS and AES for the Analysis of Thin Films", Japan. J. Appl. Phys., Suppl. 2, Pt. 2, 665 (1974).
18. Buhl, R., Huber, W.K., and Lobach, E., "Study of Surface Processes on Copper-Beryllium by Combined Secondary Ion Mass Spectrometry and Auger Electron Spectroscopy", Japan. J. Appl. Phys., Suppl. 2, Pt. 2, 807 (1974).
19. Burkhardt, F., Mertens, A., and Wagner, C., "Concentration Profiles of Implanted Phosphorus in Silicon", Phys. Status Solidi A, $\underline{22}$, K45 (1974).
20. Castaing, R., Blaise, G., and Quettier, R., "Sur les Possibilities d'Application de l'Ionisation Thermique a l'Analyse en Profondeur", Trans. 7th Int. Conf. on X-Ray Optics and Microanalysis, Moscow-Kiev, July 1974. X-Ray Optics and Microanalysis, I. Borovsky and N. Komyak Ed., (Leningrad, USSR: Mashinostrocnie 1976) p. 247.
21. Christie, W.H., Smith, D.H. and McKown, H.S., "Data Acquisition and Processing for High-Resolution Mass Spectrometry Using a Small Nondedicated Computer", Chem. Instrum., $\underline{5}$, 43 (1974).
22. Chu, W.K., Nicolet, M-A., and Mayer, J.W., "Comparison of Backscattering Spectrometry and Secondary Ion Mass Spectrometry by Analysis of Tantalum Pentoxide Layers", Anal. Chem., $\underline{46}$, 2136 (1974).
23. Coles, J.N., and Long, J.V.P., "An Ion-Microprobe Study of the Self-Diffusion of Li^+ in Lithium Fluoride", Phil. Mag., $\underline{29}$, 457 (1974).
24. Colligon, J.S., "Surface Compositional Analysis Using Low Energy Ion Bombardment Induced Emission Processes", Vacuum, $\underline{24}$, 373 (1974).
25. Colligon, J.S., Fuller, D., and Carter, G., "Secondary Ion Emission Studies of the Range Profiles of Implanted Ions", Vacuum, $\underline{24}$, 519 (1974).

26. Didenko, P.I., Litovchenko, V.G., Marchenko, R.I., and Romanova, G.F., "Study of Si-Al$_2$O$_3$ and Si-SiO$_2$-Al$_2$O$_3$ Structures by Mass Spectrometry of the Secondary Ions", Poluprovodn. Tekh. & Mikroelektron, 18, 90 (1974).

27. Evans, C.A. Jr., "Ion Probe Mass Spectrometry: Overview", Ion Beam Surface Layer Analysis, J.W. Mayer and J.F. Ziegler Ed., (Lausanne: Elsevier 1974) p. 11.

28. Evans, C.A. Jr., "Secondary Ion Mass Spectrometry", 1974 Digests of the Intermag. Conf., Toronto, Canada, May 1974, (New York: IEEE 1974), 17-3/1pp.

29. Grundner, M., Heiland, W., and Taglaver, E., "Direct Comparison of Ion Scattering and Secondary Ion Emission as Tools for Analysis of Metals Surfaces", Appl. Phys., 4, 243 (1974).

30. Harrison, W.W., and Magee, C.W., "Hollow Cathode Ion Source for Solids Mass Spectrometry", Anal. Chem., 46, 461 (1974).

31. Heiland, W., "Surface Investigation by Ion Scattering and Secondary Ion Mass Spectroscopy", Electron & Fis. Apl., 17, 151 (1974).

32. Heinrich, K.F.J., Myklebust, R.L., and Newbury, D.E., "Analysis of Layered Materials with the Ion Microprobe", Trans. 7th Int. Conf. on X-Ray Optics and Microanalysis, Moskow-Kiev, July 1974. X-Ray Optics and Microanalysis, I. Borovsky and N. Komyak Ed., (Leningrad, USSR: Mashinostrocnie 1976) p. 266.

33. Hintohorne, J.R., and Ribbe, P.H., "Determination of Boron in Chondrodite by Ion Microprobe Mass Analysis", Am. Mineralogist, 59, 1123 (1974).

34. Hofker, W.K., Werner, H.W., Oosthoek, D.P., and de Grefte, H.A.M., "Experimental Analysis of Concentration Profiles of Boron Implanted in Silicon", Ion Implantation in Semiconductors and Other Materials, B.L. Crowder Ed., (New York: Plenum Press 1974) p. 133.

35. Hofmann, A.W., Giletti, B.J., Hinthorne, J.R., Andersen, C.A., and Comaford, D., "Ion Microprobe Analysis of a Potassium Self-Diffusion Experiment in Biotite", Earth and Planetary Sci. Lett., 24, 48 (1974).

36. Hofmann, C.A., "Quadrupole Mass Spectrometers of Various Performance Groups", Vacuum, 24, 65 (1974).

37. Honig, R.E., "Analysis of Surfaces and Thin Films by Mass Spectrometry", Advances in Mass Spectrometry, A.R. West Ed., Vol. 6, (London: The Institute of Petroleum 1974) p. 337.

38. Huber, W.K., Lobach, E., and Rettinghaus, G., "Secondary Ion Mass Spectrometric Investigations of Monomolecular Layers and Thin Films", Advances in Mass Spectrometry, Vol. 6, A.R. West Ed., (London: The Institute of Petroleum 1974) p. 683.

39. Hurrle, A., and Schulz, M., "Anomalous Outdiffusion of Beryllium Implanted into Silicon", Lattice Defects in Semiconductors, Freiburg, Germany, July 1974 (London, England: Inst. Phys. 1975) p. 474.

40. Ishitani, T., Kato, M., and Shimizu, R., "Comments on the Equilibrium Topography of Sputtered Amorphous Solids", J. Mat. Sci., 9, 505 (1974).

41. Ishitani, T., and Shimizu, R., "Computer Simulation of Knock-on Effect Under Ion Bombardment", Phys. Lett., 46A, 487 (1974).

42. Jackson, D.P., and Morgan, D.V., "Computer Modeling of Collision Processes in Solids", Contemp. Phys., 15, 25 (1974).

43. Kacerovsky, P., "Mass Spectrometry of the Surface of Epitaxially Grown GaP Monogrystals", Elektrotech. Cas., 25, 386 (1974).

44. Kerhow, H., and Trapp, M., "Secondary-Ion Emission during Bombardment of Copper and Aluminum Single Crystals with Alkali Ions", Int. J. Mass Spectrom. Ion Phys., 13, 113 (1974).

45. Kondo, T., Tamura, H., and Hirose, H., "Ion Microprobe Analyzer with Wien Filter for Primary Ion Mass Separation", Mass Spectrosc., 22, 229 (1974).

46. Konnen, G.P., Tip, A., and de Vries, A.E., "On the Energy Distribution of Sputtered Dimers", Rad. Eff., 21, 269 (1974).

47. Leleyter, M., and Joyes, P., "Secondary Molecular Ion Emission from some CuBe and CuAl Alloys", J. Phys. B, 7, 516 (1974).

48. Lewis, R.K., and Vastel, J., "A High Mass Resolution Capability for the Cameca Ion Analyzer", Proc. 9th Nat. Conf. Microbeam Analysis Soc., Ottawa, Canada, July, 1974. Paper No. 50.

49. Leys, J.A., and McKinney, J.T., "Ion Scattering Spectrometry and Secondary Ion Mass Spectroscopy: Two Complementary Techniques", Proc. 9th Nat. Conf. Microbeam Analysis Soc., Ottawa, Canada, July 1974. Paper No. 52.

50. Lichtman, D., "Surface Characterization by Electron, Ion, Photon, and Surface Wave Induced Desorption", Crit. Rev. Solid State Sci., 4, 395 (1974).

51. Liebl, H., "Static Mass Spectrometers with Axial Symmetry", Advances in Mass Spectrometry, Vol. 6, A.R. West Ed., (London: The Institute of Petroleum 1974) p. 535.

52. Liebl, H., "Ion Microprobe Analysers", Anal. Chem., 46, 22A (1974).

53. Liebl, H., "The Ion Microrpobe-Instrumentation and Techniques", (Workshop), Proc. SIMS and IMMA, Gaithersburg, MD., USA, Sept. 1974, (Washington, D.C.: Nat. Bureau Standards 1975) p. 1.

54. Liebl, H., "Quadrupole Secondary Ion Mass Spectrometry Apparatus with Enhanced Transmision", Int. J. Mass Spectrom. Ion Phys., 15, 116 (1974).

55. Lobach, E., "A Secondary Ion Mass Spectrometer for Surface Analysis and Study of Surface Phenomena", Electron. & Fis. Apl., 17, 166 (1974).

56. Lodding, A., Gourgout, J.M., Petersson, L.G. and Frostell, G., "Aspects of Quantitative Determination by Ion Probe of Fluorine Concentrations in Apatites", Z. Naturforsch, 29A, 897 (1974).

57. Lovering, J.F., "Application of SIMS Microanalysis Techniques to Trace Element and Isotropic Studies in Geochemistry and Cosmochemistry", (Workshop), Proc. SIMS and IMMA, Gaithersburg, MD., USA, Sept. 1974, (Washington, D.C.: Nat. Bureau Standards 1975) p. 135.

58. MacDonald, R.J., "An Empirical Relationship between Atoms and Ions Sputtered from Single Crystal Surfaces", Surf. Sci., 43, 653 (1974).

59. Magomedov, Sh.A., Chupalaev, Ch.M., and Guseinov, A.A., "Study of Secondary Ion Emission from Solids with the MI-1305 Mass Spectrometer", Instrum. & Tech., 17, 1536 (1974).

60. Mathewson, A.G., "The Surface Cleanliness of 316 L + N Stainless Steel Studied by SIMS and AES", Vacuum, 24, 505 (1974).

3. Bakale, D.K., Colby, B.N., and Evans, C.A., Jr., "High Mass Resolution Ion Microprobe Mass Spectrometry of Complex Matrices", Anal. Chem., 47, 1532 (1975).
4. Baun, W.L., and McDevitt, N.T., "SIMS-A Useful Complement to Other Depth Profiling Techniques", J. Vac. Sci. Technol., 12, 504 (1975).
5. Benninghoven, A., "Developments in Secondary Ion Mass Spectroscopy and Applications to Surface Studies", Surf. Sci., 53, 596 (1975).
6. Benninghoven, A., Sichtermann, W., and Storp, S., "Comparative Study of Si(111), Silicon Oxide, SiC and Si_3N_4 Surfaces by Secondary Ion Mass Spectroscopy (SIMS)", Thin Solid Films, 28, 59 (1975).
7. Bernheim, M., "Microanalysis by Ion Emission", Vide, No. 176, 30, 56 (1975).
8. Blaise, G., and Bernheim, M., "Adsorption of Gases Studied by Secondary Ion Emission Mass Spectrometry", Surf. Sci., 47, 324 (1975).
9. Buhl, R., and Preisinger,A., "Crystal Structures and Their Secondary Ion Mass Spectra", Surf. Sci., 47, 344 (1975).
10. Christie, W.H., and Smith, D.H., "Ion Microrpobe Analysis of Grain Boundary Impurity Segregation in an Alloy Failure", Supp. 3, Trans. Am. Nuc. Soc., 21, 13 (1975).
11. Coburn, J.W., and Kay, E., "Abstract: Composition Profiling-A Comparison of Surface Analysis Techniques vs Methods Involving the Detection of Sputtered Species", J. Vac. Sci. Technol., 12, 403 (1975).
12. Collins, R., and Carter, G., "The Spatial Distribution of Ions Implanted into Solids Subject to Diffusion and Surface Sputtering", Rad. Eff., 26, 181 (1975).
13. Dawson, P.H., "Quadrupoles for Secondary Ion Mass Spectrometry", Int. J. Mass Spectrom. Ion Phys., 17, 447 (1975).
14. De Paz, M., and Maccio, C., "Analysis of Conducting and Insulating Surfaces by Means of Secondary Ion Mass Spectrometry (SIMS)", Z. Naturforsch, 30A, 831 (1975).
15. Dobrott, R.D., "IMMA Depth Profiling of Semiconductor Materials Systems", Electrochem. Soc. Fall Meeting, Dallas, Tex, USA, Oct. 1975 (Princeton N.J., USA: Electrochem. Soc. 1975) p. 250.
16. Doi, H., and Kanomata, I., "In-depth Analysis of Solid Surface by High Speed Ion Beam Scanning Method", Mass Spectrosc., 23, 209 (1975).
17. Dowsett, M.G., King, R.M., and Parker, E.H.C., "Modification of Existing Apparatus for SIMS in UHV", J. Phys. E, 8, 704 (1975).
18. Evans, C.A. Jr., "Surface and Thin Film Compositional Analysis", Anal. Chem., 47, 819A (1975).
19. Evans, C.A. Jr., "Surface and Thin Film Analysis", Anal. Chem., 47, 855A (1975).
20. Evans, C.A., Jr., "Status of Secondary Ion Mass Spectrometry in the United States", Japan-U.S. Joint Seminar on Quantitative Techniques in Secondary Ion Mass Spectrometry, Honolulu, Hawaii, Oct. 1975.
21. Evans, C.A. Jr., "Thin Film Compositional Analysis-A Comparison of Techniques", J. Vac. Sci. Technol., 12, 144 (1975).
22. Fair, R.B., and Pappas, P.N., "Diffussion of Ion-implanted B in High Concentration P- and As-doped Silicon", J. Electrochem. Soc., 122, 1241 (1975).
23. Fair, R.B., and Pappas, P.N., "Diffusion of Ion-implanted Boron in High Concentration P, Sb, and As Doped Silicon", Electrochem. Soc. Spring Meeting, Toronto, Canada, May 1975 (Princeton, N.J., USA: Electrochem. Soc. 1975) p. 397.
24. Gettings, M., and Coad, J.P., "A Preliminary Study of Pure Metal Surfaces Using Auger Electron Spectroscopy (AES) X-Ray Photoelectron Spectroscopy (XPS) and Secondary Ion Mass Spectroscopy (SIMS)", Surf. Sci., 53, 636 (1975).
25. Gonda, S., Matsushima, Y., Makita, Y., and Mukai, S., "Molecular Beam Epitaxial Growth of GaAs", Bull. Electrotech. Lab., 39, 361 (1975).
26. Gonda, S.,Matsushima, Y., Makita, Y., and Mukai, S., "Characterization and Substrate-temperature Dependence of Crystalline State of GaAs Grown by Molecular Beam Epitaxy", Japan· J. Appl. Phys., 14, 935 (1975).
27. Grabke, H.J., and Viefhaus, H., "New Methods in Surface Analysis and Their Application for Studies on Iron and Steel", Arch. Eisenhuettenwes, 46, 689 (1975).
28. Gries, W.H., "A Formula for the Secondary Ion Field Fraction Emitted Through an Energy Window", Int. J. Mass Spectrom. Ion Phys., 17, 77 (1975).
29. Gries, W.H., and Rudenauer, F.G., "A Quantitative Model for the Interpretation of Secondary Ion Mass Spectra of Dilute Alloys", Int. J. Mass Spectrom. Ion Phys., 18, 111 (1975).
30. Grosdover, R.S., Efremenkova, V.M., Shelyaken, L.B., and Yurasova, V.E., "Formation of Cones During Sputtering", Rad. Eff., 27, 237 (1975).
31. Hakkila, E.A., Hansel, J.M., and Hutchinson, W.B., "Effects of Sample Surface on Ion Microprobe Analysis of PtRhW Alloys", Proc. 10th Nat. Conf. on Electron Probe Analysis, Las Vegas, Aug. 1975. Paper No. 73.
32. Harrison, D.E., "Fundamentals of Ion Surface Interaction", Japan-US Joint Seminar on Quantitative Techniques in Secondary Ion Mass Spectrometry, Honolulu, Hawaii, Oct. 1975.
33. Heiland, W., and Taglauer, E., "Surface Analytical Studies Using Ion Scattering Spectrometry, Auger Electron Spectroscopy and Secondary Ion Mass Spectrometry", J. Vac. Sci. Technol., 12, 352 (1975).
34. Heinrich, K.F.J., and Newbury, D.E., "Secondary Ion Mass Spectrometry", Report NBS-SP-427, Nat. Bureau Standards, Washington, D.C., USA, Oct. 1975, 227 pp.
35. Hinthorne, J.R., and Conrad, R.L., "The Application of Peak Stripping to Problems in Ion Probe Microanalysis", Proc. 10th Nat. Conf. on Electron Probe Analysis, Las Vegas, Aug., 1975. Paper No. 74.
36. Hinthorne, J.R., and Anderson, C.A., "Microanalysis for Fluorine and Water in Silicates with the Ion Microprobe Mass Analyzer", Shimadzu Rev., 32, 103 (1975).
37. Hinthorne, J.R., and Andersen, C.A., "Microanalysis for Fluorine and Hydrogen in Silicates with the Ion Microprobe Mass Analyzer", Am. Mineralogist, 60, 143 (1975).
38. Hirose, H., Makamura, K., Shibata, A., and Tamura, H., "Hollow Cathode Ion Source for IMA", Mass Spectrosc., 23, 195 (1975).

39. Hofer, W.O., Liebl, H., and Standenmaier, G., "Depth Analysis of Thin Films with an Ion Microprobe", Electrochem. Soc. Fall Meeting, Dallas, Tex. USA, Oct. 1975 (Princeton, N.J. USA: Electrochem. Soc. 1975) p. 243.
40. Hofer, W.O., and Liebl, H., "Dept-profiling of Cu-Ni Sandwich Samples by Secondary Ion Mass Spectrometry", Appl. Phys., 8, 359 (1975).
41. Hoffman, D.W., "A Cratering Analysis for Quantitative Depth Profiling by Ion Beam Sputtering", Surf. Sci., 50, 29 (1975)
42. Hofker, W.K., Oosthoek, D.P., Koeman, N.J., and de Grefte, A.M., "Concentration Profiles of Boron Implantations in Amorphous and Polycrystalline Silicon", Rad. Eff., 24, 223 (1975).
43. Hofker, W.K., Werner, H.W., Oosthoek, D.P., and Koeman, N.J., "Redistribution of Background Impurities in Silicon Induced by Ion Implantation and Annealing", Ion Implantation in Semiconductors, S. Namba Ed., (New York: Plenum Press 1975) p. 201.
44. Hurrle, A., and Sixt, G., "Cesium Profiles in Silicon and in SiO_2-Si Double-layers as Determined by SIMS Measurements", Appl. Phys., 8, 293 (1975).
45. Ishitani, T., Tamura, H., and Kondo, T., "Quantitative Analysis with an Ion Microanalyzer", Anal. Chem., 47, 1294 (1975).
46. Ishitani, T., and Shimizu, R.,"Computer Simulation of Atomic Mixing During Ion Bombardment", Appl. Phys., 6, 241 (1975).
47. Ishitani, T., Shimizu, R., and Tamura, H., "Atomic Mixing in Ion Probe Microanalysis", Appl. Phys., 6, 277 (1975).
48. Johnson, C.E., "Electron and Ion Microprobe Analysis of Irradiated Fuels", Physical Aspects of Electron Microscopy and Microbeam Analysis, G. Siegel and D.R. Beaman, Ed., (New York: John Wiley and Sons Inc. 1975) p. 373.
49. Jonker, H.D., Morgan, A.E., and Werner, H.W., "Secondary Ion Mass Spectrometry of Compositional Changes in Garnet Films", J. Cryst. Growth, 31, 387 (1975).
50. Jurela, Z., "Average Energy of Sputtered Ions from Fifteen Polycrystalline Targets", Int. J. Mass Spectrom. Ion Phys., 18, 101 (1975).
51. Kaminsky, M., "Ion-Surface Interactions: Experimental", Japan-US Joint Seminar on Quantitative Techniques in Secondary Ion Mass Spectrometry, Honolulu, Hawaii, Oct. 1975.
52. Kato, Y., Tajima, Y., Hayakawa, H., Shibata, A., and Nishiwaki, "Development of an On-line Real Time Data Processing System for the Ion Microanalyzer", Mass Spectrosc., 24, 271 (1975).
53. Kim, H.B., Sweeney, G.G., and Heng, T.M.S., "Analysis of Metal-GaAs Schottky Barrier Diodes by Secondary Ion Mass Spectrometry", Inst. Phys. Conf. Ser., No. 24, 307 (1975).
54. Kishinevskii, M.E., "Mechanism for Secondary Ion Emission", Sov. Phys. Tech. Phys., 20, 799 (1975).
55. Komiya, S., Narusawa, T., and Satake, T., "Simultaneous Observations of Partially Oxidized Surfaces by AES and SIMS for Al, Si, Ti, V, and Cr", J. Vac. Sci. Technol., 12, 361 (1975).
56. Kondo, T., Tamura, H., Ishitani, T., and Nakamura, K., "Quantitative Analysis of Low Alloy Steel with an Ion Microanalysis", Mass Spectrosc., 23, 221 (1975).
57. Konishi, F., et al., "Effect of Ambient Oxygen on Quantitative Analysis of Solid Surface by Secondary Ion Mass Spectrometry (SIMS)", Japan-US Joint Seminar on SIMS, Honolulu, Hawaii, 1975.
58. Konishi, H., "Chemical Enhancement Effects: Metals", Japan-US Joint Seminar on Quantitative Techniques in SIMS, Honolulu, Hawaii, Oct. 1975.
59. Koshikawa, T., and Shimizu, R., "A Thermodynamic Approach to Quantitation of Semiconductor", JSPS-Technical Committee for Microbeam Analysis, Repts. No. 61, 1975).
60. Koshikawa, T., Sugata, E., Kang, S.T., and Shimizu, R., "Quantitative Analysis of Semiconductor Materials with IMA", JSPS-Technical Committee for Microbeam Analys. Repts., No. 130, (1975).
61. Koval', A.G., Bobkov, V.V., Klimovskii, Yu, A., Strel'chenko, S.S., Shubina, V.V., Lebedev, V.V., and Fogel, Ya.M., "Mass Spectrum of Secondary Ions Ejected from the Surface of a Single Crystal of Gallium Arsenide by Argon Ions", Sov. Phys. Tech. Phys., 19, 1587 (1975).
62. Kozma, L., and Riedel, M., "Application of Secondary Ion Mass Spectrometry in the Research of Tungsten", Koezl. Magy. Tud. Akad. Musz. Fiz. Kut. Intez., No. 0-16, 23 (1975).
63. Krohn, V.E., and Ringo, G.R., "Ion Source of High Brightness Using Liquid Metal", Appl. Phys. Lett., 27, 479 (1975).
64. Larrabee, G.B., "Trace Analysis of Semiconductor Materials-Emerging Technologies", Electrochem. Soc. Spring Meeting, Toronto, Canada, May 1975 (Princeton, N.J., USA: Electrochem. Soc., 1975) p. 921.
65. Larrabee, G.B., Dobrott, R.D., Keenan, J.A., and McGuire, G.E., "Establishing Detection and Determination Limits in Surface and Thin-Film Analysis", Electrochem. Soc. Fall Meeting, Dallas, Tex., USA, Oct. 1975 (Princeton, N.J., USA: Electrochem. Soc. 1975) p. 234.
66. Larsson, S.J., and Lodding, A., "Ion Analyzer Study of Non-Metals in Metals" Swed. Res. Inst. Rep. C 200559-F9, 184 (1975).
67. Lewis, R.K., "Abstract: Characterization of Multilayer Thin Films Using Secondary Ion Mass Spectrometry and Improvement of the Analytical Techniques", J. Vac. Sci. Technol., 12, 404 (1975).
68. Leys, J.A., and McKinney, J.T., "SEM and SIMS: A Unique Combination for Surface Characterization", Proc. 10th Nat. Conf. on Electron Probe Analysis, Las Vegas, Aug. 1975. Paper No. 59.
69. Liebl, H., "Ion Probe Microanalysis", J. Phys. E., 8, 797 (1975).
70. Liebl, H., "Secondary-Ion Mass Spectrometry and Its Use in Depth Profiling", J. Vac. Sci. Technol., 12, 385 (1975).
71. Lim, M., "Quantitative Impurity Analysis by Secondary Ion Mass Spectrometry Principles: Measurements in GaP", Proc. 10th Nat. Conf. on Electron Probe Analysis, Las Vegas, Aug. 1975. Paper No. 72.
72. Lodding, A., and Lundkvist, L., "Ion Probe Technique for the Study of Gallium Diffusion in Silicon Nitride Films", Thin Solid Films, 25, 491 (1975).
73. Lyon, O., Blaise, G., Roques-Carmes, C., and Slodzian, G., "Study by Secondary Ion Emission of Small Precipitates Produced During the Internal Oxidation of Cu-Al Alloys", C.R. Acad. Sci. B, 281, 313 (1975).

309

74. Mathewson, A.G. "The Surface Cleanliness of 316L + N Stainless Steel Studied by SIMS and AES", Vacuum, 24, 505 (1975).

75. Matsevich, V.G., and Zyryanov, G.K., "Determination of Secondary Ionic Emission Coefficients from Secondary Ion Energy Spectra Caused by Bombardment of PbS and LiF Single Crystals by Helium Ions with Energy from 20 to 200 eV", Vestn. Leningr. Univ. Fiz. & Khim., No. 1, p. 53 (1975).

76. Maul, J., and Wittmaack, K., "Secondary Ion Emission From Silicon and Silicon Oxide", Surf. Sci., 47, 358 (1975).

77. Morrison, G.H., and Slodzian, G., "Ion Microscopy", Anal. Chem., 47, 932A (1975).

78. Morrison, G.H., "General Aspects of Trace Analytical Methods. I. Methods of Calibration in Trace Analysis", Pure & Appl. Chem., 41, 397 (1975).

79. Nakajima, S., and Yaegashi, Y., "Analysis of Semiconductors by Means of Ion Micro Analyzer", Oyo Buturi, 44, 1303 (1975).

80. Namba, S., and Masuda, K., "Ion Implantation in Semiconductors", Advances in Electronics & Electron Phys., 37, 263 (1975).

81. Nishimura, H., and Okano, J., "An Oxygen Ion Source for the Secondary Ion Mass Spectrometer", Mass Spectrosc. 23, 9 (1975).

82. Okano, J., "Secondary Ion Mass Spectrometry(I)", Mass Spectrosc., 23, 237 (1975).

83. Pebler, A., Sweeney, G.G., and Castel, P.M., "SIMS Analysis of Doped Tungsten", Metall. Trans. A, 6, 991 (1975).

84. Perkins, W.G., and Foesch, J.A., "Qualitative Depth Profile Analysis of Metal Hydride Films, Using an Ion Microrpobe Mass Analyzer", Proc. 10th National Conf. on Electron Probe Analysis, Las Vegas, Aug. 1975. Paper No. 79.

85. Pickering, H.W., "Preferential Ion Sputtering of a Component from an Alloy", Electrochem. Soc. Fall Meeting, Dallas, Tex., USA, Oct. 1975, (Princeton, N.J., USA: Electrochem. Soc. 1975) p. 241.

86. Plew, L.E., "Automation of an Ion Microscope", Japan-US Joint Seminar on SIMS, Honolulu, Hawaii, Oct. 1975.

87. Potosky, J.C., and Wittry, D.B., "A Quadrupole Instrument for Investigation of Electron and Ion Beam Interactions with Solids, with J.C. Potosky", Proc. 10th Nat. Conf. on Electron Probe Analysis, Las Vegas, Aug. 1975. Paper No. 76.

88. Prager, M., "Effect of Residual Oxygen on the Formation of Molecular Ions in Secondary Ion Mass Spectrometry", Appl. Phys., 8, 361 (1975).

89. Riedel, M., "The Application of Secondary Ion Emission in the Chemical Analysis of Solid State", Magy. Fiz. Foly., 23, 539 (1975).

90. Rodelsperger, K., Kruger, W., and Scharmann, A., "A Simple Calculation of the Angular Distribution of Sputtered Atoms", Z. Phys., 272, 127 (1975).

91. Rudenauer, F.G., Schoberl, E., Prager, I., und Silberbauer, G., "Elektronik fur ein Ionensonden Massenspektrometer", Nucl. Instrum. Methods, 128, 309 (1975).

92. Rudenauer, F., "A Quantitative Model for Secondary Ion Emission Based on Cascade Sputtering Theory and Adiabatic Surface Ionization", Japan-US Joint Seminar on SIMS, Honolulu, Hawaii, Oct. 1975.

93. Schimko, R., Richter, C.E., Rogge, K., Schwarz, G., and Trapp, M., "Implanted Arsenic and Boron Concentration Profiles in SiO_2 Layers", Phys. Status Solidi A, 28, 87 (1975).

94. Schubert, R., "The Analysis of 301 Stainless Steel by SIMS", J. Vac. Sci. Technol., 12, 505 (1975).

95. Schulz, M., Klausmann, E., and Hurrle, A., "Correlation of Surface States with Impurities", Crit. Rev. Solid State Sci., 5, 319 (1975).

96. Seshan, K. and Washburn, J., "Some New Results in the Characterization of Defects in Phosphorus Ion-Implanted Silicon", Rad. Eff., 26, 31 (1975).

97. Shimizu, R., Ishitani, T., Kondo, T., and Tamura, H., "Practicality of the Thermodynamic Model for Quantitative Ion Probe Microanalysis of Low Alloy Steels", Anal. Chem., 47, 1020 (1975).

98. Shimizu, R., "Monte Carlo Calculation Techniques Applied to Ion Microprobe Analysis", Proc. 10th Nat. Conf. on Electron Probe Analysis, Las Vegas, Aug. 1975. Paper No. 71.

99. Slodzian, G., "Some Problems Encountered in Secondary Ion Emission Applied to Elementary Analysis", Surf. Sci., 48, 161 (1975).

100. Someno, M., Saito, H., and Kobayashi, M., "Determination of Hydrogen and Deuterium Contents in Metals and Alloys by Ion Microanalyzer", Trans. Japan Inst. Met., 16, 305 (1975).

101. Steiger, W., und Rudenauer, F.G., "A Computer Program for Peak Identification in Secondary Ion Mass Spectra", Vacuum, 25, 409 (1975).

102. Storms, H.A., Stein, J.D., and Brown, K.F.., "Evaluation of a Cesium Positive Ion Source for Seocndary Ion Mass Spectrometry", Japan-US Joint Seminar on SIMS, Honolulu, Hawaii, Oct. 1975.

103. Storms, H.A., Brown, K.F., and Stein, J.D., "Performance Evaluation of a Cesium Positive Ion Source for Secondary Ion Mass Spectrometry", Proc. of the 10th Nat. Conf. of the Microbeam Anal. Soc., Las Vegas, Nev. Aug 1975. Paper No. 77.

104. Tohyama, K., "Capability of Microanalysis Instrumentation", Shimadzu Rev., 32, 5 (1975).

105. Tsong, I.S.T., and McLaren, A.C., "An Ion Beam Spectrochemical Analyser with Application to the Analysis of Silicate Minerals", Spectrochim. Acta B, 30, 343 (1975).

106. Valencourt, L.R., Johnson, C.E., Steidl, D.V., and Davis, H.T., "Oxygen Diffusion Measurements in Porous UO_{2+x}", J. Nucl. Mat., 58, 293 (1975).

107. Walsh, J.M., and Kear, B.H., "Direct Evidence for Boron Segregation to Grain Boundaries in a Nickel-Base Alloy by Secondary Ion Mass Spectrometry", Metall. Trans. A, 6, 226 (1975).

108. Wehner, G.K., "Surface Composition Changes Under Ion Bombardment", Scanning Electron Microscopy, Vol. 1, Om Johari and Irene Corvin Ed., (Chicago, IL.: ITT Research Institute 1975) p. 133.

109. Werner, H.W., "Secondary Ion Mass Spectrometry and Its Application to Thin Film and Surface Analysis", Acta Electronica, 18, 51 (1975).

110. Werner, H.W., "Quantitative Analysis by SIMS", Japan-US Joint Seminar on SIMS, Honolulu, Hawaii, Oct. 1975.

111. Werner, H.W., Morgan, A.E., and de Grefte, H.A.M., "Interpretation of Secondary Ion Mass Spectra by Means of Fingerprint Spectra and Secondary Ion Imaging", Appl. Phys., 7, 65 (1975).
112. Werner, H.W., "Experience with Quantitative SIMS", Japan-US Joint Seminar on SIMS, Honolulu, Hawaii, Oct. 1975.
113. Werner, H.W., "Characterization of Ceramics by Means of Modern Thin Film and Surface Analytical Techniques", 8th Int. Conf. "Science of Ceramics", Cambridge, U.K. Sept. 1975, J.P. Gossez et al. Ed., (New York: Springer-Verlag 1976) p. 55.
114. Werner, H.W., "The Use of Secondary Ion Mass Spectrometry in Surface Analysis", Surf. Sci., 47, 301 (1975).
115. Werner, H.W., and Thomas, G.E., "Emissie van Ionen en van Licht Door Beschieting van Oppervlakken met Snelle Ionen: SIMS en BLE", Chem Weekblad, 71, No. 12, 24 (1975).
116. Williams, P., Evans, C.A., Jr., Grossbeck, M.L., and Birnbaum, H.K., "Ion Microprobe Analysis for Niobium Hydride in Hydrogen Embrittled Niobium", Anal. Chem., 48, 964 (1975).
117. Wittmaack, K., and Staudenmaier, G., "Diatomic Versus Atomic Secondary Ion Emission", Appl. Phys. Lett., 27, 318 (1975).
118. Wittmaack, K., "Energy Dependence of the Secondary Ion Yield of Metals and Semiconductors", Surf. Sci., 53, 626 (1975).
119. Wittmaack, K., "Pre-Equilibrium Variation of the Secondary Ion Yield", Int. J. Mass Spectrom. Ion Phys., 17, 39 (1975).
120. Wittry, D.B., "Critical Remarks on SIMS for Quantitative Methods", Japan-US Joint Seminar on SIMS, Honolulu, Hawaii, Oct. 1975.
121. Zinner, E., and Walker, R.M., "Ion Probe Studies of Artificially Implanted Ion in Lunar Samples", Proc. 6th Lunar Sci. Conf. Houston, Texas, March 1975, Compiled by the Lunar Science Institute, (New York: Pergamon Press 1975) p. 3601.

311

List of MAS Members

AARDEN,DR. H.H.*MINISTERIO DE MINES E HIDROCARBUROS*
   CENTRO SIMON BOLIVAR*CARACAS,*VENEZUELA*
ADEN, G. D.*ARIZONA STATE UNIVERSITY*DEPT. OF CHEMISTRY*TEMPE,AZ*
ADEY, J. D.*611 S. W. CAMPUS DRIVE*UNIV. OF OREGON DENTAL SCHOOL*
   PORTLAND,OR*
AGUS, Z. S.*3400 SPRUCE ST.*HOSP. OF UNIV. OF PA.*PHILADELPHIA,PA*
ALBEE, A.*CALIFORNIA INSTITUTE OF TECHNOLOGY*DIV. OF GEO. SCIENCES*
   PASADENA,CA*
ALLEMANO, E.*LONGWOOD LAKE ROAD*OAK RIDGE,NJ*
ALONZO, J. R.*P. O. BOX 45*ESSO RESEARCH + ENG. CO.*LINDEN,NJ*
AMENSON, J. L.*62 TOWN ENG.*IOWA STATE UNIV.*AMES,IA*
ANY, J. A.*1503 CLAIRMONT PLACE*BLOOMINGTON,IN*
ANAGNOSTOPOULOS, C.*EASTMAN KODAK CO.*PHYSICS DIV. RESEARCH LABS.*
   ROCHESTER,NY*
ANASTAS, D. T.*919 F M 1959*HOUSTON,TX*
ANATER, T. F.*P. O. BOX 79*WESTINGHOUSE-BETTIS*WEST MIFFLIN,PA*
ANDERSON, C. A.*163 THIRD ST.*SOLVANG,CA*
ANDERSON, J. R.*SUNY BINGHAMTON*DEPT. OF GEO. SCIENCES*BINGHAMTON,NY*
ANDERSON, R. J.*CUMMINS ENGINE CO., INC.*MC 50183*COLUMBUS,IN*
ANDERSON, R. M.*40 WESTVIEW DR.*POUGHKEEPSIE,NY*
ANDERSON, S. C.*919 F M 1959*HOUSTON,TX*
ANDRADE, J. D.*UNIV. OF UTAH*COLLEGE OF ENGINEERING*SALT LAKE CITY,UT*
ANDREWS, C. W.*5712 EDGEPARK DR.*BROOKPARK,OH*
ANNEGARN,HAROLD JOHN*N.P.R.U.*UNIV.WITWATERSRAND*JOHANNESBURGE 2001,*
   SOUTH AFRICA*
ARGENTIERI,G.J.*725 BERDIN AVE.*WAYNE,NJ*
ARMIGLIATO,ALTO*VIA CASTAGNOLI,1*BOLOGNA 40126,*ITALY*
ARMSTRONG, J. T.*CALTECH*DIV. OF GEO. + PLAN. SCI*PASADENA,CA*
ARTZ, B. E.*70 DIXBORO ROAD*ANN ARBOR,MI*
ASGAR, K.*1011 N. UNIVERSITY*110 DENTAL SCHOOL*ANN ARBOR,MI*
ASHBAUGH, P. H.*9045 COMET ST.*EL PASO,TX*
AUSTIN, C. W.*404 HILLMONT CIRCLE N. W.*HUNTSVILLE,AL*
AUSTIN, N. A.*3392 INVESTMENT BLVD.*ETEC CORP.*HAYWARD,CA*

BADGER, R. G.*818 PARK AVE.*N. TONAWANDA,NY*
BAGHDAYAN, J.*55 PENNACCOK RD.*NORTH TEWKSBURY,MA*
BAILEY, G. W.*P. O. BOX 2226*EXXON RES. AND DEV. LABS*BATON ROUGE,LA*
BAILEY, P. J.*P. O. BOX 218*YORKTOWN HGTS.,NY*
BAILEY,JOHN D.**
BAILEY,MR. MRS.HAMPTON*712 RESSELL PLACE*PLAINFIELD,NJ*
BALL, F. EMSA REP.*P.O. BOX X*OAK RIDGE NAT. LAB.*ANAL. CHEM.*
   OAK RIDGE,TN*
BALSER, J. D.*6177 SUNOL BLVD.*PLEASANTON,CA*
BANFIELD, W. G.*9000 ROCKVILL PIKE*NATIONAL INSTITUTES OF HEALTH*
   ROOM 8-B-19, BLDG. 10*BETHESDA,MD*
BANK, H. L.*MED. UNIV. CF S. C.*DEPT. OF PATHOLOGY*CHARLESTON,SC*
BARBI, N. C.*BOX 641*PRINCETON GAMMA TECH.*PRINCETON,NJ*
BARNETT, B. L.*12175 ELKWOOD DR.*CINCINNATI,OH*
BARSKY, C. K.*OWENS-CORNING FIBERGLAS*TECHNICAL CENTER*GRANVILLE,OH*
BART, J. J.*R. D. 2, DIX ROAD*ROME,NY*
BATES, T.*100 MIDLAND RD.*EG+G ORTEC, INC.*OAK RIDGE,TN*

BATT,AHRON*HADASSAH MEDICAL SCHOOL*EIN KEREM*JERUSALEM,*ISRAEL*
BEALL, J. R.*3422 W. BERRY DR.*LITTLETON,CO*
BEAMAN, D. R.*602 ROOD*MIDLAND,MI*
BEBLO, N. F.*1600 BRIARWOOD DR. A-3*LATROBE,PA*
BECKWITH, P. M.*BASF WYANDOTTE CORP.*RESEARCH BLDG.*WYANDOTTE,MI*
BEEBE, A. H.*29 EICHELBERGER DR.*GORAOPOLIS,PA*
BEEBE, E. D.*254 FORSGATE DR.*JAMESBURG,NJ*
BEESON, M. H.*38355 JACARANDA DR.*NEWARK,CA*
BENCE, A. E.*EARTH AND SPACE SCIENCES, SUNY*STONY BROOK,NY*
BENCK, R. F.*316 BYNUM RIDGE ROAD*FOREST HILL,MD*
BENEFIEL, D. C.*DOW CHEMICAL USA*B-1225*FREEPORT,TX*
BENSEY, F. N.*725 CUMBERLAND STREET*HARRIMAN,TN*
BEREZESKY, I. K.*31 S. GREEN ST.*UNIV. OF MD., SCH. OF MED.*
  DEPT. PATHOLOGH.*BALTIMORE,MD*
BERG, H. B.*165 ORANGEBURG ROAD*OLD TAPPAN,NJ*
BERNARDI, B.*37 BROWNHOUSE RD.*CAMECA INSTRUMENTS, INC.*STAMFORD,CT*
BERRY,V.K.*7703 FLOYD CURL DR.*UTHSCSA*DEPT. OF ANATOMY*SAN ANTONIO,TX
BERTA, R. L.*P. O. BOX 1959*FORT WORTH,TX*
BERTIN, E. P.*RCA LABORATORIES*ROOM E-128*PRINCETON,NJ*
BETTOLI, S. C.*38 ELM STREET*SUMMIT,NJ*
BHALLA, R. S.*ONE WESTINGHOUSE PLAZA*WESTINGHOUSE ELECTRIC CORP.*
  BLOOMFIELD,NJ*
BIELENBERG, U.*51 ORMONT ROAD*CHATHAM,NJ*
BIERWILER, T. W.*CORNING GLASS WORKS*PAINTED POST,NY*
BIGELOW, W. C.*UNIVERSITY OF MICHIGAN*DEPT. OF MATER. + MET. ENG*
  ANN ARBOR,MI*
BINGLE, W. D.*NATIONAL STEEL CORP.*SEM-ISS-MICRO PROBE DIV.*WEIRTON,WV
BIRGENSMITH, C. E.*219 S. 131ST*TACOMA,WA*
BIRKS, L. S.*NAVAL RESEARCH LABORATORY*CODE 7680*WASHINGTON,DC*
BLACK, K. M.*4100 N. HAMLINE BOX 43079*SAINT PAUL,MN*
BLAISE, J. W.*4430 DIRECTOR DRIVE*CHROMALLOY AMERICAN CORP.*
  TURBINE SUPPORT DIVISION*SAN ANTONIO,TX*
BLAZEK, H. F.*CODE 3318*CHINA LAKE,CA*
BOEKESTEIN,A*ALBARDAWEG 155*MALDEN*WAGENING,SLEEDOORN 3,*NETHERLAND*
BOHNING, J. E.*3791 N. W. 25TH*ALBANY,OR*
BOJARSKI,DR.ZBIGNIEW*15 B.DROZDOW*KATOWICE,*POLAND 40-530*
BOLON,R.B.*862 SARATOGA RD.*BALLSTON LAKE,NY*
BOMBACK, J.*P. O. BOX 2053*FORD MOTOR CO.*SCIENTIFIC RESEARCH STAFF*
  DEARBORN,MI*
BORIS, M. J.*3761 CANAL STREET*AMERICAN STEEL FOUNDRIES*
  SENIOR RESEARCH CHEMIST*EAST CHICAGO,IN*
BOROVETZ, H. S.*SCAIFE HALL*UNIV. OF PITTSBURGH*DEPT. OF SURGERY*
  PITTSBURGH,PA*
BOROVSKII,PROF.I.B.*142432 CHERNOGOLOVKA MOSCOW REG.*
  INSTITUTE OF SOLID STATE PHY*MOSCOW,*
BOUTROS, S. N.*RD 1, BOX 16*LIMESTONE,NY*
BOWER, J. F.*29 MYSTIC AVE.*WINCHESTER,MA*
BOYD, D. E.*130 COLUMBIA DRIVE*WAVERLY,OH*
BRADBERRY, J. R.*BOX 1663 MS 770*LOS ALAMOS SCIENTIFIC LAB*
  LOS ALAMOS,NM*
BRADFORD, M. N.*9607 KEMPTON AVE.*CLEVELAND,OH*
BRANCH, D. L.*2000 W. GRANDVIEW BLVD.*LORD CORP.*ERIE,PA*
BRANDIS, E. K.*ROUTE 52*IBM, D/877, B/300-41C*HOPEWELL JUNCTION,NY*
BRANKS, J. R.*219 EAST COURT ST.*JANESVILLE,WI*
BRAUN, N. M.*1899 IVANHCE ROAD*CLEVELAND,OH*
BREITER, D. N.*508 WASHINGTON AVE. 4*GOLDEN,CO*
BRENNAN, J. W.*2213 BEAUMONT ROAD*WILMINGTON,DE*
BRETON, P. J.*3392 INVESTMENT BLVD.*HAYWARD,CA*

BROMAN, R.*P. O. BOX 66*TRACOR NORTHERN*MIDDLETON,WI*
BRONN, D. G.*2205 HAVERFORD ROAD*COLUMBUS,OH*
BROOKS, E. J.*U.S. NAVAL RESEARCH LABORATORY*CODE 6310*WASHINGTON,DC*
BROOKS, G. J.*U. OF MICH.*MAT. + MET. ENG.*ANN ARBOR,MI*
BROTHERS, E. W.*3309 NO. STATE*OKLAHOMA CITY,OK*
BROWN, B. G.*8919 ALPHA DR.*STOCKTON,CA*
BROWN, D. B.*U. S. NAVAL RESEARCH LAB.*CODE 6487*WASHINGTON,DC*
BROWN, D. L.*3332 EASY AVE.*LONG BEACH,CA*
BROWN, J. H. JR.*153 WINDEMERE ROAD*ROCHESTER,NY*
BROWN, Q. A.*2034 GOLDEN GATE AVE.*QBI INTERNATIONAL*SAN FRANCISCO,CA*
BROWN,JAMES D.*95 CUMBERLAND CIRCLE*LONDON,ONTARIO,*CANADA N5X 1B7*
BRUCHER, H. G.*P. O. BOX 999*SOUTHFIELD,MI*
BRUMBAUGH, G. G.*736 RONDO ST.*ALBANY,OR*
BRUNIN,JEAN-MARIE AND.*RUE DU RIVAGE HO-6*ORROIR(B7572)*
   MONT DE L≠ENCLUS,*BELGIUM*
BRUNO, G. W.*345 SOUTH ROAD*BEDFORD,MA*
BUCZEK, D. M.*32 GORDON ROAD*NEEDHAM,MA*
BUHRKE, V. E.*2180 SAND HILL ROAD*MENLO PARK,CA*
BURNS, M. S.*111 E. 210TH ST.*MONTEFIORE HOSPITAL*BRONX,NY*
BURNSIDE, P. L.*P. O. BOX 26*BELLE CHASSE,LA*
BUSCH, G. A.*GRUMMAN AEROSPACE CO.*RESEARCH DEPT. PET 26*BETHPAGE,NY*
BUSECK, P. R.*ARIZONA STATE UNIVERSITY*DEPT. OF CHEMISTRY*TEMPE,AZ*
BUSH, D. R.*LEHIGH UNIVERSITY*BETHLEHEM,PA*
BUTLER, E. M.*40 GOULD CENTER*GOULD INC., GOULD LABORATORIES*
   ELEC. AND ELECTRONIC RES*ROLLING MEADOWS,IL*
BUTLER, J. W.*P. O. BOX 129*BUTLER ASSOCIATES*LEMONT,IL*
BUTLER, W. O.*P. O. BOX 348*DIAMOND SHAMROCK CORP.*PAINESVILLE,OH*

CAIN, J.*1701 NORTH ST.*IBM SPD DEPT. U62*BLDG. 021-2*ENDICOTT,NY*
CALDWELL, V. E.*CURTIS STREET*ARMCO STEEL CORPORATION*RESEARCH CENTER*
   MIDDLETOWN,OH*
CALK, L. C.*345 MIDDLEFIELD ROAD*MENLO PARK,CA*
CAMERON, D. P.*IBM DEPT 75P*BLDG. 320-037*HOPEWELL JUNCTION,NY*
CAMPBELL, W. J.*U. S. BUREAU OF MINES*COLLEGE PARK,MD*
CAMPBELL,D.E.*71IS AVEENUE DE VALVINS*CORNING EUROPE-CER*
   77211 AVON,CEDEX*FRANCE*
CAMPBELL,W.J.*4900 LASALLE AVE.*US BUREAU OF MINES*AVONDALE,MD*
CARDONE, F.*764 EAST 213TH ST.*BRONX,NY*
CARNWATH,J.W.(DR)*CB2 3EG*PHYSIOLOGICAL LABORATORY*CAMBRIDGE,*ENGLAND*
CASTAING,PROF. R.*UNIVERSITY OF PARIS*FACULTE DES SCIENCES*ORSAY,*
   FRANCE*
CENTURY, T.*UNIV. OF PENN.*DEPT. OF PHYSIOLOGY*PHILADELPHIA,PA*
CERNY, J. E.*1939 CHERRYLAWN DR.*TOLEDO,OH*
CERNY,J.E.*173 ESSEX AVE.*INSTRUMENTS SA,INC.*METUCHEN,NJ*
CERVEN, J.*515 E. WOODRUFF ROAD*DEPT. OF LAW ENFORCEMENT*JOLIET,IL*
CESCAS,MICHEL PIERRE*LAVAL UNIVERSITY*FACULTY OF AGRICULTURE*
   QUEBEC 10,*CANADA*
CHAMBERLAIN, N. F.*209 EDGEWOOD*BAYTOWN,TX*
CHAMBERS, W. F. DR.*SANDIA CORPORATION*ORG. NO. 5822*ALBUQUERQUE,NM*
CHANEY, C. E.*400 CROW CNY. RD.*SAN RAMON,CA*
CHANG, J.*811 BROKEN BOW TRAIL*INDIANAPOLIS,IN*
CHANG, W. H.*41 SHORT HILLS CIRCLE*MILLBURN,NJ*
CHATFIELD,CHRIS*BOX 42 056,S-12622*SANDVIK*STOCKHOLM 42,*SWEDEN*
CHATFIELD,ERIC J.*SHERIDAN PARK*ONTARIO RESEARCH FOUNDATION*
   DEPARTMENT OF PHYSICS*ONTARIO,*CANADA*
CHEN,TZONG T.*555 BOOTH ST.*CANMET COMPANY*OTTAWA,ONTARIO,*
   CANADA KIA 0G1*
CHIERO, J. A.*408 LENOX STREET*OAK PARK,IL*

CHODOS, A. A.*1201 E. CALIFORNIA STREET*
   CALIFORNIA INSTITUTE OF TECHNOLOGY*DIVISION OF GEOL. SCIENCE*
   PASADENA,CA*
CHOPRA, K. S.*P. O. BOX 579*UNION CARBIDE*MINING + METALS DIV.*
   NIAGARA FALLS,NY*
CICCARELLI, M. F.*8 WILDE DRIVE*TROY,NY*
CLANTON, U. S.*2101 NASA RD 1*NASA, JOHNSON SPACE CENTER*SN6*
   HOUSTON,TX*
CLARK, R. R.*10201 WESTHEIMER*DRESSER INDUSTRIES*HOUSTON,TX*
CLAUDE,J.M.*C.O. 140*UNIVERSITE NANCY 1*CHIMIE DU SOLIDE MINERAL*
   54037 NANCY CEDEX,*FRANCE*
CLEAVER, C. G. JR.*253 ST. PHILLIP COURT*FREMONT,CA*
CLINTON, W. C.*P. O. BOX 1125*ROLLA,MO*
CODY, T. E.*842 HAMILTON MALL*APPLIED RESEARCH LABORATORIES*
   ALLENTOWN,PA*
COHEN, A. L.*WASH. STATE UNIV.*ELECTRON MICROSCOPE CENTER*PULLMAN,WA*
COLBY, J. W.*1101 CHESS DR.*KEVEX CORP.*FOSTER CITY,CA*
COLEMAN, J. R. DR.*UNIVERSITY OF ROCHESTER MED. CTR.*
   DEPT OF RAD BIOLOGY + BIOPH*ROCHESTER,NY*
COLEMAN,L.C.*UNIVERSITY OF SASKATCHEWAN*SASKATOON,SASKATCHEWAN,*CANADA
COLMAN, D. M.*630 CLARERIDGE LANE*CENTERVILLE,OH*
COMAFORD, D. J.*9545 WENTWORTH ST.*APPLIED RESEARCH LABS*SUNLAND,CA*
COMMEAU, R. F.*U. S. GOLOGICAL SURVEY*BLDG. 8-QUISSETT CAMPUS*
   WOODS HOLE,MA*
CONLEY, D. K.*410 HILL DRIVE*ALLENTOWN,PA*
CONLIN, B. D.*ROUTE 52*IBM EAST FISHKILL*BLDG. 310 DEPT. 350 ZIP 857*
   HOPEWELL JUNCTION,NY*
CONRAD, G. H.*UNIV. OF NEW MEXICO*DEPT. OF GEOLOGY*ALBUQUERQUE,NM*
COOK, C. F.*FORT MONMOUTH,NJ*
COOPER, J. R.*NELA PARK*GENERAL ELECTRIC*EAST CLEVELAND,OH*
COOPER, T. DR.*611 HANSEN WAY*VARIAN ASSOC.*VACUUM DIV.*PALO ALTO,CA*
CORDOVA, M. H.*10201 WESTHEIMER*DRESSER INDUSTRIES*HOUSTON,TX*
CORLETT,MABEL*QUEENS UNIVERSITY*DEPT. GEOLOGICAL SCIENCES*
   KINGSTON,ONTARIO,*CANADA*
COSSLETT,PROF. V.E.*OLD SCHOOL LANE*UNIVERISTY OF CAMBRIDGE*
   CAVENDISH LAB*CAMBRIDGE,*ENGLAND*
COX,ARTHUR*P.O. BOX 460*HAMILTON,ONTARIO,*CANADA*
CRAIG, R. F.*370 MAPLE STREET*DANVERS,MA*
CRANG, R. E.*BOWLING GREEN STATE UNIV.*DEPT. BIOLOGICAL SCIENCES*
   BOWLING GREEN,OH*
CRAWFORD, C. K.*KIMBALL PHYSICS, INC.*WILTON,NH*
CRAWFORD, M. L.*BRYN MAWR COLLEGE*DEPT. OF GEOLOGY*BRYN MAWR,PA*
CRISS, J. W.*12204 BLAKETON ST.*LARGO,MD*
CRISWELL, P. J.*RTE. 100*FOOTE MINERAL COMPANY*EXTON,PA*
CROUSE, R. S.*851 WEST OUTER DRIVE*OAK RIDGE,TN*
CSONKA,PAL*KISGYAT U.7*2314-HALASZTELEK,*HUNGARY*
CULVER, H. S.*1101 CHESS DR.*KEVEX CORP.*FOSTER CITY,CA*
CUNNINGHAM, R. F. JR.*12841 RANCHWOOD ROAD*SANTA ANA,CA*
CUNNINGHAM, W. C.*3417 TULANE DR. 34*HYATTSVILLE,MD*
CURTIS, R. M.*P. O. BOX 481*SHELL DEVELOPMENT CO.*HOUSTON,TX*
CVIKEVICH, S.*IBM COMPONENTS DIVISION*DEPT 877, BLDG 300-84*
   HOPEWELL JUNCTION,NY*
CYR, J. L.*350 LOWELL ST.*RAYTHEON COMPANY*ANDOVER,MA*

DANKO, A. W.*371 SOUTHCROFT ROAD*SPRINGFIELD,PA*
DAO, J.*3392 INVESTMENT BLVD.*ETEC CORP.*HAYWARD,CA*
DAVIDSON, D. L.*P. O. DRAWER 28510*SAN ANTONIO,TX*
DAVIDSON, E.*P. O. BOX 129*APPLIED RESEARCH LABORATORIES*
   V P GENERAL MANAGER*SUNLAND,CA*

DAVIDSON,M.T.*CENTRO SIMON BOLIVAR*MINISTERIO DE MINES E HIDROCARBUROS
     DIRECCION DE GECLOGIA*CARACUS,*VENEZUELA*
DAVIS, D. P.*3301 ELECTRONICS WAY*ITT SEMICONDUCTORS*
   WEST PALM BEACH,FL*
DAVIS, R. B.*P. O. BOX 1970*RICHLAND,WA*
DAVIS,A.N.*UNIVERSITY RHODE ISLAND*SCHOOL OF OCEANOGRAPHY*
   NARRAGANSETT,RI*
DAYANANDA, M. A.*PURDUE UNIVERSITY*SCHOOL OF MATERIALS SCIENCE*
   LAFAYETTE,IN*
DE BEER, R.*883 HIGHVIEW DRIVE*CHATTANOOGA,TN*
DEAN,BILL L.*3159 EDEN AVE.*CINCINNATI,OH*
DEBRUIJN,WIM C.*RIJNSBURGERWEG 10*LEIDEN,*NETHERLANDS 2333/AA*
DEGROOT, P. B.*P. O. BOX 9077*CORPUS CHRISTI,TX*
DEICHERT, R. W.*P. O. BOX 135*EDAX INTERNATIONAL, INC.*PRAIRIE VIEW,IL
DENEE, P. B.*P. O. BOX 5890*INHALATION TOXICOLOGY RES. INST.*
   ALBUQUERQUE,NM*
DERKSEN, W.*3255-6C SCOTT BLVD.*ISI*SANTA CLARA,CA*
DESBOROUGH, G. A.*2164 ZANG STREET*GOLDEN,CO*
DEWEY, R. D.*9805 CHANNING CIRCLE*RICHMOND,VA*
DI GIACOMO, G.*P. O. BOX 390*IBM SPD DEPT F04*BLOG. 052*
   POUGHKEEPSIE,NY*
DILLON, K. M.*447 E. 18TH AVE. APT.A*COLUMBUS,OH*
DISTEFANO, M.*237 FPB*PHILLIPS PETROLEUM CO.*BARTLESVILLE,OK*
DOAN, A. S. JR.*GODDARD SPACE FLIGHT CENTER*GREENBELT,MD*
DOBROTT, R. D.*1429 LAMP POST LANE*RICHARDSON,TX*
DODD, C. G.*19 WEBSTER ROAD*WARNER-LAMBERT CO.*MILFORD,CT*
DONNELLY, W. O.*265G SOBRANTE WAY*MICROSPEC CORP.*SUNNYVALE,CA*
DOONAN,B.D.*250 NORTH ST.*GENERAL FOOD CORP.*TOXICOLOGY DEPT.*
   WHITE PLAINS,NY*
DOTY, S. B.*630 W. 168TH ST.*COLUMBIA UNIV.*ORTHOPEDIC RESEARCH LAB.*
   NEW YORK,NY*
DOYLE, J. H.*777 CAPTER ROAD*BOULDER,CO*
DRAGEN, R. F.*5916 N. GREEN BAY AVE.*MIDWEST RESEARCH MICROSCOPY, INC.
   MILWAUKEE,WI*
DROWN, H. L.*2019 DENNIS*BENTON,AR*
DUERR, J. S. DR.*230 FORREST ST.*TECHNICAL DIRECTOR*
   STRUCTURE PROBE, INC.*METUCHEN,NJ*
DUNCUMB,PETER*TUBE INVESTMENTS RESEARCH LABS.*HINXTON HALL*CAMBRIDGE,*
   ENGLAND*
DUNDORE, W. C.*105 EATON ROAD*LATROBE,PA*
DURGIN, S. A.*477 HARBOR BLVD.*BELMONT,CA*
DYMEK, R. F.*HARVARD UNIV.*DEPT. OF GEOL. SCIENCES*CAMBRIDGE,MA*

EBY,THOMAS A.*601 N 8 ST.*HAMILTON,OH*
ECHLIN PATRICK*DOWNING STREET*UNIVERSITY OF CAMBRIDGE*
   CAMBRIDGE CB2 3EA,*ENGLAND*
EDIE, J. W.*1418 PINE ST.*IOWA CITY,IA*
EDMOND, J. T.*1141 E. MARKS 303*ALLENTOWN,PA*
EICHEN, E.*THE AMERICAN ROAD*FORD MOTOR CO.*SCIENTIFIC RESEARCH STAFF*
   DEARBORN,MI*
ELLIOTT, N.*LOS ALAMOS SCIENTIFIC LAB.*MS 740*LOS ALAMOS,NM*
EPLEY, D.*P. O. BOX 1389*UNITED SCIENTIFIC CORP.*MOUNTAIN VIEW,CA*
ESHEL,AMRAN*   TEL-AVIV UNIVERSITY*DEPT. OF BOTANY*TEL-AVIV,*
   ISRAEL*
ESTILL, W. B.*P. O. BOX 969*SANDIA LABORATORIES*DIV. 8314*LIVERMORE,CA
ETZ, E.*19200 PLUMMER DRIVE*GERMANTOWN,MD*
EVANS, B. W.*UNIVERSITY OF WASHINGTON*DEPT OF GEOLOGICAL SCIENCES*
   SEATTLE,WA*

317

EVANS, C. A. JR.*1670 S. AMPHLETT BLVD.*CHARLES EVANS + ASSOC.*
   SUITE 120*SAN MATEO,CA*
EVERHART, T. E.*CORNELL UNIV.*COLLEGE OF ENGINEERING*ITHACA,NY*

FALCON, O. L.*IBM*DEPT. 877 BLDG. 300-41C*HOPEWELL JCT.,NY*
FARMELO, D. R.*5225 BIGELOW DRIVE*HILLIARD,OH*
FARMINGHAM, G. O.*THE INTERNATIONAL NICKEL CO., INC.*SUFFERN,NY*
FARR, J. D. DR.*535 KIVA 5*LOS ALAMOS,NM*
FARRAR, R. V.*116 W. 19TH AVE.*OHIO STATE UNIV.*
   METALLARGICAL ENG. DEPT.*COLUMBUS,OH*
FAUST, B. C.*330 S. FOURTH ST.*PERKASIE,PA*
FEELEY, F.*P. O. BOX 641*PRINCETON GAMMA-TECH*PRINCETON,NJ*
FEIN, N.*P. O. BOX 628*QUARTZ PRODUCTS CORP.*PLAINFIELD,NJ*
FELMLEE, W. J.*2144 GEORGETOWN BLVD.*ANN ARBOR,MI*
FERGUSON, J. E.*604 WOODLAND DR.*CLINTON,TN*
FERNALLD, T. H.*54SCHUBERT ST.*BINGHAMTON,NY*
FERNQUIST, R. G.*445 TARA LANE*WEBSTER,NY*
FERRALLI, M. W.*1635 WEST 12TH ST.*LORD CORPORATION*ERIE,PA*
FETCHKO, P. A.*3918 W. 148TH ST.*HAWTHORNE,CA*
FEUERBACHER, D. C.*P. O. BOX 6504*DRESSER INDUSTRIES*HOUSTON,TX*
FICCA, J. F.*P. O. BOX 3536*MICRON, INC.*WILMINGTON,DE*
FICCA, K.*P. O. BOX 3536*MICRON, INC.*WILMINGTON,DE*
FILE, D. M.*P. O. BOX 16*LYONS,IN*
FINKELSTEIN, G. F.*74 WESTERLOE AVE.*ROCHESTER,NY*
FINLAYSON, K. M.*RADIO CORP. OF AMERICA*LANCASTER,PA*
FINN, M. C.*244 WOOD STREET*LINCOLN LABORATORY*LEXINGTON,MA*
FIORE, R.*4606 CAMPBELLS RUN ROAD*VESUVIUS CRUCIBLE RESEARCH*
   PITTSBURGH,PA*
FIORI, C.*NIH*RM. 3W13, BLDG. 13*BETHESDA,MD*
FIRTH,MARK*MCGILL UNIVERSITY*DEPT. METALLURICAL ENGRG.*
   MONTREAL,QUEBEC,*CANADA*
FISHER, T. C.*416 OHIO AVE.*WEST SPRINGFIELD,MA*
FISHER,COLEN*IMAGE ANALYZING COMPUTER CO.*MELBOURN,ROYSTON,HERTS,*
   ENGLAND*
FITZPATRICK, F. A.*P. O. BOX 449*SANTA ANA,CA*
FLAHERTY, F.*GILLETTE PARK*GILLETTE CO.*BOSTON,MA*
FLETCHER, R.*P. O. BOX 3192*UNIVERSITY OF OREGON*EUGENE,OR*
FLOERING,D.*SUNY-STONY BROOK*HEALTH SCIENCES CENTER*DEPT OF PATHOLOGY*
   STONY BROOK,NY*
FLUTIE, R. E.*244 WOOD ST.*MIT-LINCOLN LAB.*LEXINGTON,MA*
FOLLO, P. M.*31 DOGWOOD LANE*NORTHFORD,CT*
FOORD, E. E.*BOX 25046 STOP 905*U.S. GEOLOGICAL SURVEY*
   DENVER FEDERAL CENTER*LAKEWOOD,CO*
FORNOFF, M. M.*WALCUTT DRIVE BOX 212A*BASKING RIDGE,NJ*
FORST, A. J.*2040 ASHLEY RIVER ROAD*CHARLESTON,SC*
FOSTER, M. E.*4800 W. 34TH ST.*HOUSTON,TX*
FRANKEL, R.*1101 CHESS DR.*KEVEX CORP.*FOSTER CITY,CA*
FRASER, A. J.*32 TUBWRECK DR.*DOVER,MA*
FRASER, F. W.*U. S. NAVAL RESEARCH LABORATORY*WASHINGTON,DC*
FRAZER, R. E.*317 SAN JUAN WAY*LA CANADA,CA*
FREEMAN, H. A.*5115 WEST RIVER ROAD*DOW CORNING CORP.*SANFORD,MI*
FREESE, D. D.*3400 BRIDLE PATH ROAD*EASTON,PA*
FRICKE, W.*ALCOA TECHNICAL CENTER*ALCOA CENTER,PA*
FRIEL, J. J.*BETHLEHEM STEEL CORP.*HOMER RES. LAB.*BETHLEHEM,PA*
FRITZSCHE, H.O.H.*4603 MOORE ROAD*MIDDLETOWN,OH*
FUCHS,DR. WOLFGANG*6650 HOMBURG*UNIVERSITY OF SAARLAND*
   II. DEPT. OF PHYSIOL*SAAR,*WEST GERMANY*
FUJINO,NOBUKATSU*1-CHOME NICHINAGASU*SUMITOMO METAL INDUSTRIES,3*
   CENTRAL RESEARCH LABS.*AMAGASKI,*JAPAN*

FUJISHIRO, S.*1640 SPILLAN ROAD*YELLOW SPRINGS,OH*
FULLER, W. E.*BOX 10123*PORTLAND,OR*
FURGASON, R. W.*5481 SO. PACKARD AVE.*CUDAHY,WI*

GALLAGHER, R. A.*12-13 FOX RUN DRIVE*PLAINSBORO,NJ*
GALLE,PROF.*GRUE DE GENERAL SARAIL*UNIVERSITY OF PARIS*
   LABORATOIRE DE BIOPHYSIQUE*94-CRETAIL,*FRANCE*
GAMBA, O.*BOX 79*WESTINGHOUSE ELECTRIC CORP.*BETTIS ATOMIC POWER LAB.*
   WEST MIFFLIN,PA*
GAMBLIN, W. J. JR.*P. O. BOX 135*ETEC CORP.*MIDLAND PARK,NJ*
GANCARZ, A. J.*CALIFORNIA INST. OF TECH.*DIV. OF GEO + PLAN SCI.*
   PASADENA,CA*
GANGULI, A.*3520 W. WESTMOOR BX 10*THE BENDIX CORP.*
   AIRCRAFT BRAKE + STRUT DIV.*SOUTH BEND,IN*
GARRETT, H. L.*2107 SYLVAN LANE*MIDLAND,MI*
GASPARRINI,E.*P.O.BOX 921 STATION K*TORONTO,ONTARIO,*CANADA M4P 2H2*
GAULDIN, R. E.*ROUTE 1 - BOX 45C*LITTLE ROCK,CA*
GAVRILOVIC, J. DR.*2820 S. MICHIGAN AVE*WALTER C. MCCRONE ASSOC., INC.
   CHICAGO,IL*
GECKLE, R.*BOX 3608*AMP, INC. (21-01)*HARRISBURG,PA*
GEOCKE, D.*100 MIDLAND RD.*EG+G ORTEC, INC.*OAK RIDGE,TN*
GEISS, R. H.*5600 COTTLE ROAD*IBM RESEARCH LABORATORY*DEPT. K41/281*
   SAN JOSE,CA*
GELLER, J.*477 RIVERSIDE AVE*JEOL USA, INC.*MEDFORD,MA*
GEORGAKOPOULOS,GEORGE*2057 WESBROOK PLACE*
   UNIVERSITY OF BRITISH COLUMBIA*DEPARTMENT OF GEOLOGY*VANCOUVER B.C.,
   CANADA V6T 1WS*
GEORGE, D. J.*9402 ADELPHI ROAD 203*ADELPHI,MD*
GERBER, R. M.*2680 BARRINGTON AVE.*LOS ANGELES,CA*
GERLACH, R. L.*6509 FLYING CLOUD DR.*PHYSICAL ELECTRONICS INDUSTRIES*
   EDEN PRAIRIE,MN*
GHENT,DR.E.D.*UNIVERSITY OF CALGARY*GEOLOGY DEPARTMENT*
   CALGARY 44,ALBERTA,*CANADA*
GIBBS,WARREN E.*SHERIDAN PARK*INTERNATIONAL NICKEL COMPANY OF CANADA*
   MISSISSAUGA,ONTARIO,*CANADA*
GILES, M. A. M.*P. O. BOX 641*PRINCETON GAMMA TECH.*PRINCETON,NJ*
GILES, P. M.*BETHLEHEM STEEL CORP.*HOMER RESEARCH LABS.*BETHLEHEM,PA*
GILFRICH, J. V.*U. S. NAVAL RESEARCH LAB.*CODE 6481*WASHINGTON,DC*
GILL, M. E.*RIVER ROAD*G.E. CRD*SCHENECTADY,NY*
GILMORE, J. T.*576 STANDARD AVE*CHEVRON RESEARCH CO.*RICHMOND,CA*
GILMORE, P. T.*ELASTOMERS RESEARCH, EXP. STA.*E. I. DU PNT DE NEMOURS*
   WILMINGTON,DE*
GITTER, A. J.*BOX 363, CHURCH ST. STA.*NEW YORK,NY*
GLOVER, E. D.*UNIVERSITY OF WISCONSIN*DEPT. OF GEO. + GEOPHYSICS*
   MADISON,WI*
GOFF, B.*3M CENTER*3M COMPANY*ANALYTICAL SYS BLDG. 209-B*SAINT PAUL,MN
GOLDBERG, C.*P. O. BOX 641*PRINCETON GAMMA TECH.*PRINCETON,NJ*
GOLDSTEIN, J. I.*WHITAKER LAB., LEHIGH UNIV.*DEPT. OF MET. + MAT. SCI.
   BETHLEHEM,PA*
GOLOB, H. R.*BOX 11472*PPG IND., INC.*GLASS RES. CTR.*PITTSBURGH,PA*
GOMES,CELSO BARROS*CAIXA PORTAL 20899*SAO PAULO,*BRAZIL*
GOOLEY, R. C.*UNIVERSITY OF CALIFORNIA*LOS ALAMOS SCI LAB*
   LOS ALAMOS,NM*
GORDON, G. M.*15 STEPHENS WAY*BERKELEY,CA*
GRABBE, P.*CRAWFORDS CORNER RD.*HOLMDEL,NJ*
GRACZYK, J. F.*105 POPLAR AVE.*HACKENSACK,NJ*
GRAY, L. J. DR.*NAVAL UNDERSEA CENTER*CODE 655*SAN DIEGO,CA*
GRAY, R. H.*1620 SPH IM 109 OB*THE UNIV. OF MICH.*ANN ARBOR,MI*
GREEN, D. A.*COLLINS FERRY RD BOX 880*MORGANTOWN,WV*

GREEN, F. H. Y.*944 CHESTNUT RIDGE ROAD*ALOSH*PATHOLOGY SECTION*
   MORGANTOWN,WV*
GREGG, R. Q.*3207 HENRIETTA*BARTLESVILLE,OK*
GREIFE, A. L.*944 CHESTNUT RIDGE ROAD*DHEW/NIOSH/ALOSH*MORGANTOWN,WV*
GRIDLEY, A. L.*RT. 52 - BLDG. 310-57*IBM CORP.*
   E. FISHKILL FAC. DEPT. 218*HOPEWELL JUNCTION,NY*
GRIFFITH, O. K. JR.*P. C. BOX 6411*HUGHES AIRCRAFT CO.*ANAHEIM,CA*
GROSSO, J. S.*BOX 8447*ROCHESTER,NY*
GUILEMANY,DR. J.MA.*C/PORVENIR,11.PORTAL 1*RESIDENCIA LAS FUENTES*
   ESC. DRHA. 3C*MADRID-28,*SPAIN*
GUMZ, K.*MAIDEN LANE*DURHAM,CT*
GUTHRIE, D. C.*13547 FERNHILL*SUGARLAND,TX*

HADIDIACOS, C.*16 FARSTA COURT*ROCKVILLE,MD*
HAGAN, R. C.*2738-B WALNUT*LOS ALAMOS,NM*
HAGGERTY, S. E.*UNIV. OF MASSACHUSETTS*GEOLOGY DEPT.*AMHERST,MA*
HAKKILA, A.*BOX 125*LOS ALAMOS SCIENTIFIC LABORATORY*LOS ALAMOS,NM*
HALL, H. R.*SOUTHERN ILLINOIS UNIV.*DEPT. OF ENG., MECH + MATLS.*
   CARBONDALE,IL*
HALLERMAN, G.*3001 E. COLUMBUS DR.*INLAND STEEL CO.*RESEARCH LAB.*
   EAST CHICAGO,IN*
HALLISSY, R. P.*600 SECOND ST.*YOUNGSTOWN,NY*
HAMILTON, W. J. JR.*9545 WENTWORTH ST.*SUNLAND,CA*
HAMMOND, B. L.*4002 WINFIELD COURT*BOWIE,MD*
HANCHETT, V. E.*5600 COTTLE ROAD*IBM RESEARCH LABORATORY*DEPT. K41/281
   SAN JOSE,CA*
HANKS, S. R.*300 POMPTON ROAD*WILLIAM PATERSON COLLEGE*
   DEPT. OF BIOLOGY*WAYNE,NJ*
HANNA, B.*9545 WENTWORTH ST. BX 129*APPLIED RES. LABS.*SUNLAND,CA*
HARCOURT, J. A.*3503 CHARLESTON ROAD*NORMAN,OK*
HARDY, B.*100 MIDLAND RD.*EG+G ORTEC, INC.*OAK RIDGE,TN*
HARLEY, B. N.*411 CLYDE AVE.*PERKIN-ELMER CORP.*
   SCIENTIFIC INSTRUMENTS DEPT.*MOUNTAIN VIEW,CA*
HARNSBERGER, H. F.*CHEVRON RESEARCH COMPANY*RICHMOND,CA*
HARRIS, A. B.*CATERPILLAR TRACTOR CO.*PEORIA,IL*
HARRIS,DONALD C.*555 BOOTH STREET*MINERAL SCIENCE DIVISION*
   OTTAWA,ONTARIO,*CANADA KLA OG1*
HATFIELD, W. T.*1305 KEYES AVE.*SCHENECTADY,NY*
HAYASHI, S. R.*G. E. CORP. RES. + DEV.*BLD. K-I. RM. 2020*
   SCHENECTADY,NY*
HAYDON, G. B. DR.*19500 SKYLINE BOX 429*LA HONDA,CA*
HEIDEL, R. H.*P. O. BOX 25046*DENVER FEDERAL CENTER*GEOLOGICAL SURVEY*
   DENVER,CO*
HEIDERSBACH, R. H. JR.*UNIVERSITY OF RHODE ISLAND*DEPT. OF OCEAN ENG.*
   KINGSTON,RI*
HEINRICH, K. F.*804 BLOSSOM DRIVE*ROCKVILLE,MD*
HEITUR, I. H.*107 WOODGREEN ROAD*CLAYMONT,DE*
HENOC,J.*7 RUE DES ORCHIDEES*75013 PARIS,*FRANCE*
HENRY, D. K.*P. O. BOX 584*AUSTINVILLE,VA*
HENRY, P.*101 MIDLAND RCAD*ORTEC INC.*MATERIALS ANALYSIS DIVISION*
   OAK RIDGE,TN*
HENRY, R. J.*1539 LCIS LANE*BETHLEHEM,PA*
HESSLER, R. J.*37 BROWNHOUSE ROAD*CAMECA INSTRUMENTS, INC.*
   EXECUTIVE VICE PRESIDENT*STAMFORD,CT*
HEYMAN, R.*P. O. BOX 1212*CAMERON IRON WORKS, INC.*HOUSTON,TX*
HIGGELN,R.J.*4812 WALLBANK AVE.*DOWNERS GROVE,IL*
HILL, K. A.*P. O. BOX 662*CARPENTER TECHNOLOGY CORP.*READING,PA*
HILLIER, D. R.*611 HANSEN WAY, MSG017*VARIAN ASSOCIATES*
   VACUUM DIVISION*PALO ALTO,CA*

HINTHORNE, J. R.*7545 WENTWORTH ST. BX 129*
  APPLIED RES. LAB. METHODS + APPLICATION*S DIV.*SUNLAND,CA*
HINTZ,MICHAEL B.*MATERUAKCEBTRUM*GOTEBORGS UNIVERSITET*
  CHALM≠ERS TEKNISKA HOGSKOLA*402 20 GOTEBORG 5,*SWEDEN*
HITCHINGS, J. R.*RT 100*FOOTE MINERAL CO.*EXTON,PA*
HITT, G. E.*WATKINS AVENUE*APALACHIN,NY*
HLAVA, P. F.*SANDIA LABS.*ORG. 5822*ALBUQUERQUE,NM*
HODGKIN, N. M.*3855 BIRCH ST*MICROGRAPHICS*NEWPORT BEACH,CA*
HODGKIN,M.H.*1676 KAISER AVE.*IRVINE,CA**
HOENKAMP,JOHAN C.*P.O.BOX 38*BILLITON RESEARCH B.V.*
  CITY 6800 LH ARNHEM,*NETHERLANDS*
HOFFMAN, J. R.*715 E. GRAY. ST. BOX 1475*LOUISVILLE,KY*
HOLDSWORTH, E. R.*4457 E. ARAPAHOE ST.*PHOENIX,AZ*
HOLZWARTH, W. J.*STATE UNIV. OF N.Y.*EARTH + SPACE SCI DEPT.*
  STONY BROOK,NY*
HOVLAND, C. T.*6509 FLYING CLOUD DR.*PHY ELECTRONICS IND., INC*
  EDEN PRAIRIE,MN*
HOYT, E. W.*BOX 4349*STANFORD,CA*
HREN, J. J.*UNIV. OF FLORIDA*DEPT. OF MATER SCI. + ENG.*GAINESVILLE,FL
HUGHES, B.*U. S. D. UNIV. PARK*MATERIAL SCIENCE DEPT.*LOS ANGELES,CA*
HULCE, L. A.*SAGINAW ROAD*DOW CORNING CORP.*MICROSCOPY - X-RAY SECTION
  MIDLAND,MI*
HUNT, J.*R D 2, 115 RINGWOOD CT.*ITHACA,NY*
HURLEY, R. G.*FORD MOTOR COMPANY*SCIENTIFIC RESEARCH LAB*DEARBORN,MI*
HUTCHINS, G. A.*BARBER POND ROAD*POWNAL,VT*
HUTCHINSON, W. B.*3047 WOODLAND*LOS ALAMOS,NM*
HYMAN, H. M.*18 GLEN GARY ROAD*MIDDLESEX,NJ*

IACIS,ARVID*2075 WESBROCK PLACE*UNIVERSITY OF BRITISH COLUMBIA*
  DEPARTMENT OF METALLUTGY*VANCOUVER,B.C.,*CANADA V6T 1W5*
IBARRA, S. JR.*3466 BURNETT DR.*MURRYSVILLE,PA*
INGERSOLL, R. M.*56 JASON AVE.*WATERTOWN,CT*
INGRAM, F. D. DR.*1110 COTTONWOOD*IOWA CITY,IA*
INGRAM, M. J.*1110 COTTONWOOD*IOWA CITY,IA*
IOLA, K. K.*P. O. BOX 641*PRINCETON GAMMA TECH.*PRINCETON,NJ*
IUSZOZ, S. J. JR.*SES, INC.*TRALEE IND. PK.*NEWARK,DE*

JACK, B. R.*ALLEGHENY LUDLUM RESEARCH CENTER*BRACKENRIDGE,PA*
JACKSON, M. R.*2208 MISKAYUNA DR.*SCHENECTADY,NY*
JACOBSON,BIRIT*RORSTORPSVAGEN 5*S-61200 FINSPONG,*SWEDEN*
JANNINCK, D. R.*3553 N. NEENAH AVE. 3-A*CHICAGO,IL*
JAROSEWICH, E.*TENTH + CONSTITUTION AVE.*SMITHSONIAN INSTITUTION*
  WASHINGTON,DC*
JASIENKA,STANISTAWA*SENATORSKA 25/63*KRAKOW 30-106,*POLAND*
JEAN,DANIEL G.*2 TAUNTON ST.*PERKIN-ELMER*PHYSICAL ELECTRONICS*
  PLAINSVILLE,MA*
JEITNER, W. J.*MAIL CODE - BLDG., M-101LE*WESTINGHOUSE ELECTRIC CORP.*
  MATERIALS ENGINEERING LAB.*STER,PA*
JENSEN, S. W.*NATIONAL BUREAU OF STANDARDS*BLDG. 220, RM. A123*
  WASHINGTON,DC*
JENSON, E. D.*2108 AUSTIN CT.*RICHLAND,WA*
JERNER, R. C.*3503 CHARLESTON ROAD*NORMAN,OK*
JOHARI, O. DR.*P. O. BOX 66507*CHICAGO,IL*
JOHNSON*UNIVERSITY OF WASHINGTON*SEATTLE.,WA*
JOHNSON, C. E.*9700 S. CASS AVENUE*ARGONNE NATIONAL LAB.*ARGONNE,IL*
JOHNSON, J. W.*1353 CAROLYN DRIVE*ATLANTA,GA*
JOHNSON, P. F.*UNIV. OF FLORIDA*DEPT. OF MATER SCI + ENGG.*
  GAINESVILLE,FL*
JOHNSON, R. D.*12001 HWY. 55*PLYMOUTH,MN*

JOHNSON, T. A.*208 BUCKINGHAM DR.*LYNCHBURG,VA*
JOHNSON, T. L.*1605 WARNOOK DRIVE*RAMONA,CA*
JOHNSON,S.E*10490 WEST LOYOLA DR.*LOS ALTOS,CA*
JONES, R.*2535 SOUTH CHARO AVE.*TOPANGA,CA*
JONES, R.*P. O. BOX 26224*FORT WORTH,TX*
JONGENBURGER PROF. P.*T.H.DELFT*LAB.VOOR METAALKUNDE*
    ROTTENDAMSEWEG 137 DELFT,*NETHERLANDS*
JORDAN, D. E.*RFD 2, BOX 225*LIVERMORE FALLS,ME*
JOY, D. C. DR.*600 MOUNTAIN AVE.*MURRAY HILL,NJ*
JUDD, G. DR.*RENSSELAER POLYTECHNIC INST.*MATERIALS DEPARTMENT*TROY,NY
JUDSON, C. M.*562 EAST MENDOCINO ST.*ALTADENA,CA*
JUSTI, S.*4001 MIRANDA AVE.*PALO ALTO,CA*

KADAVY, D. J.*1635 WEST 12TH ST.*LORD CORPORATION*ERIE,PA*
KANE, J. J. JR.*23 BUNGAY ROAD*MANSFIELD,MA*
KANE, W. T. DR.*CORNING GLASS WORKS*RESEARCH + DEV. LABS.*CORNING,NY*
KANNENGEISER, J. J.*4747 HARRISON AVE.*SUNDSTRAND AVIATION*ROCKFORD,IL
KARTELIAS, T. JR.*901 OAK TREE ROAD*ASARCO, INC.*
    CENTRAL RESEARCH DEPT.*SOUTH PLAINFIELD,NJ*
KASTNER, M.*P. O. BOX 109*UNIV. OF CALIF., SAN DIEGO*
    SCRIPPS INST. OF OCEAN.*LA JOLLA,CA*
KATAYAMA, B.*BATTELLE NORTHWEST LABS.*324 BLDG. T - 12*RICHLAND,WA*
KATZMAN, H. A.*432 S. BARRINGTON*LOS ANGELES,CA*
KEEGAN, W. A. DR.*48 MONROE ROAD*ENFIELD,CT*
KEERY, W. J.*NBS*A-327 BLDG. 225*WASHINGTON,DC*
KEIL, K.*THE UNIVERSITY OF NEW MEXICO*DEPT. OF GEO. + INST. METEOR*
    ALBUQUERQUE,NM*
KEISER, R. L.*1410 N. TENTH ST.*READING,PA*
KENNELLY, P. A.*3392 INVESTMENT BLVD.*ETEC CORP.*HAYWARD,CA*
KINDT, L. R.*14544 ASHTON*DETROIT,MI*
KIRKENDELL, T. D.*BOX 115*CLARKSBURG,MD*
KISS, K.*LIVINGSTONE AVENUE*STAUFFER CHEMICAL CO.*DOBBS FERRY,NY*
KLAINER, A. S. M.D.*MORRISTOWN MEMORIAL HOSPITAL*
    CHAIRMAN, DEPT. MEDICINE*MORRISTOWN,NJ*
KLEIN, C. JR.*1005 E. 10TH ST.*INDIANA UNIVERSITY*DEPT. OF GEOLOGY*
    BLOOMINGTON,IN*
KLIMENTIDIS, R. E.*CENTRAL PARK W. + 80TH ST.*
    MUSEUM OF NATURAL HISTORY*NEW YORK,NY*
KLOSS, J. W.*1635 WEST 12TH ST.*LORD CORPORATION*ERIE,PA*
KNIGHT,JOHN B.*2075 WESBROOK PLACE*UNIVERSITY BRITISH COLUMBIA*
    VANCOUVER,B.C.,*CANADA V6T 1W5*
KNISELEY, R. N.*IOWA STATE UNIVERSITY*AMES LABORATORY USAEC*AMES,IA*
KNOWLES, C. R.*UNIVERSITY OF IDAHO*BUREAU OF MINING + GEOLOGY*
    MOSCOW,ID*
KNUDSON, C.*6511 UNDESTAD STREET*EDEN PRAIRIE,MN*
KOFFMAN, D. M.*8 MADISON AVE., WEST*WINCHESTER,MA*
KOHN, E. DR.*P. O. BOX 30020*MASON + HANGER*DEVELOPMENT DIV.*
    AMARILLO,TX*
KOLB, A.*SAGINAW ROAD*DOW CORNING CORP.*MICROSCOPY - X-RAY SECTION*
    MIDLAND,MI*
KORASTINSKY, R.*WHITARER LAB.*BETHLEHEM,PA*
KOSTIC, A. D.*116 VALLEYVIEW DRIVE*MARS,PA*
KOTECKI, M. L.*3916 - 44TH ST.*ROCK ISLAND,IL*
KOVATS, W. R.*7901 S. CUSTER RD.*MONROE,MI*
KOZAK, R.*540 E. 105TH STREET*GOULD LABORATORIES*CLEVELAND,OH*
KRAJEWSKI, C. S.*20 KING DR.*POUGHKEEPSIE,NY*
KRAUSE, C. R.*67 BROOKWOOD PLACE*DELAWARE,OH*
KROHN, V. E.*9700 SOUTH CASS AVE.*ARGONNE NATIONAL LABORATORY*
    ARGONNE,IL*

KULKARNI, M. V.*WILLIAMS ST.*FISHKILL,NY*
KUNTER, R. S.*7625 W. FIFTH AVE., 100N*HOMESTAKE MINING CO.*
   LAKEWOOD,CO*
KUNZ, F. W.*8961 MORTENVIEW DR.*TAYLOR,MI*
KUPTSIS, J. D.*77-D INDEPENDENCE CT.*YORKTOWN HEIGHTS,NY*
KYSER, D. F.*1258 PAMPAS DRIVE*SAN JOSE,CA*

LAABS, F.*IOWA STATE UNIV.*AMES LABORATORY*AMES,IA*
LAAKSO, C. W.*4080 N. W. 190TH AVENUE*PORTLAND,OR*
LADURON,DOMINIQUE M.*PLACE L. PASTEUR 3*UNIVERSITY DE LOUVAIN*
   LABORATOIRE DE PETROGRAPHI*B-1348 LOUVAIN-LA-NEUVE,*BELGIUM*
LAFORCE, R. W.*103 CLIFFORDALE PARK*ROCHESTER,NY*
LAIRD, J.*UNIV. OF NEW HAMPSHIRE*DEPT. OF EARTH SCIENCES*DURHAM,NH*
LAMANEC, T.*BX 292, CRAWFORD RD., RD3*SCHENECTADY,NY*
LANDIS, F. P.*2177 STORY AVENUE*SCHENECTADY,NY*
LANDRON,CLAUDE*FACULTE DES SCIENCE ET*TECHNIQUES B.P.W.*SFAX,*TUNISIA*
LANDSTROM, D. K.*903 NEIL AVE.*COLUMBUS,OH*
LANGE, W. H.*16356 ORCHARD LANE*FRASER,MI*
LANGE,D.E.*1800 VASSAR NE NO.2*ALBUQUERQUE,NM*
LANGER, A. M.*100TH ST. + 5TH AVE.*MT. SINAI SCHOOL OF MEDICINE*
   ENVIRONMENTAL SCI. LAB.*NEW YORK,NY*
LAPIERRE, C. F.*34 FOREST ST.*TEXAS INSTRUMENTS, INC.*
   MATERIAL TESTING LAB.*ATTLEBORO,MA*
LARSON, R. R.*3144 CASTLELEIGH RD.*SILVER SPRING,MD*
LARSSON,SVEN* FACK*CHALMERS UNIV.OF TECH.*PHYSICS DEPARTMENT*
   S-402 20 GOTHENBURG,*SWEDEN*
LASCH, W. A.*2913 HUNTINGTON ROAD*SHAKER HEIGHTS,OH*
LAUCHLI, A.*UNIV. OF CALIFORNIA*DEPT. OF LAND, AIR + WATER*DAVIS,CA*
LAURIOSEN,JOHN HENRY*.A.INSTITUTE OF TECHNOLOGY*BENTLEY 61-2,*
   WESTERN AUSTRALIA*
LAWLESS, K. R.*THORNTON HALL*UNIV. OF VIRGINIA*DEPT. MATERIALS SCIENCE
   CHARLOTTESVILLE,VA*
LAWRIW, T. C.*123 BIGTREE ST.*LIVONIA,NY*
LAWSON, K. DR.*BENDIX RESEARCH LABS.*DEPT. 850*SOUTHFIELD,MI*
LEBIEDZIK, J.*1359 E. COLLEGE AVE.*STATE COLLEGE,PA*
LECHENE, C. P. DR.*45 SHATTUCK STREET*HARVARD MEDICAL SCHOOL*BOSTON,MA
LEDBETTER, M. C. DR.*BROOKHAVEN NAT. LAB.*BIOLOGY DEPT.*UPTON,NY*
LEDBURY, E. A.*511 STEVENS CT., N.W.*RENTON,WA*
LEE, D. A.*12001 HWY. 55*PLYMOUTH,MN*
LEE, M. W.*3300 RIVER DR.*MOLINE,IL*
LEE, R. J.*4070 SPRUCE RD.*MURRYSVILLE,PA*
LEGRONE, H. B.*14081 RONDEAU ST., APT. 9*WESTMINSTER,CA*
LEISZ, D. M.*P. O. BOX 348*PAINESVILLE,OH*
LEITH,D.A.*3030 BRIDGEWAY*SAUSALITO,CA*
LEITNER, J. W.*8252 ACORN DRIVE*ROSEVILLE,CA*
LENKE, J. W.*211 E. CHICAGO AVE.*AMERICAN DENTAL ASS≠N.*
   RESEARCH INSTITUTE*CHICAGO,IL*
LEROY, A. F.*9000 ROCKVILLE PIKE*NATL. INSTS. OF HEALTH*
   BLDG. 13 RM. 3W13*BETHESDA,MD*
LESHER, D. F.*305 WENZ*KUTZTOWN,PA*
LEVIN, E. R.*RCA LAB*PRINCETON,NJ*
LEWIS, C. D.*703 CURTIS ST.*ARMCO INC.*MIDDLETOWN,OH*
LEWIS,NATHAN*MOUNTAIN VIEW TER.APTS 5-4*LATHAM,NY*
LEYS, J. A.*P. O. BOX 33221*3M COMPANY*CENTRAL RES.*ST. PAUL,MN*
LIBERMAN, M. H.*145 LUNDY LANE*PALO ALTO,CA*
LIFSHIN, E.*GENERAL ELECTRIC*R + D CENTER*SCHENECTADY,NY*
LINDBERG, K.*160 MIDDLESEX TURNPIKE*ADVANCED METALS RESEARCH CORP.*
   BEDFORD,MA*
LINDBERG, R. W.*2204 ORRINGTON AVE.*EVANSTON,IL*

LLOYD, L. E.*7799 SADIE THOMAS RD.*JOHNSTOWN,OH*
LOCKHART, Z. D. JR.*715 E. GRAY ST. BX 1475*LOUISVILLE,KY*
LOH, S. E.*VIRGINIA POLYTECHNIC INST.*DEPT. OF GEO. SCIENCES*
   BLACKSBURG,VA*
LONG, P. E.*4821 CHUKAR DRIVE*WEST RICHLAND,WA*
LORD, A. E. JR.*32ND + CHESTNUT*DREXEL UNIVERSITY*
   DEPT. OF PHY. + ATMOS. SCI.*PHILADELPHIA,PA*
LORD, J. W.*783 FREEPORT ROAD*CREIGHTON,PA*
LOVE,GLYN*UNIVERSITY OF BATH*BATH,AVON,*ENGLAND*
LUBLIN, P.*40 SYLVAN ROAD*GTE LABORATORIES, INC.*
   WALTHAM RESEARCH CENTER*WALTHAM,MA*
LUNDY, D. R.*10142 GOODIN CIRCLE*COLUMBIA,MO*
LUSZCZ, S. J. JR.*20TH + RACE STS.*FRANKLIN INST. RES. LABS.*
   PHILADELPHIA,PA*
LYMAN, C. E.*RPI*MATERIALS ENGINEERING DEPT.*TROY,NY*

MACDONALD, N. C.*6589 FLYING CLOUD DRIVE*
   PHYSICAL ELECTRONICS INDUSTRIES INC.*EDEN PRAIRIE,MN*
MACDONALD, R. C.*1193 REDOAKS DR.*SAN JOSE,CA*
MACQUEEN, H. R.*28 WILWOOD DRIVE*WAPPINGERS FALLS,NY*
MADURA, A. R.*1635 WEST 12TH ST.*LORD CORPORATION*ERIE,PA*
MAGIO, M.*P. O. BOX 4874*G.C.P.O.*SCANNING*NEW YORK,NY*
MAGUIRE, W.*795 N. MOUNTAIN ROAD*ISI. INC.*NEWINGTON,CT*
MAHAR, C. E.*KODAK PARK*B-34*ROCHESTER,NY*
MAKEPEACE,CHARLES E.*2314 ELMIRA DRIVE*OTTAWA,ONTARIO,*CANADA*
MAKOSEY, J. S.*98 LOCUST ST.*IRWIN,PA*
MALICK, L. E.*42ND AND DEWEY AVE.*UNIV. OF NEBRASKA*MEDICAL CENTER*
   OMAHA,NE*
MALIZIE, E. S.*4625 ROYAL AVE.*UNION CARBIDE CORP.*METALS DIV. R + D*
   NIAGARA FALLS,NY*
MANN, M. J.*2625 NORTH VAN DORN 102*ALEXANDRIA,VA*
MANNINO, F. JR.*P. O. BOX 135*EDAX INTER., INC.*PRAIRIE VIEW,IL*
MANSKER, W. L.*UNIVERSITY OF NEW MEXICO*DEPT. OF GEOLOGY*
   ALBUQUERQUE,NM*
MANTZ, R. A.*1719 HIGHLAND ST.*ALLENTOWN,PA*
MANWARING, R.*381 PARK AVE. S.*GERHARD WITZSTROCK PUBL. HOUSE*RM. 1123
   NEW YORK,NY*
MARCINIAK, H. C.*130 SO. GAIN ST.*ANAHEIM,CA*
MARDINLY, A. J.*1545 PINE VALLEY BLVD.*ANN ARBOR,MI*
MARINENKO, R. B.*N B S*RM A121, BLDG. 222*WASHINGTON,DC*
MARSHALL,A.T.*LATROBE UNIVERSITY*ZOOLOGY DEPARTMENT*
   BUNDOORA,VICTORIA,3083,*AUSTRALIA*
MARTIN, E.*P. O. BOX 547*EDAX INTERNATIONAL, INC.*NEW ROCHELLE,NY*
MARTIN, P. W.*281 ANDOVER STREET*DANVERS,MA*
MATHEZ, E. A.*UNIVERSITY OF WASHINGTON*DEPT. OF GEOLOGICAL SCIENCES*
   SEATTLE,WA*
MATRICARDI, V. R.*WASHINGTON,DC*
MATTA, R. K.*13971 RIDGE RD.*N. HUNTINGDON,PA*
MATTERN, D. J.*2671 SOUTHCOURT*PALO ALTO,CA*
MAURICE,M.F.*B.P. 2*CEN-SACLAY*91190 GIF SUR YVETTE,*FRANCE*
MC CALL, J. L.*505 KING AVENUE*COLUMBUS,OH*
MCAFEE, W. S.*6308 W. FAIR DR.*LITTLETON,CO*
MCCAIN, W. S.*ALCO CENTER**   15C   0000
MCCARTHY, J.*2551 WEST BELTLINE HWY.*TRACOR NORTHERN*MIDDLETON,WI*
MCCLURE, D. E.*34 PORTSMOUTH ROAD*PIEDMONT,CA*
MCCONNELL, M. D.*RD 2 - WING ROAD - BX 56*REXFORD,NY*
MCCONNELL, P.*BABCOCK + WILCOX*LYNCHBURG RESEARCH CENTER*LYNCHBURG,VA*
MCCORKLE, G. E.*RT. 1, BOX 154*CHINA GROVE,NC*

MCCOY, C. D.*P. O. BOX 808*LAWRENCE LIVERMORE LABORATORY*L-404*
   LIVERMORE,CA*
MCDONALD, M. L.*7206 TENTH ST.*RIO LINDA,CA*
MCGREEVY, L. M.*4150 CITY AVE.*PHILADELPHIA COLL. OF OSTEOPATHIC MED.*
   ELECTRON MICROSCOPY S. B-42*PHILADELPHIA,PA*
MCGUIRE, G. E.*RT. 1, BOX 115B*GASTON,OR*
MCHENRY, W. D.*ROCK ISLAND ARSENAL*SARRI-ENM*ROCK ISLAND,IL*
MCKEE, T. R.*P. O. BOX 900*MOBIL RES. + DEV. CORP.*FIELD RESEARCH LAB.
   DALLAS,TX*
MCKINLEY, E. L.*BROCKWAY GLASS COMPANY*BROCKWAY,PA*
MCLEAN, J. R.*P. O. BOX 12195*IBM*DEPT. E81/B101*
   RESEARCH TRIANGLE PARK,NC*
MCMILLAN, W. R.*P. O. BOX 3909*EUGENE,OR*
MCNAMARA, L. J.*BOX 11, RD 5*TROY,NY*
MEHTA, S.*LEHIGH UNIVERSITY*DEPT. OF METALUGY*BETHLEHEM,PA*
MEISENHEIMER, R. G.*2093 ESSENAY AVE.*WALNUT CREEK,CA*
MENDONCA,HORACIO A.*TRIONVIRATO 3716*BUENOS AIRES,*ARGENTINA 1427*
MENY,LUCIENNE*BP NO 2 91190*CEN SACLAY*SRMA/O.TECH*GIFSUR YUETTE,*
   FRANCE*
MERCHANT, R. W.*8 MELODY LANE*SCHENECTADY,NY*
MERCIER, P. L.*115 W. CENTURY ROAD*DART INDUSTRIES, INC.*PARAMUS,NJ*
MERGNER, W. J.*22 S. GREEN ST.*SCHOOL OF MEDICINE*DEPT. OF PATHOLOGY*
   BALTIMORE,MD*
MERKLE,A.B.*3303 R. STREET*UNIVERSITY OF NEBRASKA*DEPT. OF GEOLOGY*
   LINCOLN,NE*
MERRIAM, G. R. MD*NATIONAL INSTITUTE OF HEALTH*BLDG. 10, RM. 10809*
   BETHESDA,MD*
MERWARTH, W. R.*IBM CORP.*DEPT. 675*ENDICOTT,NY*
MEYENHOFER*41 BRINEHAM AVE.*RUMSON,NJ*
MEYERS, P. V.*143 YOUNG AVE.*COOPERSBURG,PA*
MICHELS, L. C.*118 FOVER*LOS ALAMOS,NM*
HIGLIONICO, C. J.*2221 GLORIETTA N.E.*ALBUQUERQUE,NM*
MIHALISIN, J. R.*545 MOUNTAIN AVENUE*NORTH CALDWELL,NJ*
MILES, L. R.*2039 FERN ST.*NEW ORLEANS,LA*
MILLER, A. S.*P.O. BOX 835*BABCOCK + WILCOX*ALLIANCE,OH*
MILLER, E. L.*75 CORINTHIAN WALK*LONG BEACH,CA*
MILLER, J. L. JR.*919 GRIFFES STREET*CARY,NC*
MILLER, N. C. DR.*40 SYLVAN ROAD*GTE LABORATORIES*WALTHAM,MA*
MITCHELL, M. J.*NEW MEXICO TECH.*DEPT. OF MATERIALS SCIENCE*SOCORRO,NM
MIZER, O.*ROUTE NO. 1*SAINT LOUIS,MI*
MOLL, S. H. DR.*160 MIDDLESEX TURNPIKE*ADVANCED METALS RESEARCH CORP.*
   BEDFORD,MA*
MONIGOLD, J. R.*12435 SO. JERSEY AVE.*NORWALK,CA*
MONROE, B. L.*237 PLAINVIEW CIRCLE, NO.*LITTLE ROCK,AR*
MOORE,MICHAEL A.*1280 MAIN ST W. RM 3N38*HAMILTON,ONTARIO,*
   CANADA L85 4J9*
MORRILL, J. B.*CORNELL UNIVERSITY*DEPT. OF CHEM.*SARASOTA,NY*
MORRIS, W. G.*P. O. BOX 8*GENERAL ELECTRIC RES. + DEV. CTR.*
   SCHENECTADY,NY*
MORRISON, G. H.*NEW COLLEGE - U.S.F.*DIV. NATURAL SCIENCES*ITHACA,FL*
MOSLEY, C. W.*E. I. DU PONT*SAVANNAH RIVER LAB.*AIKEN,SC*
MOYERS, K. W.*P.O. BOX 1226*BURROUGHS CORP. ECD*PLAINIFIELD,NJ*
MOZDEN, C. A.*1835 DUEBER AVE., S.W.*THE TIMKEN CO.*RES. DEPT.*
   CANTON,OH*
MUCKER, K. F.*BGSU*PHYSICS DEPT.*BOWLING GREEN,OH*
MULHERN, J. E. JR.*UNIV. OF NEW HAMPSHIRE*DEPT. OF PHYSICS*DURHAM,NH*
MULLIGAN,TIMOTHY J.*PACIFIC BIOLOGICAL STATION*NANAIMO,B.C.,*
   CANADA V9R 5K6*

MUNKRES, M. N.*P.O. BOX 20708*UNIV. TEXAS MED. SCHOOL*
   DEPT. NEUROBIOLOGY*HOUSTON,TX*
MURATA,DR. KENJI*UNIV. OSAKA PREFECTURE*DEPT. OF ENGINEERING*
   MOZU,SAKAI,OSAKA 591,*JAPAN*
MUROSAKO, R. P.*Z FORBES ROAD*LEXINGTON,MA*
MURPHY, A. P.*P.O. BOX 39175*PROCTER AND GAMBLE COMPANY*
   MIAMI VALLEY LABS*CINCINNATI,OH*
MURPHY, J. A.*SOUTHERN ILLINOIS UNIVERSITY*ELECTRON MICROSCOPY CTR*
   CARBONDALE,IL*
MURPHY, R. J.*48 DEL BALSO BLVD.*WAPPINGERS FALLS,NY*
MUSTOE, G. E.*W. W. S. C.*GEOLOGY DEPT.*BELLINGHAM,WA*
MUSZAR, K. E. JR.*7820 SCARBOROUGH BLVD*INDIANAPOLIS,IN*
MYERS,ROBERT M.G.*P.O.BOX 149*NAVAN,ONTARIO,*CANADA KOA 2S0*
MYKLEBUST, R. L.*10222 LIBERTY ROAD*FREDERICK,MD*

NARDELLA, W. R.*239 MIDDLE RIVER ROAD*DANBURY,CT*
NASH, S. K.*1420 LOCUST ST., APT. 9-A*PHILADELPHIA,PA*
NATARAJAN,R*HYDERABAD-500258*DEFENCE METALLURGICAL RES.LAB.*
   ANDHRAPRADESH,*INDIA*
NAUMAN, D. A.*2525 SHADELAND AVE.*WESTERN ELECTRIC*INDIANAPOLIS,IN*
NELSON,MITCHELL*1529 CEDAR AVE.*MONTREAL,*CANADA H3G 1A6*
NEWBURY, D. E.*NATIONAL BUREAU OF STANDARDS*RM. A121, BLDG. 222*
   WASHINGTON,DC*
NICKOLSON, J. B.*3392 INVESTMENT BLVD.*P-E ETEC. INC.*HAYWARD,CA*
NIEGISCH, W. D.*54 TUTTLE RD.*WATCHUNG,NJ*
NIELSEN, C. H.*G.S.O., UNIV. OF R.I.*KINGSTON,RI*
NIKKEL, H.*685 N. MILDRED*DEARBORN,MI*
NISHI, J. M.*465 S. WRIGHT ST.*LAKEWOOD,CO*
NOCKOLDS,CLIVE EDMUND*UNIVERSITY OF SYDENY*ELECTRON MICROSCOPE UNIT*
   SYDNEY,N.S.W.,*AUSTRALIA 2006*
NOPANITAYA, W.*UNIV. OF NORTH CAROLINA MED. SCHOOL*
   C. E. M., DEPT. OF PATH.*CHAPEL HILL,NC*
NORDSTROM, V. P.*444 KENMORE AVE.*SCHENECTADY,NY*
NORTH, T.*2551 WEST BELTLINE HGWY.*TRACOR NORTHERN*MIDDLETON,WI*
NORVILLE*981 LOS ALTOS AVE.(HELLO)*LOS ALTOS,CA*
NORVILLE, L. R.*411 CLYDE AVE.*PERKIN-ELMER CORP.*
   SCI. INSTRUMENTS DEPT.*MOUNTAIN VIEW,CA*
NUHFER, E. B.*P. O. BOX 879*MORGANTOWN,WV*
NUNNELLEY, P. R.*2823 E. JOAN D≠ARC*PHOENIX,AZ*

O≠BOYLE, D.*314 SO. CASS AVE. A. 1*WESTMONT,IL*
O≠ROURKE, J. A.*2557 - 45TH STREET*LOS ALAMOS,NM*
OBERMEYER, C. R.*10TH AND CONSTITUTION AVE.*
   THE SMITHSONIAN INSTITUTION*MNH E-425*WASHINGTON,DC*
OGILVIE, R. E.*MASSACHUSETTS INSTITUTE OF TECH.*METALLURGY DEPARTMENT*
   CAMBRIDGE,MA*
OHNENSTETTER,D.*CO.O. 140*UNIVERSITY NANCY*LAB. CHIMIE SOLIDE MINERAL*
   NANCY CEDEX 54037,*FRANCE*
OLSON, C. M.*43 WINSLOW ROAD*NEWARK,DE*
ORDONEZ, J.*41 HAGEN DRIVE*POUGHKEEPSIE,NY*
ORTIGUERA, A. M.*5757 N. GREEN BAY AVE.*MILWAUKEE,WI*
OSTROFSKY, B.*23 RIVER ROAD*NAPERVILLE,IL*

PABST, R. E.*P.O. BOX 4255*BAYTOWN,TX*
PACKWOOD,RODNEY H.*1284 GREYROCK CRESCENT*OTTAWA,ONTARIO,**
PALACIOS*N.CANE 118(1824) LANUS*BUENOS AIRES,*ARGENTINA*
PALIK, E. S.*1899 IVANHCE ROAD*CLEVELAND,OH*
PALMBERG, P. W.*6509 FLYING CLOUD DR.*PHYSICAL ELECTRONICS INDUSTRIES*
   EDEN PRAIRIE,MN*

PANDE, C. S.*BROOKHAVEN NATIONAL LAB*BUILDING 480*UPTON, LI,NY*
PANESSA, B. J.*23 CAMP WOODBINE ROAD*PORT JEFFERSON,NY*
PARKER, M. A.*1852 - 20TH ST. N.W.*ROCHESTER,MN*
PARKES, A. S.*77 MASSACHUSETTS AVE.*M. I. T.*RM. 54-820*CAMBRIDGE,MA*
PAROBEK, L. DR.*911 S. MOUNTAIN ROAD*MONROVIA,CA*
PARRISH, W.*5600 COTTLE RD.*IBM RES. LAB.*DEPT. K 41, BLDG. 281*
   SAN JOSE,CA*
PARRISH, W. B.*1735 NEIL AVE.*OHIO STATE UNIVERSITY*COLUMBUS,OH*
PARSONS, D. F.*150 MOSHER ROAD*DELMAR,NY*
PARSONS, J. H.*BOX 11472*PPG INDUSTRIES INC.*GLASS RESEARCH CENTER*
   PITTSBURGH,PA*
PARTHASARATHY, M. V.*228 PLANT SCIENCE*CORNELL UNIV.*ITHICA,NY*
PAWLEY, J. B.*UNIV. OF WISCONSIN*HVEM FACILITY*MADISON,WI*
PAYNE, I. D.*440 RIVER ROAD*CHATHAM,NJ*
PEARSON, J. E.*4075 - 52ND ST. N.*ST. PETERSBURG,FL*
PERLAKI, F.*3500 DEER CR. RD.*HEWLETT-PACKARD CO.*PALO ALTO,CA*
PESCH, J. A.*1714 - 18TH AVE., N.W.*ROCHESTER,MN*
PETERS, E.*ACORN PARK*A. D. LITTLE*CAMBRIDGE,MA*
PETERS, K. J.*P.O. BOX 1054*NIAGARA FALLS,NY*
PETERSCHMITT,IRENE M.*LABORATOIRE DE CRISTALLOGRAPHIE*
   STRASBOURG,1 URE BLESSIG,*FRANCE 67000*
PETERSON, C. A.*1000 E. NORTHWEST HWY.*C/O UNITED STATES GYPSUM*
   DES PLAINES,IL*
PETERSON, E. A.*2655 35TH ST.*MOLINE,IL*
PETERSON, G. G.*40 GOULD CENTER*C/O GOULD LABS.*ROLLING MEADOWS,IL*
PETROV,VICTOR I.*MOSCOW ST. UNIVERSITY 117234*DEPT. PHYSICS*MOSCOW,*
PHILLIPS, B. F.*10636 YOSEMITE ROAD SO.*BLOOMINGTON,MN*
PICKETT, J. J.*5 MEADOWBROOK ROAD*BEDFORD,MA*
PIERCY,R.C.*SHERIDAN PARK*MISSISSAYGA,ONTARIO,*CANADA L5K 184*
PINARD,PIERRE JEAN-L 2*6,CHEMIN DE CHALIN*EUCULLY-69,*FRANCE*
PLANT,A.G.*601 BOOTH STREET*OTTAWA,ONTARIO,*CANADA*
PLENZLER, R. J.*1700 N. WESTWOOD*TOLEDO,OH*
PLOETZ, K. R.*31 RAMAPO PLACE*RINGWOOD,NJ*
PLOTTS, A. E.*3705 PAXTON ST. (26-50)*HARRISBURG,PA*
PLUMMER, H. K. JR.*1271 BEECHMONT AVE.*DEARBORN,MI*
PLUMMER,H.K.*1271 BEECHMONT DR*DEARBORN,MI*
POLLOCK,G.A.*22332 HAMLIN*CANOGA PARK,CA*
POSTEK, M. T.*LSU*DEPT. OF BOTANY*BATON ROUGE,LA*
POSTMA, F. W. JR.*105 MOWHAWK ROAD*OAK RIDGE,TN*
POTOSKY, J. C.*6602 PICO VISTA ROAD*PICO RIVERA,CA*
POTTER, J. S.*9301 MANCHESTER*KANSAS CITY,MO*
PRATI, J.*P.O. BOX 6971*TELEDYNE CAE TURBINE ENGINES*TOLEDO,OH*
PRESCOTT, H. E. JR.*69 ESTHERWOOD AVE.*DOBBS FERRY,NY*
PRINZ, M.*CENTRAL PK W AT 79TH ST.*AMERICAN MUSEUM OF NATURAL HISTORY*
   DEPT. MINERAL SCIENCES*NEW YORK,NY*
PRITIKIN, W. B.*915 N. MICHIGAN AVE.*DANVILLE,IL*
PRUNIER, A. R. JR.*804 DRAPER ROAD*BLACKSBURG,VA*
PYONG,KIM JAE*140-149 SINDANG-DONG*KOREA ELECTRIC CO.*SEOUL CHUNG-KU,*
   KOREA*

QUAMME,GARY*965 GLENDOWER APT. 533*RICHMOND B.C.,*CANADA V7A 2Y6*
QUINTON, P. M.*UNIVERSITY OF CALIFORNIA (RIVERSIDE)*
   DIV. BIOMEDICAL SCIENCES*RIVERSIDE,CA*
QUIRK, R. F.*286 WARREN ST.*NEEDHAM,MA*

RAMSEY, J. N.*I. B. M.*DEPT. 286, BLDG. 300-97*HOPEWELL JUNCTION,NY*
RANSON, W. A.*UNIV. OF MASS.*DEPT. OF GEOLOGY*AMHERST,MA*
RAO-SAHIB, T. S.*UNIV. OF SOUTHERN CALIFORNIA*
   DEPT. OF MAT. SC. (VHE 602)*LOS ANGELES,CA*

RASBERRY, S. D.*NATIONAL BUREAU OF STANDARDS*A 1132 ADMIN.*
   WASHINGTON,DC*
RATKOWSKI, A. J.*NYS DEPT. OF HEALTH D L R*ALBANY,NY*
RAYMOND, R. JR.*G-6, M.S. 978*UNIV. OF CALIFORNIA*
   LOS ALAMOS SCIENTIFIC LAB.*LOS ALAMOS,NM*
REED, M.*RT. 1 - BOX 10*VENUS,TX*
REED, STEPHEN J.B.*DOWING PLACE*UNIVERISTY OF CAMBRIDGE*
   DEPT. MINERALOGY-PERTROLOGY*COMBRIDGE CB2 3EW,*ENGLAND*
REESE, T. S.*NIH*BLDG. 36 38-24*BETHESDA,MD*
REESE, W. E.*4 ULSTER RCAD*NEW PALTZ,NY*
REFFNER, J. A.*1937 W. MAIN ST.*AMERICAN CYANAMID*STAMFORD,CT*
REID, W. M.*10281 WESTHEIMER*DRESSER INDUSTRIES*HOUSTON,TX*
REITAN, P. H.*4240 RIDGE LEA ROAD*STATE UNIV. OF NY*
   DEPT. GEOL. SCIENCES*BUFFALO,NY*
REMOND,MR.GY*B.R.G.M. LABORTORIRE DE MICROSONDE*   ORLEANS B.P.818*
   FRANCE*
RENTON, J. J.*1424 DOGWOOD AVE.*MORGANTOWN,WV*
RENZEMA, T. S.*3 TOLL LANE*ALBANY,NY*
REUTER, W.*P.O. BOX 218*I.B.M. RESEARCH*YORKTOWN,NY*
RIBBE,P.H.*VIRGINIA POLYTECHNIC INSTITUTE*GEOLOGY DEPT.*BLACKSBERG,VA*
RICE, S. B.*P.O. BOX 121*LINDEN,NJ*
RICHARD, N. A.*505 KING AVENUE*BATTELLE MEMORIAL INSTITUTE*COLUMBUS,OH
RIEFENBERG, D.*BOX 464*ROCKWELL INTERNATIONAL*
   ATOMICS INTERNATIONAL DIV.*GOLDEN,CO*
RIGA, G.*1489 KNOWLTON DR.*SUNNYVALE,CA*
RINALDI,ROMANO*VIA S. EUFENIA 19   MO*UNIVERSITY DI MODENA*
   INSTITUTO DI MENERALOGIA*DENA I-41100,*ITALY*
RING, J. H.*10165 DOGWOOD AVE.*PALM BEACH GARDENS,FL*
RINGO, R.*9700 SOUTH CASS AVE.*ARGONNE NATIONAL LAB.*ARGONNE,IL*
ROBERTSON,C.D.*1067 PALMER AVE.*SCHENECTADY,NY*
ROBINSON, WILLIAM H.*QUEEN ST. WEST*ALGOMA STEEL CORP.*METALS RESEARCH
   SAULT STE. MARIE,*CANADA P6A 5P2*
ROCKWELL, MARIA C.*P.O.BOX 3261 SOUTH*HALIFAZ,NOVA SCOTIA,*CANADA*
RODGERS, J. D.*85 MCKEE DRIVE*PHILIPS ELE. INSTRUMENTS, INC.*MAHWAH,NJ
ROGERS, D. J.*35215 JUNIPER*MENTONE,CA*
ROMANO,MAURICE JEAN*43,BOULEVARD DU 11 NOV.18* VILLEURBANNE 69621,*
   FRANCE*
ROMANS, P. A.*U. S. BUREAU OF MINES*ALBANY,OR*
RONIG,A.D.*980 LOUISIANA BLVD. 110C**000
ROPER, C. R. JR.*LUKENS STEEL CO.*COATESVILLE,PA*
ROSAUER, E. A.*IOWA STATE UNIVERSITY(EM-LAB.)*110 ENGINEERING ANNEX*
   AMES,IA*
ROSENSTIEL,ARNOLD P.*ADRIAAN PAUSTRAAT 34*DEN HAAG,*HOLLAND*
ROSOLOWSKI, C. A.*19 BRIDLE PATH*NEWBURGH,NY*
ROUSSEL,CHRISHAHE*1-RUE MAURICE ARNOUX*MOUTROUGE 92,*FRANCE*
ROWE, A. P.*2632 S. GREEN ROAD*UNIVERSITY HEIGHTS,OH*
ROWE, R. G.*GENERAL ELECTRIC CO.*CORPORATE RESEARCH CENTER*
   SCHENECTADY,NY*
RUCH,MARTA C.*MILLER 2850*BUENOS AIRES,*ARGENTINA 1431*
RUCKLIDGE,JOHN*UNIVERISTY OF TORONTO*DEPARTMENT OF GEOLOGY*TORONTO 5,*
   CANADA*
RUSCICA, R.*3255-6C SCOTT BLVD.*ISI*SANTA CLARA,CA*
RUSS, J.*P.O. BOX 135*EDAX INTERNATIONAL, INC.*PRAIRIE VIEW,IL*
RUTHERFORD, M. J.*BROWN UNIVERSITY*DEPARTMENT OF GEOLOGY*PROVIDENCE,RI
RYAN, J. R.*122 WINDSON DRIVE*IRWIN,PA*

SABATINI, R. L.*BROCKHAVEN NATIONAL LAB.*BLDG. 480*UPTON,NY*
SACHS, I. B.*4402 VALE CIRCLE*MADISON,WI*

SANDERS, S. M. JR.*1220 FERNWOOD CT., S.W.*AIKEN,SC*
SAUBERMANN, A. J.*330 BROOKLINE AVE.*BETH ISRAEL HOSP.*BOSTON,MA*
SAVIERS, R. H.*2101 STACKHOUSE DR.*YARDLEY,PA*
SAWATZKY,ANTON*5 TUPPER*PINAWA,MANITOBA,*CANADA ROE 1LO*
SAWRUK, S.*MOBIL OIL CORP.*RESEARCH DEPARTMENT*PAULSBORO,NJ*
SAWYER, L. C.*86 MORRIS AVENUE*CELANESE RESEARCH COMPANY*EMSA BULLETIN
   SUMMIT,NJ*
SCHAD, R. G.*164 PHYLLIS COURT*YORKTOWN HEIGHTS,NY*
SCHAMBER, F.*2551 WEST BELTLINE HWY.*TRACOR NORTHERN*MIDDLETON,WI*
SCHELL, B. E.*13113 TAMARACK ROAD*SILVER SPRING,MD*
SCHELLIN, E. P.*2001 JEFFERSON DAVIS HWY*
   INTELLECTUAL PROPERTY REPORTS, INC.*SUITE 301*ARLINGTON,VA*
SCHICK, J. D.*KUCHLER DRIVE*LA GRANGEVILLE,NY*
SCHILLING,JURGEN H.*P.O.BOX 395*CSIR-NPRL*PRETORIA,*SOUTH AFRICA 0001*
SCHMUNK, R. E.*1924 AVALON*IDAHO FALLS,ID*
SCHNEIDER, I.*1575 TENAKA PLACE APT. Q3*SUNNYVALE,CA*
SCHRADER,MANFRED*IBM DEUTSCHALAND*DEPT.0348/7032-16*
   SINDELFINGER D7032,*WEST GERMANY*
SCHRAND BILL A.*3159 EDEN AVE.*CINCINNATI,OH*
SCHREIBER, H. JR.*BELL TELEPHONE LABS., ROOM 1-A-35* OOM 1-A-35*
   MURRAY HILL,NJ*
SCHREIBER, T. P.*22918 SUNNYSIDE*ST. CLAIR SHORES,MI*
SCHUBERT, R. D.*16489 CAMELLIA TERR.*LOS GATOS,CA*
SCHULTZ, W. G.*795 N. MOUNTAIN ROAD*
   INTERNATIONAL SCIENTIFIC INSTRUMENTS*NEWINGTON,CT*
SCHURING, C. S.*P.O. BOX 1933*SCOTTSDALE,AZ*
SCHWARTZ, C. D.*247 ROLLING KNOLLS WAY*SOMERVILLE,NJ*
SCOFIELD, N.*402 VIVIAN ST.*HOUGHTON,MI*
SCOTT, M. H.*CLARK EQUIP. CO.*CORPORATE LAB. - MRL*BUCHANAN,MI*
SCRIBNER, L. L. JR.*RT. 5 - BOX 390F*CHARLOTTESVILLE,VA*
SEIBERT, J. M.*1793 WOMACK ROAD*DUNWOODY,GA*
SEIBERT, R.*16419 CRAIGHURST DR.*HOUSTON,TX*
SEISLOVE, D. A.*116 VISTA DEL PARQUE*REDONDO BEACH,CA*
SHAFFER, E. W.*BROCKWAY GLASS CO.*CENTRAL LAB.*BROCKWAY,PA*
SHAFFNER, T. J.*P. O. BOX 5936*TEXAS INSTRUMENTS, INC.*MS 147*
   DALLAS,TX*
SHEEHY, T. P.*PARK AVE. + OAK TREE ROAD*
   AMERICAN SMELTING + REFINING CO.*SOUTH PLAINFIELD,NJ*
SHERBINE, P. G. JR.*716 QUARRY ROAD*HARLEYSVILLE,PA*
SHERRY, W. M.*77 MASS. AVE.*MIT*RM. 13-5134*CAMBRIDGE,MA*
SHERWOOD, R. D. DR.*1 TIMBER TRAIL*SUFFERN,NY*
SHIKASHIO, N.*411 CLYDE AVE.*PERKIN-ELMER CORP.*
   SCIENTIFIC INSTRUMENTS DEPT.*MOUNTAIN VIEW,CA*
SHIMIZU,RYUICHI*SUITA,YAMAOKAMI*OZAKA UNIVERSITY*
   DEPARTMENT APPLIED PHYSICS*OZAKA 565,*JAPAN*
SHINODA,PROF. G.*OSAKA UNIVERSITY*OSAKA 565,*JAPAN*
SHIRAIWA,MR. T.*3,1-CHOME NICHINAGASU   AM*SUMITOMO METAL INDUSTRIES*
   CENTRAL RESEARCH LABS.*AGASKI,*JAPAN*
SHORT, J. M.*XEROX SQUARE, ROOM W-114*XEROX CORP.*RESEARCH LABS.*
   ROCHESTER,NY*
SHORT, M. A.*19275 ELDRIDGE LANE*SOUTHFIELD,MI*
SHOTT, J. E. JR.*P. O. BOX 2038*GULF RESEARCH + DEVELOPMENT CO.*
   PITTSBURGH,PA*
SHULL, V. E.*MICHIGAN STATE UNIV.*DEPT. OF HORTICULTURE*
   EAST LANSING,MI*
SICIGNANO, A.*345 SCARBOROUGH ROAD*BRIARCLIFF MANOR,NY*
SIEGEL, L. A.*1937 WEST MAIN STREET*AMERICAN CYANAMID COMPANY*
   STAMFORD,CT*

SIGURDSSON, H.* NIVERSITY OF RHODE ISLAND*UNIVERSITY OF RHODE ISLAND*
  GRADUATE SCHOOL OF OCEANOGRA*KINGSTON,NY*
SILCOX, J. PROF.*CLARK HALL*CORNELL UNIVERSITY*
  SCH. OF APPLIED + ENGIN. PHY*ITHACA,NY*
SILVA, W. J.*4800 OAK GROVE DR.*M/S 158-205*PASADENA,CA*
SIMCHICK, S. F.*1518 LA CROSSE AVE.*READING,PA*
SIMONS,D.S.*NATIONAL BUREAU STANDARDS*WASHINGTON,US**
SIMPSON, B. E.*11815 E. 62ND PL.*TULSA,OK*
SIPPEL, M. J.*SPRINGRIDGE AR M-27*WHITEHALL,PA*
SMALL, J. A.*NBS*RM. A121, BLDG. 222*WASHINGTON,DC*
SMID, R.*P. O. BOX 79*WESTINGHOUSE/BETTIS ATOMIC POWER*WEST MIFFLIN,PA
SMITH, D. T.*433 N. NW HGWY.*AMERICAN CAN CO.*BARRINGTON,IL*
SMITH, D.G.W.*   E*UNIVERSITY OF ALBERTA*
  DEPT. OF GEOLOGY*DMONTON,ALBERTA,*CANADA*
SMITH, J. V.*UNIVERSITY OF CHICAGO*DEPT OF GEOPHYSICAL SCI*CHICAGO,IL*
SMITH, J. W.*7500 E. PLEASANT VALLEY RD*INDEPENDENCE,OH*
SMITH, K. W.*1428 OTTAWA TRAIL*NILES,MI*
SMITH, N. K. R.*7703 FLCYD CURL DR.*UNIV. OF TEXAS*HEALTH SCIENCE CTR.
  SAN ANTONIO,TX*
SMITH, W. A.*777 N. BLUE PARKWAY*WESTERN ELECTRIC CO.*LEE#S SUMMIT,MO*
SOLBERG, T. N.*2703 MT. VERNON LANE*BLACKSBURG,VA*
SOLOMON, J. L.*2342 CITATION CT.*RESTON,VA*
SOLOMON, J. S.*929 N. HAMPTON ROAD*SPRINGFIELD,OH*
SONLYO, A. P. M.D.*51 N. 39TH ST.*PHILADELPHIA,PA*
SOMMAR, A. F.*16 LONG LANE*MALVERN,PA*
SOMMER, S. E.*UNIVERSITY OF MARYLAND*DEPT. OF GEOLOGY*COLLEGE PARK,MD*
SORENSEN, R. W.*178 SMITH ST.*NORTH ATTLEBORO,MA*
SOROCZAK, M.*TVA*NFDC RM. T-128*MUSCLE SHOALS,AL*
SOROKA, J.*3815 W. CLARENDON*DALLAS,TX*
SPARROW, G.*ANALYTICAL SYSTEMS/3M*BLDG 53-3S 3M CENTER*ST. PAUL,MN*
SPIELBERG, N.*KENT STATE UNIVERSITY*DEPARTMENT OF PHYSICS*KENT,OH*
SPRINGER,GUNTER*PO BOX 900   T*HORNHILL,ONTARIO,*CANADA*
SPURR, A. R.*UNIVERSITY OF CALIFORNIA*DEPT OF VEGETABLE CROPS*DAVIS,CA
STACEY, T. R.*755 SEAMASTER*HOUSTON,TX*
STAIKOFF, L. S.*10900 EUCLID AVE.*CASE WESTERN RESERVE UNIVERSITY*
  CLEVELAND,OH*
STALICA, N. R.*6442 RED FOX COURT*REYNOLDSBURG,OH*
STARKEY, J. P.*134 E. 132ND TERR.*KANSAS CITY,MO*
STATHAM,DR. PETER*HAIFAX ROAD*LINK SYSTEM*HIGH WYCOMBE,BUCKS,*
  ENGLAND HP12 3SE*
STAUB, R. E.*402 S. 36TH ST. BOX 5217*PHOENIX,AZ*
STEEL, E. B.*NATIONAL BUREAU OF STANDARDS*RM. A121, BLDG. 222*
  WASHINGTON,DC*
STEELE, I. M.*5734 S. ELLIS AVE.*CHICAGO,IL*
STEELE, W. J.*P.O. BOX 808*LAWRENCE LIVERMORE LAB.*L426*LIVERMORE,CA*
STEVENS, R. P.*A. P. GREEN REFRACTORIES CO.*MEXICO,MO*
STEVENSON, C. D.*221 W. VANDERBILT DR.*OAK RIDGE,TN*
STEWART, B.*P.O. BOX 1389*UNITED SCIENTIFIC CORP.*
                        C*MOUNTAIN VIEW,CA*
STEWART, J. H. JR.*171 NORTH SENECA RD.*OAK RIDGE,TN*
STOLTZ, D. L.*506 WEDGEWOOD DR.*BLUE SPRINGS,MO*
STONECIPHER, S. A.*P.O. BOX 269*MARATHON OIL CO.*LITTLETON,CO*
STORMS, H. A.*1165 GLENWOOD ST.*LIVERMORE,CA*
STRAUSS, B. M.*P.O. DRAWER 2038*GULF RESEARCH + DEVELOPMENT CO.*
  PITTSBURGH,PA*
STROPE, B.*2800 INDIAN RIPPLE ROAD*DAYTON,OH*
SUBIETA, M. A.*P.O. BOX 1212*HOUSTON,TX*
SULLIVAN, J. P.*188 ENDICOTT ST.*DANVERS,MA*
SULLIVAN, P. A.*848 PEARL STREET*SANTA MONICA,CA*

SUMMERS, S. E.*SPRAGUE ELECTRIC CO.*R+D CENTER*NORTH ADAMS,MA*
SUTKOWSKI, W. J.*W. REDOUBT ROAD*FISHKILL,NY*
SWANSON, D. T. DR.*816 LEXINGTON AVE.*WARREN,PA*
SWAROOP, B.*ARGONNE NATIONAL LAB.*BLDG. 212, RM. G242*ARGONNE,IL*
SWEENEY, G. G.*1310 BEULAH ROAD*WESTINGHOUSE R+D*PITTSBURGH,PA*
SMYT, C. R.*20127 LAUREL HILL WAY*GERMANTOWN,MD*
SZAPLONCZAY,MRS. ARANKA*PO BOX 3511,STATION C   O*
  BELL NORTHERN RESEARCH*TTAWA,ONTARIO.*CANADA K1Y 4H7*
SZAPLONCZAY,THEODOR*845 KINGSMERE AVE.   O*TTAWA 13,ONTARIO,*
  CANADA*

TABOCK, J.*18278 UNIVERSITY PARK DR.*LIVONIA,MI*
TAFT, S.*P.O. BOX 348*DIAMOND SHAMROCK CORP.*PAINESVILLE,OH*
TALLBALLA,MOHAMED*KING ABDUL AIZIZ UNIVERSITY*JEDDAH,*SAUDA ARABIA*
TARPLEY, J. L.*5101 RUSSETT RD.*ROCKVILLE,MD*
TATE, P. H.*PO BOX 8361 BLDG 770/124*UNION CARBIDE CORPORATION*
  SOUTH CHARLESTON,WV*
TAYLOR, C. M. DR.*P. O. BOX 7087*CHARLES M. TAYLOR CO.*STANFORD,CA*
TAYLOR, DR J.M.*CANADIAN CONSERVATION INSTITUTE*
  NATIONAL MUSEUM OF CANADA*OTTAWA,QUEBEC,*CANADA K1AOM8*
TAYLOR, T. N.*1735 NEIL AVE.*THE OHIO STATE UNIV.*DEPT. OF BOTANY*
  COLUMBUS,OH*
TAYLOR,M.E.*11586 HIGHVIEW AVE.*WHEATON,MD*
TENNY, H.*P.O. BOX 999 BATTELLE BLVD*RICHLAND,WA*
TEORSKY, R. K.*ALLEGHENY LUDLUM RESEARCH CENTER*BRACKENRIDGE,PA*
TESKA, T. M.*UNIV. OF ARIZONA*LUNAR LAB.*TUCSON,AZ*
THIELEN, C. J.*S.U.N.Y.*DEPT OF EARTH + SPACE SCI*STONY BROOK,NY*
THOMAS, R. S.*800 BUCHANAN ST.*WESTERN REGIONAL RES. CENTER*
  BERKELEY,CA*
THOME, G. P.*P.O. BOX 2953*MOTOROLA INC.*DISCRETE SEMICONDUCTOR D162*
  PHOENIX,AZ*
THOMPSON, A. W. DR.*UNIV. OF WISCONSIN-MILWAUKEE*DEPT. OF CHEMISTRY*
  MILWAUKEE,WI*
THOMPSON, D. P.*P.O. BOX 641*PRINCETON GAMMA TECH.*PRINCETON,NJ*
THOMPSON, K. F.*UNIV. OF ROCHESTER*BIOPHYSICS DEPT., 8-6833*
  ROCHESTER,NY*
THURSTON, E. L. DR.*TEXAS A + M UNIVERSITY*DEPT. OF BIOLOGY*
  COLLEGE STATION,TX*
TIXIER,DR.*IRSID*ST.GERMAIN EN LASE,*FRANCE 78104*
TONGIER, M. JR.*44 BRANDON RD.*NEWPORT NEWS,VA*
TORMEY, J. M.*UCLA*CTR FOR HLTH SCI DPT OF PHY*LOS ANGELES,CA*
TORREY, C. T.*4467 GARDENIA DR.*PALM BEACH GARDENS,FL*
TOTH,ATTILA L.*ISABELLA U 40.*BUDAPEST,*HUNGARY H 1077*
TOUSIMIS, A. J. DR.*P.O. BOX 2189*TOUSIMIS RESEARCH CORP.*ROCKVILLE,MD
TRABER, W. F.*MONTEREY + COTTLE ROADS*IBM*E40-013*SAN JOSE,CA*
TREGILGAS, J. H.*P.O. BOX 225936 MS-147*DALLAS,TX*
TRL WENDT-SONIS R-D*285 N. 13 ST.*ROGERS,AR*
TRZCIENSKI,WALTER E.*2500 AVE.MARIE GUYARD*ECOLE POLYTECHNIQUE*
  DEPARTMENT GENIE MINERAL*MONTREAL,QUEBEC,*CANADA*
TURNBULL, T. P.*2436 S. LOWELL ST.*SANTA ANA,CA*
TURNER, J. F.*NORTH ST.*ENDICOTT,NY*
TZENG, W. V.*1200 FIRESTONE PKWY.*FIRESTONE TIRE AND RUBBER CO.*
  AKRON,OH*

UTMACHER,RA.,G.*P.O.BOX 1663 MS 541*LOS ALAMOS SCIENTIFIC LAB.*
  LOS ALAMOS,NM*

VALLONE, J.*P.O. BOX 101*ESSO RESEARCH AND ENGINEERING CO.*
  FLORHAM PARK,NJ*

VALLYATHAN, W. N.*UNIV. OF VERMONT*DEPT. OF PATHOLOGY*BURLINGTON,VT*
VAN AMELSVOORT,J.M.M.*6525 GA NIJMEGEN*GEERT GROOTEPLEIN ZUID 24*
   DEPT. SUBMICROSCOPIC MORPH.*NETHERLANDS*
VAN DEMARK, G. D.*P.O. BOX 50*MILLBROOK,NY*
VANNIER, M. W. MD*510 S. KINGS HIGHWAY*MALLINCKRODT INSTITUTE*
   SAINT LOUIS,MO*
VASSAMILLET, L. F.*4400 FIFTH AVENUE*PITTSBURGH,PA*
VENUTI, J. P.*20 OXFORD ST.*CAMBRIDGE,MA*
VEZZALINI,G.M.*VIA S. EUFEMIA 19*UNIVERSITY DI MODENA*
   INSTITUTO DI MINERALOGIA*MODENA,*ITALY I-41100*
VIGNA,GUSTAVO L.*ARENALES 3644 6 #A#*BUENOS AIRES,*ARGENTINA 1425*
VIGNESOULT,MME NICOLE*B.P. NO.2*CEN-SACLAY*SECS/LECI*GIF-SUR-YVETTE,*
   FRANCE 91190*
VILMOS,DR.STEFANIAY I.*FEHERVARI UT 144*BUDAPEST,*HUNGARY H-1116*
VIRTA, R. L.*4708 - 67TH AVE.*HYATTSVILLE,MD*
VOLIN, T. E.*BOX 2358, LAUREL RIDGE*TUXEDO,NY*
VOTAVA, W. E.*BOX 552*ALFRED,NY*

WAGENBLAST, H. W.*1567 OLD ABENS CREEK ROAD*
   MATERIALS CONSULTANTS + LABS, INC.*MONROEVILLE,PA*
WAGMAN, J.*4504 PAMLICO DRIVE*RALEIGH,NC*
WALITSKY, P.*1 WESTINGHOUSE PLAZA*WESTINGHOUSE*DEPT. 82010-5*
   BLOOMFIELD,NJ*
WALKER, D. DR.*20 OXFORD ST.*CAMBRIDGE,MA*
WALKER, E. R.*WEST VIRGINIA UNIVERSITY*ANATOMY DEPT.*MORGANTOWN,WV*
WALKER, M.*37 BROWNHOUSE RD.*CAMECA INSTRUMENTS, INC.*STAMFORD,CT*
WALKER, J. L.*P.O. BOX 8, BLDG. 560*FCRC*FREDERICK,MD*
WALL, C. M.*3600 DUNCANVILLE ROAD*DALLAS,TX*
WALLNER, J. L.*465 LINCOLN AVE. N.W.*HIGHLAND PARK,IL*
WALTER, E. R.*821 SPRING ROAD*CHARLESTON,WV*
WALTER, N. M.*P.O. BOX 16858*THE BOEING VERTOL CO.*PHILADELPHIA,PA*
WARD, C. M.*1627 PINEHURST CT.*LIVERMORE,CA*
WARD, P. C.*WESTINGHOUSE PLAZA*DEPT. 8002.02*BLOOMFIELD,NJ*
WARNER, R. R.*25 SHATTUCK ST.*HARVARD MEDICAL SCHOOL*
   DEPT. OF PHYSIOLOGY*BOSTON,MA*
WARNER,R.W.*VALLECITOS ROAD*PLEASANTON,CA*
WASYLYK, J. S.*AGR P.O. BOX 149*BUTLER,PA*
WEAVER, R. E. F.*304 GREGORY COURT*MONROEVILLE,PA*
WEAVERS, B. A.*HERCULES, INC. RESEARCH CENTER*ANALYTICAL DIV.*
   WILMINGTON,DE*
WEI, S. H. Y.*UNIVERSITY OF IOWA*DEPARTMENT OF PEDODONTICS*
   IOWA CITY,IA*
WEILL, D. F.*UNIV. OF OREGON*DEPT. OF GEOLOGY*EUGENE,OR*
WEISER,WISICHARD,T.*C/O BUNDESANSTALT FUER*ALFRED-BENTZ-HAUS*HANNOVER,
   WEST GERMANY D-300*
WELCH, B. M.*P.O. BOX 12195*IBM*DEPT. E 81*RESEARCH TRIANGLE PARK,NC*
WELLS, O. C.*1324 LELAND DRIVE*YORKTOWN HEIGHTS,NY*
WELTER, L. M.*777 N. PASTORIA AVENUE*COATES + WELTER INSTRUMENT CORP.*
   SUBSIDIARY OF AMER OPT CORP*SUNNYVALE,CA*
WENKHOUSE, D. R.*P.O. BOX 11472*PPG INDUSTRIES, INC.*
   GLASS RESEARCH CENTER*PITTSBURGH,PA*
WERGIN, W. P.*10108 TOWHEE AVE.*ADELPHI,MD*
WERNER,HELMUT W.*PHILLIPS RESEARCH LABS.*EINDHOVEN,*NETHERLAND*
WESTBY, G. R.*641 VIOLET LANE*BATAVIA,IL*
WESTON, N. E. DR.*DUPONT EXPERIMENTAL STATION*
   TEXTILE FIBERS DEPT BLDG 302*WILMINGTON,DE*
WEY, S.*5600 COTTLE ROAD*IBM CORP.*D-348-006*SAN JOSE,CA*
WHATLEY, T. A.*701 S. AVIATION BLVD.*XEROX CORPORATION*MAIL STOP M2-19
   EL SEGUNDO,CA*
WHITE, E. W.*RD 1 - BOX 182*ROSSITER,PA*

WHITE, R. A.*BOX 50408*CITIES SERVICE OIL CO.*EXPLORATION + PROD RES.*
   TULSA,OK*
WHITE, R. G.*3231 WALNUT ST.*L.R.S.M. UNIV. OF PENN.*PHILADELPHIA,PA*
WHITLOCK, R. R.*BOX T*COLLEGE PARK,MD*
WHITNEY, W. P.*SULLIVAN PARK*CORNING GLASS WORKS*CORNING,NY*
WHITTAKER, E. F. JR.*60 EVANDALE ROAD*ROCHESTER,NY*
WIGGINS, L. B.*12201 SUNRISE VALLEY DR.*RESTON,VA*
WILD, T. J.*2604 CROSS COUNTRY ROAD*FAIRBORN,OH*
WILLGALLIS,DR.ALEX.*GUTZMANNSTR.31*BERLIN,*WEST GERMANY*
WILLIAMS, D. B.*LEHIGH UNIVERSITY*DEPT. OF METALLURGY*BETHLEHEM,PA*
WILLIAMS, J. P.*CORNING GLASS WORKS*RESEARCH AND DEVELOPMENT*
   CORNING,NY*
WILLIAMS, M. G. DR.*7703 FLOYD CURL DRIVE*
   UNIV. OF TEXAS HEALTH SCIENCE CTR.*DEPT OF ANATOMY*SAN ANTONIO,TX*
WILLIAMS, T.*CHROMALLOY AMERICAN CORP.*R + T DIVISION*ORANGEBURG,NY*
WILLIAMS,PETER M.*HEYDEN SONS LTD.SPECTRUM HOUSE*HILLVIEW GARDENS*
   LONDON,*ENGLAND NW4 2JQ*
WILSON, D. C.*RT. 1, BOX 150*CHAPEL HILL,NC*
WILSON, J. W.*STERLING FOREST*INTERNATIONAL NICKEL CO.*
   P. D. MERICA RESEARCH LAB.*SUFFERN,NY*
WINCHELL, H.*2161 YALE STATION*YALE UNIV.*DEPT. OF GEOLOGY*
   NEW HAVEN,CT*
WIRSING, A. E.*R D 1*EAST FAIRFIELD,VT*
WISE, W. N.*2776 RIVER ROAD*HAMILTON,OH*
WISNIEWSKI, A. W.*19 WRIGHT ST.*LOWELL,MA*
WITTRY, D. B. DR.*UNIV. PARK*UNIVERSITY OF SOUTHERN CALIFORNIA*
   MATERIALS SCIENCE DEPT.*LOS ANGELES,CA*
WOLF, E. D.*18627 KINZIE STREET*NORTHRIDGE,CA*
WOLF, R. C.*883 LILAC LANE*LOS ALTOS,CA*
WOLFE, G. J.*1234 VENIOC DR.*KNOXVILLE,TN*
WOLFF, U. E.*VALLECITES ROAD*GENERAL ELECTRIC CO.*PLEASANTON,CA*
WOLLAM, J. S.*555 TECHNOLOGY SQ.*CAMBRIDGE,MA*
WOLLENBERG, R. L.*1356 SO. SECOND ST.*LOSHOCTON,OH*
WON,LEE TAE*148-149 SINGANG-DONG*KOREA ELECTRIC CO.*CHUNG-KU*SEOUL,*
   KOREA*
WONSIDLER, D. R.*555 UNION BLVD.*BELL TELEPHONE LABS., INC.*
   ALLENTOWN,PA*
WOODHOUSE, J. B.*UNIVERSITY OF ILLINOIS*MATERIALS RESEARCH LAB.*
   URBANA,IL*
WOODS, J. W.*8 RICHARDS ROAD*THE KEARNS GROUP NORTHHEAST*LYNNFIELD,MA*
WRIGHT, J. R. JR.*2596 BRYDEN ROAD*BEXLEY,OH*
WU, C.*UNIVERSITY OF SOUTHERN CALIFORNIA*DEPT. OF MATERIALS SCIENCE*
   UNIVERSITY PARK,CA*

YAGUNOFF, G. G.*176 WINFIELD ST.*SAN FRANCISCO,CA*
YAKOWITZ, H.*14212 WOODCREST DRIVE*ROCKVILLE,MD*
YANG, N. Y.C.*G.E. VALLECITOS NUCLEAR CENTER*M/C V03*PLEASANTON,CA*
YEN, A. C.*IBM 300/41C*DEPT. 877*HOPEWELL JUNCTION,NY*
YEW, N. C.*3392 INVESTMENT BLVD.*ETEC CORP.*HAYWARD,CA*
YONKO, J. A.*3110 MANOR WAY*PITTSBURGH,PA*

ZELEZNY, W. F.*560 BRYCE*LOS ALAMOS,NM*
ZERCHER, C. R.*882 PEPPERTREE LANE*SANTA CLARA,CA*
ZIMMERMAN, S. D.*CITIES SERVICE CO.*DRAWER 4*CRANBURY,NJ*
ZINGARO, P. W.*22 CLUBWAY*HARTSDALE,NY*
ZINNERMAN, M.*P.O. BOX 4874 G.C.P.O.*SCANNING*NEW YORK,NY*
ZIPP, R. D.*7 S. 600 COUNTY LINE ROAD*HINSDALE,IL*
ZULLIGER, H. DR.*1400 STERLIN RD BOX 1389*UNITED SCIENTIFIC CORP.*
   ANALYTICAL INSTRUMENT DIV.*MOUNTAIN VIEW,CA*

Author Index

Notes

Notes

Notes

Notes